



# City Research Online

## City, University of London Institutional Repository

---

**Citation:** Gami, A. (2016). Experimental and computational analysis for insect inspired flapping wing micro air vehicles. (Unpublished Doctoral thesis, City, University of London)

This is the accepted version of the paper.

This version of the publication may differ from the final published version.

---

**Permanent repository link:** <https://openaccess.city.ac.uk/id/eprint/17454/>

**Link to published version:**

**Copyright:** City Research Online aims to make research outputs of City, University of London available to a wider audience. Copyright and Moral Rights remain with the author(s) and/or copyright holders. URLs from City Research Online may be freely distributed and linked to.

**Reuse:** Copies of full items can be used for personal research or study, educational, or not-for-profit purposes without prior permission or charge. Provided that the authors, title and full bibliographic details are credited, a hyperlink and/or URL is given for the original metadata page and the content is not changed in any way.



CITY UNIVERSITY  
LONDON

Experimental and Computational  
Analysis for  
Insect Inspired Flapping Wing Micro Air Vehicles

*Anish Gami*

Submitted to City University London  
in partial fulfilment for the Degree of  
*Doctor of Philosophy*

School of Mathematics, Computer Science and Engineering  
September 2016

# Contents

|  |           |
|--|-----------|
| <b>Contents</b>  | <b>1</b>  |
| <b>List of Tables</b>                                      | <b>5</b>  |
| <b>List of Figures</b>                                     | <b>7</b>  |
| <b>Acknowledgement</b>                                     | <b>29</b> |
| <b>Declaration</b>   | <b>30</b> |
| <b>Abstract</b>  | <b>31</b> |
| <b>Nomenclature</b>  | <b>34</b> |
| <b>Abbreviations</b>                                       | <b>40</b> |
| <b>1 Introduction</b>                                      | <b>44</b> |
| 1.1 Motivation . . . . .                                   | 44        |
| 1.2 Nature and Insects . . . . .                           | 46        |
| 1.3 Insect Thorax Structure and Flapping Muscles . . . . . | 53        |

|          |   |            |
|----------|---|------------|
| 1.4      | MAV Applications . . . . .  | 55         |
| 1.5      | Various Types of MAVs . . . . .   | 58         |
| 1.5.1    | Fixed Wing Aircraft and MAVs . . . . .  | 58         |
| 1.5.2    | Rotary Wing Aircraft and MAVs . . . . .                                       | 63         |
| 1.5.3    | Flapping Wing Aircraft and MAVs . . . . .                                     | 67         |
| <b>2</b> | <b>Review of Literature and Background</b>                                    | <b>80</b>  |
| 2.1      | Insect Wing Motion . . . . .  | 80         |
| 2.2      | Large Experimental Flapping Rigs . . . . .                                    | 86         |
| 2.3      | Ornithopter to MAV Scale Flapping Rigs and Models . . . . .                   | 104        |
| 2.4      | Further Review of Aerodynamics . . . . .                                      | 126        |
| 2.4.1    | Wagner Effect . . . . .   | 128        |
| 2.4.2    | Added Mass Effect . . . . .   | 129        |
| 2.4.3    | Kramer Effect . . . . .   | 129        |
| 2.4.4    | An Additional Review of LEV, TEV, Wake Capture, Clap & Fling and TV . . . . . | 130        |
| <b>3</b> | <b>FWMAV Design and Analysis</b>  | <b>146</b> |
| 3.1      | Traditional FWMAV Design . . . . .  | 147        |
| 3.2      | Model I: Design Exploration . . . . .   | 151        |
| 3.2.1    | Gears and Gearbox . . . . .   | 158        |
| 3.3      | Model II: Design Exploration . . . . .  | 161        |
| 3.4      | Flapping Wing Model Linkage Comparison . . . . .                              | 166        |
| 3.5      | Kinematic Modelling . . . . .   | 174        |

|          |  |            |
|----------|--|------------|
| 3.5.1    | Linkage Movement . . . . .   | 175        |
| 3.5.2    | Kinematic Results . . . . .  | 180        |
| 3.6      | Wing Morphology and Experimental Wings . . . . .                             | 182        |
| 3.6.1    | Wing Morphology . . . . .  | 182        |
| 3.6.2    | Experimental Wings . . . . .   | 186        |
| 3.7      | Measurements for Both MAV Models . . . . .                                   | 188        |
| <b>4</b> | <b>Experimental Methodology</b>  | <b>206</b> |
| 4.1      | Experimental Equipment and Arrangement . . . . .                             | 206        |
| 4.2      | Force Measurement System . . . . .   | 233        |
| 4.3      | Experiments Performed with Analysis . . . . .                                | 240        |
| 4.4      | Wing Kinematics Measurement . . . . .  | 260        |
| <b>5</b> | <b>Simulation Results</b>  | <b>280</b> |
| 5.1      | Wing Kinematics, Non-Dimensional Parameters & Further Aerodynamics . . . . . | 283        |
| 5.1.1    | Wing Kinematics . . . . .  | 283        |
| 5.1.2    | Non-Dimensional Parameters . . . . .   | 290        |
| 5.1.3    | Further CFD Review Related to Flapping Wings . . . . .                       | 292        |
| 5.2      | Cases Simulated . . . . .  | 304        |
| 5.2.1    | Drosophila . . . . .   | 304        |
| 5.2.2    | Rectangular Wing . . . . .   | 314        |
| 5.2.3    | Flapping Experimental Wing . . . . .   | 360        |

|          |  |            |
|----------|--|------------|
| <b>6</b> | <b>Experimental Results</b>  | <b>367</b> |
| 6.1      | Force & Moment Measurements for Model 1 (Sym Only) . . . . .                 | 369        |
| 6.1.1    | Flapping Only for 47 mm Wings (WT3) . . . . .                                | 369        |
| 6.1.2    | Wing Motion Analysis for Model 1 . . . . .                                   | 376        |
| 6.1.3    | Flapping Only for 60 mm Wings (WT4) . . . . .                                | 385        |
| 6.1.4    | Flapping & Rotation for 60 mm Wings (WT4) . . . . .                          | 393        |
| 6.1.5    | Flapping & Rotation with Asymmetric Pitching for 60 mm Wings (WT4) . . . . . | 410        |
| 6.2      | Force & Moment Measurements for Model 2 (Sym & Asym) . . . . .               | 421        |
| 6.2.1    | Wing Motion Analysis for Model 2 (Sym & Asym) . . . . .                      | 421        |
| 6.2.2    | Flapping Only for 60 mm Wings (WT4) . . . . .                                | 428        |
| 6.2.3    | Flapping and Rotation for 60 mm Wings (WT4) . . . . .                        | 431        |
| <b>7</b> | <b>Conclusion and Recommendations</b>  | <b>440</b> |
| 7.1      | Conclusion . . . . .   | 440        |
| 7.2      | Recommendations . . . . .  | 448        |
|          | <b>Bibliography</b>  | <b>451</b> |
| <b>A</b> | <b>Experimental Images and Arrangements</b>                                  | <b>461</b> |
| <b>B</b> | <b>Further Experimental Results</b>  | <b>464</b> |
| <b>C</b> | <b>Further CFD Results and Grids etc.</b>                                    | <b>469</b> |
| <b>D</b> | <b>FWMAV Models I and II extras</b>  | <b>480</b> |

# List of Tables

|     |   |     |
|-----|---|-----|
| 1.1 | <i>Insect Data for Various Species (Azuma 2006)</i>   | 52  |
| 1.2 | <i>Flapping Wing Aircraft and MAVs</i>  | 79  |
| 3.1 | <i>Specifications For Traditional Style MAVs shown in Figures 3.1 and 3.2</i>                     | 151 |
| 3.2 | <i>Stroke Angles &amp; Percentage Differences</i>   | 173 |
| 3.3 | <i>Specifications For Wings shown in Figure 3.18</i>  | 187 |
| 3.4 | <i>Statistical Power Data for Model 1 Mechanism Only</i>  | 195 |
| 3.5 | <i>Statistical Power Data for Model 1 with 52 mm Carbon Fibre Bars</i>                            | 204 |
| 3.6 | <i>Summary of Flapping Models</i>   | 205 |
| 3.7 | <i>Summary of Wings Utilised</i>  | 205 |
| 4.1 | <i>Names of The Equipment Shown in Figures 4.1 and 4.2</i>  | 210 |
| 4.2 | <i>Arri Light Illuminance Data</i>  | 213 |
| 4.3 | <i>Materials Used in The 0 degree Inclination Experimental Setup Shown in Figures 4.4 and 4.5</i> | 218 |
| 5.1 | <i>Insect Data for Hovering Flight Mode (Liu et al. 2009)</i>                                     | 300 |
| 5.2 | <i>Grid Density for Drosophila Wing</i>   | 307 |

|     |  |     |
|-----|--|-----|
| 5.3 | <i>Rectangular Wing Specifications</i> . . . . .   | 317 |
| 5.4 | <i>Simulations Performed for a Rectangular Wing Moving in a Horizontal Plane</i> . . . . . | 317 |
| 5.5 | <i>Grid Density for 60 mm Experimental Wing (WT4)</i> . . . . .                            | 360 |
| 6.1 | <i>Experiments Performed with Both Models</i> . . . . .                                    | 368 |
| 6.2 | <i>Flapping Cases for 60 mm Wings (WT4)</i> . . . . .                                      | 386 |
| 6.3 | <i>Flapping and Rotation Cases at 0 Degree Inclination for 60 mm Wings (WT4)</i> . . . . . | 393 |
| 6.4 | <i>Flapping and Rotation with AP Cases for 60 mm Wings (WT4)</i> . . . . .                 | 411 |

# List of Figures

|      |   |    |
|------|---|----|
| 1.1  | <i>Bee Alighting Sequence Side View Whilst Carrying Pollen (Goodman 2003)</i> . . . . .   | 49 |
| 1.2  | <i>Bee Alighting Sequence Front View (Goodman 2003)</i> . . . . .   | 49 |
| 1.3  | <i>Insect Flight Muscles; A: Direct and Indirect Dorsoventral Muscles, B: Indirect Dorsoventral and Longitudinal Muscles. Dark Muscles are Contracted, Light Muscles are Relaxed and Stretched, Dark Arrows are The Direction of Wing Movement and Light Arrows are The Direction of The Notum (Goodman 2003)</i> . . . . . | 54 |
| 1.4  | <i>Pointer FQM-151A (AeroVironment Inc A)</i> . . . . .   | 58 |
| 1.5  | <i>Black Widow (AeroVironment Inc B)</i> . . . . .  | 59 |
| 1.6  | <i>Wasp III (Designation Systems)</i> . . . . .   | 59 |
| 1.7  | <i>Wasp AE (AV media gallery)</i> . . . . .   | 60 |
| 1.8  | <i>Gust Resistant MAV (Galinski et al. 2010)</i> . . . . .  | 61 |
| 1.9  | <i>Carbon Butterfly (Plantraco A)</i> . . . . .   | 61 |
| 1.10 | <i>Micro MAV Chevron (Plantraco B)</i> . . . . .  | 62 |
| 1.11 | <i>MAV-07 (Prox Dynamics A)</i> . . . . .   | 63 |
| 1.12 | <i>Picoflyer (Prox Dynamics A)</i> . . . . .  | 64 |
| 1.13 | <i>1 Gram Helicopter (Prox Dynamics A)</i> . . . . .  | 64 |

|      |  |    |
|------|--|----|
| 1.14 | <i>Skybotix Autonomous UAV Micro Helicopter Drone (Skybotix Helicopter Robot Shop B)</i> . . . .   | 65 |
| 1.15 | <i>Xtreme 2.0 Gen II Quadcopter (Xtreme Quadcopter Robot Shop)</i> . . . . .   | 66 |
| 1.16 | <i>One Gram Ornithopter (Prox Dynamics B)</i> . . . . .  | 67 |
| 1.17 | <i>Micromechanical Flying Insect (Steltz et al. 2007)</i> . . . . .  | 68 |
| 1.18 | <i>Microrobotic Fly - RoboBee (Wood 2008a)</i> . . . . .   | 69 |
| 1.19 | <i>i-Fly Vamp (Go Radio Controlled)</i> . . . . .  | 70 |
| 1.20 | <i>Microbat; A: Super Capacitor Powered; B: Battery Powered; C: Battery Powered with R/C Navigation (Pornsin-Sirirak et al. 2001)</i> . . . . .  | 71 |
| 1.21 | <i>Beetle Mimicking Flapper (Nguyen et al. 2009)</i> . . . . .   | 72 |
| 1.22 | <i>Konkuk Ornithopters &amp; MAVs; A: 360 mm Wing Span; B: 280 mm Wing Span; C: 150 mm Wing Span; D: 100 mm Wing Span (Park et al. 2008)</i> . . . . .   | 73 |
| 1.23 | <i>Nano Hummingbird (AeroVironment Inc G)</i> . . . . .  | 74 |
| 1.24 | <i>Delfly I: A &amp; Delfly II: B (Delfly Website B)</i> . . . . .   | 76 |
| 1.25 | <i>Micro Delfly (Delfly Website C)</i> . . . . .   | 76 |
| 1.26 | <i>Hummingbird MAV (Nakata et al. 2011)</i> . . . . .  | 76 |
| 1.27 | <i>Cornell MAV (Richter &amp; Lipson 2011)</i> . . . . .   | 78 |
| 2.1  | <i>Stages of Wing Motion</i> . . . . .   | 81 |
| 2.2  | <i>Wingtip Paths for Various Insects; A: Albatross (Fast Gait), B: Pigeon (Slow Gait), C: Horseshoe Bat (Fast Flight), D: Horseshoe Bat (Slow Gait), E: Blow Fly, F: Locust, G: June Beetle, H: Fruit Fly (Shyy et al. 2013)</i> . . . . . | 82 |
| 2.3  | <i>Bumblebee Flight Mode Alteration (Shyy et al. 2013)</i> . . . . .   | 83 |
| 2.4  | <i>Insect Body Coordinate Frame</i> . . . . .  | 84 |

|      |  |     |
|------|--|-----|
| 2.5  | <i>Insect Wing Coordinate Frame</i> . . . . .  | 85  |
| 2.6  | <i>Robofly Experimental Rig (University of California Berkeley)</i> . . . . .  | 88  |
| 2.7  | <i>Two-Dimensional Wing Path. Black Line: Instantaneous Wing position, Black Dot: Leading Edge, Red Arrow: Instantaneous Force Vectors. (Dickinson et al. 1999)</i> . . . . .                      | 88  |
| 2.8  | <i>PIV Images of Fluid Dynamics for Three Different Wing Rotation Phases (Dickinson et al. 1999)</i>   | 90  |
| 2.9  | <i>Diagram Portraying A Summary of Flow Dynamics, red: counter-clockwise vorticity, blue: clockwise vorticity, lighter shades represent vorticity from the previous stroke (Birch et al. 2003)</i> | 92  |
| 2.10 | <i>Smoke Visualisation via A Hawkmoth Flapping Rig (Van Den Berg et al. 1997)</i> . . . . .  | 93  |
| 2.11 | <i>Sketch of Flow Behaviour (Van Den Berg et al. 1997)</i> . . . . .   | 95  |
| 2.12 | <i>Diagram of Test Setup for a Flapping Wing in a Water Tunnel (Nagai et al. 2008)</i> . . . . .   | 96  |
| 2.13 | <i>Single Wing and Two Wing Fluid Visualisation for Interval of End Upstroke-Start Downstroke (Lehmann et al. 2005)</i> . . . . .  | 99  |
| 2.14 | <i>Overview of Clap-and-Fling Flight Mechanism (Lehmann et al. 2005)</i> . . . . .   | 100 |
| 2.15 | <i>Iso-Surface of Vorticity Magnitude for Flexible Wing (Percin et al. 2011)</i> . . . . .   | 103 |
| 2.16 | <i>U.S. Army Research Lab FWMAV (Hall et al. 2012)</i> . . . . .   | 105 |
| 2.17 | <i>Hummingbird inspired FWMAV (Nakata et al. 2011)</i> . . . . .   | 105 |
| 2.18 | <i>Cybird P1 with Body Attached and Mounted on Sting (left), Crank-Gear Mechanism with Flapping Arms (right) (Hu et al. 2010)</i> . . . . .  | 109 |
| 2.19 | <i>Four-Winged MAV (Bolsman et al. 2009)</i> . . . . .   | 110 |
| 2.20 | <i>Flapper Actuated by LIPCA Version 1 (Syarifuddin et al. 2006)</i> . . . . .   | 112 |
| 2.21 | <i>Flapper Actuated by LIPCA Version 2 (Nguyen et al. 2008)</i> . . . . .  | 113 |
| 2.22 | <i>Flapper Actuated by LIPCA Version 3 with Acrylic Links (Nguyen et al. 2007)</i> . . . . .   | 114 |
| 2.23 | <i>Flapper Actuated by LIPCA Version 4 Complete Acrylic Frame (Nguyen et al. 2009)</i> . . . . .   | 116 |

|      |   |     |
|------|---|-----|
| 2.24 | <i>Flapping Wing MAV with Two Actuators (Anderson 2011a)</i>  | 119 |
| 2.25 | <i>Clap-and-Fling X-Type MAV (Kawamura et al. 2008)</i>   | 121 |
| 2.26 | <i>Harvard RoboBee with A Hybrid Power-Control Actuator (Finio et al. 2009a)</i>  | 123 |
| 2.27 | <i>Harvard RoboBee with Stabilising Dampers (Teoh et al. 2012)</i>  | 125 |
| 2.28 | <i>Re Influence on the Drag Coefficient for a Circular Cylinder (Anderson 1986)</i>   | 126 |
| 2.29 | <i>Flow Around A Circular Cylinder (Anderson 1986)</i>  | 127 |
| 2.30 | <i>Simplified Wake Capture Schematic During Stroke Reversal (Sane 2003)</i>   | 131 |
| 2.31 | <i>Vorticity Images for Both Cases (Birch et al. 2003)</i>  | 141 |
| 3.1  | <i>Single Gear MAV Enclosed in a Bee-Like Body</i>  | 149 |
| 3.2  | <i>Two Gear MAV Enclosed in a Elliptic Body</i>   | 150 |
| 3.3  | <i>Model 1 Shown in a Variety of Views with Maximum Dimensions; A: Front View, B: Side View, C: Top View, D: Back Isometric View, E: Front Isometric View</i>   | 155 |
| 3.4  | <i>Parts from The Model with Their Designated Titles</i>  | 157 |
| 3.5  | <i>Model 2 Shown in a Variety of Views with Maximum Dimensions; A: Front View, B: Side View, C: Top View, D: Back Isometric View, E: Front Isometric View</i>   | 162 |
| 3.6  | <i>Vertical Guide Comparison for Both Models with Plate Connection Diagram; A: Model 1, B: Model 2 Sym Configuration, C: Model 2 Asym Configuration, D: Model 2 Sym Configuration Isometric View, E: Model 2 Asym Configuration Isometric View, F: Model 2 Connection of Vertical Guide Plate</i> | 165 |
| 3.7  | <i>Experimental and CAD Images of the Linkage Mechanism During Downstroke</i>   | 169 |
| 3.8  | <i>Experimental and CAD Images of the Linkage Mechanism During Upstroke</i>   | 170 |
| 3.9  | <i>Experimental and CAD Stroke Angles from Linkage Mechanism</i>  | 171 |

|      |  |     |
|------|--|-----|
| 3.10 | <i>Tolerance Data for CAD Model in Symmetric Configuration</i> . . . . .   | 172 |
| 3.11 | <i>Links and Co-ordinates for Mechanism; Blue Dots: Fixed Pivot Location, Red Dots: Variable Location</i> . . . . .  | 174 |
| 3.12 | <i>Linkage Mechanism in Neutral Position with Angles</i> . . . . .   | 175 |
| 3.13 | <i>Linkage Mechanism Displaced from Neutral Position with Angles</i> . . . . .   | 177 |
| 3.14 | <i>Linkage Mechanism in Three Different Positions; Blue: Neutral Position, Red: Start Downstroke Position, Green: Start Upstroke Position</i> . . . . .  | 181 |
| 3.15 | <i>Angle Input to The System Related to Output Angle</i> . . . . .   | 181 |
| 3.16 | <i>Linkage Mechanism with Angle In and Angle Out</i> . . . . .   | 182 |
| 3.17 | <i>Schematic Illustration of a Generic Wing Planform with Geometrical Details</i> . . . . .  | 184 |
| 3.18 | <i>Experimental and CAD Wings; A: 26 mm SR Wing (WT2), B: CAD of 26 mm SR Wing (WT2), C: 47 mm Wing (WT3), D: CAD of 47 mm Wing (WT3), E: 60 mm Wing (WT4), F: CAD of 60 mm Wing (WT4)</i> . . . . .   | 187 |
| 3.19 | <i>Power and Force Measurements of Mechanism Only; A: Model 1, B: Model 2 (sym), C: Model 2 (asym), D: Model 1, E: Model 2 (sym), F: Model 2 (asym), Coloured Dots in Graphs D,E,F Represent Axes Projections Such As Blue: Frequency Vs Vertical Force, Magenta: Frequency Vs Power, Green: Power Vs Vertical Force</i> . . . . . | 191 |
| 3.20 | <i>Power and Force Measurements of Mechanism Only; A: Model 1, B: Model 2 (sym), C: Model 2 (asym), D: Average Vertical Force Comparison, E: Average Power Comparison, F: Average Power / Average Vertical Force Comparison</i> . . . . .  | 193 |
| 3.21 | <i>Normal Distribution for Power Measurements of Model 1 Mechanism Only; A: 5 Hz, B: 8 Hz and C: 12 Hz</i> . . . . .   | 194 |

|      |   |     |
|------|---|-----|
| 3.22 | <i>Power and Force Measurements of 52 mm Carbon Fibre Bar Flapping; A: Model 1, B: Model 2 (sym), C: Model 2 (asym), D: Model 1, E: Model 2 (sym), F: Model 2 (asym), Coloured Dots in Graphs D,E,F Represent Axes Projections Such as Blue: Frequency Vs Vertical Force, Magenta: Frequency Vs Power, Green: Power Vs Vertical Force</i> | 197 |
| 3.23 | <i>Power and Force Measurements of 52 mm Carbon Fibre Bar Flapping; A: Model 1, B: Model 2 (sym), C: Model 2 (asym), D: Average Vertical Force Comparison, E: Average Power Comparison, F: Average Power / Average Vertical Force Comparison</i>  | 201 |
| 3.24 | <i>CAD Diagrams and Measurements for Model 1 with Carbon Fibre Bars Flapping; A: Front View of Model with Bars, B: Isometric View of Model with Bars, C: Comparison of Experimental Measurements and Theoretical Calculations, D: Power Required to Actuate Carbon Fibre Bars</i>   | 202 |
| 3.25 | <i>Normal Distribution for Power Measurements of Model 1 with 52 mm Carbon Fibre Bars; A: 3 Hz, B: 6 Hz and C: 9 Hz</i>   | 203 |
| 4.1  | <i>Schematic of Tests in Air</i>  | 208 |
| 4.2  | <i>Schematic of Vacuum Chamber Tests</i>  | 209 |
| 4.3  | <i>Vacuum Chamber</i>   | 216 |
| 4.4  | <i>Experimental Setup Top View</i>  | 219 |
| 4.5  | <i>Experimental Setup Side View</i>   | 220 |
| 4.6  | <i>Photograph of 0 Degree Inclination Setup Side View</i>   | 221 |
| 4.7  | <i>Photograph of 0 Degree Inclination Setup Angled View</i>   | 221 |
| 4.8  | <i>Hovering Experimental Setup Top View</i>   | 222 |
| 4.9  | <i>Hovering Experimental Setup Side View</i>  | 223 |
| 4.10 | <i>CAD of 0 Degree Inclination Setup Iso View</i>   | 224 |
| 4.11 | <i>CAD of 90 Degree Inclination Setup Iso View</i>  | 224 |

|      |  |     |
|------|--|-----|
| 4.12 | <i>Photograph of 90 Degree Inclination Setup</i>                   | 225 |
| 4.13 | <i>CAD of 0 Degree Inclination Vacuum Chamber Setup Top View</i>   | 227 |
| 4.14 | <i>CAD of 0 Degree Inclination Vacuum Chamber Setup Side View</i>  | 227 |
| 4.15 | <i>CAD of 90 Degree Inclination Vacuum Chamber Setup Top View</i>  | 228 |
| 4.16 | <i>CAD of 90 Degree Inclination Vacuum Chamber Setup Side View</i> | 228 |
| 4.17 | <i>CAD of 0 Degree Inclination Vacuum Chamber Setup Iso View</i>   | 229 |
| 4.18 | <i>CAD of 90 Degree Inclination Vacuum Chamber Setup Iso View</i>  | 229 |
| 4.19 | <i>Photograph of 0 Degree Inclination Vacuum Chamber Setup</i>     | 230 |
| 4.20 | <i>GUI of Software to Acquire Voltage Measurements</i>             | 231 |
| 4.21 | <i>GUI of Software to Acquire F/T Measurements</i>                 | 231 |
| 4.22 | <i>Signal Produced by Reflective Sensor</i>                        | 232 |
| 4.23 | <i>Photograph of Signal Displayed on Oscilloscope</i>              | 232 |
| 4.24 | <i>F/T Sensor Axes Top View</i>                                    | 235 |
| 4.25 | <i>F/T Sensor Axes Side View</i>                                   | 235 |
| 4.26 | <i>F/T Sensor Axes Iso View</i>                                    | 236 |
| 4.27 | <i>Model at 0 Degree Inclination with Force Axes Front View</i>    | 237 |
| 4.28 | <i>Model at 0 Degree Inclination with Force Axes Side View</i>     | 237 |
| 4.29 | <i>Model at 90 Degree Inclination with Force Axes Top View</i>     | 238 |
| 4.30 | <i>Model at 90 Degree Inclination with Force Axes Side View</i>    | 238 |
| 4.31 | <i>Model at 0 Degree Inclination with Force Axes Iso View</i>      | 239 |
| 4.32 | <i>Model at 90 Degree Inclination with Force Axes Iso View</i>     | 239 |

|      |  |     |
|------|--|-----|
| 4.33 | <i>Photograph of Cracked Mylar During Experiments</i>  | 242 |
| 4.34 | <i>Distances from Transducer Tool Plate</i>  | 243 |
| 4.35 | <i>Flapping Setup at 0 Degree Body Inclination with 60 mm Wings (WT4)</i>                                | 244 |
| 4.36 | <i>Photograph of Flapping Setup at 0 Degree Body Inclination with 60 mm Wings (WT4)</i>                  | 244 |
| 4.37 | <i>Flapping Setup w/Table at 0 Degree Body Inclination with 60 mm Wings (WT4)</i>                        | 245 |
| 4.38 | <i>Photograph of Flapping Setup w/Table at 0 Degree Body Inclination with 60 mm Wings (WT4)</i>          | 245 |
| 4.39 | <i>Flapping Setup w/GE at 0 Degree Body Inclination with 60 mm Wings (WT4)</i>                           | 246 |
| 4.40 | <i>Photograph of Flapping Setup w/GE at 0 Degree Body Inclination with 60 mm Wings (WT4)</i>             | 246 |
| 4.41 | <i>Flapping Setup w/TE wall at 0 Degree Body Inclination with 60 mm Wings (WT4)</i>                      | 247 |
| 4.42 | <i>Photograph of Flapping Setup w/TE wall at 0 Degree Body Inclination with 60 mm Wings (WT4)</i>        | 247 |
| 4.43 | <i>Flapping Setup w/TE wall and GE at 0 Degree Body Inclination with 60 mm Wings (WT4)</i>               | 248 |
| 4.44 | <i>Photograph of Flapping Setup w/TE wall and GE at 0 Degree Body Inclination with 60 mm Wings (WT4)</i> | 248 |
| 4.45 | <i>Flapping Setup w/TE wall 1S at 0 Degree Body Inclination with 60 mm Wings (WT4)</i>                   | 249 |
| 4.46 | <i>Flapping Setup w/TE wall and GE 1S at 0 Degree Body Inclination with 60 mm Wings (WT4)</i>            | 249 |
| 4.47 | <i>FR Setup at 90 Degree Body Inclination with 60 mm Wings (WT4)</i>                                     | 250 |
| 4.48 | <i>FR w/GE Base Setup at 90 Degree Body Inclination with 60 mm Wings (WT4)</i>                           | 250 |
| 4.49 | <i>Photograph of Model 1 at 90 Degree Body Inclination</i>   | 252 |
| 4.50 | <i>Photograph of FR Setup at 90 Degree Body Inclination with 60 mm Wings (WT4)</i>                       | 252 |
| 4.51 | <i>Photograph of FR w/GE Base Setup at 90 Degree Body Inclination with 60 mm Wings (WT4)</i>             | 253 |
| 4.52 | <i>Additional Photographs of FR Setup at 90 Degree Body Inclination with 60 mm Wings (WT4)</i>           | 253 |

|      |  |     |
|------|--|-----|
| 4.53 | <i>Photograph of Model 2 Setup at 90 Degree Body Inclination with 60 mm Wings (WT<sub>4</sub>) . . . .</i>   | 254 |
| 4.54 | <i>Photograph of Model 2 Setup at 90 Degree Body Inclination with 60 mm Wings (WT<sub>4</sub>) with Mirror Reflection View . . . . .</i>   | 254 |
| 4.55 | <i>Vacuum Chamber Setup with Model at 0 Degree Body Inclination with 60 mm Wings (WT<sub>4</sub>)</i>  | 256 |
| 4.56 | <i>Vacuum Chamber Setup with Model at 90 Degree Body Inclination with 60 mm Wings (WT<sub>4</sub>)</i>   | 256 |
| 4.57 | <i>Photograph of Vac Chamber with Model at 0 Degree Body Inclination with 60 mm Wings (WT<sub>4</sub>)</i>   | 257 |
| 4.58 | <i>Photograph of Vac Chamber with Model at 90 Degree Body Inclination with 60 mm Wings (WT<sub>4</sub>) . . . . .</i>  | 257 |
| 4.59 | <i>Photograph of FW Model Flapping (Top) and Vac Chamber with Photography Equipment (Bottom) . . . . .</i>   | 258 |
| 4.60 | <i>CAD of Camera and Light In-Line With Wing . . . . .</i>   | 261 |
| 4.61 | <i>CAD of Camera In-Line With Mirror Above Wing . . . . .</i>  | 261 |
| 4.62 | <i>Wing Angle of Attack for Positive and Negative Halves (Circle Represents Leading Edge) . .</i>  | 262 |
| 4.63 | <i>Wing Motion for 26 mm Semi-Rigid Wings (WT<sub>2</sub>) 50 microns 1.5 mm exposed flexible area, Vertical Stroke Plane, D: Downstroke and U: Upstroke . . . . .</i>   | 263 |
| 4.64 | <i>Wing Motion for 26 mm Semi-Rigid Wings (WT<sub>2</sub>) 50 microns 1.5 mm exposed flexible area Side View, Vertical Stroke Plane, D: Downstroke and U: Upstroke . . . . .</i>   | 264 |
| 4.65 | <i>Wing Kinematic Data for 26 mm Semi-Rigid Wings (WT<sub>2</sub>) 50 microns 1.5 mm exposed flexible area; A:Wing Displacement Plot; B:Wing Velocity Plot; C:Wing Acceleration Plot; D:Flapping Stroke Plot; E:Angle of Attack Plot; F:Deviation Plot . . . . .</i> | 265 |
| 4.66 | <i>Wing Motion for 26 mm Semi-Rigid Wings (WT<sub>2</sub>) 75 microns 2 mm exposed flexible area, Vertical Stroke Plane, D: Downstroke and U: Upstroke . . . . .</i>   | 269 |

|      |  |     |
|------|--|-----|
| 4.67 | <i>Wing Kinematic Data for 26 mm Semi-Rigid Wings (WT2) 75 microns 2 mm exposed flexible area; A:Wing Position Plot; B:Wing Velocity Plot; C:Wing Acceleration Plot; D:Flapping Stroke Plot; E: Angle of Attack Plot . . . . .</i>             | 270 |
| 4.68 | <i>Wing Motion for 26 mm Rigid Wings (WT1) 75 microns 2 mm exposed flexible area, Vertical Stroke Plane, D: Downstroke and U: Upstroke . . . . .</i>   | 271 |
| 4.69 | <i>Wing Motion for 26 mm Rigid Wings (WT1) 75 microns 2 mm exposed flexible area Side View, Vertical Stroke Plane, D: Downstroke and U: Upstroke . . . . .</i>   | 272 |
| 4.70 | <i>Wing Kinematic Data for 26 mm Rigid Wings (WT1) 75 microns 2 mm exposed flexible area; A:Wing Position Plot; B:Wing Velocity Plot; C:Wing Acceleration Plot; D:Flapping Stroke Plot; E:Angle of Attack Plot; F:Deviation Plot . . . . .</i> | 273 |
| 4.71 | <i>Wing Motion for 26 mm Rigid Wings (WT1) 75 microns 3 mm exposed flexible area, Vertical Stroke Plane, D: Downstroke and U: Upstroke . . . . .</i>   | 277 |
| 4.72 | <i>Wing Kinematic Data for 26 mm Rigid Wings (WT1) 75 microns 3 mm exposed flexible area; A:Wing Position Plot; B:Wing Velocity Plot; C:Wing Acceleration Plot; D:Flapping Stroke Plot; E:Angle of Attack Plot; F:Deviation Plot . . . . .</i> | 278 |
| 4.73 | <i>Rigid Wing Deviation Trajectory 75mic 2 mm exposed flexible area; A:Deviation with Tracking Path; B:Deviation with Velocity Path . . . . .</i>  | 279 |
| 4.74 | <i>Wing Movement Comparison for Various Mylar Thickness's and Lengths; A:Flapping Stroke Plot; B:Angle of Attack Plot; C:Deviation Plot; D:Deviation Motion Plot . . . . .</i>   | 279 |
| 5.1  | <i>Wing Kinematics for Instantaneous Position and Velocity . . . . .</i>   | 285 |
| 5.2  | <i>Drosophila with Ring Shaped Vortex and Downwash . . . . .</i>   | 293 |
| 5.3  | <i>Flow Field Around Insect Wings; A: Hawkmoth, B: Drosophila . . . . .</i>  | 295 |
| 5.4  | <i>Computational Domain with a Drosophila Wing . . . . .</i>   | 305 |
| 5.5  | <i>Drosophila Wing Computational Domain with Dimensions . . . . .</i>  | 306 |

|      |  |     |
|------|--|-----|
| 5.6  | <i>Drosophila Wing Kinematics and Measurement Comparison for Various Grid Densities; A: Wing Kinematics, B: Wing Motion (green arrow: flapping, blue arrow: pitching), C: Lift Force Comparison, D: Drag Force Comparison, E: Lift Force Comparison Close-Up . . . . .</i>           | 310 |
| 5.7  | <i>Drosophila Wing Measurement Comparison; A: Lift Force Comparison, B: Drag Force Comparison . . . . .</i>  | 311 |
| 5.8  | <i>Drosophila Wing with Streamlines; A: Inner and Outer Vortex at <math>\tau = 0.25</math>, B: Flow Field Around Wing at <math>\tau = 0.25</math>, C: Full Outer Vortex Travelling from Root to Tip at <math>\tau = 0.25</math> . . .</i>  | 313 |
| 5.9  | <i>Rectangular Wing with Force Axis, Flapping is About <math>F_y</math> &amp; Pitching is About <math>F_z</math> (Moments Are Positive in The Anti-Clockwise Direction About Each Axes) . . . . .</i>  | 316 |
| 5.10 | <i>Wing Pitching Schematic for Rotation Duration (Circle Represents Leading Edge) . . . . .</i>  | 316 |
| 5.11 | <i>Kinematic and Flow Details for the Rectangular Wing; A: Kinematic Plot for Rectangular Wing Simulations, B: Cells Surrounding The Wing, C: Rotational Positions Investigated, D: Flow Around The Wing for case 11 at <math>\tau = 0.045</math>. Velocity Units: m/s . . . . .</i> | 318 |
| 5.12 | <i>Rectangular Wing Motion Through a Stroke (green arrow: flapping, blue arrow: pitching) . .</i>  | 319 |
| 5.13 | <i>Flow Around The Rectangular Wing with Rotation Position D and Duration of 1.1s, Early Downstroke . . . . .</i>  | 320 |
| 5.14 | <i>Lift Force Comparison; A: Rotation Position D, B: Rotation Position D (average), C: Rotation Position C, D: Rotation Position C (average), E: Rotation Position B, F: Rotation Position B (average) . . . . .</i>   | 324 |
| 5.15 | <i>Lift Force Comparison; A: Rotation Position A, B: Rotation Position A (average), C: Rotation Duration 3.3s, D: Rotation Duration 3.3s (average), E: Rotation Duration 2.2s, F: Rotation Duration 2.2s (average) . . . . .</i>   | 325 |
| 5.16 | <i>Lift Force Comparison; A: Rotation Duration 1.1s, B: Rotation Duration 1.1s (average), C: Leading Edge Mid-Chord Positions, D: Leading Edge Mid-Chord Positions (average), E: Average Lift For All Cases (Legend Represents Lift Force) . . . . .</i>                             | 326 |

|      |   |     |
|------|---|-----|
| 5.17 | <i>Rectangular Wing Motion for Cases 1-3; A: Case 1, B: Case 1 with Pressure on Wing Surfaces, C: Case 2, D: Case 2 with Pressure on Wing Surfaces, E: Case 3, F: Case 3 with Pressure on Wing Surfaces . . . . .</i>   | 327 |
| 5.18 | <i>Horizontal Force Comparison; A: Rotation Position D, B: Rotation Position D (average), C: Rotation Position C, D: Rotation Position C (average), E: Rotation Position B, F: Rotation Position B (average) . . . . .</i>  | 332 |
| 5.19 | <i>Horizontal Force Comparison; A: Rotation Position A, B: Rotation Position A (average), C: Rotation Duration 3.3s, D: Rotation Duration 3.3s (average), E: Rotation Duration 2.2s, F: Rotation Duration 2.2s (average) . . . . .</i>  | 333 |
| 5.20 | <i>Horizontal Force Comparison; A: Rotation Duration 1.1s, B: Rotation Duration 1.1s (average), C: Leading Edge Mid-Chord Positions, D: Leading Edge Mid-Chord Positions (average), E: Average Thrust For All Cases (Legend Represents Thrust Force) . . . . .</i>  | 334 |
| 5.21 | <i>Pressure Contours of Flow Around Rectangular Wing at Mid-Span (Case 2); A: During Downstroke <math>\tau = 0.161</math>, B: During Downstroke <math>\tau = 0.219</math>, C: During Downstroke <math>\tau = 0.277</math>, D: During Downstroke <math>\tau = 0.335</math>, E: During Downstroke <math>\tau = 0.393</math>, F: During Downstroke <math>\tau = 0.451</math>. Pressure Units: Pa . . . . .</i> | 335 |
| 5.22 | <i>Velocity Vectors of Flow Around Rectangular Wing at Mid-Span (Case 2); A: During Downstroke <math>\tau = 0.161</math>, B: During Downstroke <math>\tau = 0.219</math>, C: During Downstroke <math>\tau = 0.277</math>, D: During Downstroke <math>\tau = 0.335</math>, E: During Downstroke <math>\tau = 0.393</math>, F: During Downstroke <math>\tau = 0.451</math>. Velocity Units: m/s . . . . .</i> | 336 |
| 5.23 | <i>Pitching Moment Comparison; A: Rotation Position D, B: Rotation Position D (average), C: Rotation Position C, D: Rotation Position C (average), E: Rotation Position B, F: Rotation Position B (average) . . . . .</i>   | 340 |
| 5.24 | <i>Pitching Moment Comparison; A: Rotation Position A, B: Rotation Position A (average), C: Rotation Duration 3.3s, D: Rotation Duration 3.3s (average), E: Rotation Duration 2.2s, F: Rotation Duration 2.2s (average) . . . . .</i>   | 341 |

|      |   |     |
|------|---|-----|
| 5.25 | <i>Pitching Moment Comparison; A: Rotation Duration 1.1s, B: Rotation Duration 1.1s (average), C: Leading Edge Mid-Chord Positions, D: Leading Edge Mid-Chord Positions (average), E: Average Pitching Moment For All Cases (Legend Represents Pitching Moment)</i> . . . . .   | 342 |
| 5.26 | <i>Rectangular Wing in Downstroke Motion with Rotation about Mid-Chord and Leading Edge for <math>\chi = 2.2s</math>; A: Pressure on Wing with Mid-Chord Rotation View 1, B: Pressure on Wing with Mid-Chord Rotation View 2, C: Wing Motion with Mid-Chord Rotation, D: Pressure on Wing with Leading Edge Rotation View 1, E: Pressure on Wing with Leading Edge Rotation View 2. Pressure Units: Pa</i> . . . . .  | 343 |
| 5.27 | <i>Rectangular Wing in Downstroke Motion with Rotation about the Leading Edge; A: Pressure Contour of Flow Around Wing Tip with Rotation Duration as <math>\zeta = 3.3s</math> at <math>\tau = 0.125</math>, B: Pressure Contour of Flow Around Wing Tip with Rotation Duration as <math>\zeta = 2.2s</math> at <math>\tau = 0.125</math>, C: Pressure Contour of Flow Around Wing Tip with Rotation Duration as <math>\zeta = 1.1s</math> at <math>\tau = 0.125</math>, D: Velocity Magnitude Contour and Vectors through the Mid-Span at <math>\tau = 0.219</math>. Pressure Units: Pa, Velocity Units: m/s</i> . . . . . | 344 |
| 5.28 | <i>Aerodynamic Power Comparison; A: Rotation Position D, B: Rotation Position D (average), C: Rotation Position C, D: Rotation Position C (average), E: Rotation Position B, F: Rotation position B (average)</i> . . . . .   | 349 |
| 5.29 | <i>Aerodynamic Power Comparison; A: Rotation Position A, B: Rotation Position A (average), C: Rotation Duration 3.3s, D: Rotation Duration 3.3s (average), E: Rotation Duration 2.2s, F: Rotation Duration 2.2s (average)</i> . . . . .   | 350 |
| 5.30 | <i>Aerodynamic Power Comparison; A: Rotation Duration 1.1s, B: Rotation Duration 1.1s (average), C: Leading Edge Mid-Chord Positions, D: Leading Edge Mid-Chord Positions (average), E: Average Aerodynamic Power For All Cases (Legend Represents Aerodynamic Power)</i> . . .   | 351 |
| 5.31 | <i>Rectangular Wing with Rotation About the Leading Edge Cases 1-3 at <math>\tau = 0.125</math>; A: Streamlines &amp; Pressure Contour on Wing Surface for <math>\zeta = 3.3s</math>, B: Streamlines &amp; Pressure Contour on Wing Surface for <math>\zeta = 2.2s</math>, C: Streamlines &amp; Pressure Contour on Wing Surface for <math>\zeta = 1.1s</math>. Pressure Units: Pa</i> . . . . .  | 352 |

|      |  |     |
|------|--|-----|
| 5.32 | <i>Rectangular Wing with Rotation About the Leading Edge Cases 1-3 at <math>\tau = 0.125</math>; A: Streamlines with Velocity Magnitude for <math>\zeta = 3.3s</math>, B: Flow Field Around the Wing for <math>\zeta = 1.1s</math>, C: Streamlines with Velocity Magnitude for <math>\zeta = 2.2s</math>, D: Streamlines with Velocity Magnitude for <math>\zeta = 1.1s</math>. Velocity Units: m/s . . . . .</i>                        | 353 |
| 5.33 | <i>Fx Vs Lift Limit Cycle Comparison; A: Rotation Position D, B: Rotation Position C, C: Rotation Position B, D: Rotation Position A . . . . .</i>   | 354 |
| 5.34 | <i>Fx Vs Lift Limit Cycle Comparison; A: Rotation Duration 3.3s, B: Rotation Duration 2.2s, C: Rotation Duration 1.1s . . . . .</i>  | 355 |
| 5.35 | <i>Contour Plot for Average Aerodynamic Power / Average Lift Force For All Cases (Legend Represents Average Power, W / Average Lift, N) . . . . .</i>  | 356 |
| 5.36 | <i>Rectangular Wing with Rotation About the Leading Edge Cases 1-3 at <math>\tau = 0.125</math>; A: Streamlines with Velocity Magnitude at Wing Tip for <math>\zeta = 3.3s</math>, B: Streamlines with Velocity Magnitude at Wing Tip for <math>\zeta = 2.2s</math>, C: Streamlines with Velocity Magnitude at Wing Tip for <math>\zeta = 1.1s</math>. Velocity Units: m/s . . . . .</i>   | 358 |
| 5.37 | <i>Rectangular Wing with Rotation About the Leading Edge Cases 1-3 at <math>\tau = 0.125</math>; A: Frontal View of Streamlines with Velocity Magnitude at Wing Tip for <math>\zeta = 3.3s</math>, B: Frontal View of Streamlines with Velocity Magnitude at Wing Tip for <math>\zeta = 2.2s</math>, C: Frontal View of Streamlines with Velocity Magnitude at Wing Tip for <math>\zeta = 1.1s</math>. Velocity Units: m/s . . . . .</i> | 359 |
| 5.38 | <i>Computational Domain with The Experimental Wing . . . . .</i>   | 360 |
| 5.39 | <i>Experimental Wing in The Computational Domain with Dimensions . . . . .</i>   | 361 |
| 5.40 | <i>60 mm Wing (WT<sub>4</sub>) Data with Motion and Pressure Visualisation; A: Grid Sensitivity Comparison for Lift Force Data, B: Experimental and CFD Lift Force Comparison, C: Flapping Wing Motion of Downstroke, D: Flapping Wing Motion of Downstroke with Pressure Contours on Wing Surfaces. Pressure Units: Pa . . . . .</i>  | 362 |
| 5.41 | <i>60 mm Experimental Wing (WT<sub>4</sub>) with Pressure Distribution; A: Coarse Mesh, B: Medium Mesh, C: Dense Mesh, D: Hyper Dense Mesh. Pressure Units: Pa . . . . .</i>   | 364 |

|      |  |     |
|------|--|-----|
| 5.42 | <i>60 mm Experimental Wing (WT<sub>4</sub>) with Streamlines and Mesh; A: Flow Characteristics During Downstroke at <math>\tau = 0.25</math>, B: Flow Field Around Wing at <math>\tau = 0.25</math>, C: Mesh on Wing Surface, Velocity Units: m/s</i>  | 365 |
| 6.1  | <i>Flapping Wing Measurements for 47 mm Wings (WT<sub>3</sub>); A: 3 Hz Spectrogram, B: 3 Hz Force &amp; Power Data, C: 4 Hz Spectrogram, D: 4 Hz Force &amp; Power Data E: 5 Hz Spectrogram, F: 5 Hz Force &amp; Power Data. Colour Bar Represents Size of Amplitude. UI: M1-F-WT<sub>3</sub>-S-V</i> | 372 |
| 6.2  | <i>Flapping Wing Measurements for 47 mm Wings (WT<sub>3</sub>); A: 6 Hz Spectrogram, B: 6 Hz Force &amp; Power Data, C: 7 Hz Spectrogram, D: 7 Hz Force &amp; Power Data E: 8 Hz Spectrogram, F: 8 Hz Force &amp; Power Data. Colour Bar Represents Size of Amplitude. UI: M1-F-WT<sub>3</sub>-S-V</i> | 373 |
| 6.3  | <i>Flapping Wing Measurements for 47 mm Wings (WT<sub>3</sub>); A: 9 Hz Spectrogram, B: 9 Hz Force &amp; Power Data, C: 10 Hz Spectrogram, D: 10 Hz Force &amp; Power Data. Colour Bar Represents Size of Amplitude. UI: M1-F-WT<sub>3</sub>-S-V</i>   | 374 |
| 6.4  | <i>Flapping Wing Measurements for 47 mm Wings (WT<sub>3</sub>); A: Aerodynamic Force Comparison, B: Power Data for Inertia and Aerodynamic Forces, C: Aerodynamic Power &amp; Force Relation. UI: M1-F-WT<sub>3</sub>-S-V</i>  | 375 |
| 6.5  | <i>Wing Position for Flapping Motion Sequence with Non-Dimensional Time. UI: M1-F-WT<sub>4</sub>-S-V</i>   | 378 |
| 6.6  | <i>Wing Position for FR Motion Sequence with Non-Dimensional Time. UI: M1-FR-WT<sub>4</sub>-S-V</i>  | 379 |
| 6.7  | <i>Wing Position for FR with AP Motion Sequence with Non-Dimensional Time. UI: M1-FRAP-WT<sub>4</sub>-S-V</i>  | 380 |
| 6.8  | <i>Wing Position for FR Motion in Hovering Mode Sequence with Non-Dimensional Time. UI: M1-FR-WT<sub>4</sub>-S-H</i>   | 381 |
| 6.9  | <i>Wing Position from Ground Effect Base for FR Motion in Hovering Mode, 1-8 Downstroke, 9-15 Upstroke. UI: M1-FRwB-WT<sub>4</sub>-S-H</i>   | 382 |
| 6.10 | <i>Wing Position from Ground Effect Base for FR with AP Motion, 1-8 Downstroke, 9-15 Upstroke. UI: M1-FRAPwB-WT<sub>4</sub>-S-V</i>  | 382 |

|      |   |     |
|------|---|-----|
| 6.11 | <i>Wing Kinematics for a Compilation of Arrangements Tested with Model 1; A: Flapping, B: FR with 0 Degree Inclination, C: FRAP with 0 Degree Inclination, D: FR with 90 Degree Inclination, E: AOA Comparison for FR and FRAP Configurations . . . . .</i>   | 384 |
| 6.12 | <i>Various Experimental Layouts; A: Cases F1, FR1 &amp; FRAP1, B: Cases F5 &amp; FRAP2, C: Case FR3, D: Model at 90degrees, E: Model at 90 degrees w/GE . . . . .</i>   | 390 |
| 6.13 | <i>Various Experimental Layouts; A: Case F2, B: Cases F3, FR2 &amp; FRAP4, C: Cases F4, FR4 &amp; FRAP3, D: Case FR5 . . . . .</i>  | 391 |
| 6.14 | <i>Flapping Wing Measurements for 60 mm Wings (WT4); A: Flapping Only Aero and Inertial Forces with Stroke Angle, B: Comparison of Flapping Aero Forces, C: Aerodynamic Power &amp; Force Relation, D: Spectrogram for Vertical Axis in Air. Colour Bar Represents Size of Amplitude. UI: M1-F-WT4-S-V &amp; M1-FwB-WT4-S-V . . . . .</i> | 392 |
| 6.15 | <i>Flapping and Rotation Measurements with Uncertainty Applied . . . . .</i>  | 394 |
| 6.16 | <i>Flapping &amp; Rotation Wing Measurements for 60 mm Wings (WT4); A: Case FR1, B: Spectrogram for Vertical Axis in Air, C: Case FR2, D: Case FR3, E: Case FR4, F: Case FR5. Colour Bar Represents Size of Amplitude. UI: M1-FR-WT4-S-V &amp; M1-FRwB-WT4-S-V . . . . .</i>  | 401 |
| 6.17 | <i>Flapping &amp; Rotation Wing Measurements for 60 mm Wings (WT4); A: Comparison of Lift Force, B: Comparison of Thrust Force, C: Comparison of Pitching Moment. UI: M1-FR-WT4-S-V &amp; M1-FRwB-WT4-S-V . . . . .</i>   | 402 |
| 6.18 | <i>Flapping &amp; Rotation Wing Measurements for 60 mm Wings (WT4); A: FR Only Data with Wing Displacement Kinematics, B: Average Thrust Force for All Cases, C: Average Pitching Moment for All Cases, D: Average Aerodynamic Power &amp; Force Relation. UI:M1-FR-WT4-S-V &amp; M1-FRwB-WT4-S-V . . . . .</i>                           | 403 |
| 6.19 | <i>Flapping &amp; Rotation Wing Measurements for 60 mm Wings (WT4) with Model in Hovering Position; A: FR Only (90 Deg), B: FR w/GE Boundary (90 Deg), C: Comparison of Thrust Force, D: Comparison of Lift Force, E: Comparison of Pitching Moment. UI: M1-FR-WT4-S-H &amp; M1-FRwB-WT4-S-H . . . . .</i>                                | 408 |

|      |   |     |
|------|---|-----|
| 6.20 | <i>Flapping &amp; Rotation Wing Measurements for 60 mm Wings (WT<sub>4</sub>); A: FR Only (90 Deg) with Wing Displacement Kinematics, B: Average Pitching Moment, Average Lift &amp; Average Power (90 Deg Data), C: Comparison of Vertical &amp; Horizontal Forces at Different Inclinations, D: Comparison of Horizontal &amp; Vertical Forces at Different Inclinations. UI: M1-FR-WT<sub>4</sub>-S-V, M1-FR-WT<sub>4</sub>-S-H &amp; M1-FRwB-WT<sub>4</sub>-S-H . . . . .</i> | 409 |
| 6.21 | <i>Flapping with Restricted Wing Pitching; A: Schematic of Wing Pitching Motion, B: Wing Kinematic Motion for Complete Cycle; Circle Represents Leading Edge . . . . .</i>  | 410 |
| 6.22 | <i>Flapping and Rotation with Asymmetric Pitching Measurements for 60 mm Wings (WT<sub>4</sub>); A: Case FRAP1, B: Case FRAP2, C: Case FRAP3, D: Case FRAP4, E: Spectrogram for Vertical Axis in Air. Colour Bar Represents Size of Amplitude. UI: M1-FRAP-WT<sub>4</sub>-S-V &amp; M1-FRAPwB-WT<sub>4</sub>-S-V . . . . .</i>  | 417 |
| 6.23 | <i>Flapping and Rotation with Asymmetric Pitching Measurements for 60 mm Wings (WT<sub>4</sub>); A: FRAP Only with Wing Displacement Kinematics, B: Spectrogram for Vertical Axis in Vacuum Chamber, C: Average Lift Force, D: Average Thrust Force, E: Average Pitching Force, F: Average Thrust Force Based Upon AOA Duration. Colour Bar Represents Size of Amplitude. UI: M1-FRAP-WT<sub>4</sub>-S-V &amp; M1-FRAPwB-WT<sub>4</sub>-S-V . . . . .</i>                         | 418 |
| 6.24 | <i>Flapping and Rotation with Asymmetric Pitching Measurements for 60 mm Wings (WT<sub>4</sub>); A: Comparison of Lift Force, B: Comparison of Thrust Force, C: Comparison of Pitching Moment, D: Aero Power &amp; Thrust Force Relation. UI: M1-FRAP-WT<sub>4</sub>-S-V &amp; M1-FRAPwB-WT<sub>4</sub>-S-V . . . . .</i>   | 419 |
| 6.25 | <i>Power Input for Various Wing Motions with Model 1 Inclined at 0 Degrees . . . . .</i>  | 420 |
| 6.26 | <i>Wing Position for Model 2 in Sym Configuration Undergoing Flapping Motion Sequence with Non-Dimensional Time. UI: M2-F-WT<sub>4</sub>-S-V . . . . .</i>  | 422 |
| 6.27 | <i>Wing Position for Model 2 in Asym Configuration Undergoing Flapping Motion Sequence with Non-Dimensional Time. UI: M2-F-WT<sub>4</sub>-A-V . . . . .</i>   | 423 |
| 6.28 | <i>Wing Position for Model 2 in Asym Configuration Undergoing FR Motion Sequence with Non-Dimensional Time. UI: M2-FR-WT<sub>4</sub>-A-V . . . . .</i>  | 424 |

|      |   |     |
|------|---|-----|
| 6.29 | <i>Wing Kinematics for a Compilation of Arrangements Tested with Model 2; A: Sym Configuration with FR Motion, B: Asym Configuration with FR Motion, C: Asym Configuration with FR Motion with 90 Degree Inclination, D: AOA Comparison for Sym &amp; Asym Configurations, E: AOA Comparison for Asym Configuration in 0 Degree &amp; 90 Degree Inclinations . . . . .</i>  | 427 |
| 6.30 | <i>Flapping Wing Measurements of 60 mm Wings (WT<sub>4</sub>) for Model 2; A: Symmetric Configuration, B: Asymmetric Configuration, C: Comparison of Lift Force and Peak Data, D: Aero Power &amp; Lift Force Relation, E: Spectrogram for Vertical Axis in Air for Asymmetric Configuration, F: Spectrogram for Vertical Axis in Vacuum Chamber for Asymmetric Configuration. Colour Bar Represents Size of Amplitude. UI: M2-F-WT<sub>4</sub>-S-V &amp; M2-F-WT<sub>4</sub>-A-V . . . . .</i> | 430 |
| 6.31 | <i>Flapping &amp; Rotating Wing Measurements of 60 mm Wings (WT<sub>4</sub>) for Model 2; A: Symmetric Configuration Force &amp; Power Data, B: Symmetric Configuration Moment Data, C: Spectrogram for Vertical Axis in Air for Asymmetric Configuration. Colour Bar Represents Size of Amplitude. UI: M2-FR-WT<sub>4</sub>-S-V &amp; M2-FR-WT<sub>4</sub>-A-V . . . . .</i>   | 436 |
| 6.32 | <i>Flapping &amp; Rotating Wing Measurements of 60 mm Wings (WT<sub>4</sub>) for Model 2; A: Asymmetric Configuration Force &amp; Power Data, B: Asymmetric Configuration Moment Data, C: Comparison of Lift &amp; Thrust, D: Aero Power &amp; Thrust Force Relation, E: Comparison of Moments. UI: M2-FR-WT<sub>4</sub>-S-V &amp; M2-FR-WT<sub>4</sub>-A-V . . . . .</i>   | 437 |
| 6.33 | <i>Flapping &amp; Rotating Wing Measurements of 60 mm Wings (WT<sub>4</sub>) for Model 2 in Hovering Position; A: Asymmetric Configuration Force &amp; Power Data, B: Asymmetric Configuration Moment Data. UI: M2-FR-WT<sub>4</sub>-A-H . . . . .</i>  | 439 |
| A.1  | <i>Table for Experiments . . . . .</i>  | 462 |
| A.2  | <i>Ground Effect Boundary for Experiments . . . . .</i>   | 462 |
| A.3  | <i>Trailing Edge Wall Boundary for Experiments . . . . .</i>  | 463 |
| A.4  | <i>CAD of Ground Effect Boundary for 90Deg Body Inclination Experiment . . . . .</i>  | 463 |

|     |   |     |
|-----|---|-----|
| B.1 | <i>Spectrogram Plots for 60 mm Wings (WT<sub>4</sub>) in FR &amp; FRAP Configurations; A: FR for Fx Axis, B: FR for Ty Axis, C: FRAP for Fx Axis, D: FRAP for Ty Axis, E: FR in Hovering Mode for Fx Axis, F: FR in Hovering Mode for Ty Axis. Colour Bar Represents Size of Amplitude. UI: M1-FR-WT<sub>4</sub>-S-V, M1-FR-WT<sub>4</sub>-S-H &amp; M1-FRAP-WT<sub>4</sub>-S-V . . . . .</i>                             | 466 |
| B.2 | <i>Spectrogram Plots for 60 mm Wings (WT<sub>4</sub>) in FR &amp; FRAP Configurations During Vacuum Chamber Tests; A: FR for Fx Axis, B: FR for Ty Axis, C: FRAP for Fx Axis, D: FRAP for Ty Axis, E: FR in Hovering Mode for Fx Axis, F: FR in Hovering Mode for Ty Axis. Colour Bar Represents Size of Amplitude. UI: M1-FR-WT<sub>4</sub>-S-V, M1-FR-WT<sub>4</sub>-S-H &amp; M1-FRAP-WT<sub>4</sub>-S-V . . . . .</i> | 467 |
| B.3 | <i>Example of Experimental Images to Capture Wing Motion with Various Arrangements; A: Flapping Only, B: Flapping with TEwall and GE Boundaries, C: FR Only, D: FR with TEwall and GE Boundaries, E: FR Only in Hovering Mode, F: FR in Hovering Mode with GE Boundary, G: Flapping Only in Vacuum Chamber, H: FR Only in Vacuum Chamber . . . . .</i>  | 468 |
| B.4 | <i>Point Tracking for Flapping Wing and Location Data Output . . . . .</i>  | 468 |
| C.1 | <i>Fx Vs Lift Limit Cycles; A: Rotation Position D, B: Rotation Position D, C: Rotation Position D, D: Rotation Position C, E: Rotation Position C, F: Rotation Position C . . . . .</i>  | 471 |
| C.2 | <i>Fx Vs Lift Limit Cycles; A: Rotation Position B, B: Rotation Position B, C: Rotation Position B, D: Rotation Position A, E: Rotation Position A, F: Rotation Position A . . . . .</i>  | 472 |
| C.3 | <i>Moments for Rotation Position D and Rotation Position C ; A: Rotation Position D and Duration 3.3s, B: Rotation Position D and Duration 2.2s, C: Rotation Position D and Duration 1.1s, D: Rotation Position C and Duration 3.3s, E: Rotation Position C and Duration 2.2s, F: Rotation Position C and Duration 1.1s . . . . .</i>   | 473 |
| C.4 | <i>Moments for Rotation Position B and Rotation Position A ; A: Rotation Position B and Duration 3.3s, B: Rotation Position B and Duration 2.2s, C: Rotation Position B and Duration 1.1s, D: Rotation Position A and Duration 3.3s, E: Rotation Position A and Duration 2.2s, F: Rotation Position A and Duration 1.1s . . . . .</i>   | 474 |

|     |   |     |
|-----|---|-----|
| C.5 | <i>Aerodynamic Power for Rotation Position D and Rotation Position C ; A: Rotation Position D and Duration 3.3s, B: Rotation Position D and Duration 2.2s, C: Rotation Position D and Duration 1.1s, D: Rotation Position C and Duration 3.3s, E: Rotation Position C and Duration 2.2s, F: Rotation Position C and Duration 1.1s . . . . .</i> | 475 |
| C.6 | <i>Aerodynamic Power for Rotation Position B and Rotation Position A ; A: Rotation Position B and Duration 3.3s, B: Rotation Position B and Duration 2.2s, C: Rotation Position B and Duration 1.1s, D: Rotation Position A and Duration 3.3s, E: Rotation Position A and Duration 2.2s, F: Rotation Position A and Duration 1.1s . . . . .</i> | 476 |
| C.7 | <i>Mesh Around Drosophila Wing for Grid Independence Study; A: Coarse Mesh, B: Medium Mesh, C: Dense Mesh, D: Hyper Dense Mesh, E: Dense Mesh with Stationary Inner Domain</i>  | 477 |
| C.8 | <i>Mesh on Drosophila Wing for Grid Independence Study; A: Coarse Mesh, B: Medium Mesh, C: Dense Mesh, D: Dense Mesh with Stationary Inner Domain, E: Hyper Dense Mesh, F: Wing Rotation Location . . . . .</i>   | 478 |
| C.9 | <i>Two Dimensional Slices of the Grid and Drosophila Wing at the Leading Edge; A: Coarse Mesh, B: Medium Mesh, C: Dense Mesh, D: Dense Mesh with Stationary Inner Domain, E: Hyper Dense Mesh . . . . .</i>   | 479 |
| D.1 | <i>Model 1 with Body and 60 mm Wings (WT4) in Flapping Arrangement; A: Front View, B: Side View (Opaque and Transparent), C: Top View, D: Front Isometric View (Opaque and Transparent), E: Back Isometric View (Opaque and Transparent) . . . . .</i>  | 482 |
| D.2 | <i>Model 1 Support Board and Linkage Mechanism with Connection Lines; A: Top View, B: Front Isometric View, C: Back Isometric View, D: Side View . . . . .</i>  | 483 |
| D.3 | <i>Model 1 Complete Linkage Mechanism with Connection Lines; A: Top View, B: Back Isometric View, C: Side View, D: Front Isometric View . . . . .</i>   | 484 |
| D.4 | <i>Model 1 Base and Gearbox with Connection Lines; A: Back View, B: Back Isometric View, C: Side View, D: Top View, E: Back Isometric View, F: Side View . . . . .</i>  | 485 |
| D.5 | <i>Photograph of Model 2 Backboard and Linkage Mechanism . . . . .</i>  | 486 |

|      |  |     |
|------|--|-----|
| D.6  | <i>Photograph of Model 2 Linkage Mechanism with White Lines for Measurements . . . . .</i> | 486 |
| D.7  | <i>Photograph of Model 2 Linkage Mechanism and Base . . . . .</i>                          | 487 |
| D.8  | <i>Photograph of Model 2 Linkage Mechanism Marked and Base . . . . .</i>                   | 487 |
| D.9  | <i>Photograph of Model 2 Top View . . . . .</i>  | 488 |
| D.10 | <i>Photograph of Model 2 Linkage Mechanism and Base . . . . .</i>                          | 488 |

**THE FOLLOWING PARTS OF THIS THESIS HAVE BEEN REDACTED  
FOR COPYRIGHT REASONS:**

- p. 58, Figure 1.4**
- p. 59, Figure 1.5 and 1.6**
- p. 60, Figure 1.7**
- p. 61-2, Figure 1.9 and 1.10**
- p. 63, Figure 1.11**
- p. 64, Figure 1.12 and 1.13**
- p. 65-7, Figure 1.14-6**
- p. 70, Figure 1.19**
- p. 74, Figure 1.23**
- p. 76, Figure 1.24 and 1.25**
- p. 88, Figure 2.6**

Dedicated to my Parents,

For their patience, sympathy and continual support in all aspects of my life

&

Dedicated to my Daughter,

Her beautiful smile, adorable personality and presence brightens up life & makes everything worthwhile

# Acknowledgements

Firstly, I would like to thank my supervisor, Prof. M. Gavaises for his professional and human support during the duration of this research project. I am grateful for the opportunity, funding and freedom provided to pursue my research work and grow as an engineer. It has been an invaluable experience, which has helped me develop so many skills and formed the foundation for my professional career.

I would also like to thank my second supervisor, Dr. C. Cheung for his support, advice and knowledge in this field of science. I hope you enjoyed our extensive research conversations as much as I did. Lastly, I am grateful for the continuous motivation and courage you have given me during these past years.

In addition, I would like to thank Mr. M. Smith for his valuable advice and skills to manufacture the components required for the experimental work of this project. Furthermore, I would like to thank Mr. R. Leach and the technical staff for their support. Moreover, I would like to thank Mr. J. Hooker and Mr. T. Barnes for giving me access to all your tools and workshop to manufacture components for the experiments.

A big thank you to my friends and colleagues in City University research group, for all of the insightful conversations and support in one way or another.

Last, but not least, I would like to thank my family and friends for their guidance and support in my personal life. A very warm thank you to my parents, sister, wife and daughter for their patience, loving encouragement and strength you have given me.

# Declaration

I hereby declare that the work presented in this thesis is my own unless stated and referenced in the text accordingly.

City University London

Anish Gami

# Abstract

Many creatures in nature have evolved the ability to fly and some seem to do so effortlessly with captivating movement. The flight characteristics of these natural fliers have greatly fascinated biologists and engineers for a long time that to this day researchers continue to actively work in this field of science with the aim of one day developing a Flapping Wing Micro Aerial Vehicle (FWMAV) which can replicate the flight of nature's creatures. These types of autonomous robotic vehicles can fulfil tasks which are not suitable for manned vehicles especially when risks to human safety are present. Flight techniques such as control, stability and manoeuvrability are flight characteristics which an FWMAV must possess if such a device is employed for various rescue missions. With this in mind symmetrical and asymmetrical wing motions are studied experimentally in the current research programme in such a way that the methodology employed for this type of flight can be implemented into future FWMAVs.

This research study is composed of investigations carried out in various fashions such as design & development, experimentally testing and computational evaluations of hovering aerodynamics of an FWMAV with variable parameters. The design of the first FWMAV, led to the creation of the second model which has the ability to perform symmetric and asymmetric flapping motions. Both models were tested thoroughly with various wing motion arrangements to assess the forces and moments generated along with the power required to actively move the wings through the air. A range of Reynolds numbers were studied within the experiments, the 47 mm wing (WT3) was flapped from 3 Hz to 10 Hz which meant that the Reynolds number ranged from 749 to 2498. The 60 mm wing (WT4) was flapping at a frequency of 5 Hz with a range of different flapping motions, the Reynolds number for this was in the region of 2716. The experiments were performed on the experimental rig which incorporated a six component force transducer whilst images were captured via a high-speed camera to analyse the cyclic wing motion. Along with the various styles of wing

motion tested, stationary rigid boundaries were also positioned in the near vicinity of the wings to study the effect this has on flight forces and moments, in addition to the power drawn in such scenarios.

Aside from the design and experimental investigations, computational studies were conducted involving a rectangular wing in hovering mode where the rotational duration and location are varied to determine key aerodynamic measurements and flow phenomena. The Reynolds number for this analysis was 155 and the flapping stroke frequency was 0.145 Hz. This extended study was composed of twelve cases to thoroughly investigate three rotational durations and four locations of wing rotation along the chord. In general, maximum lift force was achieved when the wing pitched about the spanwise axis at the leading edge whilst rapidly rotating at its smallest rotational duration. As a result, the maximum aerodynamic power was also required in this situation. Furthermore, grid quality assessments were carried out to determine the accuracy of the solution against the type of grid methodology adopted as mesh deformations are experienced in a time dependent manner. Prior to expanding the CFD study, a drosophila insect wing was simulated in a hovering mode analysis to evaluate the computational methodology adopted. It was found that the computational data produced in this thesis had good agreement with experimental and computational results from literature. Further to this, the 60 mm wing (WT4) was modelled in a flapping only simulation for which the trend of the curves agreed well between the experimental and computational data.

In general, for the tests where the wings on both sides produce a single motion in the form of flapping only, the force measurement data followed in a consecutive fashion as the frequency was increased. Likewise, in relation to the augmenting frequency and force output, the aerodynamic power increased as the flapping frequency grew. Following this the experimental tests became more complex with the introduction of a rigid stationary boundary in the proximity of the wings. In this flapping only motion, the boundaries seemed to augment the aerodynamic forces generated by a maximum of approximately 10 mN (peak-peak) on average when compared to the base case of flapping only with no boundary present, particularly the TE wall boundary case which seemed to generate the greatest aerodynamic force of approximately +/-25 mN.

With the addition of passive wing rotation the model could now perform a coupled flapping with rotating wing motion whilst a single actuator is utilised to drive the mechanical system. Building from the previous work, stationary boundaries were also exploited for these experiments, where it was found that the peaks of the lift force measured for both strokes were greater when stationary boundaries were present near the dynamically active wings. Furthermore, the thrust generated was found to be larger for all the boundary cases

compared to the base case. As a direct relation to the thrust force data, the same result as aforementioned was found for pitching moment. However, a consequence for the greater force generation in the presence of boundaries, is that greater aerodynamic power was required by the mechanical device for the boundary tests with this coupled wing motion when compared to the base case. The passive wing pitching motion is unique as it is created via elastic elements attached to the root section of each wing. The flapping stroke produces a sinusoidal motion through its controlled actuation, whereas the wing pitching motion is dependent on many factors that determine its motion during a cycle. The Flapping and Rotation with Asymmetric Pitching (FRAP) experiments seemed to generate more lift force in the downstroke phase with a thrust generation in the upstroke phase, such a result was found as the wing created a large AOA during the upstroke promoting thrust generation whilst reducing the vertical force generation in the downwards direction. Similar to previous tests, when the wings were performing this FRAP motion, the greatest lift force was produced when a wall was located in the near vicinity of the trailing edge of both wings. For the second model, it was found that greater thrust was generated in the asymmetrical configuration as opposed to its symmetrical counterpart, and overall yawing moments were generated during asymmetric wing motions which are essential for lateral control and manoeuvrability. This result was consistent when the model was positioned to have its stroke plane in the vertical axis as well as the horizontal axis.

In summary, the research performed during the course of this project produced innovative results in the form of the creation of two micro air vehicles with a thorough explanation of the development process and examination under experimental tests. Various parameters were analysed during the experimental tests such as force, moment, power and wing position measurements. The tests were performed on both models, one of which has the functionality to perform asymmetrical flapping and successfully generate moments about two different axes. A unique wing motion which favoured the upward vertical force production was investigated under various scenarios. The wings keep a fixed angle of attack during the downwards flapping motion and are allowed to passively rotate during the upstroke motion. Computational simulations were performed to investigate the hovering fluid dynamics, forces, moments and power required for various chordwise rotational positions and durations of wing rotation. This investigation aided in understanding the full effects of altering these parameters under hovering conditions for a rectangular wing. The valuable results found from this research program provide a better insight into various topics involving micro air vehicles in addition to developing future flight worthy insect inspired vehicles.

# Nomenclature

K - Kelvin

Hz - Hertz

N - Newtons

F<sub>x</sub> - Force in X direction

F<sub>y</sub> - Force in Y direction

F<sub>z</sub> - Force in Z direction

M<sub>x</sub> - Moment about X axis

M<sub>y</sub> - Moment about Y axis

M<sub>z</sub> - Moment about Z axis

$\omega_m$  - Motor Speed

V - Voltage

W - Watts

D<sub>G</sub> - Distance Between the Central Gear Locations

T<sub>N</sub> - Number of Teeth in a Gear

D<sub>P</sub> - Diametral Pitch

$Pitch_D$  - Pitch Diameter

$G_{rr}$  - Gear Reduction Ratio

$T_{NL}$  - Number of Teeth in Larger Gear

$T_{NS}$  - Number of Teeth in Smaller Gear

$\zeta$  - Wing Rotation Duration

$\tau$  - Non-Dimensional Time (based on instantaneous time and time required for a complete period)

$\chi$  - Wing Rotation Position Along Chord

$\hat{r}$  - Non-Dimensional Radial Distance (based on position from wing root and wing span)

$\hat{c}$  - Non-Dimensional Chord (based on length of chordwise strip and mean chord)

$c$  - Chord

$\bar{c}$  - Mean Chord

$R$  - Single Wing Span

$r'$  - Radial Distance from Wing Root

$Y_{LE}$  - Leading Edge Profile

$\hat{Y}_{LE}$  - Non-Dimensional Leading Edge Profile (based on distance from mid-axis to LE and mean chord)

$f$  - frequency

$q$  - Dynamic Pressure

$\Phi$  - Stroke Amplitude

$\Psi$  - Angle of Attack Amplitude

$\Theta$  - Deviation Amplitude

$S$  - Wing Area

$S_T$  - Total Wing Area

AR - Aspect Ratio

VAR - Variance

$\sigma_{SD}$  - Standard Deviation

$R_g$  - Radius of Gyration

$R_r$  - Distance from Rotation Axis to Wing Root

$R_t$  - Distance from Rotation Axis to Wing Tip

$\alpha_{LM}$  - Angle Between Lengths in Linkage Mechanism

$\beta_{LM}$  - Angle created from Linkage Movement

$\theta_{LM}$  - Angle Alters with Link Movement

$\epsilon_{LM}$  - Outer Angle in Neutral Position

$L_n$  - Length

L - Link

$F_L$  - Lift Force

$F_I$  - Inertial Force

$F_D$  - Drag Force

$C_{FL}$  - Lift Coefficient

m - Mass

a - Acceleration

$\phi(t)$  - Stroke Angle as a Function of Time

t - Time

$U_{\text{ref}}$  - Velocity

$L_{\text{ref}}$  - Length

$\nu$  - Kinematic Viscosity

$\mu$  - Dynamic Viscosity

$\rho$  - Density

$\omega$  - Angular Velocity

$v$  - Velocity

$Re$  - Reynolds Number

$Re_{\text{hover}}$  - Reynolds Number for a Hovering Condition

$St$  - Strouhal Number

$S_{BF}$  - Frontal Body Area

$L_B$  - Length of Body

$\bar{\tau}$  - Stress Tensor

$h_a$  - Linear Stroke amplitude

$k$  - Reduced Frequency

$p$  - Pressure

$J$  - Advanced Ratio

$L_a$  - Arc Length

$L_{\Phi}$  - Length with Reference to Stroke Amplitude

$T$  - Time Taken for a Complete Cycle

$\psi(t)$  - Angle of Attack as a Function of Time

$\vartheta(t)$  - Deviation Angle as a Function of Time

$V$  - Maximum Translational Velocity

$v(\tau)$  - Translational Velocity as a Function of Non-Dimensional Time

$\tau_{acc}$  - Non-Dimensional Time At Onset of Translational Acceleration

$\Delta\tau_{acc}$  - Non-Dimensional Duration of Translational Acceleration

$\tau_{dec}$  - Non-Dimensional Time At Onset of Translational Deceleration

$\Delta\tau_{dec}$  - Non-Dimensional Duration of Translational Deceleration

$\omega_{rot}$  - Angular Velocity Constant

$\omega(\tau)$  - Angular Velocity as a Function of Non-Dimensional Time

$\tau_{turn}$  - Non-Dimensional Time at Onset of Wing Rotation

$\tau_{rot}$  - Non-Dimensional Duration of The Rotational Phase

$\Delta\theta$  - Total Angle of Wing Rotation

$\omega$  - Angular Velocity

$Mx_{wing}$  - Moment about Wing Base Fixed X Axis

$My_{wing}$  - Moment about Wing Base Fixed Y Axis

$Mz_{wing}$  - Moment about Wing Base Fixed Z Axis

$P_{req}$  - Power Required

$\xi$  - Measure of Stroke Reversal Duration

$\gamma$  - Measure of Angle of Attack Reversal Duration

$\varphi$  - Body Rotation about X Axis

$\sigma$  - Body Rotation about Z axis

$\zeta$  - Body Rotation about Y axis

# Abbreviations

Aero - Aerodynamic

AOA - Angle of Attack

Asym - Asymmetrical

AV - AeroVironment

CAD - Computer Aided Design

CCD - Charge-Coupled Device

CFD - Computational Fluid Dynamics

CG - Centre of Gravity

Ch. - Channel

DARPA - Defence Advanced Research Projects Agency

DC - Direct Current

DOF - Degree of Freedom

DVID - Dynamic Virtual Inner Domain

ESC - Electronic Speed Controller

Exp - Experimental

fps - Frames Per Second

FR - Flapping and Rotation

FRAP - Flapping and Rotation with Asymmetric Pitching

FSI - Fluid Structure Interaction

F/T - Force/Torque

FW - Flapping Wing

FWMAV - Flapping Wing Micro Aerial Vehicle

FWNAV - Flapping Wing Nano Aerial Vehicle

GE - Ground Effect

GUI - Graphical User Interface

HS - High Speed

IFPS - Interface and Power Supply

iso - Isometric

LD - Larger Distance

AP - Asymmetric Pitching

LE - Leading Edge

LEV - Leading Edge Vortex

Li-Po - Lithium Polymer

LW - Light Weight

MAV - Micro Aerial Vehicle

Mf - Multifunction

MFI - Micromechanical Flying Insect

NAV - Nano Aerial Vehicle

NI - National Instruments

PIV - Particle Image Velocimetry

PSU - Power Supply Unit

R/C - Radio Control

RSV - Rotational Starting Vortex

SR - Semi-Rigid

SS - Combination of Starting and Stopping Vortex

SVID - Stationary Virtual Inner Domain

Sym - Symmetrical

TE - Trailing Edge

TEV - Trailing Edge Vortex

TTL - Transistor-Transistor Logic

TSV - Translation Starting Vortex

TV - Tip Vortex

RV - Root Vortex

UAV - Unmanned Aerial Vehicle

UDF - User Defined Function

USL - Under-wing Shear Layer

VI - Virtual Instrument

VID - Virtual Inner Domain

WE - Wall Effect

1S - One Side Only

WT - Wing Type

UI - Unique Identifier

# Chapter 1

## Introduction

This first chapter presents a brief insight regarding the motivation to research flight mechanics, in-particular insect flight and MAVs. Following this, a few biological aspects of an insect are described and the applications of small flying objects. A brief review of various types of MAVs which have been developed by researchers, engineers and even hobbyists will be presented.

### 1.1 Motivation

To date, a variety of aerial vehicles of many different sizes have been seen, which are built for specific purposes and continually improved as researchers pursue their passion and interests to advance existing knowledge in this field of science. In 1902, the Wright brothers completed the design of their new glider, which included significant improvements compared to its predecessor. After years of experimental research carried out in order to determine the flaws of their previous glider design, they designed and built a wind tunnel with a two blade fan powered by a gasoline engine, where they tested hundreds of different models some of which were aerofoils, flat-plates, curved plates, rounded leading edges and many others. The findings of their experimental research were vital to their new design and led to their success. Following their successful glider design, they commenced a new challenge to develop powered flight. The field of aeronautics has experienced continuous advancements in technology over the past century involving the development and

constant improvements to flight vehicles. Various types of flying machines have been created some of which are aeroplanes, helicopters, airships, space vehicles, rockets, missiles and so on. Flying vehicles within nature have evolved over millions of years ago and have recently become a key topic for aerial defence machines as technology continues to improve in various aspects of engineering. The maximum positive g-forces permitted in most general aviation aircraft is 4-5 g and select military aircraft withstand 8-10 g. However, many birds routinely experience positive g-forces in excess of 10 g and up to 14 g (Shyy et al. 2008). Early stages of flight were inspired by natural flyers in the form of flapping wings from the sketches of Da Vinci, the designs of flying vehicles were based on flapping wings, years later we witness the rebirth of these flying machines attempting to mimic bird and insect like wing motion, in the hope to one day fly like these extraordinary creatures.

For decades, researchers have been fascinated by nature's flyers and wondered how these creatures can fly so effortlessly, efficiently and with such remarkable control characteristics. Biological flyers have several manoeuvring characteristics, flight control body motions which are difficult to implement in man-made flyers. They adapt to wind gusts, deform their wings to control speed, change direction and even reduce their lift. Further to this, birds have the ability to take-off and land from a solid foundation or water. They are able to bend and spread their wings to position them at a high angle of attack producing a large drag force (whilst also maintaining sufficient lift compared to its weight at low speed) in order to reduce their approaching speed, before touching down on land or water. Larger birds such as American eagles with their large wing area can afford to stop flapping whilst looking for prey and remain airborne for a long duration simply by taking advantage of the thermal in the air, while smaller birds must flap their wings continuously in order to fly. As the size of the animal decreases its wing flapping frequency increases where the smallest insects seem to flap their wings violently at frequencies above 200 Hz, with swift directional changes displaying manoeuvrability.

In order to progress in this multi-disciplinary field of UAVs and MAVs, technology advancement is a key factor to succeeding in this area of science. Various fields of engineering are required to understand and develop such vehicles including aeronautics, CFD, electronics, robotics among others. A highly developed MAV with a set of stringent mission requirements requires a diverse range of parts which are continually being developed to improve efficiency, size, weight, manufacturing time, structural strength which all in future will need to lead to cost effectiveness and performance enhancement for the vehicle. The miniaturisation of

parts and devices is very challenging but is imperative to the growth of MAVs. Mechanical parts, actuators, sensors, gyroscopes, cameras, power sources, control circuitry along with other components are all critical for the development of a complete autonomous MAV.

The need for such small scale aerial vehicles is invaluable, a core reason for the continual evolution is rescue surveillance. A collapsed building will pose a threat to any human life entering this site, whereas it would be an ideal environment in which an MAV can be used most effectively. They can also be used in surveillance missions in hazardous and confined environments. Such devices can be sent in to explore the area, determine the locations of human lives and even seek out the best route to follow. A MAV equipped with manoeuvrability skills similar to that of insects and the information captured via its sensors and cameras would be intricate to all search and rescue teams in all parts of the world. This is just one role a MAV device can execute, there are many more which such devices are necessary for.

## 1.2 Nature and Insects

Nature has shown us various flying techniques from gliding to hovering where the latter can only be performed by insects and smaller birds. Their take-off methods vary from using their legs as a spring mechanism and leaping into the air to extended runs through water or land to gain enough speed and raise their entire body above the surface. Hummingbirds are capable of hovering for prolonged periods whilst flapping its wings in a similar fashion to insects along a horizontal stroke plane, bats are also known to hover but not like Hummingbirds who share similar hovering characteristics to insects. “Most of the total energy required for flight is dissipated as heat in the flight musculature. For hovering animals, the remaining mechanical energy is divided into three components: induced power required to generate lift, profile power necessary to overcome drag on the wings, and inertial power required to accelerate and decelerate the wings during stroke reversal” (Dickinson et al. 1995). An animal’s ability to hover are based upon four parameters according to (Shyy et al. 2008), which are the moment of inertia of its wings, overall size, wing shape and especially the degree of freedom for wing movement. Hovering requires wing characteristics which exist primarily in small biological flyers.

This project is based on insect flight due to their size, manoeuvrability, flight characteristics (such as control and fluid dynamic enhancing phenomenas), hovering ability, low speed flight among many other enticing

features. A highly sought after feature is the insect's capability to develop its own flow field and raise its entire body without the need of any forward flow acting on its wings. These characteristics make an insect an ideal flyer for all indoor and enclosed environment operations.

Insects have the ability to translate along three degrees of freedom and rotate about any of these axes. Its ability to manoeuvre swiftly is available due to its rotational capabilities such as pitch, roll and yaw about their respective translational axes. To undergo controlled take-off and landing the insect adopts a similar method to hovering, where its stroke plane will be close to horizontal and thrust production is controlled, especially during landing. The stroke plane on either side of the body can be varied, and if the stroke plane is different on either side then a turning motion can be created (further discussed below). The insect would be seen to turn away from the side which has the largest stroke plane angle, thus the largest stroke plane angle will be on the outside of the turn. The lift force production is proportional to the angle of attack of the wing, thus altering the pitch angle of the wing on one side will produce an unbalanced lift force on both sides resulting in a rolling moment, insect manoeuvrability will be further elaborated upon below. Moving the flapping motion position either forwards or backwards achieves a pitching moment as the CG point of the insect is modified.

It is clear that insect muscles play a large part in the aerial ability of an insect via their controllability, endurance, strength and co-ordination to perform in such a manner. The level of control and co-ordination involves immense complexities and in mechanical terms somewhat impossible to create at the size of a fly or wasp with the current technology available. Along with the wings, the insects body also holds a significant role to aid insect aerodynamics. During forward flight the insect would attempt to almost streamline its body via positioning it horizontally, when landing the abdomen section seems to be lowered to assist stability and increase drag production in order to reduce its approaching speed. Thus, developing an MAV to imitate an insect in flight and manipulate its fascinating flight characteristics is an incredibly complex task. In addition, as the insect approaches to land it moves the legs outwards ready for touch down which can also act to augment drag force and reduce the insect landing speed (an image of a bee alighting on a platform is shown in Figure 1.1, in which the bee is also carrying pollen). An additional view of the bee alighting on a platform is shown in Figure 1.2, where it is clearly seen that the wings are stretched out to augment the production of drag force. "Tiny changes in the timing of separate elements and components of the wing-flapping cycle and the way in which the wings rotate, for example, can substantially alter both the

magnitude and direction of the resultant forces. It has been shown in hoverflies that a change of 8% in the timing of the wing edge rotation, relative to the timing of the flap, increased the amount of lift generated by 67%” (Goodman 2003).



Figure 1.1: *Bee Alighting Sequence Side View Whilst Carrying Pollen* (Goodman 2003)

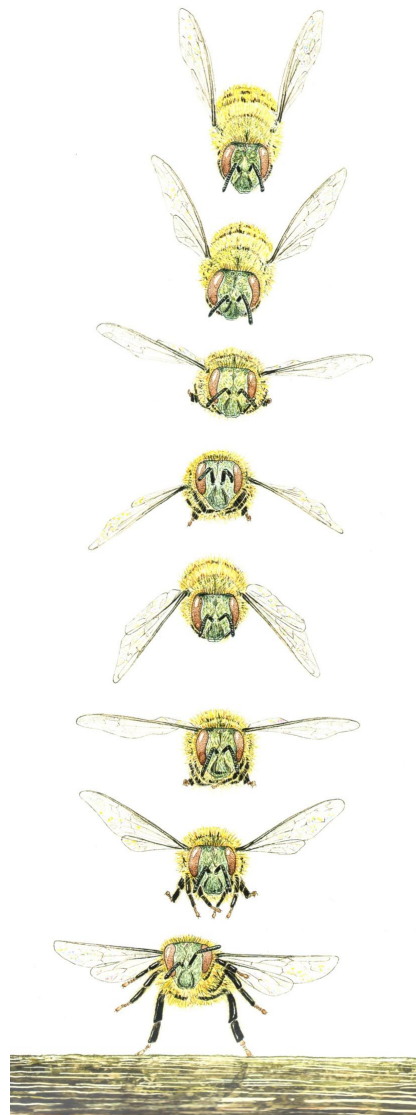


Figure 1.2: *Bee Alighting Sequence Front View* (Goodman 2003)

An insect needs to generate enough aerodynamic power to raise its entire body weight and remain aloft. This aerodynamic power must be produced during its complete flapping wing motion of down and upstrokes. However, the inertial power creation is quite contrasting to the preceding, as positive power would be needed for the first half stroke as this phase involves accelerating the wing from rest. The second half stroke would require decelerating the wing as it will come to rest at the end of the stroke. At the start of a flapping motion inertia is of a maximum value, this decreases towards the midstroke where the acceleration has reached a value of zero. Following on, the wing continues to move in its prescribed path whilst the acceleration is now of opposite sign. “ The energy yielded by this deceleration could be used to minimise the cost of flight in one of two ways. The flies could decelerate their wings by stretching elastic elements within the thorax. This work could then be recovered during the next half stroke and provide energy to accelerate the wings. Alternatively, the work of deceleration could be used directly as a source of aerodynamic power during the second half of each stroke. Any inertial energy stored in elastic elements is unavailable as an immediate source of aerodynamic power” (Dickinson et al. 1995).

The wings of any animal which has the ability to fly must withstand considerable aerodynamic forces and moments which are produced by its wings during flight. Any reduction of these forces and moments due to wing loading would affect its flight performance and efficiency. Insects wings are constructed of a thin membrane reinforced with cuticular veins. These veins provide a structured surface with flexibility and the capability to change the shape of the wing to adapt under various conditions of aerodynamic and inertial loading. A birds wing is much larger made up of a skeletal structure, muscles and feathers. Due to this it has a better resistance to damage compared to insects wings. The root section of the birds wing has the highest thickness and camber where both reduce towards the tip of the wing. The birds wing can be streamlined where the  $Re$  of the wing is approximately of the order of  $10^5$ . The wing camber can be transformed to develop favourable aerodynamics via the muscles or passively by aero-elastic motion of the feathers, in addition camber can also be modified actively to some extent.

Among the animal flight group gliding and soaring can only be performed by birds, the larger the bird, the better its ability to glide and soar. Animals usually flap their wings in order to produce thrust and lift. Upon gliding the bird can produce lift only, no thrust is produced as there is no flapping motion. Thrust can be generated by gliding through a slightly downward angle whilst moving forwards through the air, this is known as the gliding angle. Thus, thrust is actually produced by the gravitational force acting on

the animal. “A wandering albatross, with a wing span of over 3 m, has a reported lift-to-drag ratio of 19 whereas the fruit fly, which has a span of 6 mm, has a ratio of 1.8” (Alexander 2002). Another option to continue flying without excess wing motion would be to soar, where the bird would maintain its altitude or even ascend by using rising air currents. “Biological flyers also tilt their flapping stroke plane: down and forward on the downstroke and up and backward on the upstroke. To fly faster, biological flyers make the stroke more vertical by increasing the up-and-down amplitude of the movements. When biological flyers decrease their speed, they tend to flap their wings more horizontally, similar to the way helicopters change their rotors” (Shyy et al. 2008). Relevant data of a variety of insect species is shown in Table 1.1, the data is tabulated to provide an insight of the large range of masses, flapping frequencies and total wing areas among other parameters.

| <b>Insect</b>                           | <b>Mass (mg)</b> | $S_T(mm^2)$ | $S_{BF}(mm^2)$ | <b>R (mm)</b> | <b>f (Hz)</b> | <b>V (m/s)</b> | $L_B$ (mm) | <b>AR</b> | <b>k</b> |
|---|------------------|-------------|----------------|---------------|---------------|----------------|------------|-----------|----------|
| <i>Diptera (Tabanus Borinus)</i>        | 276              | 184         | 63             | 15.5          | 96            | 4              | 23         | 5.32      | 0.244    |
| <i>Diptera (Sarcophaga Carnaria L.)</i> | 45               | 36          | 12             | 7             | 160           | 2              | 12         | 5.44      | 0.281    |
| <i>Diptera (Musca Domestica)</i>        | 12               | 20          | 4.5            | 5.5           | 190           | 2              | 6.5        | 6.05      | 0.210    |
| <i>Hymenoptera (Bombus Terrestris)</i>  | 388              | 142         | 74             | 16            | 130           | 3              | 19.5       | 7.21      | —        |
| <i>Hymenoptera (Vespa Germanica)</i>    | 187              | 98          | 29             | 14            | 110           | 2.5            | 18         | 8         | 0.16     |
| <i>Hymenoptera (Apis Mellifica L.)</i>  | 78               | 42          | 27             | 8.5           | 250           | 2.5            | 13         | 6.88      | —        |
| <i>Lepidoptera (Papilio Podalirius)</i> | 300              | 3600        | 52             | 37            | 10            | 3.5            | 25         | 1.52      | 0.54     |
| <i>Lepidoptera (Pieris Brassica L.)</i> | 127              | 1840        | 35             | 31            | 12            | 2.5            | 23         | 2.09      | —        |
| <i>Lepidoptera (Plusia Gamma L.)</i>    | 144              | 440         | 36             | 18            | 48            | 1.5            | 19.5       | 2.95      | —        |

Table 1.1: *Insect Data for Various Species (Azuma 2006)*

### 1.3 Insect Thorax Structure and Flapping Muscles

MAV designers must keep in mind that to directly replicate an insects muscular structure and flight concepts will not lead to a micro-robotic device which will perform exactly like an insect in flight. As researchers we need to understand and manipulate their flight mechanisms and use existing as well as novel technology to develop an MAV which has the ability to fly like an insect. “For their size insects are very efficient fliers. The ratio of power input to power output lies between 4% and 15% for insects in flight. The same ratio for birds like starlings and pigeons is around 10%, but physiologically the efficiency of muscle increases with increasing body size for all types of locomotion. Based on this relationship, we would expect insects to fly at lower efficiencies, between 1% and 2%, because their smaller muscles have to move faster and so would have higher costs associated with the chemistry of muscle contraction” (Goodman 2003).

The insect anatomy can be categorised into three body sections known as the head, thorax and abdomen. The internal part of the head houses the insects brain, whereas the external structure consists of the eyes and antennae. The thorax consists of the muscular parts acting as a driving mechanism for its legs and wings. And finally the abdomen contains the reproductive and digestive systems. The flight muscles are specifically found in the pterothorax. The maximum load lifting capacity for a variety of flying animals, from tiny bugs to bats and birds, has been measured by attaching progressively larger weights to their bodies and encouraging them to take-off. “It was found that all the animals could lift somewhere between 10% and 300% of their own body weight, with birds and bats at the lower end of the range and insects like butterflies and damselflies, known to use the clap and fling mechanism of lift enhancement, at the higher end of the range. Insects are better at lifting than birds or bats because a higher proportion of their body mass is flight muscle (20-50% of mass, compared with less than 20% for vertebrates)” (Goodman 2003).

“Mechanically driven systems of given stiffness and damping (internal resistance to motion) exhibit resonant oscillatory frequencies at which advantageous energetic expenditure is highest. Any mechanical system can be driven at a frequency different from the resonant frequency, but the driving force is then out of phase with motion of the structure or object in question. The amplitude of oscillation is reduced considerably and substantial energy is dissipated in non-useful work. The presence of the elastic recoil within the thorax and antagonistic action between wing depressors and elevators suggest that the insect flight thorax is a mechanically resonant system driven periodically through muscular contraction” (Dudley 2002).

“The presence of elastic elements within the pterothorax is of particular importance for flight energetics. Such elements stretch at the end of a down or upstroke (i.e. at the end of any given half-stroke) and store wing kinetic energy as strain energy. This energy is subsequently released and contributes to the generation of subsequent half-strokes. Such action is energetically important because a major component of power expenditure during flight is the inertial energy required to accelerate the wings during each half-stroke” (Dudley 2002). The flapping wing motion can be produced via two methods in most insects, these are direct and indirect muscle systems. The direct flight muscles are linked directly to the wing, and contraction of these muscles creates a downwards flapping motion directly on the wing. The indirect flight muscles are composed of two sets known as the dorsoventral and dorsolongitudinal flight muscles. A diagram of this can be seen in Figure 1.3. The upper surface of the thorax is known as the notum which rises when the longitudinal muscles are contracted, and lowers when the dorsoventral muscles contract. Alternate contractions of these indirect muscles causes the thorax to flex with the notum continually changing its vertical direction of movement, resulting in the creation of a flapping motion applied to its wings. “In bees the direct muscles serve as steering muscles adjusting the rotational motion and other subtle movements of the wing during beating, through alteration of the mechanical configuration of the wing hinge sclerites and tensioning of the thorax” (Goodman 2003). The insects airspeed is monitored via its antennae, thus they use this part of their body as speed sensors.

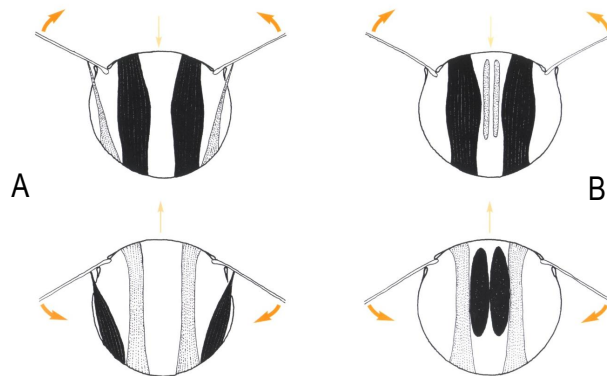


Figure 1.3: *Insect Flight Muscles; A: Direct and Indirect Dorsoventral Muscles, B: Indirect Dorsoventral and Longitudinal Muscles. Dark Muscles are Contracted, Light Muscles are Relaxed and Stretched, Dark Arrows are The Direction of Wing Movement and Light Arrows are The Direction of The Notum (Goodman 2003)*

The direct flight muscles are synchronous muscles which are activated individually, whereby there is a direct

correspondence between muscle contraction and output action in this case a flapping motion. Indirect flight muscles operate asynchronously in the manner of once they are activated via neural signal they will remain in this state and muscle contractions and relaxations will continue to occur until a stop signal is received. “Approximately three-quarters of the known insect species have asynchronous flight muscles. It follows, therefore, that asynchronous muscle powers flight in most animal species that fly” (Josephson et al. 2000). From the two types of muscles mentioned asynchronous muscles have the ability to operate at high frequencies as they can be activated and require no further input from the nervous system for continual contraction and relaxation movements. Synchronous muscles perform at lower frequencies due to the continual necessity of neural signals for muscle movements and this chain of information transfer is the core reason for lower frequency operation. “Myogenic muscles (also known as asynchronous muscles) allow greatly increased wing-beat frequencies than would be possible in a neurogenic system which, because of the inherent delays in the neuro-muscular activation chain, are unlikely to exceed 100 Hz whereas 1000 Hz has been recorded in small flies such as gnats which possess myogenic muscles. While a bee is in flight, 80% of the energy consumed by the flight muscles is lost as heat, and up to half of the remainder is spent accelerating and decelerating the wings. This means that only 5-10% of the energy consumed by a flying bee actually goes into generating the aerodynamic forces necessary for flight” (Goodman 2003). The wing root is a multi-degree of freedom joint which rotates to produce flapping, pitching and deviation motions during a stroke cycle. The wings of insects do not have muscular features thus the deformation of the wings due to inertia and aero loading must be passively stabilised, and bending stiffness is aided by the venation formation of the wings.

## 1.4 MAV Applications

Researchers, engineers and hobbyists working in the field of MAVs are aware of the requirements a MAV should fulfil to be the answer for the future generation to use as an asset in a variety of tasks. In order to improve on the work already accomplished in this field, technology will need to advance as well as the scientists and engineers researching this field of aeronautics/robotics. These aerial drones need to be small and light weight similar to insects, thus distinguishable and hopefully a somewhat replication. A highly sought after function would be low noise levels, a robotic flying vehicle which can remain quiet in operation would prove to be suitable for an array of assignments. They should be slow speed flyers to achieve flight indoor, outdoor and in extremely confined areas. It should maintain impressive control features whilst flying

at such low speeds and be highly manoeuvrable in all applications of flight. Vertical take-off and landing are mandatory due to flight in cramped areas, in addition take-off and landing on various surfaces would be a desirable characteristic but at present not essential. Other traits a MAV should possess are efficiency, equipped with multiple sensors and a camera to provide important data. Using its sensors autonomous flight would prove to an admirable quality, but control via a remote device from a ground based pilot would be sufficient for the initial stage. Albeit, it should be borne in the readers mind that a device which would satisfy the aforementioned criteria does not exist at present and is unlikely to be produced in the near future. Having said this, the above are criteria which would form a near perfect FWMAV which is not a requirement for all applications, thus developing a FWMAV device which appeases most of the core characteristics from the above or consists of features that are required to carry out its job would be enough in most circumstances. In effect, this would suit scientists and engineers a lot more rather than designing a perfect device applicable to all applications. Another desirable trait would be driving the thoracic mechanism at resonance. Exploiting the functionality of resonance would in essence reduce the amount of energy spent by amplifying the stroke amplitude, fundamentally reducing payload or extending the duration of missions.

Flapping MAVs are suitable for a wide variety of applications which is explained below, as far such a device has not been sent out for missions for which a quad rotor drone can fulfil as research for such small aerial vehicles is still young and slowly progressing from its preliminary stages. As research in the field of insect flight MAVs continually advances, these devices will be deployed for rescue missions and reconnaissance. In many situations it may not be safe for a human life to enter certain places or be within a certain radius, in such circumstances the importance of MAVs would be immeasurable to avoid fatal incidents.

#### ***Space Investigations:***

MAVs due to their small size, lightweight, efficiency, ability to take-off and land on a selection of surfaces (when replicating biological flight) would be a suitable tool to explore in space. Installed with various sensors and visual equipment it could collect vital information from aerial as well as ground position. Its hovering technique would allow visual mapping, thus scientists could gather large amounts of data, such tasks cannot be accomplished by a ground based vehicle or one that cannot hover with incredible control characteristics.

#### ***Reconnaissance:***

A small lightweight aerial device with insect flight characteristics would be invaluable to defence institutions. The number of casualties can be vastly reduced by deploying such a device to collect information such as

positioning of the enemy, weapons and equipment the enemy are using for combat and other relevant information. Adopting the appearance of an insect would be highly advantageous for spying missions where priceless information can be gathered via the FWMAVs on-board camera and microphone systems. Surveillance tasks involving monitoring the activities and movements of terrorist organisations or even individuals would immensely assist the security authorities of all governments. Exploring sites where mines have been planted to save lives of soldiers. These are only some of the military and defence tasks which a FWMAV can accomplish.

#### ***Investigations of Hazardous Areas:***

Locations where radioactive elements have leaked or chemical spillages have occurred. In such situations, it would be dangerous for humans to enter without appropriate equipment and attire, employing a MAV would help gather significant information and even resolve the problem without a human entering the hazardous site.

#### ***Rescue Explorations:***

As aforementioned these machines would prove to be invaluable when used in situations which involve collapsed buildings, buildings with uncertain structural integrity, rescue searches for survivors after a natural disaster has occurred. In such circumstances time is extremely limited and searching for survivors over a large area can prove to be a difficult task. MAVs provide the option of aerial vision and moving close towards the ground, into confined spaces, manoeuvring around obstacles seeking out human life using thermal mapping equipment and providing feedback to rescue teams of the vast data gathered via its on-board sensors and cameras. Large groups of these micro robotic flyers can be deployed in order to examine large areas rapidly and efficiently.

#### ***Accident Traffic Monitoring:***

Locations which are statistically prone to road vehicle accidents can be monitored and the level of accidents can be reduced by reducing congestions, monitoring problems with traffic flow and rectifying any situations which are of concern or will be of concern in the foreseeable future. If an accident occurred, the device could approach near ground level, collect and transmit feedback to its headquarters where ambulance and police authorities could be notified. If a vehicle is partly crushed, due to its small size and manoeuvring skills the FWMAV could enter the vehicle (without touching any obstacles which can cause further structural concerns) and report the condition of the passenger(s) via images and data from its sensors.

## 1.5 Various Types of MAVs

An assortment of MAVs exist which originally had to satisfy specific dimensional and mass constraints of 150 mm maximal dimension or smaller and less than 100 grams respectively. Numerous toy aerial vehicles can be purchased from commercial hobby stores, and manufacturers have introduced a large variety of toy indoor flyers. As expected, these are not suitable for the applications mentioned previously.

### 1.5.1 Fixed Wing Aircraft and MAVs

#### *Pointer FQM-151A:*

Fixed Wing UAVs have been in production for a very long time and have established their position in the UAV community. In 1986, AeroVironment released a hand launched UAV known as Pointer FQM-151A (Figure 1.4) which would allow soldiers to have a view over the forthcoming hills, this aircraft was used for light military operations to reconnoitre. AeroVironment has developed numerous UAV devices for defence purposes, most of which have been fixed-wing aircraft models. Refer to (AeroVironment Inc C) to find information of many other UAVs designed by AeroVironment.

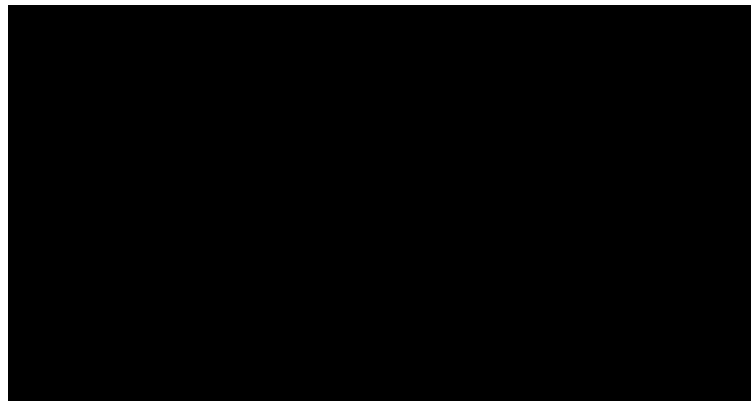


Figure 1.4: *Pointer FQM-151A (AeroVironment Inc A)*

#### *Black Widow:*

AeroVironment developed a fixed-wing MAV model formed of a simple wing shaped body with active control surfaces and a propeller positioned in the centre of the leading edge, this was known as the Black Widow (Figure 1.5) and the US Tech company claim that this was the first operating MAV system in the world.

This gadget weighed in at approximately 85 grams, with a span of 15 cm and could be launched from its carrying case which was a protective cassette. When launched the MAV had a flight duration of over 30 minutes, for a distance of up to 1.8 km and approaches speeds up to 30 mph. The aircraft was loaded with numerous sensors to collect relevant data and a camera which transmits its visual data to the remote pilot. Refer to (AeroVironment Inc B) and (Grasmeyer & Keennon 2001) for more information. Specialists in the field of UAVs, the engineers at AeroVironment had to reduce the size of all the avionics equipment and cram them into a payload capacity which was vastly reduced compared to the large fixed wing UAVs.



Figure 1.5: *Black Widow* (AeroVironment Inc B)

***Wasp III:***

Another UAV developed by AeroVironment has a wing span of 72 cm, and a weight of 430 grams. The Wasp III (Figure 1.6) performs autonomous flight, has a high resolution camera with zoom and tilt functions which can be hand-launched. It can fly up to speeds of 24-40 mph and travel for a duration of 45 minutes. For more information on the Wasp III aircraft, refer to (AeroVironment Inc D)

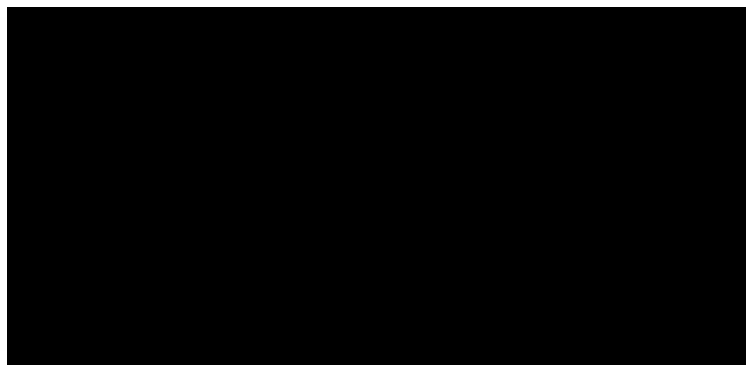


Figure 1.6: *Wasp III* (Designation Systems)

***Wasp AE:***

A larger and improved version of the Wasp III was created, which was designed to fly in all environments, and fly for a longer duration. This model has a wing span of 102 cm and weighs in at 1.3 kg. In addition to the hand-launch method mentioned above, the Wasp AE (Figure 1.7) can also be remotely launched. It has a cruising speed of 23 mph and can perform a dash when required up to speeds of 51 mph. Refer to (AeroVironment Inc E) for further details of this aircraft.

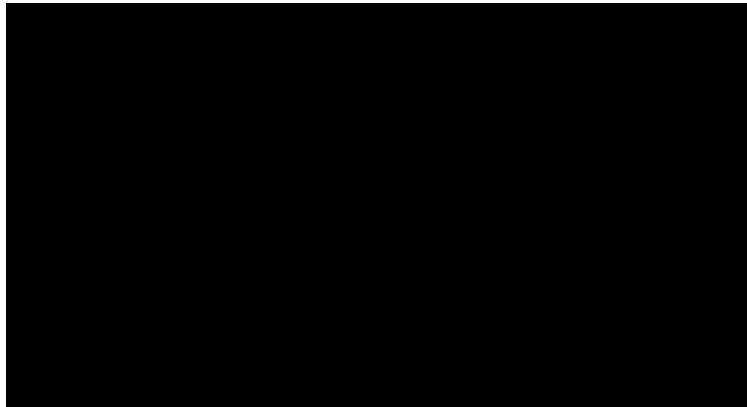


Figure 1.7: *Wasp AE (AV media gallery)*

***Gust Resistant MAV:***

Researchers at Warsaw University of Technology have put their efforts into developing a fixed-wing MAV (Figure 1.8) which is resistant to gust. In outdoor flight a MAV can experience vertical gust which may subject the vehicle to a high angle of attack or near stall manoeuvre, limiting the vehicles flight capability. Attempting to rectify the problem in hand, they opted to design a MAV which has a very high stall angle of attack. A cranked delta wing configuration with a propeller placed within it was tested experimentally in wind tunnel studies which determined that with the motor ON the CL is higher for AOAs of 8-30 degrees compared with results of motor off. With this data in mind flight tests were performed which showed that the model was able to fly controllably at very high angles of attack. Further work was needed as the MAV would tend to drift which was a result of rpm changes of the propeller's motor, nonetheless they seemed to find a work around which was proposed as future work. Refer to (Galinski et al. 2010) for further information.



Figure 1.8: *Gust Resistant MAV* (Galinski et al. 2010)

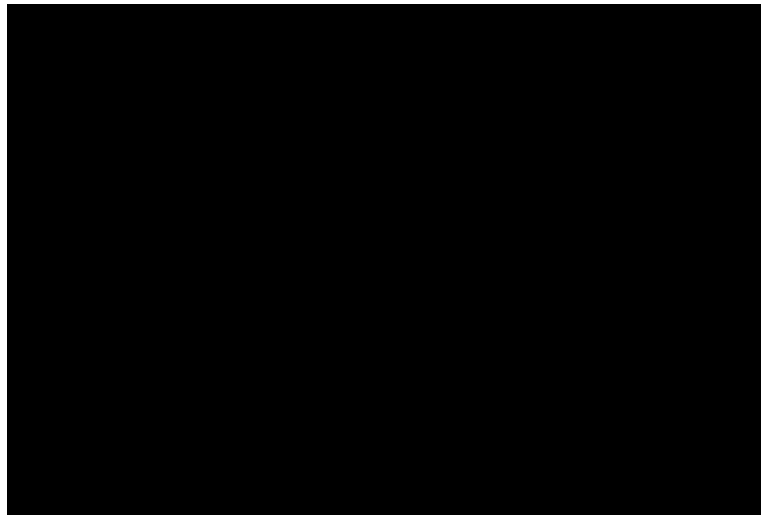


Figure 1.9: *Carbon Butterfly* (Plantraco A)

***Carbon Butterfly:***

Plantraco is a company based in Canada, who stock small scale and lightweight parts for aerial vehicle applications. Along with parts they also manufacture MAVs which can be commercially purchased. The Carbon Butterfly (Figure 1.9), is Plantraco's own creation which can be flown indoors and has been developed

using the components which they sell. Although slightly larger than a MAV this aerial gadget has a wing span of 19 cm, is extremely light at 3.6 grams, with its structural frame and wings constructed of carbon fibre and mylar respectively. Its average flight time is 10 minutes but has been reported to be airborne for longer durations.

***Micro MAV Chevron:***

Another aerial invention by Plantraco is the Micro MAV (Figure 1.10), similar in appearance to the Black Widow it is a single wing MAV with a propeller located at the front. A small wingspan of 11.4 cm below the requirement of a MAV and very lightweight at 4 grams, this aerial toy can be used indoors with cruising speeds of approximately 1.5-2 m/s. The body is constructed of durabatic foam and it has a flight duration of 6-10 minutes. Keep in mind all of Plantraco's MAVs are toys used mainly by hobbyists.

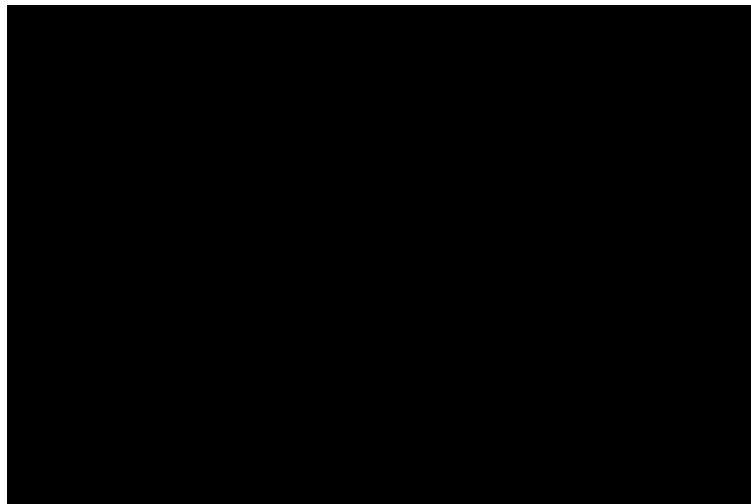


Figure 1.10: *Micro MAV Chevron (Plantraco B)*

## 1.5.2 Rotary Wing Aircraft and MAVs

### *MAV-07:*

Prox Dynamics founded by Petter Murren, is a technology company specialising in MAVs. Numerous contributions have been made by Prox Dynamics more so in the field of rotary wing MAVs. The MAV-07 (Figure 1.11), is a micro coaxial helicopter which is a radio controlled device with an on-board camera transmitting feedback to its grounded pilot for navigation. It utilises a gyro and passively stable rotor system to gain sufficient stability. The helicopter has a rotor diameter of 160 mm, length of 180 mm, weight of 30 grams and a flight duration of 10 minutes. Considering the fact that the MAV has four coreless motors, two of which are used for the main rotor and the remaining for control devices, this helicopter has a low flight weight.

### *Picoflyer:*

The Picoflyer (Figure 1.12) operates with a passively stable rotor system, but does not have a gyro. At the time of production this was presented as the worlds smallest radio controlled helicopter. This is another production by Prox Dynamics which is operated by a remote pilot but needs to be viewable when in operation, as there is no camera fitted. This helicopter includes a very small rotor of 60 mm in diameter, length of 85 mm, flight weight of 3 grams and a flight duration of 2-3 minutes.

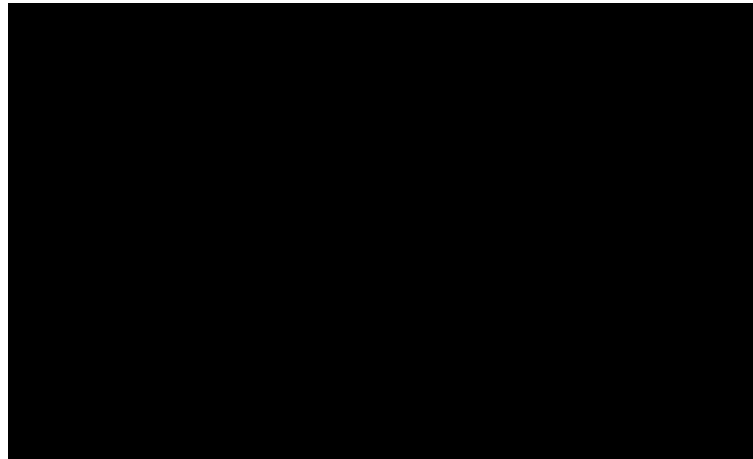


Figure 1.11: *MAV-07 (Prox Dynamics A)*

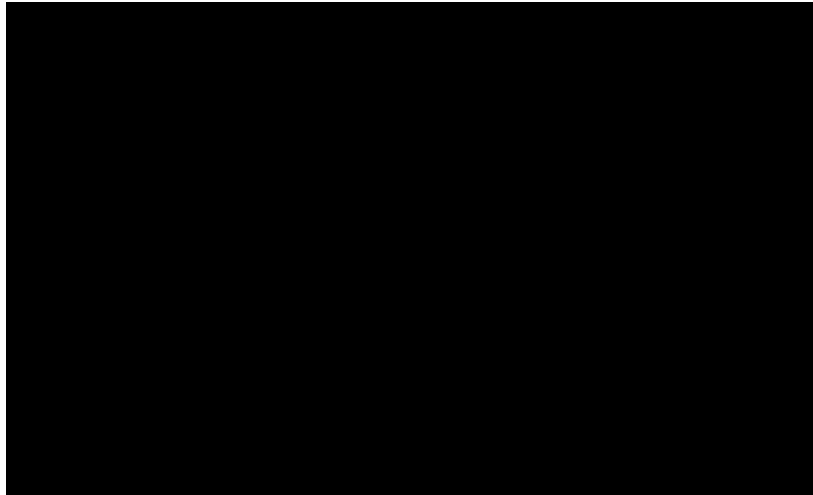


Figure 1.12: *Picoflyer (Prox Dynamics A)*

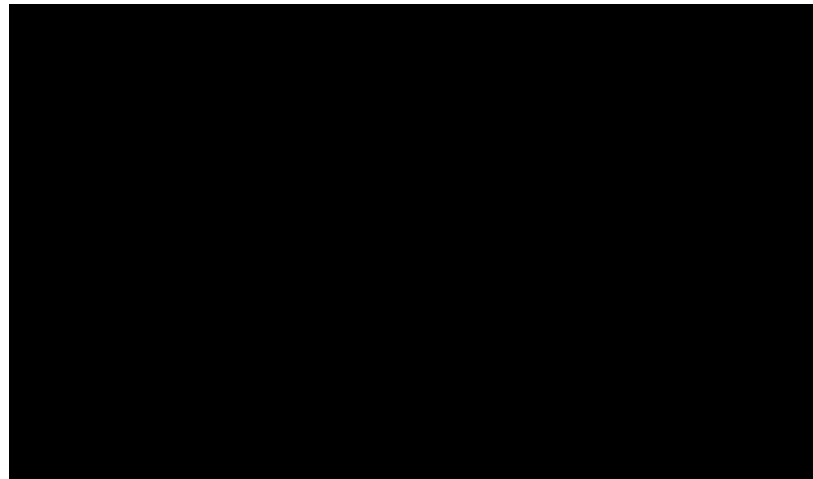


Figure 1.13: *1 Gram Helicopter (Prox Dynamics A)*

***1 Gram Helicopter:***

Another tiny helicopter produced by Prox Dynamics was the 1 Gram Helicopter (Figure 1.13), which has a rotor diameter of 70 mm, was extremely lightweight, a length of 85 mm and a flight duration of less than a minute. A very small battery was fitted to this due to weight limitations which consequently affects the

flight duration. This helicopter is operated by a single channel board and navigated by a remote pilot, but the device needs to be viewable by the pilot when in flight. Refer to (Prox Dynamics A) and (Muren 2008) for more information on the MAVs developed by Prox Dynamics.

***Skybotix Autonomous UAV Micro Helicopter Drone:***

The Skybotix Auto UAV Helicopter Drone (Figure 1.14), was designed for educational and research purposes. It carries an on-board motherboard, which is the smallest and least expensive Linux computer available at the time of production. The helicopter has a blade span of 340.8 mm, height of 168.4 mm and width of 165.1 mm. It can perform autonomous flight for up to 20 minutes and equipped with its full configuration it has a mass of 340 grams. To aid stability it holds a dual axis gyroscope for both roll and pitch axes. A 1D gyroscope is also on-board which operates in the vertical direction (Z axis). There are two types of cameras installed and images are sent via WiFi. Refer to (Skybotix Helicopter Robot Shop A) and (Skybotix Helicopter Robot Shop B) for more information.

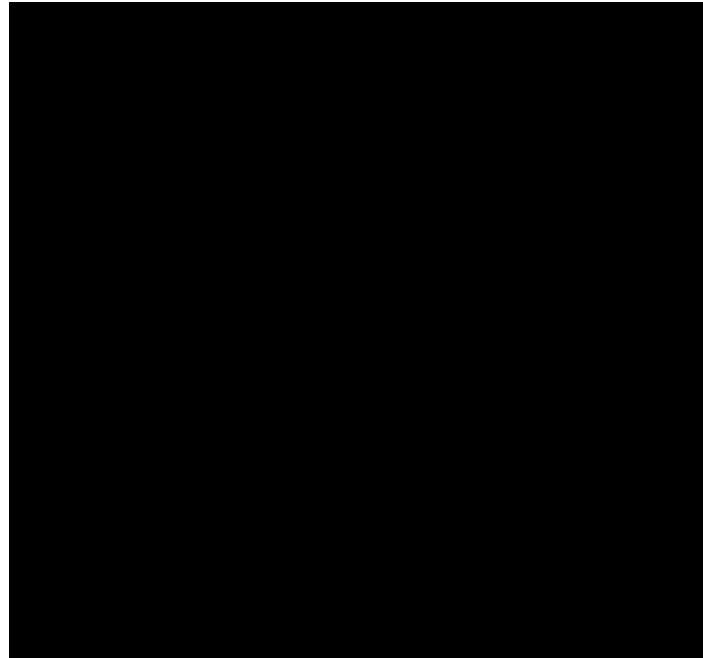


Figure 1.14: *Skybotix Autonomous UAV Micro Helicopter Drone (Skybotix Helicopter Robot Shop B)*

***Xtreme 2.0 Gen II Quadcopter:***

The Xtreme 2.0 Gen II Quadcopter (Figure 1.15), is an aerial vehicle whose design was based on the traditional helicopter but consists of 4 rotors which enhance its overall stability even in hover mode. In terms of size this particular model is quite large with dimensions of 610 mm x 610 mm x 305 mm which are length, width and height respectively. Holding 4 motors, 4 ESCs, a camera, transmitter, control and stability components, in addition to its toughened framework including its landing gear, the model weighs slightly above 4.5 kg. The protective outer circular guards around the rotor protect the blades from any damage if the model was to collide with any obstacle or crash land due to zero battery life. Furthermore, working alongside today's tablet PC technology it can be controlled by an iPad. Refer to (Xtreme Quadcopter Robot Shop) for further information.

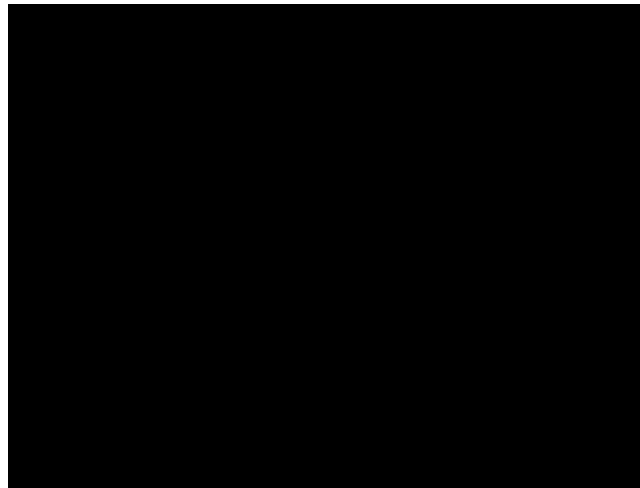


Figure 1.15: *Xtreme 2.0 Gen II Quadcopter (Xtreme Quadcopter Robot Shop)*

### 1.5.3 Flapping Wing Aircraft and MAVs

Details of the FWMAV models is provided here in brief, a detailed analysis involving experiments and improvements to the models will be provided in the literature review chapter of this thesis.

#### ***1 Gram Ornithopter:***

Prox Dynamics has also developed a flapping wing MAV which they released in 2007. The FWMAVs wings are actuated via a single motor-gearbox arrangement, where the motor is controlled by the on-board single channel receiver and is operated via a remote pilot that needs to have the model in sight at all times. The 1 gram ornithopter (Figure 1.16), has a wing span of 100 mm, length of 85 mm and a flight duration of less than one minute. The MAV has a flight weight of 1.1 grams and sports a tail which aids its stability in flight. The wing membrane would flex according to the aerodynamic loading acting on it, coincidentally this would set its angle of attack which would vary with wing stroke position as do most MAVs / ornithopters that adopt a highly flexible material for its wings. See (Prox Dynamics B) for further information regarding this model.

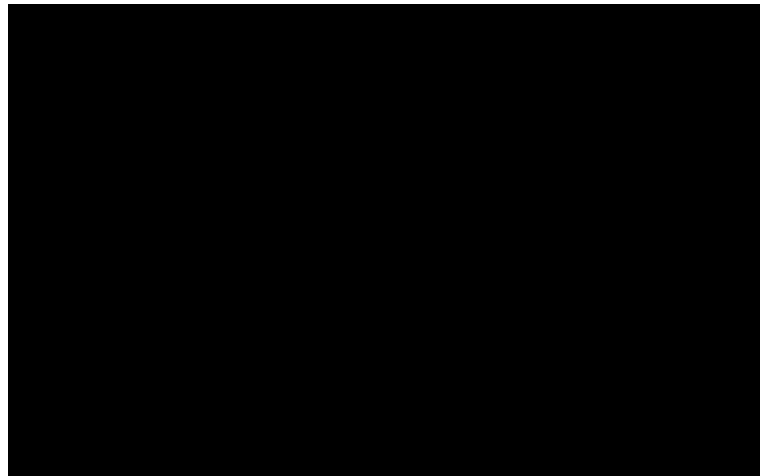


Figure 1.16: *One Gram Ornithopter (Prox Dynamics B)*

#### ***MFI:***

The University of California, Berkeley developed its own MAV more commonly known as the MFI (Figure 1.17). Scientists at Berkeley have been working on this MFI model since 1998 as stated in (Steltz et al. 2007). Their optimum goal in short was to create a flying vehicle which can mimic insect flight and perform this role at the scale of an insect. Via experimentation and improvements they arrived at a model which had

the ability to flap its wings at 275 Hz and produce a lift force of 1.4 mN from a single wing. This was a significant improvement from their previous work which reported a lift force of 0.5 mN from a single wing which flapped at 160 Hz (Avadhanula et al 2003). By reducing the wing inertia leads to an increase in the resonant frequency of the thorax, the piezo actuators stiffness was increased, in addition to other favourable modifications the end result demonstrated an increase in flapping frequency. The mechanism is composed of two four-bar linkages, that amplify the minor linear displacement provided by the piezo actuators to result in a wing flapping and rotation motion. Each wing needs two piezos, thus the complete MFI uses 4 piezo actuators. See (Avadhanula et al 2003) and (Steltz et al. 2007) for further details.

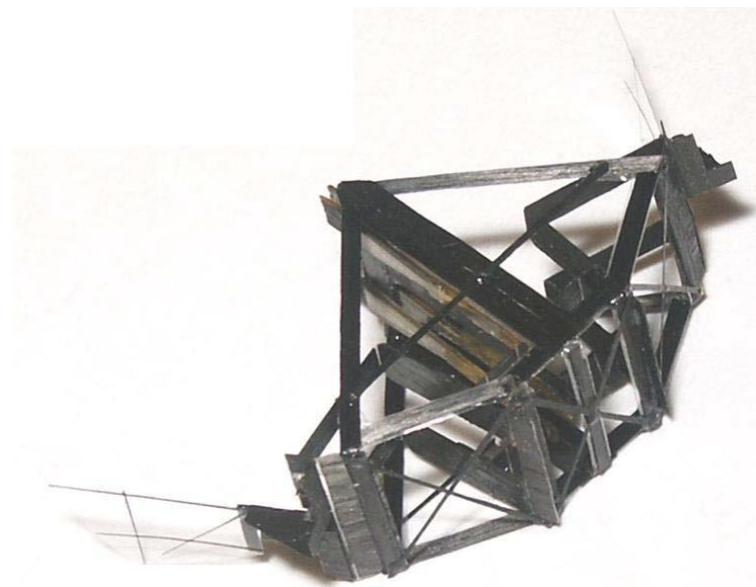


Figure 1.17: *Micromechanical Flying Insect* (Steltz et al. 2007)

### ***Microrobotic Fly - RoboBee:***

Harvard University has their own version of a tiny, lightweight MAV which like the Berkeley model utilises flexures for its mechanical linkage thorax structure. The outcome from the research produced an insect scale MAV (Figure 1.18) which could lift its own weight when powered by an external power source. Their model has a mass of only 60 mg and 30 mm wing span. This was reported as the first insect-sized MAV to lift its own weight (Wood 2007). Wood's optimum goal like Berkeley was to produce an insect like MAV which possesses the flight characteristics of an insect and furthermore at insect scale. The thorax mechanism was actuated by a single piezo which had a mass of 40 mg, which accounted for two-thirds of its total flight mass. The remaining 20 mg of mass is made up of the transmission, wing and airframe. The MAV had a

flapping stroke of approximately 110 degrees, a wing rotation of 50 degrees at mid-stroke for both down and up-strokes at a flapping frequency of 110 Hz. Its large stroke amplitude along with adequate wing rotation is a massive advantage in terms of aerodynamics. Taking advantage of the aerodynamic enhancements that some biological flyers experience the wings of this MAV have fairly constant AOA for a sufficient amount of time during the translation phase of both strokes, aiding in the growth and stabilisation of the LEV. However, the aerodynamics cannot be sufficiently analysed without fluid visualisation. Further details of this model can be found in (Wood 2007), (Wood 2008a) and for a video demonstration of its wing motion see (Wood 2007a).

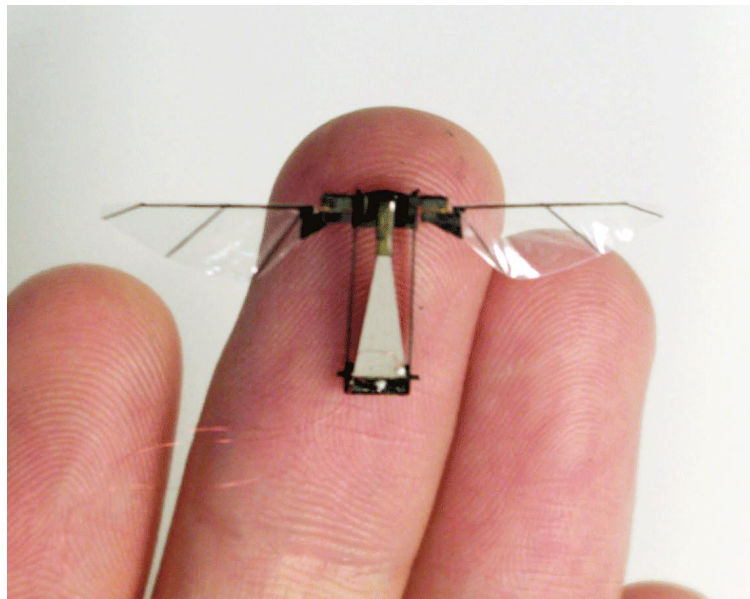


Figure 1.18: *Microrobotic Fly - RoboBee* (Wood 2008a)

### ***i-Fly Vamp:***

The toy market has also released its versions of flying flapping vehicles such as the i-fly Vamp (Figure 1.19) which is a product of Interactive Toys. The toy is radio controlled by the grounded pilot who needs to be in line of sight of the vehicle in order to navigate it. A single set of wings are actuated by a motor-gearbox configuration, its flight weight is 13 grams, a wing span of 265 mm, length of 215 mm and a flight duration of approximately 10 minutes. They also released an i-fly Wasp which had the same specifications but a different appearance. It has been claimed that control is carried out by the wings rather than the tail which is more common among MAVs of this type, as their flight mode is closer to that of birds rather than insects. See (Remote Controlled Toys) for further details which includes a video demonstrating the i-Fly Vamp in

flight. Commercial toy flapping models are difficult to control in flight whereby the users efforts are usually focused on keeping the flapping machine airborne, rather than directing it and manoeuvring it in the desired directions or through a specified flight path.

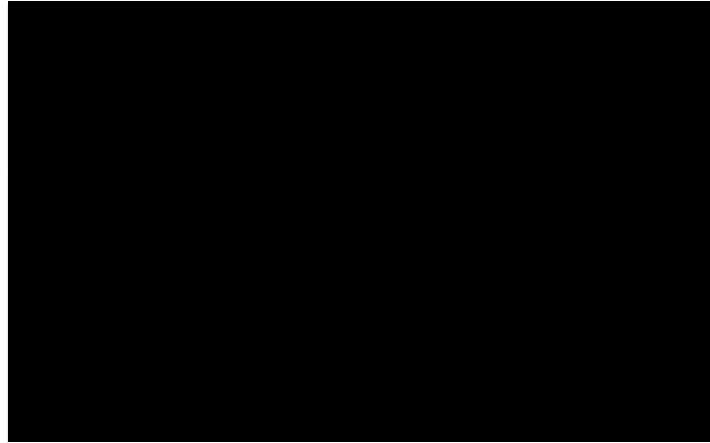


Figure 1.19: *i-Fly Vamp* (Go Radio Controlled)

***Microbat:***

According to Pornsin-Siriak et al (Pornsin-Sirirak et al. 2001), Microbat (Figure 1.20) was the first electrically powered aerial vehicle to take to the air. They developed three versions of the Microbat which had a different power source and the final model had a R/C system. Its flapping behaviour is similar to that of a bird and a flexible membrane allows for wing deformation in effect creating an angle of attack, which is controlled by the aerodynamic loading acting on the wings surface. In all, its design is based on a traditional ornithopter similar to the i-fly vamp, one gram ornithopter and numerous others reviewed below. The flapping arms were actuated by a DC-motor and gearbox configuration. The first version (Figure 1.20A) of the Microbat had a super capacitor powered electric motor, which has a flight weight of 7.5 grams and its free flight duration was only 9 seconds. As this was far too short, a battery was used in the second version (Figure 1.20B) but due to the requirement of a DC-DC converter to step up the voltage required by the motor and the weight of the battery itself this version had a flight weight of 10.5 grams. The fuselage length was increased to aid stability and when tested it flew for 18 seconds. Increasing the wing span to 9 inches from the previous 6 inches led to an even longer flight duration of 22 seconds. The final Microbat version (Figure 1.20C) retained the longer wingspan and had a flight weight of 12.5 grams, many components were improved to reduce the flight weight but the addition of R/C components meant that its weight would

still be higher than the previous version. A ground based pilot would now have control over the throttle, elevator and rudder whilst navigating it when airborne. This aircraft had a flight duration of 42 seconds, with sufficient improvements implemented such as weight reduction the flight duration will increase. With a function such as motor on/off under the pilots control during flight would have a huge long term benefit for flight duration as future vehicles with the ability to glide could take advantage of this.

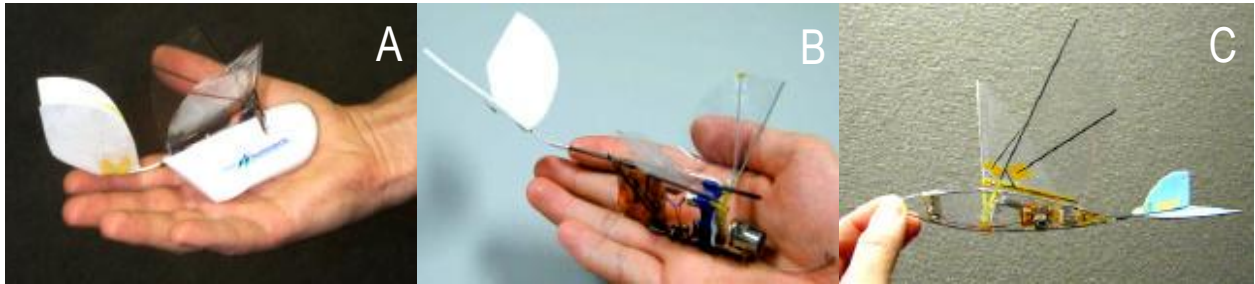


Figure 1.20: *Microbat*; A: *Super Capacitor Powered*; B: *Battery Powered*; C: *Battery Powered with R/C Navigation* (Pornsir-Sirirak et al. 2001)

#### ***Beetle Mimicking Flapper:***

Konkuk University have been actively researching insect flight through experimentation to develop a MAV which could possibly fly. As far, they created a MAV (Figure 1.21) based on a beetle which is a fairly large creature with a sufficient body size that allows for adequate space to house mechanical and electrical components. A typical male beetle has a wing span of 129 mm, with body dimensions of 48 mm x 24 mm which are the length and width respectively. A male biological beetle has a weight of 6-10 grams and a flapping frequency of approximately 35-40 Hz. Their MAV was composed of mechanical linkages which were actuated by a small DC motor and carried its own power supply in the form of a lithium battery. The mass of the MAV was 5.71 grams which rose to 10.26 grams with the inclusion of the battery. It had a wing span of 125 mm, the body length and heights were 35 mm x 22 mm respectively. With a flapping frequency of 17 Hz, they decided that improvements were needed with the change of a motor to one which has a higher stall torque. The flapping frequency is affected by the aerodynamic and inertial forces acting on the wings, these resistive forces are transferred to the linkage arrangement which transmits resistive forces on to the driving mechanism, thus improving the stall torque of the motor would assist with the problem in hand. Installing a different motor augmented the flapping frequency to 25 Hz, with a very small addition in weight. Their second version had the same dimensional properties with a flight weight of 10.37 grams (including its power

source). Overall this led to a vertical increase in flight force by 50%. The biological beetle has extremely large flapping angles of 180 degrees during hovering flight with a flapping frequency of approximately 37 Hz and 165 degrees for forward flight with a flapping frequency of approximately 34 Hz. For both flight modes the beetle has a wing rotation angle of 140 degrees. This data was found from (Nguyen et al. 2010a). Konkuk's mechanical flapper had a flapping angle of 148 degrees and a wing rotation of 105 degrees, the wing rotation increased in accordance with the flapping frequency to 115 degrees for the second version of their MAV. Further information regarding their model and experimental work can be found in (Nguyen et al. 2009), (Nguyen et al. 2010a) and (Nguyen et al. 2010b).

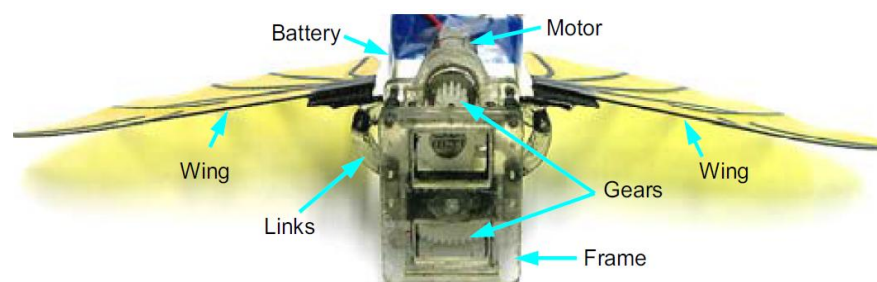


Figure 1.21: *Beetle Mimicking Flapper* (Nguyen et al. 2009)

### ***Konkuk Ornithopters & MAVs:***

Park and Yoon of Konkuk University, developed four flying vehicles with spans ranging from 360 to 100 mm, with weights ranging from 50 to 4.32 grams respectively, all shown in Figure 1.22. They constructed 2 winged (monoplane) and four winged (biplane) models which were all actuated via linkage-motor combination. The smallest model (Figure 1.22 D) which sports a wing span of 100 mm, had the highest flapping frequency of 35 Hz, but it also had the shortest flight duration. The largest model (Figure 1.22 A) had a wing span of 360 mm, flight weight of 50 grams, with a flapping frequency of 20 Hz, its flapping amplitude was 30 degrees and its flight duration was 15 minutes. Their second model with a reduced wing span of 280 mm (Figure 1.22 B) had a flight weight of 30.6 grams, flapping frequency of 24 Hz, a flapping amplitude of 35 degrees and a flight duration of 8 minutes. The third model (Figure 1.22 C) had a wing span of 150 mm, flight weight of 8.7 grams, flapping frequency of 30 Hz, and a stroke amplitude of 45 degrees, these properties produced a flight duration of 1 minute. The final model (Figure 1.22 D) was the smallest they produced which consisted of four wings with a total wing span of 100 mm, flight weight of 4.32 grams, a total flapping amplitude of 60 degrees and a flight duration below 30 seconds. A lighter gearbox and motor along with a

battery of larger capacity should lead to an extended flight duration. The largest ornithopter (Figure 1.22 A), is capable of landing and take-off within 3 m, it has an on-board camera to view its surroundings and can offer visual surveillance on missions. The ornithopter in Figure 1.22 B was reduced in size and the fuselage frame removed to reduce weight. The purpose of this model was to possess high speed and manoeuvrability, due to the latter they opted to have a rudder and elevator that both deflect under the pilots authorisation. All the models create a single flapping wing motion, where the flexible membrane surface deforms during wing motion and produces a relative angle of attack. See (Park et al. 2008) for further information.

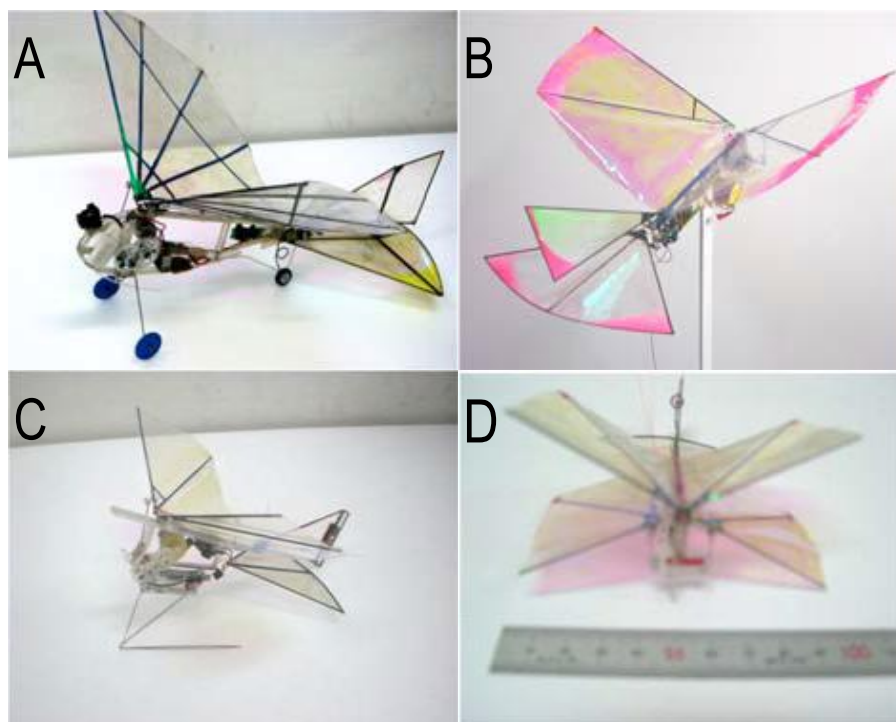


Figure 1.22: *Konkuk Ornithopters & MAVs; A: 360 mm Wing Span; B: 280 mm Wing Span; C: 150 mm Wing Span; D: 100 mm Wing Span (Park et al. 2008)*

***Nano Hummingbird:***

AeroVironment widely known for specialist skills in designing miniature fixed winged aircrafts as previously reviewed, developed a flapping wing NAV Hummingbird (Figure 1.23), which has a wing span of 160 mm and a total flight weight of 19 grams. AeroVironment were awarded a 5 year contract from DARPA to design a NAV which has the flight characteristics of a hummingbird. The NAV Hummingbird has a flight duration of 5-11 minutes, and capable of flight in directions such as forward, backwards, left and right. The NAV

can descend and climb vertically as well as rotate in both directions around its vertically aligned body. The wings flap along a horizontal stroke plane actuated by a configuration of linkages and motors. It carries an on-board daylight colour video camera, transmitter and power source. Furthermore, the NAV can hover with stability by using aerodynamic characteristics of an actual hummingbird. See (AeroVironment BBC) and (AeroVironment Inc F) for further information regarding this FWNAV.



Figure 1.23: *Nano Hummingbird* (AeroVironment Inc G)

### ***Delfly:***

Delft University have produced three of their own flying flapping vehicles. The Delfly I (Figure 1.24 A) is the largest of the three models with a wing span of 500 mm, flight weight of 21 grams, with a stroke amplitude of 25 degrees and a flapping frequency of 12 Hz. This vehicle was equipped with an on-board camera including a video transmitter to allow visual observation of its surroundings and to construct a control loop between itself and the ground controls via PC. A weakness was that when the model performed fairly tight turns with a low angle of attack it would start to spiral dive. Delfly I, was operated by a coreless pager motor which would wear out very quickly, due to low efficiency that led to overheating. This led to the second phase which was the creation of Delfly II (Figure 1.24 B) where the wing span was downsized to 280 mm, had a flight weight of 16 grams, a stroke amplitude of 35 degrees and an increased flapping

frequency of 21 Hz. This model had the ability to take-off and land vertically, loaded with a brushless motor which consumed less energy and provided enough power so that the model could hover. Overall the brushless motor is more efficient, durable and can reach higher power densities. Building on the lessons learnt from the design, and flight tests performed with the previous two delfly ornithopters, the smallest of their collection was formed known as the micro Delfly (Figure 1.25). The micro Delfly has a wingspan of 100 mm, with a flight weight of 3.07 grams, a stroke amplitude of 48 degrees and a flapping frequency of 30 Hz. The micro Delfly could not perform hovering mode flight, due to insufficient lifting forces which were down to the brushed motor overheating, this was the same problem revealed in the Delfly I, and the use of a brushless motor was not possible for the micro model due to brushless motors being larger and heavier. All the Delfly vehicles were of a biplane configuration equipped with a camera and video transmitter as these pieces of equipment were basic requirements for the developers. The micro Delfly performed a clap-and-fling motion to enhance its lift force, details about this aerodynamic mechanism will be provided in the next chapter of this thesis. Initially elastic rubber band powered models were constructed for obvious reasons such as simplicity and inexpensive in terms of both cost and time. They explored three designs known as the monoplane ornithopter, biplane ornithopter and tandem wing ornithopter, from this they concluded that the biplane configuration although slower than the monoplane would suit their purpose best as they wanted to place a camera on-board, thus the vehicle would need to be very stable in flight. For further information see (Delfly Website A), (Croon et al. 2009) and (Lentink et al. 2010).



Figure 1.24: *Delfly I: A* & *Delfly II: B* (*Delfly Website B*)

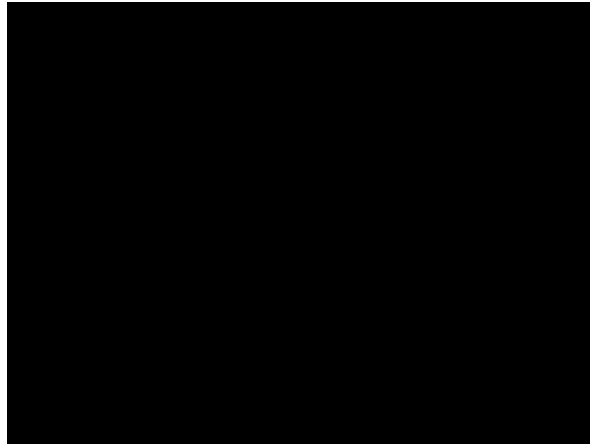


Figure 1.25: *Micro Delfly* (*Delfly Website C*)

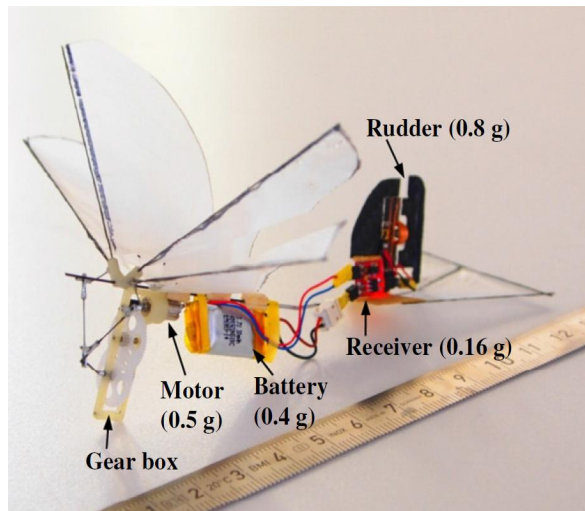


Figure 1.26: *Hummingbird MAV* (*Nakata et al. 2011*)

### ***Hummingbird MAV:***

Chiba University have a robotic flying vehicle through the work of H. Liu, whom developed a four-winged hummingbird-like-aerial vehicle (Figure 1.26) which flaps its wings at 30 Hz and has the ability to turn in four directions (up, down, left and right) and has a flight weight of 2.4-3 grams. The MAV has a wing span of 120 mm, where each wing is 60 mm in length with a chord at wing base of 30 mm. Each wing has a mean chord length of 23.6 mm. The driving mechanism of the flapping wings is similar to the system used in the Delfly MAV. Taking note from insect flight the hummingbird MAV adopts the clap-and-fling technique, where the top wings (on both sides) clap at the end of upstroke and at the end of down-stroke the top wings clap together with the bottom wings on their respective sides. After each clapping scenario a fling would take place (both of these should be regarded as separate mechanisms), as aforementioned this technique will be expanded upon in the next chapter. Through this four-wing design the wings come in contact with one-another on three occasions in a single flapping cycle. The hummingbird has a light weight linkage mechanism composed of thin metal links and is actuated by a small DC motor-gearbox configuration. The wings have a rigid leading edge with a flexible membrane surface which will deform under aerodynamic loads which act upon wing motion, when deformed the pressure generation under the wings surface will contribute to the production of lift and thrust forces. Another advantage is that flexible wings are also much lighter than rigid wings, which is vital when developing a MAV. Controllable flight offering a rotation to turn left or right is achieved by an active rudder system attached to the tail which is actuated by a micro electromagnetic actuator. These types of actuators have a history of providing a control method for small fixed wing aircraft, and are now commonly used for ornithopters and FWMAVs. The MAV carries an on-board battery to power both of its actuating devices and has performed a successful flight with a duration of 6 minutes, reaching a maximum height of 10 m, and covered an overall ground area of 20 m x 20 m when in flight. See (Nakata et al. 2011) for further details.

### ***Cornell MAV:***

Cornell University took an alternative approach in manufacturing parts for their MAV (Figure 1.27) by using a technique better suited for some of today's engineering applications. With the use of a 3D printer they created a four-winged MAV which are actuated by linkages that are connected to a small DC geared motor. This method of manufacturing allowed them to create wings of any geometry they desire, even a replication of insect wings, which can all be done in a matter of minutes, and an entire ornithopter can be manufactured in 60 minutes (Richter & Lipson 2011). This rapid turn around time would help advance

experimental work which usually requires a significant amount of time due to the long durations needed to manufacture components. A complete single piece wing with the inclusion of the skeletal features (to provide structural rigidity) was constructed as the printer had the capability to output a thin film for the wings membrane surface. Numerous wings were tested to perform investigations for the most desirable characteristics in terms of size, weight and lift force produced. The wings were quite difficult to maintain, as they tend to curl up after certain durations and dis-assembly of the model is required in order to place the wings under sufficient weight to retain its flat plate properties. Their MAV has a flight weight of 3.89 grams and demonstrated hovering for a duration of 85 seconds with the use of upper and lower stabilisers, thus a guide was not needed when hovering. Via experiments a single wing was tested with properties of 80 mm length x 30 mm maximum chord which produced a lift force of 2.92 grams by flapping its wings through a stroke amplitude of 110 degrees at 30 Hz, the total wing span was reported to be 143 mm. When hovering each wing of the MAV completed an 80 degree sweep for flapping angle and two Li-Po batteries were fitted to the model which powered the motor. Refer to (Richter & Lipson 2011) for more information.

Table 1.2, summarises some of the characteristics of the flapping MAV machines reviewed in this sub-section. The outright goal for this research community is to develop a MAV that incorporates the flight characteristics of an insect and beyond. From the work evaluated above monumental efforts have been dedicated to emulate insect flight. Progressions made to the models and experiments carried out to create some of these models will be reviewed in chapter 2.

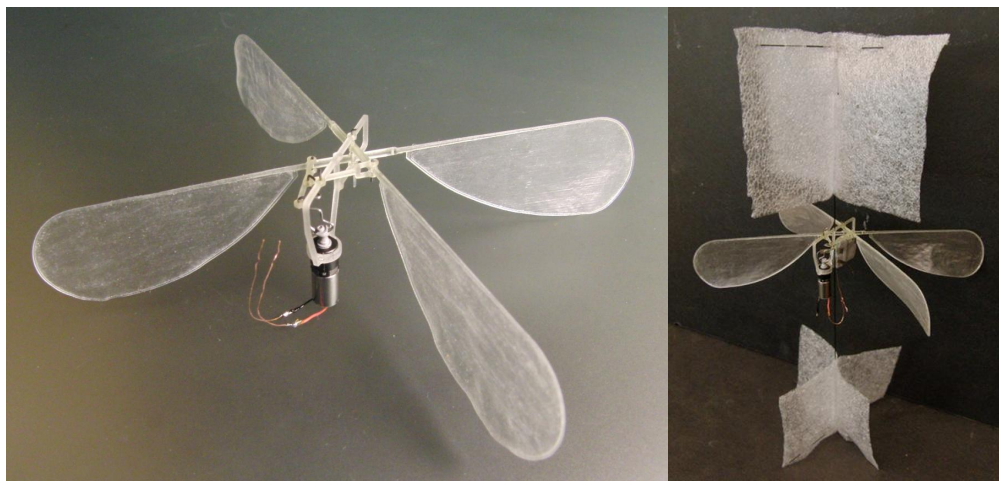


Figure 1.27: *Cornell MAV (Richter & Lipson 2011)*

| Model                    | Weight (grams) | Span (mm) | Actuator | Power   | f (Hz) | Wing Rotation | No. of Wings |
|--------------------------|----------------|-----------|----------|---------|--------|---------------|--------------|
| 1 Gram Ornithopter       | 1.1            | 100       | Motor    | Battery | –      | No rotation   | 2            |
| MFI                      | > 0.1          | > 25      | Piezo    | Mains   | 275    | Passive       | 2            |
| Microbotic Fly – Robobee | 0.06           | 30        | Piezo    | Mains   | 110    | passive       | 2            |
| <i>i</i> – Fly Vamp      | 13             | 265       | Motor    | Battery | –      | No rotation   | 2            |
| Microbat                 | 12.5           | 228.6     | Motor    | Battery | 30     | No rotation   | 2            |
| Beetle Mimicking Flapper | 10.37          | 125       | Motor    | Battery | 25     | Passive       | 2            |
| Konkuk Ornithopter A     | 50             | 360       | Motor    | Battery | 20     | No rotation   | 2            |
| Konkuk Ornithopter B     | 30.6           | 280       | Motor    | Battery | 24     | No rotation   | 2            |
| Konkuk MAV C             | 8.7            | 150       | Motor    | Battery | 30     | No rotation   | 2            |
| Konkuk MAV D             | 4.32           | 100       | Motor    | Battery | 35     | No rotation   | 4            |
| Nano Hummingbird         | 19             | 160       | Motors   | Battery | 30     | Actuated      | 2            |
| Delfly I                 | 21             | 500       | Motor    | Battery | 12     | No rotation   | 4            |
| Delfly II                | 16             | 280       | Motor    | Battery | 21     | No rotation   | 4            |
| Delfly Micro             | 3.07           | 100       | Motor    | Battery | 30     | No rotation   | 4            |
| Hummingbird MAV          | 2.4 – 3        | 120       | Motor    | Battery | 30     | Passive       | 4            |
| Cornell MAV              | 3.89           | 143       | Motor    | Battery | 30     | Passive       | 4            |

Table 1.2: Flapping Wing Aircraft and MAVs

## Chapter 2

# Review of Literature and Background

The second chapter of this thesis will present a review of some of the research which has been carried out in the field of insect flight and also to gain knowledge from this research and implement this during this project. Researchers have been highly active in a field which still requires a lot of work before we see a FWMAV which can fly and trim like an insect autonomously and at the size of an insect. As a community we are yet to develop this even at the scale of a reasonably large insect such as a beetle. An overview will be provided of the experimental work accomplished in this field in two parts, firstly the experiments involving large flapping experimental rigs and secondly experiments involving smaller flapping models towards the scale of MAVs. Following this, the aerodynamics revolving around low Reynolds number flyers specifically insects will be reported along with some CFD work which has been carried out in order to thoroughly understand the flow physics. A supplementary CFD review is provided in chapter 5.

### 2.1 Insect Wing Motion

The periodic wing motion of an insect travels through four main stages, which are downstroke, supination, upstroke and pronation. The translating phases are carried out during the downstroke and upstroke motions where the wings tend to hold a relatively consistent AOA. These translation phases are followed by rotational phases which occur at either end of the stroke. The end of downstroke is followed by supination and the end

of the upstroke is followed by pronation. Typically, the wing rotates (upper surface pointed upwards) and accelerates at the start of every stroke translating through the air with a somewhat fixed AOA (that can vary during the translation phases), which rapidly reverses during the rotational phase. The previous upper surface is now the lower surface which experiences large pressures on its face as it travels through its stroke where maximum velocity is obtained by the wing tip at mid-stroke. Thus, as shown in Figure 2.1, the wing pronates followed by the translating downstroke and then supinates which is again followed by a translating motion termed the upstroke. This periodic motion continues in the same fashion dependent on the insects flight mode as corrections for stability would require adjustments made by the wings.

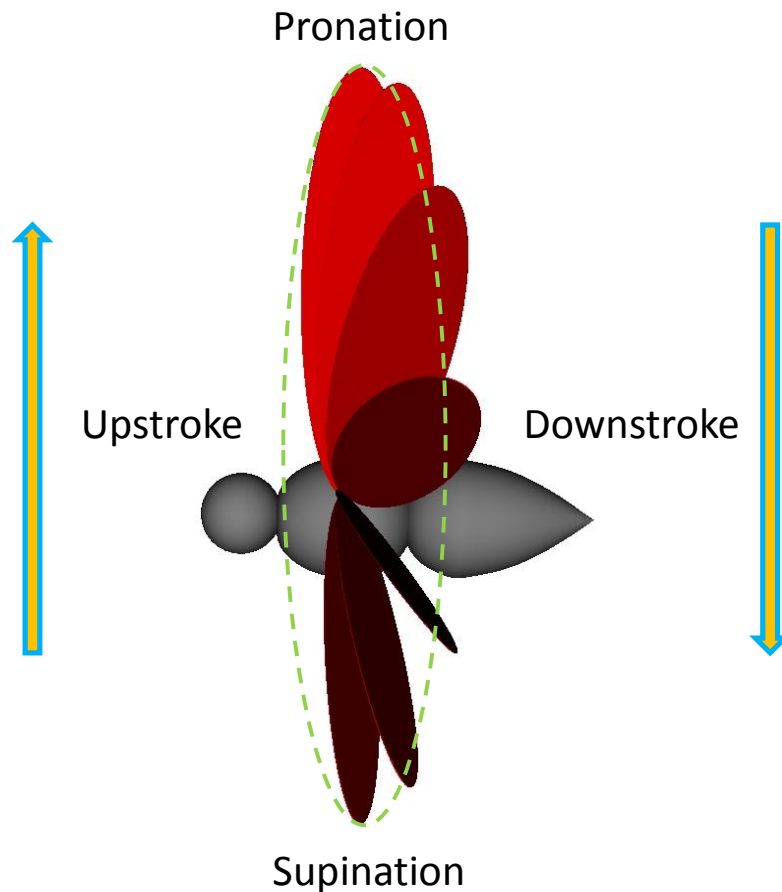


Figure 2.1: *Stages of Wing Motion*

Further to flapping and wing rotation, flying animals can deviate their wings as the wing tips trace out

irregular shapes during their motion in forward flight, some of these have been shown in Figure 2.2. Some are seen to trace out a figure-of-eight like shape intersecting their previous tip path, others tend to have much more complex motions such as the June beetle which traces out tiny loops at either ends of its stroke and some opt for tight curvilinear paths such as a thin banana-like loop.

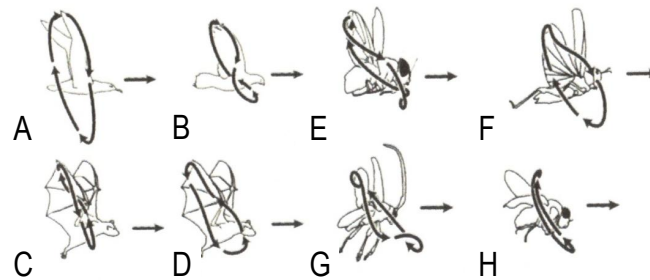


Figure 2.2: *Wingtip Paths for Various Insects; A: Albatross (Fast Gait), B: Pigeon (Slow Gait), C: Horseshoe Bat (Fast Flight), D: Horseshoe Bat (Slow Gait), E: Blow Fly, F: Locust, G: June Beetle, H: Fruit Fly (Shyy et al. 2013)*

In steady flight an insect's body experiences both lift and parasite drag forces. Due to the sectional body parts, exceptional streamlined flight to reduce the overall pressure drag generated is improbable, however at the greater forward flight velocities the body angle is rotated to more favourable drag reducing profiles especially when compared to the positioning of its body during hovering flight. During forward flight alterations to the stroke plane are carried out by altering thoracic inclination in relation to the horizontal which effectively applies changes to the body angle. The body angle can be altered by aerodynamic forces produced from the wings motion which would create a pitching moment about the axis located at the wing base, this seems to be the only controllable method to achieve body angle alteration. Although passive pitching can occur during forward flight dependent on the location of the resultant aerodynamic forces from body lift and drag. However, active wing motion would be seen as the appropriate mechanism to maintain stability. Thus, body pitching torques are generated by the wing motion during the stroke, this includes both the translational and rotational phases, subtle modifications in wing kinematics during stages of high accelerative movements of the wing can aid in pitch control, resulting in changes to the body angle.

For hovering flight the wing kinematics in general are symmetrical for both down and up strokes which in turn leads to an equivalent force generation for each stroke, where drag forces balance out cyclically whilst the insect remains airborne from the vertical lift force vector. When transforming to forward flight the advance

ratio inclines as does the asymmetry of aerodynamic forces for each half stroke where they become more pronounced. The wing orientation alters as the downstroke becomes more horizontal whilst the upstroke is more vertical at higher advance ratios, in addition the downstroke has a higher wing motion velocity than the upstroke stage. Thus, at higher advance ratios the downstroke motion aligns and travels faster to generate greater forces in the vertical direction, whilst the force vector of the upstroke motion is oriented more towards the horizontal for forwards motion and overcome the overall drag generated (Dudley 2002). An image of the stroke plane orientation from hovering flight to fast forward flight has been shown in Figure 2.3.

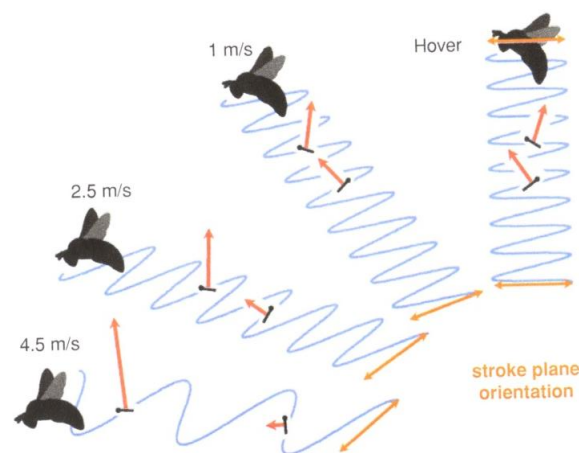


Figure 2.3: *Bumblebee Flight Mode Alteration* (Shyy et al. 2013)

During steady forward flight, both stability and manoeuvrability are distinguished factors which are constantly performed fluently with subtle alterations to kinematics in a rapid manner. To perform manoeuvres, an insect must generate moments in either a concurrent or temporally decoupled manner which is accomplished essentially by the generation of a variety of forces directed vertically, horizontally and sideways. As stated in (Dudley 2002), in addition to wing movements, insects tend to use their bodies and even their legs for manoeuvring, thus they choose to optimise their bodies features by exploiting its various parts to aid its flight path. Moments such as roll and yaw are derived from asymmetric movement of the wings which effectively generates asymmetric forces. When performing a yawing moment the stroke amplitude is smaller on the inside of the turn, thus the translational velocity of the wings is smaller which results in a smaller force production. Whilst the wing on the outer side has a larger stroke amplitude, with a larger translational velocity which in turn generates a larger force, this imbalance will generate a yawing moment for the entire insect (Dudley 2002). This technique of force imbalance has been adopted in the second FWMAV model

designed as part of this thesis which will be elaborated upon in Chapter 3. Needless to mention, manoeuvring flight can be accompanied with small instabilities due to an imbalance of forces generated, which an insect corrects with small kinematic alterations. Overall torque generation is paramount for insect flight and the key mechanism to produce such torques is an asymmetric wing motion for either side. Thus for the inside of a turn the muscular activity of the inside wing may be reduced or the muscular activity on the outside is immensely augmented. In furtherance of asymmetric wing motions, to restore flight stability an insect can deflect its abdomen to generate torque, which is created by the pressure drag acting on the deflected abdomen. Thus, during fast forward flight the deflection of the abdomen would generate even more torque as the drag forces are greater and this can again be used for stability or even assist in manoeuvring flight, furthermore due to the large cross-sectional area of the abdomen significant asymmetries in flight can be obtained.

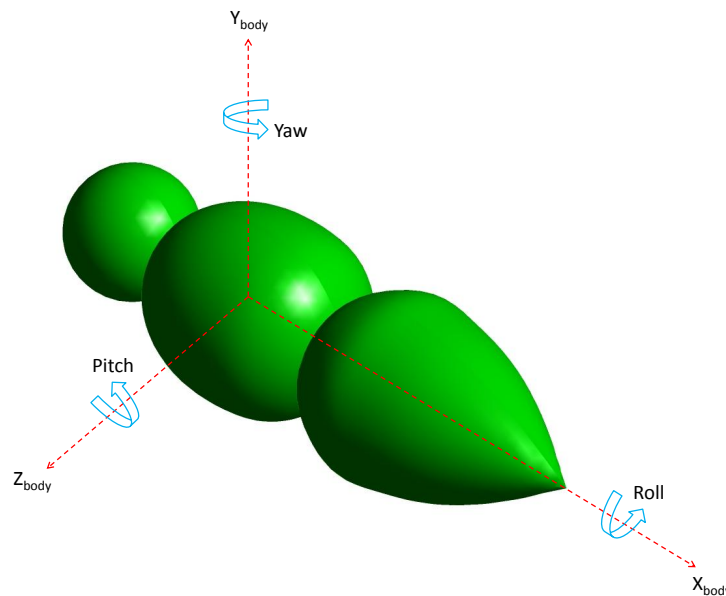


Figure 2.4: *Insect Body Coordinate Frame*

During the translation phase the AOA for each stroke does not have to be symmetric as mentioned above and its position is flight dependent. Although the AOA is somewhat fixed during both the translation phases, alterations do occur but these dynamic changes in AOA are not extreme which is why the AOA is denoted as 'relatively fixed'. Furthermore, according to (Ellington 1984) the wing has a twisted configuration where the AOA is largest at the wing base and declines towards the tip, the actual amount of twist present is

relatively small. The smaller angle of attack at the wing tip compared to the wing base would also induce less drag forces, and as the tip travels with the highest velocity, less energy is consumed. Active control for the wing twist parameter in mechanical terms is something which would require control of the wing spars or venation formation to force the wing membrane to twist in specified directions, the apparatus required for such control characteristics would immensely contribute to the additional mass the FWMAV would carry on-board. Dependent on the type of flight an insect can vary the wing rotational timings at the start and end of a stroke (during pronation and supination motions), this assists in generating torques. However, under hovering conditions it is acceptable to generalise that the rotational durations of pronation and supination are identical, which would also aid in flight stability.

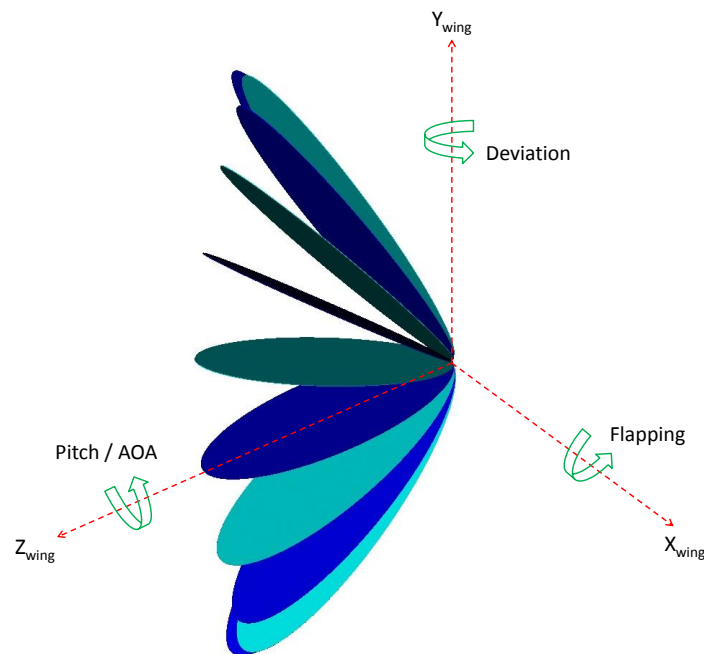


Figure 2.5: *Insect Wing Coordinate Frame*

In general, several coordinate systems are incorporated due to the various sectional parts involved and the singular movements performed during the periodic motion of the wings. A single body fixed coordinate frame has been shown in Figure 2.4, which is a simplified approach as the body sections do have singular movements. However, this approach is appropriate for this study as the body is considered stationary under the hovering conditions for the experimental and computational investigations (where no body is present). Thus, in such a case the body fixed coordinate frame and global world fixed coordinate frame are both

aligned. However, the generation of torque from wing motion would cause the body to rotate, so long as it has been provided with the freedom to do so. The wing kinematics are fundamentally formed from three separate motions which are flapping (sweeping stroke), pitching (angle of attack) and deviation (out of stroke plane movement), these have been shown in Figure 2.5 where the wing is travelling through a downstroke motion. For the body, the vertical axis is denoted as  $Y_{body}$ , the longitudinal axis is denoted as  $X_{body}$  and the lateral axis is denoted as  $Z_{body}$ , where the lift, drag and side forces act along these axes respectively. Likewise, the forces acting on the wings are in the same directions as shown in both the aforementioned diagrams. Each wing would have its own wing base fixed coordinate frame, but under the condition of symmetrical wing motions, a single wing base fixed coordinate frame is sufficient which can simplify matters and especially computational efforts. Thus, in various scenarios multiple coordinate frames are needed which will reference to one another and the global world fixed coordinate system. Note, insects have the freedom to rotate clockwise and counter-clockwise with the control functions it has for its body parts.

## 2.2 Large Experimental Flapping Rigs

A key part to unlocking, understanding and manipulating the findings of how insects fly is via experimentation. Experiments performed in liquid have huge advantages as opposed to gas, due to its more viscous nature, which in essence allows for vast simplifications. Thus, the speed of wing movement can be drastically reduced, but correct scaling conditions would need to be in place in order to preserve the Reynolds number to achieve the required fluid properties. Unsteady fluid motions can be visualised more easily, measurements are much easier to acquire as the sensor can be placed directly on the wing arm, normally near the root. The inertial effects of accelerating the wing is much smaller, as the wings movement through the liquid is much slower compared to gas. Furthermore, the larger mechanical models have control over wing AOA throughout the entire flapping cycle. Thus, the user will input the wing kinematics, and the mechanical model will act this out as programmed to do so. Thus if the inertial measurements are carried out they are straight forward to perform compared to experiments using passive wing rotation. Passive wing kinematics are dependent on many factors which have been detailed later in this thesis. The third rotational motion known as stroke deviation could also be performed accurately and consistently at various frequencies. With passive wing rotation and deviation, the path produced will be dependent on the flapping frequency and the properties of the material(s) and linkages used to produce these motions.

Robofly (Figure 2.6) was constructed to investigate the flight aerodynamics of insects, in particular the *Drosophila melanogaster*. The experimental rig was composed of six stepper motors which are controlled by input functions via a PC. The motors are attached to the wings via timing belts and drive shafts which actuate two wings that flap along the horizontal stroke plane with a force sensor attached to one of the wings, to measure the forces acting in the parallel and perpendicular directions. The experiments were conducted in a tank filled with mineral oil which had a density of  $880\text{kg}/\text{m}^3$ . The Reynolds number of 136 was matched by selecting a fluid with a specific viscosity, in addition to altering the wing size and flapping frequency. Each wing had a length of 250 mm and a thickness of 3.2 mm, they were swept through a stroke angle of 160 degrees, at a very slow frequency of 0.145 Hz.

They state that the instantaneous forces act approximately perpendicular to the wings flat surface throughout the flapping cycle, presenting that at these Reynolds numbers the pressure forces are dominant compared to the shear viscous forces which act parallel to the wings surface, this can be seen from the 2D wing-force vector plot shown in Figure 2.7. The wing path shown at the top of Figure 2.7 has an AOA at midstroke of 20 degrees for upstroke and 40 degrees for downstroke. The wing path shown at the bottom of Figure 2.7, is for a symmetrical AOA of 40 degrees at mid-stroke for both up and down strokes. Due to mis-alignment of the wing an inaccuracy of  $\pm 4.5$  degrees for AOA occurred during the symmetrical wing motion, this led to differences in the temporal force measurements for each flapping stroke per cycle.

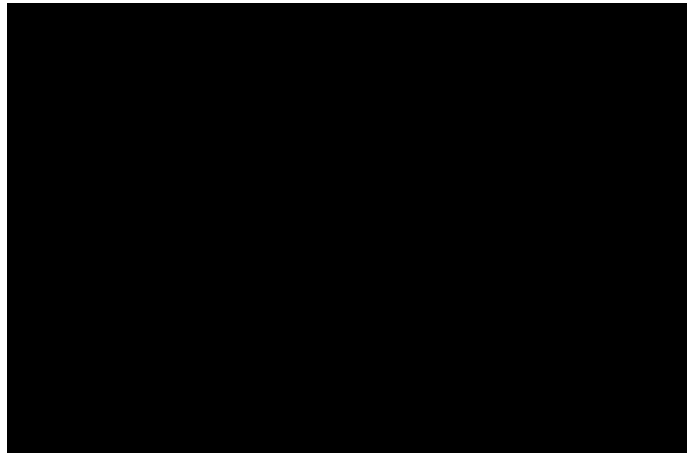


Figure 2.6: *Robofly Experimental Rig (University of California Berkeley)*

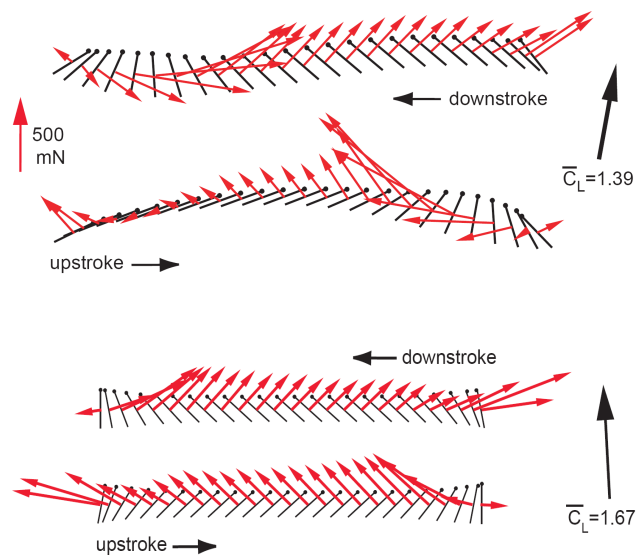


Figure 2.7: *Two-Dimensional Wing Path. Black Line: Instantaneous Wing position, Black Dot: Leading Edge, Red Arrow: Instantaneous Force Vectors. (Dickinson et al. 1999)*

The stepper motors can be programmed to carry out a variety of wing kinematics, thus experiments were conducted to determine the vertical and horizontal aerodynamic forces for symmetrical AOA rotation, advanced AOA rotation and delayed AOA rotation. In summary, it was revealed that advanced rotation produces the highest average lift force followed by symmetrical AOA rotation and the delayed AOA rotation showed the

least lift force production.

By obtaining the  $C_L$  and  $C_D$  for translation motion by experiments where the wing is held at a fixed angle of attack and swept through 180 degrees they approximately calculate the translation force contribution to the actual lift and drag forces produced. Using this they subtract the actual lift and drag measured data from the respective translation force contribution measured data to determine the approximate rotational force contribution. Exploiting this method they determine the rotational lift force contributions for the advanced, symmetrical and delayed sets, where two peaks are observed at the end and start of a cycle. At the end and start of a stroke the advanced case would produce two positive peaks, the symmetrical case would produce two positive followed by a negative peak and finally the delayed case would produce two negative peaks. As the two peaks occur at different times it has been suggested that they may occur this way as contributions from two different aerodynamic enhancing techniques. The first peak has been denoted to be a contribution from the wings rotation at the end of the stroke, and the second possibly due to wake capture where the wing interacts with the shed vorticity from the previous stroke.

In order to test the hypothesis of wake capture that a wing should continue to generate a certain amount of force even if it came to a complete rest at the end of half stroke, the wing was brought to a sudden stop at the end of upstroke. It was found that for advanced AOA rotation a significant peak is observed for a few hundred milliseconds after the wing is brought to rest, for the symmetrical motion no lift force is produced but a considerable amount of drag force is produced, and for the delayed case positive drag and negative lift force is produced. Also temporal consistency is observed for the second peak between the forces produced for all three cases when the wing is brought to rest and the half-stroke positions when the wing is continuously flapping. In the case of advanced rotation the wing is oriented at a preferable AOA with the leading edge pointing forwards (as a starting position), and interacting with the shed vorticity from the previous stroke produces positive lift force, as a jet of high velocity collides with the underside of the wing. The case of delayed rotation does not benefit in this manner as the wing is placed at an angle that will generate negative lift forces with the shed fluid directly pressing down on the upper surface with the leading edge (previous LE) now facing the wrong direction when compared to the wings direction of translation. Furthermore, the symmetrical case has no AOA at mid-stroke reversal, thus it benefits from no lift generation, but substantial drag acting on its flat upright surface, leading to large form drag when inclined in this position.

Figure 2.8, are flow visualisations produced from 2D PIV analysis, which depicts the wing just before coming

to rest, the aforementioned statements relate to the fluid dynamics seen in these images. The vorticity shed in the advanced image would be stronger as the wing underwent a complete wing rotation generating much more rotational circulation at the end of the previous stroke. The effect of the wake strength for the advanced case is much stronger, resulting in a large peak lift force. Essentially as the wing is held stationary when brought to rest, the shed vorticity from the previous stroke impacts the surface of the wing like a jet of fluid. In addition if the wings were travelling through still fluid then a peak in lift force, like the one seen here should not occur, but when travelling through the vortex jet a peak should be observed in reaction to the forces experienced due to the vortex jet interaction.

The wake shed from the prior stroke can be seen as an energy source as lift enhancement is achieved dependent on the wings inclination angle when in contact with the vortex jet. When a body moves through a fluid, energy is essentially lost to the external medium and a wake formation is produced. The energy present in this wake can be partially extracted as kinetic energy exists within the motion of this fluid, thus wing-wake interaction can be seen as re-capturing the energy which departed in the form of a wake in the prior stroke, this transfer of fluid momentum to the wing augments the efficiency of insect flight. Once the wing has reversed its stroke direction, a transfer of fluid momentum occurred in all the 3 cases mentioned above, albeit, it may not have always been beneficial in terms of lift production due to the wing AOA. Further information regarding insect flight fluid dynamic mechanisms can be found from (Lehmann 2004).

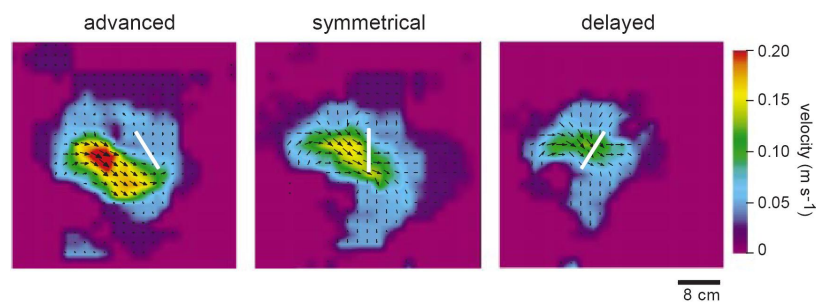


Figure 2.8: *PIV Images of Fluid Dynamics for Three Different Wing Rotation Phases (Dickinson et al. 1999)*

The influence of wing-wake interaction was investigated using the robofly experimental rig at Berkeley. PIV flow visualisation is used to quantify the fluid behaviour around the chord of an active wing, synergetically force measurements were also recorded. The wing was swept through a 160 degree flapping stroke angle, with an AOA of 45 degrees at mid-stroke. No wing deviation occurred, and the wing kinematic motion for down

and upstrokes were programmed to be the same (but inaccuracies due to gear slippage and misalignments results in inaccuracies of  $\pm 4.5$  degrees), the wing motion was also set to be advanced by 12% of stroke reversal. The flapping frequency was set to be 0.168 Hz which brings the Re to approximately 160. See (Birch et al. 2003), for details regarding the laser and camera setup.

They subtracted the forces and velocity flow field images generated from the first stroke by that of the fourth stroke to isolate the influence of the wake aerodynamics of the current stroke. By doing so, the wake from prior strokes can be analysed and the forces produced related to this. During the first cycle the wake is still developing whereas on the fourth cycle the flow field has fully developed, thus the fluid dynamics and force measurements are now periodic and considered as converged solutions. Thus, the resulting images and forces are of the vorticity shed during the previous stroke. The trends noticed for force production for the first cycle and fourth cycle present very similar results except for the onset of the stroke where the fourth cycle has a much larger peak which indicates an influential factor from wake capture. When a wing starts from rest rotating to position its orientation at the required AOA it experiences an instantaneous magnitude of vorticity as it performs this motion resulting in the production of a force peak. This is not the same for wake capture where the wing now interacts with a jet of shed vorticity from the prior stroke, resulting in a peak of lift force production. Following this there is a decline in force production which is related to the attenuation of translation circulation which is the result of downwash induced by the wake.

At the onset of the first stroke as the fluid is initially at rest the flow dynamics are much simpler compared to the onset of the fourth cycle where the flow field is fully developed consisting of the shed vortices from the prior stroke. In addition to the lifting force enhancement experienced from the previous wake shed, the LEV growth rate increases as opposed to when wing motion commenced through a stationary fluid. The diagram in Figure 2.9, recounts a summary of the flow dynamics discovered from the PIV images. The onset of downstroke shows the development of an LEV and a USL, followed by the development of a TSV that detaches soon after moving into the wake during translation whilst the LEV grows and seems to stabilise, the TSV is a creation from the roll-up of the vorticity from the under-wing surface. Towards the end of the downstroke the wing velocity decreases as the wing will start to rotate, at this time the USL moves downwards towards the TE, which is followed by the detachment of this USL and the formation of a RSV.

During the commencement of the upstroke the wing interacts with the LEV and RSV of the previous stroke, and this wake capture augments the forces produced in addition to accelerating the growth of a new LEV.

During the translation of the upstroke a new USL forms which is partially connected to the newly shed TSV2, where the combination of the new TSV2 and the old RSV1 form a doublet. Thereafter the doublet is shed into the wake as the wing continues to translate where the LEV2 grows and stabilises, and so forth.

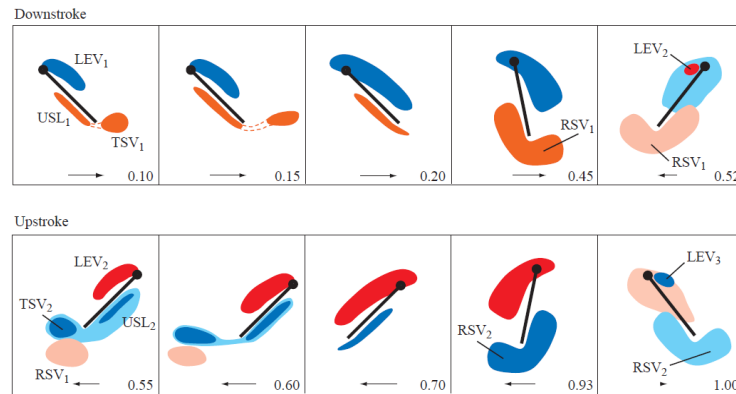


Figure 2.9: *Diagram Portraying A Summary of Flow Dynamics, red: counter-clockwise vorticity, blue: clockwise vorticity, lighter shades represent vorticity from the previous stroke (Birch et al. 2003)*

From the image subtraction method, a jet of fluid upstream of the wing was found, where within this two high velocity vortices are located from which the authors suggest the upper region of vorticity is composed of a combination of the counter-clockwise LEV and the clockwise TV both from the previous stroke, and lower region is composed of a combination of the counter-clockwise LEV and the clockwise RSV. The jet of fluid moves upstream towards the wing just under the TE, inducing an upward thrusting force on the under-wing surface, as the wing continues its translating movement through the downstroke the vortices which portrayed a strong presence previously have now moved into the wake and by stroke reversal are no longer present.

Along with an augmentation of forces the shed vortices also give rise to downwash, which grows during the first half of the stroke, this downwash reduces the aerodynamic AOA in turn altering the circulation created by the wing, overall the downwash reduces the force generated by the wing. Furthermore, it was found that although the growth of the LEV is accelerated in the fourth stroke for reasons aforementioned, shortly after whilst the wing is translating through the downstroke motion it was noticed that the strength of this is less than the LEV formed in the first stroke. Proceeding this it was observed that the LEV in the fourth stroke is more closely attached to the wing surface compared to that of the first stroke. The results presented, clearly display that although a wing started from rest will generate acceleration dependent forces, a wing which performs rotation with time dependent AOA and interacts with shed vorticity from the prior stroke

will benefit from both aerodynamic mechanisms, thereby augmenting the forces significantly more in the latter scenario.

In a different experiment, a large flapper consisting of two wings and a body was constructed to model the hovering kinematics of insects, specifically a hawk moth *manduca sexta*. The body houses 4 DC servo motors and a gearbox which are used to actuate the drive shafts that displace the wings according to the input kinematics. Although the hawk moth has a fore and hind wing, tests are done using a single wing and the wings on either side of the body are coupled, thus they both create identical motions. The wing can travel through 4DOF which are the flapping stroke angle, stroke deviation, AOA control at the leading edge and AOA control at the trailing edge, exploiting these the wing kinematics of a hawk moth were replicated on this machine. The wings are x9.6 larger than a real hawk moth's wings, thus bringing the wing length to 46.5 cm long, with a surface area of  $513 \text{ cm}^2$ , thickness of 0.34 cm and each weighs 189 grams. A smoke rake was attached to the leading edge of the wing to allow flow visualisation in the form of smoke streaklines. The authors stated that in order to maintain flow dynamic similarity the  $Re$  needs to match that of a real hawk moth, applying this the flapping frequency was reduced to be 0.3 Hz allowing for the wing length to be massively increased. Their flow visualisation images revealed a highly three-dimensional strong LEV with a large axial velocity component, where they state that this LEV seems to resemble a roll up of a vortex sheet, rather than present a trapped vortex. The diameter of this vortex increases from wing base to tip, where it detaches from the wing surface at approximately 75% of its span (measured from wing base) on the second half of downstroke as the core became unstable towards the wing tip, where it connects to a large tangled tip vortex. The vortex connection is shown in Figure 2.10 along with the mechanical flapper. The neighbouring fluid above the LEV possesses a strong spanwise component.



Figure 2.10: *Smoke Visualisation via A Hawkmoth Flapping Rig (Van Den Berg et al. 1997)*

Following wing reversal at pronation stage a stopping vortex is shed which later combines with the starting vortex that is shed from the translating wing during the early stages of downstroke to create a SS vortex which consists of a broken down core. This unification there after connects with the tip vortex where the growth of the wake occurs, this can be seen in the diagram shown in Figure 2.11. Following this at the end of downstroke the vortex detached from the wing surface and the cycle would start again with the production and amalgamation of vortices, but a difference the authors observed was the generation of a weaker starting vortex shed during the upstroke translation.

Figure 2.11, shows representations of the LEV from different views, where the movement of the axial flow component of the LEV is presented along with dividing stream surfaces (DSS). Figure 2.11 (bottom left), illustrates the axial flow component feeding vorticity into the TV which produces a three dimensional vortex ring in its wake. This axial flow component helps stabilise the LEV which is vital for lift production, especially in hovering mode but also results in a decrease of the vortex diameter. Through the centre of this ring exists a downwash of high velocity.

Analysing the images from above the stroke plane they observed that a vortex ring is generated during the downstroke and its position moves away from the central body line as downstroke proceeds, so in effect two rings are produced by the entire model (smoke visualisation is on one side). As Kelvin's circulation theorem states that the total circulation within a system must remain constant, implies that any change in circulation of the bound vortex of a wing must be followed by the shedding of a vortex of opposite circulation and equal strength. As the bound vortex of the wing experiences a gradual growth and decline in relation to its acceleration and deceleration during its downstroke translation, this must be followed by the continual shedding of vorticity.

A spanwise gradient in circulation exists in the LEV where the circulation from wing base to tip increases peaking at some point as mentioned earlier followed by a decline to zero. This form of spanwise gradient must be followed by a gradient in the trailing vorticity in the wake, thus a vortex sheet is shed from the wing, which due to its instability will roll-up instantaneously into a shape resembling a vortex ring (composed of the base vortex, tip vortex and SS vortex). Before the roll-up the sheet will have an arc-like structure based on the swept area of the wing. Now, a generation of two vortex rings exist on the flapper, which could combine into a single ring if the root vortices are close together, due to entanglement of these vortices which are composed of equal strength but circulating in opposite directions, leading to a break down of the root

vortices. However, the authors state that a single vortex ring is not composed as sufficient distance remains between the two root vortices which they observed from their images. But as the flapper had a large distance between both wings due to its body housing the mechanical components is much larger than that of a hawk moth insect, this will differ from the wake generated for the real hawk moth insect where, the root vortices will in essence amalgamate with the wake of the body, leading to cancellation of vortices and the production of a single vortex ring in a shape resembling a dumbbell.

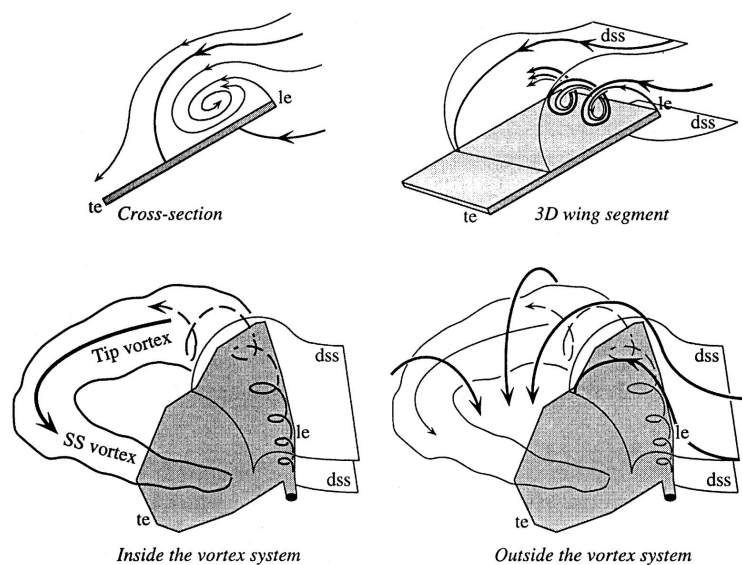


Figure 2.11: *Sketch of Flow Behaviour* (Van Den Berg et al. 1997)

Utilising a water tunnel (Nagai et al. 2008), aerodynamic force measurements on a single wing undergoing two motions for hovering and forward flight were investigated to determine which sequence of kinematics would prove to be most efficient and produce the largest amount of force to suit its respective flight mode. The kinematic wing motions explored are a combination of trapezoidal and approximate sinusoidal (a pure sinusoidal curve was beyond the limit of the stepper motors used in the setup, thus proximities were modelled), furthermore all motions were symmetrical. A diagram of their setup is shown in Figure 2.12, where the wing motion was created by two stepper motors (1 for each motion) which are controlled individually and strain gages were used to acquire force measurements. The wing planform was based on a bumble bee (*bombus terrestris*), which had a span of 100 mm and represented a somewhat rigid plate as any deformations were small. The flapping angle and AOA were the same as that of the bumblebee which are 60 degrees and 45 degrees respectively. Attempting to match the flow properties the Re was between 1000-5000, dependent

on the frequency which was ranged from 0.2-0.5 Hz. From the tests they found that the combination of sinusoidal + trapezoidal for flapping + AOA respectively, produces greater lift but also requires more power and the combination of trapezoidal + trapezoidal for flapping + AOA respectively, proved to be more efficient than the previously mentioned kinematic combination. The primary reason why the former produces a larger force was due to its larger velocity as an approximate sinusoidal curve was produced for the flapping stroke. Thus for better efficiency in hovering or forward flight modes a combination of trapezoidal waves for both flapping and AOA is more suitable. However, larger lift forces can be obtained by selecting the sinusoidal + trapezoidal for flapping and AOA motions respectively for both modes of flight as found in their results.

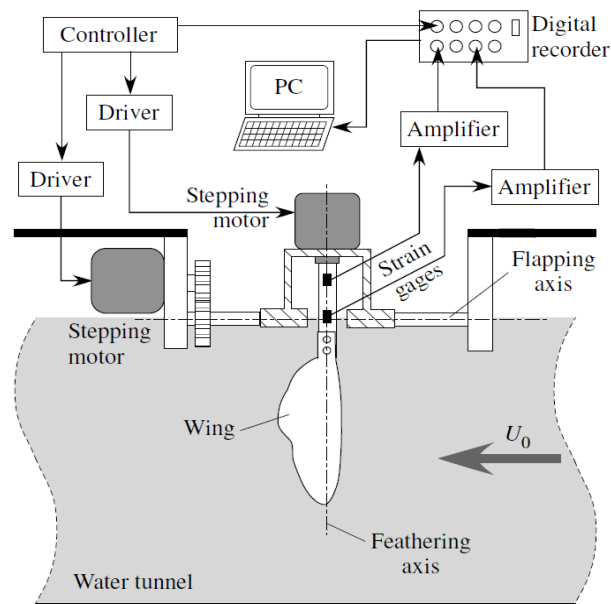


Figure 2.12: *Diagram of Test Setup for a Flapping Wing in a Water Tunnel (Nagai et al. 2008)*

The large robotic 'robofly' experimental rig submerged in a tank filled with mineral oil was employed to investigate the flow physics surrounding the clap-and-fling mechanism via experimentation. Details of the experimental rig have been elaborated upon in the early part of this sub-section, and further information can be sourced from (Dickinson et al. 1999) and (Lehmann et al. 2005). The wings do not come in physical contact with one-another during the clap phase in-order to protect the sensor, instead they come in close proximity to model the clap-and-fling effect, and the wing bases are farther apart compared to the wing tip during the clap phase. The stroke amplitude which the wings sweep through is 160 degrees with a flapping

frequency of 0.16 Hz, the midstroke AOA is held at  $\pm 45$  degrees and the fluid Reynolds number has a mean value of 134.

Force measurements demonstrated force production enhancements through parts of both the clap-and-fling phase, where the latter phase produced a very large lift force peak, as opposed to the lift force peak measured for a single wing in the same time interval. At the position of clap the force augments producing a small lift enhancement thereafter slightly declining, which is followed by a very large peak produced from the fling phase, where the drag force acting on the wing also produces a peak in force.

PIV flow visualisation was conducted to investigate the fluid dynamics in the near wing territory along the chord of the wing at approximately 65% span length (this is the position at the centre of wing area). In the two wing case as the wings approach each other leading up to the clap phase its found to be more strenuous to accelerate fluid, which affects the development of aerodynamic forces. The generation of circulation around the wings is heavily affected due to the presence of the second wing whereby both have regions near their surface with opposing circulations that cancel out one-another. Due to this effect, the amount of vorticity shed from the trailing edge of the two wing case is considerably less than observed in the single wing case, this is shown in the beginning images of Figure 2.13. In addition, the bound circulation about the wing in the single wing case is stronger than the bound circulation about the wings in the two wing case.

As the wings undergo rotation towards the end of the upstroke a stopping vortex is shed in both cases and the total force increases from the generation of bound circulation. Furthermore, the strength of vorticity in the LEV of the two wing case approaching clap phase (or it can be said towards end of upstroke) is considerably stronger than that seen in the single wing case. This may be due to the closing gap created from the leading edge of both wings approaching and compressing the fluid. Combined, their directional rotational motions cause the fluid to eject upwards towards the LEVs of both wings. Synchronously an outflux jet takes place near the lower half of the wings where the fluid is squeezed in the opposite direction leading to force enhancement in the two wing case.

The second part is known as the fling phase where the leading edges rotate away from one another, where the fluid from above would rush into the gap between the wings where a low pressure region exists which aids the rapid build up of leading edge vorticity. However, the LEV development is slower than that observed for the single wing case due to the counter-circulation created by the second wing. The authors mention that

the prevention of LEV growth in the very early stages of fling could be due the generation of the TEV which inhibits the growth of the LEV due to the upward momentum of the fluid through the open cleft (they also suggest this may have been partly to do with the drosophila shaped wings used). Furthermore, the presence of the shed LEV from the prior stroke has a stronger appearance and persists around the LE during the initial fling phase. A stronger USL is noticed for the two wing case, but seems to be slightly detached as opposed to the single wing case where the USL is pressing against the surface of the wing. The generation of the starting vortex is faster in the single wing case compared to the two wing case where the trailing edges are in close proximity to one another hindering the growth of this vortex. Inhibition of the growth of both LEV and TEV is observed in the two wing case due to the small distance between the wings. During the latter stages of fling, strong LEVs are identified on both wings, which seem to be fairly stronger than that of the single wing and as the wings proceed with the downstroke stage, starting vortices are shed from both wings.

During the clap stage the wings are juxtapositional, but do not touch or deform in any way, by producing a much smaller cleft thereafter coming in contact with one-another may enhance force production. Deformation of the wing would produce a smaller cleft at the lower part as the trailing edges would be much closer or even touching would allow less upward momentum of the fluid, which may possibly lead to faster generation of LEVs, effectively enhancing force production. The inter-vortex stream generated through the vortex system consisting of the LEV and TEV at the end of upstroke, has the effect of enhancing force production by a momentum transfer mechanism. The two wing configuration does not take full advantage of this due to the weak TEV accompanying the wings at the end of upstroke (towards wing clap), this is shown in the top set of images in Figure 2.13. A diagram of this has been shown in Figure 2.14 A-D, which presents a brief summary of the fluid behaviour during the clap-and-fling motion. Once the wings clap the TEVs are shown to be in the wake, with a downwash present on the outer sides of the wings. On the onset of the fling phase, fluid is pulled in around the wings LE (for both wings) and the growth of the LEV is observed during early downstroke, where fluid is drawn in and around both trailing edges.

LEV peak vorticity was analysed at 5 sections along the wing span from the base to the tip. This was accomplished for the single wing and two wing data sets, where the average LEV peak velocity was presented at time intervals leading up to the clap of the wings to a time sufficiently after the fling phase in order to analyse the complete mechanism. Significant differences existed between the peak LEV average vorticity

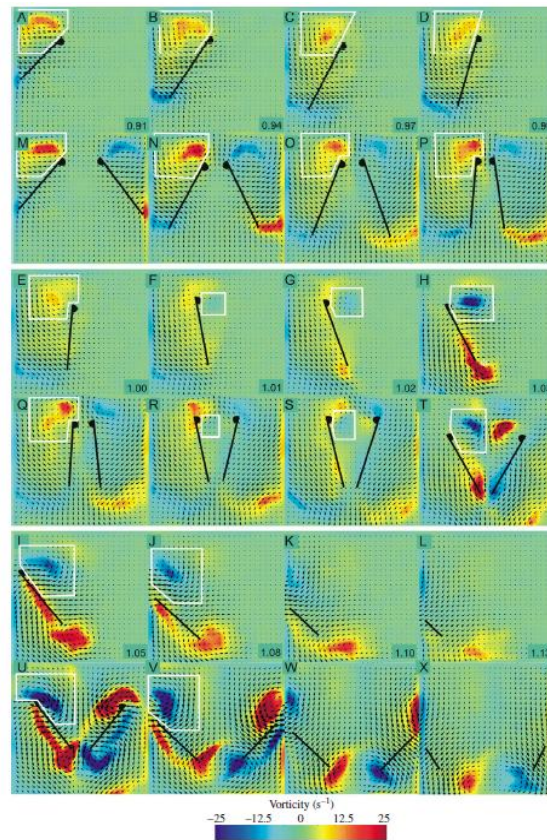


Figure 2.13: *Single Wing and Two Wing Fluid Visualisation for Interval of End Upstroke-Start Downstroke (Lehmann et al. 2005)*

measurements for the one wing and two wings cases, where the single wing had a much lower vorticity. For majority of the time interval previously mentioned the LEV average vorticity was higher for the two wing case, and the differences significantly grew during and after the fling phase.

In general from the data collected a lift enhancement is noticed when the wings are in close proximity of one-another and the separation angle should be no more than 10-12 degrees, thereafter the enhancement effect diminishes. In addition the enhancement was found when the wings do not come in contact, thus the wings need to come in close proximity to one-another to experience aerodynamic lift force enhancement and do not necessarily have to press against one-another. The major force enhancement occurs when the wings fling apart and an influx of fluid travels into the opening region, which in effect adds to the strength of the LEV, although this does occur a delay is observed as seen in Figure 2.13, where the build up of the LEV occurs shortly after the fling phase. A related hypothesis to consider is that the clap-and-fling may actually

occur as part of the insect attempting to maximise its stroke amplitude. Increasing the stroke amplitude in turn will escalate the wing velocity so long as the flapping frequency remains consistent. As the total flight forces are dependent on wing flapping velocity squared, an increase in stroke amplitude will consecutively provide an increase in total lift force. Through viscous enhancement for flight at very low Reynolds number a faint escalation in lift forces will be observed, but as a consequence the drag force will rise considerably, to a degree where one would question the benefit of lift augmentation. Overall the lift to drag ratio would be seen to be cataclysmic at lower Reynolds number flight, especially when energy consumption will inordinately inflate due to drag force.

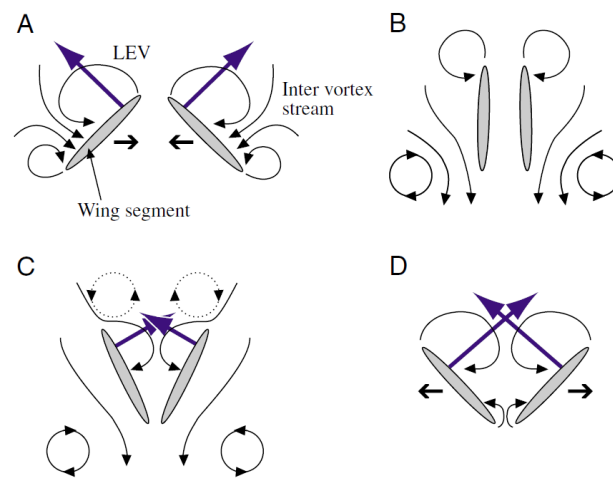


Figure 2.14: *Overview of Clap-and-Fling Flight Mechanism (Lehmann et al. 2005)*

A water tank experiment using time resolved tomographic PIV was conducted based on the Delfly II flapping model by Percin et al (Percin et al. 2011). A single wing was placed in a water tank in a hovering position, where the wing had a rigid leading edge and a flexible transparent membrane. The clap-and-fling mechanism was exploited and the flow interaction was simulated by the use of a mirror. In order to compare aero-elastic features in air and in water, dynamic similarity is seen as an important factor. This analysis is considerably vital when examining highly flexible wings, which encounters different forms of structural dynamics and fluid dynamics when in motion in two different mediums. In attempting to reproduce the Delfly II flapping motion in a much denser medium such as water, parameters such as the same amount of maximum deformation and bending stiffness need to be kept similar. Moreover the Reynolds number needs to be matched. Considering this they used a 100 micron metre polyester sheet as the membrane material and the wing was flapped

at 0.75 Hz. Deformation data was compared and significant differences were observed, the primary reason behind this is that inertial forces in air are far from negligible, but in water they are very close to zero for a complete flapping cycle. They summarised it was too difficult to achieve the same wing deformation behaviour in both mediums. Following this they carried out tests on polyester wings with a thickness of 100 and 250 micro meters, and dimensions of 100 mm x 57 mm which are the span and mean chord respectively.

A motor actuated a crank rocker mechanism that swept the wing through a 50 degree amplitude. The Re under hovering flight mode was found to be 6700 based on the mean chord of the wing and its tip velocity. The wing was placed vertically in the water tank which was constructed of Plexiglass allowing full optical access for illumination. Spherical polymide particles were used to aid visualisation, and the motion of the liquid was captured by three HS cameras, where each of them are placed at an angle of 45 degrees from one another (two cameras would be 90 degrees to one another). The cameras were all synchronised by software from LaVision for calibration purposes and visualisation of the fluid flow.

Iso-surfaces of vorticity magnitude were presented to display the vortical structures present in the flow field during the wings motion, this is shown in Figure 2.15. The presence of the LEV and TEV are clearly noticed as the wing moves towards the mirror. The strength of the LEV decreases as the wing decelerates as it approaches the wall as shown in Figure 2.15 in images  $t=-0.012$  to  $t=0$ , the LEV seems more concentrated in the image shown in the top left as opposed to the image in the top centre ( $t=-0.06$ ) where shear layers of fluid are pulling away from the wing surface. The separation of this shear layer is even more evident in the image labelled  $t=0$  where the LEV seems to be slightly detached off the wing surface and its cylindrical formation has deteriorated compared to the images in  $t=-0.12$ , in addition the fluid composing the LEV has moved downwards. The fluid present on the frontal surface of the wing aids in the attachment of the TEV to the wing and remains in the near proximity of the wing as shown in image  $t=-0.12$ , and as the wings membrane rotates the fluid is stretched and leads to the detachment of the TEV and clearly a distance away from the wing. At the end of the stroke where wing clap is simulated the TEV is shed into the wake of the wing.

During supination the leading edge now moves away from the mirror plate where the trailing edge moves in the opposite direction most probably undergoing the peel technique, but the fluid behaviour is not clear as the image has not focused on this category. The detached TEV which shed into the wake from the previous stroke is still present but a considerable distance away from the wing. Also the shed LEV from the previous

stroke is present in the near vicinity of the wing further vertically downwards from the leading edge and interacts with the wing surface and its diminishment is clear in image  $t=0.12$ , where the generation of a new LEV is seen. The fluid which collides with the wing seems to have been torn into smaller sections due to the collision with the wing and reduction in vorticity. As the wing continues its sweeping motion the newly developed LEV significantly grows, the reason for the rapid growth of this LEV could be due to fluid which rushes into the gap created during the fling phase.

Comparing vorticity contours for the two different wing membranes with a difference in thickness, provided interesting information where the flexible wings seems to have its LEV close to its leading edge, whereas 250 micro meter wing had the LEV a distance away as if it has been stretched. An LEV a distance away would most probably lead to a smaller lift force as the suction acting is a distance away. However, for the 250 micro meter wing the stretched shear layer towards the bottom of the wing undergoing separation was curved downwards like its being dragged by the trailing edge of the wing, this could be due to an increased downwash. Overall the thicker membrane seems to produce more downwash and upwash as observed at the clap phase, where the vortices are forced to convect downwards and upwards due to the more rigid nature of the membrane interacting with the mirror plate wall. Due to this up-down convection of vortices at the time of supination the more rigid wing probably will not benefit from the wake capture aerodynamic technique, whereas with the more flexible wing the shed vortices in the previous stroke interact with the wing. The thinner membrane experiences significant deformation during each stroke in comparison to the wing with a thicker membrane. When approaching the clap phase, a stronger LEV is present for the thicker membrane wing but as mentioned above it is a distance away from the leading edge. The wing membrane swings in the opposite direction to the flapping stroke motion creating an AOA for each stroke, where the thinner membrane obtains a greater AOA due to its more flexible nature. Fluid visualisation via CFD provides huge amounts of data which would prove to be very time consuming to produce experimentally and certainly difficult to produce during a single flapping cycle (during experimental visualisation certain sections are analysed rather than the entire wing). The fluid flow shown in the above figure was for a certain section of the wing, computational simulation would allow us to view the entire flow field encompassing the wing providing qualitative as well as quantitative data. CFD continually proves to be paramount in the field of engineering, but must not be seen as a replacement for experimental research but as an additional scientific method.

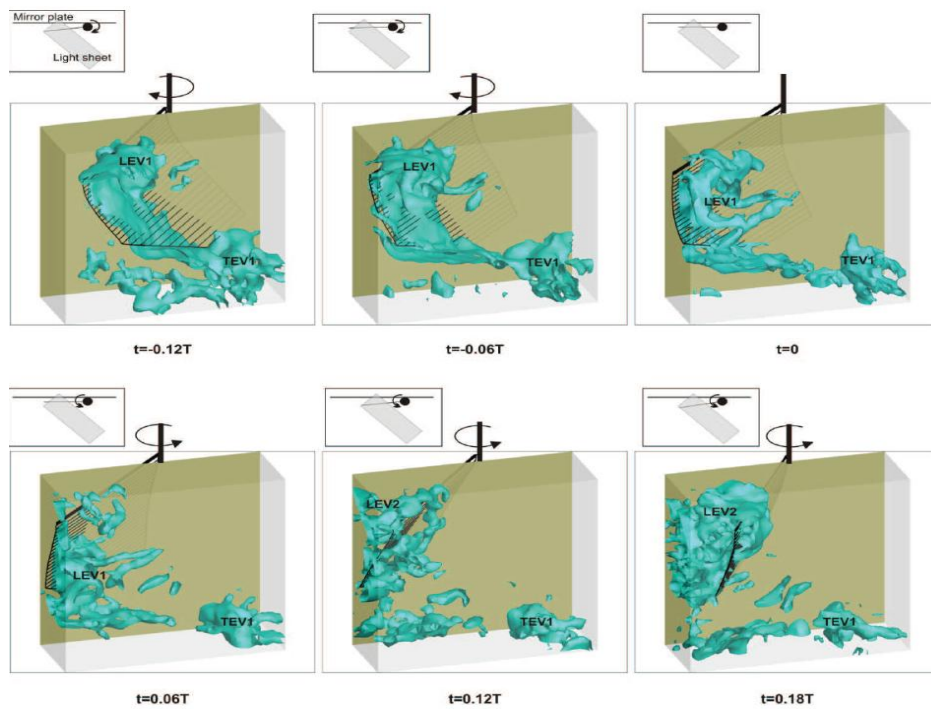


Figure 2.15: *Iso-Surface of Vorticity Magnitude for Flexible Wing* (Percin et al. 2011)

## 2.3 Ornithopter to MAV Scale Flapping Rigs and Models

Experimental work at the scale of FWMAVs is rather complicated due to factors such as mechanical vibrations, reasonably high flapping frequency, wear and tear of moving components, measurement of small forces and moments, passive wing rotation, acquiring small scale components and even the assembly and repairing of such delicate flapping models can be problematic. Research at this scale can also be expensive because of the equipment needed such as, highly sensitive sensors and high speed cameras. In addition, experiments investigating the fluid dynamic forces would need to be completed in air and then again in a vacuum chamber to extract the final aerodynamic forces and moments, unless a liquid is used but this is usually conducted for larger scale experimental rigs. When developing a small experimental rig MAV, the designer should keep in mind that future work will be in the direction of this model performing a successful take-off and moreover stable flight with similar flight traits of an insect. With this in mind, weight, size, efficiency, number of components required for the desired mechanical movements and simplicity of the mechanism will all be factors. Needless to mention the more components a MAV has, the heavier it will be.

Hall et al (2012), presented vertical thrust measurements determined via experimentations on a FWMAV (Figure 2.16) which was actuated by a bimorph piezoelectric PZT actuator and a modified version which underwent a two DOF motion (bending and twisting) to actuate a simple mechanism which consisted of a set of wings. They tested three different wings, and in order to obtain the largest wing displacement possible the mechanism was driven at resonant frequency of 21 Hz via a piezo actuator. The FWMAV was placed in a hovering position, with the wing leading edge aligned perpendicularly to the vertical force axis. However, during the experiment they captured asymmetric flapping which they believe was the reason they obtained negative values for their average vertical force measurements. Although the overall vertical force production was negative the modified piezoelectric actuator produced larger forces for both up and downstrokes, the reason for this is primarily due to the increased displacement of the modified actuator compared to the traditional bi-morph. They used a six-component nano 17 F/T (ATI Automation) transducer to record vertical force measurements, similar to the sensor used for the experiments detailed in this thesis. The forces measured for example in one case were 15 mN (upstroke) and -24 mN (downstroke). The force resolution of the sensor using the Netbox configuration is 3.1 mN. The authors stated that the negative value during the downstroke represents the delay in wing rotation. Although such small forces were recorded which are relatively close to the resolution of the sensor, the data produced was repeatable and consistent

over many flapping cycles, deeming the data accurate. The forces measured and described above are total force measurements of the entire FWMAV.

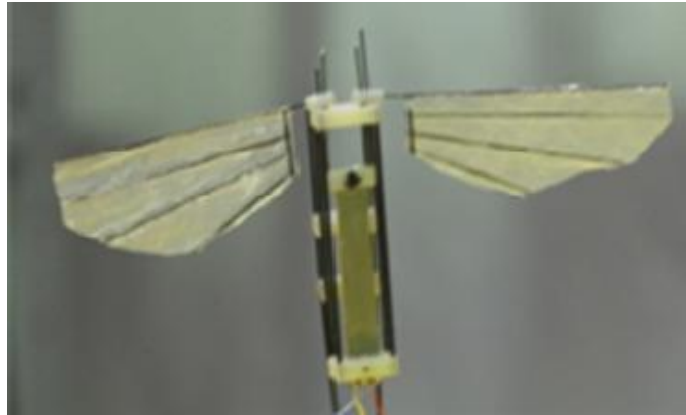


Figure 2.16: *U.S. Army Research Lab FWMAV (Hall et al. 2012)*

A hummingbird inspired MAV (Figure 2.17) has been developed at Chiba University by Prof. Liu, (Nakata et al. 2011). It has been rumoured that the production of this hummingbird (in the form of an MAV) costed in the region of 2.1 Million Dollars. Details about this MAV were provided in chapter 1. The MAV was composed of a range of parts which are commercially available from stores such as Didel and Plantraco. Aerodynamic investigations were executed by way of experimentations and CFD to explore the clap-and-fling force generation enhancement, as well as the physical interaction of the flexible wings concerning the amount of deformation.

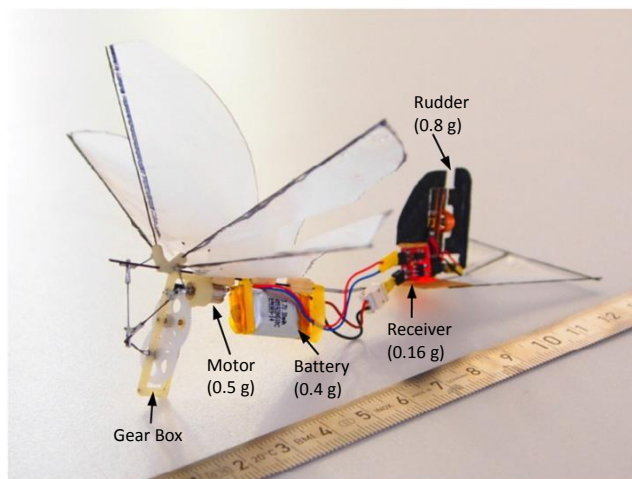


Figure 2.17: *Hummingbird inspired FWMAV (Nakata et al. 2011)*

Wing kinematics were captured and mapped out three dimensionally by using 3 cameras which were synchronised and operated for a brief period providing the complete temporal history for a flapping cycle. The MAV was mounted onto a 2 configuration load cell balance (to measure lift and drag forces) and was placed inside a low speed wind tunnel. The flapping frequency was controlled by the power input to the DC motor (which can be simply modified by altering the input voltage), based on a freestream velocity of 1.6 m/s, the  $Re$  and reduced frequency are found to be 2500 and 0.93 respectively. For sake of comparison they also tested a two wing MAV which was based on the wing mechanical system of the lower wings of the four winged (x-type) MAV system.

The MAV showed thrust force production in the case of zero oncoming flow but this changed to drag force for oncoming flows greater than 3 m/s, which demonstrates that gust of this speed or more would have a significant impact on this type of MAV. The four winged MAV produces more lift than the 2 winged MAV. However, in addition to the extra set of wings, the wings of the x-type MAV would travel a larger combined flapping amplitude as the two winged MAV was only based on the lower wings of this x-type design. Contrary to the aforementioned when a softer membrane is installed on the two winged MAV, it produced larger lift forces than the four winged MAV, which led to the authors highlighting the importance of the wing flexibility in the production of a successful MAV.

Single mean values of the aerodynamic forces for experimental and computational measurements showed good agreement, and the time history of the computational measurements shows that the upstroke produces more lift force than the downstroke due to the upper and lower wings on both sides now performing the clap-and-fling motion, opposed to the single clap-and-fling motion produced on the downstroke. However, the peaks are observed at the mid-stroke position of both up and downstrokes, which may be due to the AOA of the wings at this portion of the cycle. They employed a multi-blocked overset (Chimera) grid in their simulation, where the wing had a separate grid domain placed around it, which is dynamic just like the grid methodology exploited for the research in this thesis. Unlike the experiment, the CFD analysis was done with the model under hovering mode (zero freestream velocity). The reconstructed wing kinematics are modelled using the Fourier series function as the wing deformation is time dependent, under the assumption that the wing deformation is symmetric for both sides, one half is simulated. Under hovering mode the  $Re$  and  $k$  are 3400 and 0.59 respectively. The flow structures around the wings strongly represent the fluid dynamics of insect flapping flight with the development of LEV, TEV and TV (these will be explained in detail in

the latter sections of this chapter). Analysing the fluid visualisations the authors conclude their MAV with highly flexible wings practices the aerodynamic lift force enhancements namely the clap and peel, as the wings exhibit a peeling effect due to its flexible membrane, which overall leads to a rapid increase in force production. Also during the phase of clap and fling, the technique assists in adjusting the feathering angle close to the wing tip to avoid wing rotational phase delay as this would lower the aerodynamic performance.

An additional payload or significant change in wing properties would markedly affect any commercial toys flight performance. This is in addition to the difficult control characteristics it originally possesses. In simple terms, leaving aside flight stability, additional payload would require the generation of extra lift which is understandable. However, simply increasing the wing area or flapping frequency may not be a suitable solution due to the motors characteristics such as stall torque or the gearbox ratio. The latter of the aforementioned would also apply to FWMAVs which have been designed by researchers. This is primarily due to researchers focusing on developing a flapping flight vehicle which can fly and carry certain payload due to the limited lift force production. Most commercial flapping toys were designed to fly as they were originally provided, changes to this would relate to the requirement of further modifications. For example, an increase to the original wing area would require more torque and power leading to changes to the gearbox, motor and power source. In addition the structural integrity of the model should be questioned, due to the immense number of hours the mechanism is in operation.

A commercial toy flapper, namely Cybird P1 (Figure 2.18) has been used in numerous experiments involving wind tunnel studies and various types of wings. The toy was designed by (Kim et al. 2003), boxed as a fully assembled model and equipped with a remote control for a ground situated pilot. The wings are driven by a four-bar crank mechanism which is actuated by a large single motor that draws energy from the on-board power supply. As with all DC motors connected to a mains power supply the rpm can be varied by adjusting the input voltage, this in turn when connected to a linkage system with a wing will vary the flapping frequency accordingly.

The Cybird P1 was used for flapping experiments by the following authors (Hu et al. 2010), (Mazaheri et al. 2011) and (Ebrahimi et al. 2012) to investigate the production of aerodynamic forces. Hu et al (2010), tested the ornithopter to determine the benefits of flapping wing flight compared to fixed wing soaring. The tests were undertaken in a low speed wind tunnel and tested under forward flight speeds of 1-10 m/s, which corresponding to the wing chord have Reynolds numbers of 10000-100000. Lift and drag measurements were

recorded for all the tests by a load cell which was located at the lower end of the sting arm. They concluded that flapping wing motion has significant aerodynamic advantages as opposed to a fixed wing configuration when considered under an advance ratio of below 1 (where the flow is classified to be in an unsteady state).

They tested 3 different wings for which the structural skeleton remained consistent but the membrane was different as two were flexible and one was rigid. Specifically these were, nylon and latex for flexible wings and wooden for the rigid wing. Each wing of the original Cybird P1 ornithopter has a span of 368 mm, this length remained unchanged in these tests. However, due to the variation of materials used for the wing membrane the masses of each wing differed, this would have a direct effect on the flapping frequencies of each wing under the same gearbox-motor arrangement; due to this the maximum flapping frequency achieved for the rigid wing was 4 Hz which is half of what the flexible wings could be tested at. The latex wing performed best when considering thrust force production, but the rigid wing seemed to perform best in terms of lift force production. And the nylon wing was found to have the best soaring flight behaviour but performed on the contrary for flapping flight. Both flexible wings performed better than the rigid wings for thrust force production under a flapping motion scenario. Furthermore the flexible wings also proved to show a better aerodynamic performance under soaring flight conditions compared to the rigid wings.

Further wind tunnel studies were undertaken using the flexible membrane wings supplied with the Cybird P1, the results have been detailed in (Mazaheri et al. 2011) and (Ebrahimi et al. 2012). Similar to the tests performed by (Hu et al. 2010), they varied the flapping frequency, AOA and wind speeds to explore the aerodynamic performance of the ornithopter. Utilising a one-component force balance they measured lift and thrust forces (not simultaneously), thus sensor direction was altered in reference to the axis which they needed to measure. Freestream velocities ranged from 6-12 m/s in increments of 2 m/s, and the flapping frequency was varied from 0-9 Hz. They concluded that thrust force production increased as the flapping frequency increased and this trend seems to remain consistent at the AOAs explored, and the lift component increased as the freestream velocity increased, consequently this proved to be detrimental to propulsive forces as expected. Following this work, tests were performed as detailed before but this time power measurements were recorded using the input voltage to the motor. From the data gathered they attempted to create a flight envelope for this particular flapping model, see (Ebrahimi et al. 2012) for further information. The experimental power measurements show that as flapping frequency increases, the power required by the motor also increases.

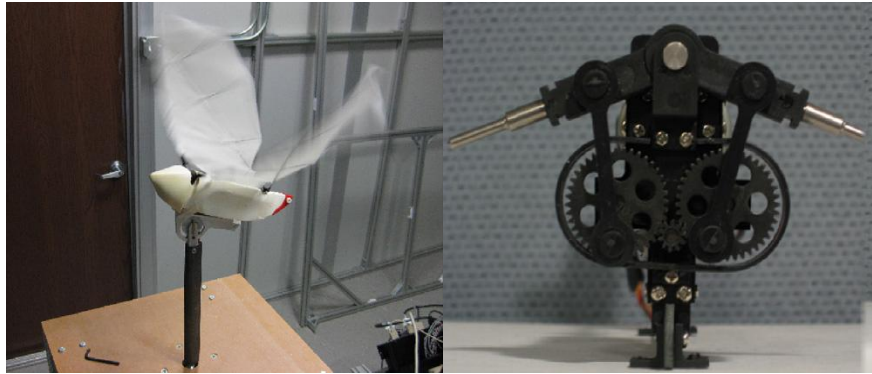


Figure 2.18: *Cybird P1 with Body Attached and Mounted on Sting (left), Crank-Gear Mechanism with Flapping Arms (right)* (Hu et al. 2010)

Research in this field at Delft University aside from the Delfly flapping models reviewed earlier has led to the design of an insect inspired four-winged MAV which is actuated by a solenoid with linear movement (see Figure 2.19). The thorax structure is composed of two circular rings which includes a flexural linkage arrangement (constructed from materials such as carbon fibre and polyester). The model developed performs a flapping and wing pitching motion, whereby the AOA is produced passively about the leading edge. The wing skeleton was created from carbon fibre and reinforcement is enforced at the leading edge and wing root by using larger diameter carbon fibre rods. Mylar sheet was used for the wing membrane, and due to its high deformation properties it was strengthened with the addition of two spars made of smaller and lighter carbon fibre rods compared to that used at the leading edge.

In order to create the desired wing kinematics, the model needs to be driven at resonance frequency of 28 Hz. The flapping amplitude achieved at resonance was 68 deg, in order to preserve stability in flight all wings would need to have a symmetric motion. The wings used for the final model in tests were geometrically quite similar to that of hummingbirds and they had parameters such as a span of 50 mm, a maximum wing chord of 20 mm and a mean chord of 16.75 mm. Various transmission designs were considered, with an end goal to produce the desired wing kinematics in this case larger flapping amplitude, which was produced by driving the model at resonance. This would reduce the power spent on creating such large flapping amplitudes, the reader should refer to (Bolsman et al. 2008) and (Bolsman et al. 2009) for more information regarding the designs considered and their analysis.

A 12V amplitude sinusoidal signal was input into the solenoid, and the plunger movement was monitored

as the solenoid needed to react effectively to the input signal. To test the lift force production of the MAV, a simple beam cantilever with a ruler was setup. The model was suspended from the cantilever beam and deflection changes were used to determine lift production. It was reported this model produced approximately  $8.75 \times 10^{-3} N$  of lift force, which was expected to be below its flight weight. One of the core functions which Bolsman looks to adopt from an insect is resonance, and emphasises the importance of this function through the 4 flexible thorax structures considered, of which two were considered more in-depth as they had more desirable features which are better suited to hovering, more specifically carrying four wings which would overall produce more lift. The FWMAV is shown in Figure 2.19 and more information regarding the model can be found in (Bolsman et al. 2009).

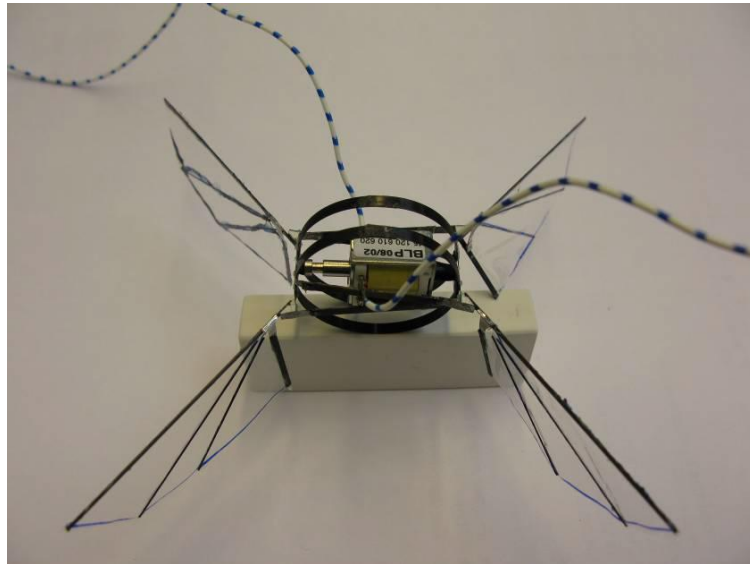


Figure 2.19: *Four-Winged MAV (Bolsman et al. 2009)*

Konkuk University have built a team which have been highly active in this field of research, the development of the beetle mimicking MAV is part of their most recent research which can be said to be the result of their prolonged work in the field of insect flight experimental investigations. Their research seemed to begin from the design of a lightweight piezo composite actuator, which was termed as LIPCA (lightweight piezo ceramic actuator). The actuator requirements were to create a large displacement whilst generating a high force output, even though similar actuators were commercially available they opted to improve them in the form of weight reduction via replacing the metal layers, which are used to produce the actuator by lightweight fibre reinforced plastic layers. Following this they tested their custom built actuator against a commercial

actuator THUNDER (which is available from FACE International) and found their actuator produced larger displacements, see (Yoon et al. 2002).

Earlier publications regarding flapping wings commenced with the design of a fourbar linkage system (Figure 2.20) which was actuated by a piezoceramic actuator, more specifically LIPCA. LIPCA produces small curvature deflections which can be considered almost vertically linear due to the small displacement produced (keep in mind dependent on the clamping configuration adopted for LIPCA its displacement is at maximum a few millimetres, hence the need for a mechanism to amplify this minute displacement). The actuator needs a mains power supply that can provide a very high voltage of 300V peak-peak (-150 V to +150 V) and a signal to instruct its motion which in this case was a sine wave, which was produced by the in-built function generator of the power supply. The actuator will perform best at its resonant frequency as it stores vibrational energy and this will provide the largest deflection, in turn producing the flappers largest stroke amplitude. The actuator needs to be clamped either at one end in a cantilever configuration or both in a simply supported arrangement, this is dependent on the mechanism it is actuating. The actuator was placed in a simply supported position as they found this benefited the actuation force.

The total mass of the flapping device was 20 grams and a wing area of  $29 \text{ cm}^2$ . The flapping model was tested at frequencies from 4-12 Hz and the resonant frequency was found to be 9 Hz, for which the flapping amplitude produced was approximately 80 degrees. Passive wing rotation was produced by exploiting the aerodynamic loading acting on the wing during its flapping motion, which was a maximum of around 55 degrees, this rotation was limited by the use of stoppers. The wing rotation limits were set as 45 degrees maximum AOA for the upstroke motion and 10 degrees maximum AOA for the downstroke motion. The wing rotation was captured by a high speed camera which was operated at 2000 fps. The images can then be analysed to investigate the pitching motion throughout a flapping cycle. The wings were based on the planform of a drosophila insect and were constructed from a thin sheet of polyethylene which was understood to have sufficient qualities such as ease of fabrication, stiff and lightweight. Force measurements were taken in the vertical and horizontal directions using a load cell which was setup with its strain gage in a wheatstone quarter bridge arrangement. The data measured showed that maximum forces were produced when the model was driven at its resonant frequency, and also the average forces displayed positive results which were 2.49 and 0.83 grams of forces in the vertical and horizontal directions respectively. This data represents the total force of the model, refer to (Syiafuddin et al. 2006) for further information.

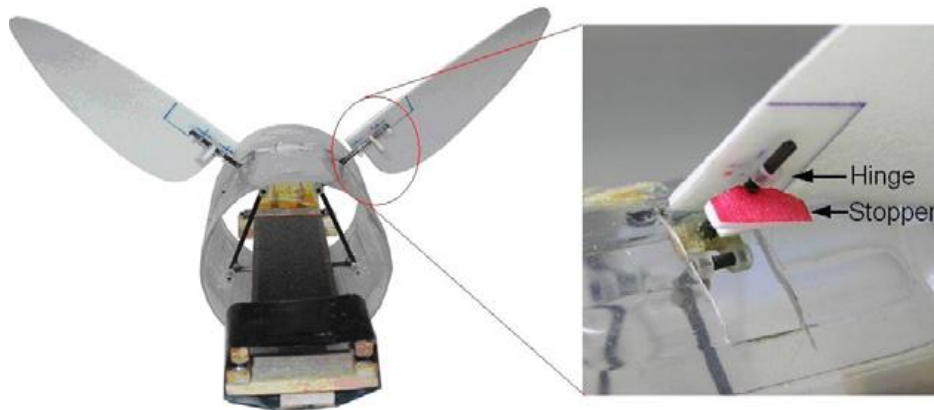


Figure 2.20: *Flapper Actuated by LIPCA Version 1 (Syaifuddin et al. 2006)*

Further tests were performed using a slightly altered LIPCA actuator and linkage mechanism (Figure 2.21), but on this occasion the type of wing surface was analysed. They experimentally tested the vertical force production dependent on the type of wing surface comparing the difference between a flat wing and a corrugated wing, which are common for insects where the veins span out from wing root to tip on both upper and lower surfaces. The vein structure will provide a higher bending stiffness compared to a simple flat wing constructed from the same materials. Both wings they tested had identical mass, planform area, geometry and material (polyethylene, same as the previous experiment). The corrugated wing would however, have a different side view profile due to the vein formation. During tests the wings LE was re-enforced by the addition of a carbon fibre rod leading to an increase of its bending stiffness.

Along with the wing structure, the mechanism was slightly altered to include the clapping of the wings at the end of upstroke. However, the authors could not conclude on the effect of the clapping clearly and stated that further tests would be needed with the use of a vacuum chamber as all the forces measured in this experiment were total force recordings. However, the total force measurements are the actual forces that this flapping model produces, and if flight was possible for this model it is paramount to consider this form of force measurement. The setup was the same as that used for their tests in (Syaifuddin et al. 2006), in addition to the flapping model now placed at a 45 degree inclination to the horizontal axis. During flapping flight some insects tilt their body to create a flapping stroke angle at 30-60 degrees to the horizontal axis (Grodnitsky 1999), hence the choice of 45 degrees. Another change was the choice of wave input for the actuator which was now a square wave. The wing rotation angles remained the same as the previous tests.

Overall they found that the corrugated wing produced a larger vertical force, whilst the mechanism was flapped at a resonant frequency of now 10 Hz (Nguyen et al. 2008). Lastly, flow visualisation was performed on the corrugated wings inside a wind tunnel with a flow of 5 m/s via the smoke wire technique, which depicted the generation of a LEV and TEV during downstroke wing motion, with detachments to the freestream observed thereafter.

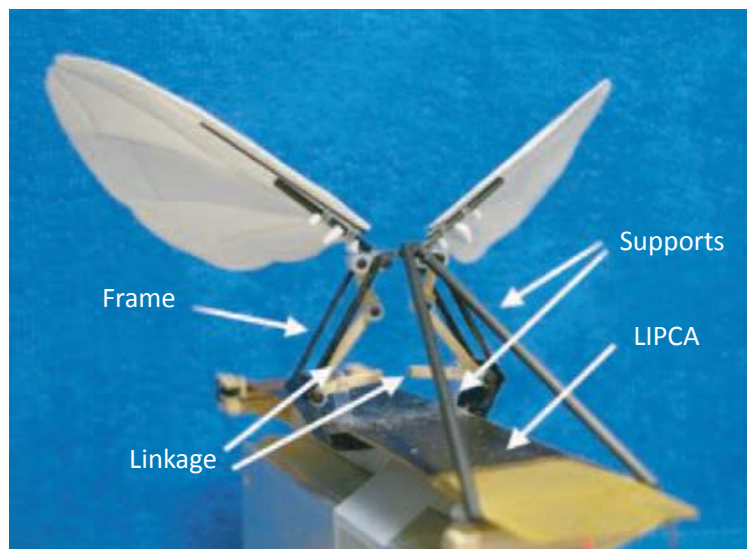


Figure 2.21: *Flapper Actuated by LIPCA Version 2 (Nguyen et al. 2008)*

To unfold the curiosity surrounding the vertical aerodynamic force generation of the present flapping model and its wing motion production, researchers at Konkuk University continued with their experimental investigations on their flapper, with some changes to improve its previous state. Retaining most of the flappers previous characteristics, they implemented changes in the form of a revised actuator now using a compressed LIPCA which should in effect enhance the flapping amplitude of the flapping device. A different type of wing was also adopted which is a geometric clone of a horse botfly insect, where its skeletal profile is fabricated of carbon/epoxy fibres and kapton film (Figure 2.22). The wings were bonded together by vacuum bagging and cured at very high temperatures of 177 deg celcius (Nguyen et al. 2007). Using the new compressed LIPCA the flapping angle was now 110 degrees and with the employment of a vacuum chamber the mechanism now adopted the clapping technique as the aerodynamic force could now be found, their vacuum level was stated as 95%. Their setup now included application of the nano 17 load cell. The actuator had 300V (peak to peak) applied to it with the instruction of a square wave. The model was mounted to the load cell by a sting

manufactured from a carbon rod and was tilted at 40 degrees to the horizontal axis, for reasons mentioned previously.

The wing rotation amplitude was now increased to 70 degrees, where the downstroke rotation was 10 degrees and upstroke rotation was 60 degrees. The Reynolds number under hovering conditions with a flapping frequency of 9 Hz is 3684. Flapping at larger frequencies does not necessarily mean that you will always get larger vertical forces when considering passive wing rotation, the primary reasons are the size of wing rotation amplitude and the duration of wing rotation at set angles. These factors heavily influence the fluid dynamics surrounding flapping wing flight. As a whole, they reported the temporal variations of aerodynamic force production for two tests of which the summary shows that the mean vertical aerodynamic forces found were 0.025 N for the compressed LIPCA and 0.021 N for the original LIPCA, thus they concluded that due to an increased actuator displacement and actuation force, the compressed LIPCA produced better results. Refer to (Nguyen et al. 2007) and (Nguyen et al. 2009a) regarding their tests, the latter is an extended edition.

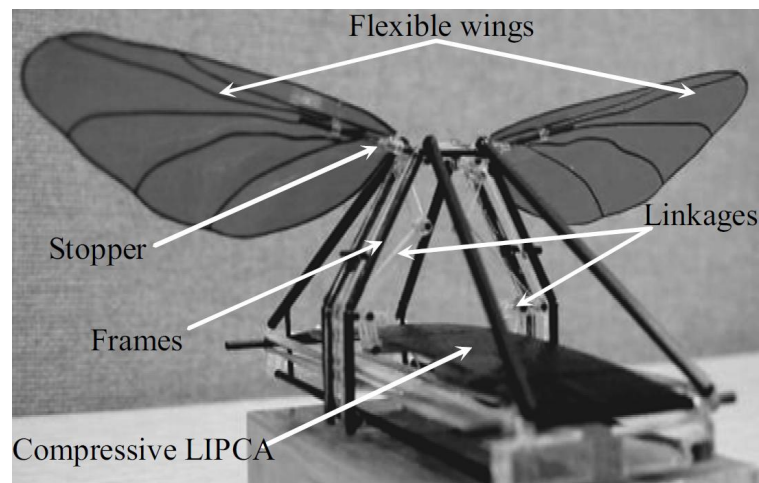


Figure 2.22: *Flapper Actuated by LIPCA Version 3 with Acrylic Links (Nguyen et al. 2007)*

With modifications applied to the appearance of the model (Figure 2.23) in addition to a new experimental rig, the model was now placed above the transducer by a carbon fibre fabricated sting, as opposed to previous tests where the flapper was placed below the transducer. The new stand has a pivot point beneath the model connection where its body axis can be tilted. They tested the aerodynamic force generation of two artificial wings for which the geometries were based on two insects which were the horse botfly and hawk moth, both were constructed by the same method mentioned previously. The artificial horse botfly wings had an area

of  $22 \text{ cm}^2$ , span of 11.4 cm, an AR of 2.96 and Re of 5890. The hawk moth artificial wings had the exact same area, span of 10.6 cm, an AR of 2.55 and a Re of 5654. For both sets of wings the resonant frequency was found to be 9 Hz and the flapping angle created was 130 degrees using the compressed LIPCA.

Temporal variations of the aerodynamic forces were provided and in summary the mean vertical aerodynamic forces were found to be 2.38 gram force for the horse botfly wings and 2.49 gram force for the hawk moth wings. The authors state that the reason why the hawk moth wing produces a larger vertical aerodynamic force is due to its exact replication of a real hawk moth insect wing, whereas for the artificial horse botfly was scaled up in this experiment. However, capturing the time history images of the wing motion (flapping angle and wing rotation) alongside force measurement may help to explicate on the difference of force generation, as aforementioned the aerodynamic forces are considerably influenced by the wing pitching motion.

Moreover, when comparing differences in forces which are not substantial deems to be quite difficult without the use of techniques such as PIV which would allow the experimentalist to grasp a complete insight of the flow development throughout a flapping cycle step-by-step. Smoke visualisation was performed in a low speed wind tunnel as smoke streaklines travelled at 1 m/s along the horizontal axis flowing towards the mid-span of the hawk moth wing, whilst the flapping model was tilted so its flapping stroke plane is at 45 degrees to the horizontal axis. From the images they noticed the development of the LEV and TEV during downstroke motion and detachments of these vortices moving into the freestream thereafter. For more information regarding their setup refer to (Nguyen et al. 2009b).

The fourbar linkage mechanism was modified to achieve an optimal flapping frequency by investigating the lengths of their present flappers linkages. Previously in (Syaifuddin et al. 2006), (Nguyen et al. 2007), (Nguyen et al. 2008), (Nguyen et al. 2009a) and (Nguyen et al. 2009b), the flapper demonstrated its largest vertical force production at resonant frequency of 9 or 10 Hz, the researchers at Konkuk University wish to better these results by producing the largest vertical force production beyond the frequencies reported as far. Following their analysis they found that altering the linkage lengths results in an improved moment transmission leading to flapping at higher frequencies. To summarise, they found that the optimal frequency of their improved flapper was now 17 Hz, however, this was at the expense of a decrease in flapping amplitude which was now 92 degrees. They concluded that this was an improvement on their work from (Nguyen et al. 2008). See (Truong et al. 2011) for an in-depth review of their linkage length and flapping model evaluation.

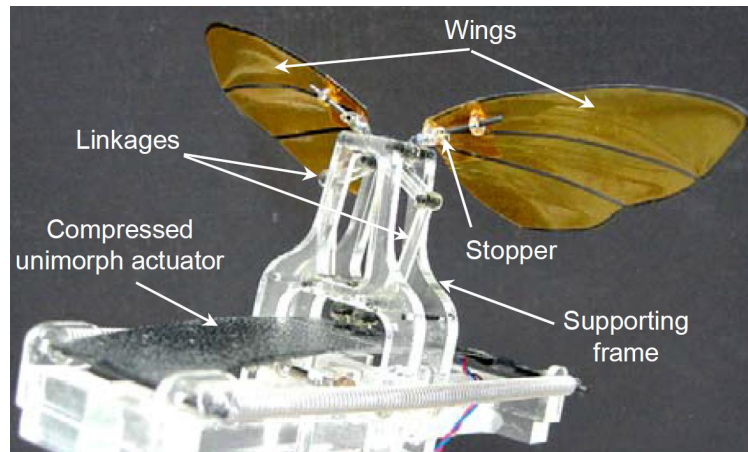


Figure 2.23: *Flapper Actuated by LIPCA Version 4 Complete Acrylic Frame (Nguyen et al. 2009)*

In order to design an MAV based on a particular insect, it is paramount to study this insect and understand its flight parameters. They used two high speed cameras operated at 2000 fps (placed perpendicularly to one-another to capture the side and back views simultaneously) to record the beetle in free flight, which was accomplished by suspending a beetle in the air by a hanger. Thereafter, the images are taken to obtain information such as flapping stroke angle, frequency of flapping and the rotation of the hind wing. Analysing the images, the stroke plane for hovering free flight was found to be 11 degrees from the horizontal axis and -21 degrees from the horizontal axis for forward flight. For hovering free flight the beetle has a flapping amplitude of 180 degrees and for forward flight an angle of 165 degrees. The wing rotation for both modes of flight is reported as found to be 140 degrees, the flapping frequency was found to be 37 Hz for hovering and 34 Hz for forward flight (Nguyen et al. 2010a).

Exploiting the knowledge gained from their previous work (Syaifuddin et al. 2006), (Nguyen et al. 2007), (Nguyen et al. 2008), (Nguyen et al. 2009a), (Nguyen et al. 2009b) and (Truong et al. 2011), the team at Konkuk University developed an MAV known as the beetle mimicking flapper whose specifications have been explained in Chapter 1 of this thesis. Due to the present technology in terms of actuation and power source, it seemed more feasible to resort to a DC motor (Didel) due to its many attractive features for robotics at this small scale. Their design adopted a popular Scotch yoke mechanism which converts the rotary motion output from the motor to result in a linear motion which in turn creates a flapping motion. As the motor rotates, it forces the crank which is attached to it to move with it, now as this crank rotates it moves the slider whose motion is restricted to move linearly in the vertical direction by the guides on either side. This

slider is connected to a set of links which will transform the motion now into a flapping motion as they pivot about a point. Refer to (QTRCO) and (Wolfram Scotch) for more information regarding the Scotch yoke mechanism, including a wide range of animations available on the internet.

Wing rotation was created by the use of 0.05 mm thick polyimide, this was placed in between two glass/epoxy sheets and bonded together. The role of the glass/epoxy layers was to act as a stopping device to limit the amount of wing rotation. The components of the flapper were constructed from 1 mm thick acrylic sheet, and the total weight including the on-board battery comes to 10.26 grams. The artificial beetle like wings were fabricated from carbon fiber for its frame and venation formation which replicated that of a beetle and its membrane from thin Kapton film (7.7 micro metres). The two materials were bonded together by vacuum bagging and curing in an oven. The leading edge was the only skeletal feature that was re-enforced to increase bending stiffness.

Forward velocity was measured by mounting the model on a horizontal guide rail where its distance travelled is measured by a ruler. As the wing rotation function is the prime reason behind forward velocity, various materials were tested to determine the forward velocity. The maximum average forward velocity was found to be 360 mm/s at a travelling distance of 420 mm. Thereafter the model was placed on a sting which is mounted to the F/T nano 17 transducer, to flap through a stroke plane of -5 degrees from the horizontal axis (which was the mid-angle between a real beetle in hovering flight and forward flight).

Vertical force measurements were recorded in time history of the entire model and the average total force generated from the model was 2 grams. Average vertical force can be improved by incorporating a motor which has a higher stall torque and reducing the weight of some of the components used especially the battery. A change in the motor and reduction of linkage/frame mass results in an increase in flapping frequency of 25 Hz and a total mass of 10.37 grams. The average vertical force produced now was 3 gram force which is an increase by 50% compared to the previous tests. The MAV still cannot lift its own weight and the flapping frequency is still lower than the real beetle. When the forward velocity was tested again using the same setup as described above, the flappers performance improved as the maximum average velocity was now 700 mm/s at a travelling distance of 800 mm. Tests were also carried out to determine which body angle would produce the highest forward velocity and as expected the body angle parallel to the horizontal axis produces the best results, thus forward flight would be ideal in this manner, but would mean that the MAV would need to rotate its body in flight as this would not be suitable for hovering flight mode. The thrust force was

found to be 2.83 grams.

The Air Force Institute of Technology have also taken a keen interest in flapping flight, they created a MAV very similar to the RoboBee of Harvard University through direct collaboration with Harvard Microrobotics Laboratory. They present a method for the manufacture of small components such as wings with a repeatable process. The MAV (Figure 2.24) utilises a four-bar linkage to create the flapping motion, which is actuated by a single bimorph piezoelectric strip which is mounted in a cantilever configuration. The flapping amplitude produced is 110 degrees and wing rotation is created by a flexible material located at the hinge position near the wing root. The piezo was sourced from Omega Piezo (a commercial supplier of piezo products), this is one of many companies which manufactures piezo components. The MAV was constructed of flexure linkages which is fabricated by sandwiching kapton film in between two pieces of carbon fibre, this can then be cut as the part is still a somewhat 2D object (due to its minute thickness), thereafter another two laminates can be joined and folded to create a 3D part. The process needs to be repeatable and also the parts need to be fabricated accurately, thus the parts were cut using a laser. For more details regarding the manufacturing refer to (Anderson et al. 2011).

Another manufacturing method which has been developed recently by Harvard Microrobotics Laboratory has been denoted as the 'pop-up book MEMS'. Using this method 3D structures can be manufactured at the micron to centimetre scale. Previously flexures were constructed by sandwiching rigid and flexible layers together (such as carbon fibre and kapton film), a large bulk of parts would be required to make an MAV as spare parts are also needed and assembly mis-alignments may be a common occurrence for such small scale components. Pop-up books on the other hand is a single part, where the links are on the multiple interconnected layers, where mechanisms of much more complexity can be created. The main advantage is the fabrication of complex mechanisms from a single part. Refer to (Whitney et al. 2011) for further details regarding this method.

The MAV had a mass of 0.35 grams, fairly heavier than the Robobee. When flapped at resonance the model could operate at 30 Hz, however, this was heavily dependent on the wings attached due to wing mass and aero loading acting on the wings. The model generated a vertical force of 1.5 mN per wing. Several modifications could be applied, foremost of these would be a custom designed actuator which would need to be lighter and maintain or improve the power density among other properties provided by the Omega Piezo strip. Similar to wings used on MAVs of this scale they were constructed from carbon fibre and Kapton polyimide, with

the latter as the membrane material. Force measurements were performed with the incorporation of a new piezo. The measurements were conducted using the nano 17 with the Netbox, which they state has a force resolution of 3.125 mN for all axes. Referring to (Anderson 2011a), lift force measurements with temporal variation were recorded in the range of 2 mN to -4 mN, even though measurements were conducted below the force resolution of the sensor at certain periods and close to the noise floor level the data obtained was accurate as they showed consistency in cycles and repeatability. Averaged force measurements per wing type were quite close to one another. They conclude their manufacturing procedure of developing wings produces sufficient repeatability in terms of mass, structural dynamics and force generation properties as seen from the averaged force measurements. Producing wings of very similar properties is of high importance as instabilities would result in an FWMAV when in flight, furthermore it would be easier to implement flight control methods if this factor of wing property differences was eliminated or drastically reduced. Refer to (Sladek et al. 2011) for a detailed analysis of the wing manufacturing procedure.

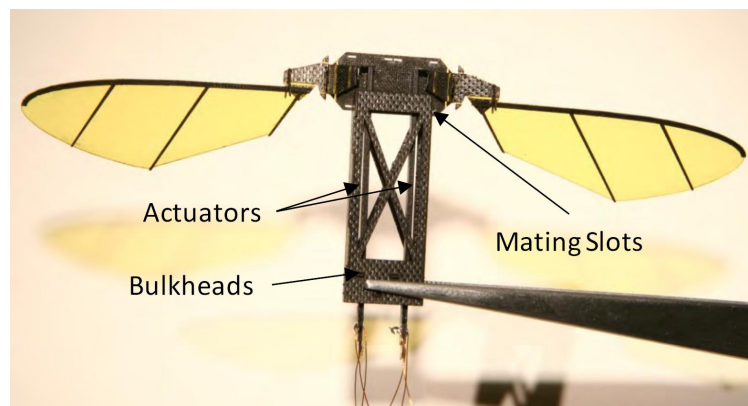


Figure 2.24: *Flapping Wing MAV with Two Actuators (Anderson 2011a)*

Force measurements were performed on the Delfly II in its most expensive mode of flight in terms of energy, which is hovering flight (Lentink et al. 2009). Their work describes the process of how Delfly and Delfly II were designed from fundamental rubber band actuated flappers to electrically actuated via motors and on-board power supplies. In addition they provide details concerning the components selected for the flapping vehicles and the locations of these components on the vehicle itself which is important to aid flight stability. Average lift force readings were produced where tests are conducted in a vacuum chamber as well as air. The deformation of the wing membrane during air and vacuum tests differed, evidently due to no aero loading acting during vacuum tests, summarising that large aero-elastic wing deformations are observed when the

model is flapping in air. They conclude that the efficiency in Delfly like designs are poor due to high inertial and frictional losses. Following this an analysis regarding the efficiency of flapping wings compared to revolving wings was conducted, demonstrating that revolving wings have more efficiency in hovering flight mode, for both tests they used insect like wings where one set was flapped and the other rotated in a circular plane.

Although they summarised that revolving insect wings would be more efficient, further tests via experiments or computational simulations should be carried out, as insect wings under the correct Reynolds number and wing motion can produce large lift forces compared to the insects weight. Thus a lift to energy expenditure study would provide more insight into this and help clarify as well as aid in the production of efficient micro flyers at insect scale. The fluid dynamics encountered in this type of study may reveal a prolonged attachment of the stabilised LEV for the rotating wings as AOA change and pronation/supination would not exist, resulting from this the forces produced and energy spent on each case would be analysed. Further to this, the study could become rather involved as mechanisms such as clap-and-fling prove to be highly beneficial for insects, thus insect flight mechanisms would need to be included in the complete study amongst other vital factors. Fluid visualisation should be captured for all these experiments to directly compare the flow physics encompassing these types of wing motion, including the vortical shedding at the strokes reversal, and continued vortical shedding may occur for the revolving wing case, to fully investigate this the flow dynamics need to be visualised in a time dependent comparison.

Kawamura et al (2008), conducted a force measurement study on flapping wings encompassing a two-directional force balance system composed of vertical and horizontal directional load cells. The MAV adopted the clap-and-fling technique (wing clap was performed at the end of the downstroke by both sides and at the end of upstroke), which had a span of 100 mm and a flight weight of 2.3 grams, which are said to be close to that of a real Hawk moth insect, namely the *Manduca sexta* (Kawamura et al. 2008). For preliminary tests they used a flapping model of span 150 mm with a motor actuating the gearbox powered by a mains DC PSU. Tests were carried out in a wind tunnel run at 0-5 m/s, and the model had a flapping amplitude of 46 degrees. The body angle was varied from 0-40 degrees from the horizontal axis during experiments and average force measurements were presented. In general the results showed larger vertical force production at higher freestream velocities and flapping frequencies. From the results of their tests they developed an x-type MAV, where the clap-and-fling was performed 3 times per flapping cycle, with a stroke amplitude of

100 degrees and adopted a tail which consisted of a rudder for control purposes. The CG position of the MAV was adjusted by altering the position of the on-board battery, more flapping frequency was required for hovering flight as opposed to forward level flight.

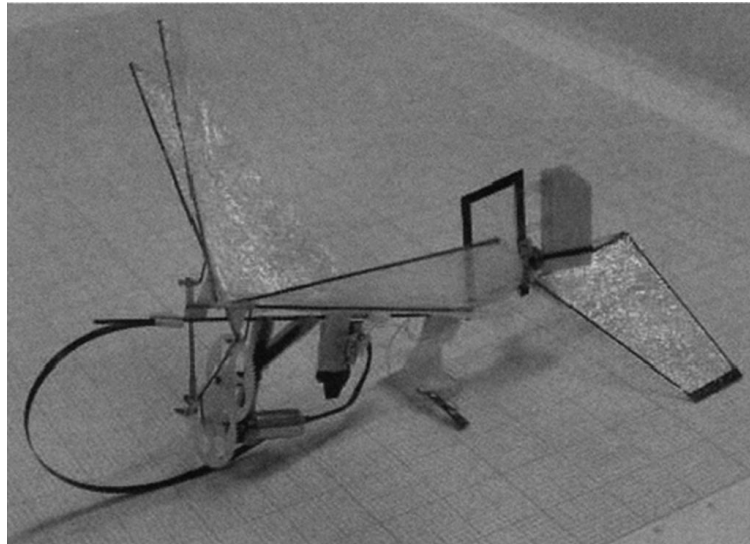


Figure 2.25: *Clap-and-Fling X-Type MAV* (Kawamura et al. 2008)

Harvard Microrobotics Laboratory (HML) as mentioned in the introductory section of the thesis have developed an insect scale MAV composed of flexure linkages, which are actuated by a custom manufactured piezoelectric strip and can perform high frequency flapping up to 110 Hz. As mentioned earlier the MAV is capable of multiple motions through the use of a 1DOF transmission, one is flapping and the second is created by passive wing rotation using the aerodynamic loading acting upon the wing when travelling through its respective stroke motion. A flexible material known as polyimide is used to create this rotational action, this material has been used for various MAV applications to carry out the same job role. Robert Wood of HML was the core developer of the model (Wood 2008a), having initially worked on the MFI at Berkeley University, the RoboBee was a creation from the experience gained during the development and enhancements made to the MFI (details of this MAV were provided in the introductory section).

The piezo like its LIPCA counterpart requires a signal input to provide instructions for the action which it needs to perform, in addition to this, extremely high voltages are required which cannot be provided by the standard mini Li-Po batteries. Thus a step-up transformer would be needed which would usually be accompanied by a large mass due to the sheer number of electrical components required. Due to the high

frequency requirement of the RoboBee the amount of deflection output from the piezo had to be minimised as much as possible, however at the same time the flapping stroke amplitude has to be sufficiently large as well. Considering this, the linkage mechanism needs to be setup in such a manner where both are actioned appropriately. The blocking force of the piezo is also a vital factor as the aero loading acting on the wings will be transformed through the linkages to the actuator, thus the smaller the deflection required, the higher the output blocking force and frequency will be. With this in mind they designed a lightweight mini piezo strip which deflects at  $\pm 0.4$  mm, with a mere mass of 40 mg and length of 12 mm.

Under hovering flight conditions the MAV has a maximum  $Re$  of 1200 for hovering flight, a wingtip speed of greater than 6 m/s and an astounding wing mass of 0.5 mg (Wood 2007). The design process of the RoboBee has been detailed in (Wood 2007b), where in-depth details for fabrication of the model have been provided regarding the transmission, actuation and wing material properties. The MAV demonstrated an average vertical lift force of approximately 1.14 mN, the time history of this is presented in (Wood 2007b).

Through the continuous active research by the team at the HML lab, modifications were made to supply the model with some form of control, which was accomplished in the form of asymmetric flapping motion. At the time, the only form of manoeuvrable flight was the adoption of asymmetric flapping and to achieve this two control actuators would be needed along with some alterations to the existing MAV. Maintaining a constant flapping frequency for both wings but a change of amplitude signifies that the flapping velocity of one side is larger which will result in the generation of larger lift forces, which will create a body torque from the asymmetric force production. With the addition of the control actuators in essence changes the model into a 3DOF transmission creating a 5DOF system (one power, two control and two passive). The power actuator is used to create the flapping motion, and the very small linear displacements from the control actuators are used to alter the kinematics of the wings.

The MAV structure was setup on a testbed with inclusion of one power and one control actuator. Thus only one wing was tested for control, and the results showed that through the activation of the control actuator a difference in flapping amplitude was produced dependent on the direction of deflection of the control actuator. Thus the addition of this actuator on flight vehicles will administer asymmetric force production. Refer to (Finio et al. 2009) for further information regarding the installation of control actuators.

In light of this asymmetric technique improvements were made by (Finio et al. 2009a), with the conversion

of two control actuators into one. By attaching this control actuator to the power actuator (used for flapping), reduces the mass and improves the efficiency of the future model. The hybrid power-control actuator was tested via a testbed composition shown in Figure 2.26, to determine the angles produced by the wings when actuated under the influence of the combined actuator. With the control actuator under displacement from its equilibrium position asymmetry was produced, but the amount of asymmetry differed when the control actuator was placed at each extreme point ( $\pm 0.75$  mm), which may have been due to imperfections in the manufacturing process of transmission components or actuator or slight misalignments in the assembly stage of the MAV. Moreover the asymmetric results demonstrate that the unification of a hybrid power-control actuator is suitable for controlled flight, and should produce enough torque to create body rotations.

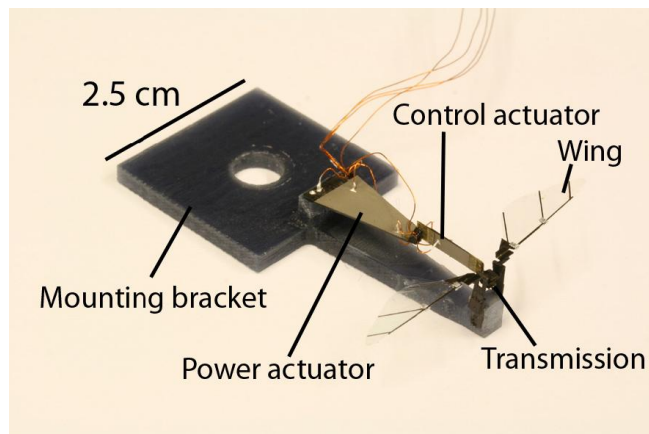


Figure 2.26: *Harvard RoboBee with A Hybrid Power-Control Actuator* (Finio et al. 2009a)

Stroke deviation was implemented on the RoboBee (Finio et al. 2010), to investigate more efficient wing trajectories that some insects can perform. Analysis was carried out by a quasi-steady model to determine the lift force generated and the power required per trajectory. And experimental images were captured of the wing performing the various trajectories at two different frequencies. With adjustments applied to the transmission and the installation of an additional actuator to create stroke deviation, one half of the model was setup on a testbed to analyse the trajectory created by the wing. The three trajectories created by the wing tip were flat, oval and a figure-of-eight.

At low frequencies (1-2 Hz) the wing tip path seemed to perform well, creating sufficiently accurate replications of its input signal to the control the piezo which controls the wing deviation during a stroke. On the other hand, under high frequency tests (100 Hz) the wing tip trajectory did not match the shapes re-

quired even the flat line was erroneous. Differences would be expected from the two cases tested as one has minimal aero and inertial loading whilst the other experiences substantial contributions from both of these components. Possible reasons stated were that due to the transmission layout, the wing experiences undesired vertical motions due to coupling with the lift forces and the flexibility of the flexure joints allows motions in more than one axis. Even though a motion is usually required as a rotation about one axis, this would be possible from a revolute joint but this would not offer the desirable characteristics which flexures consist of.

As shown in the wing kinematic measurements sub-section of this thesis, wing deviation is an idiosyncrasy which accompanies the use of flexible materials for wing rotation, further details have been discussed in this sub-section. From the quasi-steady analysis they found that the flat wing trajectory produces the largest averaged lifting force, but consumes the most power whilst doing so. Furthermore, the figure-of-eight trajectory consumes the least energy but also produces the least amount of lift force, however, it did produce the best lift-to-power ratio. Finally, the oval trajectory produced a slightly larger lift force than that found for the figure-of-eight but consumed a significant amount of more power. Despite the improvement in efficiency presented from the quasi steady theoretical results, implementing a third rotational motion would involve additional linkages which will increase the weight of the MAV, which may actually more or less balance out the efficiency enhancement. Further to this, the more linkages placed inside such confined areas (due to the size of these MAVs) would increase the chance of mechanical failure via wear and tear. An experimental analysis comprising of the measurement of force production, energy consumption and fluid visualisation would need to be administered on a MAV scale model to thoroughly analyse the effects of wing deviation. A variation of trajectories based on insects as well as others should be investigated whilst ensuring the wing trajectory and moreover complete kinematics remain consistent.

Dynamic stability is a key problematic factor relating to flapping flight for MAV and insect scale models, with an attempt to address this issue the group at HML installed upper and lower aerodynamic dampers to the existing RoboBee (Figure 2.27), which assists in vertical stabilisation by attempting to remain in an upright orientation when in hovering flight. The dampers were constructed from carbon and polyester sheet used as its membrane, and the carbon fibre structure was purposely increased in length from all sides to act as a form of protection against damage. When powered, the RoboBee vertically ascended with sufficient stability without its body rolling back over and crash landing, thus the damper proves to be effective whilst

vertically ascending. For hovering attempts the RoboBee is ascended vertically upwards (say through a z-axis) and then moves laterally through the x and y axes, it could not hover in one position, hence its lateral movement along the xy plane, but it did hold its altitude well. In addition the tests were conducted indoors where no wind effects exist, which would highly affect this damper configuration. Overall, the RoboBee did demonstrate some form of stability which allowed it to fly without the use of vertical guides.

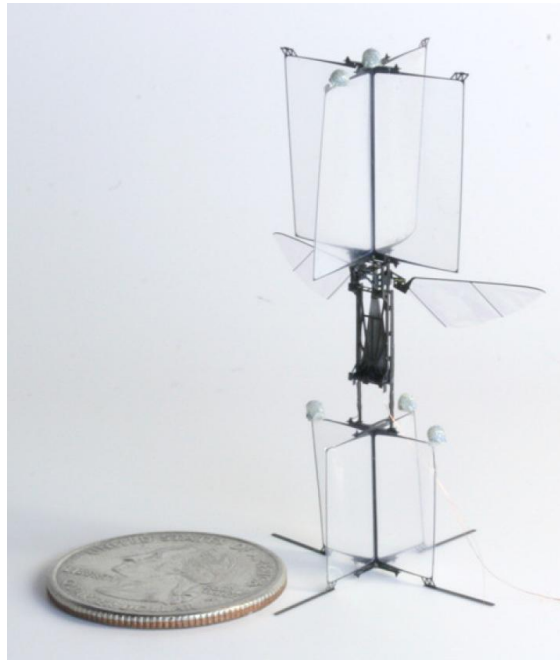


Figure 2.27: *Harvard RoboBee with Stabilising Dampers* (Teoh et al. 2012)

With an endeavour to cover all aspects of their RoboBee design and make improvements in various categories the HML group developed a methodology to manufacture very light weight artificial insect like wings. Furthermore, in order to replicate insect flight one needs to investigate the wing morphology of real insects in correspondence to their flight performance and apply these items to the robotic MAV. Their intricate venation formation would provide certain strengths of bending stiffness to the wings which will have an affect on their passive deformation, in turn determining the temporal aerodynamic forces generated by the wings. The fabrication of the wings was a combination of smart composite microstructures and lithography, the complete process in detail has been presented in (Shang et al. 2009). Various wings were created where their new wing enhanced the spanwise and chordwise stiffness to provide a closer resemblance to insect wings as opposed to their previous wing set that was used on the initial design of the RoboBee (shown in Figure

1.18). The correlation between the venation formation and mass distribution would simplify the replication of insect wings, thus if the venation structure is mimicked accurately the mass distribution throughout the wings should not pose much of an issue.

## 2.4 Further Review of Aerodynamics

The  $Re$  of the flow has significant effects on the behaviour of the fluid when a bluff body such as a circular cylinder is placed in a freestream condition. The flow dynamics dramatically change through a range of Reynolds numbers, which has a direct impact on the drag coefficients generated by the bluff body, a comparison for the impact of  $Re$  on drag coefficient has been shown in Figure 2.28. From the data present in Figure 2.28, the drag coefficient is very large at extremely low  $Re$  which decreases as the  $Re$  of the flow increases. At a  $Re$  of approximately 300,000 there is a drastic plunge in drag coefficient values which gradually increase until a  $Re$  of  $10^7$ , the rapid decline in drag coefficient values is due to the sudden transition from laminar flow to turbulent flow within the boundary layer.

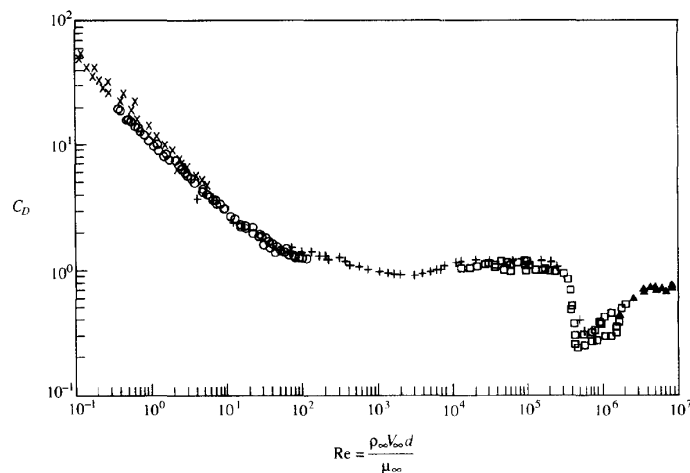


Figure 2.28:  $Re$  Influence on the Drag Coefficient for a Circular Cylinder (Anderson 1986)

For a very low  $Re$  ranging from 0-4, the flow around the cylinder in freestream conditions remains attached and is nearly symmetrical (see Figure 2.29A). This type of flow is commonly known as Stokes flow or creeping flow, the velocity of the flow is very slow, thus inertia effects are very small and the viscous effects are very large. As the Reynolds number is increased and lies within a range of  $4 < Re < 40$ , the flow seems to separate

on the back half of the cylinder where two stable vortices are formed which maintain this position (shown in Figure 2.29B). Thereafter, the vortices which were present behind the cylinder are shed alternatively from the body as the flow becomes unstable as the  $Re$  is escalated above 40. This formation of alternate vortex shedding behind the cylinder continues and is termed von Karman vortex street, a sketch of the shedding formation can be seen in Figure 2.29C.

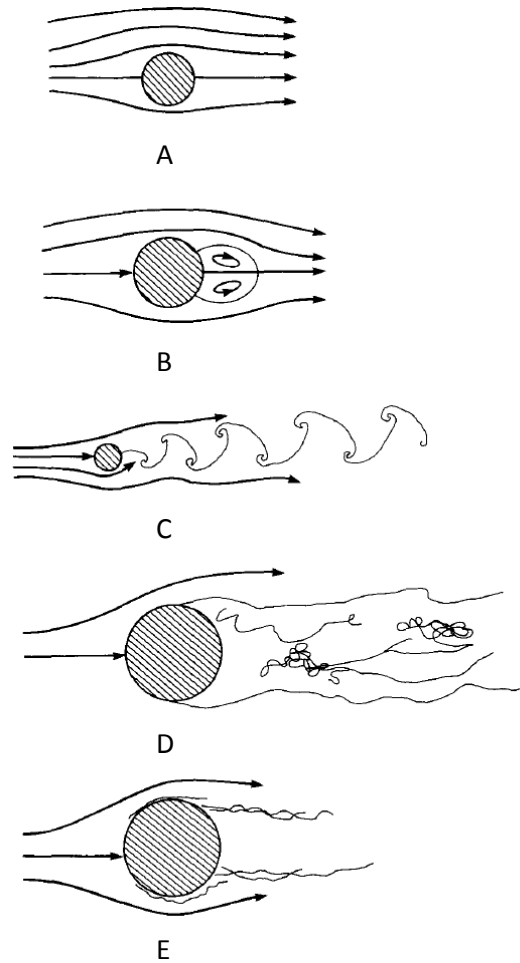


Figure 2.29: *Flow Around A Circular Cylinder (Anderson 1986)*

As the  $Re$  increases to the order of  $10^5$  the laminar boundary layer on the surface of the cylinder separates at approximately 80 degrees from the stagnation point located at the centre of the frontal face (see Figure 2.29D). The previous alternate shedding of vortices becomes turbulent and no pattern is present in the wake downstream of the cylinder. For larger  $Re$ , laminar flow separation occurs on the frontal face as mentioned

previously, but transition to turbulent flow takes place in the free shear layer above the separated region, where re-attachment of the flow occurs towards the back half of the cylinder. Thereafter separating again at 120 degrees from the stagnation point. The  $Re$  for this flow phenomena is  $3 \times 10^5 < Re < 3 \times 10^6$ , from the transition to turbulent flow and thinner wake moving downstream behind the cylindrical body (see Figure 2.29E). The pressure drag generated is diminished, thus the drag coefficient declines as mentioned above. As the  $Re$  increases above  $3 \times 10^6$  a wider wake is produced relating to a larger pressure drag behind the cylinder which is why the drag coefficient increases in the data shown in Figure 2.28. At a location on the frontal face the boundary layer transits directly to turbulent flow, and separation occurs below an angle of 120 degrees on the back half of the cylinder from the stagnation point (located at the front of the cylinder) which is why a wider wake is produced. The creation of a wider wake via flow separation relates to the production of a larger pressure drag force. In general, the size of drag force that would be produced in Figure 2.29E is greater than the size of drag force that would be produced in Figure 2.29A. For further information see (Anderson 1986).

### 2.4.1 Wagner Effect

When a wing with an inclination starts moving from its previous rest state through a fluid, the circulation formed around the wing will not reach a steady state instantaneously. As the wing travels through a fluid, vorticity will be generated at the trailing edge which will eventually roll up and shed into the wake. The shed vorticity from the trailing edge is commonly known as the starting vortex. Thus, as the wing continues to move through the fluid, the bound circulation around the wing gradually strengthens and will reach its maximum steady circulation when this starting vortex has travelled a sufficient distance from the wing. To elaborate, the steady circulation is reached only when the starting vortex has travelled a sufficient distance from the wing, as the growth of circulation is hindered by the velocity field induced in the proximity of the wing due to the vorticity which is shed at the trailing edge. This phenomena of delayed growth in circulation was discovered by (Wagner 1925), for further information refer to (Sane 2003).

### 2.4.2 Added Mass Effect

Consider a wing at rest in a vacuum chamber, if this wing is now accelerated by translating through a single axis, an inertial force is generated as the mass of the wing is accelerated. If the same scenario were now performed within a fluid, as before an inertial force would be generated by accelerating the mass of the wing but now an additional force is required to also accelerate the fluid which is present around the wing, thus in effect the inertia of the wing has increased. This effect is known as added mass and is also commonly known as virtual mass (Sane 2003) and (Ellington 1984). As an additional force is required to accelerate the fluid, consequently more power will be required which will evidently have an effect on insect flight due to the variable accelerations that exist in a stroke cycle.

### 2.4.3 Kramer Effect

A wing which is performing a steady translating motion through a fluid which abruptly alters its angle of attack will enhance its lift generated during this time, and is directly related to the angular velocity of rotation, where larger angular velocities will generate greater lifting forces. This fluid phenomena was discovered by (Kramer 1932), further information can be found in (Ellington 1984). A wing which is flapping and rotating about a span-wise axis, will cause a deviation from the Kutta condition as the stagnation position will displace from the trailing edge. Such a motion will develop shear, which a fluid will naturally resist due to viscosity. Thus, the fluid will produce additional circulation in order to once again agree with the Kutta condition where the stagnation region is at the trailing edge. However, as re-establishing the Kutta condition cannot be accomplished immediately, which effectively deems that time is required to fulfil the condition. If the wing continues to rotate rapidly during this time, the fluid will naturally attempt to meet the Kutta condition, and in doing so will generate additional circulation until the Kutta condition is established. Albeit, whether the additional rotational forces increase or decrease the net force generated from the wing translation is dependent upon the direction of wing rotation. Further information can be found in (Sane 2003).

This form of fluid phenomena regarding rotational circulation was also noticed in the experiments performed by (Sane & Dickinson 2002), where a wing was rotated at constant angular velocities whilst it was concurrently carrying out a steady translation. From the measurements obtained, improvements were made to

current quasi-steady analytical models, where they found that the rotational forces varied linearly with the position of the rotational axis for all the angular velocities measured. Revising the quasi-steady method to include the effect of rotational circulation demonstrated improvements in the comparison between analytical and experimental data.

#### **2.4.4 An Additional Review of LEV, TEV, Wake Capture, Clap & Fling and TV**

A wake flow field is continually produced from the periodic motion of each wing, as an action of the cyclic motion the wing will pass through this flow field consisting of shed vorticity from the prior stroke as it continues its prescribed kinematic motion introducing a wing-wake interaction which is commonly known as wake capture. Albeit, the effect of wake capture may be near negligible in forward flight as the wake is stretched out and left behind the insects forward flight path, but during hovering mode its contribution seems to be paramount aiding both lift force production as well as flight force efficiency.

The schematic shown in Figure 2.30, presents a hypothesis of the wake interference with the cyclic motion of the wing. During the translation phase an LEV is attached to the upper surface of the wing, the freestream velocity is produced as the wing travels through the fluid and the light blue arrow is the resultant force acting on the wing. As the wing approaches the end of the current stroke it starts to rotate around an axis along the chord plane and as a result, vorticity is generated at the trailing edge and thereafter shed from both the leading and trailing edges. An inter-vortex velocity field (velocity field has been shown by dark blue arrows) is generated by the two vortices that are rotating in opposite directions. The strength and favoured direction of the inter-vortex stream is governed by the two vortices shed from both edges. Upon the completion of stroke reversal the wing interacts with the velocity field where fluid momentum is transferred to the wing and as a result enhanced aerodynamic forces are achieved, which has a supplementary benefit in the form of flight efficiency. The wing kinematics determine the magnitude of the vortices shed from each edge, therefore the sizeable effect of wake capture is dependent upon the wing kinematics before and after stroke reversal. At the onset of the next stroke vortices form at the leading and trailing edge, as this motion progresses to translation the trailing edge starting vortex is shed into the wake and the Kutta condition is established.

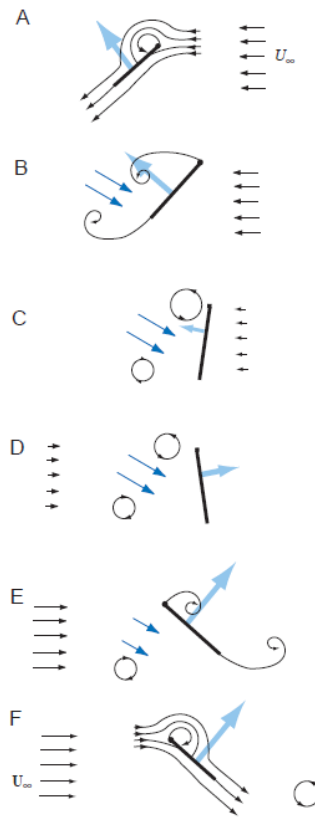


Figure 2.30: *Simplified Wake Capture Schematic During Stroke Reversal (Sane 2003)*

Sun et al. (2002), conducted an investigation utilising CFD to determine the flight forces and fluid dynamics surrounding a wing planform based on the drosophila fairly similar to that experimented upon by Dickinson et al. (1999). They briefly explain that under steady-state analysis the wing will produce approximately half the lift coefficient opposed to that produced under unsteady conditions where the dynamic stall vortex generates lifting forces. Simulations were performed firstly, where the wing undergoes stroke reversal with a dynamic wing rotation altering its pitch angle and travelling through the flow field generated from the previous stroke, and secondly where the wing performs the same kinematic motion but it is started in still air. From a comparison of the data they conclude that the force peak produced at the beginning of the stroke is due to rapid acceleration of the wing rather than wake capture, as they found the force peak was more or less similar in both cases. In addition, a brief analysis was carried out on the location of the pitching axis and its effect on force production where they found that a rotational axis located at  $0.2c$  from the leading edge would produce larger force peaks and overall larger averaged force opposed to a rotational axis located

at  $0.5c$  from the leading edge. The discrepancies between the results of Dickinson et al. (1999) and Sun et al. (2002) remains unclear, but the aerodynamic phenomena of wing-wake interaction and its significance was clearly shown by the experiments of Dickinson et al. (1999) which was reviewed earlier.

An experimental investigation on real-life butterflies in particular Vanessa Atlanta was performed by Srygley et al. (2002), where the insects were freely flying to and from artificial flowers placed within a wind tunnel run to assess the topology of the three-dimensional separated fluid motion around its wings via high resolution smoke wire flow visualisation. They noticed that the butterflies took advantage of numerous unsteady aerodynamic mechanisms such as the LEV, wake capture, clap-and-fling, in addition to active and inactive upstroke motion (upstroke motion which has positive, neutral or negative loadings on the upstroke).

The insect has the ability to select freely which mechanism it requires to use from the aforementioned dependent on its flight behaviour. The authors found that the vortex structure generated at the leading edge was composed of a more consistent diameter rather than a conical formation which has been noticed in other experimental investigations (Van Den Berg et al. 1997). Thus a sufficient geometrical difference existed in the topological structure of both LEVs. Flow separation is noticed above the insects body and the authors state that a conical style of LEV requires that the flow along the lengthwise direction of the insects body would need to remain attached to the surface of the body and not separate, further information regarding this can be found in (Srygley et al. 2002). Furthermore they found the existence of sub-parallel dual leading edge vortices with the same sense of rotation on the upper wing surface. The production of these dual vortices is a result of two forms of acceleration during the downstroke, firstly the peeling stage where the wings are moving away from one another followed by the acceleration of the wings once they have separated. When this fashion of vortices are generated at the leading edge during the downstroke motion, the insect experiences very large accelerations. The vortices which are shed at the end of a stroke are known as stopping vortices which possess significant amounts of energy, where part of the energy can be usefully extracted upon interaction with the wing. The interaction of the wing moving through its wake and stopping vortex would reduce the amount of circulation of the stopping vortex whilst reducing the velocity of the wake, and dependent on the wing inclination lift enhancements can be achieved. A hypothesis mentioned by the authors states that circulation can be extracted from the collision of the wing and stopping vortex to create the bound vortex on the wing for the following wing stroke.

The clap and fling mechanism also termed as the Weis-Fogh mechanism was first proposed by (Weis-Fogh 1973),

where the author mentioned that distinct motions such as the clap and fling occur during the wing motion of the *encarsia formosa* stating that the wings are brought together at the top of the morphological upstroke (clap effect) and the fling occurs at the beginning of the morphological downstroke.

Researchers have further investigated this aerodynamic phenomena via experimentations and computational means to further understand the fluid dynamics and resultant forces generated from such wing motions. The clap-and-fling / clap-and-peel should be treated as two separate aerodynamic mechanisms as they actually act independently in a fashion one after another. Sane (2003), mentions that in the clap phase for the *encarsia formosa*, the leading edge of both wings come in contact prior to the trailing edges of both wings meeting one another, thus the gap is not closed abruptly, but in a rather gradual manner. The circulation on each wing is acting in opposing directions which leads to the result of cancelling one-another when the wings are in contact. Assuming the stroke plane is along the horizontal axis an additional thrust force is generated by the closing gap between the two wings as the fluid is pushed outwards (downwards). As the wings continue to pronate following the clap phase, the leading edges fling apart which creates a low pressure region that is then filled with fluid rushing in from the surroundings which augments the rate of growth for circulation. Both of the wings then move away from one another with opposite signs of bound circulation, however Kelvin's law regarding the conservation of circulation is conserved as the net circulation results to zero around the two wing system.

Miller et al (2005), took a computational approach to study the clap-and-fling technique by conducting two-dimensional simulations, lift coefficients were determined for a range of Reynolds numbers from 8-128 with an analysis of the flow field formation around the wings. In regards to the clapping phase, a small gap remains when the wings are in their final clap position. A fling motion only along with a combined clap-and-fling motion were studied for two forms of cases which were composed of a single and dual set of wings. The kinematic motions were modelled using the following equations for acceleration during translation (refer to Equation 2.1) and for deceleration during translation (refer to Equation 2.2).

$$v(\tau) = \frac{1}{2}V \left\{ 1 + \cos \left[ \pi + \frac{\pi(\tau - \tau_{acc})}{\Delta\tau_{acc}} \right] \right\} \quad (2.1)$$

$$v(\tau) = V - \frac{1}{2}V \left\{ 1 + \cos \left[ \pi + \frac{\pi(\tau - \tau_{dec})}{\Delta\tau_{dec}} \right] \right\} \quad (2.2)$$

$$\tau = \frac{tV}{c} \quad (2.3)$$

At the end of the upstroke the wings were rotated about the leading edge, whereas the fling phase was commenced by rotation taking place about the trailing edge. Wing rotation occurs at the end of the upstroke and start of the downstroke phases, during translation the wing is held at a constant angle of 45 degrees. The angular velocity during the rotational phase at the end of upstroke is modelled using Equation 2.4, the fling phase of wing rotation which occurs at the onset of downstroke is also carried out in this manner.

$$\omega(\tau) = \frac{1}{2}\omega_{rot} \left\{ 1 - \left( \cos \left[ 2\pi \frac{\tau - \tau_{turn}}{\Delta\tau_{rot}} \right] \right) \right\} \quad (2.4)$$

$$\omega_{rot} = \frac{2\Delta\theta V}{\Delta\tau_{rot}c} \quad (2.5)$$

Flow formation of the numerical results were compared to experimental results from another author for a pair of wings performing the fling motion, where a good agreement was found in both sets of images, even though the Reynolds number of the two varied quite significantly as the numerical simulation had an Re of 128 whereas the experiment had an Re of 3000. Analysing the flow field visualisations, displayed that on the commencement of the fling motion (at a Re equal to 8), the vorticity at the leading edge is generated and grows as the wings continue their rotational motion.

Shortly after as the wings move apart on the commencement of translation, trailing edge vortices are created which develop in strength, consequently this leads to lift reduction. However, positive lift generation prevails as the LEVs are prominently stronger than the TEVs in the vortical asymmetrical structure, this relationship is observed throughout the stroke. With the same wing motion carried out for a single wing, both LEV and TEV develop and are of equal strength whilst rotating in opposite directions implying that the principle behind total vorticity conservation is met. During translation the TEV has a stronger presence opposed to that observed in the dual wing case, thus lower lift forces are produced for the single wing case when compared to the two-wing case. During translation motion both the vortices at the leading and trailing edges remain attached to the wing until the point of wing reversal. For the dual wing case in the fling motion at a larger Reynolds number of 128 the LEVs are formed during the early fling stages, however, on the onset of translation the LEVs seem to stretch and eventually shed from the surface of both wings whilst concurrently

the TEVs form on both wings. Following this the TEV grows and eventually detaches from the wing surface and a new LEV begins to develop, this continual shedding and development of the vortices displays the von Karman vortex street, this fashion of alternate vortex shedding does not occur in three-dimensional insect flight. The TEV would be shed early and the LEV would remain attached to the wing until wing reversal for three dimensional insect flight. Thus, for the same kinematic motion vortex shedding is experienced for the larger Reynolds number case in the two-dimensional simulations. The vortices generated at the leading and trailing edges were circulating in opposing directions, this applies for both the dual wing and single wing cases.

Measurements acquired for a range of Reynolds numbers for the two-wing set under a fling followed by translation motion results in decreasing lift values during the translation phase for all the Re cases as the TEV grows. The lift measurements for cases which have a higher Reynolds number produce even lower lift values for certain periods due to the shedding of the leading edge vortex, but the values tend to rise when the LEV has once again formed and the TEV is shed. The largest peaks of lift coefficient, and largest lift coefficient during translation was found for the lowest Reynolds number case, and lowest lift coefficient values were produced for the highest Reynolds number case, thus as the Reynolds number increased the time dependent lift coefficient values decreased. The same relationship is observed for the drag coefficients where they seem to increase as the Reynolds number decreases, thus maximum values are produced for the lowest Re case, and minimum values are produced for the largest Re case, the drag coefficients will reach steady values as the wings continue to translate at a constant angle of attack. For the single wing set, the same analysis was performed where the authors found that as the Reynolds number increases the lift coefficient values decrease where the peak lift coefficients decrease as the Reynolds number increases. Furthermore, for an Re of 64 and above, the lift coefficients during translation experiences a substantial decline as the LEV detaches from the surface of the wing and moves downstream. The width of the boundary layer around the wing grows for the cases with decreasing Reynolds number and the mass of the fluid pulled along with the wing is greater. The drag coefficients for the single wing set are seen to increase with decreasing Reynolds number, these values also reach a steady state as the translation phase progresses. For the two winged set, the initial drag coefficient peak during the wing rotation phase was much larger opposed to the first peak produced in the one wing set. Overall, the drag coefficient for the dual winged set is larger than that found for the single wing set due to the drag peak produced during the two wing fling phase. As the drag coefficient has been found to increase with decreasing Re, more energy would be consumed especially in the

wing rotation phase by smaller insects which fly at the lower Reynolds number range.

Further simulations were conducted to investigate the combined motion (clap and fling) in a similar manner as described above, where a dual set of wings and a single wing were operated in a fluid domain which had a Reynolds number of 8, and a similar case with a dual set of wings where the Re was modelled at 128. For all sets, the wings were started from a rest position with a fixed angle of attack of 45 degrees. Firstly, for a Re of 8, as the wings translated through the upstroke moving in opposite directions approaching one-another each wing had an attached leading and trailing edge vortex which were shed when the wings approached one-another to perform the clap phase where they rotate about the leading edge to close the gap. Following this, the fling phase occurs as described previously where leading edge vortices form and the wings now travel through the wake of the prior stroke and weak trailing edge vortices form as the wings progress through their translational phase. Likewise at a Re of 8, the single wing during the upstroke motion has attached leading and trailing edge vortices which are shed from the wing surface during the rotation phase at end upstroke. In continuation of the wing rotation new leading and trailing edge vortices form which grow as the wing continues to translate through its downstroke motion and move through its wake from the prior stroke. For the larger Reynolds number as both wings translate in opposing directions moving towards each other, the LEVs develop whilst they shed their trailing edge vortices. As the wings perform the clap motion the leading edge vortices are shed and move a distance above the wings leading edge. During the fling phase, leading edge vortices begin to develop on each wing as they rotate about their trailing edge. Thereafter, as the wings translate away from one-another the leading edge vortices are shed, and TEVs develop which grow as the wing translates through the downstroke. Following this as described previously the trailing edge vortices will detach and move downstream as new leading edge vortices develop during this translational phase resulting in an enhancement in lift force.

In the two winged set where the Re is 64 or above, lift coefficients are enhanced during the rotation phase of the clap motion when compared to the single wing case. Following this, larger peaks are found at the start of the fling rotational phase for the two winged set opposed to the single wing set, this also applies to the lower Re cases as well. During this fling rotation, two large leading edge vortices form for the two winged case and no formation of trailing edge vortices takes place as the trailing edges are close together, but for the single wing although a leading edge vortex does develop, a trailing edge vortex of opposing rotational direction also develops which reduces the effect of the leading edge vortex and reduces the lift coefficients produced

for the single wing set. Furthermore, large drag coefficient peaks are also produced during the duration of the combined motion, where drag coefficient increases as the Reynolds number decreases, this latter result was also found for the single wing simulations. During the clap phase, the drag coefficient values produced for the single wing are significantly lower than the two winged set, thus more energy would be consumed when a mirror wing is present for the combined motion. Overall, the lift coefficient measurements for the two winged set are not significantly larger than the single wing set. Analysing the average lift coefficient data, they found that when the combined motion is performed by the two wings opposed to the fling motion only, the lift coefficients are larger for all the Re cases as the wings travel through their wake which was produced in the prior stroke. In general, the authors concluded that the lift enhancing effects of clap and fling were found to be greater for lower Re compared to the higher Re. After the clap and fling motion the lift is significantly enhanced for Re equal to 32 and below for the dual wing set opposed to the single wing set which has no mirrored motion, and this enhancement is more noticeable as the Re decreases.

Exploring the high lift mechanism related to the flight of hawk moths Ellington et al. (1996), stated that an intense LEV is developed during the downstroke motion of their model which is strong enough to explain the lifting forces generated. This downstroke is known as the power stroke as its primary role is to support the insects weight. They go on to mention that the vortex is developed by dynamic stall, and this vortex spirals out from the root towards the tip of the wing with a conical structure which has a resemblance to the leading edge vortex produced by delta wing aircraft.

The authors performed an experimental study on real-life hawk moth insects on this occasion, where the insect was situated in a wind tunnel and stereo-photography was exploited to investigate the three dimensional flow dynamics around the insects wing. A vertical smoke rake installed within the wind tunnel was utilised along different spanwise positions of the wing.

A comparison of the images taken just after mid-downstroke along the span of the wing, illustrated flow separation at the leading edge and re-attachment to the upper surface with a leading edge vortex enclosed between these two points which grew in diameter towards the tip. The leading edge vortex breaks down at approximately 75% span from the root, where it rolls up and attaches to the tip vortex which is composed of a much larger diameter. Further to this, they noticed that flow re-attached behind the LEV and travelled towards the tip of the wing into to the TV. In order to examine the vortex structure at the leading edge of the hawk moth insect further and replicate its formation robotically, they developed a flapper mechanical

model which has been reviewed in an earlier stage of this literature review. During the downstroke motion, a conical structured vortex formed which was swept along the leading edge of the wing by a spiralling axial spanwise flow. The axial flow velocity was manually measured where they found that it steadily inclined along the inner half of the wing and peaking at approximately 60% span from the wing base. Thereafter, the axial velocity declined more rapidly along the remaining wing span until it lifts off from the wing surface. In relation, the circulation data decreases on the outer wing during a position in late downstroke, which is an outcome of both vortex breakdown and the detachment of the vortex at the leading edge from the wings surface. The stability of the leading edge vortex is vital in order for the insect to generate sufficient lifting forces, this is accomplished by the transfer of spanwise axial flow travelling from the wing root to tip within the structure of the LEV as it drains energy from the vortex core in effect limiting its growth so the vortex remains attached to the leading edge for a prolonged duration. Techniques such as active spanwise suction or blowing along the upper surface of the wing can be adopted to induce axial flow to promote the stability of the LEV. In two dimensional conditions the spanwise pressure gradient required to drive the axial flow is non-existent, thus the LEV on a wing translating in two dimensional conditions under the Re of the hawk moth (6300) would most probably become unstable and detach from the wing surface moving downstream in the wake, such an effect has been reported previously above for a much lower Re under two-dimensional conditions. In general, as the axial flow transfers momentum out of the leading edge vortex, the momentum in the flow acting in the chord-wise axis is effectively reduced, thus the outcome ensures that the growth of the leading edge vortex is limited, and this lift enhancing aerodynamic phenomena is also a self-stabilising mechanism.

Birch et al. (2001), investigated the formation of the leading edge vortex on the large dynamically scaled mechanical device immersed in mineral oil with a wing planform replicating the geometry of the drosophila melanogaster insect. The features of the mechanical model have been expounded upon in an earlier section of this literature review. The Re of the flow considered in this experiment is 160, where a single wing is flapped through 180 degrees at a frequency of 0.168 Hz, further information regarding the setup of the apparatus can be sourced from (Birch et al. 2001).

Experimental flow visualisation in the form of PIV demonstrated that a shear layer of vorticity concentrated into a vortex at the leading edge via clear flow separation. Axial flow velocity was noticed within the core of the LEV, but was said to be considerably small compared to the average velocity of the wing tip, thus

the pressure gradients within the vortex core must be small relating to the weak axial velocity. A reason as to why the axial flow velocity is so low within the core could be due to the large viscous forces present at very low Reynolds numbers, thus large axial flow velocity is present in the LEV of the hawk moth model as previously mentioned where the viscous forces are much smaller opposed to the fruit fly flow conditions. In general, as the viscosity forces increase with decreasing Reynolds numbers, insects which fly at the very low Reynolds number range would most probably also have low axial flow velocity travelling through the vortex attached at the leading edge. Furthermore the larger viscosity present in the fluid at very low Re flows may allow the vortex to remain stable and attached to the leading edge for a prolonged duration as vortex stability is augmented by smoothening the disturbances which are present in the flow. The variation of the strength of vorticity along the span of the wing generates a spanwise pressure gradient which has been specified previously as a driving factor of the axial flow.

Their results also showed that maximum axial velocity exists behind the LEV, rather than acting through its core which as stated previously showed weak axial velocity. Chord-wise vorticity directs the flow towards the tip of the wing which essentially rolls up into the TV. The axial flow velocity hypothesis is quite different to that found by Ellington et al. (1996) for the hawk moth flapper, as both operate at substantially different Reynolds numbers which may be the critical factor in determining the structure of the LEV. In addition, as the velocity of the spanwise flow within the vortex cores differ significantly, the structural appearance of both vortices are likely to differ.

In order to investigate the effect and importance of the low axial flow velocity in the core of the LEV for the drosophila wing, fences were attached at 40% and 60% span from the wing base, to limit spanwise flow and determine the effect this has on the LEV. The installation of the teardrop fences reduced the axial flow velocity in the core of the vortex to velocity levels which were too small to measure, however, the structure of the LEV was barely affected, thus maintenance of the LEV in this case is not dependent on the axial flow through the core of the LEV.

Alternatively, the teardrop shaped fence was relocated and positioned rearwards at the trailing edge (still occupying a sufficient chord-wise distance with maximum height near the trailing edge), in order to determine whether the axial flow behind the leading edge assists in maintaining the LEV by removing energy from the developing vortex. This resulted in a reduction of vortex strength and overall lift reduction. Furthermore, the time course of force generation throughout a stroke was unaltered with the overall use of the teardrop fences

when compared to force data of the wing only, which meant that vortex attachment was barely affected. As a final investigation, a cylindrical wall acting as a stationary rigid boundary was placed in close proximity to the wing tip. This boundary was found to have no effect on the dynamics of vortex attachment, but force generation was augmented as the LEV was strengthened and extended a longer distance along the wing span before separating from the wing surface. Furthermore, Lehmann (2004) mentions in a review that the presence of this wall boundary would reduce the axial flow travelling out of the LEV structure which in effect limits the amount of energy exiting the vortex. Thus, it is important to note that even though the LEV grew in size, detachment from the surface still did not occur. The authors suggest that the flow conditions at this Reynolds number for the fruitfly wing, the LEV growth is limited (and its attachment to the wing surface is prolonged) by the reduction in the effective angle of attack, and this angle of attack is reduced due to the downwards flow induced by the combination of the tip vortex and the vorticity shed into the wake from the prior stroke. Thus, as the flapping wing moves through the translation phase, the fluid approaching it from the free stream is deflected downwards until it is in parallel alignment to the lower wing surface near the boundary layer. In more detail the flow vector of the fluid approaching the wing changes direction largely due to the vertical induced momentum jet of flow (downwash).

The initial stroke performed by an insect will develop the largest forces during the translation phase as induced flow is minimal at this flight duration. Proceeding strokes will produce less aerodynamic force during the translation phase, as the aerodynamic angle of attack is reduced as the direction of the flow vectors alters as a result of the induced downwash effect, and the vorticity present in the wake formation from the previous stroke. This decline in lift is made under the assumption that the insect maintains the same wing kinematics in the proceeding strokes as was carried out in the initial stroke.

The leading edge vorticity generated at two different Reynolds numbers specifically  $Re=120$  and  $Re=1400$ , was studied via experimentations to analyse the effect of Reynolds number on the structure of the vortex and the aerodynamic phenomenas of vortex stability under both flow conditions on the drosophila wing. The experimental research was conducted on the experimental rig at Berkeley University, the apparatus setup has been explained earlier in this report and can be found from (Birch et al. 2003). The switch in  $Re$  for this experiment was accomplished by altering the viscosity of the fluid which the wing travels through. The overall results suggest that the phenomena regarding vorticity transport and moreover LEV stability is an effect of the  $Re$  of the fluid, and not the differences in wing geometry (which would have negligible influence

in comparison to the  $Re$  of the flow) or experimental methodologies carried out for tests with the hawk moth and drosophila wings, reviewed previously. From the force measurements presented for AOA's ranging from  $-10$  to  $50$  degrees, after an initial force transient, stable force generation was produced for all angles mentioned and both Reynolds numbers which states that the LEV was stabilised for the entire duration of the stroke. If vortex shedding occurred the lift force would reduce, likewise reducing circulation around the wing, however, such an action did not occur hence the force measurements illustrated stability. For all AOA's greater than  $10$  degrees the stable lift coefficient values are greater for the case  $Re=1400$  than the lower  $Re$  case. In addition, the authors state that net force vector approaches an angle of  $90$  degrees (normal to the wing plane), faster for the higher  $Re$  case, than the lower  $Re$  case due to the larger presence of viscous drag. Furthermore, the drag coefficient values for  $Re=1400$  were lower than the case of  $Re=120$  for angles of attack below  $30$  degrees, which is most probably due to the contribution of viscous skin friction at an AOA lower than  $30$  degrees. Stronger vorticity exists near the core of the LEV for the higher  $Re$  case compared to the lower  $Re$  case, the greater vorticity will result in higher lift generation which is seen from their data of lift coefficient values. In the region of the LEV, clockwise vorticity is present for both cases, and this vorticity has been stretched from the leading edge to nearly  $40\%$  of the chord for the higher  $Re$  case due to the larger leading edge vortex. An under wing vorticity layer exists on the lower surface of the wings where counter-clockwise vorticity is present which is much weaker than the vorticity present near the core of the LEV (see Figure 2.31), this applies to both cases.

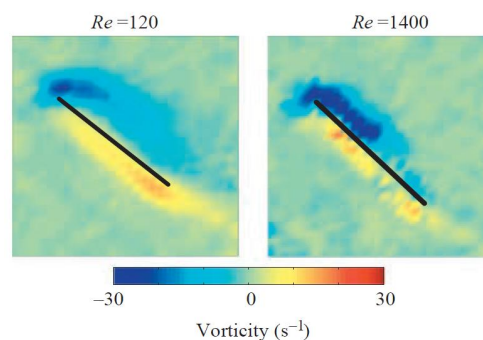


Figure 2.31: *Vorticity Images for Both Cases (Birch et al. 2003)*

As a whole, the circulation along the span of the wing is greater for the higher  $Re$  case opposed to the lower  $Re$  case, which coincides with the stronger vorticity on the upper wing surface for the higher  $Re$  case. Beyond  $70\%$  span from wing root the circulation seems to decrease for the higher  $Re$  case, whereas this decline occurs

earlier for the lower Re case at approximately 60% from wing root, where the decline in circulation will relate to LEV detachment. The lower Re case has more influence from viscosity, thus it generates less circulation and lower forces are produced. The LEV for the higher Re case was larger and grew in diameter towards the tip of the wing, although a growth in diameter is also noticed for the lower Re case, the vortex itself in comparison to the higher Re case is smaller in diameter and composed of a tighter structure. Furthermore, velocity data presented that although axial flow velocity was present through the vortex core of the LEV it was small and essentially no peak axial flow was found within the vortex for the lower Re case, but much greater axial flow velocity is observed behind the LEV where the peak axial flow velocity is located. In comparison, peak axial flow velocity was found within the core of the LEV for the higher Re case, where the maximum axial flow velocity at 55% span from wing root was greater than the tip velocity. The flow near the leading edge of the high Re case is much more complicated when compared to the flow near the leading edge of the lower Re case where viscous forces are greater. As the LEV grows towards the tip, its instability becomes clear, where sufficient fluctuations in velocity exist within the flow in the near upper surface of the wing.

The overall velocity vector flow field presented a similar formation for both cases, nevertheless, significant differences in flow formations are likely to exist and become more conspicuous towards the wing tip. Clockwise rotating tip vortices are visible in both cases where as mentioned previously within the LEV core for the higher Re case a strong axial flow velocity travels from base to tip. For the lower Re case within the LEV exists a somewhat smooth and organised weak axial flow velocity which travels along the span towards the tip vortex which it connects to. The same motion exists in the flow behind the LEV but the axial flow velocity is much stronger than what existed within the LEV. As aforementioned strong axial flow velocity exists within the core of the LEV for the higher Re case, which drains energy into the tip vortex from the core. However, the flow moving towards the tip is not as smooth and organised as observed for the lower Re case, and the flow motion although directed from base to tip (travelling into the tip vortex) augments in complexity, where the intensity of the tip vortex is greater than the tip vortex formed in the lower Re case.

The directions of the velocity vectors in the DPIV images suggested that a spiral vortex formation exists for the LEV of the high Re case. This was confirmed by images produced from further experiments where a bubble rake was placed at the leading edge of the wing and a clear spiral structured vortex was formed at the leading edge, such a structure is formed from the spiralling axial flow travelling through the vortex. In

general, LEV stabilisation in both cases is governed by different flows, which is evident as vortex stabilisation in the low Re case does not require high axial flow velocity through the vortex core. Fundamentally, stability is achieved by momentum equilibrium where the vorticity which is generated at the leading edge during the stroke, must be balanced by the transport of vorticity into the wake. Such an intrinsic scenario must exist in order to maintain equilibrium which will result in stabilisation of the leading edge vortex. This hypothesis applies for both the Reynolds numbers examined in the experiment of (Birch et al. 2003), and the previous experiments carried out on the drosophila and hawk moth (aforementioned in this literature review).

From the various literature, differences in the methodology of leading edge vortex stability has revealed the influence that Re has on the flows constructed from the complex wing motion, moreover the critical Re where the switch in methodology occurs is actually unknown. Furthermore, in addition to the Re of the fluid, the wing kinematics will also have an influence on the LEV formation, lastly wing geometry may have a small effect but this would be negligible in comparison to the influence of the Re of the flow. Nevertheless, at present this may not be of concern as nature's animals forming such a vortex at the leading edge of its wings have the ability to self-stabilise this vortex and maintain its condition for a duration which is sufficient for successful and highly manoeuvrable flight with admirable control abilities. Further information regarding the LEV can be found in (Shyy et al. 2007), which expands upon the LEV generated on a fixed wing aircraft. As stated by Wei Shyy et al. (2007), a large contribution to the lifting force is due to the vortex which is created at the leading edge of the wing with a growth in diameter as it moves rearwards along the aircraft. The vortex forms on either side of the wing, where the core of the vortices have a strong axial flow travelling through it with low pressure. The intense axial flow velocity through the core of the vortex is effectively a low pressure region which results in lifting forces from the suction effect created. The vortices tend to break down at a high AOA, unlike insect flight which have LEVs present when the wings hold a high AOA. During the breakdown, the size of the vortex grows and the axial flow component is no longer travelling in one direction. In turn, as the axial flow velocity is lost, the pressure will increase and losses are experienced in lifting forces.

Under the condition of flapping wings dominated by unsteady flows, tip vortices seem to increase lift force by the production of a low pressure region near the wing tip and interacting with the LEV in the form of an anchoring effect which acts as a technique to delay or prevent the shedding of the LEV. Shyy et al (2009), performed a comparison of computational simulations concerning a flat plate with an aspect ratio of

4, flapping under a hovering mode through a Reynolds number of 100. Their study focused on 2 different kinematic cases, such as translation with a delay in wing rotation and translation with synchronised wing rotation, for which 2D and 3D simulations were performed to investigate the effect of TVs. For the delayed case, significant differences were found between both 2D and 3D simulations, this was not the case for the synchronised case as the variation in flow field along the spanwise direction was weak. The synchronised effect had a significantly larger angular amplitude during its motion, which led to a small AOA during the translation phase which did not sufficiently experience delayed stall as the LEV formation was rather weak as was the generation of the tip vortex which had little impact on lift generation. For low aspect ratio flapping wings, the effect of the tip vortex was seen to produce either a significant or small impact on the aerodynamic benefits, and were found to be highly dependent upon the wings kinematics. The formation of the TV is paramount for lift enhancement and its function in vortex stability at low Re aerodynamics.

The literature review has covered a broad range of documented work within the field of insect flight mechanics. Several types of models have been developed for experimental and flying purposes, some of which have been initially created for experimental work with a view to progression towards controlled flight. The models discussed operate via various methods most of which require a set of linkages which are actuated by electrical devices and powered by either a mains connection or battery. Various forms of actuators were utilised in both small test models and the large experimental rigs such as pager motors, DC motors, piezo strips, LIPCA strips, linear solenoid and AC stepper motors. Some models require several actuators in order to perform specific types of wing motions which have been discussed previously. For the models designed for this project DC pager motors have been used as they hold many advantages and are in economical terms, very cost effective. Furthermore, they are small and light enough to adopt into a fully radio controlled flying model which can be effortlessly operated by off-the-shelf Li-Po batteries. Most of the experimental work is based on force measurements or flow visualisations to investigate the fluid dynamics surrounding various scenarios regarding flapping wings. Any work performed to investigate moment and power measurements has been very minimal where a full set hasn't been evaluated. In addition to this the larger experimental rigs have full control of the instantaneous wing motion which is extremely difficult to adopt into a smaller flight scaled model. The smaller models which incorporate wing rotation (varying angle of attack) adopt a passive mechanism where control is again very difficult. A technique to control the passive wing rotation upto a limitation has been investigated in this report. Both vertical and horizontal flapping strokes have been considered in this report, primarily due to the types of tests performed, which include various boundary

configurations and different styles of wing motions. For the computational work only a horizontal stroke plane was considered. Both forms of analysis experimental and computational were performed in the hovering condition.

## Chapter 3

# FWMAV Design and Analysis

The third chapter of this thesis discloses the design of the FWMAV, commencing with traditional MAV designs which have been discussed in great detail in the previous chapters. The second and third sections will display the FWMAVs designed and experimented upon in this study, along with the gearbox design. The various essential parts will be detailed in these designs as well as their connections. Thereafter, the linkage kinematics will be explored along with the wing morphology and wings tested in these experiments. Finally, experimental measurements will be presented of the mechanical system for the FWMAV models. The analysis performed in this chapter would define changes that are necessary to improve the models, this will be expanded upon throughout the chapter.

### 3.1 Traditional FWMAV Design

The traditional FWMAV design involves a group of linkages which are actuated by a gearbox system consisting of a DC (brushed or brushless) motor dependent on the characteristics of the model. The basis of this design is its simplicity, where the wings perform a simple flapping only motion with a limited stroke amplitude, large wing area and maximum dimension of 150 mm. Various types of traditional designs have been reviewed in chapter 1 and 2, such as the 1 gram ornithopter, i-Fly Vamp, Cybird P1 and Delfly (I,II and micro) among numerous others. In addition to their undesirable large size, these types of flapping models have small flapping amplitudes compared to an insect which renders a colossal disadvantage to lift force production. To compensate for that, the flapping frequency will need to increase, leading to a more powerful gearbox system (including larger power source), which in turn will augment the weight; an unfavourable outcome. This can be somewhat over-ridden by an increase in wing size to enhance lift production (or provide a sufficient lifting force for continuous flight) but again presents an undesirable effect of geometrical and weight increment. Although one could argue that a small flapping amplitude will undergo less wing loading during flapping motion which in effect will reduce energy consumption, the amount of lift produced when wing size is reduced (in order to transfer the design to resemble insect flight form or even smaller birds) will not be enough. In summary, even though they do not possess the characteristics which an insect like flapping vehicle requires, the traditional FWMAVs have physically demonstrated successful flight, where some have even proven the ability to hover. One of their most sought after qualities is the sheer simplicity of its design, such a simple system cannot be designed at insect scale which requires severe amounts of research alongside expenditure.

Figures 3.1 and 3.2, illustrate the designs of conventional FWMAVs in one and two gear configurations. Both designs are encased in streamlined bodies which encompass the entire mechanism exposing the relevant components which would assist flight such as the wings and tail. Although the tail in both figures is fairly simple serving as a stability aid, control facilities can easily be incorporated with the addition of a vertical rudder and elevator which are actuated by electromagnetic hinges that are very lightweight and quite common amongst these types of flying vehicles. Both designs carry on-board power supplies such as Li-Po batteries and receivers to allow the ground based pilot to control the FWMAV. These designs are not ready for manufacture at present and require some modifications before construction, they merely represent the layout of this type of MAV along with the components needed and type of mechanisms required. Carbon

fibre is the dominant material required for construction of this model, as the frame, linkages, wing leading edges and wing spars are all carbon fibre parts.

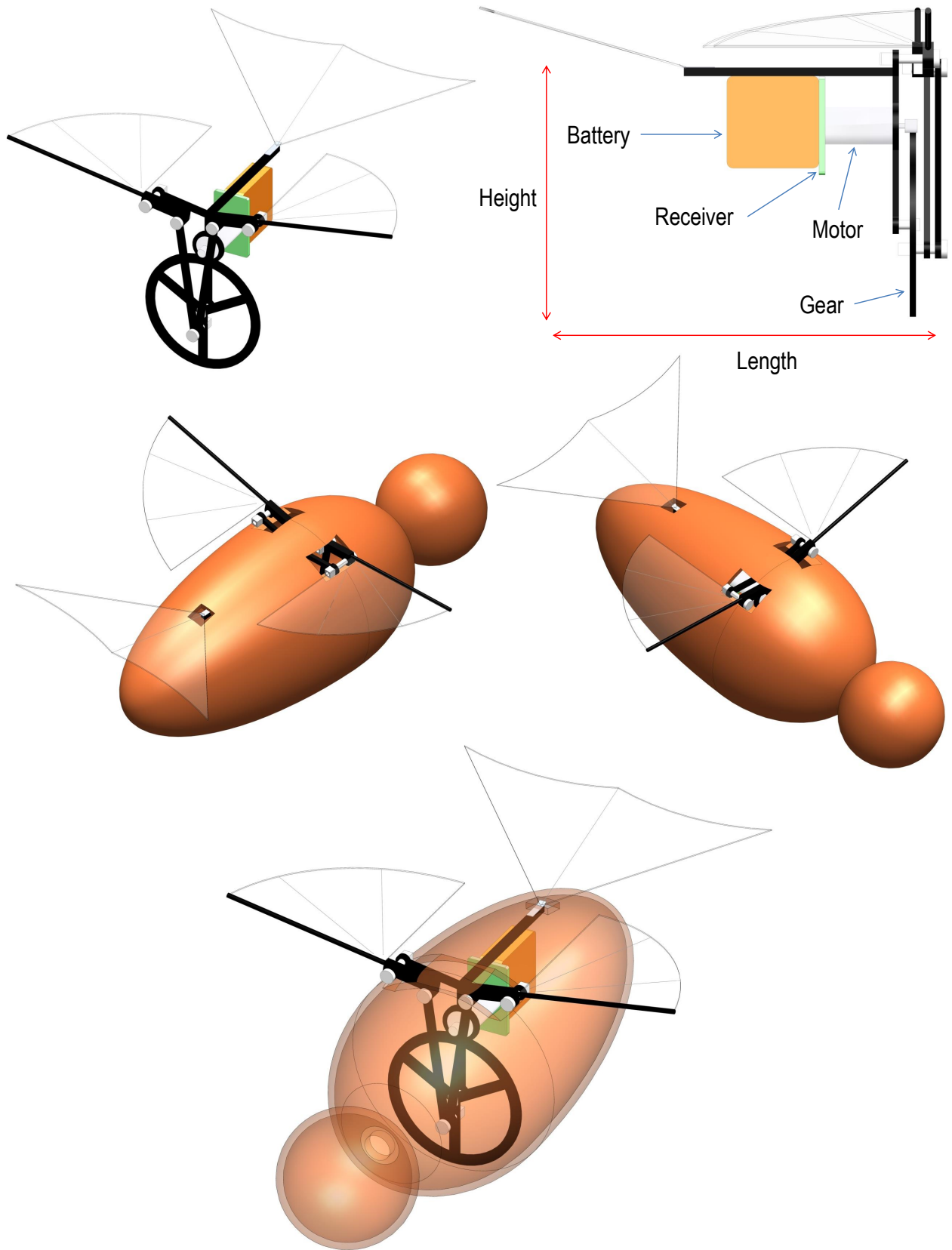


Figure 3.1: *Single Gear MAV Enclosed in a Bee-Like Body*

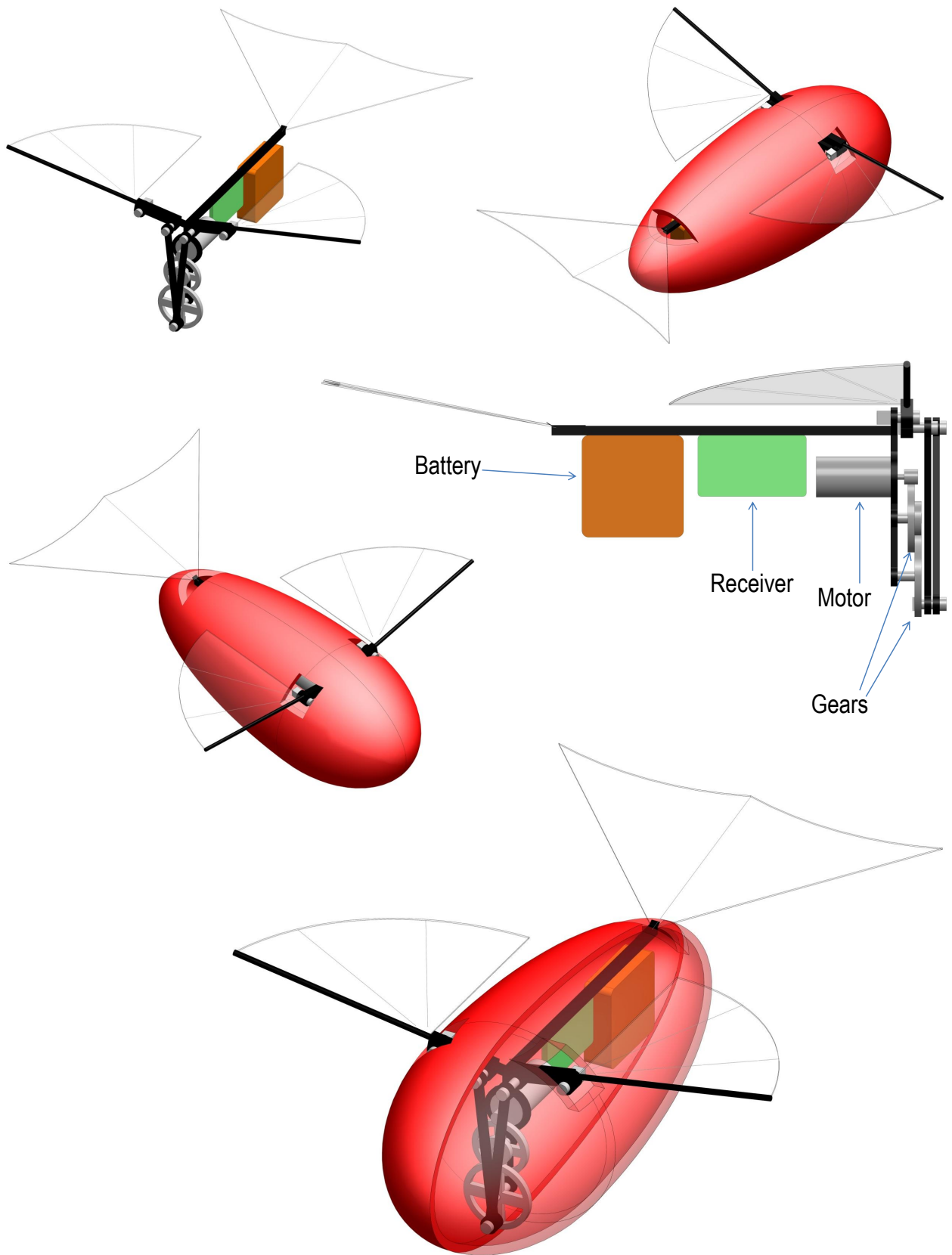


Figure 3.2: *Two Gear MAV Enclosed in a Elliptic Body*

| <b>Parameter</b>            | <b>One Gear Design</b> | <b>Two Gears Design</b> |
|-----------------------------|------------------------|-------------------------|
| <i>Total Wing Span (mm)</i> | 102.5                  | 99.8                    |
| <i>Total Tail Span (mm)</i> | 70                     | 70                      |
| <i>Length (mm)</i>          | 76.1                   | 92.1                    |
| <i>Height (mm)</i>          | 50.5                   | 34.7                    |
| <i>Body Length (mm)</i>     | 124                    | 88                      |
| <i>Body Width (mm)</i>      | 46                     | 37.2                    |
| <i>Body Height (mm)</i>     | 46                     | 37.2                    |
| <i>Receiver</i>             | <i>Micro9 2 Ch.</i>    | <i>Micro9 2 Ch.</i>     |
| <i>Battery</i>              | <i>LP20 Cell</i>       | <i>LP20 Cell</i>        |
| <i>Gear(s)</i>              | <i>G381L</i>           | <i>G336L and G360L</i>  |

Table 3.1: *Specifications For Traditional Style MAVs shown in Figures 3.1 and 3.2*

Table 3.1, contains further specific details of both designs and lists some of the components required. Note the dimensions listed in relation to the wings and tail are approximate figures based on various flapping models found in literature, test results would be required prior to any implementation to a flying model. The components shown serve merely as an example of the type of equipment that could be chosen for MAVs and are commonly used on MAVs. Four channel receivers are also available which would be needed if additional control surfaces were installed onto these designs such as those aforementioned. The receiver and battery have been chosen from Plantraco, and the gears have been selected from Didel. A wide selection of components are available from numerous distributors which include devices such as ESCs to control the rpm of brushless motors, cameras and gyroscopes to aid stability, commonly seen amongst rotorcraft models.

## 3.2 Model I: Design Exploration

Due to the limitations of traditional FWMAV designs, researchers focusing on FW vehicles which somewhat resemble insect flight mechanics have implemented linkage systems which require very small linear actuations and output larger angular flapping motions, where the linear input is at the scale of mm. Thus, the FWMAV designs for which physical models were constructed adopt the ideology of insect flight mechanics in the form

of a linkage system which requires a few mm of linear actuation to output a larger arc-like flapping movement. This principle is indispensable when designing at this scale due to the continuous and critical requirement for weight reduction. A larger flapping amplitude will escalate lift force production under the condition that flapping frequency and wing area remain constant resulting in an overall augmentation of wing flapping velocity, which as explained previously the flight force is dependent upon wing velocity squared. During the design stage it was essential to keep in mind that the overall size and design of the model must provide the potential for further down-sized development, in addition to, reducing the amount of linear actuation with near zero or minimal loss of stroke amplitude which can be accomplished with various modifications in the kinematics of this linkage system.

In order to design a flapping vehicle, one needs to fully understand the mechanical aspects of the system and amalgamation of components required. Further to this, it is paramount to consider economical costs in terms of finance and time. Thus, the process needs to incorporate an initial design, development of this design and finally fundamental and meticulous tests need to take place in order to study the design to thoroughly understand its behaviour. Thereafter the design can be downsized, reduced in weight, incorporate essential equipment such as an on-board camera, improved efficiency and force / torque production. In addition, the design must be feasible to manufacture, be able to perform to initial design specifications and requirements with the option for modifications and repairs during the experimental phase.

Both models designed for the experimental evaluations of this thesis were constructed from ready to use materials and components. Majority of the parts were constructed from carbon fibre of 1.5 mm thickness, which can be purchased in sheet form in a variety of thickness's. The parts can be cut to size via CNC and pin holes drilled with the use of carbide cutters and reamers to provide high accuracy for hole diameters. Due to the substantial amount of tests planned for the model and in an attempt to perform minimal amounts of repairs, a stiff, hard wearing and highly crack resistant material was employed in these models. Although carbon fibre layers can peel-off due to wear and tear or unforeseen damage, this would not affect the part much and repairs would not be needed unless mechanism performance was affected. Another benefit was the ease of modifications from manufacturing defects or inaccuracies when the hole diameter was slightly too small or machining/filing down parts which need to sit well in order to be bonded appropriately or connected in a similar manner.

The pins and pin ends were created from readily available carbon fibre rods which require basic tools to cut

to size and prepare for model assembly. The linkage backboards secured to an acrylic base, where the legs of the backboards slot perfectly into the designated gaps on the base. Connection diagrams have been shown in Figures D.2 to D.4 located in the appendix of this thesis, which demonstrates the procedure of connections required in order to assemble such a model. M2 screws were used to secure and maintain the distance between the two backboards as they are only fully supported at the legs by the base and the upper shoulder section has been supported via screws. The backboards act as a support for the linkage system, which consists of fixed pivot points that the links can rotate about when instructed to do so by their connecting members. The legs of these support frames are fastened to the base via screws and nuts, as shown in Figure D.4. The pins were secured to pin ends and mounts via cyanoacrylate adhesive (which is essentially a strong fast acting glue). The linear plunger which travels through the vertical slots is constructed of tufnol, which is more of a fabricated material that is readily available as sheets or blocks. The small crank controller was also manufactured from tufnol which like carbon fibre can be amended to allow pertinent connections between parts. All the linkages were attached via pins and were secured to remain in their set position via pin ends. The reader should refer to Figure 3.4, which illustrates the model in a simpler form where each section has been taken apart and labelled.

The solenoid consists of a plunger which is placed in the centre of the device that undergoes a pulling force from the electromagnet surrounding it. As the plunger is forced to move only in one direction in this case pull, an opposite movement is required to produce a +/- (upwards/downwards) motion, this is accomplished by implementing a spring. When a current is passed through the electromagnet the plunger is pulled downwards towards the core by a set distance, whilst the current remains through the coil the plunger will remain in this position, thus a varying waveform is needed to continually activate and deactivate the electromagnetic device. Using a spring, frequency generator and signal amplifier the solenoid can be operated to produce a continuous +/- linear motion, which was suitable to drive the thorax linkage structure of the FWMAV presented in this thesis. Although utilising the solenoid as an actuation device demonstrated successful movement of the mechanism outputting a flapping wing motion, it was not used in F/T experiments as the plunger produces significant vibrations due to its bouncing behaviour. This vibration would have augmented the mechanical vibrations already present in such a mechanical linkage device, thus it seemed more feasible to research into another actuating device that does not produce such vibrations. Solenoids are easily available from companies such as Farnell and RS Components based in the UK, the solenoids tested in this project were sourced from these companies.

Without the addition of wings the model had a span of 84 mm, a height of 75 mm and maximum width of 57 mm. The linkage support frame had a length of 58 mm which is the distance between both its shoulders. The dimensions provided in Figure 3.3, are the maximum lengths as seen in the pictures, and the span would increase dependent on the span of the wings attached. For example, the attachment of the 47 mm span wings (WT3) brought a significant rise in total span length of 178 mm. The pictures displayed in this Figure show the model positioned in various views, further information regarding the gearbox system and wings have been detailed in the following sections of this chapter.

The size of the model was paramount during the design stages as the underlying design principle of an MAV is based on its small dimensions, but adequate spatial requirements must be provided as this is an experimental model for an experimental rig at present, with future downsizing applicable exploiting the same mechanical methodology to create a flapping motion. Certain spatial requirements are suitable for experimental rig models as repairs would need to be carried out. And in order to complete them certain connections would need to be broken apart and subsequently bonded together again. A larger and more robust linear slider was designed and implemented into the present model, in order to ensure that it is unlikely to experience any damage from the motion conversion it executes, and the loading forces it experiences from the wings which are transmitted through the linkage mechanism.

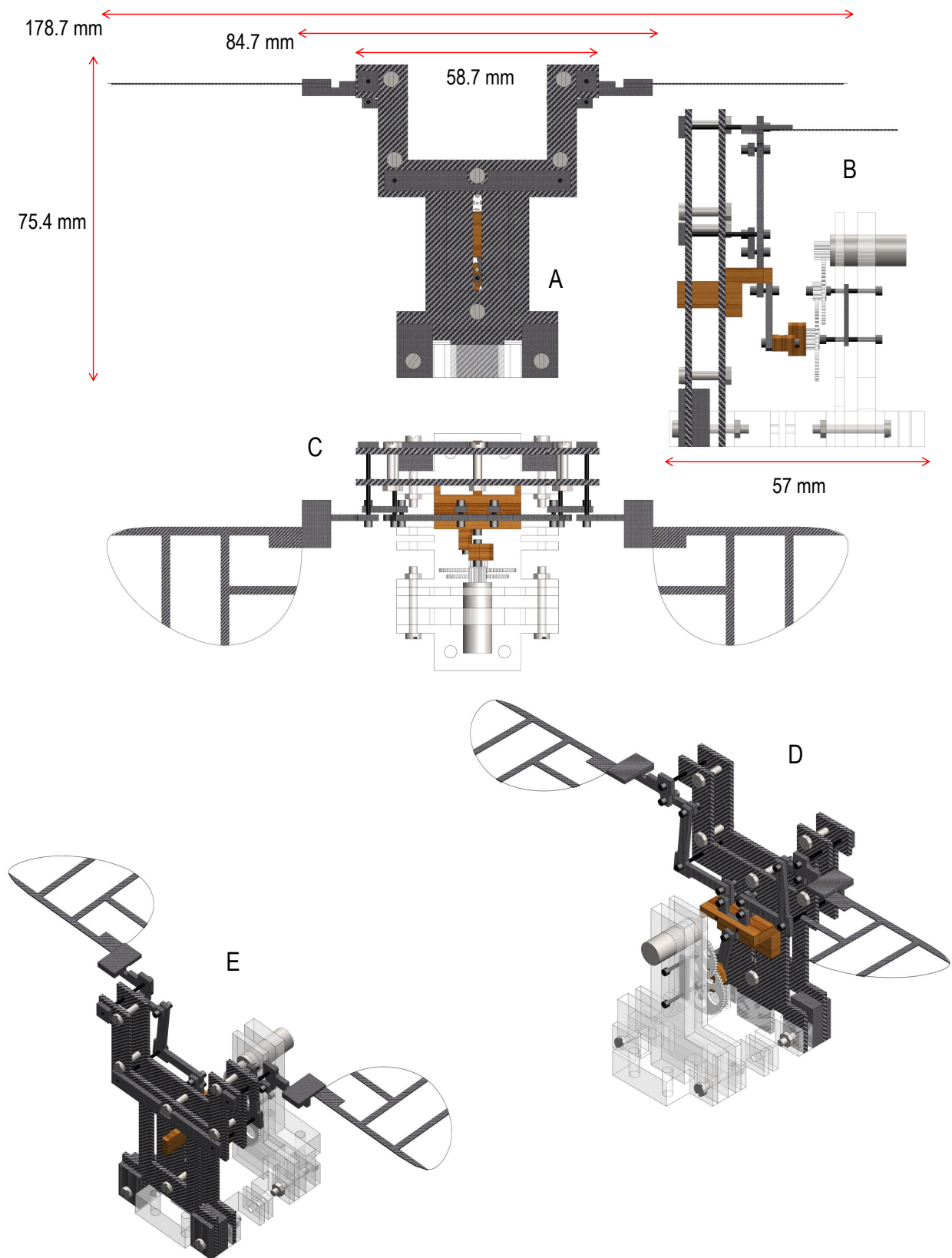


Figure 3.3: Model 1 Shown in a Variety of Views with Maximum Dimensions; A: Front View, B: Side View, C: Top View, D: Back Isometric View, E: Front Isometric View

The primary purpose of this four-bar linkage system is to amplify and convert the small linear actuation into a large semi-rotary flapping motion. The linkage mechanism rotates about four fixed pins which are known as pivots, and the remaining rotations between the links occur about freely hanging pins which can be denoted as hinges. Numerous hinges are required in order to create such a flapping motion, and their rotational properties need to be continually assessed during the assembly process as stiff hinges would cause further complications in the mechanical motion of the system, which could lead to unwanted asymmetries and unnecessary energy consumption. Furthermore the linkages should be stiff to transmit the dynamic forces output from the gearbox to the wings, and the periodic aerodynamic force acting on the wings will be transmitted to the motor via the linkage system.

The linkages should also be lightweight in order to reduce the amount of mass the gearbox has to actuate, and effectively consume less energy. Only a small linear amplitude is required to create a large flapping angle, where in the present design the smaller the amplitude the less friction the slider will experience when sliding along the vertical slot, and the future design would see an additional benefit as a smaller linear actuator could be incorporated to replace the gearbox. However, the same motion conversion method can be implemented and downsized for a future model, and the flat surface of the slider can be replaced by two cylindrical rigid rods which will move linearly along the slot and would result in a reduction of friction generated from the plunger and vertical slot technique as the surface areas in contact are diminished. The connections which form the entire mechanical linkage system has been shown in Figure D.3, the guide lines show the connections of all the parts including the linear slider and crank arm. The methodology behind the mechanical movement of this system applies to both models with a modification incorporated to produce asymmetrical flapping.

As the crank controller rotates with the gear, it causes the crank arm to also rotate in a circular fashion as they are connected via a pin which is located within the crank controller component. As the crank arm rotates it will naturally push/pull the plunger which is enforced to travel through a linear path only due to its tongue section which is placed within the vertical slot. Enforcement by such a method creates a linear motion which is transferred and amplified by the linkage system. However, even though the rotational motion has been converted to a linear motion, a consequence of this particular method is the friction which is accompanied with it. This additional friction will consume more energy, reducing the efficiency of the system and add to the already long list of energy consumptions when an on-board power supply is considered in

future models. Thus, maintaining the conversion methodology and reducing the amount of friction produced will aid the efficiency levels of the design, this can be implemented by using the approach outlined previously.

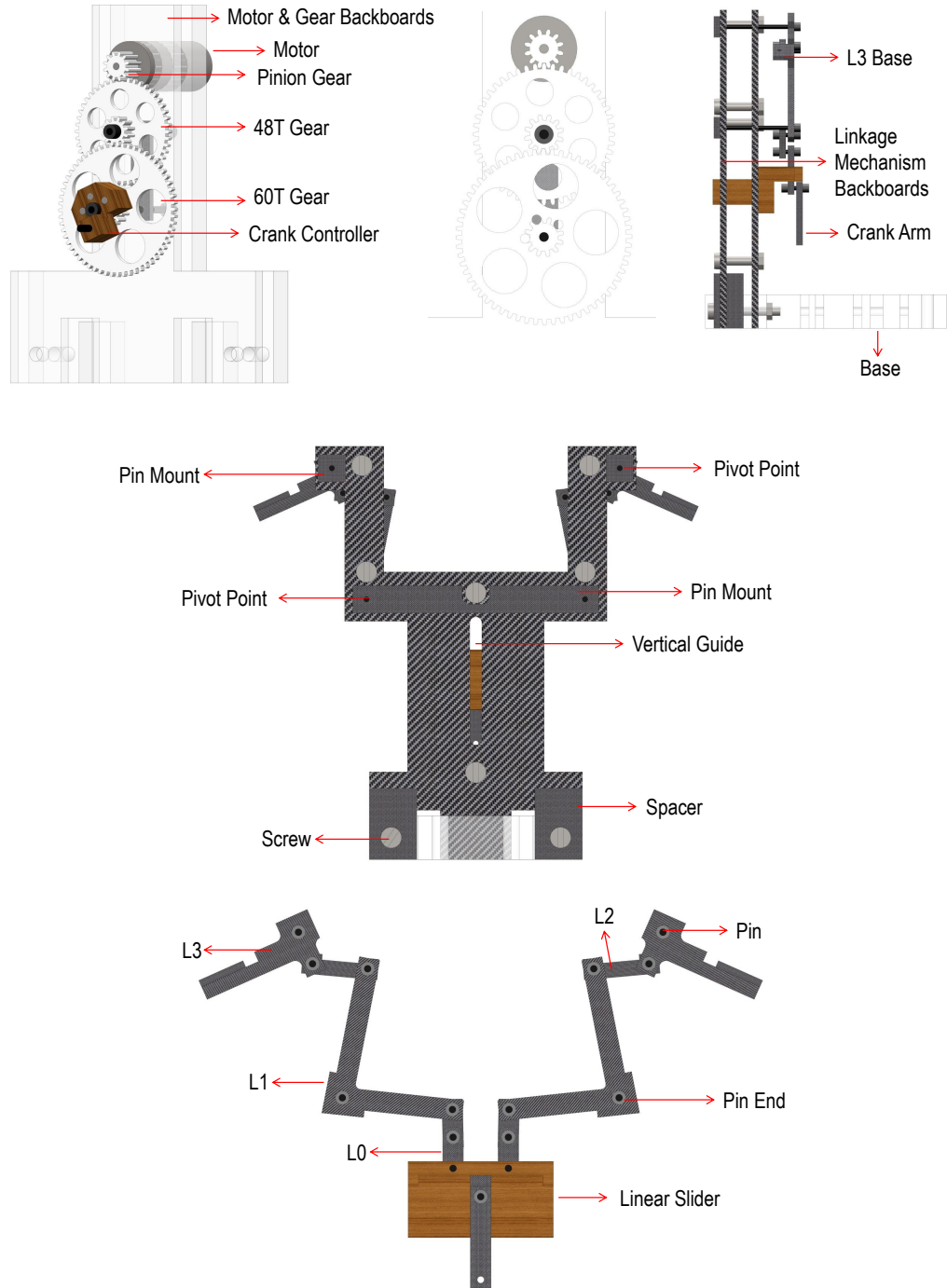


Figure 3.4: *Parts from The Model with Their Designated Titles*

### 3.2.1 Gears and Gearbox

The motor and gear support boards were manufactured from acrylic which slotted comfortably into the base of the model through its designated slots. The legs of the motor/gear support boards were fastened to the base via screws and nuts on either side of the model in the same manner employed for the linkage backboards. The motor slots into the top allocated hole which provides a very tight fit in order to hold the motor in place as any movement of the motor would affect the rotation of the gears (possibly leading to damaging the teeth of the gears, which would require knotty repairs as various connections would have to be taken apart) and effectively terminate the motion of the mechanical flapping system. The positioning of the gears on the support boards are extremely important as the teeth need to be aligned properly in order to interact with each other creating a rotary motion, as forced to do so by the actions of the motor which has a 12T pinion gear attached to its shaft. The gears were attached to the backboards via pins and secured by pin ends. The crank controller is attached to the 60T gear by steel rods which ensures synchronous motion of the crank controller and gear. A diagram presenting the alignment of teeth from each gear has been shown in Figure 3.4, where the gearbox mechanism parts can be seen with their names. Refer to Figure D.4, where a complete dissection of all parts and their connections related to the gearbox has been shown. It is worth noting that spur gears were used for both models as shown in the aforementioned figures and the same gearbox arrangement was utilised for both models.

The flapping frequency is heavily affected by the aerodynamic loading acting on the wing. The aerodynamics acting on the wings during flapping become resistive forces, and these forces are transmitted to the motor by the linkage mechanism and in turn converted to an overall loading on the motor shaft, reducing the rate of rotation or even stalling the motor resulting in zero rotation. If the motor torque is not large enough the end effect is a reduction in flapping frequency, this is where the application of the gear ratio assists. In addition to the fluid loading applied to the wings during motion, inertial force produced via mass acceleration would also contribute to the energy needed to produce a flapping wing motion. Thus, the amalgamation of these loadings need to be considered as resistive actions which the motor will need to work against. Further to this, energy will also be consumed by the actuation of the mechanism itself (without the wings), thus a combination of numerous loads applies significant overall resistive action to the rotational motion of the motor. The gearbox, driven by the motor needs to provide a sufficient amount of torque to overcome the resistive fluid dynamic forces acting upon the wings. Future models should incorporate a motor with a higher

stall torque but a direct consequence of this will be the additional weight which would need to be balanced or outweighed by a sufficient improvement in lift force production. As the gearbox needs to overcome an amalgamation of resistive forces as aforementioned including its own frictional and inertial forces (which are relatively small in comparison to metal gears), it is not a straightforward task to select the ratio. In addition, a required flapping frequency (see Equation 3.2) must be kept in mind as well as torque output. The selection was made with the assistance of the literature review and using the summation of the peak results from the CFD data of a simple flapping wing as a resistive force for both wings (shown in chapter 5). This was considered to act through the linkage system on the output gear and work against the electrical motor. However, as the full set of resistive forces were not considered due to the complex nature of the complete mechanical system, a considerably larger gear ratio was chosen which would also allow for the usage of wings with a greater area and mass if need be during the experimental stage.

The gear reduction ratio (Equation 3.1) will influence the rpm that the crank arm will operate at, where a higher gear reduction ratio will provide more torque to the system. But the rotational speed of the crank arm will be reduced, thus the higher ratio compromises the rotational speed for an augmentation in torque output. The opposite will apply for a lower gear reduction ratio, thus to increase flapping frequency specific details such as torque, rpm, mass and size need to be considered. A motor of a higher stall torque will allow the model to flap at higher frequencies, at a lower gear ratio, thus reducing the amount of spatial room needed for the gearbox within the model but will be accompanied by a considerable amount of weight. Similarly, opting for a brushless motor opposed to the coreless brushed motor chosen for these models would aid in efficiency and reliability as the only contact parts are the ball bearings which are hard wearing. A brushed motor creates its rotational motion via contact between the commutator and the brushes which causes significant wear over time.

$$G_{rr} = \frac{T_{NL1}}{T_{NS1}} \frac{T_{NL2}}{T_{NS2}} \quad (3.1)$$

The flapping frequency output is determined by Equation 3.2.

$$f = \frac{\omega_m V}{60 G_{rr}} \quad (3.2)$$

The motor speed ( $\omega_m$ ) is measured in revolutions per minute and voltage (V) is measured in volts. The central hole pierced into the gears needs to be aligned properly in order for the teeth to have the correct amount of contact so that they are synchronised in movement rather than the upper gear resting on the one below. With this in mind, dual support boards were integrated into the model which will ensure that

the pin used to position the gear remains perfectly horizontal as it passes through two holes a set distance apart which fit well around the diameter of the pins. The vertical locations of these holes can be found using Equation 3.3 which relates to the number of teeth the gears have and the diametral pitch. The distances need to be determined for all gear hole locations, this includes the pinion gear attached to the motor shaft. The diametral pitch can be determined by Equation 3.4.

$$D_G = \frac{(T_{N1} + T_{N2})}{2 D_P} \quad (3.3)$$

$$D_P = \frac{T_N}{Pitch_D} \quad (3.4)$$

However, if the pitch diameters are known the central difference between the holes for each gear placement can be expressed by Equation 3.5 which opts to use the pitch diameter of both the gears.

$$D_G = \frac{(Pitch_{D1} + Pitch_{D2})}{2} \quad (3.5)$$

Gears consisting of 48/12 and 60/12 teeth were used for these experiments which in combination provided a reduction ratio of 20:1. The 60/12 teeth gear was attached to the crank controller where steel pins were used to connect them to one another which were inserted into the tight fit holes of both components. The pins were then secured with cyanoacrylate adhesive. The gears were fabricated from delrin which is a form of plastic that proved to be a difficult material to work with due to its requirement for specific adhesives during bonding and the amount of time required in order to create a complete bond, which was not actually strong enough. Thus, combining any part to the delrin gear via glue was not seen as an option and connections were implemented via pins whilst ensuring that the gear and crank controller remain connected by closing them off with pin ends on either side, as seen in Figure D.4.

### 3.3 Model II: Design Exploration

An MAV which has the ability to produce asymmetrical forces can in essence perform controlled flight with successful manoeuvring by modulating the difference in amplitude and the frequency of flapping. However, whilst performing body torques the MAV must be capable of producing enough lift force to keep itself airborne. Whilst hovering the MAV's main objective is to generate a thrust force vertically in opposite to the force of gravity, but for forward flight this aerodynamic force vector would need to contribute accordingly to thrust in the flight direction. A balance would be needed in order to generate enough thrust force to allow the MAV to move forwards with a sufficient speed but also to remain airborne with sufficient lift force. Any flight mode change as performed by a manoeuvre should ideally be executed gradually in order to maintain maximum flight stability and controllability, but realistically this usually is not the case. When an insect is in flight it would execute flight mode change swiftly in order to manoeuvre around any obstacles encountered, the application of unbalanced torque exploited in order to travel around objects is not pre-planned. An FWMAV would need to adopt these characteristics to successfully resemble the flight control and manoeuvring skills that an insect possesses. Similar to RC helicopters, the FWMAV would need to be equipped with a gyroscope to aid stability in order to adopt the skill of flight manoeuvrability.

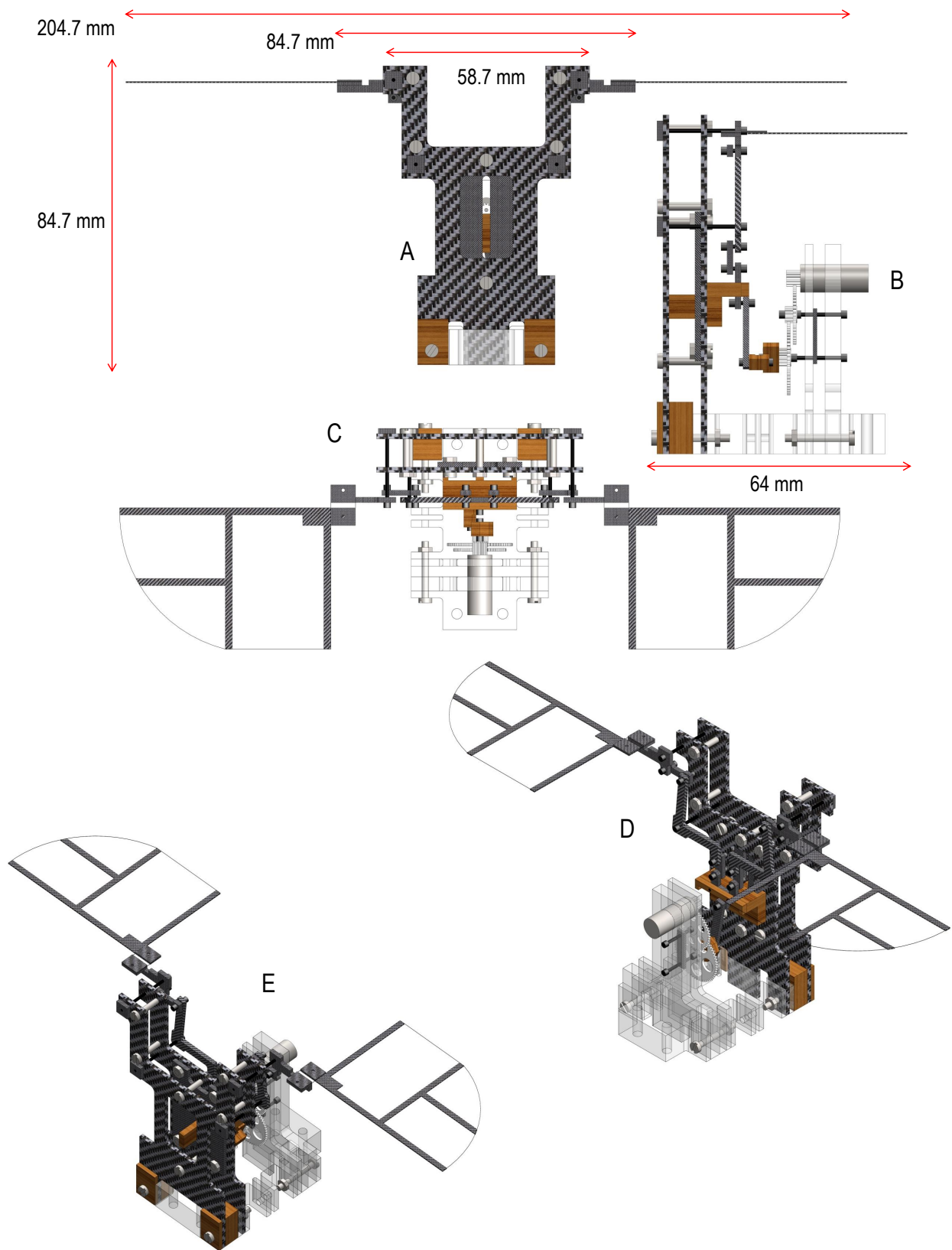


Figure 3.5: Model 2 Shown in a Variety of Views with Maximum Dimensions; A: Front View, B: Side View, C: Top View, D: Back Isometric View, E: Front Isometric View

This discrete system consists of linkages which move in an individual fashion when forced to do so under the rotational action of the crank arm is symmetrical for model 1 and model 2, when in a symmetrical configuration. This mirror line does not exist when in the asymmetrical configuration for obvious reasons. The maximum span of model 2 is 204.7 mm with the attachment of the larger 60 mm wings (WT4), this span length is dependent on the span of the wings affixed to the model. The width of the model measures 64 mm, which is the maximum recorded length with the 60 mm wings (WT4) affixed, otherwise the side length of model 2 is the same as model 1. Pictures of model 2 with the dimensions stated have been shown in Figure 3.5.

Both models 1 and 2 operate similarly by exploiting the same techniques of actuation and flapping output, but differ in category as model 2 can perform two flight modes. An active change in flight mode was not implemented into model 2 initially as it was more feasible to physically change the flight mode type when the model is not in operation as this was the initial phase of the design and experimentation. It was imperative to first test whether this technique of flight mode change is successful and also to perform various tests in order to evaluate its performance. Thereafter an active mechanism can be designed and implemented into a future design.

The change in flight mode is executed by simply displacing the vertical plunger horizontally from its zero position by 2 mm which causes the L0 links to slant in a direction dependent on the direction of displacement of the plunger. This slanting action affects the remaining links of the mechanism connected to L0 and when the plunger is actuated an asymmetrical motion will be output. In the present design the horizontal displacement required to perform asymmetrical flapping is implemented via a backing plate which has a vertical slot offset by 2 mm from the line of symmetry, and symmetrical flapping is carried out with the attachment of another plate which has the vertical slot placed along the line of symmetry. Figure 3.6 illustrates both models in images A-C, where the offset of the plunger can be clearly seen in image C when compared to images A and B. Isometric views have been shown to merely present a three dimensional view of model 2 in both configurations of symmetrical and asymmetrical flapping and the placement of the plate. A connection diagram has also been shown in Figure 3.6, illustrating where the backing plate secures onto the backboard via screws and nuts. A desirable characteristic of this form of flight mode change is its simplistic implementation, a small horizontal displacement of the linear plunger will create an asymmetrical flapping wing amplitude on both sides. It is essential that any change in flight can be executed in a simple manner,

and in mechanical terms the simpler the method, the better suited it is for such small scale flight applications. Incorporating numerous moving parts to perform such a change in the type of flight would mean extra weight and additional friction resulting in larger energy consumption. Active change in the type of flight is possible with an additional actuator which will only be called upon when change of flight mode is required, which would aid efficiency substantially as opposed to two electronic devices continually in operation to flap each wing independently. With the technique presented here the second actuator would only need to displace the backing plate by 2 mm and a second flight mode is achieved, this will prove to be vital in terms of energy consumption which is a key factor to consider when designing lightweight aerial vehicles.

Model 2 had a larger overall height due to the additional length on the support board when compared to model 1. The additional length was primarily adopted in the design to hinder/avoid linkage locking when flapping in asymmetrical mode as one side will produce a larger angle than the other. Linkage locking can cause severe damage to the gears and even the motor, as the motor will still be drawing power from the PSU trying to force the gears to move. If the motor succeeds in forcing the gears to move when the linkages are locked and are restricted to move in the fashion they were designed for, the teeth of the gears would now grind against one-another, effectively resulting in a failure to the gear mechanism. The mechanism can approach a position where locking will occur, and thus careful consideration has been given in the mechanical design with precautions to prohibit this happening were put in place during the design of model 2. Linkage locking can only occur beyond end downstroke, thus the flapping amplitude this mechanism can produce is limited due to this effect. Beyond the maximum upstroke set for the present linkage design, locking will not occur but the wings can physically collide which will contaminate force measurements and damage both wings, thus a limitation also exists here. This restraint is common among all flapping wing vehicles as wing-wing interaction during a flapping stroke can have disastrous effects for all flapping wing vehicles due to the damage caused. However, this does not apply to FW models that produce a clapping of the wings at the end of a stroke as they meet at the point when the wings are at rest and not part way through the stroke. Furthermore, the clapping mechanism has fluid dynamic effects and does not affect the physical condition of the wings.

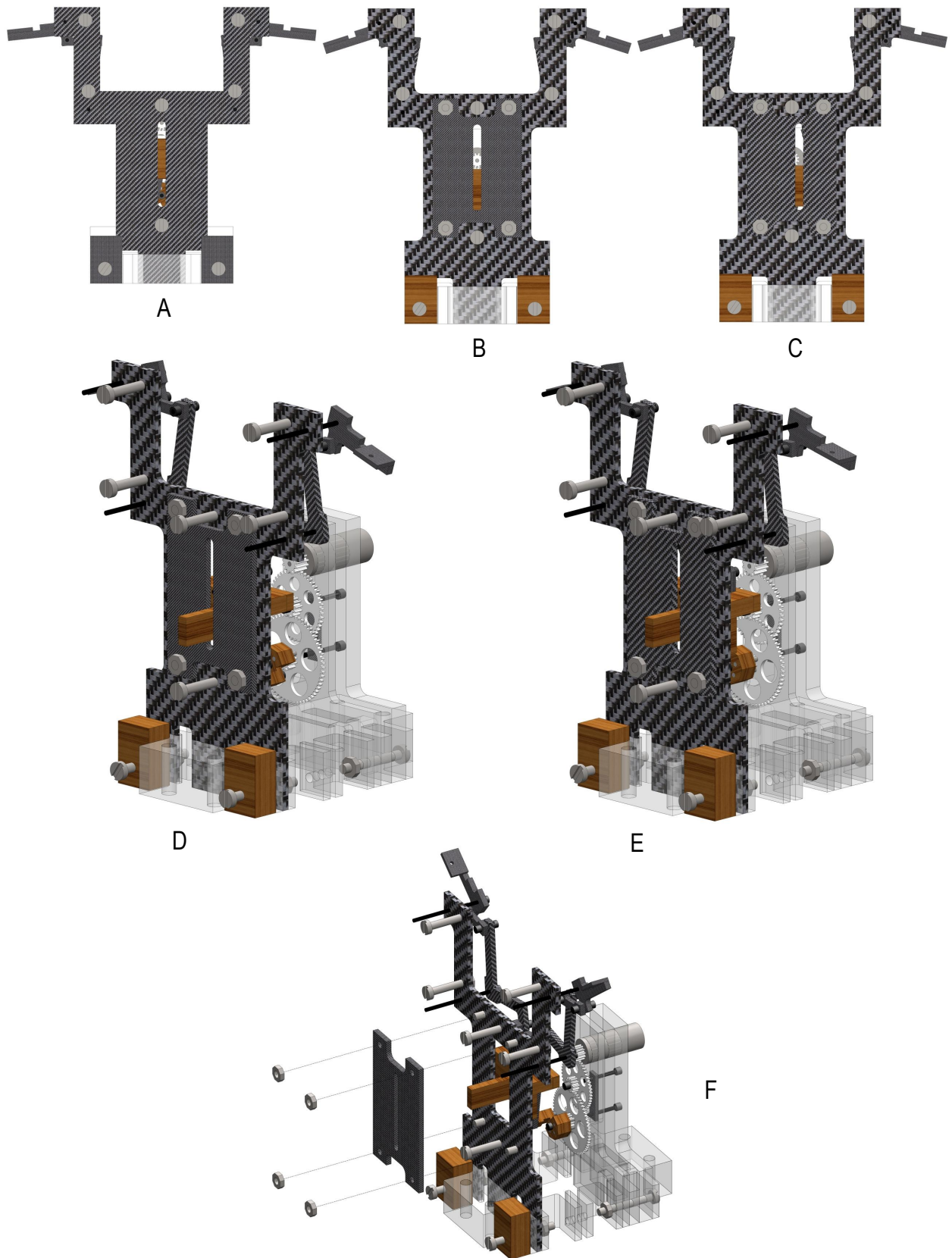


Figure 3.6: *Vertical Guide Comparison for Both Models with Plate Connection Diagram; A: Model 1, B: Model 2 Sym Configuration, C: Model 2 Asym Configuration, D: Model 2 Sym Configuration Isometric View, E: Model 2 Asym Configuration Isometric View, F: Model 2 Connection of Vertical Guide Plate*

Although both models are larger than what we would require from a FWMAV, future designs could be considerably downsized as well as severely reduced in weight with substantial miniaturisation of many parts. Overall, with specific modifications the height of the model can be more or less halved, improvements in the linkage system would see a benefit in the gear reduction ratio favouring rpm, which effectively would increase the flapping frequency and would also reduce the amount of space required for the gearbox system. Although severe weight reduction would be undertaken, an antithetical effect would also take place which will bring about a small weight increase with the change in motor to one which has a higher stall torque and also the addition of another electrical actuation device which will allow control over the flapping mode. Nonetheless, the overall weight of the model will still be heavily reduced even with changes to the electrical actuation devices. A future design would also need to carry an on-board power supply in the form of a Li-Po battery which can be readily purchased. Through the knowledge gained from the design, manufacturing, assembly and experimental testing stages an MAV which incorporates the above additional components can be designed in future with the vast information gathered during this process. One must keep in mind that even with the incorporation of additional control and more powerful components the model will not be able to fly without further research carried out in the same manner as carried out in this project because flight stability is an issue which will affect all flying vehicles, more so for one which consists of dynamic wings which continually accelerate mass at high frequencies. In addition to the stability issues, the intensely paradoxical fluid dynamics surrounding flapping wing flight with multiple coupled wing motions performed in a periodical manner pose great complications in insect inspired flight, especially at a dimensional scale which is directed more towards that of a real insect. The linkage system could also be downsized in both length and width, but a study will need to be carried out in order to determine the kinematic and moment effects. Subsequently experimental investigations will also need to be performed to research the implications of these alterations. Nevertheless, the preeminent downsizing should be aimed towards the frame and base as these are substantially larger than the linkage mechanism which is minuscule in comparison.

### **3.4 Flapping Wing Model Linkage Comparison**

Images were acquired of the linkage mechanism including the vertical plunger to demonstrate its motion and compare its movement to CAD images of the model and determine the difference between experimental to CAD modelling. The plunger was physically positioned and an image was taken, this could have been done

using the electro-mechanical system incorporated in the model (by physically turning the gears) but due to its size it was blocking the view of the plunger, thus it was removed for this analysis.

A small linear displacement of the vertical plunger will cause link L0 to move which will in effect push/pull L1 creating a moment as L1 is restricted to rotate about a fixed pivot. Consequently L1 will push/pull L2 which will affect the position of its connected member L3. As L3 is restricted by a pivot point as well, a rotational motion will occur which in this case creates a method of flapping. Since symmetry of linkages has been integrated into the design, a flapping motion is produced on either side, both linkage sets are actuated by the same vertical plunger, which is the part that couples the linkage mechanism. The linkage mechanism of model 2 has been evaluated only as the operative principles are the same for both.

Images have been shown in Figures 3.7 and 3.8, to present a visual comparison of the stroke angle produced from the CAD and physical linkage mechanism. The former illustrates the mechanism demonstrating a downstroke motion, where the starting point is the top left corner and the end of the motion is the bottom of the third column (in reference to the experimental images). The slider of the physical model was placed in random linear positions in order for the L3 arms to create a flapping motion. There was no need for the slider to be set to specific positions or equivalent increments as the vertical displacement of the slider can be determined using a fixed coordinate system and a variable coordinate system which dynamically moves with the plunger, thus known as the slider coordinate system. However, this is heavily simplified as the plunger can only travel through a single axis in positive and negative directions, in this case known as vertically up or down. The acquired vertical displacement of the slider from each image can be inserted into the CAD design which will output a stroke angle. Thereafter, both the experimental and CAD mechanism stroke angles can be compared to determine how well the physical system relates to the theoretical CAD model. For such a mechanism which is the key contributor in creating the flapping motion required, it is paramount that such an evaluation is conducted to determine how well the theoretical design performs in reality. Various factors such as strength of pivot bars, mounting condition of the pivot bars, positioning of the linkage mechanism on the bars, stiffness due to pressure applied on linkages from pin ends and even the size of the hole diameters are all critical factors that will effectively determine whether the mechanism will operate in the manner in which it was designed to do so. For example, if the holes are too large the links will slant resulting in inconsistency of the alignments of each link which will affect the motion and even the condition of the pivots as additional stress is applied to the pivot arms when diagonal links are continually forced to rotate

around these bars which have zero freedom of movement. This highlights the need to conduct fundamental evaluations of a dynamic system, and a distinct advantage of such an evaluation is the validation of the CAD model as future designs can be carried forward with more confidence based on the results determined through this comparison procedure.

The images shown in both Figures 3.7 and 3.8, seem to present a very good visual comparison between physical and CAD mechanisms. The images compare very well even at extreme flapping angles (maximum downstroke and maximum upstroke) where one would anticipate this to be the most precarious comparison as the structure approaches its limitation point. White lines were drawn onto the carbon fibre linkages to aid visualisation against a dark background, which effectively allowed for accurate measurements from the experimental images. A poorly assembled mechanism would have significant differences due to the factors stated above, if such a case was presented we would need to investigate what the core differences were between the physical and CAD models and rectify the problematic areas. As evidently seen from the images, as the slider vertically descends the linkages follow this by forming a downstroke where the lowest position of the slider is the largest downstroke angle created. The opposite applies in the upstroke position whereby the upstroke motion is created as the slider vertically ascends, and the maximum upstroke is found at the maximum vertical position of the slider. The complete linear distance travelled by the slider during the downstroke motion was 10.78 mm, which produces a stroke angle of 140.5 degrees. Under electro-mechanical actuation from the linkage gearbox system the upstroke and downstroke angles would undoubtedly be of the same size with the same linear actuation from the slider. During these fundamental validation tests the up and downstroke angles varied as the slider was physically positioned by hand to random locations in order to merely investigate the motion of the mechanism and compare the angle output between the CAD and physical models. Thus, the total linear distance travelled by the slider during the upstroke case was 10.26 mm, which output a stroke angle of 125.97 degrees. Clearly a larger stroke angle is produced when the slider travels a farther distance as seen from the values of the up and downstroke cases. In all, the distance travelled by the slider will determine the size of the output angle from the linkage mechanism, this is a key principle which applies to a linkage system with this type of design.

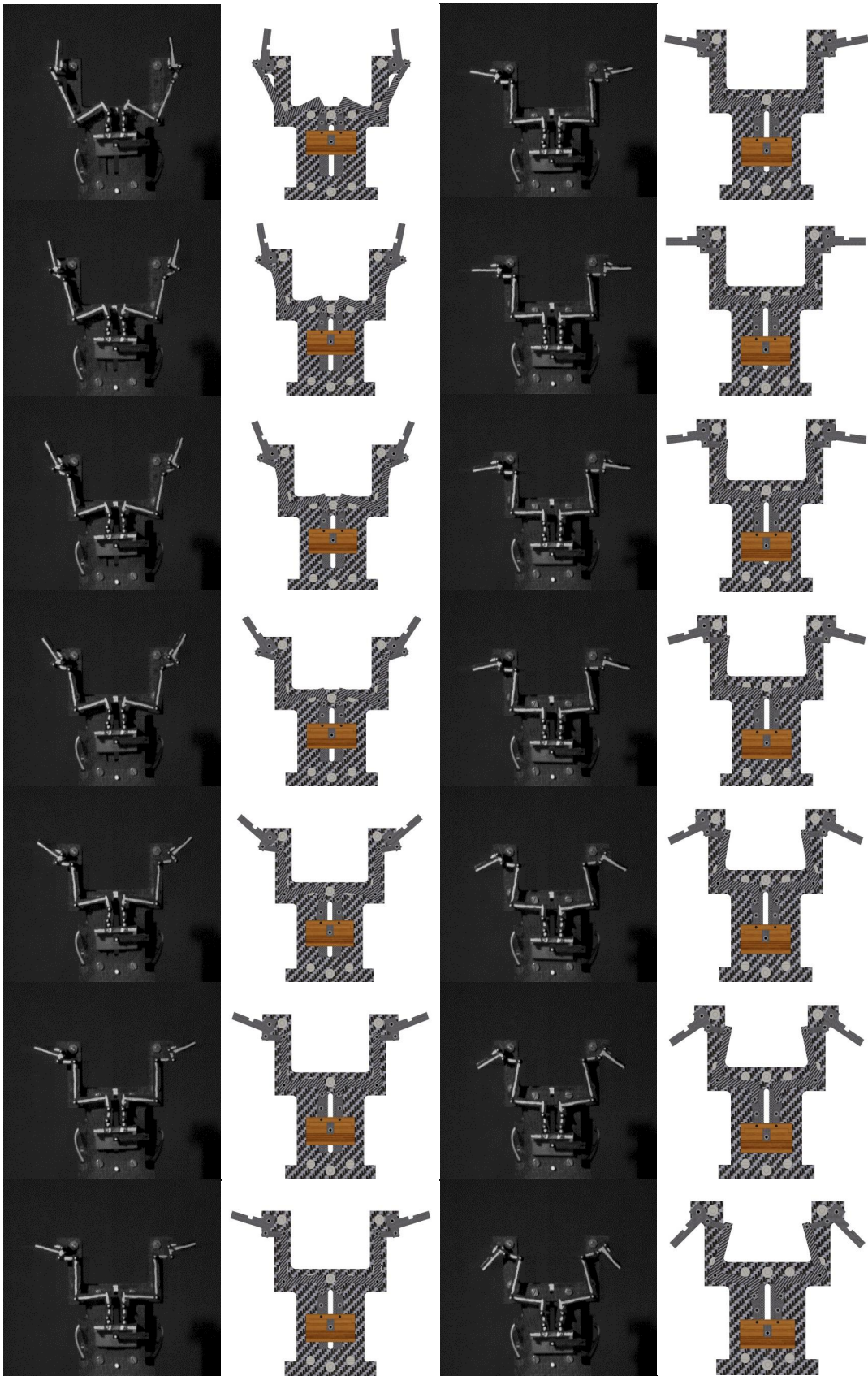


Figure 3.7: *Experimental and CAD Images of the Linkage Mechanism During Downstroke*

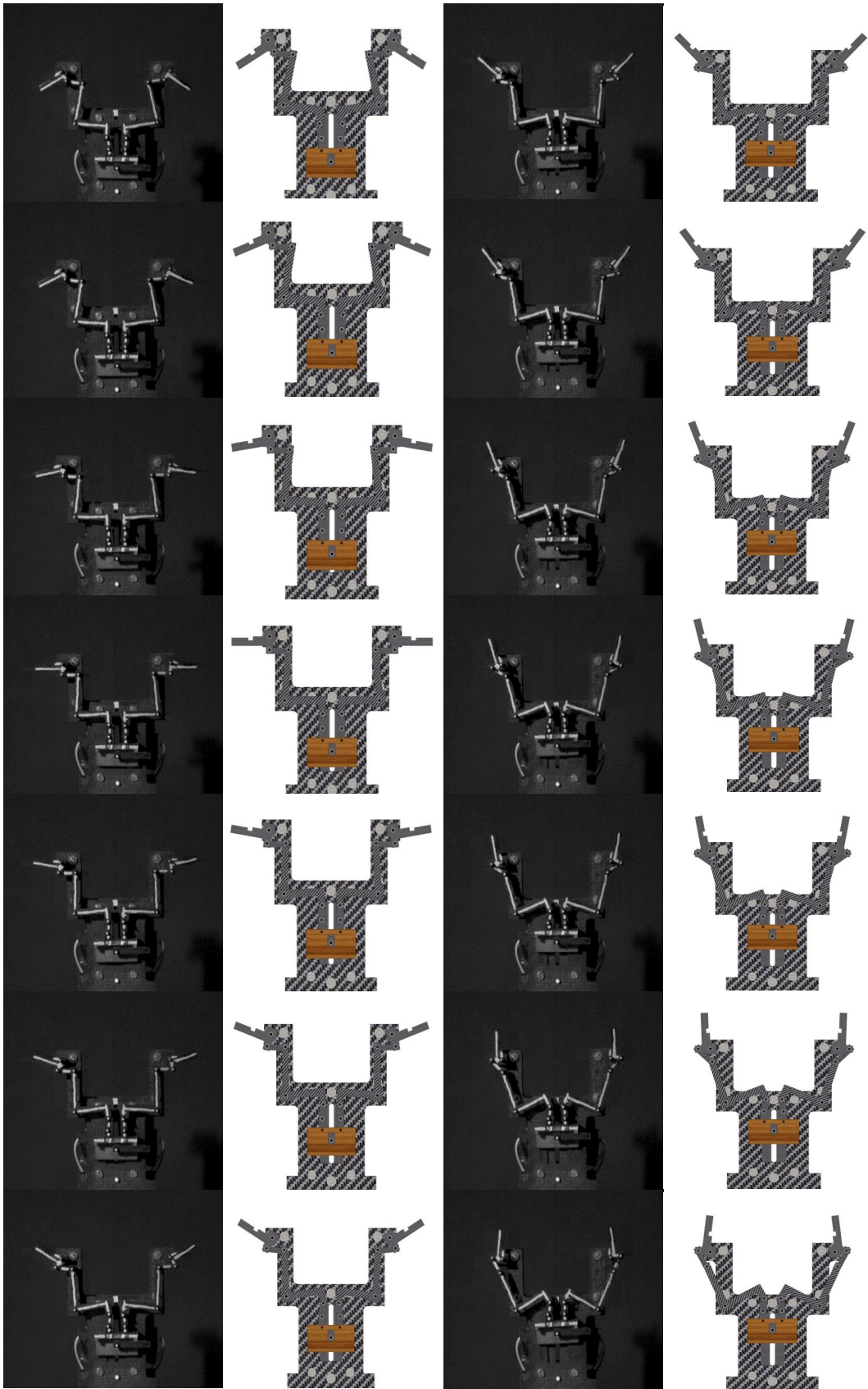


Figure 3.8: *Experimental and CAD Images of the Linkage Mechanism During Upstroke*

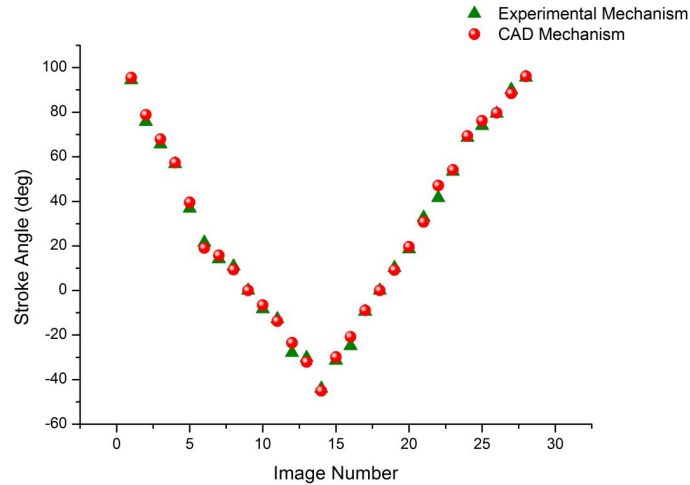


Figure 3.9: *Experimental and CAD Stroke Angles from Linkage Mechanism*

Figure 3.9, displays a data comparison of the output stroke angles for both the experimental and CAD models. The measurement uncertainty for all the physical measurements can be taken as  $\pm 2$  degrees, as the physical readings are acquired by initially capturing images and then measuring via software. When the flapping arms are positioned along the horizontal axis, the stroke angle has been taken as zero degrees. Thus, naturally during a complete cycle zero degrees will be encountered twice as seen in the graph, where the data found from both cases compares very well when the slider is located at the same vertical position. The first half of the data (from left to right) refers to downstroke followed by upstroke, where the lowest negative point can be referred to as maximum downstroke in this current analysis. As a whole, the data between both cases compares very well, although certain points do show a clear difference in output stroke angle values such as image numbers 12, 16 and 22. The differences are not alarming and could most possibly be due to slight inaccuracy in measurement from experimental images. Other causes for the differences could be due to the slider having a slight inclination which would alter the linkage positioning, in turn creating a small error in the flapping arm position. Small differences in the data between both cases are bound to emerge as many individual actions are carried out to create such a mechanism, and defects could occur during these stages from manufacturing the components, placement of holes, diameter of holes and even the circularity of the carbon fibre bars can come into interrogation for the cause of differences. Overall the data shown in the graph compares well and furthermore it also conforms well with the visual images in Figures 3.7 and 3.8.

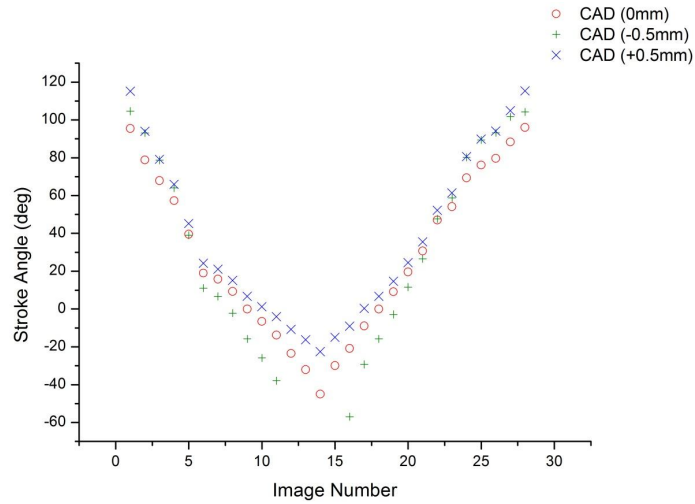


Figure 3.10: *Tolerance Data for CAD Model in Symmetric Configuration*

The tolerance data is found by analysing the CAD model and applying a stacked tolerance effect to the linkage mechanism. The original (0 mm) case was compared with the physical mechanism which has been analysed singularly in Figure 3.9. Leading on from this the extreme tolerance values of  $\pm 0.5$  mm are applied to each of the linkages to determine how the stroke amplitude values are affected when the linear slider is moved to the same positions as the original (0 mm) case. For the -0.5 mm case the holes on linkages L0-L3 were moved inwards (closer to one-another) and the opposite applies for the +0.5 mm case where the holes are moved outwards. As the hole movement is applied to all of the linkages an accumulated tolerance effect is found which leans towards a worst case scenario at both extreme ends. Dependent on the method of manufacture a reduced level of accuracy is possible where the extreme distance from the original centre point of a hole is  $\pm 1$  mm. This will affect the mechanism even more where the linkage mechanism will lock at smaller linear actuation distances, thus changes would need to be made if such extreme tolerances were found in the manufactured parts. Figure 3.10, presents a comparison of the stroke angle values for both extreme tolerances investigated here. It is clearly evident that linkage locking occurs for the -0.5 mm case towards the lowest positions for the linear slider, this situation would require alterations as such a scenario would cause severe problems. The largest positive stroke angles are found for the +0.5 mm case, however when approaching the lowest linear positions the smallest negative flapping angle is output. The original case stroke angle values are placed in between the stroke angles for both extreme tolerance values for most of the linear actuated positions. Of most importance is the total stroke angle created during the down and up strokes in comparison to the instantaneous individual stroke angle per linear actuator position.

| <b>Parameter</b>              | <b>0 mm-A</b> | <b>+0.5 mm-B</b> | <b>-0.5 mm-C</b> | <b>% Diff. A &amp; B</b> | <b>% Diff. A &amp; C</b> |
|-------------------------------|---------------|------------------|------------------|--------------------------|--------------------------|
| <i>Min. Downstroke (deg)</i>  | 95.5          | 115.19           | 104.61           | 18.69                    | 9.10                     |
| <i>Max. Downstroke (deg)</i>  | -45           | -22.5            | -37.9            | 66.67                    | 17.13                    |
| <i>Min. Upstroke (deg)</i>    | -29.91        | -14.99           | -56.94           | 66.46                    | 62.25                    |
| <i>Max. Upstroke (deg)</i>    | 96.06         | 115.34           | 104.22           | 18.24                    | 8.15                     |
| <i>Total Downstroke (deg)</i> | 140.5         | 137.69           | 142.51           | 2.02                     | 1.42                     |
| <i>Total Upstroke (deg)</i>   | 125.97        | 130.33           | 161.16           | 3.40                     | 24.51                    |

Table 3.2: *Stroke Angles & Percentage Differences*

Table 3.2, presents stroke angle values for all three tolerance cases. As aforementioned, the plunger was physically positioned to set distances, this was then replicated in all the CAD tolerance cases to determine stroke angle values. The percentage differences lie within a large range of values for both down and upstrokes. Analysing the data plot in Figure 3.10 and the values within the aforesaid table it can be seen that the extreme tolerance values have a noticeable effect. Some of the percentage differences are very large > 60%, which shows that the linkage mechanism capabilities are clearly affected or enhanced in some scenarios by the introduction of these tolerance values. Majority of the total down and up stroke percentage differences have reasonable values except for the difference between cases A and C for total upstroke angle. This has a relatively large value because of the very large minimum upstroke value of -56.94 degrees, which is a resultant of the lowest linear actuation position achievable by the mechanism at this tolerance setting.

### 3.5 Kinematic Modelling

The linkage mechanism has been modelled with a set of equations which effectively produce the output flapping angle from a vertical length. The input displacement is applied to Link L1 (refer to Figure 3.11) which is located at the bottom of the mechanism, as aforementioned this forces the connected members to move from their current position where the size of displacement is dependent upon the actuation distance along with the direction of actuation. The flapping motion is created by link L3 which is located at the top of the mechanism, the part is a single piece with an 'L' shaped geometry which is restricted in terms of directional movement as it is positioned on the fixed pivot rod of the frame. Thus, L3 cannot translate and is restricted to output rotational motions only. The output angle must be greater than the input angle applied to L1 as this is the overall purpose of using such a linkage method, and the greater the output angle the more effective the linkage system performance is seen to be. If the difference in angle is not large enough the system would need to be reviewed and a revised version should be produced with an end result of a sufficiently greater output angle opposed to the input angle. The co-ordinate positions have been shown in Figure 3.11, the fixed locations have been assigned blue dots as these are the pivot locations which L1 and L3 rotate about, and some of the variable locations shown in red have the option to translate as well as rotate.

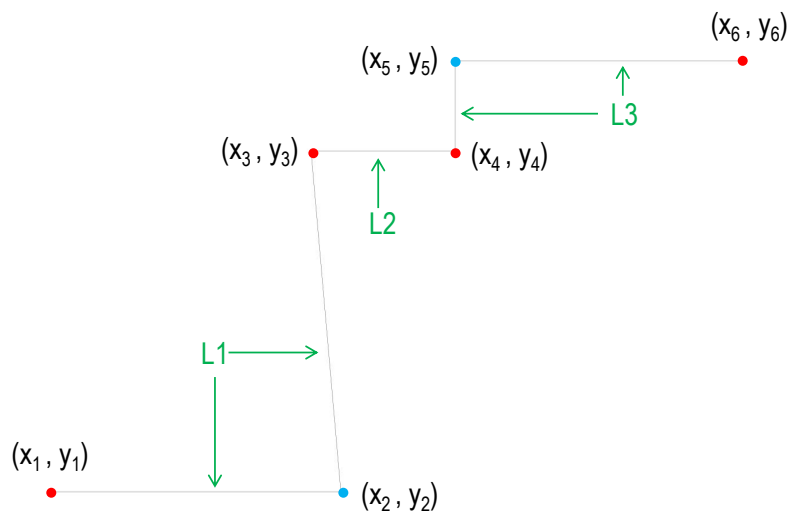


Figure 3.11: *Links and Co-ordinates for Mechanism; Blue Dots: Fixed Pivot Location, Red Dots: Variable Location*

### 3.5.1 Linkage Movement

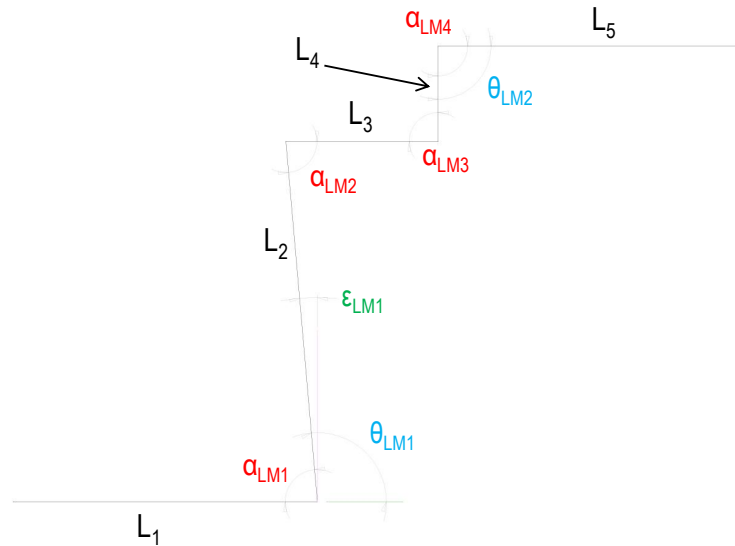


Figure 3.12: *Linkage Mechanism in Neutral Position with Angles*

Figure 3.12, illustrates the linkage mechanism in the neutral position and the angles which apply when in this state. The  $\alpha$  angles refer to the angles between each length of link, for example,  $L_1$  and  $L_2$  has an angle between them which is referred to as the inner angle of  $L_1$  (refer to Figure 3.4 to identify this link), it also referred to as the angle between lengths  $L_1$  and  $L_2$ .  $\alpha_{LM1}$  and  $\alpha_{LM4}$  are fixed angles as they were assigned to a single link and do not refer to an angle between two links such as  $\alpha_{LM2}$  and  $\alpha_{LM3}$ , which are both variable angles that will alter upon any change applied to the links.  $\epsilon_{LM1}$  is the angle positioned between  $L_2$  and the vertical axis, this angle will change, and effectively is replaced by  $\beta$  which is shown in Figure 3.13. The final variable angles are  $\theta_{LM1}$  and  $\theta_{LM2}$ , the former is the angle between the horizontal and the outside of  $L_2$ . The latter, is the angle on the inner part of  $L_3$  in the current diagram, but this in fact varies as it actually measures the entire angle from the vertical axis to  $L_5$ .

$$\alpha_{LM1} = \alpha_{LM2} \quad (3.6)$$

$$\alpha_{LM3} = \alpha_{LM4} \quad (3.7)$$

Equations 3.6 and 3.7, apply to the linkage system when the links are positioned in the neutral state as shown in Figure 3.12, any change would discard these equations as the relationship would no longer apply, as  $\alpha_{LM2}$  and  $\alpha_{LM3}$  are variable angles.

$$\theta_{LM1} = 180^\circ - \alpha_{LM1} \quad (3.8)$$

$$\epsilon_{LM1} = \theta_{LM1} - 90^\circ \quad (3.9)$$

$$\epsilon_{LM1} = \cos^{-1} \left( \frac{y_3 - y_2}{L_2} \right) \quad (3.10)$$

$$\epsilon_{LM1} = \sin^{-1} \left( \frac{x_2 - x_3}{L_2} \right) \quad (3.11)$$

When the linkage system is in neutral state, Equations 3.8 and 3.9 both apply, and can be determined as the initial angle of  $\alpha_{LM1}$ , this is known as it should be prescribed when selecting the initial linkage mechanism parameters. Additionally  $\epsilon_{LM1}$  can be calculated using either Equation 3.10 or 3.11, similar equations can be derived to determine angular properties for all linkage mechanisms.

Upon the displacement of L1 all of the connected members displace from the original position which leads to the introduction of various  $\beta$  angles which are utilised in the process to determine the output angle through the method of firstly calculating the co-ordinates of each point in the linkage system.  $\beta_{LM1}$ , is the first displacement angle which represents the change in angle from the original horizontal position to the new position of L<sub>1</sub>, this is shown in Figure 3.13.  $\beta_{LM2}$ , defines the change in angle of L1, but in this case the vertical displacement is under consideration and  $\beta_{LM3}$  demonstrates the change in angle of L2 from the neutral position in accordance to the horizontal axis. The relationship of  $\beta_{LM4}$  and  $\beta_{LM6}$  is in accordance to Equation 3.12.

$$\beta_{LM4} = \beta_{LM6} \quad (3.12)$$

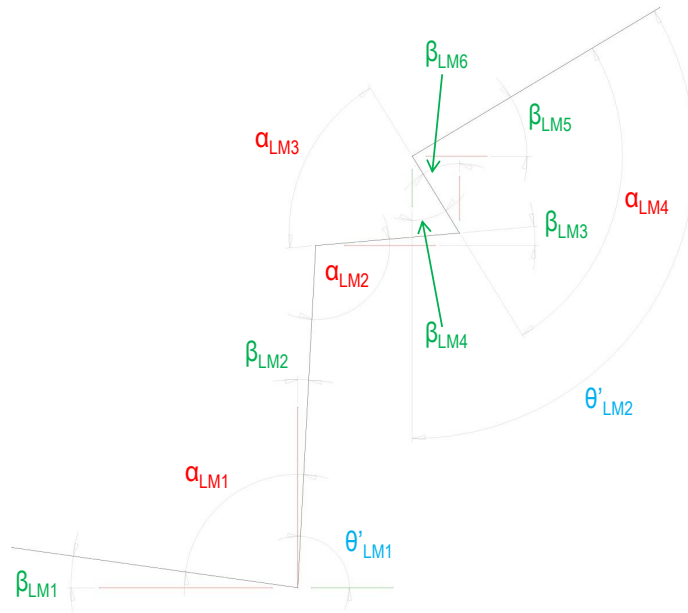


Figure 3.13: *Linkage Mechanism Displaced from Neutral Position with Angles*

$\beta_{LM5}$ , is the final output angle which is more commonly known as the flapping angle. The angle is measured from the horizontal axis to  $L_5$ , and when taking the horizontal axis as a zero point the upper half will produce a larger arc as opposed to the bottom half due to linkage locking as explained previously.

The following equations calculate the angle properties in reference to Figure 3.13,

$$\beta_{LM1} = \epsilon_{LM1} - \beta_{LM2} \quad (3.13)$$

$$\beta_{LM2} = \theta'_{LM1} - 90^\circ \quad (3.14)$$

$$\theta'_{LM1} = 180^\circ - \alpha_{LM1} - \beta_{LM1} \quad (3.15)$$

$$\theta'_{LM1} = 180^\circ - \alpha_{LM1} - \beta_{LM1} \quad (3.16)$$

$$\theta'_{LM2} = \alpha_{LM4} + \beta_{LM4} \quad (3.17)$$

The selection of equations shown below can be used in various arrangements to determine the coordinates of the links, once the coordinates are found the angular output can be determined. This is dependent on the initial linkage lengths and positioned angles. The pivot points are fixed to the frame, thus the coordinates assigned to these positions are fixed and due to this they are already known, so long as the lengths and link angles are defined.

$$y_1 = \tan\beta_{LM1}(x_2 - x_1) + y_2 \quad (3.18)$$

$$y_3 = \frac{1}{\tan\beta_{LM2}}(x_2 - x_3) + y_2 \quad (3.19)$$

$$y_4 = \tan\beta_{LM3}(x_4 - x_3) + y_3 \quad (3.20)$$

$$y_5 = \frac{1}{\tan\beta_{LM4}}(x_4 - x_5) + y_4 \quad (3.21)$$

$$y_6 = \tan\beta_{LM5}(x_6 - x_5) + y_5 \quad (3.22)$$

$$\beta_{LM3} = \sin^{-1} \left( \frac{y_4 - y_3}{\sqrt{(x_4 - x_3)^2 + (y_4 - y_3)^2}} \right) \quad (3.23)$$

$$\beta_{LM4} = \sin^{-1} \left( \frac{x_4 - x_5}{\sqrt{(x_5 - x_4)^2 + (y_5 - y_4)^2}} \right) \quad (3.24)$$

$$y_3 = L_2 \cos\beta_{LM2} + y_1 - L_1 \sin\beta_{LM1} \quad (3.25)$$

$$y_3 = x_1 + L_1 \cos \beta_{LM1} - L_2 \sin \beta_{LM2} \quad (3.26)$$

$$y_4 = L_3 \sin \beta_{LM3} + L_2 \cos \beta_{LM2} + y_2 \quad (3.27)$$

$$x_4 = L_3 \cos \beta_{LM3} - L_2 \sin \beta_{LM2} + x_2 \quad (3.28)$$

$$y_5 = L_4 \cos \beta_{LM4} + L_3 \sin \beta_{LM3} + z_3 \quad (3.29)$$

$$x_5 = L_3 \cos \beta_{LM3} + x_3 - L_4 \sin \beta_{LM4} \quad (3.30)$$

$$y_6 = L_5 \sin \beta_{LM5} + L_4 \cos \beta_{LM4} + z_4 \quad (3.31)$$

$$x_6 = L_5 \cos \beta_{LM5} + x_4 - L_4 \sin \beta_{LM4} \quad (3.32)$$

Equations 3.23 and 3.24, calculate the angles of  $\beta_{LM3}$  and  $\beta_{LM4}$  respectively. All other  $\beta$  angles can be determined in a similar manner according to the angle to be calculated.

A future design would require an optimisation process performed to determine the optimum lengths and angles that each individual link should be and positioned at in the system. Although the mechanism was continually scrutinised during the design stage, the end product for this project was bound to be an experimental test rig which meant that a larger actuation distance than what would be desired for a future design was allowable and would aid in overcoming the wing loading which is expected to act on the linkage mechanism. It is worth noting that the first and second derivatives of the linkage equations determine the velocity and acceleration which can be utilised to determine the forces and torques of the linkage movements. However, this is beyond the requirements of the current analysis and such values would only be theoretical as frictional forces and tolerance gap sizes which lead to slight inclinations and minor mis-alignments would not

be considered. The core necessity of this analysis was to determine the output angular positions in comparison to the input displacements. Some other flapping mechanisms based on the small input angle and large output angle methodology which have been developed are shown in (Nguyen et al. 2008), (Steltz et al. 2007) and (Wood 2008a). All the aforementioned utilise a linear actuator to drive the linkage mechanism and create a flapping motion. Rigid linkage and flexure transmission based connections can be utilised to create a successful flapping motion, where alterations can be made in both to create a greater output angle. The mechanical flapping motion produced by the FWMAVs within this research project is categorised as a rigid linkage based mechanism.

### 3.5.2 Kinematic Results

The kinematic equations were solved using Matlab where all the required data can be determined systematically and the final  $\beta_{LM5}$  angles were produced. The linkage mechanism is shown in two of its extreme positions along with the neutral zero position in Figure 3.14. Both the vertical and horizontal axes represent the distance of the linkage mechanism, which provides insight into the maximum length of the mechanism when positioned in start upstroke and start downstroke positions. The methodology applied here, can be utilised for a future design where the link lengths, angles and pivot positions can be modified and optimum flapping angle for a minimum input angle can be determined. The pivot points have been shown in 'circles' which refer to co-ordinates  $(x_2, y_2)$  and  $(x_5, y_5)$ .

Figure 3.15, illustrates the relation between the angle input into the system and the resultant stroke angle output.  $\beta_{LM1}$  evidently has a much smaller range compared to  $\beta_{LM5}$ , whilst the  $L_1$  arm travels through 5 degrees the  $L_3$  arm travels through approximately 40 degrees. Thus, the design of the linkage system is clearly performing well and fulfilling its role. A steep linear relationship is observed in this plot for both angles with rapid growth shown for the  $\beta_{LM5}$  angles. At the start and end of the stroke the plots seem to have a slight curvature which is formed at the most extreme angles where the growth in angle is more gradual.

Figure 3.16, presents the arc input and output angles along with the linkage system in the neutral position. The arcs are the graphical results from the movement of both  $L_1$  and  $L_3$  arms. Presenting the data under the measurement axes of distance travelled aids in understanding the actual motion the arm travels through

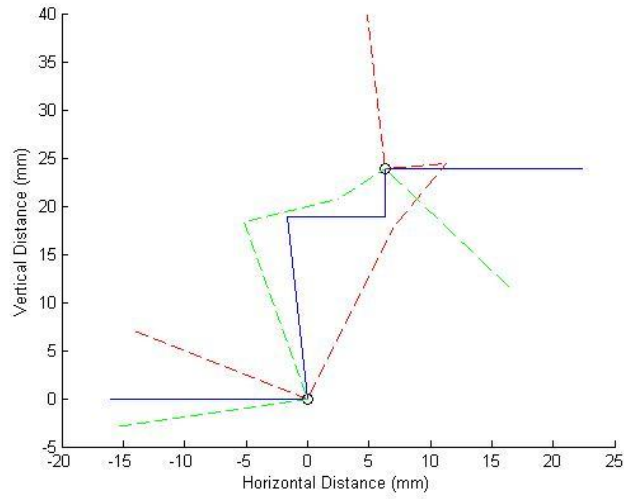


Figure 3.14: *Linkage Mechanism in Three Different Positions; Blue: Neutral Position, Red: Start Downstroke Position, Green: Start Upstroke Position*

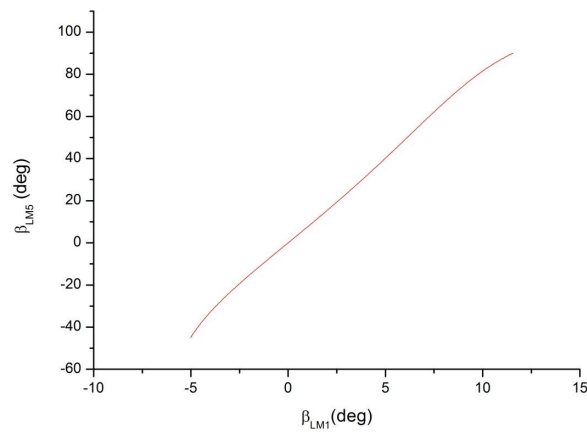


Figure 3.15: *Angle Input to The System Related to Output Angle*

and the flapping angle output from the linkage system. The graphical output of both arcs formed from the coordinate locations of  $(x_1, y_1)$  and  $(x_6, y_6)$  clearly present the consequential difference between the input and output angles.

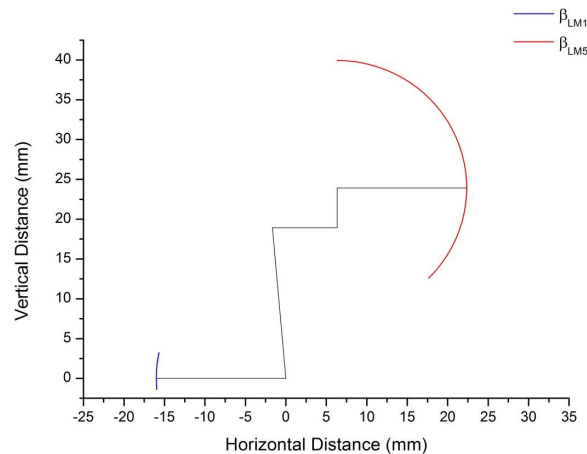


Figure 3.16: *Linkage Mechanism with Angle In and Angle Out*

## 3.6 Wing Morphology and Experimental Wings

### 3.6.1 Wing Morphology

In order to successfully mimic insect flight it is essential to understand the morphological wing parameters of a real insect. During flight an insect's wing will passively deform from the aerodynamic and inertial loadings experienced when in motion which effectively results in unpredictable aerodynamic behaviour, such a feature would need to be incorporated into the wings of the FWMAV to stand a chance in performing like an insect when in flight. The dynamic loading applied to the wing when in motion is dependent on the three dimensional kinematics, thus the three dimensional formation of the artificial wing must match that of an insect in order to behave in the same manner under the same prescribed wing kinematics.

The wings of an insect essentially act as reactive aerofoils through their modification of wing curvature in either of the strokes, which are direct responses to the inertial and aerodynamic forces experienced. The passive deformation would strongly depend on the venation formation, membrane material, mass distribution,

planform, size and even the structural profile of the leading edge. In general, the insect wing is thought to be a flat plate which consists of load bearing beams (in reality these are the tubular veins) which are spread out throughout the wing area. However, the reality of it is not so straightforward, as the wings actually have a corrugated structure in the chordwise direction that is more pronounced at the root of the wing. The corrugation pattern is essentially a delicate process to replicate and would require numerous pieces of equipment in addition to materials. Information regarding the construction of such wings can be found in (Tanaka & Wood 2010), where the process and materials used have been explained in detail. The paper describes an artificial insect wing consisting of corrugation along the chord and successful manufacture at the same scale of an insect wing with a span of 11.7 mm.

To gain a thorough understanding of the aerodynamic effects of wing corrugation investigations would need to be carried out on wings which replicate the deformational characteristics of an insect's wing along with a replication of its entire three dimensional surface, and tests must be performed under the same wing kinematics which an insect carries out. Although at such high angles of attack where the flow is largely separated, the fluid would effectively be less sensitive to the variation in wing profile, thus the corrugated profile may not play such a sufficient role in terms of aerodynamic benefits due to its irregular profile. The wing corrugation provides a higher flexural stiffness opposed to a chordwise flat beam, this corrugation will remain effective so long as the venation formation is present in both spanwise and chordwise directions, see (Dudley 2002) for further information. Thus, although the profile of corrugation may have a limited effect under separated flows, the structural benefits of stiffness that wing corrugation enhances is essential to the aerodynamic performance of insect wings. The venational formation reduces the amount of bending and torsion of the wing, where majority of the venational mass is located at the root of the wing (denoting that the vein density is highest here) as the wing bending moment during a flapping motion is largest at the root. As majority of the venational mass is located at the root, less energy is consumed to accelerate the wings during a flapping cycle.

A generic wing planform is shown in Figure 3.17, which displays specific wing parameters and there dimensional properties according to the wing. Non-dimensionalisation can be carried out to the radial distance (Equation 3.33) of the wing root by using the span of a single wing as shown in (Ellington 1984).

$$\hat{r} = \frac{r'}{R} \quad (3.33)$$

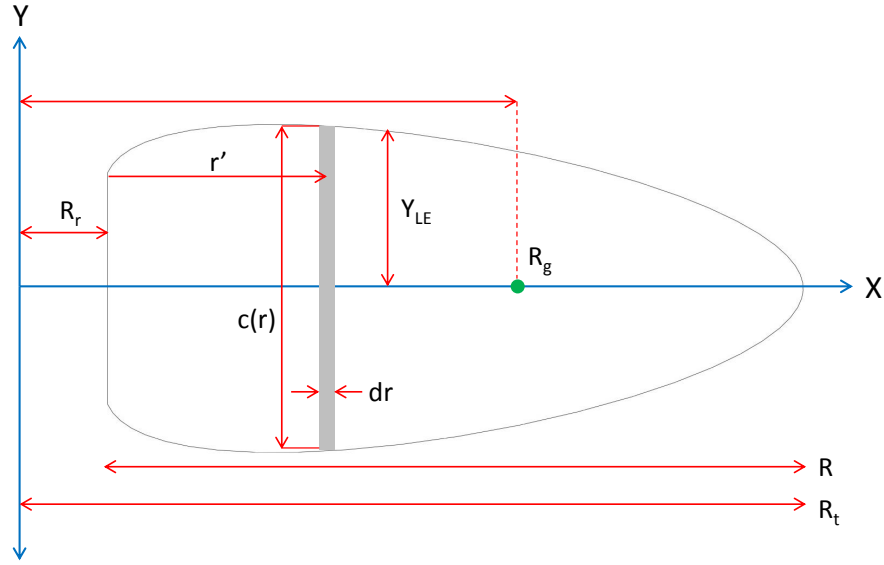


Figure 3.17: *Schematic Illustration of a Generic Wing Planform with Geometrical Details*

A similar non-dimensionalisation can be applied to the chord-wise component of the wing as shown in Equation 3.34,

$$\hat{c} = \frac{c}{\bar{c}} \quad (3.34)$$

Where the mean chord length can be determined by the average length of a set of chord-wise lengths or from Equation 3.35. The leading edge profile can be non-dimensionalised (shown in Equation 3.36) by using the mean chord as this entity exists in the same plane as  $Y_{LE}$ ,

$$\bar{c} = \frac{1}{R} \int_0^R c(r) dr = \frac{S}{2R} \quad (3.35)$$

$$\hat{Y}_{LE} = \frac{Y_{LE}}{\bar{c}} \quad (3.36)$$

The planform area of the wing can be found using a strip method, where the wing is split into sections along its chord-wise direction and corresponding difference in radial distance and chord length are used to

determine the area. Integrating in the span-wise direction and accounting for both wings will determine the total wing area as shown in Equation 3.37. The Aspect ratio of a wing is found using Equation 3.38,

$$S = 2 \int_0^R c \, dr \quad (3.37)$$

$$AR = \frac{(2R)^2}{S} \quad (3.38)$$

The moment of wing area can be found using Equation 3.39, where k refers to the order of the moment,

$$S_k = 2 \int_0^R c r^k \, dr \quad (3.39)$$

The non-dimensional radius of the moment of wing area is determined from Equation 3.41, where the first order of the radial moment is the wings centre of area, and orders above are the area distribution of the wing,

$$\hat{r}_k^k(S) = \int_0^1 \hat{c} \hat{r}^k \, d\hat{r} \quad (3.40)$$

The radius of gyration is the spanwise location of the position where the mean lift acts, as the local velocity at each cross section varies during flapping motion. Additionally its also equal to the second moment of inertia which is defined as the torque needed to move a rigid body of fixed mass through a desired change in angular velocity about a rotational axis, see (Ellington 1984).

$$R_g = \sqrt{\frac{1}{S} \int_0^{R_r} r^2 c(r) \, dr} \quad (3.41)$$

The approximate location of the radius of gyration has been shown in Figure 3.17, which is usually positioned beyond the mid-position of the radial length from the rotational axis to the wing tip. The above formula of radius of gyration refers to hovering flight only.

### 3.6.2 Experimental Wings

Deformation modes can be used to store potential energy with the application of an external force causing the material to deform. Upon the removal of this external force the energy can be released and exploited in a beneficial manner dependent on its connections and surroundings. Thus the application of suitable materials which can take advantage of the energy storage associated with deformations, would prove to be very beneficial for designs which are continuously energy conscious, due to a limited supply of energy stored within its power supply. When selecting a material with the ability to store energy the mass and overall morphology must be considered as it is paramount this material bonds/connects to other materials which are incorporated in the system.

Deformations which can exist from the exploitation of a material such as mylar for the application of wing rotation are bending and torsion. Due to the flexible nature of mylar, when flexed it stores elastic energy and can gradually release this energy dependent upon the amount of pressure acting on the surface and the positioning of this pressure. However, in some situations this energy can be rapidly released overcoming the pressure resisting its motion. When applied in the role of wing rotation in a flapping wing system, the fluid loading acting upon the wing will cause the mylar to deform in the manner of bending (wing rotation) and torsion (small amount of wing deviation). This can add to the rapid rotation the wing performs with the release of this elastic energy, resulting in the acceleration of the fluid surrounding the wing. Thus, the mylar hinge not only aids in performing passive wing rotation but also stores energy and enhances force production when this energy is released rapidly. However, this is not to say that passive wing rotation will aid more force enhancement over controlled wing rotation, as this would not be true. The important information to acknowledge here is that passive wing rotation allows the wing to rotate with the use of a light weight material and experiences an additional benefit from the elastic energy stored.

In terms of force enhancement a controlled wing rotation will definitely prove to be more beneficial, but with the amount of additional mass this is not a feasible option for FWMAVs. Ideally engineers would want to control the wing angle of attack throughout the flapping stroke, this would allow the designer to tailor the vehicle to take full advantage of the enhancing aerodynamic phenomena known in the field of insect flight and create the ultimate FWMAV. This form of active control would allow for more controllability in terms of manoeuvring and stability, but as mentioned would introduce more mass. As controlling the wing angle of attack through the flapping stroke is not an option, certain limitations or simple mechanical mechanisms

can be implemented into the FWMAV designs, to incorporate different types of wing motion to enhance other features such as thrust or lift or even a rotating moment. Such an attempt was explored in parts of this thesis via FRAP wing rotation and even asymmetrical flapping.

| Parameter                      | 26 mm SR Wings | 47 mm Wings | 60 mm Wings |
|--------------------------------|----------------|-------------|-------------|
| <i>Wing Span (mm)</i>          | 26             | 47          | 60          |
| <i>Mean Chord (mm)</i>         | 12.7           | 22.3        | 34.7        |
| <i>Area (mm<sup>2</sup>)</i>   | 728            | 2198        | 4274        |
| <i>Aspect Ratio</i>            | 3.7            | 4           | 3.4         |
| <i>Radius of Gyration (mm)</i> | 27.6           | 37.8        | 44.9        |
| <i>Mylar Thickness (mm)</i>    | 0.036          | 0.05        | 0.05        |

Table 3.3: Specifications For Wings shown in Figure 3.18

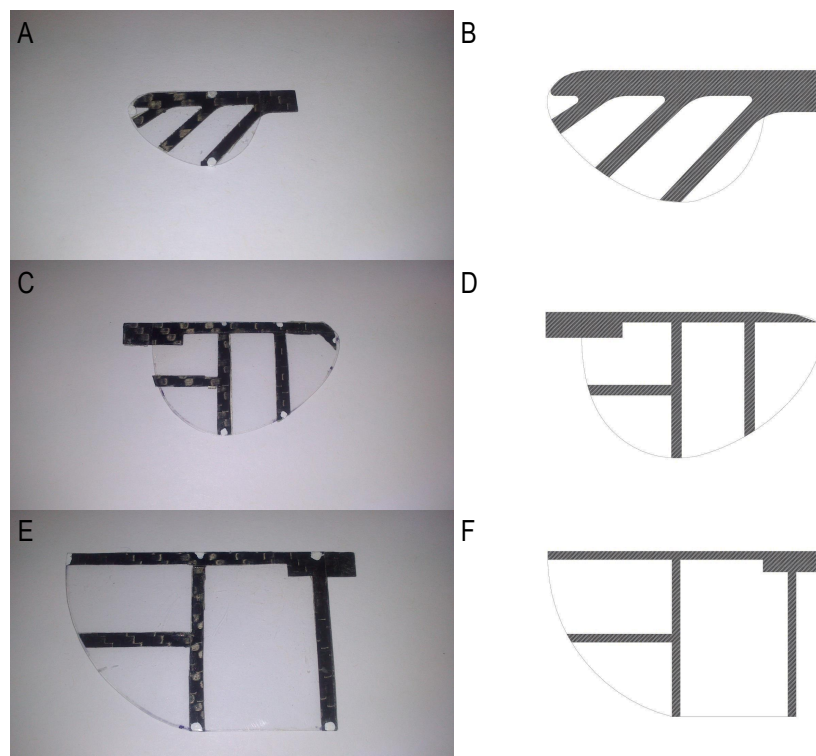


Figure 3.18: Experimental and CAD Wings; A: 26 mm SR Wing (WT2), B: CAD of 26 mm SR Wing (WT2), C: 47 mm Wing (WT3), D: CAD of 47 mm Wing (WT3), E: 60 mm Wing (WT4), F: CAD of 60 mm Wing (WT4)

The wings shown in Figure 3.18, have been utilised during the experimental and kinematic analysis. The skeletal wing structure for the semi-rigid wings was manufactured using the CNC machine along with the fully rigid wings, and the remaining others were manufactured by hand using essential crafting tools. The fully rigid wing set was constructed of carbon fibre only, it had the same profile and specifications as the 26 mm semi-rigid wings (WT2). The semi-rigid and fully rigid wings had to be manufactured via CNC as they had a greater thickness of 0.45 mm which was found to be too difficult to craft by hand into the desired shape. The wings skeletal structures which were crafted by hand were constructed from a carbon sheet of thickness 0.3 mm, this could be accurately cut using sharp blades attached to the x-acto knife and a template of each wing frame. Table 3.3 displays the specifications of each wing set (all lengths are for singular wing span), where the radius of gyration of each is 9-13 percent greater than the distance from the axis of rotation to the mid-span of the wing for all wing sets. Mylar was used as the membrane surface, it was taped down to the frame of the wing where care was taken to ensure additional pieces of tape do not stick to the membrane which is not in contact with the frame. The mylar material is evenly distributed to avoid any positions of membrane material gathering which would affect the surface smoothness. Each wing was attached to both the models with the exact same method, which was by the attachment of the small tongue section located near the root of all the wings that would securely connect to the base which was glued to the L3 flapping arms of the model.

### 3.7 Measurements for Both MAV Models

Both models were tested to determine the base measurements when the model has no extra mass or aerodynamic surface to translate through a flapping motion. Conducting tests on the fundamental models, allows the designer to analyse the mechanical motion and determine which component or mechanism would require modifications in future designs. Furthermore, through comparisons of multiple models which in principle are based on the same mechanical design with infinitesimal differences aids in understanding what is causing the diversification in the relevant measurement(s). The same tests were performed on both models whilst measurements were recorded for vertical force produced and the requisite power input.

Figures 3.19 A-C, illustrate the power readings recorded during each test on model 1 and model 2 in both of its configurations. From the data, its evident at a lower flapping frequency there is low power input and

the same relationship exists for higher frequency flapping where higher power is drawn by the mechanical system. A brief glance at these plots clearly displays a vast difference in the power required and the shape of the curves. At lower frequencies the power plots for model 1 show a sinusoidal behaviour, until 7 Hz onwards where the attitude of the curve becomes capricious. It should bear in mind that these power measurements are not recorded at the same rate as the force measurements, thus they do not relate to any specific position of the flapping arms, moreover they represent real time power readings during numerous flapping cycles. The power readings have merely been shown to demonstrate the unpredictable behaviour of the power input to the system, and this capricious behaviour exists due to the current drawn by the motor from the PSU, as the voltage was constant throughout all the tests. As a greater level of power is drawn from the power supply, the amplitude is compressed where the cyclic sinusoidal waveform no longer exists, during small sections the power drawn is somewhat consistent. This fluctuating behaviour is present in both the power graphs for model 2, and at the lowest flapping frequency of 2 Hz in the symmetric configuration model 2 shows large peaks in the power required to move the mechanical linkages. A hypothesis for the difference in power required between both models is due to the friction the plunger experiences during its vertical motion which is imposed by its linear guide. Further to this, although great care was taken when assembling both models, stiffness in linkages between both models is bound to have small differences. Reducing the surface area of the plunger which is in contact with the guide would theoretically reduce the level of friction produced, however, such changes were not made to the model at the time as this design served solely as an experimental rig design and such favourable implementations would be made for future flight worthy models.

Analysing these data plots allows one to understand that the shear power drawn under base tests with no additional physical or aerodynamic loading, model 2 seems to require substantial amounts of power when compared to model 1, and this applies to both configurations of model 2. In order to create asymmetrical flapping motion the plunger was slightly shifted along the horizontal axis, which was done by a change of plates which attach to the frame of the model, any differences in the smoothness of the surface which the plunger is in contact with during its vertical motion would affect the power needed, and also shifting the plunger has a direct consequence on the attached linkages which are displaced from their original position which may have an effect on power. From the data, model 2 (asym) seems to have a smoother mechanical motion as the power data is lower at all frequencies and the lower frequencies do not show such high peaks as seen for model 2 (sym) results.

Figure 3.19 D-F, presents three-dimensional plots describing a clear relation between frequency, vertical force and power. It should be noted that when power is stated as a single value it is the average power required per cycle, this was determined by averaging the real time power readings over numerous flapping cycles. As long as the forces and moments generated show a consistent periodic behaviour, the average power value can be directly related to a complete cycle. As the frequency increases both vertical force and power measurements escalate as shown by the red plots. At the greatest flapping frequency of 12 Hz, a comparison showed that model 1 requires lower power input and produces a larger vertical force output when compared to both sets of results shown for model 2. Model 1 clearly has a smoother mechanical motion throughout its system especially in its vertical guide, as it consumes nearly three times less power at the same flapping frequency which concludes that this model is more efficient than model 2. The conjecture behind this is that the vertical guide slot was probably smoother or slightly wider which will create less frictional forces when in motion. The blue two-dimensional plots show the relation between flapping frequency and the average vertical force measured as expected where the latter appears to increase parabolically with frequency. Plots in magenta present the average power variation with increasing flapping frequency, where a somewhat linear trend is observed as the frequency increases, the power input follows which is an expected relationship. And finally the green plots in all the graphs present the results for average vertical force in relation to the average power required to move the mechanical system to output these force values. Note the vertical force measurements displayed in these graphs present the peak-peak forces. Force measurements alone are not enough to analyse such a system as they are formed from various contributions such as the inertial forces of the R3 arms (composed of mass and accelerations), vibrations of the system, frictional forces from the slider and all connections present in the system. Therefore a power analysis is essential to complete a fundamental investigation on the bare models which proves to provide a valuable form of comparison.

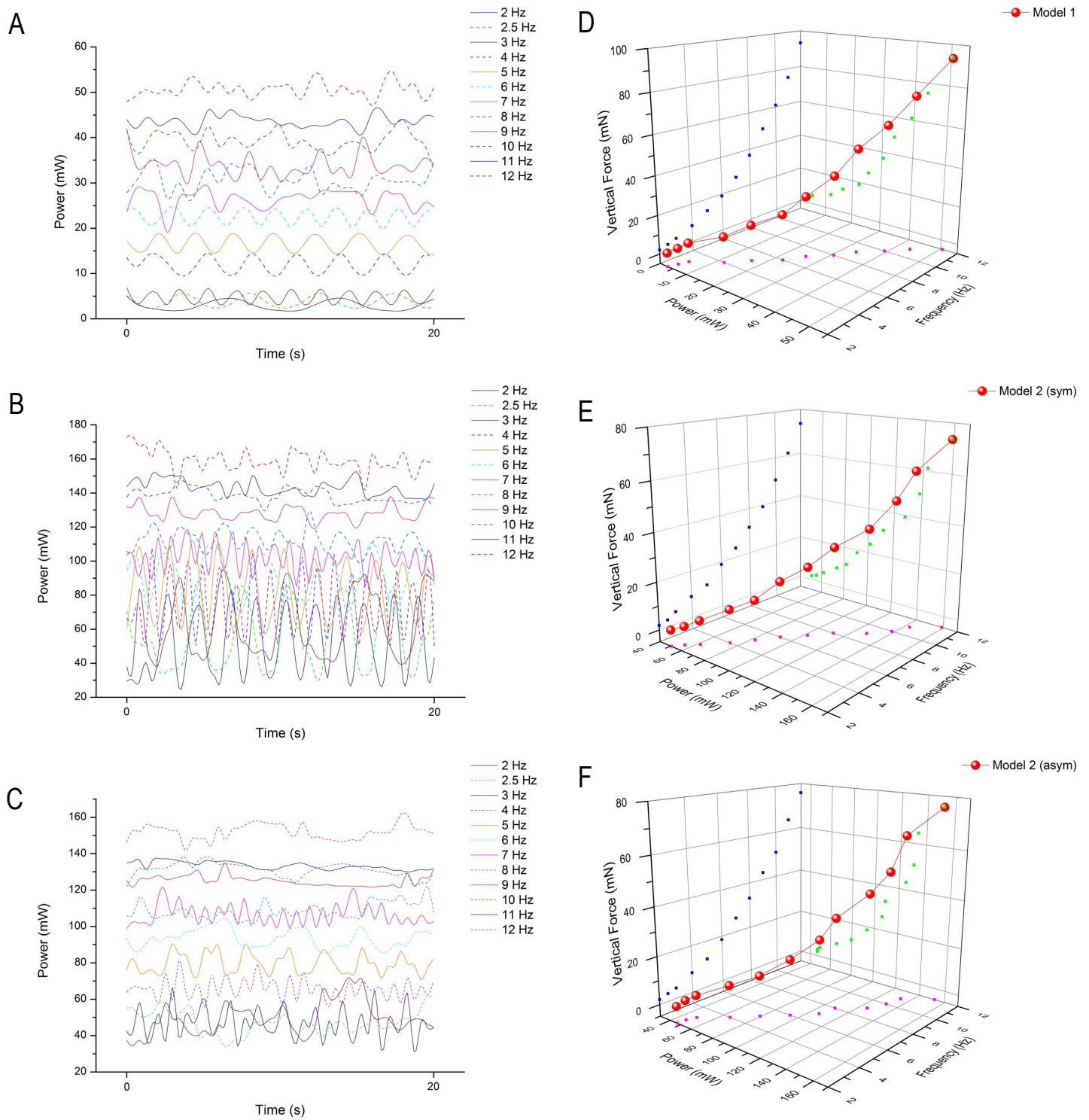


Figure 3.19: Power and Force Measurements of Mechanism Only; A: Model 1, B: Model 2 (sym), C: Model 2 (asym), D: Model 1, E: Model 2 (sym), F: Model 2 (asym), Coloured Dots in Graphs D,E,F Represent Axes Projections Such As Blue: Frequency Vs Vertical Force, Magenta: Frequency Vs Power, Green: Power Vs Vertical Force

Time history data for vertical force measurements has been shown in Figure 3.20 A-C. All the graphs illustrate smooth sinusoidal curves for a duration of 1 second. A very good consistency in terms of cyclic formation is shown in these plots indicating that the mechanical forces produced from both models should be smooth and consistent unless unforeseen vibrational forces contaminate data. This time history data has been presented in an average peak-peak vertical force format in graph D located in the same Figure. The force measurements at 2 Hz are minuscule compared to that of 12 Hz, and as aforementioned the force gradually increases with increasing flapping frequencies. From 2-8 Hz both models in all possible configurations produce very similar force measurements, thereafter the difference seems to gradually increase where model 1 seems to be producing larger forces, the difference of steady escalation in force production is seen from 9-12 Hz. Model 2 shows very similar force data for all frequencies in both symmetrical and asymmetrical configurations which is a positive result because a substantial difference would mean that one flight mode is not performing as the other, which would lead to further design work in the future in order to make sufficient adjustments. The vertical forces shown in these graphs are an evaluation of the mechanical system only.

Average power data has been shown in Figure 3.20 E, which clearly shows the minuscule power required by model 1 compared to model 2, this observation is consistent through all flapping frequencies. The power input to model 2 under symmetrical mode is slightly larger than that compared to the asymmetrical mode, which becomes more evident towards the larger flapping frequencies. Graph F (located in the same Figure) shows a power-force ratio at each flapping frequency. Model 1 has much more desirable results as opposed to model 2 where the power input is very large as mentioned previously. The data displays a larger ratio at lower frequencies as the force produced at these slow flapping speeds is very small. A substantial difference exists between both models as model 2 requires so much more power at each frequency. Modifications and further tests would need to be carried out on model 2 in future to reduce the amount of power required to move the mechanical system. The power analysis presented, clearly shows the significance of these fundamental tests carried out on the mechanism alone, prior to the addition of aerodynamic surfaces which would further complicate matters.

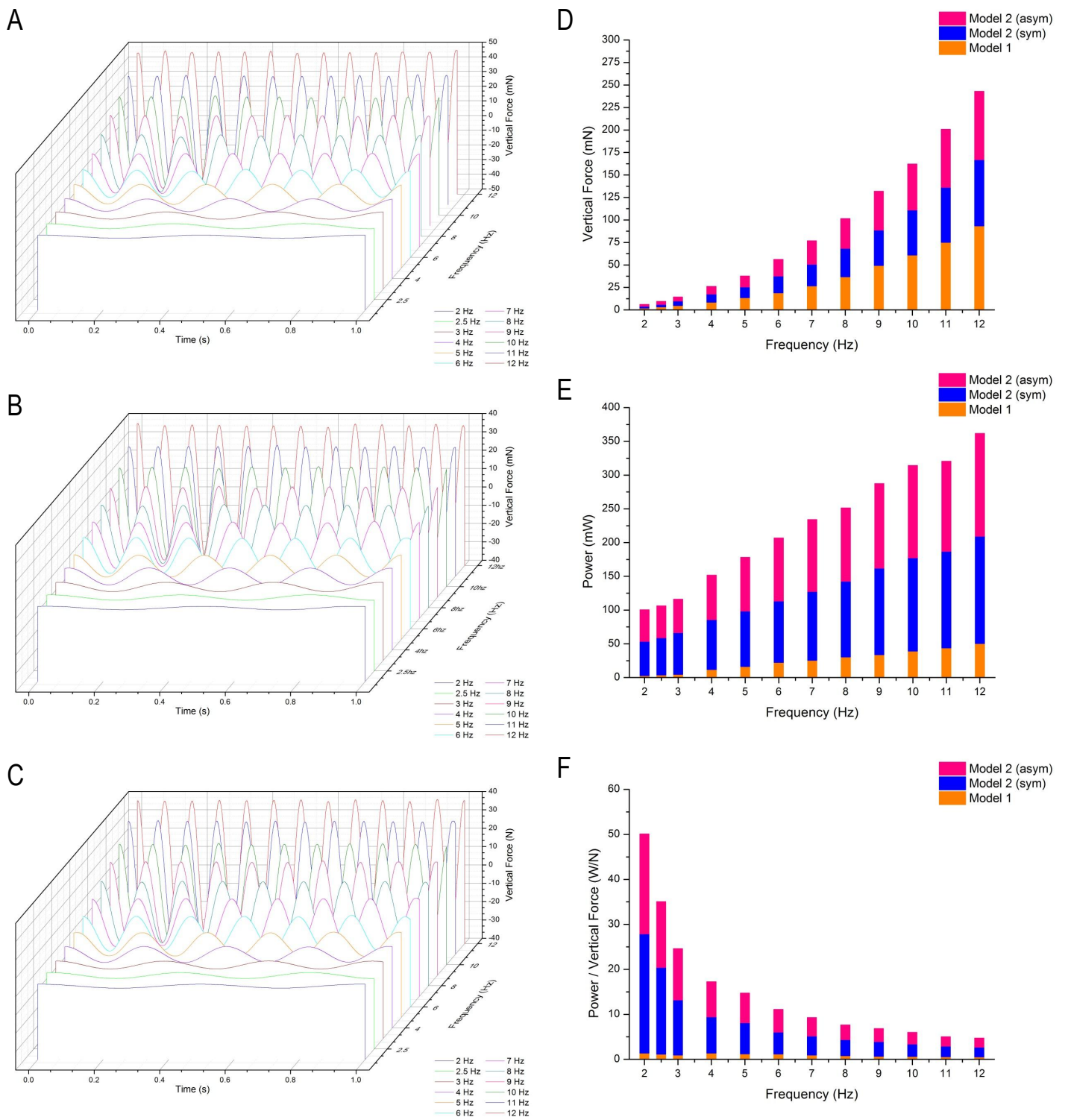


Figure 3.20: Power and Force Measurements of Mechanism Only; A: Model 1, B: Model 2 (sym), C: Model 2 (asym), D: Average Vertical Force Comparison, E: Average Power Comparison, F: Average Power / Average Vertical Force Comparison

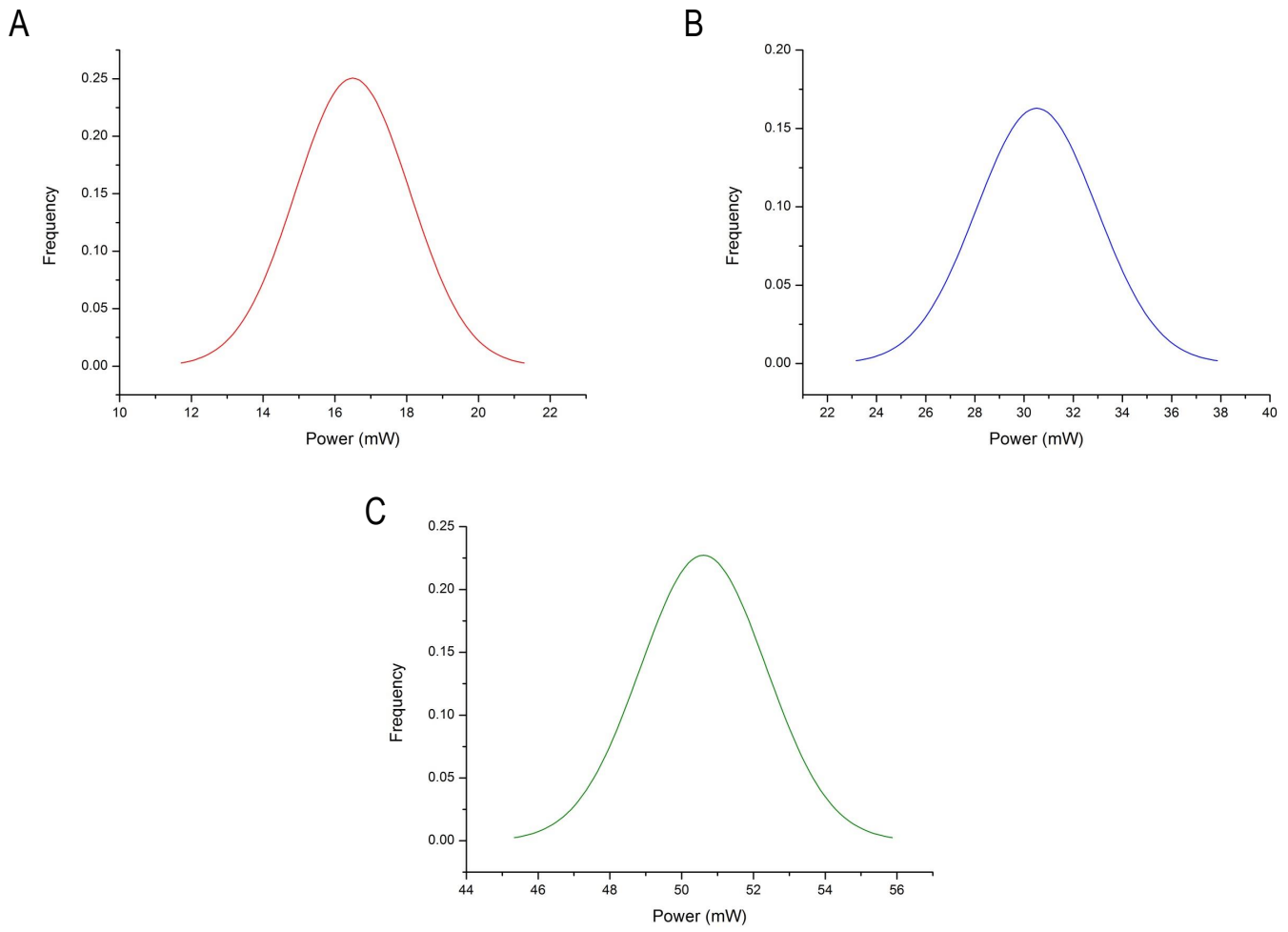


Figure 3.21: *Normal Distribution for Power Measurements of Model 1 Mechanism Only; A: 5 Hz, B: 8 Hz and C: 12 Hz*

Figure 3.21, presents several samples of normal distribution plots in relation to the power drawn by the mechanical system when flapping at the respective frequencies. The curves provide a clear statistical dispersion of the power data recorded. The standard bell curve shape is shown where the peak in each occurs at the mean power value. The plots were calculated to the third standard deviation to cover the range of power values for each flapping frequency. It should be noted that the frequency axis in these plots has no relation to flapping frequency. The mean, variance and standard deviation data is shown in Table 3.4. The standard deviation values quantify the level of dispersion for all the flapping frequencies, where it is found that the data lies within a small spread of 1-2.71 mW. As previously discussed the mean power drawn by the system increases as the flapping frequency increases.

Further examinations were carried out on the models, in this case carbon fibre rods were attached to both

| Flapping Frequency (Hz) | Mean (mW) | VAR ( $mW^2$ ) | $\sigma_{SD}$ (mW) |
|-------------------------|-----------|----------------|--------------------|
| 2                       | 2.97      | 1.07           | 1.03               |
| 2.5                     | 3.81      | 1.36           | 1.17               |
| 3                       | 4.74      | 1.75           | 1.32               |
| 4                       | 12.04     | 2.96           | 1.72               |
| 5                       | 16.53     | 2.54           | 1.60               |
| 6                       | 22.43     | 2.32           | 1.52               |
| 7                       | 25.58     | 4.76           | 2.18               |
| 8                       | 30.59     | 6.00           | 2.45               |
| 9                       | 33.92     | 7.33           | 2.71               |
| 10                      | 39.21     | 5.18           | 2.28               |
| 11                      | 43.82     | 1.84           | 1.36               |
| 12                      | 50.57     | 3.08           | 1.76               |

Table 3.4: *Statistical Power Data for Model 1 Mechanism Only*

flapping arms which had a length of 59 mm, diameter of 2 mm and each had a mass of 0.27 grams. The rods had a uniform mass and diameter distribution along its spanwise length. During these tests the rods were flapped at various frequencies from which power and vertical force measurement data sets were obtained. Aerodynamic force contribution is minuscule compared to the inertial forces produced when flapping the carbon bars. The bars were flapped at frequencies from 3-9 Hz with consistent increments of 1 Hz, the same tests were conducted on both models. A diagram of the model with the carbon bars attached is shown in Figure 3.24.

Figure 3.22 A-C, displays the power curves for both models. At lower frequencies for model 1 the power curve demonstrates a repeatable trend which disappears as the frequency increases from 6 Hz onwards and random fluctuations are observed. However, as mentioned earlier this power data is not consistent with the time history of force measurements and is not the time history power data per flapping cycle, it is the real time power recorded from numerous flapping cycles. From all three graphs, it is evident that model 2 requires much more power for all frequencies compared to model 1, but this is unsurprising as this power input result was previously seen in the mechanism only tests. However, with additional mass acting on both

flapping arms model 2 (asym) has a fairly larger power requisite over its symmetrical configuration and this becomes even more evident at higher frequencies.

Graphs D-F in Figure 3.22, display the vertical force, power and frequency data for both models. As observed from previous plots whilst the flapping frequency augments the vertical force and power measurements follow. The force measurements produced for both models are not too far apart, but as an example at 12 Hz flapping frequency model 1 generates the largest force of all the tests and requires much less power. Furthermore, even though model 2 (asym) generates a larger force than its partnering configuration it requires a considerable amount of power at this same frequency. The blue dots in these graphs show a parabolic movement, where vertical force produced parabolically escalates with flapping frequency. Magenta dots present the same relationship, on this instance power input is compared to flapping frequency, and although a linear trend is not observed, the growth in power requisite for increasing flapping frequency is clearly witnessed. Higher vertical force measurements will draw more current from the PSU essentially outputting a larger amount of power, thus as the vertical force produced increases, the power needed grows in relation and this is shown in the results of the green dots. Thus, for a given frequency with the attachment of additional load model 2 will consume more energy compared to model 1 and this same relation was observed from the measurements for the mechanism only.

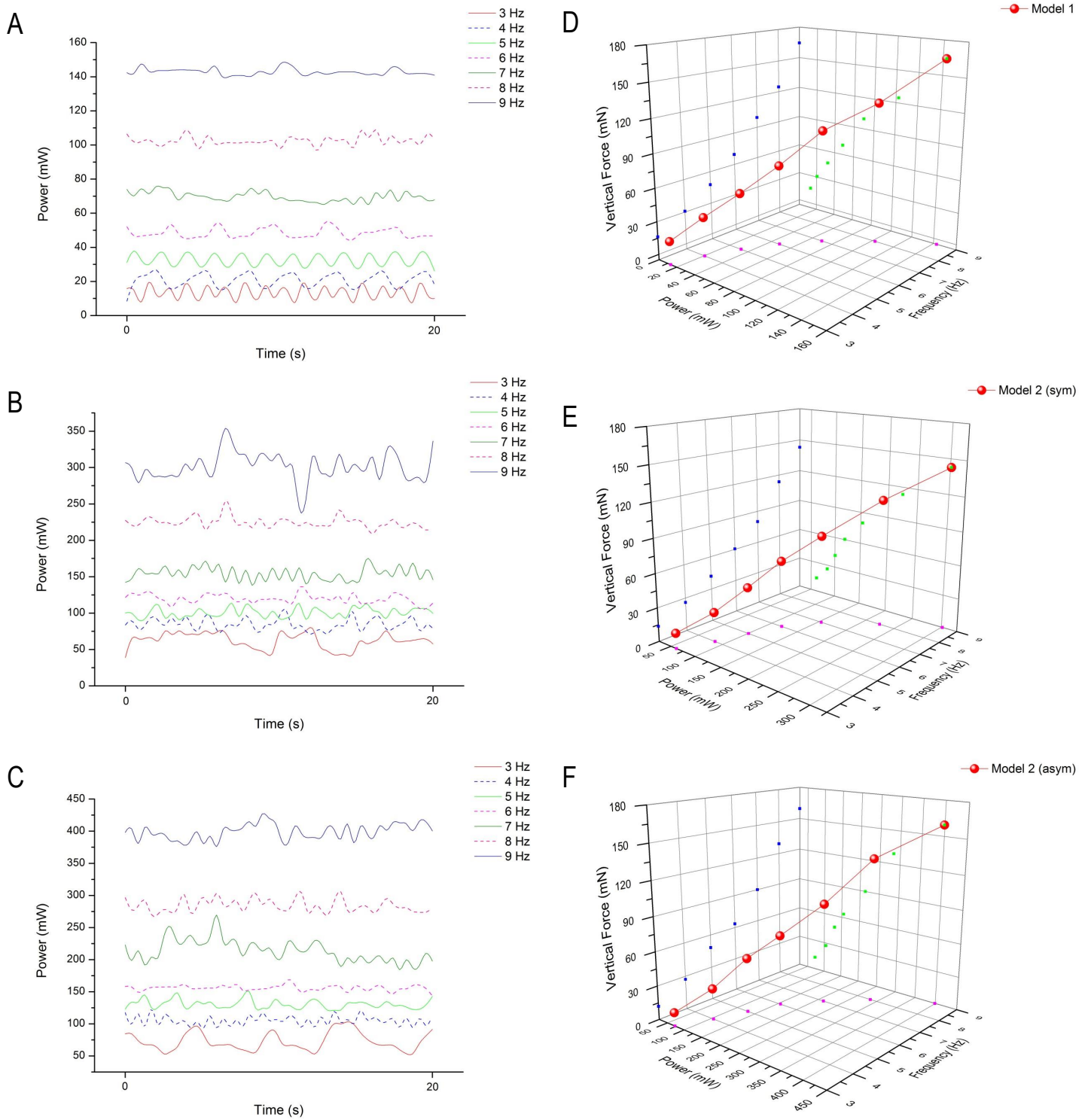


Figure 3.22: Power and Force Measurements of 52 mm Carbon Fibre Bar Flapping; A: Model 1, B: Model 2 (sym), C: Model 2 (asym), D: Model 1, E: Model 2 (sym), F: Model 2 (asym), Coloured Dots in Graphs D,E,F Represent Axes Projections Such as Blue: Frequency Vs Vertical Force, Magenta: Frequency Vs Power, Green: Power Vs Vertical Force

Figure 3.23 A-C, illustrates the time history data of the total vertical force measurements for both models and all frequencies scrutinised in these experiments. All the plots show a smooth and consistent behaviour resembling a sinusoidal wave. This result has a direct relation to the force measurements taken for the mechanism only, and as the same result has been seen again it can be concluded that the mechanical models will continue to perform well with the addition of mass on both sides, this applies to all the configurations tested. Thus, the additional inertial force has not affected the performance of the motion for the flapping arms.

Graph D in Figure 3.23 presents the average peak-peak vertical force measurements for all tests conducted, which clearly shows that the amount of force produced at every frequency is very similar for both models. As mentioned previously the parabolic growth of vertical force production for these tests are very clear. Stack graph E, demonstrates the low power requirement from model 1 opposed to model 2 in both its configurations where the demand in power is greater for asymmetrical flapping mode especially at the higher flapping frequencies. A possible hypothesis for the greater demand in power of asymmetrical flapping mode opposed to symmetrical flapping mode could be due to the tightening of linkages experienced from the additional mass applied on both sides especially when the plunger has been shifted, and the linkages are now slanted from their default position.

Although previous results have shown that the symmetrical flapping mode of model 2 has a greater power input demand to move the mechanism compared to asymmetrical flapping mode, the data in graph E (Figure 3.23), clearly presents a conflicting result. Thus, this result aids in understanding the power requirement of model 2 under asymmetrical flapping mode with the addition of mass, and overall a greater inertial force which will be an important factor when wings are attached to the model, as all wings which are accelerated through a flapping motion will generate inertial forces. In furtherance, this inertial force for a fixed mass will grow with augmenting flapping frequencies.

In comparison to force output and power input model 1 performs very well compared to model 2 and a more or less consistent result is observed with augmenting frequency. For all frequencies tested the size of the values for average power / average vertical force data are very similar, thus although accelerating a fixed mass at escalating frequencies would draw increasing amounts of power as the size of acceleration increases, the output force follows this relation as the acceleration element is the main contributor to the total inertial force produced as the flapping frequency increases. At lower frequencies model 1 does not

require significant amounts of power to actuate the mass at such low speeds, and the mechanism is clearly performing smoothly. This relation is more or less observed for frequencies of 6-9 Hz for model 2 as lower frequencies tend to draw considerable amounts of power, where model 2 in asymmetrical mode is the more power demanding arrangement for this model.

In order to compare experimental results to theoretical calculations the average peak-peak vertical force measurements of model 1 with carbon fibre rods attached, were subtracted from the measurements of model 1 mechanism flapping only. As a result the peak-peak average vertical force produced from the flapping bars only is determined and this can then be compared to theoretical calculations. The equations used are shown in 3.42 and 3.43, where the latter solves for the time dependent acceleration.

The results have been presented in Figure 3.24 C, which clearly presents a good agreement between experimental and theoretical results. The difference between the plots grows as the flapping frequency increases but this is expected as the vibrational forces increase with increasing frequency, and although the aerodynamic forces generated are very small they will grow with increasing frequencies. Nonetheless, the main contribution to the differences is due to the vibrational effects. As the force measurements were taken for the entire model vibrational forces will affect the data measured, but this actually represents realistic situations as these types of models will always experience vibrational forces from all of its moving parts. As the flapping frequency increases the acceleration of the fixed mass also augments thus the inertial force produced will increase as well. Although the data presented for experimental and theoretical results have a good agreement, theoretical calculations are more suited to lower flapping frequencies when considerable vibrational effects are involved, as larger frequencies than those tested here would have even greater differences in both sets of results.

$$F_I = m a = m \frac{\partial^2 L_a}{\partial t^2} \quad (3.42)$$

$$\frac{\partial^2 L_a}{\partial t^2} = L_\Phi \omega^2 \cos(\omega t) \quad (3.43)$$

Graph D in Figure 3.24, presents the power required at each frequency tested in order to flap the carbon fibre bars. The data was determined by subtracting average power recorded for the mechanism and flapping bars from the average power required for driving the mechanism only at each respective actuation frequency.

The power required by the mechanism is much lower than that needed for the mechanism and flapping bars, this becomes extremely evident towards the higher flapping frequencies. The power required for flapping the bars only is quite similar at 3 and 4 Hz because at these frequencies the black (mechanism + bars) and red (mechanism only) lines seem to have a very similar growth rate, which deteriorates as the frequency increases as the differences rapidly augment. An interesting discovery to note here is the growth of the power required for the bars only compared to the mechanism only. As the flapping frequency increases, the amount of energy consumed increases considerably, which confirms that the mass of the wings needs to be kept as low as possible in order to reduce the amount of energy consumed in translating the wings.

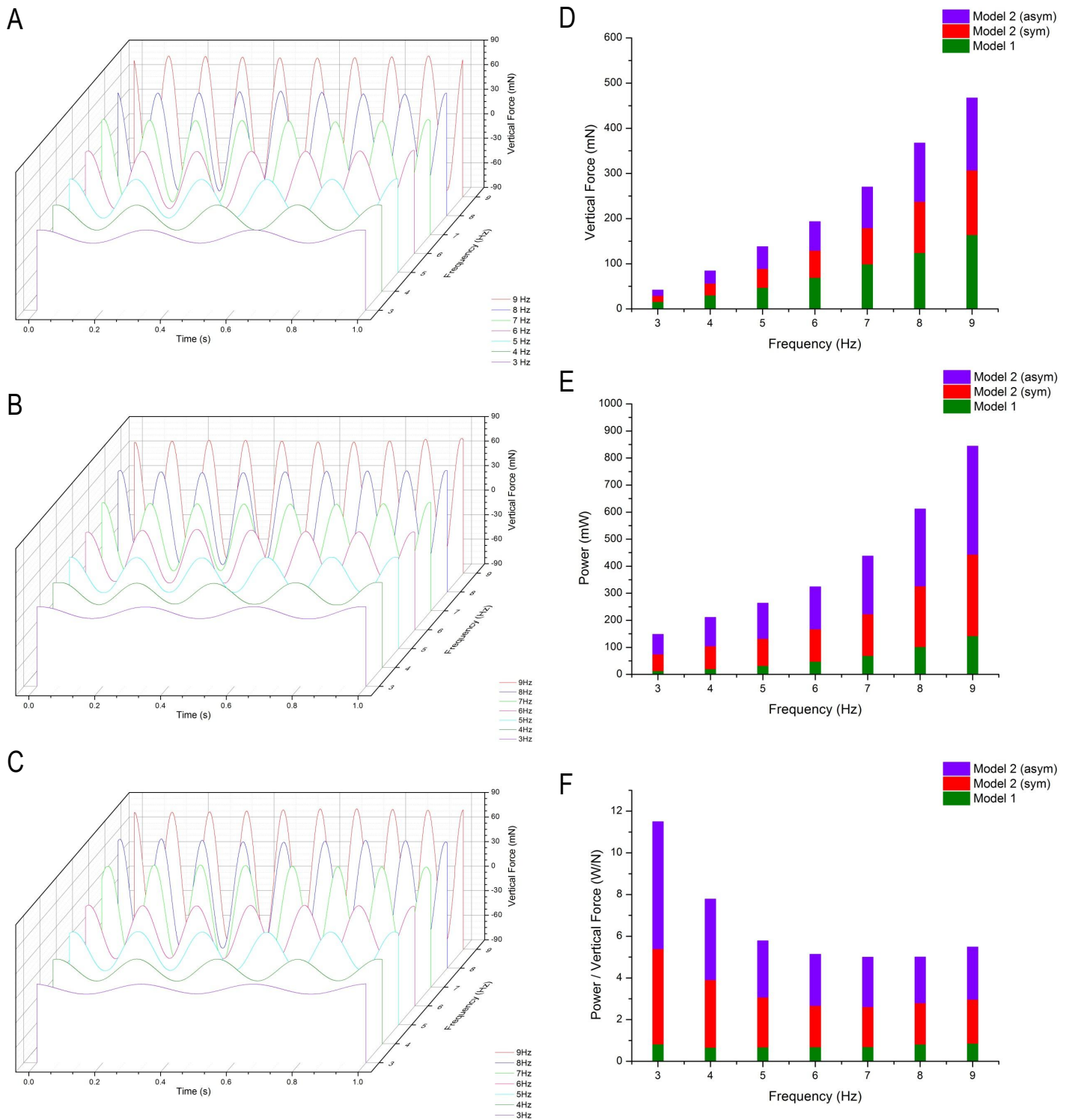


Figure 3.23: Power and Force Measurements of 52 mm Carbon Fibre Bar Flapping; A: Model 1, B: Model 2 (sym), C: Model 2 (asym), D: Average Vertical Force Comparison, E: Average Power Comparison, F: Average Power / Average Vertical Force Comparison

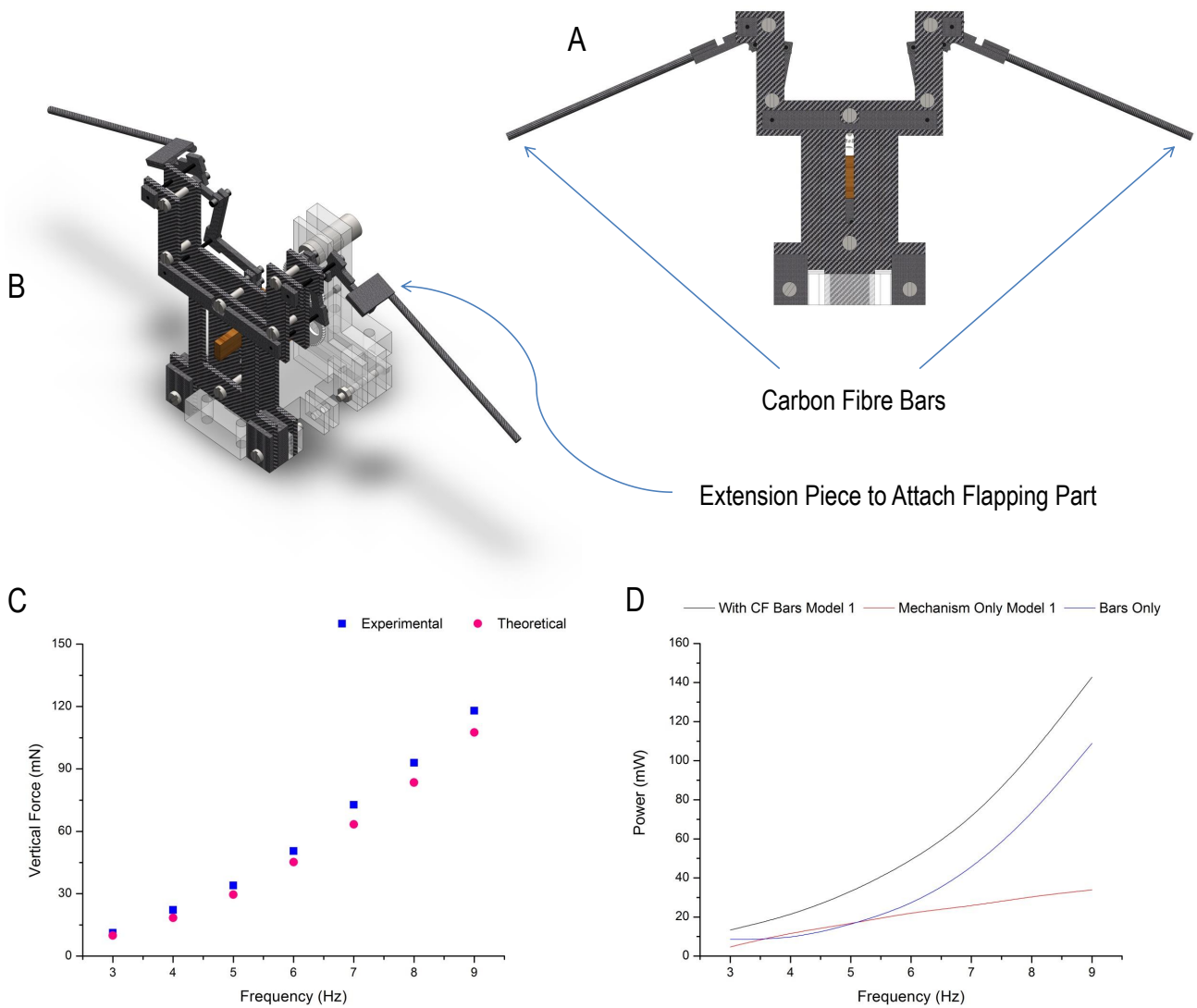


Figure 3.24: CAD Diagrams and Measurements for Model 1 with Carbon Fibre Bars Flapping; A: Front View of Model with Bars, B: Isometric View of Model with Bars, C: Comparison of Experimental Measurements and Theoretical Calculations, D: Power Required to Actuate Carbon Fibre Bars

The experimental results reveal quantitatively the performance of the models and allow the model designer to apply appropriate modifications to improve the mechanical system. Although Model 2 was successful in performing asymmetrical flapping the amount of power drawn is fairly large and specific adjustments must be thoroughly considered in order to improve this model. Nonetheless it should be borne in mind that this model produced successful results with an interchanging flapping mode. Future designs would incorporate a second actuator which would provide a flapping mode change during flight, and this actuator would only be used when flight mode change is required thus only a single actuator will be required to perform the flapping motion and asymmetrical flapping would be possible.

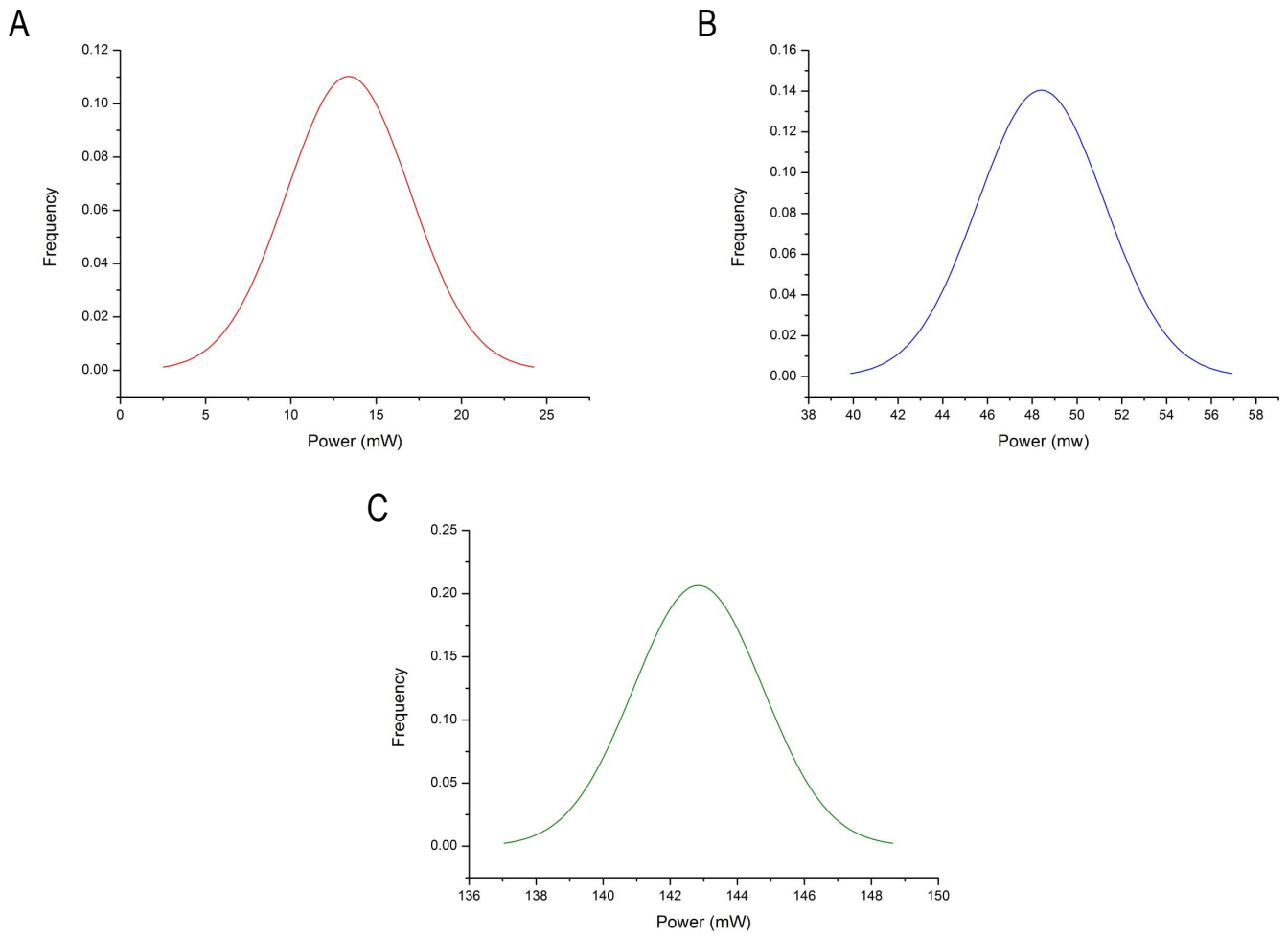


Figure 3.25: Normal Distribution for Power Measurements of Model 1 with 52 mm Carbon Fibre Bars; A: 3 Hz, B: 6 Hz and C: 9 Hz

The normal distribution curves shown in Figure 3.25 display the traditional bell shaped curve for three flapping frequencies for consecutive intervals. The curves peak at the mean value which is also the line of symmetry. The dispersion of the statistical data is to the third standard deviation, in order to ensure the full spread of power drawn is included in this analysis. Majority of the values would lie in the region of one standard deviation of the mean results. Similar to the previous result of mean power shown for the mechanism only, the mean power drawn increases as the flapping frequency increases, see Table 3.5. The standard deviation of 9 Hz has the smallest spread of data collected where majority of the values lie close to the mean of 142.84 mW, a greater spread of data exists for a flapping frequency of 4 Hz where the standard deviation value is noticeably larger.

| <b>Flapping Frequency (Hz)</b> | <b>Mean (mW)</b> | <b>VAR (<math>mW^2</math>)</b> | <b><math>\sigma_{SD}</math> (mW)</b> |
|--------------------------------|------------------|--------------------------------|--------------------------------------|
| 3                              | 13.38            | 13.09                          | 3.618                                |
| 4                              | 20.67            | 16.47                          | 4.06                                 |
| 5                              | 32.55            | 10.49                          | 3.24                                 |
| 6                              | 48.40            | 8.06                           | 2.84                                 |
| 7                              | 69.74            | 8.21                           | 2.86                                 |
| 8                              | 102.55           | 7.35                           | 2.71                                 |
| 9                              | 142.84           | 3.73                           | 1.93                                 |

Table 3.5: *Statistical Power Data for Model 1 with 52 mm Carbon Fibre Bars*

Any future design would adopt the adjustments that are necessary to improve the design, which can only truly be discovered after the rigorous design procedure and experimental evaluations discussed in this chapter. Core improvements would be along the lines of down-sizing the model, reducing the weight of the final model to ensure the lift forces produced are sufficient for the MAV to demonstrate successful flight and the addition of a second actuator to simply alter the position of the vertical slider (plunger) dependent on the type of flight required.

The design and manufacture procedures were discussed in great detail for both models with the concept of the symmetrical/asymmetrical model. A comparison was formed for the physical and CAD linkage system to understand the level of accuracy and differences developed during the several stages from design to manufacture to assembly. Lastly, fundamental experiments were performed on the bare models to determine the force and power measurements without additional mass and aerodynamic surfaces. A comparison between experimental and analytical calculations was performed in which it was found that the two seem to agree well especially for the lower flapping frequencies considered. Tables 3.6 and 3.7, summarise the flapping models and types of wings utilised within this research project. The tests performed on each model and wing have been described to present the type of analysis they have been utilised within. As mentioned within the table, the 26 mm wings (wing types 1 and 2) have been assessed in a preliminary kinematic study to understand the wings motion under passive wing pitching conditions. The system test for maximum power drawn when the models are flapping at 12 Hz without wings has been shown to demonstrate the power requirement differences in model 1 and 2, the full details have been aforementioned within this chapter.

| <b>Flapping Models</b> | <b>Flapping Config.</b> | <b>Actuation Method</b> | <b>Tests Performed</b>                       | <b>System Test Max. Power (mW)</b>             |
|------------------------|-------------------------|-------------------------|--|--|
| <i>Model 1</i>         | <i>Sym.</i>             | <i>Rotary to Linear</i> | <i>Flapping, FR and FRAP with Boundaries</i> | 50.57  |
| <i>Model 2</i>         | <i>Sym. and Asym.</i>   | <i>Rotary to Linear</i> | <i>Flapping and FR</i>                       | 159.00( <i>sym</i> ) and 152.01( <i>asym</i> ) |

Table 3.6: *Summary of Flapping Models*

| <b>Wing Type</b> | <b>Material</b>               | <b>Singular Span (mm)</b> | <b>Analysis</b>               | <b>Tests Performed</b>                       |
|------------------|-------------------------------|---------------------------|-------------------------------|--|
| 1                | <i>Carbon Fibre Only</i>      | 26                        | <i>Kinematic Only</i>         | <i>FR</i>                                    |
| 2                | <i>Carbon Fibre and Mylar</i> | 26                        | <i>Kinematic Only</i>         | <i>FR</i>                                    |
| 3                | <i>Carbon Fibre and Mylar</i> | 47                        | <i>Kinematic and Forces</i>   | <i>Flapping</i>                              |
| 4                | <i>Carbon Fibre and Mylar</i> | 60                        | <i>Kinematic, CFD and F/T</i> | <i>Flapping, FR and FRAP with Boundaries</i> |

Table 3.7: *Summary of Wings Utilised*

## Chapter 4

# Experimental Methodology

This fourth chapter expounds the experimental techniques implemented for this research project by providing details of the equipment utilised and the physical arrangement of the experimental set-up. Details of the force measurement device along with data acquisition software are presented. Various tests were carried out involving both FWMAV models and all wing sizes mentioned in the previous chapter, some details and images will be presented in this section.

### 4.1 Experimental Equipment and Arrangement

The experiments performed in this project required the design, manufacture and assembly of a new experimental rig to suit both FWMAV models and one which was also partially transferable to a vacuum chamber of circumscribed space. Prior to any experimental examinations, both FWMAVs were tested thoroughly for endurance during mechanical motion and consistency of kinematic flapping motion. This is an important step as any inconsistency in the mechanism or slight shift caused by loosening in the linkages can affect the wing motion resulting in inconsistencies/inaccuracies in force measurements during any single test. Both models were tested on numerous occasions for extended periods of time, far beyond the duration required for force measurement recordings. If any small repairs or alterations were required to any of the models, force measurements and kinematic analysis would be carried out and the data acquired would be compared to a

previous test to ensure consistency is maintained throughout the experimental investigation. The same test was also performed numerous times to ensure accuracy in force/torque measurements, voltage measurements for reflective sensors, current and voltage measurements to determine power and images of wing motion.

Many complications were found during the design and experimental stages, where the foundation of these complexities were due to small scale models and components (including wings) leading to small force measurements. Experimental examinations on such small scale (realistic) models flapping at moderate frequencies requires the measurement of forces for the entire model as opposed to directly measuring forces from a single or two large wings, where the sensor can be located at the root of the wing or near enough to this position. Measurements taken directly from the wings consist of far less mechanical vibration contributions to the overall measurements, requiring less severe filtering methods when compared to measurements from an FW-MAV. Experimental research carried out at real size for MAV applications is vital for the growth of research in this field of Engineering, projects which involve the design and experimental analysis of such small devices are usually interdisciplinary involving numerous fields of Science and Technology. The mechanical aspects of both models have been discussed in the previous chapter along with the wing properties and materials.

One of the primary requirements of accurate force/torque measurements is the rigid mounting of the sensor. The experimental rig itself would need to be robust and mounted to an extremely sturdy surface. Considering the aforementioned an Optical (breadboard) table was used as the base of the experimental rig. In addition to providing a firm and equally balanced surface, its breadboard like features provides many advantages such as screwing experimental equipment directly to the table, or to extended mounts custom designed for the Optical table.

In order to map the time history of the measurements and wing kinematics accurately, the data acquisition of both measurements and images must be activated at the same time. This can be achieved by interacting with both the sensor and camera, by providing a common signal via triggering. Also this method is vital when the flapping model is placed in the vacuum chamber as there is no access to the model, further information will be provided in a later stage of this chapter.

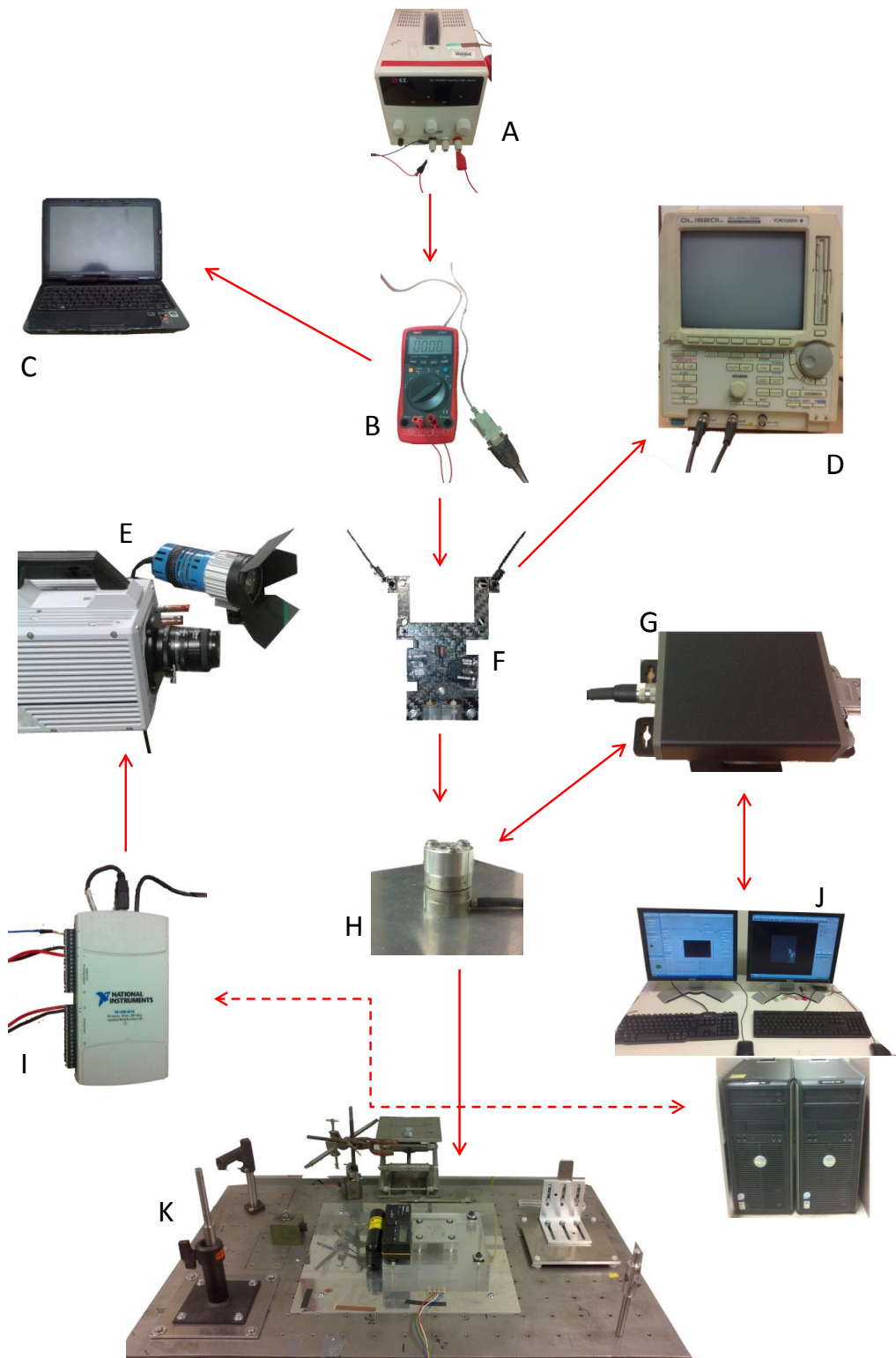


Figure 4.1: *Schematic of Tests in Air*

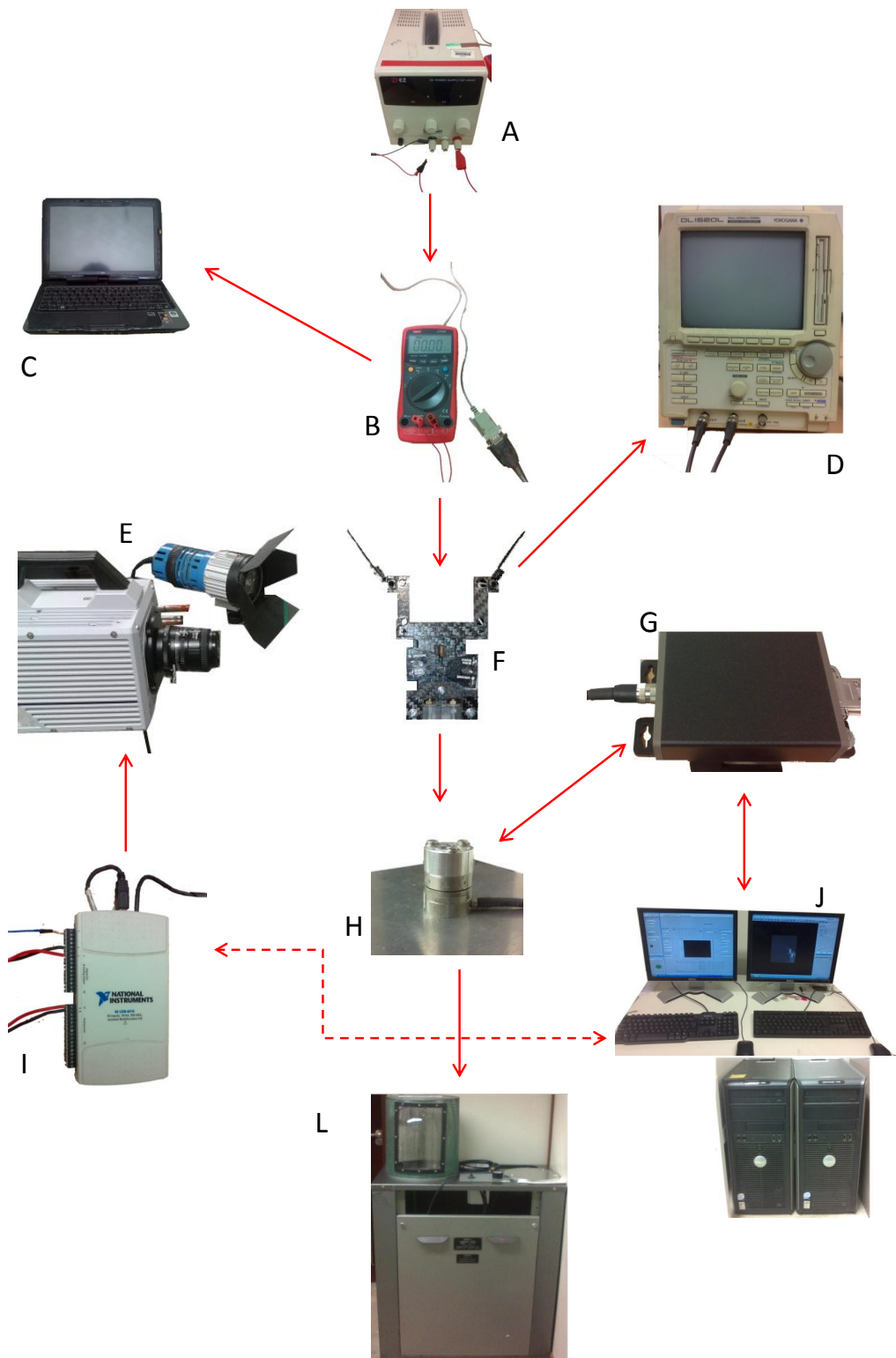


Figure 4.2: *Schematic of Vacuum Chamber Tests*

| <b>Label</b> | <b>Title</b>                             |
|--------------|--|
| <i>A</i>     | <i>Power Supply</i>                      |
| <i>B</i>     | <i>Multimeter</i>                        |
| <i>C</i>     | <i>Laptop / PC</i>                       |
| <i>D</i>     | <i>Oscilloscope</i>                      |
| <i>E</i>     | <i>HS Camera and Light Source</i>        |
| <i>F</i>     | <i>Flapping Model</i>                    |
| <i>G</i>     | <i>Sensor Interface and Power Supply</i> |
| <i>H</i>     | <i>Load Cell / Transducer</i>            |
| <i>I</i>     | <i>NI USB – 6215 I/O Multifunction</i>   |
| <i>J</i>     | <i>PC with DAQ Card</i>                  |
| <i>K</i>     | <i>Optical Table</i>                     |
| <i>L</i>     | <i>Vacuum Chamber</i>                    |

Table 4.1: *Names of The Equipment Shown in Figures 4.1 and 4.2*

The apparatus used for this research project are shown in Figures 4.1 and 4.2. It can be seen from the schematics that majority of the equipment for both tests are the same. Other equipment needed will be shown in the latter sections (via experimental setup diagrams and photographs) and have not been shown in the figures as they are seen as the minute utensils of the experiment. The names of the equipment have been shown in Table 4.1 . The apparatus was tested and examined numerous times to ensure consistency in results for the same experiment.

Majority of the materials, equipment and tools necessary for this experimental work had to be researched and purchased specifically for this project and also have the capability to be utilised in different fields of engineering research for future work. Descriptions of components used and how they functioned with one-another is written below. The components for the experimental set-up and flapping models were manufactured in-house at the university using existing machinery and some specialist tools/accessories such as carbide cutters, reamers, a selection of tweezers, various glues etc. Following the manufacturing process finishing touches (small amendments) are required to some components, especially those related to the flapping models, this is imperative as the parts need to connect accordingly for the models to operate correctly. Holes with large

diameters for linkages can prove to be problematic as the pin (providing the connection between parts) would be too loose when placed in this hole, creating an inclination leading to numerous problems as explained in the previous chapter. Due to the hard and polished surface finish of carbon fibre material, the amount of surface area which is in contact with another part did not pose a problem, and any flaking of the textured material is easily resolved by gently filing down and smoothing the appropriate areas.

A fundamental prerequisite for both flapping models was that they should be able to accomplish hundreds to even thousands of flapping cycles before any maintenance is required. This requirement meant that the designer of such models would need to consider numerous conditions, one of which would be that the parts can be replaced with moderate effort and foreseen failures should be considered during the design stage. Mechanical linkage locking seems to be a common fault with linkage mechanisms, limiters can be placed in appropriate positions to avoid this from occurring. However, any limiting feature should not affect the operation of the flapping model, and should not reduce the smoothness of motion. The designer should also bear in mind that any unnecessary friction would result in a waste of energy from a MAVs power supply.

When assembling the flapping model, the assembler should keep in mind that these parts may need to be dis-assembled due to accidental damage, improvement to a part or an adjustment in the model. Thus, it is vital that appropriate adhesive is used where needed and the correct adhesive dependent on the materials being joint together. Once the correct adhesive is applied the parts which are joined would need adequate time to create a strong bond. Multiple adhesives were needed some of which were cyanoacrylates, plastic weld, 2 part Epoxy, glue for all plastics etc. Using an incorrect adhesive for materials which are not suitable can and most likely will lead to failures in bonds which can cause damage to parts. Thus, it is essential that the correct adhesive is used for each material, and once a strong bond has developed it is tested by applying a force greater than what it would experience when in operation.

During the preliminary stages of empirical research a CCD sensitive camera (CCD sensi-cam) was used for wing kinematic investigations. LabView was used to send a pulse signal to the camera as a triggering process to capture the wing images at various locations in its flapping cycle. The CCD camera was found to be sufficient for all flapping tests, but as it is important to accurately map the wings movement throughout its flapping cycle especially for all wing rotation tests, a HS camera was used as a final choice for all the tests shown in this thesis. Taking many images throughout each cycle provides the entire history of wing movement in much smaller time-steps. The HS Camera used for these experiments was the Photron Fastcam

SA1.1. The camera is capable of capturing thousands of images a second, more precisely ranging from 5400 fps at a resolution of 1024x1024 to 675000 fps at a resolution of 64x16. Also with its on-board memory, the images can be acquired onto the camera and then transferred to the PC reducing the load on the PC CPU during the time of recording images, and BNC connections are provided to connect trigger signals. This camera was more than adequate for this research and proved to be crucial by capturing good quality images at small time-steps. Using such a camera requires a sufficiently powered light source, such as the ARRI PocketPar 125W used in this arrangement. Using a brighter light source in some tests may have been more beneficial, however, this would have also accumulated to the temperatures in the laboratory (especially when focused on the wing of the model) and more importantly affected the condition of the mylar a lot more, causing it to crack which would eventually lead to its failure.

In order to view the entire wing during its cyclic motion sufficient resolutions were selected and various frame rates were used ranging from 2000 fps to 36000 fps. Only one half of the model was viewed by the camera as the wing motion performed by model 1 was symmetric, and to produce good quality images with the light source available during experiments it was best to record a single side. For model 2 both sides had to be viewed by the camera as this model can produce symmetric and asymmetric wing motions. Although more light (from a greater power light source) would have been beneficial to attain better quality images (as a much larger resolution was being recorded), the data needed from the images could be extracted effortlessly and the presentation of the images is more than satisfactory. For a short period during the experiments, a second light source was available which was utilised for asymmetric experiments. This was needed as reflecting the single light source off the mirror was not producing images of acceptable quality. Example images have been shown in Figure 6.28 to provide an insight on the quality and detail needed from the images.

For a brief period an Arri L7-C Colour LED light source was tested to see if this will deliver enough intensity and help produce the same quality of images as was achieved using the PocketPAR 125W, but it was found that the intensity from this light was far too low (even when fully focused on the wing section) for these experiments and the variation of colour temperatures (2700 K-10000 K which can be selected from the cameras on-board control system) did not show the benefit expected. On the other hand due to the lights low intensity it did show a very admirable feature which was its extremely low temperature output, this will prove to be a major advantage for some scientific experiments. For the experimental tasks in this

project low temperature would be beneficial, but a few more Arri L7-C's would be needed to provide enough intensity. From the photometric data shown in Table 4.2, we can clearly see there are significant differences between the illuminance values of both light devices, thus the Arri PocketPAR 125W is better suited for these experiments to allow for a choice of a sufficient shutter speed setting for the camera. Furthermore, the PocketPAR is much smaller in physical size, proving to be easier to work around, re-position effortlessly and occupies less space on the optical table to allow for further fixtures to be added to the table if needed. The barn door fixture installed on the Arri Lamp was set in a wide open configuration during the experiment as the light did not need to focus on a specific spot, rather the region in which the wing travelled through.

| Arri Device          | Colour Temp (K) | Flood-3m (lx) | Middle-3m (lx) | Spot-3m (lx) | Flood-5m (lx) | Middle-5m (lx) | Spot-5m (lx) |
|----------------------|-----------------|---------------|----------------|--------------|---------------|----------------|--------------|
| <i>PocketPAR125W</i> | 5600 – 6000     | 1200 – 5000   | 6500 – 17000   | 32000        | 430 – 1800    | 2350 – 6100    | 11500        |
| <i>L7 – CLED</i>     | 5600 – 6000     | 754           | 1774           | 5742         | 271           | 639            | 2067         |

Table 4.2: *Arri Light Illuminance Data*

Single channel power supply units (PSUs) were used in these experiments to power the DC motor, reflective sensors and Schmitt trigger circuits. The PSUs could provide an output of 0-30V maximum and a current of 0-3A. These units were sufficient for the power needed for the circuitry mentioned, and tested numerous times to ensure the voltage and current output was reading correctly on the digital display. To attain a better accuracy of voltage and current readings, multimeters were used which provided readings up to 3 decimal places (deemed as acceptable accuracy for this project). The multimeter was also tested for reading accuracy numerous times by comparing measurements to other multimeters. And as mentioned previously the same tests were carried out multiple times to ensure accuracy in all data measurements. The voltage values set for flapping wing frequencies had to be repeatable in order to carry out further tests in different arrangements and wings etc. Thus, a multimeter was used to measure the exact voltage value once a desired frequency was set and thereafter this method was continuously used in order to obtain a precise frequency efficiently.

The multimeter was used to record real-time current values during the tests, the multimeter read the data and this was transferred to the laptop which was used to record all the current data. This meant that we could obtain the power required during each test accurately and also study the variations in power. Unfortunately

the current was not recorded at the same sampling frequency as all other measurements as the equipment to accomplish this was not available for this experiment. However, as the current was recorded in real-time per test and F/T measurements showed periodic consistency, this displays that the current drawn can be averaged to determine the amount required per cycle. From the average current value and set voltage, the average power drawn by the complete system can be determined. Although the reader should keep in mind that current plots normally show a volatile behaviour illustrated via the continuous fluctuations which can be seen in some of the recorded measurements (these have been shown in chapter 3).

A small DC pager motor was used as an actuation device to drive the gearbox subsequently creating a flapping motion via linkages. The motor had a mass of 2.78 grams which is fairly high for MAV applications but as this was a stationary experimental rig it seemed feasible to perform tests with this and due to its small dimensional size a realistic choice for future concept designs. Furthermore a motor of half this mass can be sought after in future from specialist companies such as Maxon motors and Faulhaber. The motor has a resistance winding of 3.3 ohms, with body and shaft dimensions of 7 mm x 17 mm and 1 mm x 3 mm respectively. The same type of motor was used for both models and for all experiments so power measurements can be compared. The motors were powered directly by the mains DC power supply and measurement properties recorded as explained previously.

The F/T sensor is placed directly under the flapping model to feel all the effects of the flapping model and measure this in six components. A highly sensitive sensor was chosen for this application as the measurements obtained would be fairly small from the planned experiments. The sensor was powered via an interface power supply which drew its power directly from the DAQ card located in the PC. The power cable connected to the DAQ card provides 5V to the interface PSU and also transmits the signals read from the F/T sensor to the DAQ card. The cable is specially designed at NI and slightly modified by ATI (manufacturers of the F/T sensor) to connect to the interface PSU and utilise specific channels required for reading strain gage voltages from the transducer (these voltage readings are amplified and conditioned in order to be read by the DAQ card). The IFPS acts as a power source as well as a data collector and transmitter, for which the interface is specifically designed for the transducer used. From the interface devices available to operate with this sensor the DAQ option proved to be the more suited apparatus for this project, for reasons such as its high sampling rate of 250kHz (41.6kHz per channel), filtering availability, most accurate synchronisation and sufficient control via LabView software. The DAQ card which was purchased with this transducer package

was designed by NI to operate with the cable provided.

The multifunction NI device was used for receiving, transmitting and acquiring signals. This device has digital and analog I/O capabilities with multiple channels as well as high data acquisition rates of 250,000 samples per second. The reflective sensors would continuously pass signals to the NI MF device which would then communicate with the PC and instructed by the software for its next commands. The signal is what triggers the start of data recordings, this wave produced from the reflective sensors is also passed to the NI box which is recorded by the software simultaneously. Thus all data measurements and images are acquired in real-time, and is done so concurrently.



Figure 4.3: *Vacuum Chamber*

The vacuum chamber had a bell jar dome to enclose the vacuumed area, which then had to be covered by the metallic perforated guard due to extremely dangerous conditions created when the glass bell jar is in approximately 99.5% vacuum condition. Oil fumes exhausted from the pump contained within the lower section of the vacuum machine had to be let out of the enclosed laboratory, which was done so by feeding the hose pipe out of the lab and into an open area. In order to allow optical access into the chamber when in vacuum condition Lexan was used to create a window for the camera to view the wing motion. “Lexan Polycarbonate is characterised by its excellent mechanical behaviour, maintaining high strength and stiffness when exposed to elevated temperatures over a long period of time. Lexan Polycarbonate sheet is one of the toughest, transparent thermoplastic materials and can withstand impact from all kinds of objects, from stones to hammers without shattering. Its proven energy absorbing characteristics are maintained at

sub-zero winter temperatures to high summer temperatures. Polycarbonate sheet has 250 times the impact strength of glass and so gives greater protection” (PAR-Group). The chamber needed 3 electrical feeds for the transducer, reflective sensors and motor. The same configurations which were used in open air experiments were maintained in vacuum chamber tests to uphold accuracy within the experiments. When placing the chamber in vacuum condition checks were continually made to ensure that no small pieces from the model have fallen off and the rubber seal (placed around the vacuum dome) is placed down onto a clean base to avoid any leakages and maintain safe experimental conditions. An enlarged image of the vacuum machine is shown in Figure 4.3. Ideally a very high vacuum level is required for vacuum chamber tests to acknowledge that any effect from the medium is minimal and minute force contributions can be deemed negligible. The vacuum gauge was monitored during tests to ensure a high vacuum level was maintained.

The experimental arrangement for tests in air can be seen in Figures 4.4 to 4.5. Both diagrams show the primary setup for acquiring force measurements from the flapping model. In Figure 4.4, the part labelled 'Optics Base' is bolted to the Optical table and is the connection for the experimental base and Optics table. The experimental base can also be extended by adding an attachment and securing it to the extension slot pre-made in the design, this would secure an attachment part to the experimental base. It was designed as an additional accessory to mount a digital inclinometer in line with the base of the flapping model to directly measure and accurately pitch the body of the model(s). The transducer is directly mounted to the sensor base via the threaded holes located on the sensor.

From the side view image of the setup (Figure 4.5), the body inclination pivot point (located on the hinge connected to the flapping model base) can be seen, this would allow measurements to be taken at a range of inclination angles from 0 to 90 degrees. When the body is pitched its vital that the angle is measured precisely, which was accomplished by the digital inclinometer. However, if experiments were performed at say 45 degrees body pitch angle a sufficient mirror setup would be needed which would require a larger optics table, numerous mirrors and lasers in order for the camera to view the wing motion accurately. Or a simpler method would be to use a sturdy tripod with the capability of pitching the camera to the same angle as the body, unfortunately this was not available during the experimental period. The sting is the direct connection from the flapping model to the sensor. It is extremely vital that the flapping model is rigidly mounted to the sensor to avoid any additional vibrational forces contributing to the already present mechanical vibrations from moving parts of the flapping model. A stiff mounting was always ensured and

checks were continually carried out through the experimental period. Thus, all connections from the flapping model to the transducer needed to be very tight and secure. The sting attaches onto the transducer via a top cylindrical base which is secured by the threaded holes located on the top of the transducer similar to the bottom half the transducer. Table 4.3, shows a list of the materials used for the parts labelled in Figures 4.4 to 4.5.

| <b>Part Name</b>              | <b>Material</b>  |
|-------------------------------|------------------|
| <i>Optics Base</i>            | <i>Aluminium</i> |
| <i>Exp Base</i>               | <i>Acrylic</i>   |
| <i>Sensor Base</i>            | <i>Aluminium</i> |
| <i>Flapping ModelBase</i>     | <i>Acrylic</i>   |
| <i>Sting</i>                  | <i>Aluminium</i> |
| <i>Body Inclination Hinge</i> | <i>Acrylic</i>   |
| <i>Sting Secure</i>           | <i>Aluminium</i> |

Table 4.3: *Materials Used in The 0 degree Inclination Experimental Setup Shown in Figures 4.4 and 4.5*

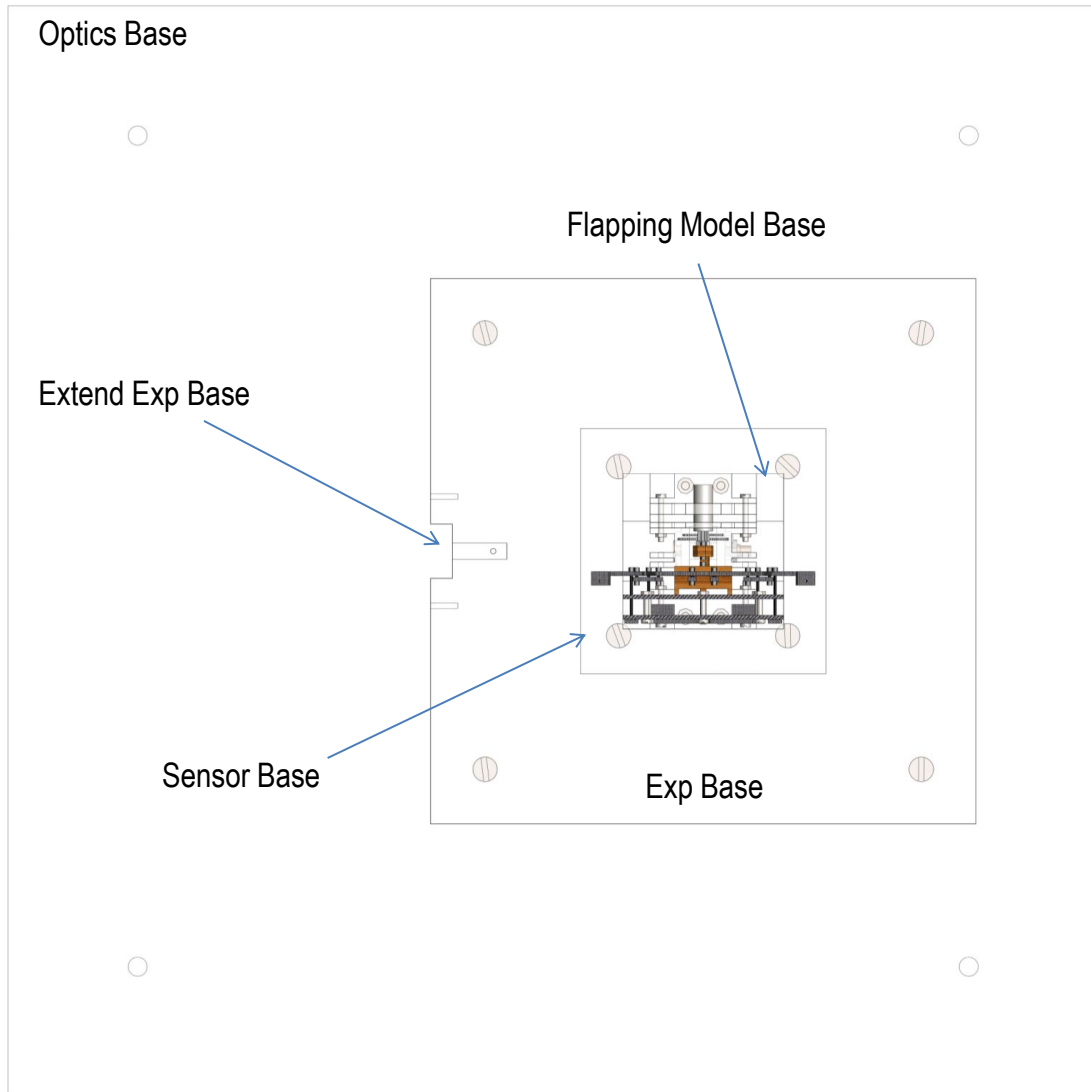


Figure 4.4: *Experimental Setup Top View*

The software shown in Figure 4.20 was used to acquire voltage measurements from the F/T sensor and reflective object sensor. The reflective object sensor creates a signal when it is exposed to a 'shiny' substance or when the beam is cut. This signal is used as a trigger method to activate both the camera and F/T sensor to start recording. The high speed camera requires its own software to view the images, but the triggering is controlled using NI equipment and the VI software created on LabView. The real-time measurements for both can be viewed in the software during experiments, but the measurements observed are the raw voltage measurements which require a conversion into F/T readings using the calibration matrix specifically for this sensor and thereafter appropriate filtering is necessary.

ATI also provided a LabView VI software which directly outputs the F/T measurements. This software was edited to allow for triggering and capture the reflective object sensor signal all simultaneously, a screen shot of this software has been shown in Figure 4.21. Either of the aforementioned softwares can be used for data acquisition where both would in effect have the same outcome. However, to reduce the unnecessary computational loading during real-time data recordings it would be best to use the voltage software and apply conversions in a separate software, once real-time data recordings are complete.

The software proves to be an integral part of the experimental arrangement, it controls some of the experimental equipment and acquires measurement data. As LabView is an open-source software where the user can freely edit and develop existing softwares to each projects specific requirements it demonstrates colossal benefits for experimental researchers. The DAQ card and multi-function devices are also designed to work well with LabView as they are all manufactured by National Instruments.

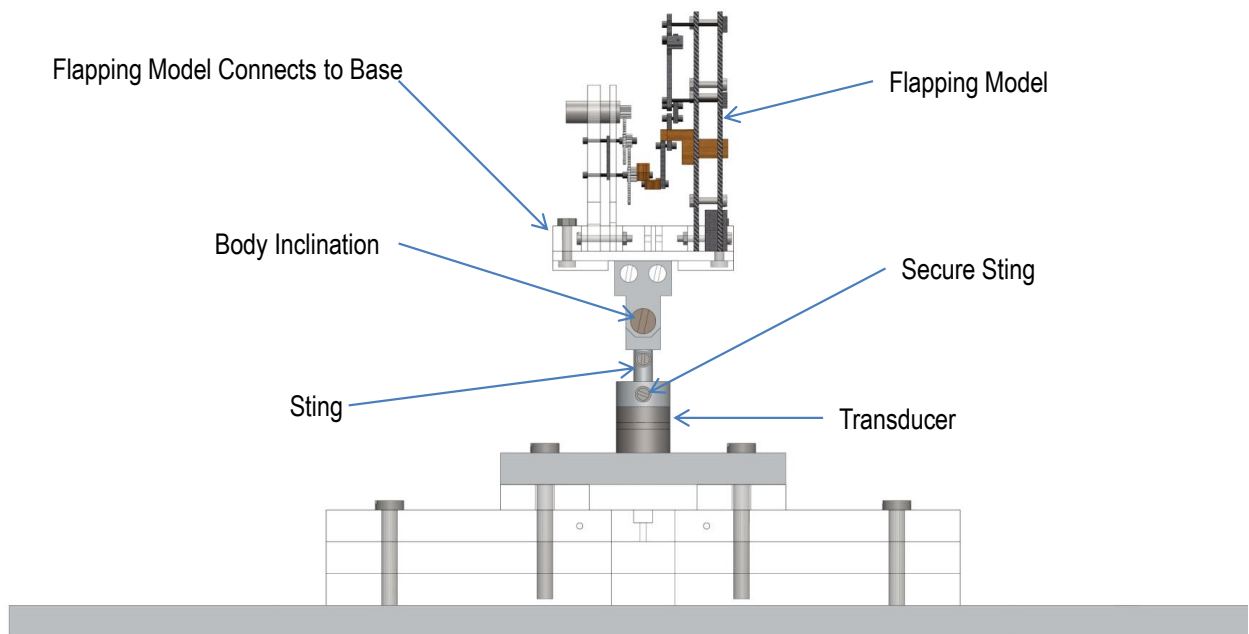


Figure 4.5: *Experimental Setup Side View*

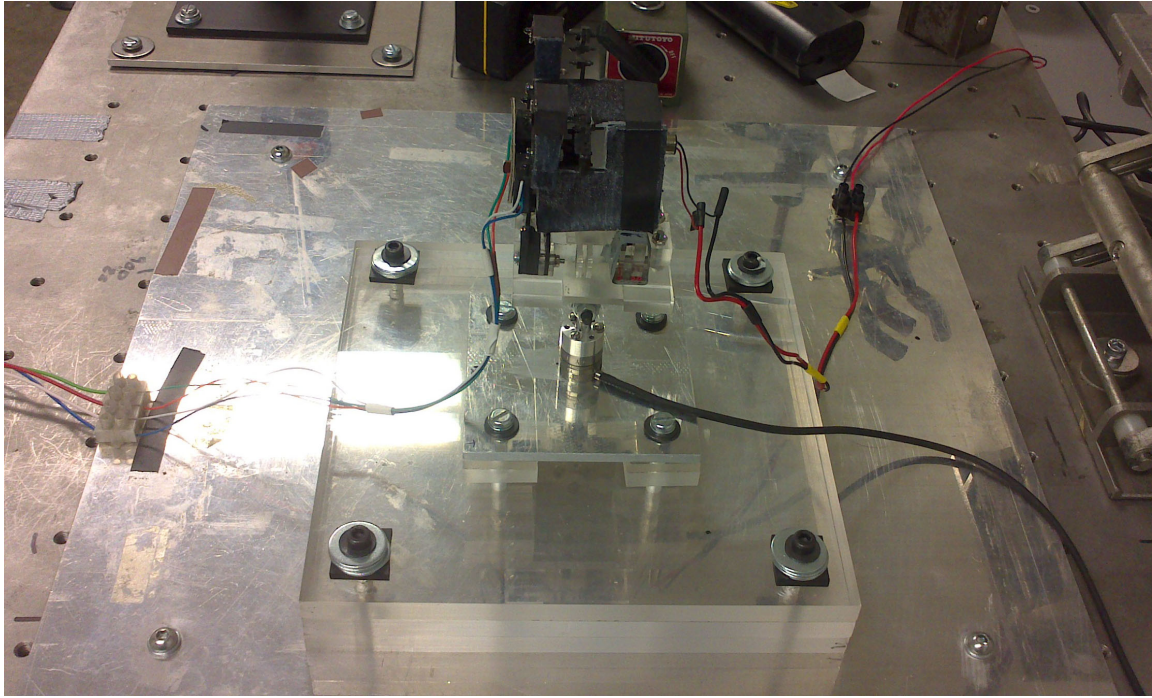


Figure 4.6: *Photograph of 0 Degree Inclination Setup Side View*

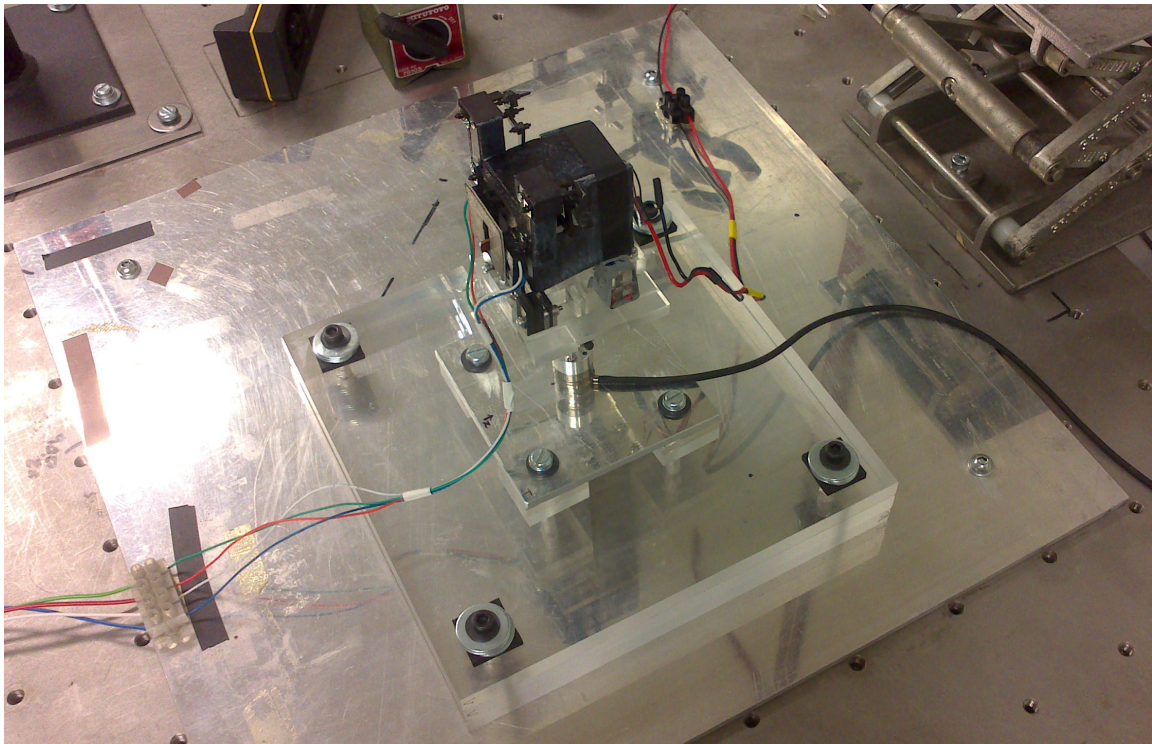


Figure 4.7: *Photograph of 0 Degree Inclination Setup Angled View*

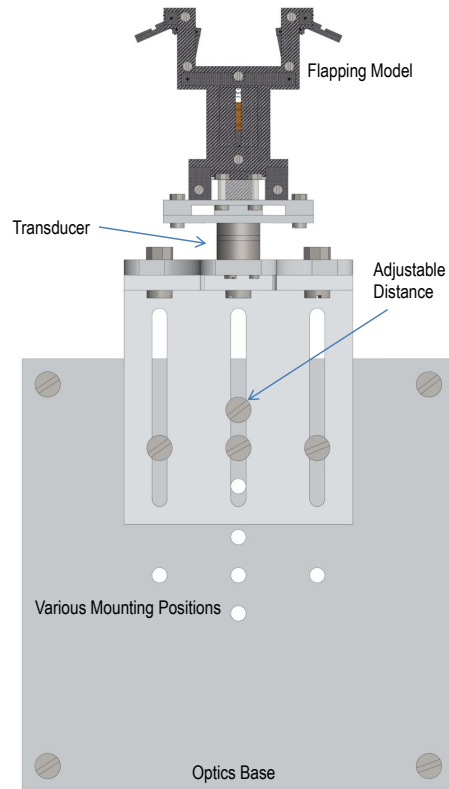


Figure 4.8: *Hovering Experimental Setup Top View*

The 90 degree body inclination (hovering position) experimental setup has been shown in Figures 4.8 and 4.9. All base, bracket and extensions are constructed from Aluminium for this setup. The position of the right angle bracket can be varied and the height at which the model is placed from ground level can also be adjusted. The variable positioning proved to be very helpful when setting up boundary experiments and to ensure the model is in good view of the camera by slightly adjusting its height prior to any experiments undertaken on this setup.

The F/T sensor is now placed directly under the model which seems to look like its in a compressed position (between the top and bottom transducer mounts). This configuration would decrease the level of mechanical vibrations accumulated between the force/torque producing locations and the sensor. As a result, the transducer would experience less mechanical vibrations, opposed to using the sting configuration shown in the 0 deg setup and rotating the body of the model to create an angle greater than zero degrees. Both 0

degree and 90 degrees experimental configurations produce accurate F/T measurements, an advantage of the hovering setup is that the level of mechanical vibrations are reduced as the distance between the flapping model and transducer is reduced. As always all components need to be stringent and joints via screws need

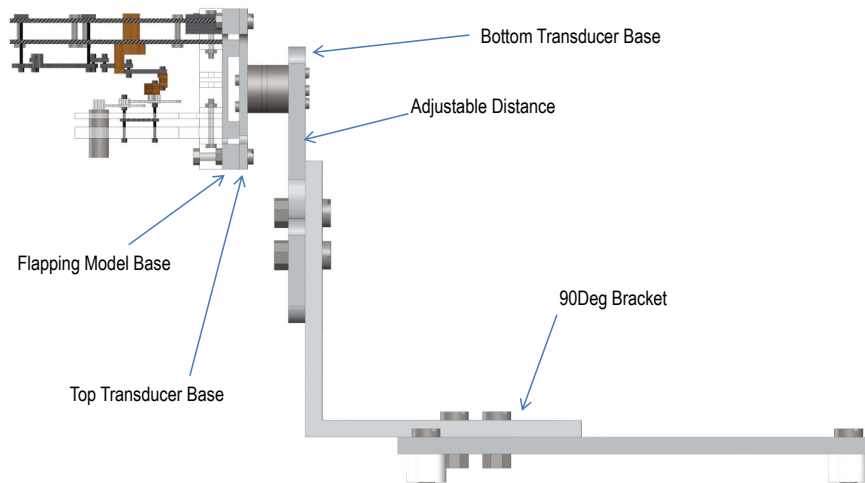


Figure 4.9: *Hovering Experimental Setup Side View*

to be very tight to ensure experiments are performed on a rigid setup to augment accuracy in results. The optics base for the hovering setup will mount directly onto the optics table, all other parts are secured via nuts and bolts as shown in the experimental diagrams (Figures 4.8 and 4.9). Isometric diagrams have been shown in Figures 4.10 and 4.11 of the two experimental configurations mentioned above. The reflective sensors have not been shown in the setup diagrams as their position on the flapping model had to be slightly varied when positioning the emitter and collector devices. But the beam which was cut was always located at either max or min stroke angle position, where the maximum flapping angle would be produced when the linear heaving part was at maximum position and minimum flapping angle would be produced when the heaving part was at its minimum position. The position of the reflective sensors can be seen on the photograph of the experimental setup shown in Figure 4.12, additional pictures have been shown in the appendix. Any wiring or connectors linked to the flapping model setup had to be taped down to a base or the optics table to guarantee that no additional forces are produced from the movement of these wires which would add to the forces experienced by the highly sensitive sensor during tests. In all setups the flapping model had to be kept well above the ground to assure there is no fluid-wall interaction which would affect the results.

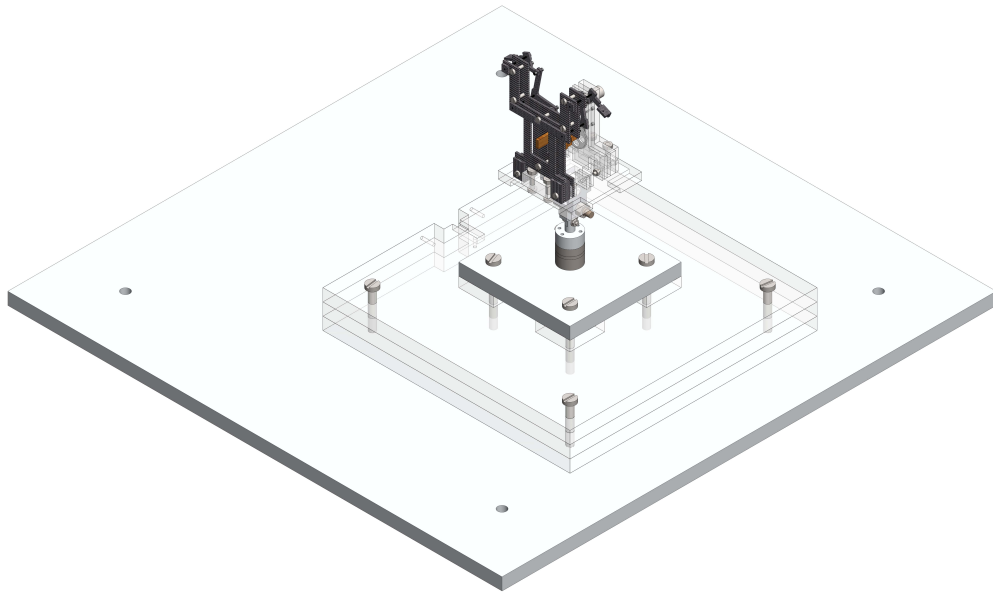


Figure 4.10: *CAD of 0 Degree Inclination Setup Iso View*

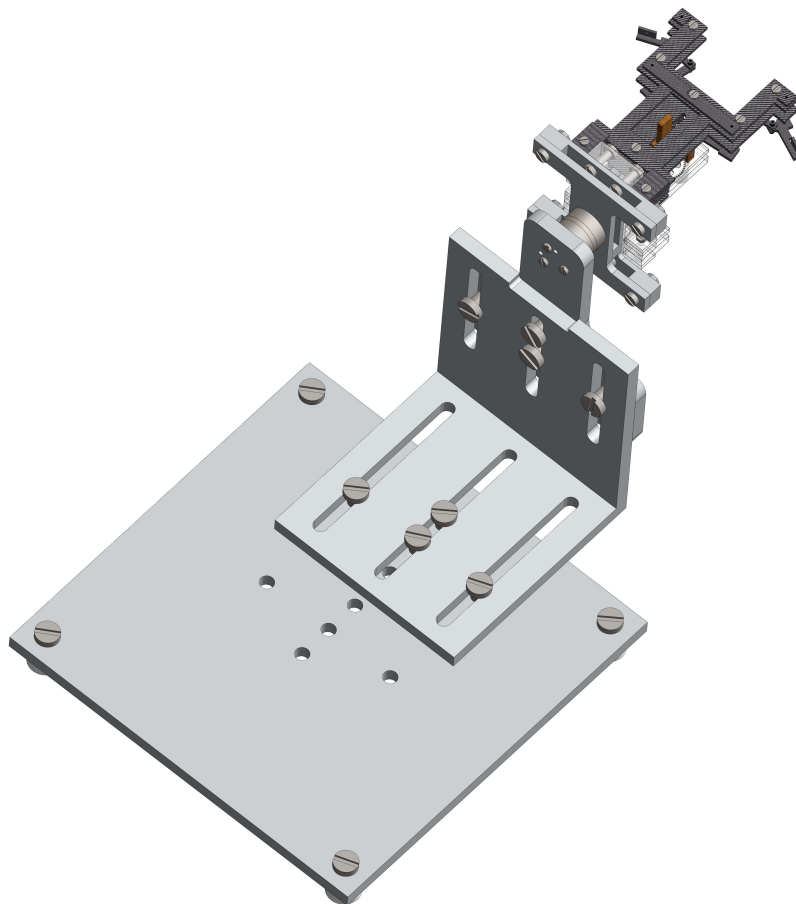


Figure 4.11: *CAD of 90 Degree Inclination Setup Iso View*

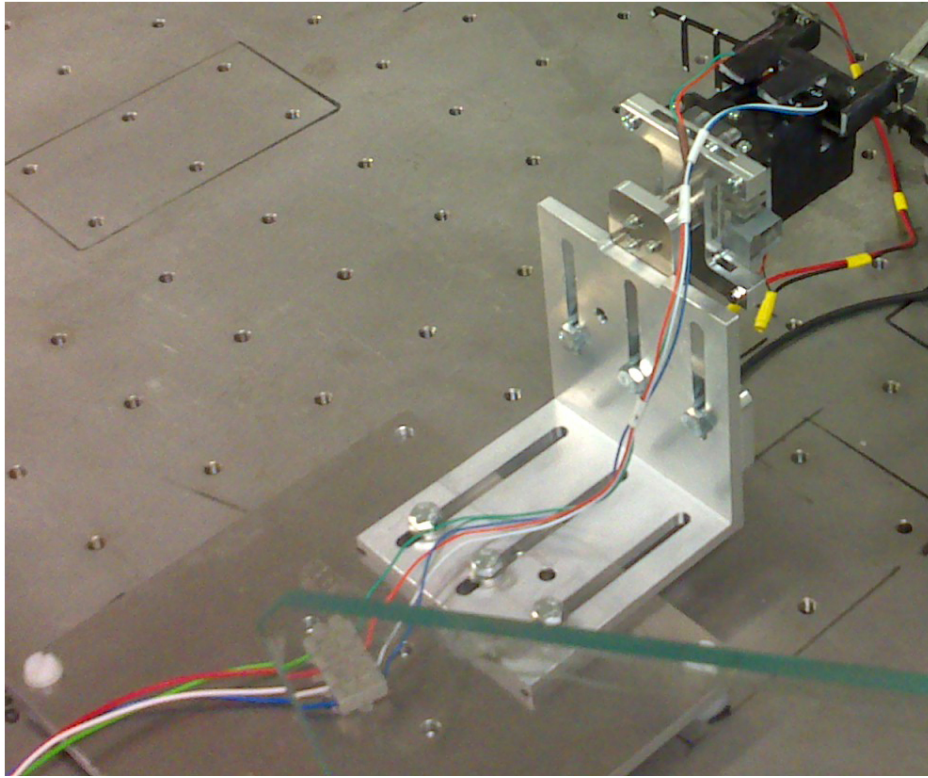


Figure 4.12: *Photograph of 90 Degree Inclination Setup*

The signal output from the reflective object sensor (shown in Figure 4.22) does not require any filtering, a TTL pulse is produced representing the activity of the beam from this sensor. Once the beam is cut/blocked a rising signal is produced (ending the low-time duration), this signal triggers the acquisition of the F/T measurements, reflective object beam measurements and images. The signal was viewed on the oscilloscope (shown in Figure 4.23) to determine the flapping frequency of the model and examine electrical noise amplitudes which would corrupt the signal from the sensors. The photographs show the exact same wave which is recorded by the DAQ device and used as an effective triggering technique. In Figure 4.23, the photo on the right has a larger time per grid division (spacing), thus the wave observed seems to be at a higher frequency when its actually at a very similar frequency to its neighbouring image.

The same configurations which were used in air had to be used in the vacuum chamber as well, this would maintain consistency. Some of the parts used had to be reduced in size and altered as the vacuum chamber had limited space and various pieces of equipment and wiring had to be enclosed in the glass dome. During vacuum tests once the air was extracted and a vacuum of 99.5% was achieved, the conditions were then held using the controls on the vacuum machine which blocked the port exiting the air from the chamber and the pump was turned off. It was necessary to turn the pump off due to the vibrations it created during operation. All wiring within the dome had to be kept clear of the wings and the parts which are connected from the flapping model to the sensor, this would assure accuracy of force/torque measurements. The 0 degree and 90 degrees experimental arrangements in the vacuum chamber have been shown in Figures 4.13 to 4.18. Figures 4.13 and 4.15, show a birds eye view of the vacuum chamber setup which displays the layout of the electrical feeds required for the experiment.

All parts were fitted to the primary base which had clearance holes for all electrical feeds, and is firmly mounted to the vacuum machine, a necessary requirement to ensure no vibrations affect the F/T measurements. A smaller transducer base was used in this setup as opposed to the arrangement used in air, this base served as a base for the right angle bracket in hovering experiments. As seen in the diagram, the transducer for hovering experiments in the vacuum chamber is in the same position as it was for hovering tests in the air, shown in Figures 4.8 and 4.9. The same parts were used in the vertical (0 degree) flapping experiments in the vacuum chamber as shown in Figure 4.5 except for the base. It is immensely important that the same setup is used when making comparisons between air and vacuum chamber experiments as the results may have small differences and they should be due to the influence of the fluid and not the components used in the experiments, this applies to all experiments conducted which require such comparability's. Overall any change of the experimental components should not affect the results and in this case need to provide a rigid platform for mounting the transducer. Due to space limitations a smaller 90 degree bracket was used in the hovering vacuum chamber setup as illustrated in Figure 4.16, however this would have no effect at all on the results obtained during tests as the purpose of this part is to provide a solid foundation for the transducer which it exceedingly fulfills. Isometric diagrams of both vacuum chamber setups have been shown in Figures 4.17 and 4.18, this provides a complete view of the core vacuum chamber arrangements.

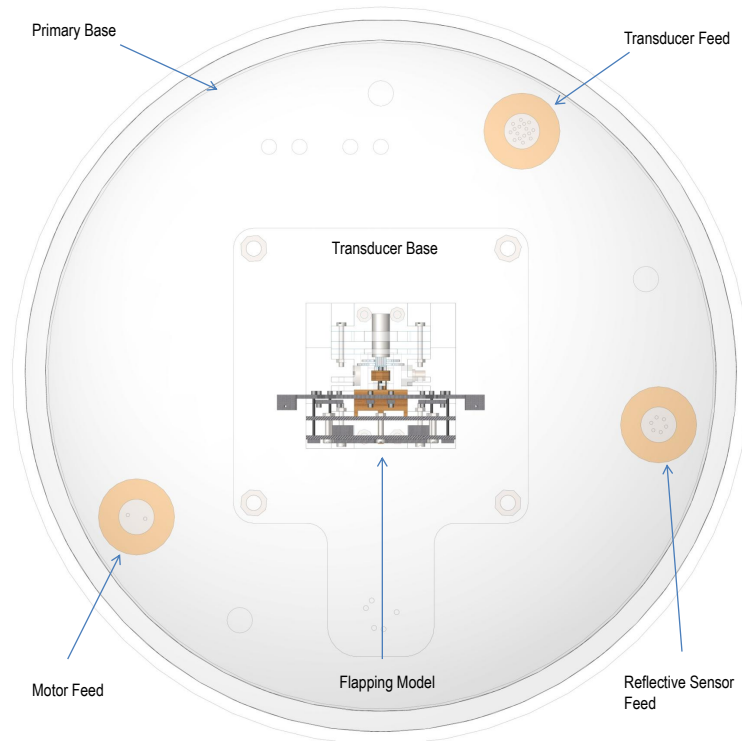


Figure 4.13: *CAD of 0 Degree Inclination Vacuum Chamber Setup Top View*

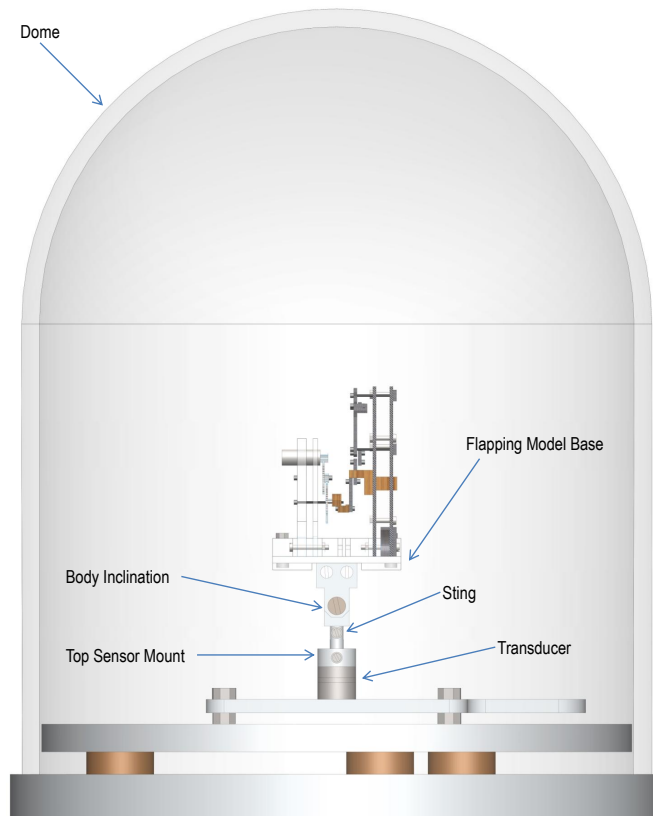


Figure 4.14: *CAD of 0 Degree Inclination Vacuum Chamber Setup Side View*

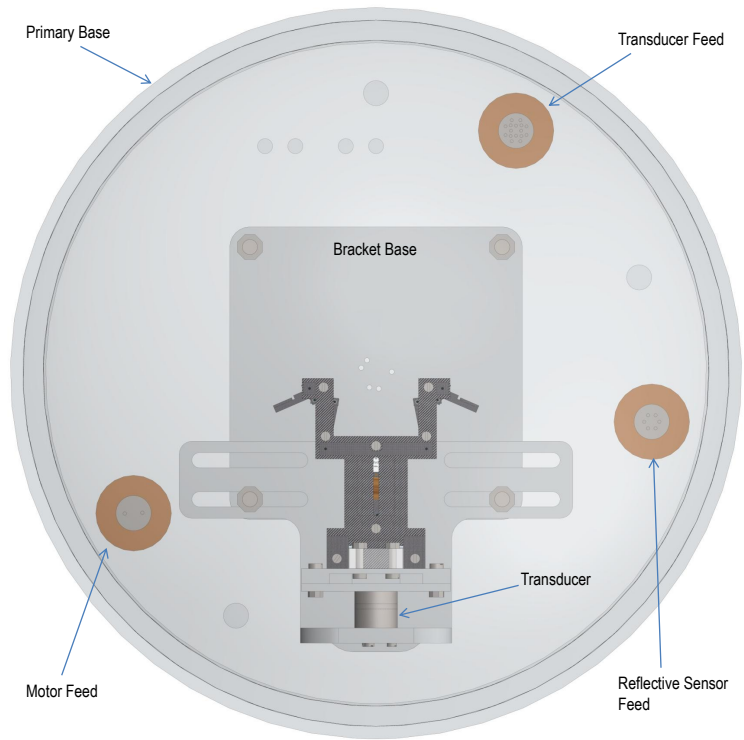


Figure 4.15: CAD of 90 Degree Inclination Vacuum Chamber Setup Top View

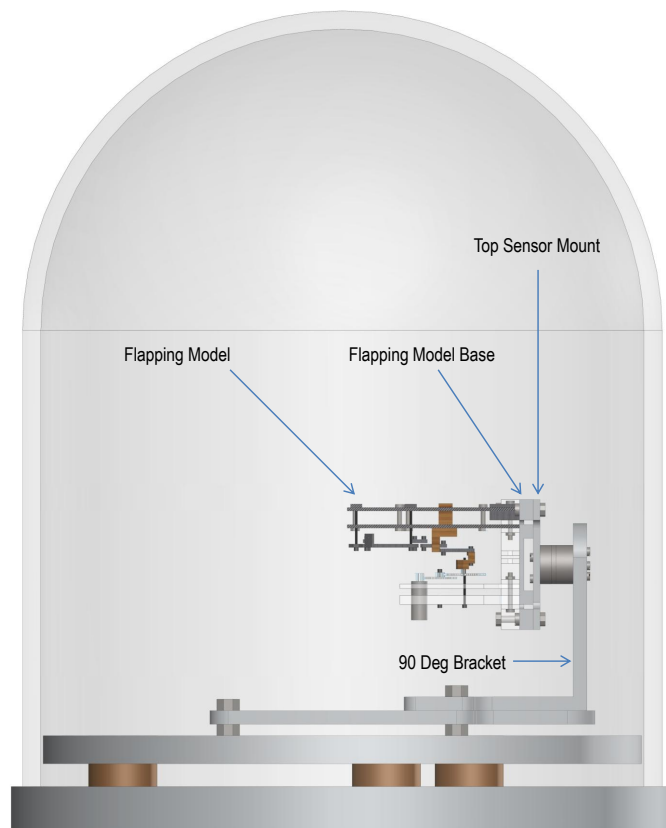


Figure 4.16: CAD of 90 Degree Inclination Vacuum Chamber Setup Side View

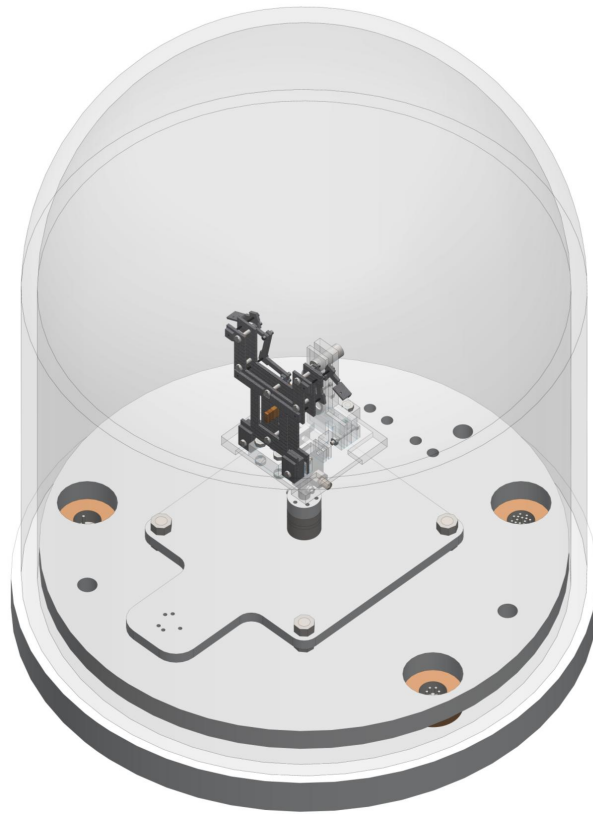


Figure 4.17: *CAD of 0 Degree Inclination Vacuum Chamber Setup Iso View*

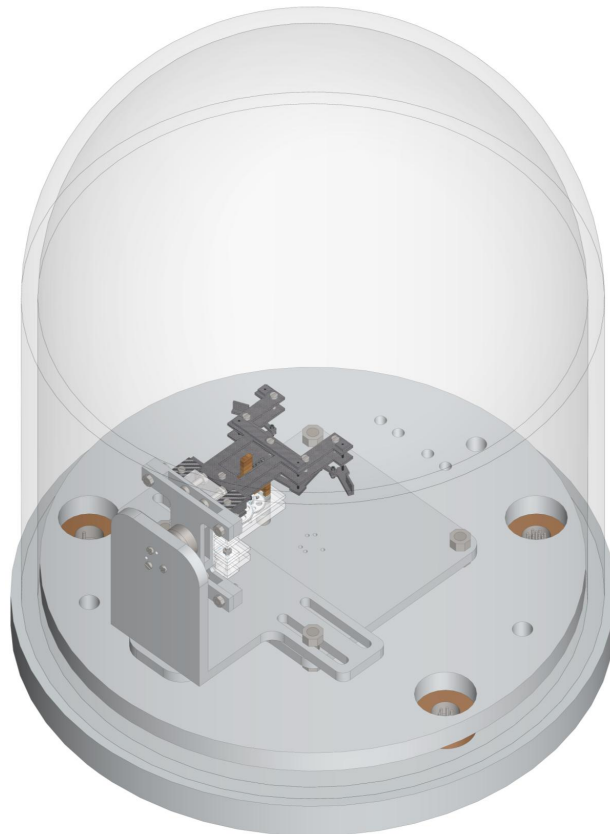


Figure 4.18: *CAD of 90 Degree Inclination Vacuum Chamber Setup Iso View*

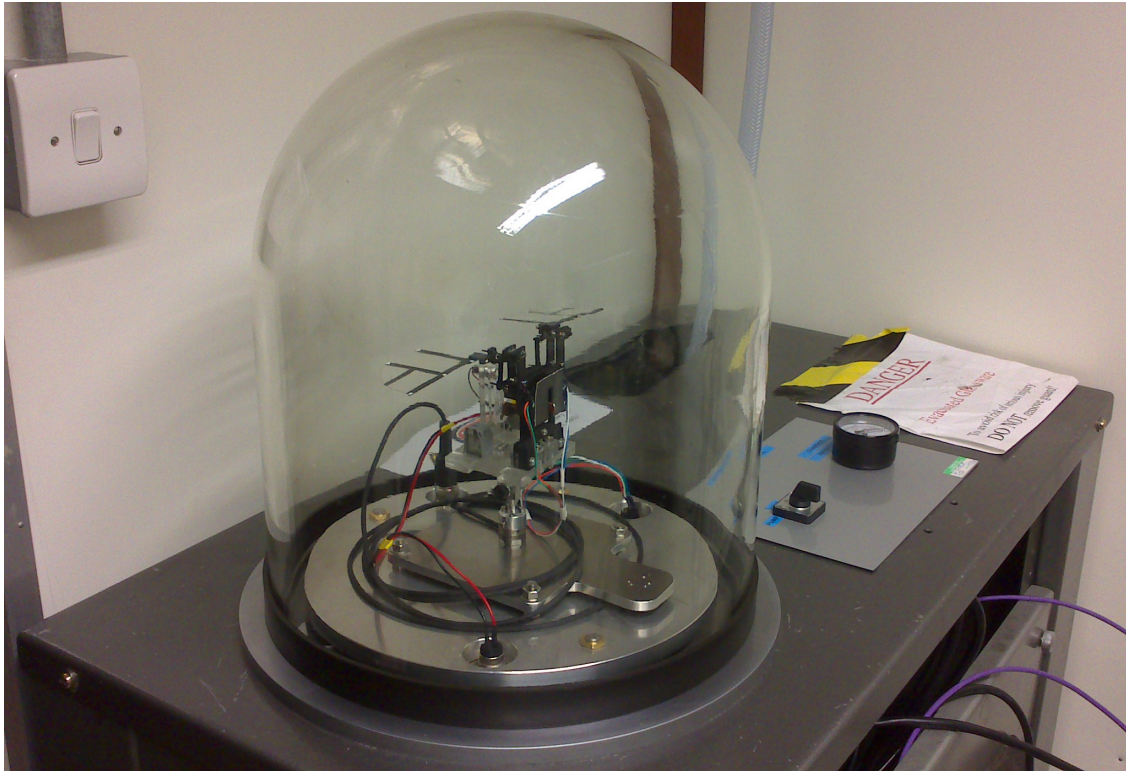


Figure 4.19: *Photograph of 0 Degree Inclination Vacuum Chamber Setup*

Figure 4.19 shows a photograph of the vacuum chamber in the vertical setup. The rubber seal is placed at the bottom of the glass dome as shown in the photograph. Smaller electrical sockets were used for the motor and reflective sensor to reduce any chance of the wings interacting with them and also to improve visibility of the wing. The socket for the transducer could not be altered without cutting the transducer cable which was not an option. The cable shields the carried signals from external influences to deliver accurate readings. For this reason the F/T sensor socket was placed more or less behind the flapping model, where visibility and wing interaction was not an issue. The control panel consisted of a dial which controls the pump and a gauge to display the level of vacuum in the chamber.

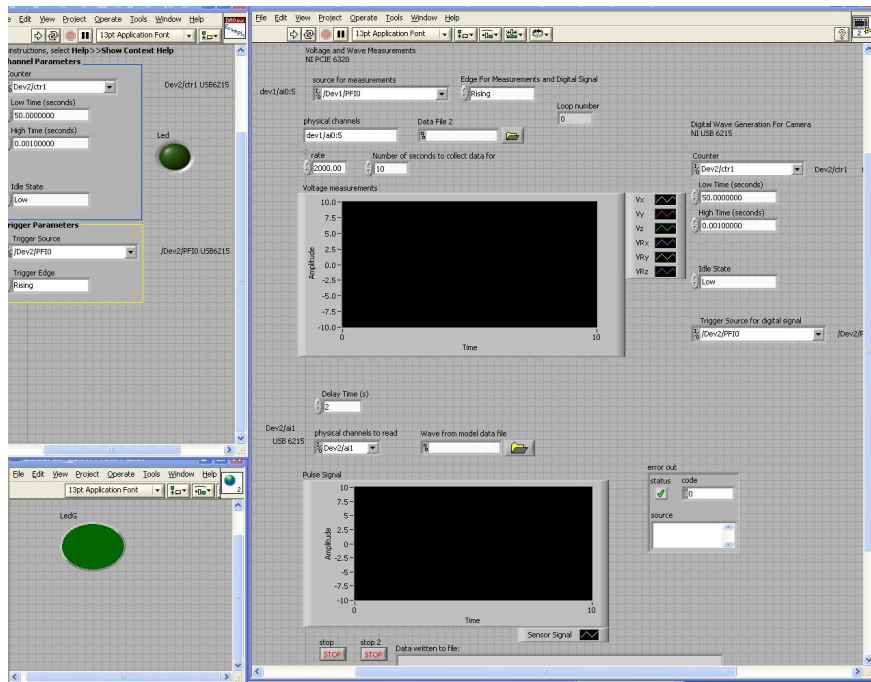


Figure 4.20: GUI of Software to Acquire Voltage Measurements

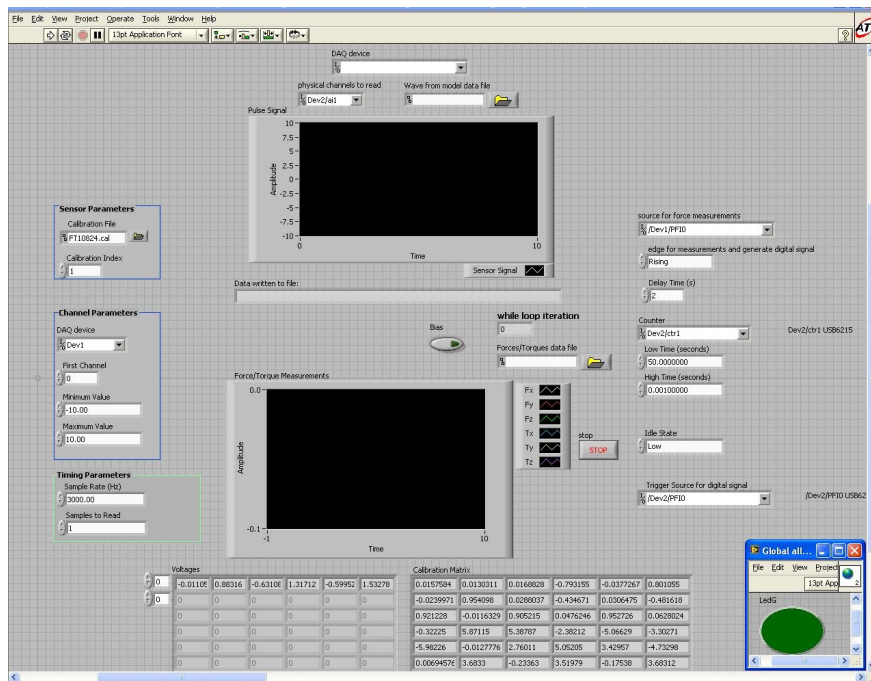


Figure 4.21: GUI of Software to Acquire F/T Measurements

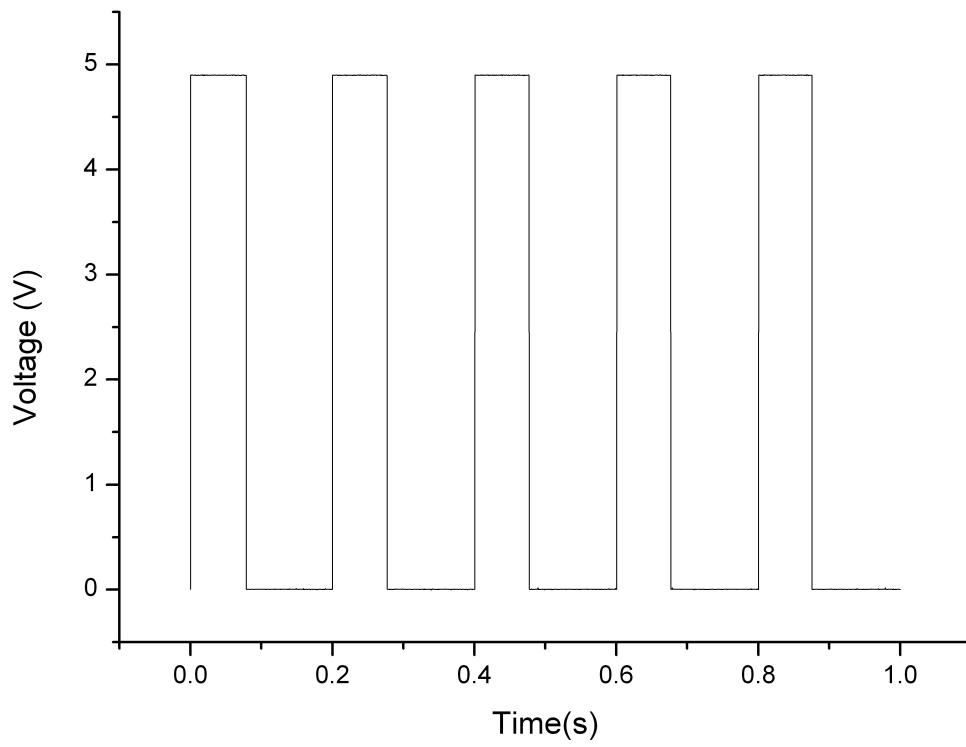


Figure 4.22: *Signal Produced by Reflective Sensor*

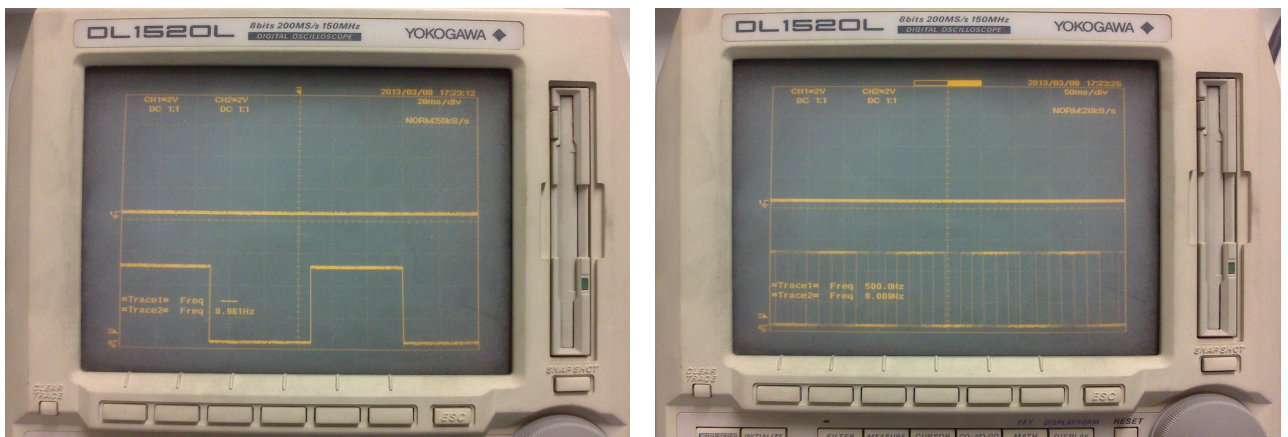


Figure 4.23: *Photograph of Signal Displayed on Oscilloscope*

## 4.2 Force Measurement System

Due to the nature of these experiments in order to capture small force/torque measurements a very sensitive multi-axis transducer is required. With this in mind the smallest resolution sensor commercially available with the ability to measure data in multiple axes was chosen. The Nano 17Ti has the lowest measuring range per axis available from ATI, combined with the 16-bit DAQ card the sensor has a force measurement resolution of  $\pm 0.24$  mN, torque measurement about  $T_x$ ,  $T_y$  of  $\pm 1.84$  mN-mm and  $T_z$  of  $\pm 1.53$  mN-mm. The Nano 17Ti utilises strain gauges to measure displacements and outputs an electrical voltage. "The positioning of the strain gauges plays a vital role in allowing the sensor to perform properly, three strain gauges are mounted in a close formation to allow the resolution about all three axes (x,y,z) to be the same even though the maximum force measured by the x and y axes is  $\pm 8$ N and the maximum force measured along the z axis is  $\pm 14.1$  N" (ATI-Staff). The maximum moment that can be measured about any of the three axes is  $\pm 50$  N-mm.

The transducer was calibrated by ATI Automation and fundamental validation tests were performed before commencing experiments on the flapping wing models. Weights were placed on the sensor to determine its accuracy for all six components. Various weights of up to 30 grams were used for this procedure and average measurements were determined for each F/T axis in the region of expected force and torque measurements. The maximum weight size used (30 grams) is well beyond the maximum total force measured for all the tests, thus it covered the required range but was not an extreme value as it is paramount to perform validations near to the range of measurements for the experiment. The average percentage errors found were 1.41%, 1.83%, 1.61% for  $F_x$ ,  $F_y$  and  $F_z$  respectively. Torques about each axis were also recorded by placing the masses at a set distance of 20 mm from the central location of the tool plate of the transducer. The average percentage errors found were 2.13%, 1.89%, 2.03% for  $T_x$ ,  $T_y$  and  $T_z$  respectively. As the load placed on each axis was increased the percentage error seemed to slightly reduce. The x-axis proved to be the most accurate for force measurements and the  $T_y$ -axis proved to be the most accurate for torque measurements. All axes seemed to be comparable in terms of accuracy for force and torque measurements. Measurements were also analysed for the sensor unloaded and FFT was performed to clarify that no electromagnetic interference is noticed in the data as this would compromise the accuracy of the results. This was essential as there were a number of electrical devices in operation during the experiment. Very small axis interaction is noticed which was found to be below 1mN. Contributing to these measured values in the two axes which the mass is not

directly affecting is the signal noise. The measured values need to be recorded above the noise threshold of the transducer to ensure data is not contaminated with signal noise. Repeatability of the results obtained via several data sets collected per experiment, proves that the results obtained are accurate and averaging is performed solely to slightly improve the accuracy of the results.

Along with this sensor numerous others were considered during the design stages. Along with the common strain gauged load cells, a piezo sensor (Kistler 9215) was considered due to its ability to measure forces at very low resolutions and had the ability to measure a sufficient range of forces. However, as this was a single axis sensor at least two would be necessary and further accessories such as cables and charge amplifiers would be required, thus it did not prove to be cost effective at all in comparison to the Nano 17Ti. Moreover the mounting of these piezo sensors would not have been as stiff and tightly secured to the model(s) as there was no actual mounting surface, unlike the Nano 17Ti transducer which allows test pieces to be screwed down to its tool plate. Among requirements such as low resolution and sufficient measuring range per axis, the transducer should also have the ability to acquire data at large frequencies, have a large resonant frequency, high stiffness and large overloads per component (the latter is a preferred feature but is not imperative). Many other sensors were considered but these were the only two at the time of purchase which were commercially available and offered very low resolution measurements. Sensors which have the ability to directly measure forces from insects have been produced by FemtoTools and tested on real-life insects where measurements have been obtained along a single axis. “The FemtoTools FT-S MicroForce Sensing Probes feature the required sensitivity and measurement speed to measure the lift forces of the fruit fly, generated during a single wing beat cycle” (Femto-Tools).

ATI transducers have been utilised for FW research by other Institutions some of which are Konkuk University and Air Force Institute of Technology. A review of the research accomplished has been presented in the literature review chapter some of which consisted of experimental work at MAV scale.

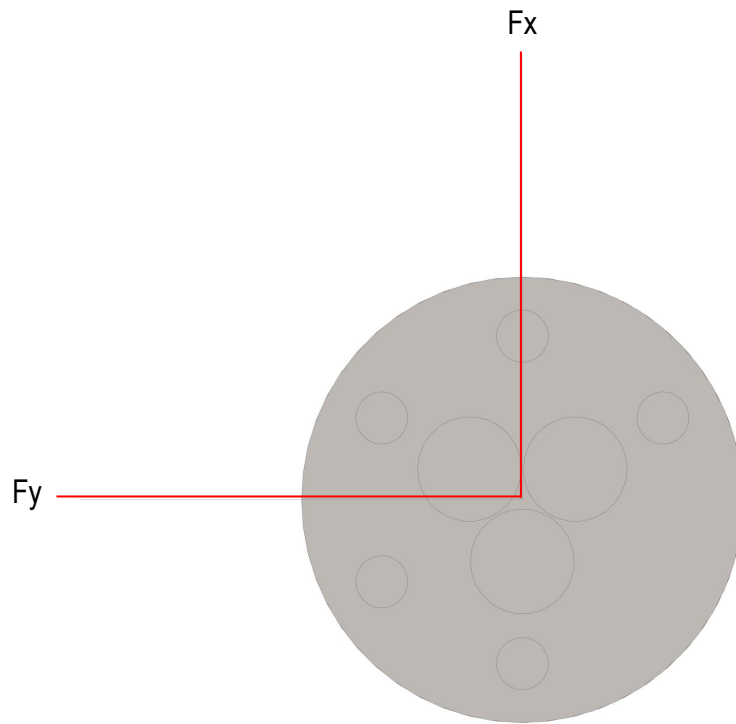


Figure 4.24: *F/T Sensor Axes Top View*

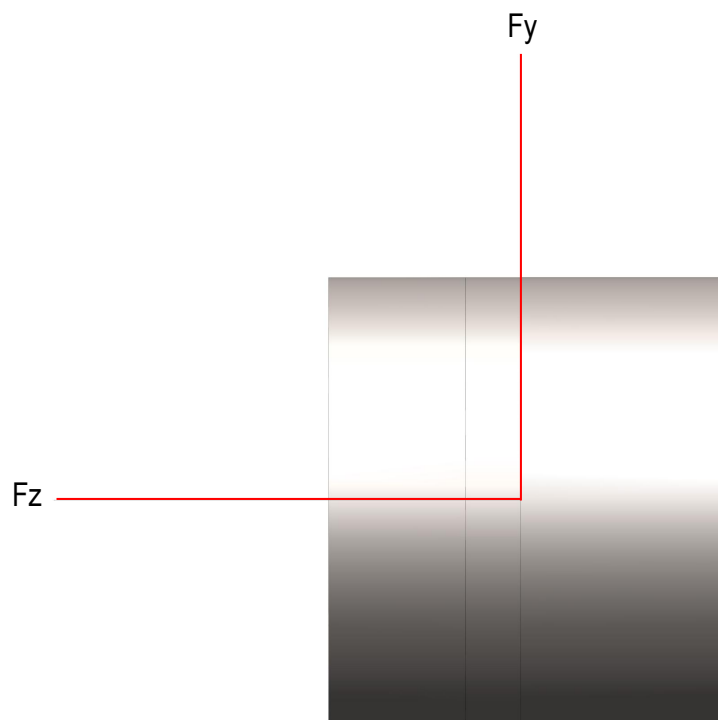


Figure 4.25: *F/T Sensor Axes Side View*

Two Dimensional diagrams of the force sensor in 2 different views presenting all three axes are shown in Figures 4.24 and 4.25. A three Dimensional diagram is shown in Figure 4.26 which displays all three axes and moments that act around each axis. For all 0 degree inclination tests the x-axis was the thrust force axis, y-axis was the side force axis and the z-axis was the lift force axis. According to the aforementioned the moments are labelled as follows,  $T_x$  is the rolling moment,  $T_y$  is the pitching moment and  $T_z$  is the yawing moment about each of their respective axes. As the position of how the model mounts to the transducer changed for all hovering tests, some of the force labels also changed. The x-axis was now the lift force axis, y-axis remained as the side force axis and the z-axis was now the thrust axis. The moment about the x-axis,  $T_x$  was the rolling moment,  $T_y$  was the pitching moment and  $T_z$  was the yawing moment. Moments about each of the axis are positive in the anti-clockwise direction.

Figures 4.27, 4.28 and 4.31 show the model positioned at 0 degrees inclination with all three force axes. The moments for the 0 degree inclination are positive in all three axes in the anti-clockwise direction, and the same applies for the hovering tests. Force axes direction for the hovering tests have been shown in Figures 4.29, 4.30 and 4.32. The isometric views show a clear representation of the directions of each force axes and as aforementioned the y-axis remains as side force.

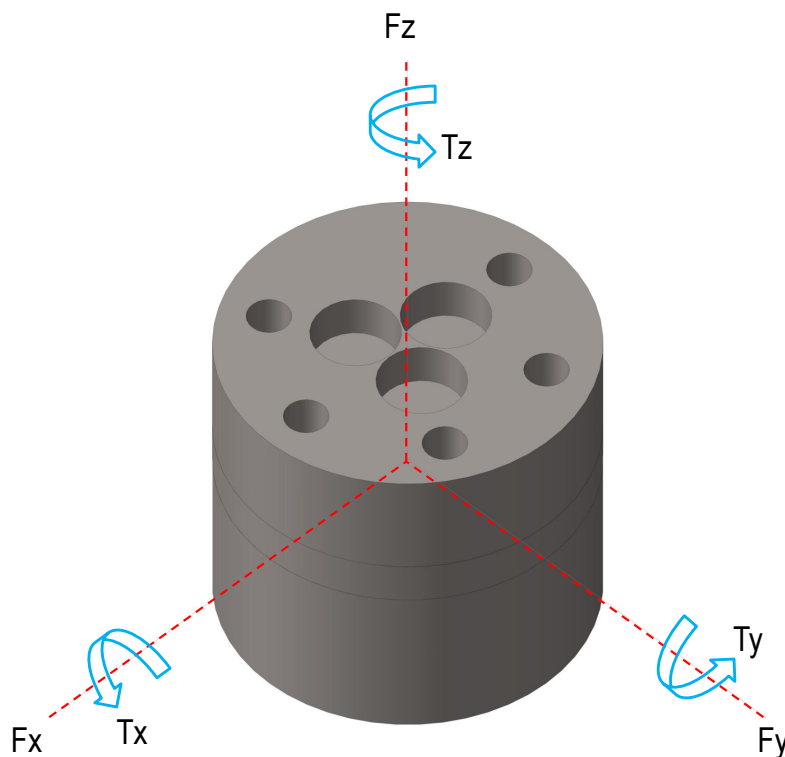


Figure 4.26: *F/T Sensor Axes Iso View*

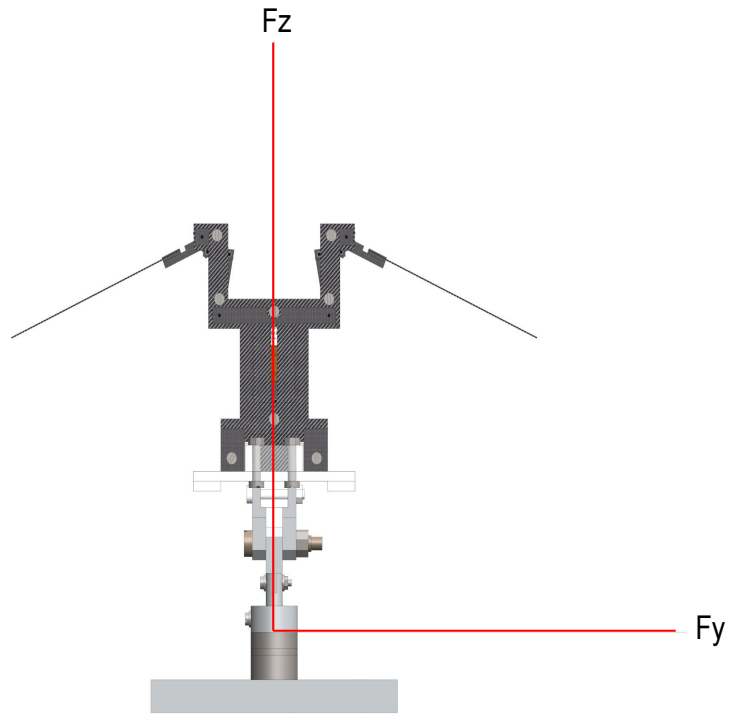


Figure 4.27: *Model at 0 Degree Inclination with Force Axes Front View*

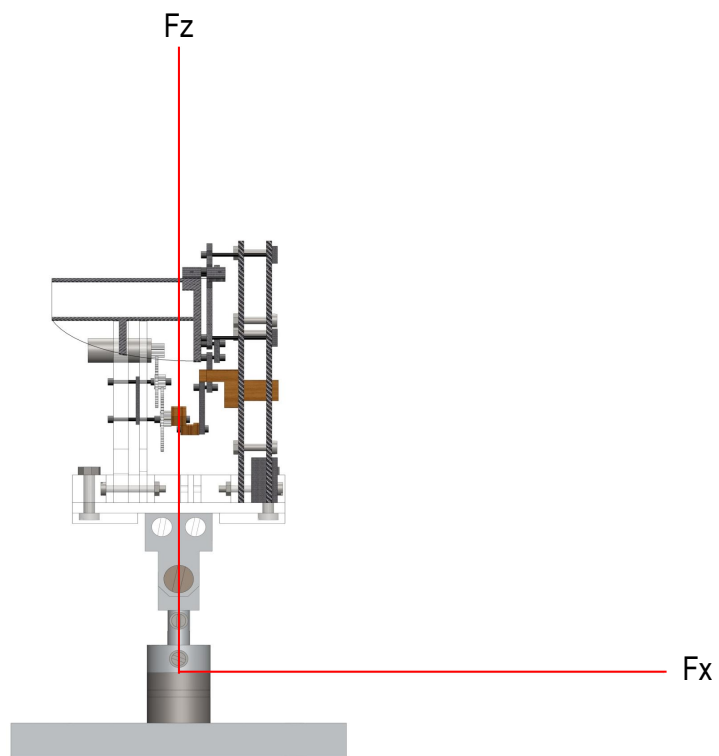


Figure 4.28: *Model at 0 Degree Inclination with Force Axes Side View*

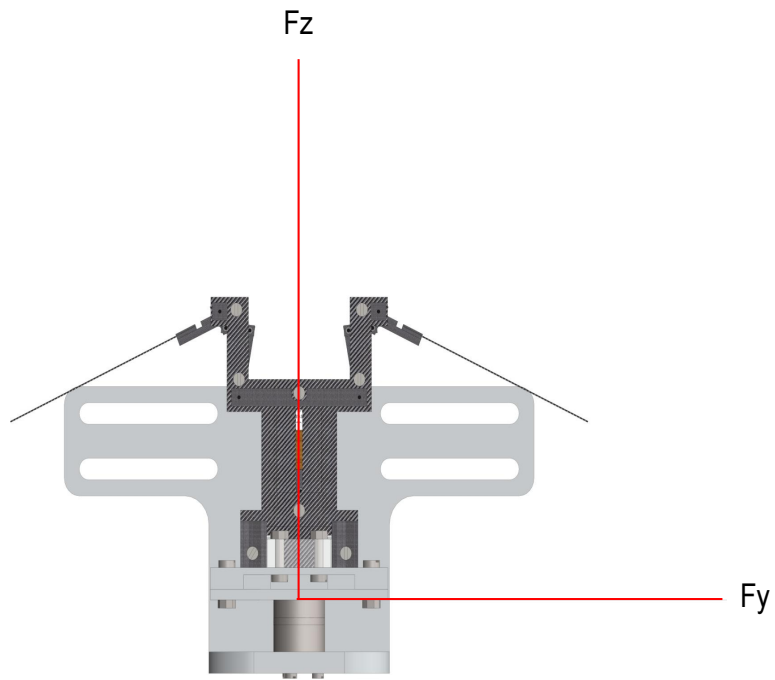


Figure 4.29: *Model at 90 Degree Inclination with Force Axes Top View*

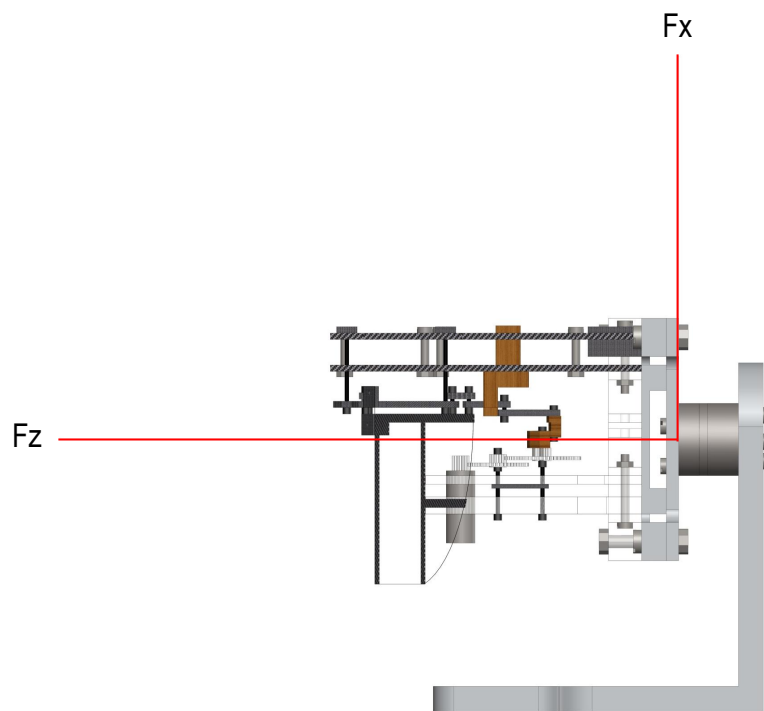


Figure 4.30: *Model at 90 Degree Inclination with Force Axes Side View*

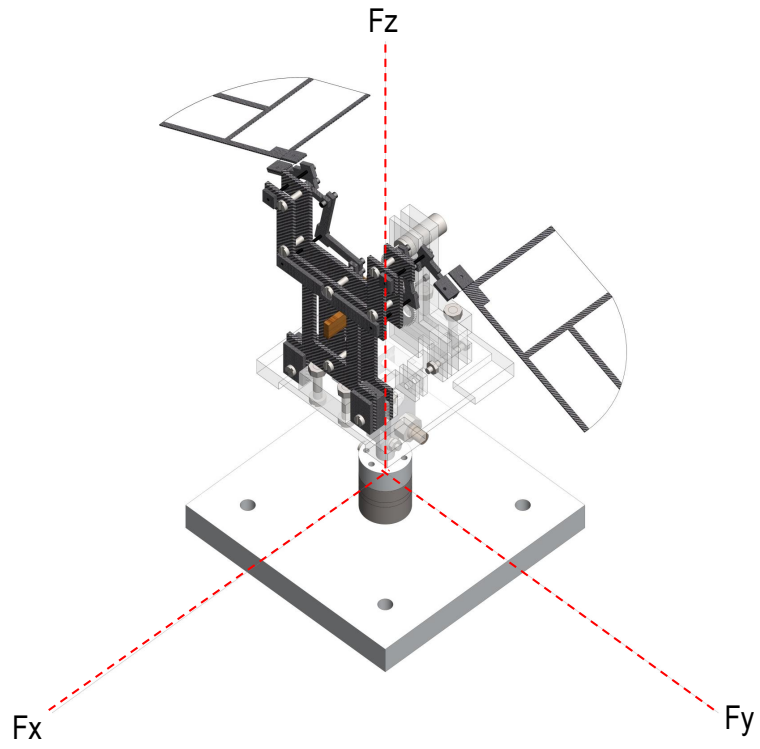


Figure 4.31: *Model at 0 Degree Inclination with Force Axes Iso View*

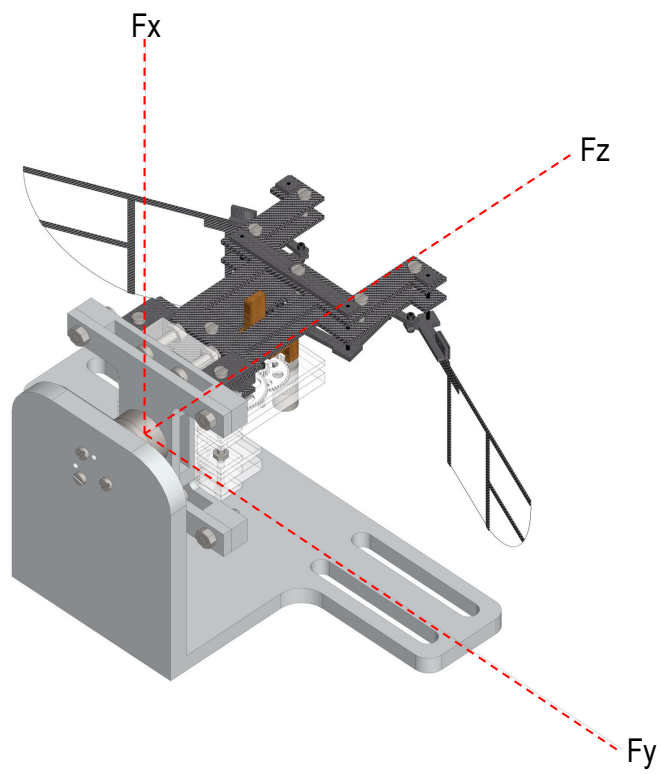


Figure 4.32: *Model at 90 Degree Inclination with Force Axes Iso View*

### 4.3 Experiments Performed with Analysis

The experiments performed through this research project were designed having certain scenarios in mind which FWMAVs would experience when flying in a confined space, as well as the effect of a change in wing stroke motion would have on kinematics and measurements. To develop a better understanding of flapping wing experimental work and data evaluations it was mandatory to commence the experimental stage with simpler experiments before moving on to more complex tests involving a combination of wing motions such as flapping with wing rotation and flapping with AP wing rotation.

A description of some arrangements explored are briefly detailed below:

Flapping only - A simple flapping motion is produced in the form of a sinusoidal wave

Flapping and Rotation - A flapping motion is produced and the wing rotates passively due to the aerodynamic and inertial loads acting on the wings.

Flapping and Rotation with Assymmetric Pitching (AP rotation) - A flapping motion is produced and the wing rotates passively due to aerodynamic and inertial loads acting on the wings, but they are only free to rotate during the upstroke motion.

A range of experiments such as symmetric wing motion, asymmetric wing motion and boundary wall investigations were carried out for the above arrangements. This was done for the wings mentioned in the previous chapter, as the wing rotation was passive, it meant that consistency of wing motion had to be monitored and tolerances should be allowed for small variations of wing kinematics during tests. Further to this, the condition of the Mylar used for passive wing rotation needs to be monitored as well, dependent upon many factors the condition of this flexible material does deteriorate with the number of flapping cycles completed. However, a substantial number of cycles would need to be completed before any decline in condition is noticed. Factors which affect the lifetime of the Mylar are - flapping frequency, Mylar thickness, Mylar length exposed for rotation motion, max/min wing rotation angle and even the mass of the wing will have an effect. All boundary experiments were only performed on model 1 (symmetrical flapping only).

If the wing(s) were to collide with any form of wall or stiff boundary the mylar will take the impact and its condition would weaken, the extent would be dependent on the type and force of contact with the rigid boundary. However, this mainly applies for rigid wings, for a very flexible wing surface, the rotation piece

(mylar in this case) would not be affected as much as the wing membrane would now suffer. Needless to mention that any flexible material used for passive wing rotation would have a reduced weakening if it were to undergo a flapping with AP rotation motion compared to flapping with full wing rotation.

The boundary distances set from the wing edge were planned during the design process of the experiment, but for certain tests which involved passive wing rotation the appropriate boundary distances (predominantly for ground effect tests) had to be located after capturing images of the wing motion and analysing the images. For example, the height of the foam piece acting as the ground for GE tests was set after the wing rotation height from the experimental rig was determined from the HS images.

Figures 4.35 to 4.46, illustrate the test arrangements for the 60 mm wing (WT4) in a flapping configuration. Similar setups were used for the FR and FRAP model configurations where the distances of the boundaries were altered due to passive wing rotation. The Figures also show photographs of the setup to display that the planned arrangements during the design phase were replicated sufficiently with minor alterations as mentioned in this chapter.

The tests which utilised a ground effect base for the FR and FRAP configurations required the use of the HS camera for the initial setup. Due to the passive rotation of the wing estimating the angular position of the wing during the rotation phase relating to its height above a ground effect base is far from trivial, thus images recorded from the HS camera were used to align the wing frame edge and the GE base so the distance between the two is approximately 1-1.5 mm. Needless to mention a consistent distance between the wing frame and GE base is vital to maintain accuracy in results and make comparisons between data sets of different arrangements. The boundaries were designed in accordance to the wing size and motion performed by the wings.

The boundary parts such as the GE base and TE wall were stuck down to the table to assure there was no movement or mis-alignment during the tests. The tables were also stuck down to the acrylic base, it was vital to ensure the table or any of the boundary parts were not touching the model or the force balance arrangement as this would immensely compromise the accuracy of the results obtained. Several data sets were recorded for each setup, even though all boundary parts were stuck down during the experiments the boundary and wing distances were still checked to maintain consistency and produce accurate data during all tests.

In the flapping tests the wing tip was approximately 1 mm away from the GE base part and for the FRAP tests as the wing rotates the tip is no longer the closest section to the base part. A section between the wing tip and trailing edge of the wing is now the closest part to the wing, this edge distance is approximately 1-1.5 mm away from the GE base. For flapping only, the distance between the wing edge and TE wall was consistent. This varied for FR and FRAP as the wings passively pitched during the wings motion. Brown cardboard was used as a backing for 'TE wall' experiments to aid the visibility of the white dots on the wings. Figure 4.33, shows a photo of the mylar used to perform the pitching of the wing with a crack

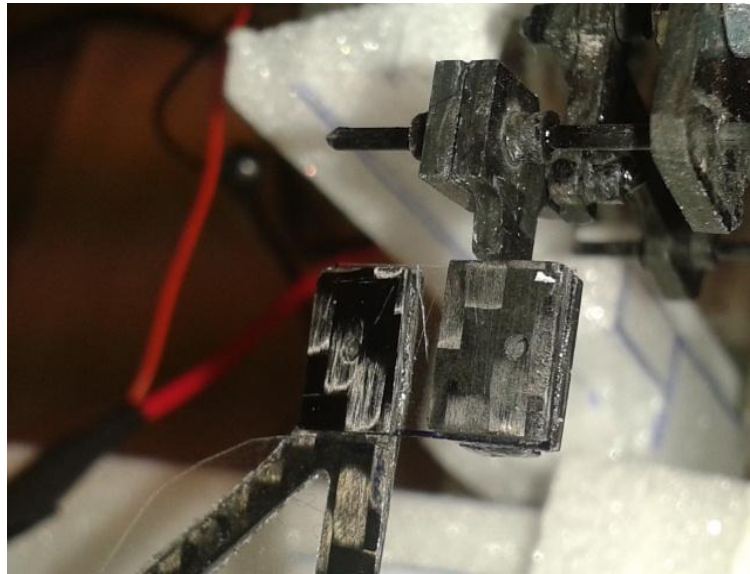


Figure 4.33: *Photograph of Cracked Mylar During Experiments*

which is followed by tearing of the mylar along the cracked path. The crack formed after many cycles where the wing was purposely setup to collide with a rigid boundary placed beneath it to effectively visualise the damage caused to the mylar. As aforementioned wing rotation will eventually cause the mylar to crack along the line with which the wing performs the pitching motion. This will lead to the mylar tearing along this cracked trail, this entire process combined will result in inconsistent wing pitching per cycle, at first the inconsistency will be very small (deemed as negligible) but this will later worsen as the condition of the mylar deteriorates further. Finally leading to inconsistent F/T production, and when in flight an unstable FWMAV which will ultimately fail.

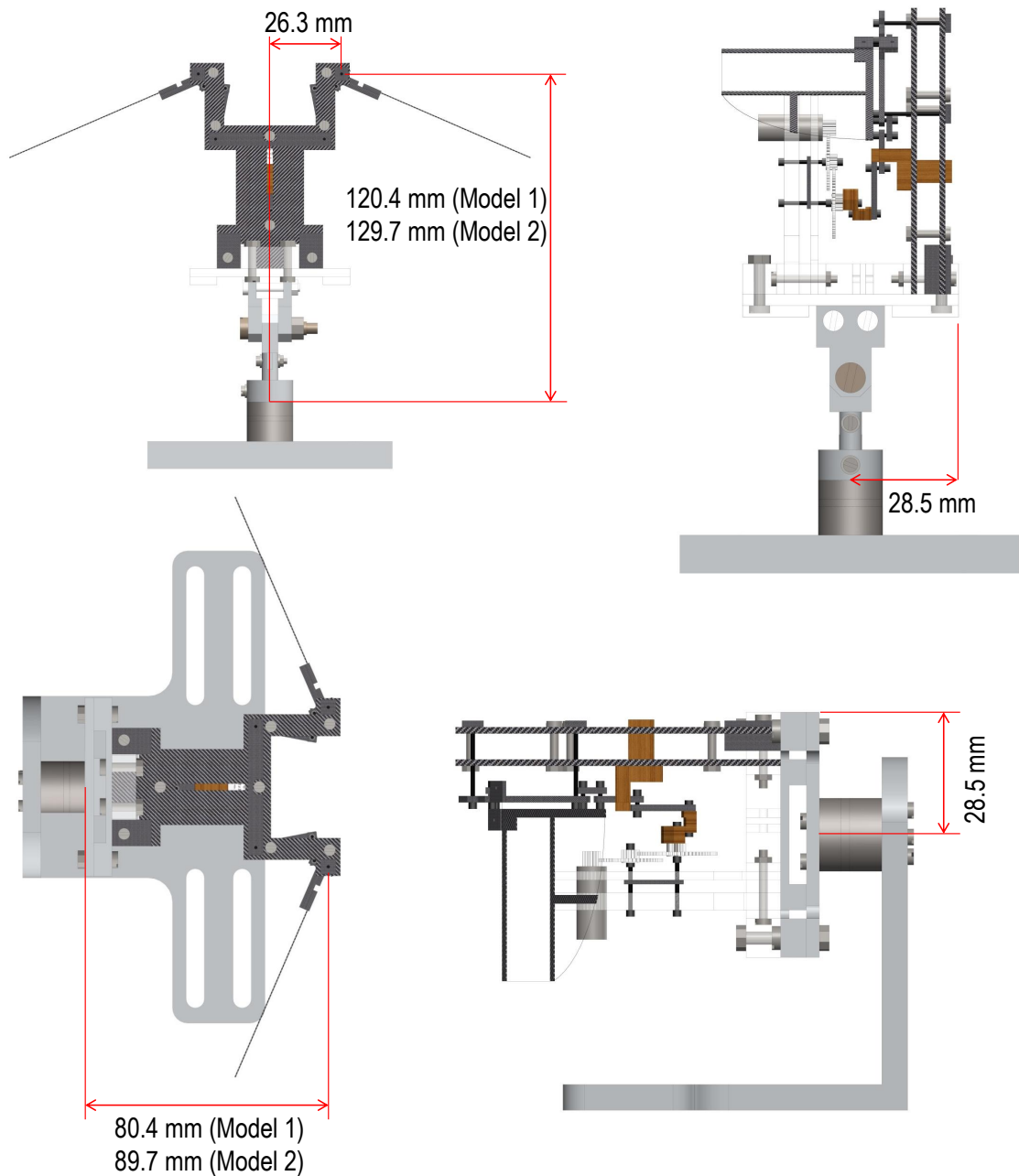


Figure 4.34: *Distances from Transducer Tool Plate*

Figure 4.34, displays diagrams of the model in both 0 degree and 90 degree inclinations. Distances have been shown of the model positioning from the top tool plate of the transducer. As mentioned in chapter 3, model 2 is longer in the vertical direction than model 1, thus its distance is greater in reference to the tool plate.

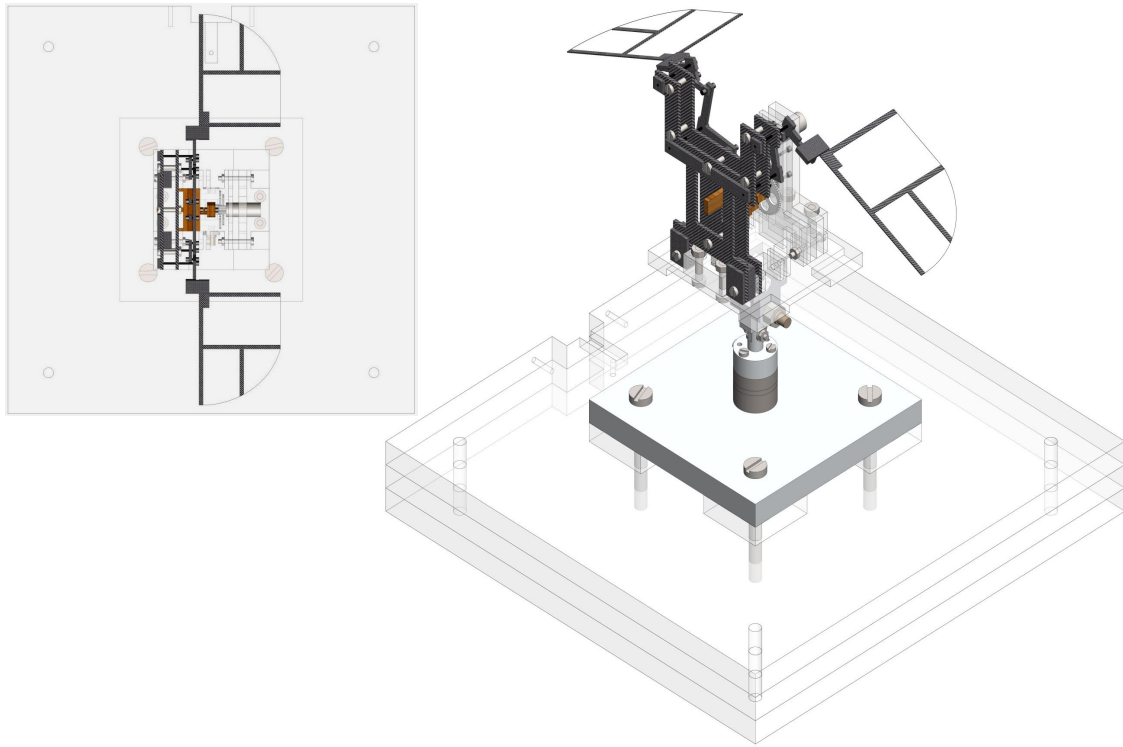


Figure 4.35: *Flapping Setup at 0 Degree Body Inclination with 60 mm Wings (WT4)*



Figure 4.36: *Photograph of Flapping Setup at 0 Degree Body Inclination with 60 mm Wings (WT4)*

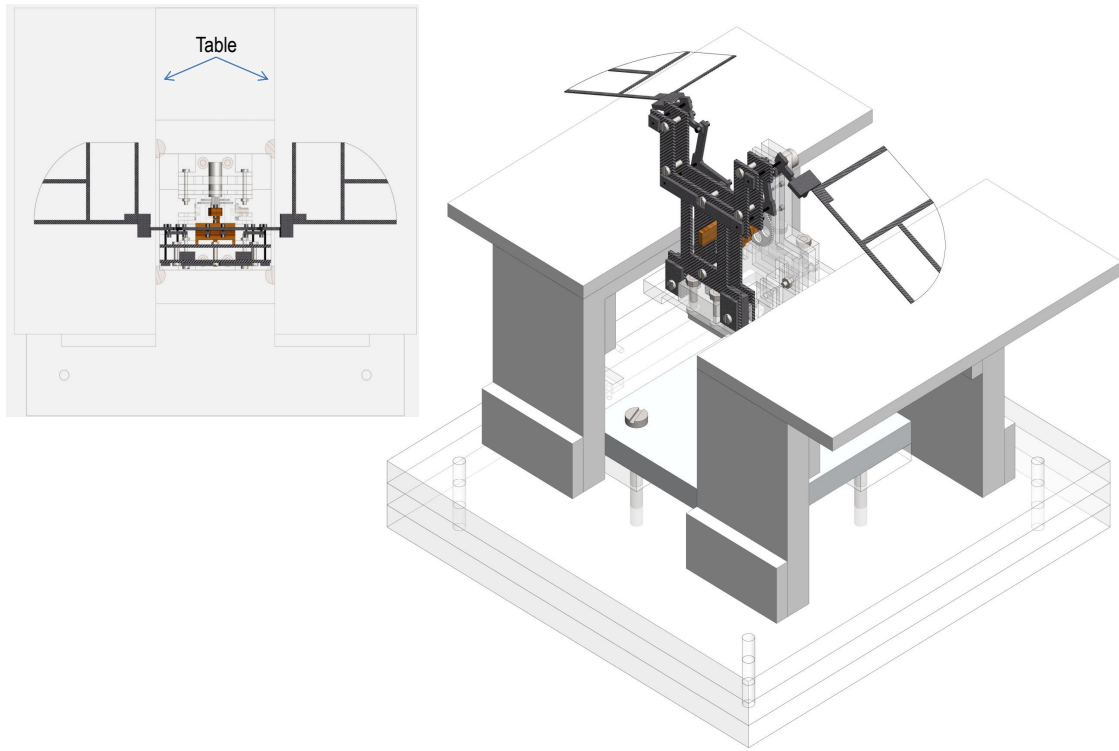


Figure 4.37: *Flapping Setup w/Table at 0 Degree Body Inclination with 60 mm Wings (WT4)*

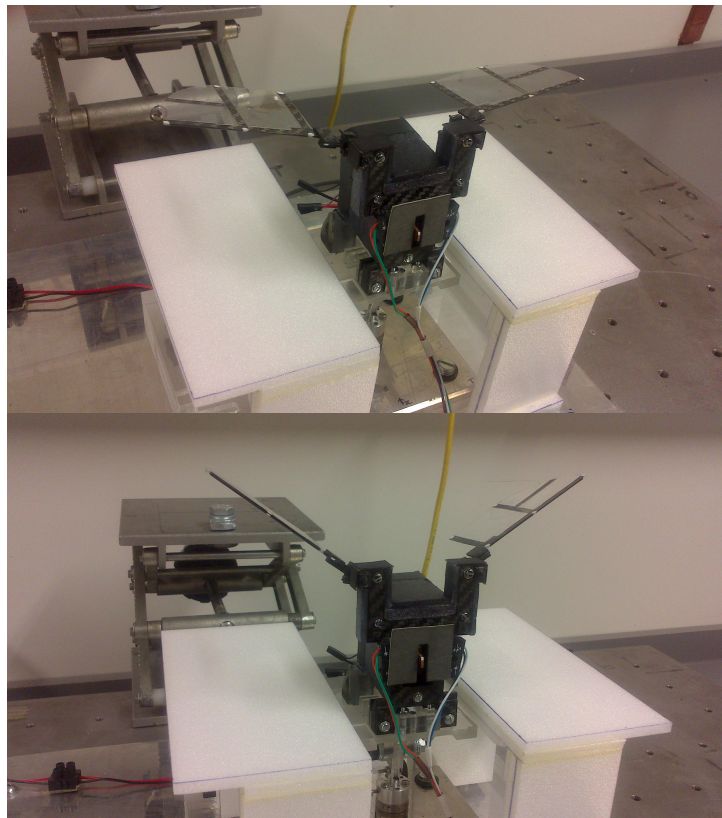


Figure 4.38: *Photograph of Flapping Setup w/Table at 0 Degree Body Inclination with 60 mm Wings (WT4)*

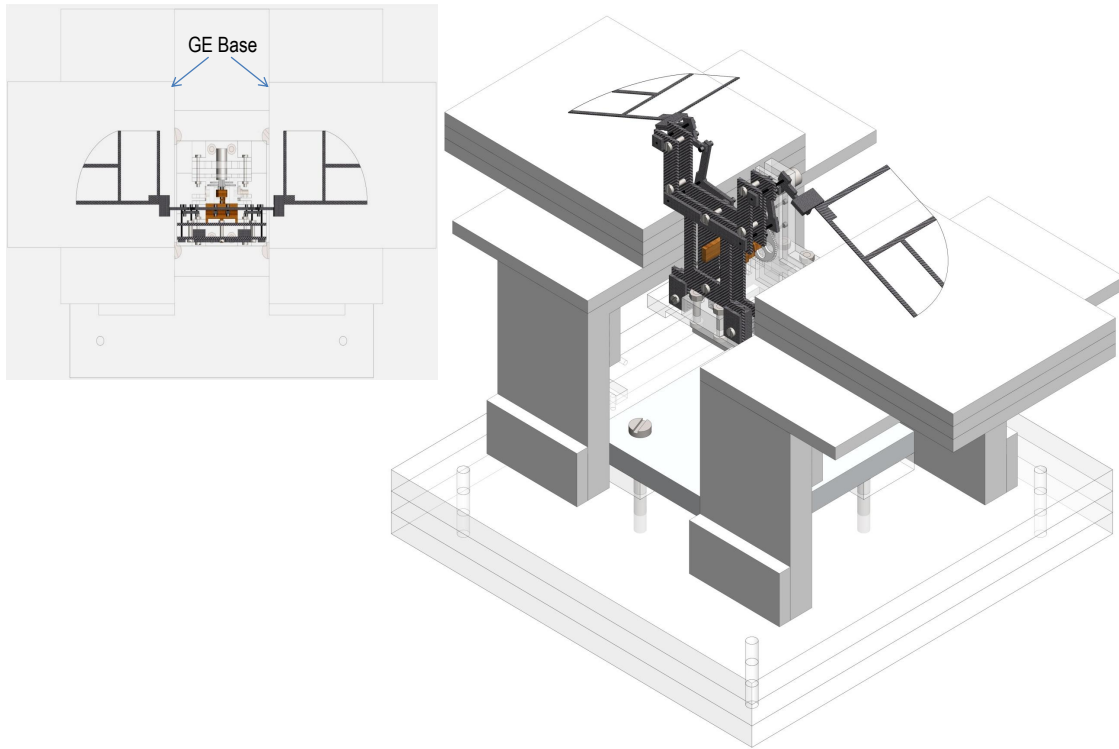


Figure 4.39: *Flapping Setup w/GE at 0 Degree Body Inclination with 60 mm Wings (WT4)*

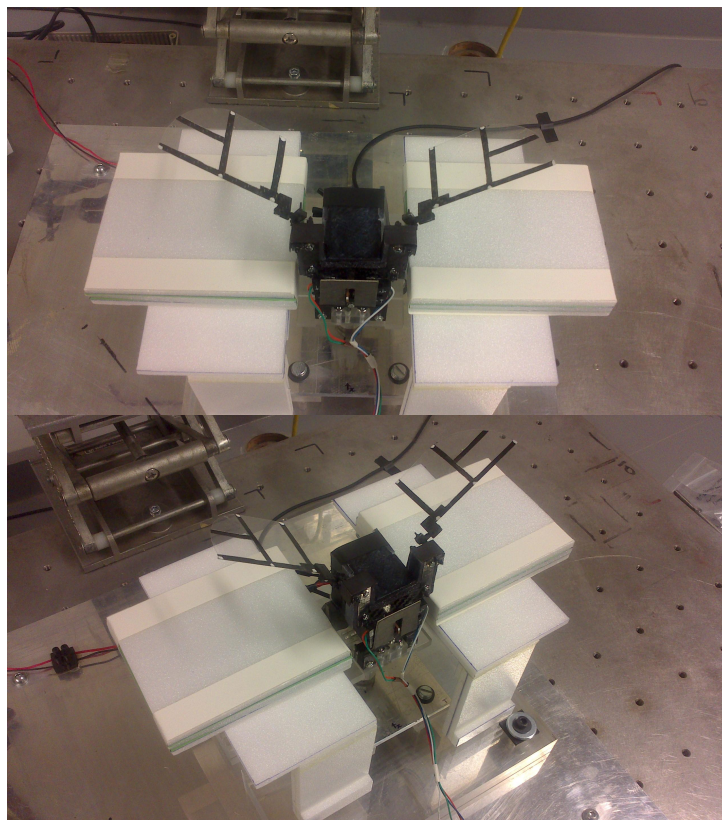


Figure 4.40: *Photograph of Flapping Setup w/GE at 0 Degree Body Inclination with 60 mm Wings (WT4)*

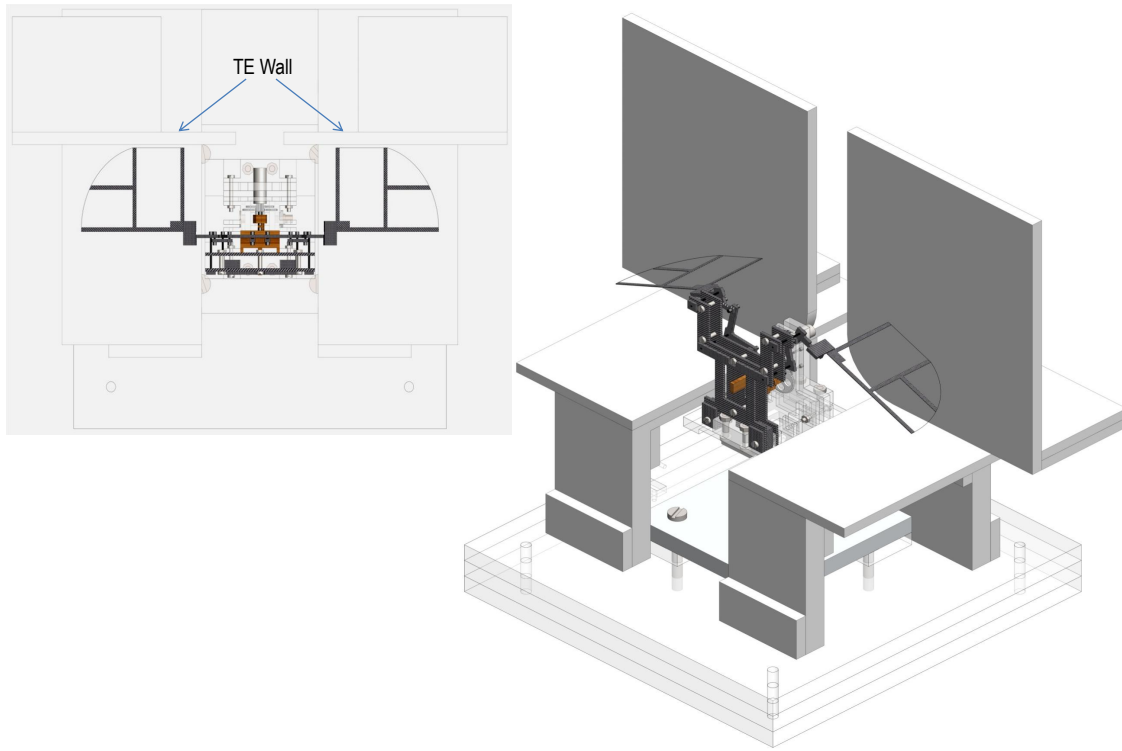


Figure 4.41: *Flapping Setup w/TE wall at 0 Degree Body Inclination with 60 mm Wings (WT4)*

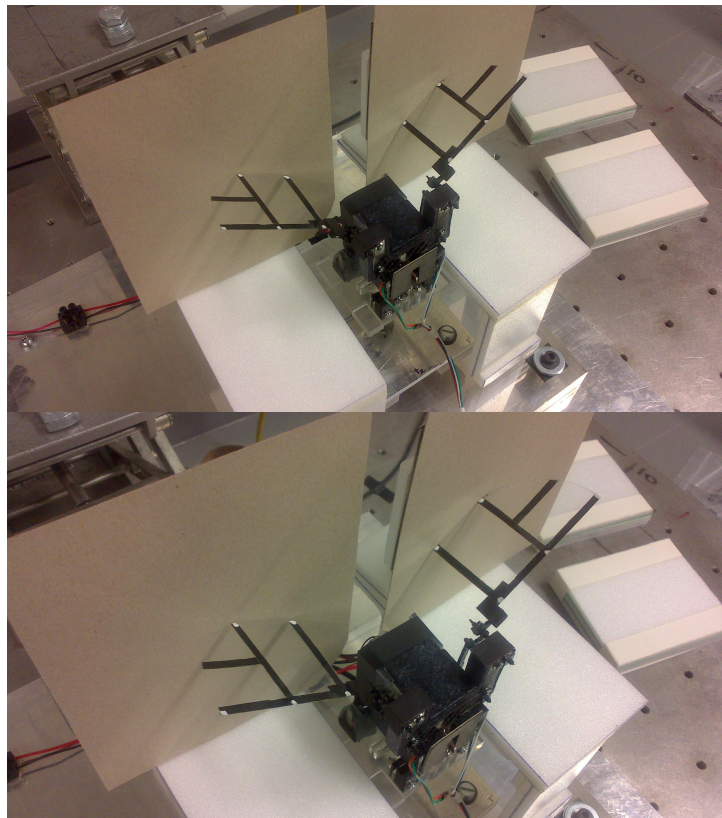


Figure 4.42: *Photograph of Flapping Setup w/TE wall at 0 Degree Body Inclination with 60 mm Wings (WT4)*

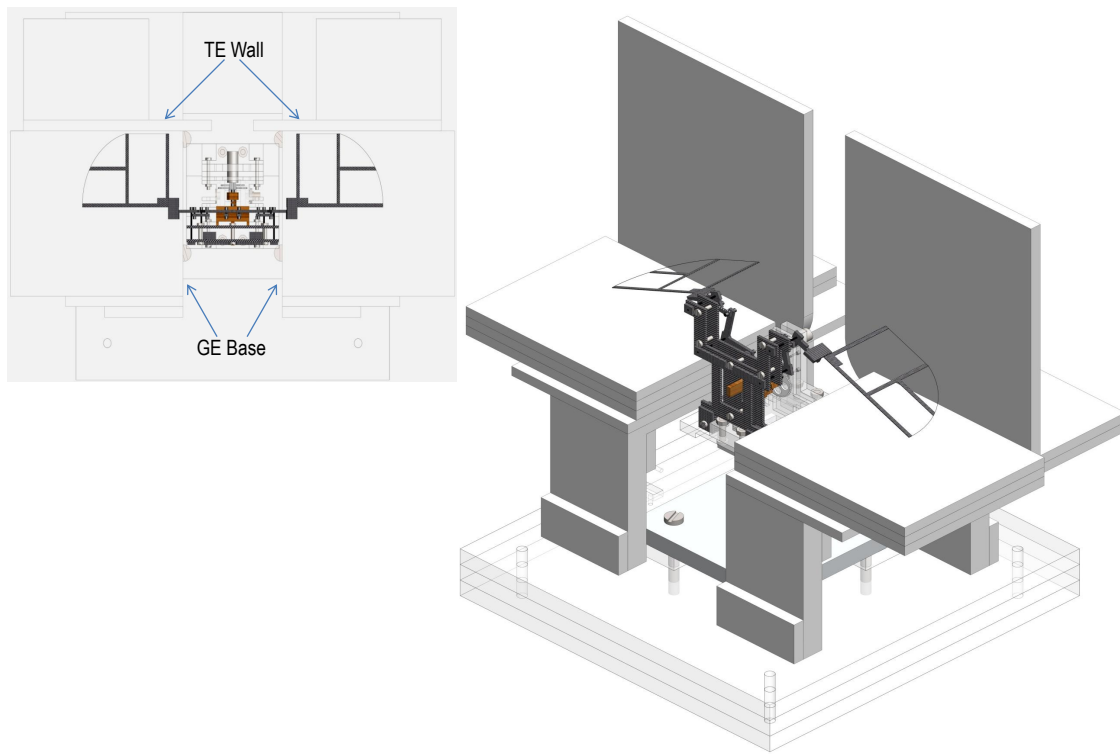


Figure 4.43: *Flapping Setup w/TE wall and GE at 0 Degree Body Inclination with 60 mm Wings (WT4)*

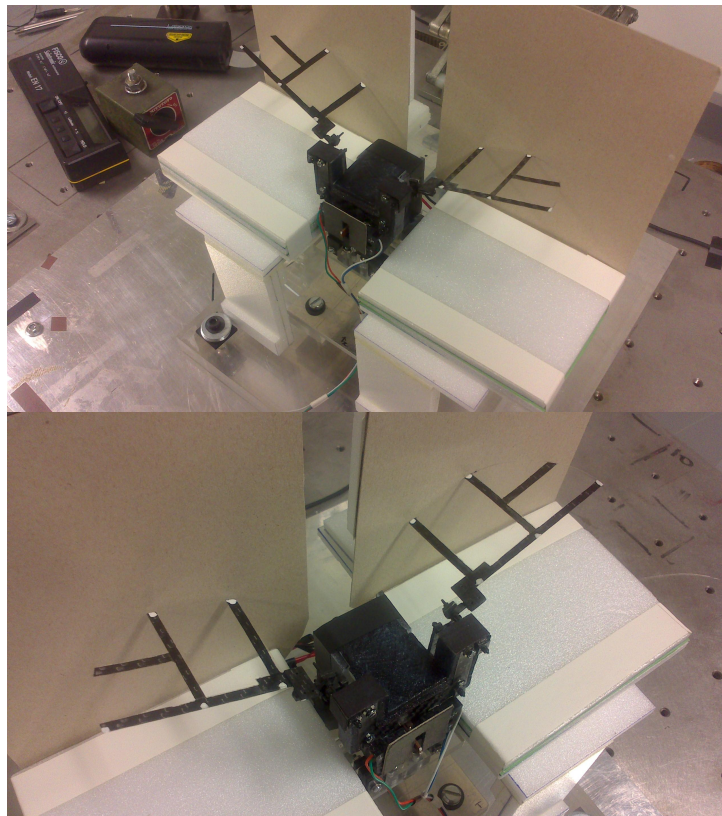


Figure 4.44: *Photograph of Flapping Setup w/TE wall and GE at 0 Degree Body Inclination with 60 mm Wings (WT4)*

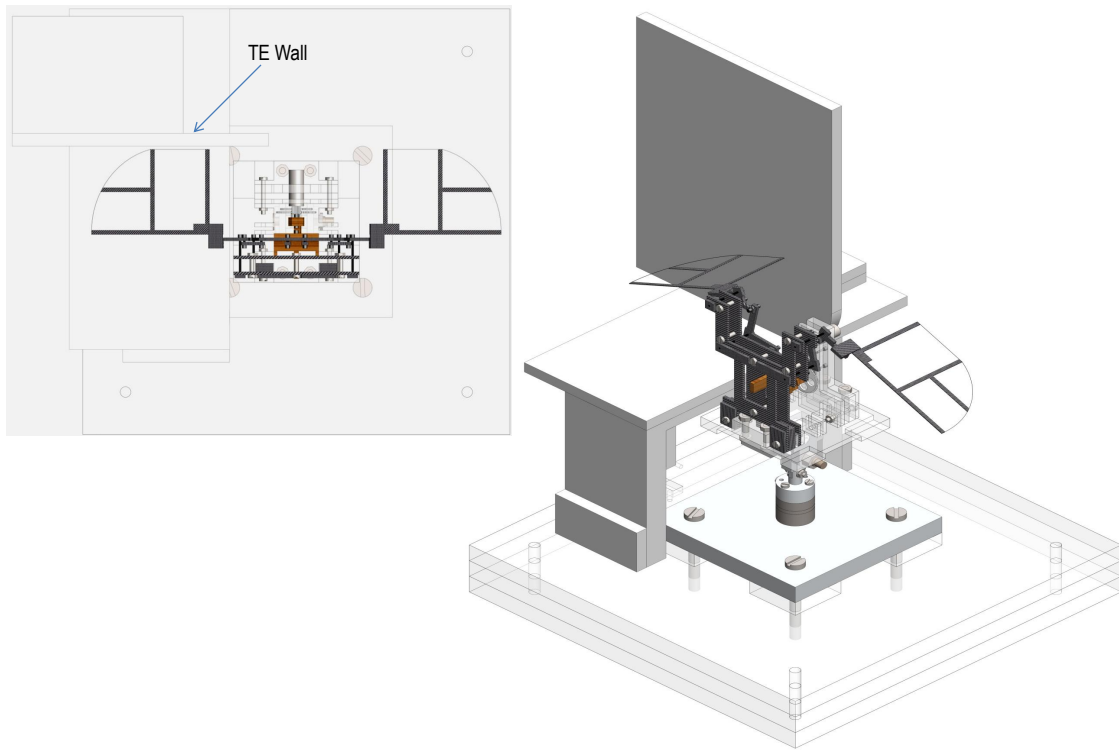


Figure 4.45: *Flapping Setup w/TE wall 1S at 0 Degree Body Inclination with 60 mm Wings (WT4)*

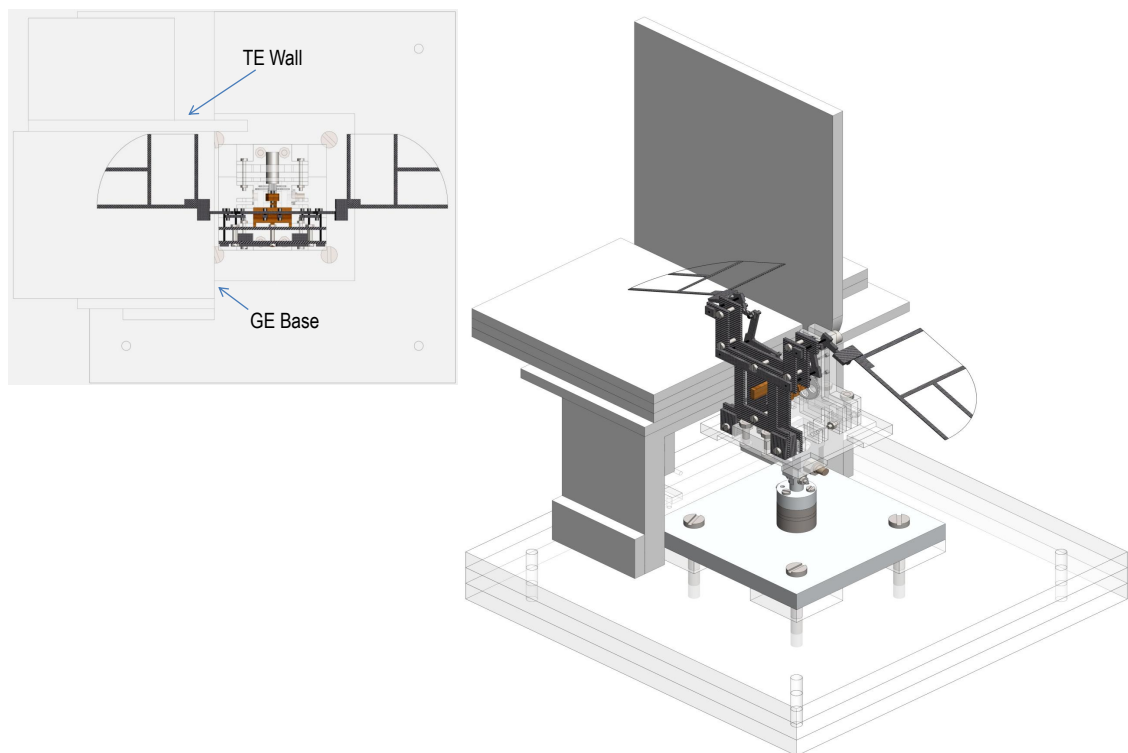


Figure 4.46: *Flapping Setup w/TE wall and GE 1S at 0 Degree Body Inclination with 60 mm Wings (WT4)*

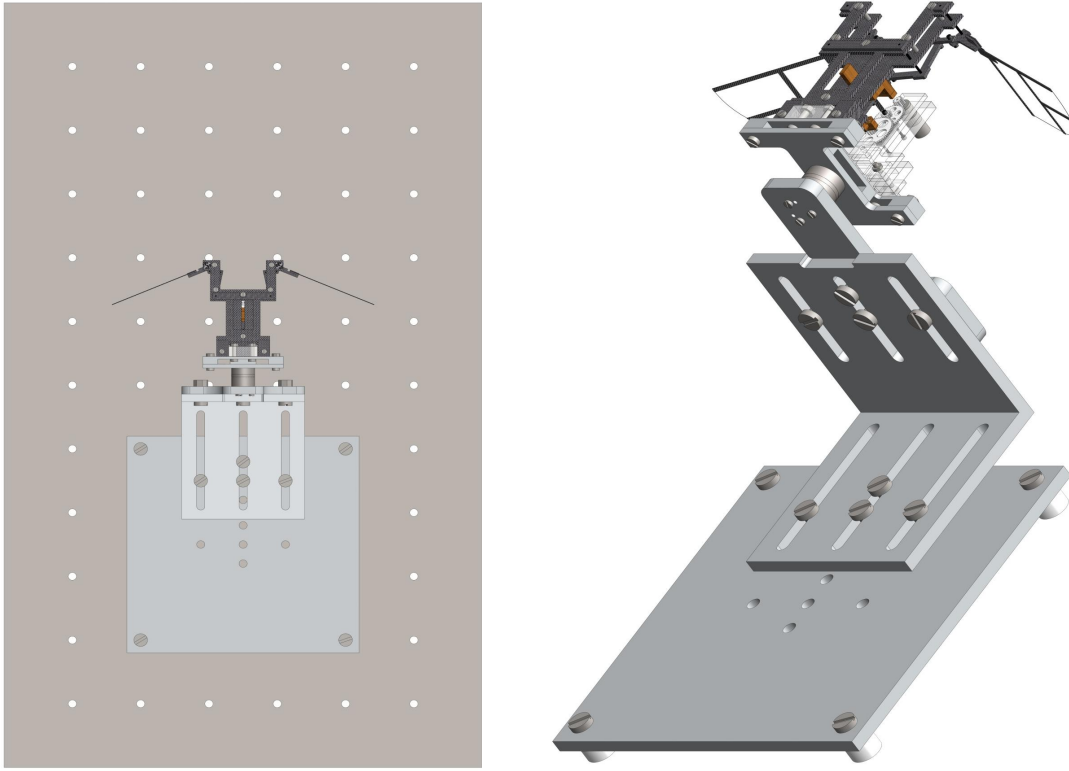


Figure 4.47: *FR Setup at 90 Degree Body Inclination with 60 mm Wings (WT4)*

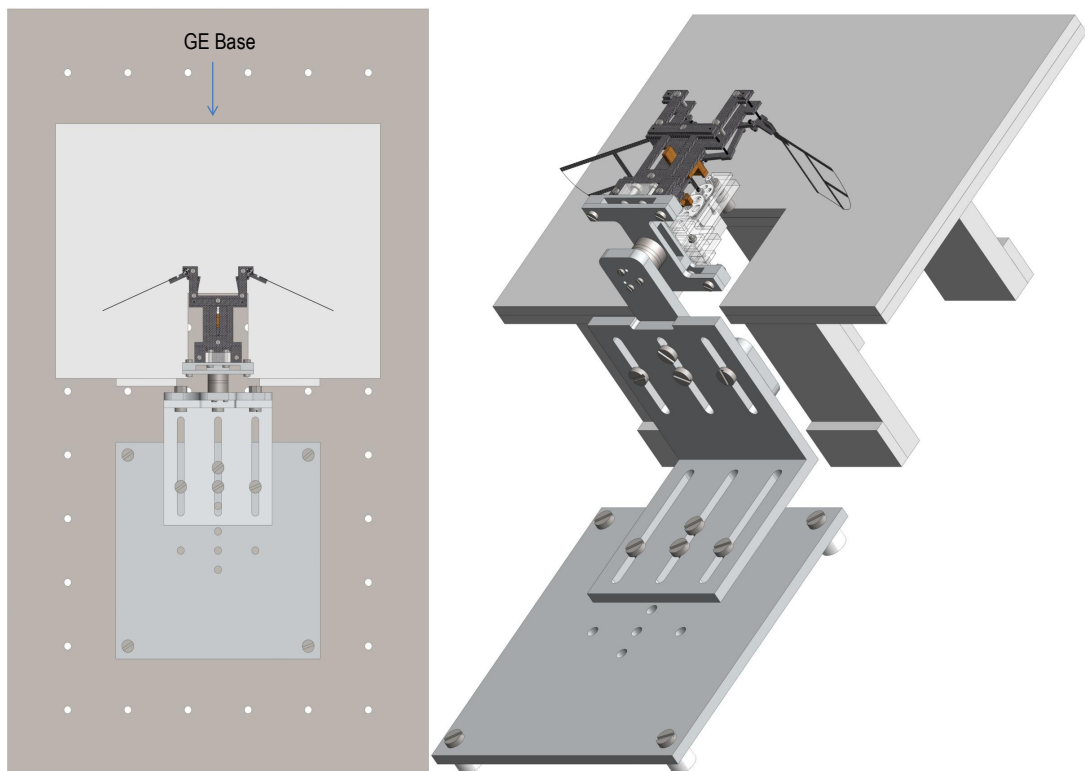


Figure 4.48: *FR w/GE Base Setup at 90 Degree Body Inclination with 60 mm Wings (WT4)*

Hovering experiments were performed on both models, as the setup is exactly the same for both models on the experimental rig, images have only been shown for model 1, these can be found in Figures 4.47 and 4.48. The GE base part performs a similar role to the TE wall part used for the 0 degree inclination tests. Both are placed near the trailing edge of the wing, however it should be borne in mind that the lift force vector has changed in the hovering tests, thus the lift forces produced will now experience the effect of the GE base placed near the TE of the wing. For the 0 degree inclination tests the thrust axis would experience the effect of the TE wall, lift forces may also be affected during the 0 degree inclination experiments, but not as much as the thrust axis.

All boundaries used for hovering experiments were secured down to the foam table for reasons previously mentioned and the foam table is also securely taped to the optics table. Experimental visualisation would provide very interesting results as a boundary is located in its near region, understanding the fluid motion with a boundary placed near the wing would assist researchers in the field of FWMAVs and would immensely help designers of such devices.

It is paramount that the boundary parts do not come in contact with the model, experimental rig and wings as inaccurate results would be produced. Any wing-boundary contact would produce results which need to be analysed separately as the collision would affect F/T measurements. In reality this is a situation which should be avoided for reasons discussed earlier in this chapter, primarily to protect the mylar.

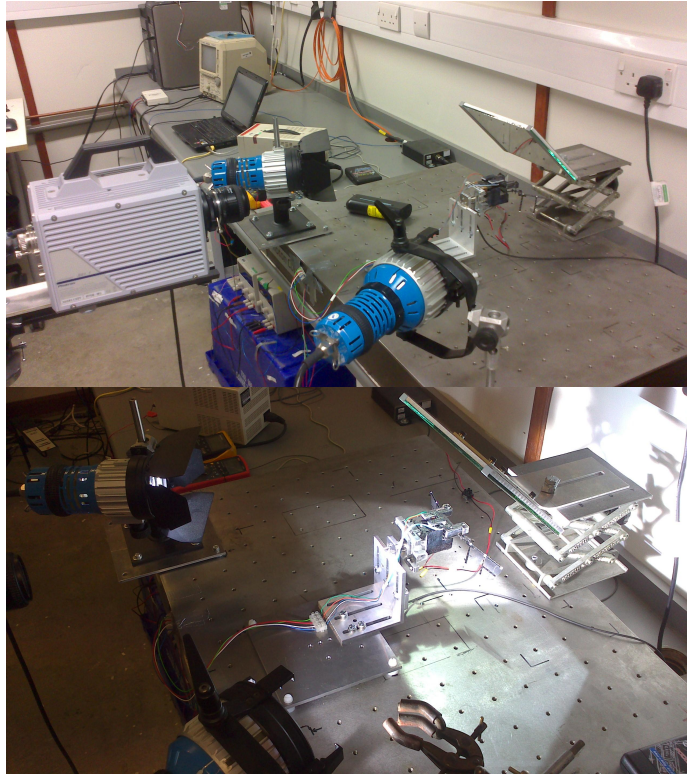


Figure 4.49: *Photograph of Model 1 at 90 Degree Body Inclination*

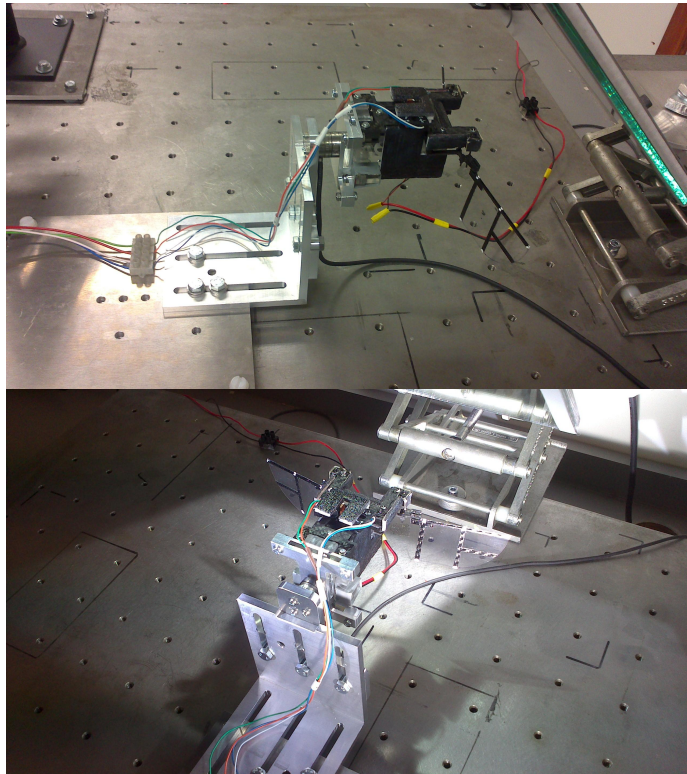


Figure 4.50: *Photograph of FR Setup at 90 Degree Body Inclination with 60 mm Wings (WT<sub>4</sub>)*

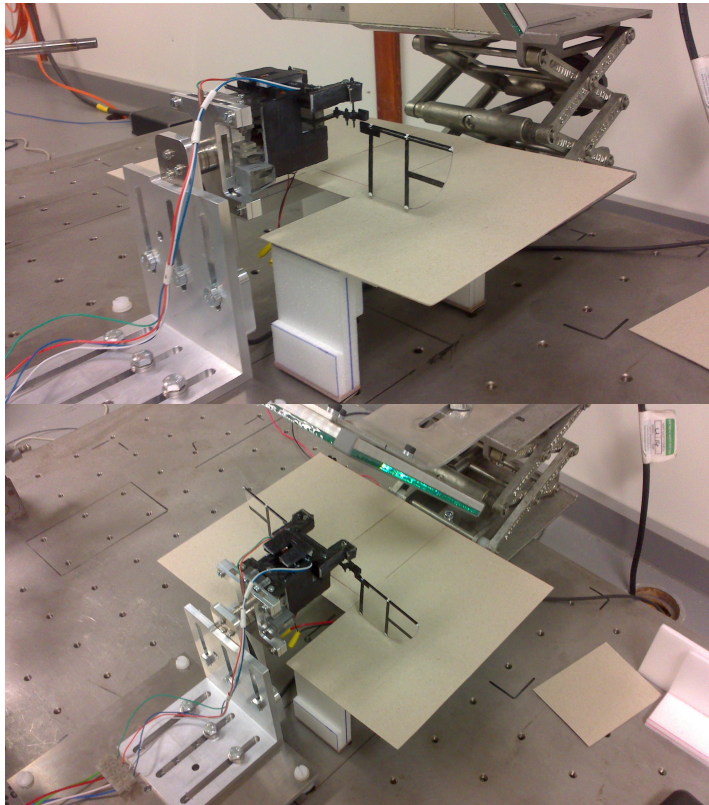


Figure 4.51: *Photograph of FR w/GE Base Setup at 90 Degree Body Inclination with 60 mm Wings (WT4)*

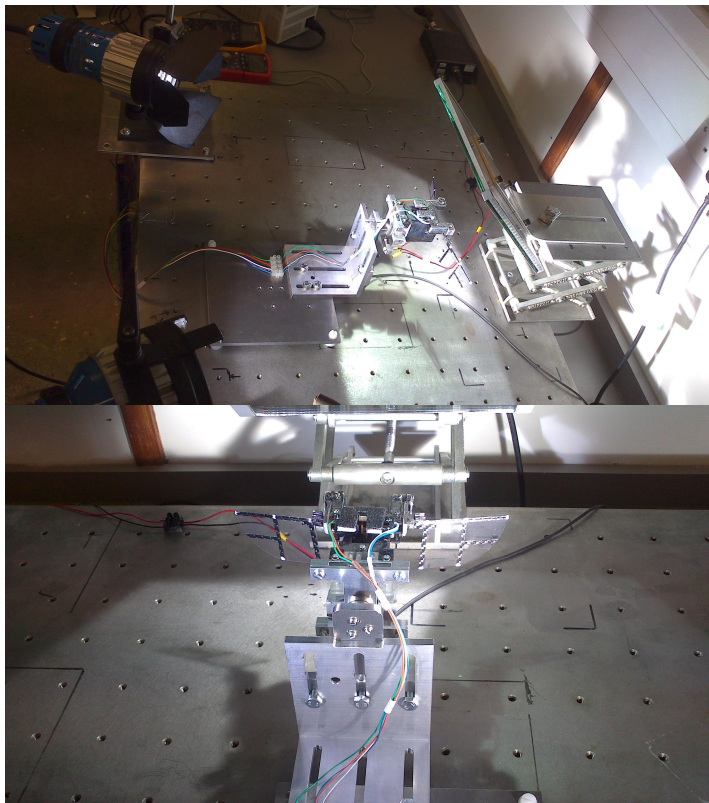


Figure 4.52: *Additional Photographs of FR Setup at 90 Degree Body Inclination with 60 mm Wings (WT4)*

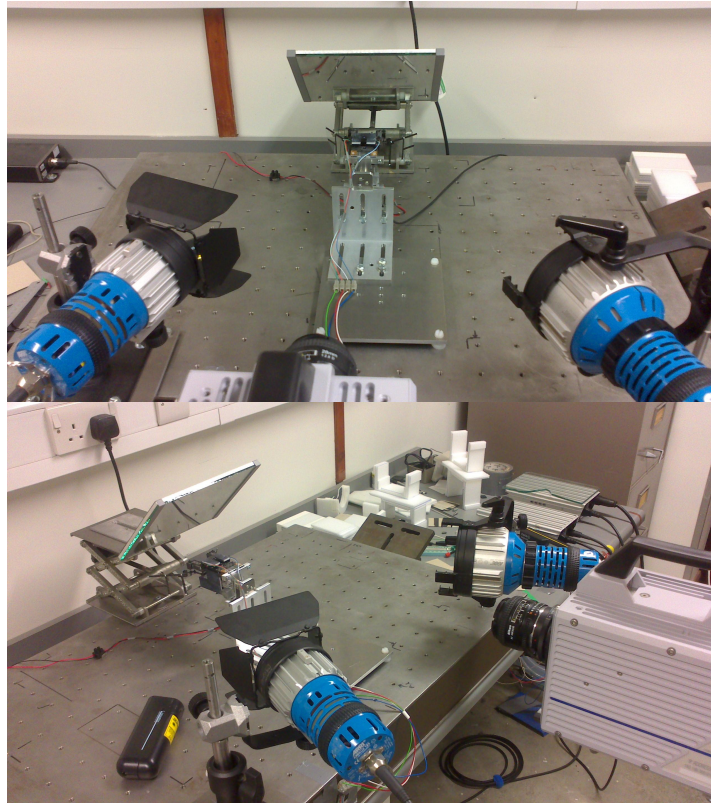


Figure 4.53: *Photograph of Model 2 Setup at 90 Degree Body Inclination with 60 mm Wings (WT4)*

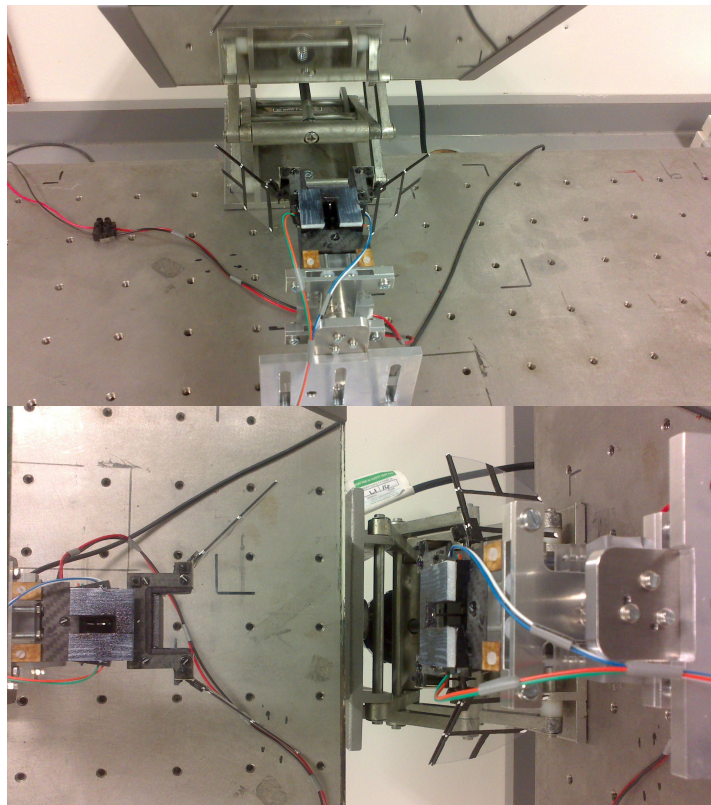


Figure 4.54: *Photograph of Model 2 Setup at 90 Degree Body Inclination with 60 mm Wings (WT4) with Mirror Reflection View*

Figures 4.49 and 4.50, consist of photographs showing the hovering experimental setup. A mirror was placed at 45 degrees above the wings of the FW model with the camera aligned to it so the entire wing motion can be captured and analysed. The top half of Figure 4.49, provides an insight of the lab used for these experiments. The HS camera was placed on a tripod with a lockable horizontal guide a certain distance away from the model. The mirror was placed on a vertical traverse to accurately position the height of the mirror above the model, the horizontal distance could also be adjusted using the guide slot cut out on the aluminium mirror mount.

The physical representation of the experimental rig is an excellent replication of that designed, evidently seen by the comparison of Figures 4.47 and 4.49. The boundary designs required small alterations such as height and location from the wing. Boundaries were placed around the model, as the model could not be moved during a set of experiments. Figure 4.51, demonstrates the GE boundary placed in the vicinity of the model in a GE base arrangement. Comparison of all the results is found in the results section.

Model 2 (capable of asymmetrical) flapping is shown in Figures 4.53 and 4.54 in its experimental arrangement. For these experiments the camera had to capture the wing motion of both wings due to its asymmetrical flapping. The experimental setup is exactly the same as that used for model 1, and both symmetrical and asymmetrical tests were performed on this model. Comparisons of the wing motion and test results can be found in the results chapter. The bottom picture in Figure 4.54 shows the difference in stroke positions for both sides when in an asymmetrical configuration, this is the view seen by the mirror inclined above the wings. No boundaries were used in these investigations as these tests were designed to solely explore the affect of the asymmetrical nature on the forces/torques produced when compared to its flapping configuration. Applying boundaries would have complicated matters even further, and such investigations can be performed as part of future research.

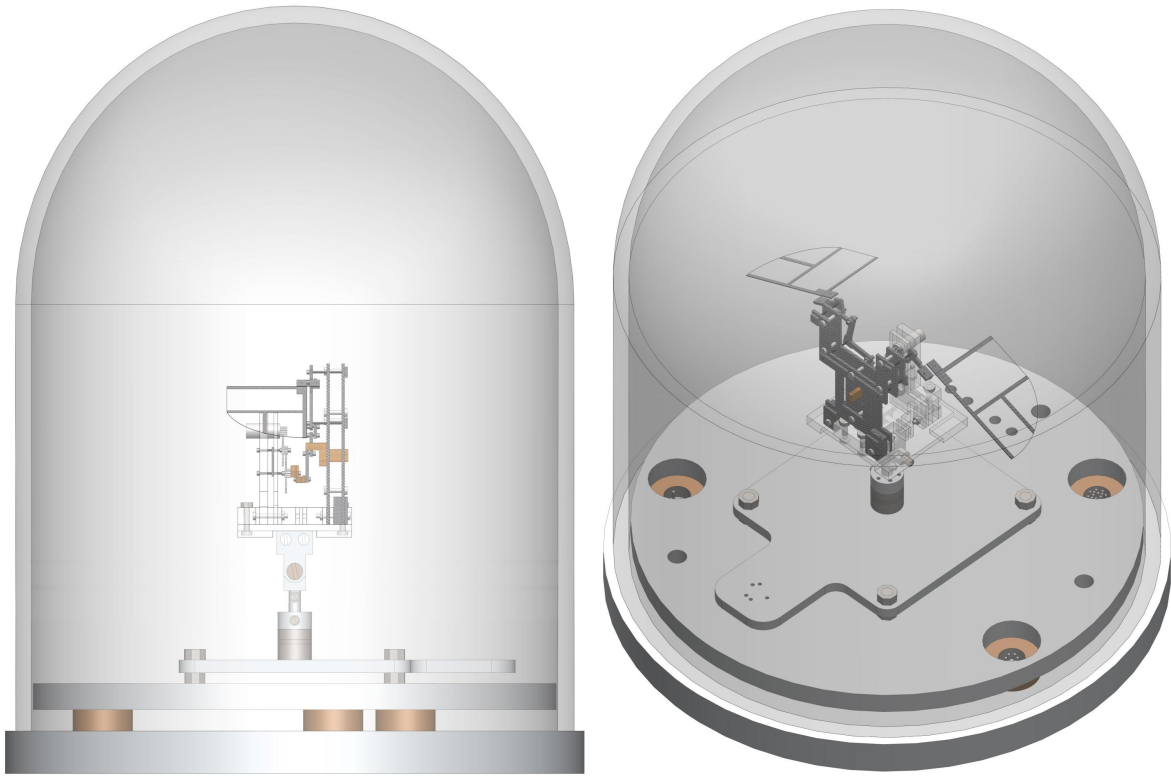


Figure 4.55: *Vacuum Chamber Setup with Model at 0 Degree Body Inclination with 60 mm Wings (WT4)*

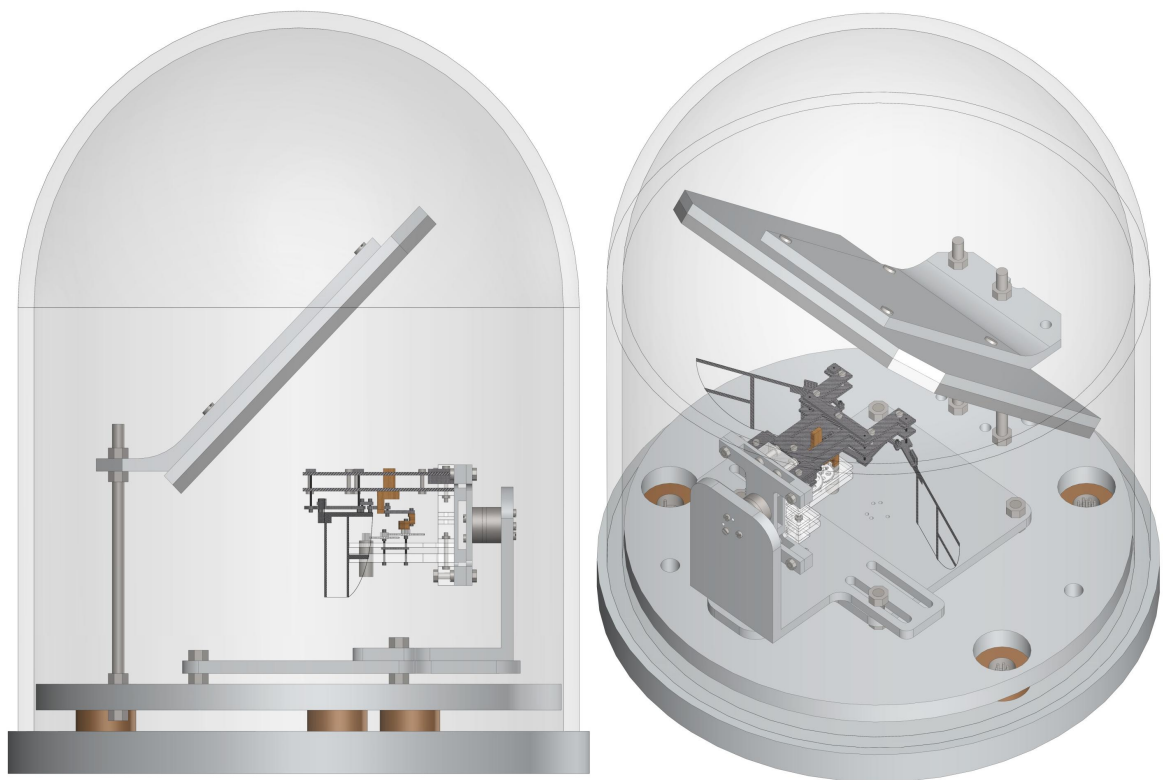


Figure 4.56: *Vacuum Chamber Setup with Model at 90 Degree Body Inclination with 60 mm Wings (WT4)*



Figure 4.57: *Photograph of Vac Chamber with Model at 0 Degree Body Inclination with 60 mm Wings (WT4)*



Figure 4.58: *Photograph of Vac Chamber with Model at 90 Degree Body Inclination with 60 mm Wings (WT4)*



Figure 4.59: *Photograph of FW Model Flapping (Top) and Vac Chamber with Photography Equipment (Bottom)*

CAD diagrams and photographs of the vacuum chamber setup have been shown in Figures 4.55, 4.56, 4.57 and 4.58 respectively. As aforementioned the setup in the vacuum chamber and air utilised almost the same equipment. The setup in the vacuum chamber is a direct replication of that used in air tests. Due to space restrictions some parts in the experimental rig such as the base for the F/T sensor had to be re-designed, but this does not affect F/T measurements as the base connects on the mounting side of the sensor and moreover its role is solely to provide a rigid foundation. All components stationary or dynamic placed within the chamber were not touching the glass bell jar. The bell jar was also continually checked for cracks during test intervals to reduce the risk of implosion.

When the model was placed in the vac chamber setup initial tests were performed in the air and the results

were compared to previous air test results to maintain accuracy. The aforementioned was carried out for 0 deg and 90 deg inclination tests. Thereafter, the model was placed under vacuum conditions and this set of tests could commence. A mirror placed in the vacuum chamber for hovering experiments, inclined at 45 deg above the wings within a confined space meant that its positioning would become more intricate, to assist with this the mirror mount was placed between two M6 nuts along two threaded rods which was a method adopted to act like a vertical traverse. A large mirror was needed to view the wing motion for both wings when testing the asymmetrical configuration of Model 2, this has been shown in the CAD diagrams and photographs. Ideally a larger vacuum chamber could have been used for these experiments where the fitting of all components shown may have been easier and in simpler terms not so tight, however as this chamber was readily available at the university it was more feasible in monetary terms to use this piece of equipment.

The mirror was aligned to the wings at mid-stroke position in view of the camera via a laser pointer. Although very satisfactory wing motion images were obtained using the single light source, an additional light source would have been beneficial due to the vacuum guard placed above the bell jar. Some additional photos have been shown in Figure 4.59, the top picture shows the FW Model performing a flapping motion, the bottom picture shows the model enclosed by the bell jar and guard. Both the light and camera were placed on tripods which were bolted down to the ground to prevent any movement of the tripods.

## 4.4 Wing Kinematics Measurement

As aforementioned the wing kinematic motion was recorded using a HS camera, thereafter the images can be analysed to determine the position of the wing during a flapping cycle and also its AOA. To determine the wing position the white dots which were marked on the wing can be tracked via software ( $\mu$ ETA, for more information see (Beta CAE)) or manually. For many images the software cannot complete the task of tracking the wing AOA, this is due to the dot disappearing during certain parts of wing rotation and rather than predicting the position of the dot for this short period the tracking program aborts. However, selecting specific pictures to be processed via software and processing the remaining manually for wing kinematic positioning the task of finding the flapping and AOA angles becomes easier and more efficient. The measurement uncertainty as previously mentioned in chapter 3 can be taken as  $\pm 2$  degrees, as the size of the dot is fairly significant and measuring via software manually and automatically matched well. As a dot is monitored and measured for a dynamic wing this level of uncertainty seems reasonable and should be within the acceptable tolerance given the nature and complexity of these experiments.

Once the wing kinematic angles have been extracted from the images the displacement curve can be plotted according to time. Furthermore the velocity and acceleration of wing kinematics can also be determined and examined against the F/T measurements. The wing motion kinematics will determine the amount of lift and thrust produced, along with any moment created throughout the cyclic wing motion. The axis of wing motion is the same as that shown in Figure 2.5, where flapping is about the X-axis, pitch about the Z-axis and out of plane deviation about the Y-axis.

As the MAV in this experiment produces an AOA via passive wing rotation, it is vital that the motion is analysed thoroughly for each experiment to understand the effect the polyester thickness, and length has on the wing rotation and also the approximate timings for enhancing F/T values. Optimising the wing rotation is key to producing better F/T measurements during flapping motions, however this is not a trivial task when using a passive wing rotation feature. For this exercise only the wing kinematics are analysed to understand the motion created under passive conditions.

An appropriate method to determine the wing AOA produced for different Mylar thickness's and lengths was to experimentally test them and examine the images. The kinematic results were then compared to determine the preferable option. Also small differences in the kinematic angles did not affect the F/T measurements

significantly which was a beneficial factor as small differences can occur when using the passive wing rotation method. The camera was always pointed directly at the wing, as the wing barely deviates out of position we can assume the leading edge of the wing is always in plane with the camera lens. Any small deviation is taken as negligible especially when compared to the flapping or wing rotation angles. As shown in Figure 4.60, the camera was pointed at the wing and remained in this position for all the tests to obtain accurate comparable images.

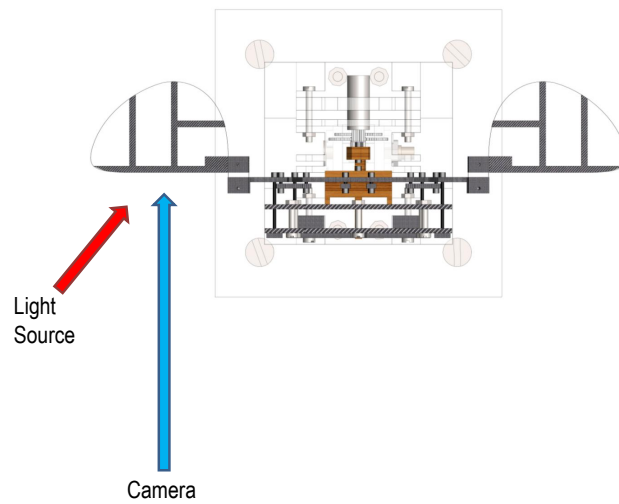


Figure 4.60: *CAD of Camera and Light In-Line With Wing*

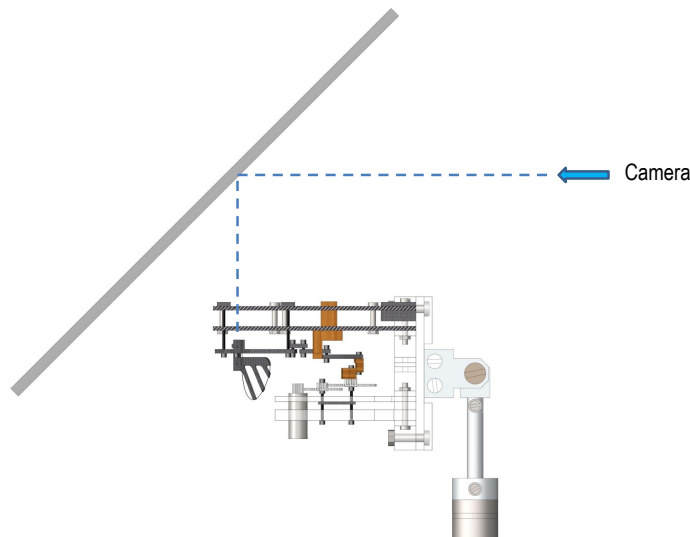


Figure 4.61: *CAD of Camera In-Line With Mirror Above Wing*

Figure 4.61, shows a diagram of how the camera was lined-up for hovering tests. The camera was pointed towards the mirror which was placed at a 45 degree angle directly above the wing. Using this method the camera is still in plane with the wing as it is pointed to a mirror inclined above the wing which views the entire wing motion. The wing kinematics can vary immensely due to inertia, in general it is desirable to use a very light wing which is flexible but this would obviously complicate things further, as wing deformation and leading edge bending would also need to be considered which would also affect F/T measurements. Thus, to simplify matters somewhat, semi-rigid and full rigid wings were used for these experiments. Beyond wing rigidity other factors could also affect wing rotation most of which have already been mentioned earlier in this chapter. The purpose of this preliminary study is to understand passive wing rotation for different inertial effects such as rigid and semi-rigid wings, in addition to, different thickness and exposed area of mylar for passive wing pitching. Thus, the preliminary study is to focus on wing motion under different conditions prior to looking at other types of measurements which are described in the experimental results chapter. The 26 mm (wing types 1 and 2) singular span wings have only been utilised for this kinematic analysis, they have not been discussed in the results presented in chapters 5 or 6.

A flapping and rotation motion for 26 mm semi-rigid wings using 50 microns thickness Mylar and an exposed flexible area of 1.5 mm is shown in Figure 4.63, where time has been shown in a non-dimensional format. The downstroke motion is shown on the left and proceeds to the upstroke motion, denoted as D and U respectively next to the non-dimensional time. As this was a preliminary test the white dots were not marked on the wings at this point. However, the kinematics of the wing can still be acquired (although this is more time consuming as manual methods are utilised) and provided a good starting point for experiments to understand the passive motion at the start of the experiments. Figure 4.62, displays the regional halves for positive and negative AOA when the wing pitches under passive conditions.

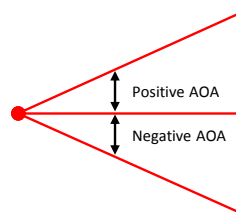


Figure 4.62: *Wing Angle of Attack for Positive and Negative Halves (Circle Represents Leading Edge)*

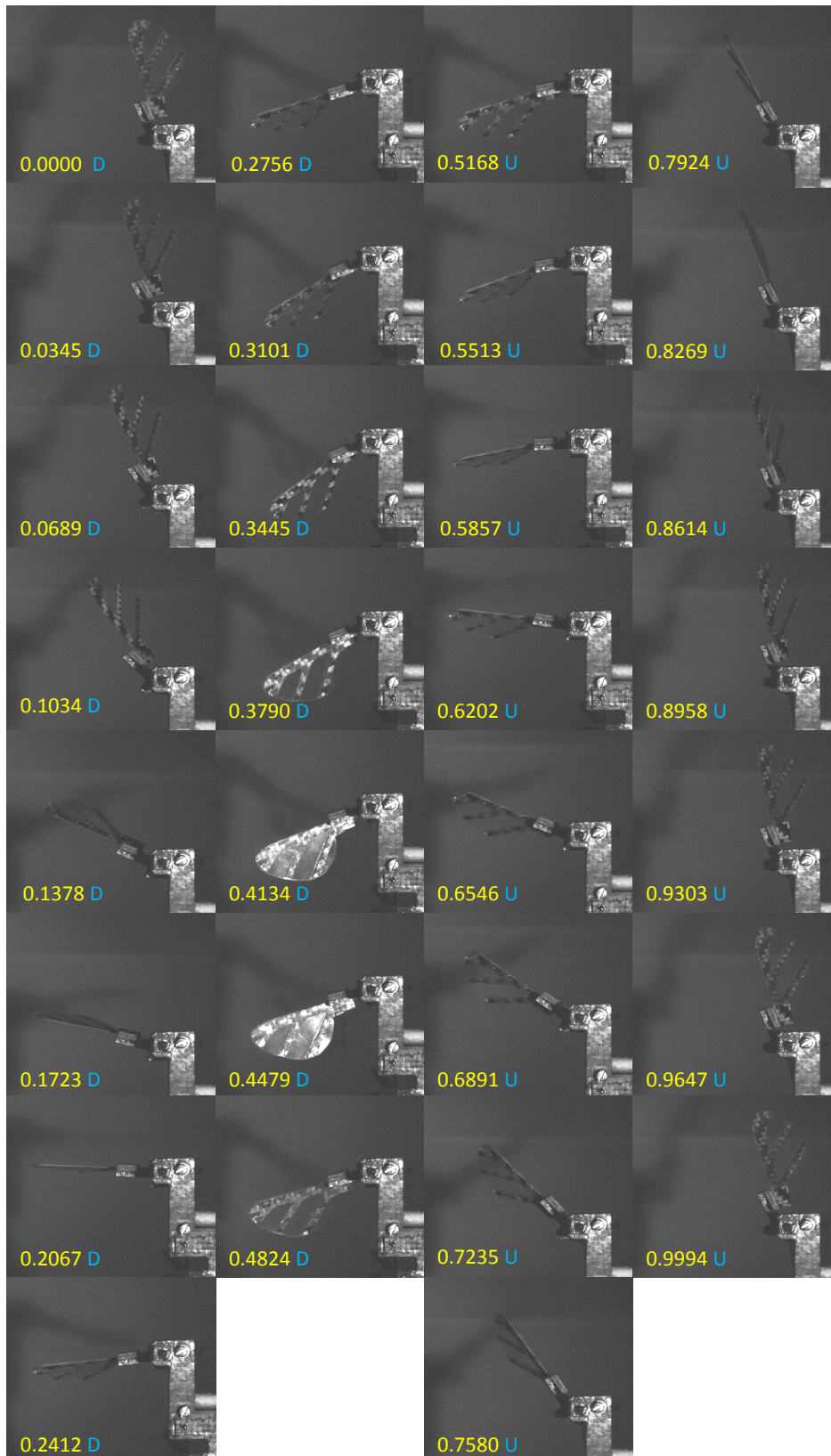


Figure 4.63: *Wing Motion for 26 mm Semi-Rigid Wings (WT2) 50 microns 1.5 mm exposed flexible area, Vertical Stroke Plane, D: Downstroke and U: Upstroke*

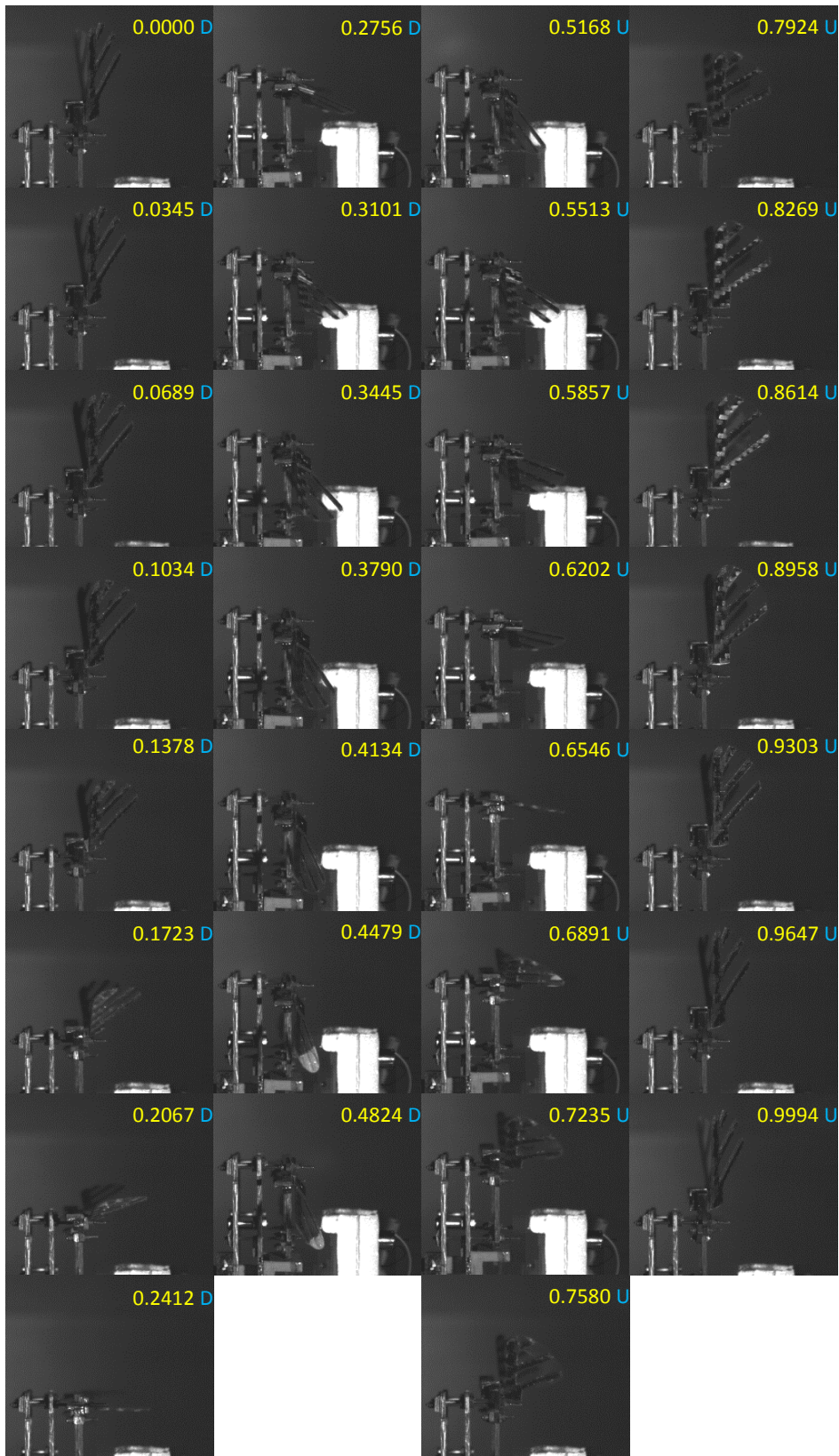


Figure 4.64: *Wing Motion for 26 mm Semi-Rigid Wings (WT2) 50 microns 1.5 mm exposed flexible area Side View, Vertical Stroke Plane, D: Downstroke and U: Upstroke*

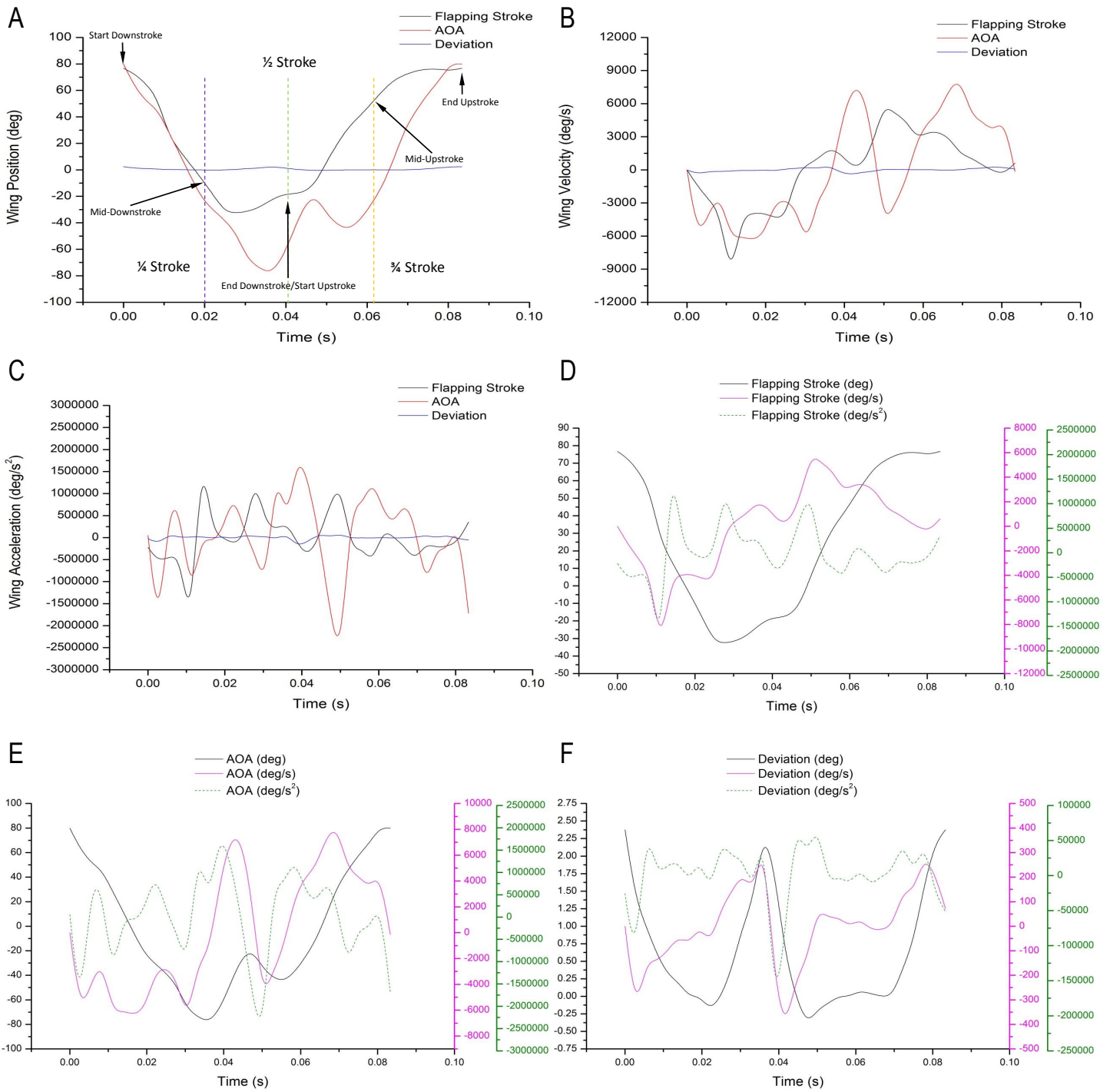


Figure 4.65: *Wing Kinematic Data for 26 mm Semi-Rigid Wings (WT2) 50 microns 1.5 mm exposed flexible area; A:Wing Displacement Plot; B:Wing Velocity Plot; C:Wing Acceleration Plot; D:Flapping Stroke Plot; E:Angle of Attack Plot; F:Deviation Plot*

Figure 4.63, displays a flapping and passive wing rotation motion for a 26 mm span semi-rigid wing (WT2), which was set to flap at 12 Hz. These images provide data for the flapping stroke angles, velocity and acceleration. In addition the same data can be extracted for the angle of attack. These tests were carried out primarily to examine the wing motion and understand the behaviour of wing rotation under passive conditions. Inertial forces have a significant impact on the passive wing rotation motion and in the long term will also affect the condition of the mylar. However, from numerous tests it was concluded that the condition is not affected to the extent where the mylar would only last tens of cycles but to the extent that it would last up to hundreds to even thousands of flapping cycles.

The images in Figure 4.63 show the wing performing a downstroke motion (starting from the images on the left side) and this later progresses to an upstroke motion (shown in the images of columns 3 and 4) to complete a cycle. At the start of the downstroke motion, the wing angle of attack is at its peak position. As the wing continues its downstroke the angle of attack now starts to decrease and reaches 0 degrees at the same time when the flapping stroke angle is 0 degrees at mid-downstroke position. Inertial forces seem to dominate through part of the downstroke cycle, as we would expect the wing to remain at a positive angle of attack at the mid-downstroke position. The angle of attack continues declining falling into the negative AOA region and near to end downstroke position the wing has its peak negative AOA. During the start of the upstroke portion of the cycle, the wing angle of attack is rotating in the opposite (positive) direction to decrease the negative angle of attack. As the wing reaches end-downstroke position the AOA is highly negative and bends inwards compressing the mylar (bending it into an uncomfortable position) which it then reacts to by flicking out of this position during the initial stages of the upstroke motion. This is due to the small exposed flexible area selected and thickness of mylar (for such a small exposed flexible area a thinner mylar may have been better but would weaken quicker). A smaller dimension for rotation causes this type of rotation as opposed to the images for the tests performed in Figure 4.71 which has a much larger exposed flexible area and abrupt reactional rotations are not noticed. In addition, a small reactional rotation may occur due to the sudden change of direction caused by the upstroke motion causing a slight jerk reaction on the passively rotating wing. The aforementioned only lasts for a very brief period as the AOA remains negative and is actually quite large and gradually rotates back to a positive AOA and peaks maximum positive at the start of the downstroke position. The motion can be more easily interpreted by viewing Figure 4.65A. Without the use of experimental flow visualisation it is difficult to understand the exact behaviour of the fluid around such a wing rotation. Ideally we would prefer the AOA to remain positive

for majority of the time during the downstroke and negative for majority of the time during its upstroke motion. A large stroke amplitude ( $>80$  degrees) is necessary to assist in prolonging the desired angle of attack among many other features related to the mylar properties and wing itself. The stroke amplitude and angle of attack (both peak to peak) produced for the wing motion in Figure 4.63 is 108 degrees and 155 degrees respectively.

Figures 4.65B and 4.65C, illustrate the fluctuation in velocity and acceleration that the wing undergoes during its cyclic motion. The flapping stroke angles should produce a wave similar to a cosine wave, the wave produced in Figure 4.65A approximately represents a cosine wave. If we analyse only a flapping motion a better representation of a cosine wave is produced but due to the passive wing rotation the flapping stroke angles are affected. Notice the elongated period in stroke angles at the same time the AOA undergoes a reactional rotation, these types of passive motions seem to affect the flapping stroke motion. If we could control the AOA via a rotary encoder we could avoid this, but as this is not feasible at MAV scales, researchers need to utilise a passive wing rotation implementation. Figures 4.65D and E, show the flapping stroke and wing rotation evaluations through a complete cycle. Theoretically we would expect to see a symmetrical motion for both down and up flapping strokes, the motion actually produced in reality is somewhat symmetrical and one which would be difficult to predict. The wing rotation is near to impossible to predict with its unorthodox behaviour at certain portions of the wings rotational motion. The accelerations and velocities have large alterations, especially for wing angle of attack, producing various sized peaks throughout the flapping cycle and very rarely maintaining a constant acceleration.

The size of wing deviation is very small from the neutral axis basically near to negligible in comparison to the other two measured angles (stroke and AOA). This is clearly shown in the images displayed in Figure 4.64 and in the wing positioning graph shown in Figure 4.65A. The mylar thickness and moreover the exposed flexible area set between the rigid carbon fibre pieces allow the wing to create its rotation, these are the core factors which determine the deviation of the wing from its original position. An analysis for just the wing deviation can be seen in Figure 4.65F, the maximum deviation produced is 2.63 degrees as this is such a small value we deem it as negligible. The accelerations and velocities show a more or less symmetrical trend for both up and down strokes, a motion that is simpler to follow and much smaller vacillations, however this is immensely due to such small angular movement. The wing kinematics were examined for a few cycles and the data always presented a consistent wing motion from cycle to cycle, if this were not the case the

Forces/Torques would also show an inconsistency.

Figure 4.66, shows the wing motion created with the wing flapping at 12 Hz. The same SR wing has been used but a different mylar thickness was chosen and the exposed flexible area is now 0.5 mm larger. As a thicker mylar was used the exposed flexible area had to be increased in order to try and produce a sufficiently large AOA. A thicker mylar piece was also used to determine whether this would delay the transition of AOA, from positive AOA during downstroke transferring into a negative AOA by the end of the downstroke motion, or even reaching a 0 degree AOA at mid-downstroke position, but as seen in the images this was not the case. Advanced wing rotation is noticed again as the wing reaches end downstroke position, and its also interesting to note that the wing has its peak negative AOA during the end phase of downstroke. In addition during the upstroke phase the wing does not really produce a negative AOA, certainly not one that can be considered as a sufficient AOA. The AOA is more or less zero degrees and seems to vacillate between 0 degrees AOA and positive AOA. Towards the end of the upstroke the acceleration of the flapping stroke along with the reduction in velocity and the wing stopping when it reaches its maximum flapping stroke point are some of the reasons which cause the wing to flick to its maximum positive AOA, the rotation is created as part of the reaction to the changes in flapping motion speed.

Again experimental flow visualisation would help to understand whether the wing interacts with any fluid shed from the previous time the wing was in this same position, and what effect this has on the wings motion. When the wing flicks in this manner due to reasons aforementioned it must overcome the fluid pressure acting on its surface and around its geometry producing a resistance to this motion. Thus sufficient momentum is needed for the wing to rotate as it does in the images shown at end-downstroke and end-upstroke motions. A similar flicking motion is seen in vacuum chamber tests, which validates that this flicking is majorly influenced by the wing flapping mechanical movement, with part influence provided by the fluid surrounding the wing but again experimental fluid visualisation would be needed to understand and analyse the amount of influence the medium has. Data extracted from the images is shown in Figure 4.67, the peak-peak AOA produced is 58 degrees this is rather small compared to the motion shown in Figure 4.63. As this AOA is smaller and less dominating a better cosine wave representation is produced for the flapping stroke angle curve. The flapping stroke velocity also shows a less volatile trend, showing a similar curve to a sine wave. As expected with alternating velocities throughout a cycle, acceleration will be continuously fluctuating. The accelerations of the AOA is also much larger compared to flapping stroke accelerations.



Figure 4.66: *Wing Motion for 26 mm Semi-Rigid Wings (WT2) 75 microns 2 mm exposed flexible area, Vertical Stroke Plane, D: Downstroke and U: Upstroke*

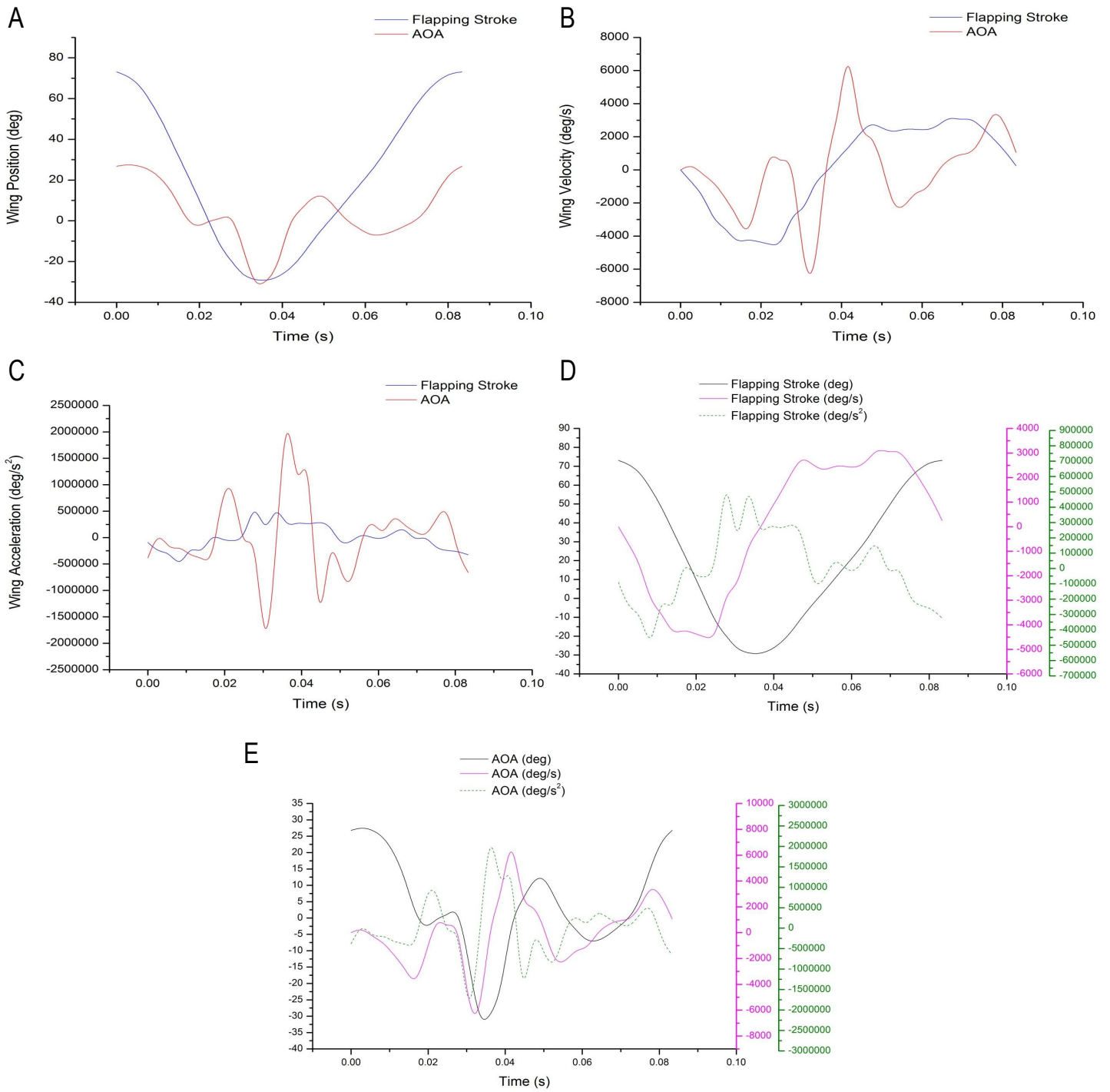


Figure 4.67: *Wing Kinematic Data for 26 mm Semi-Rigid Wings (WT2) 75 microns 2 mm exposed flexible area; A:Wing Position Plot; B:Wing Velocity Plot; C:Wing Acceleration Plot; D:Flapping Stroke Plot; E: Angle of Attack Plot*

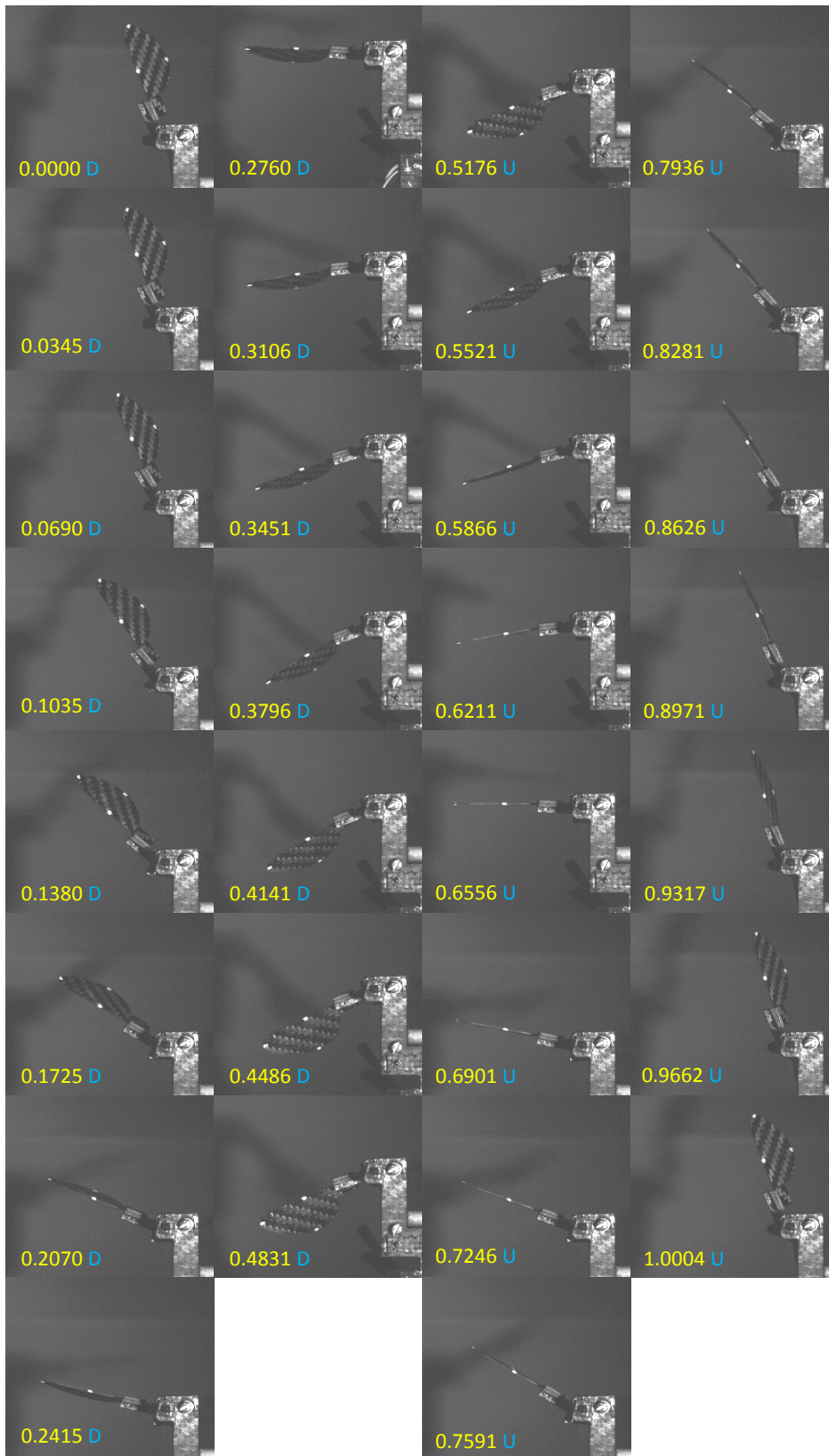


Figure 4.68: *Wing Motion for 26 mm Rigid Wings (WT1) 75 microns 2 mm exposed flexible area, Vertical Stroke Plane, D: Downstroke and U: Upstroke*

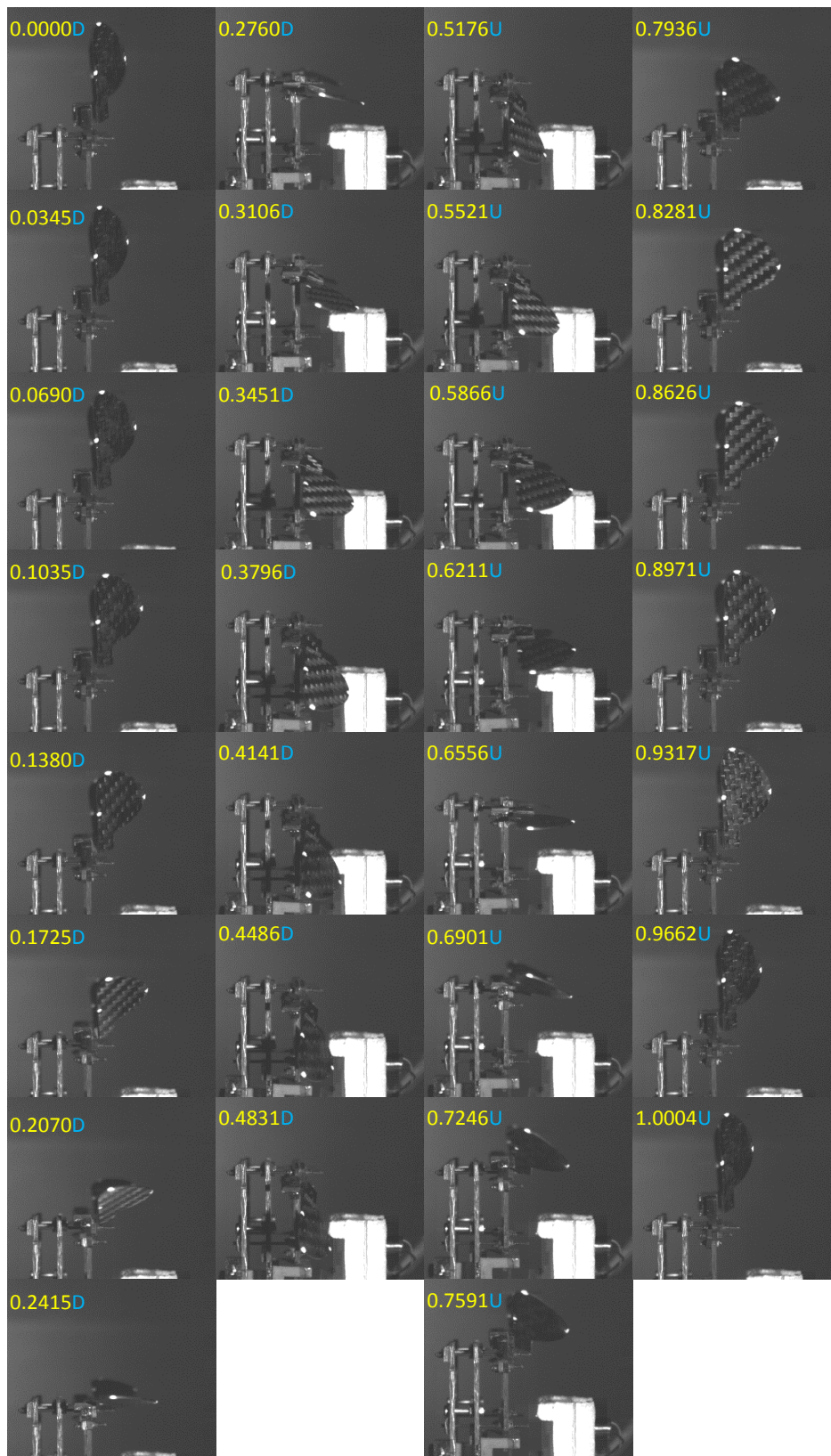


Figure 4.69: *Wing Motion for 26 mm Rigid Wings (WT1) 75 microns 2 mm exposed flexible area Side View, Vertical Stroke Plane, D: Downstroke and U: Upstroke*

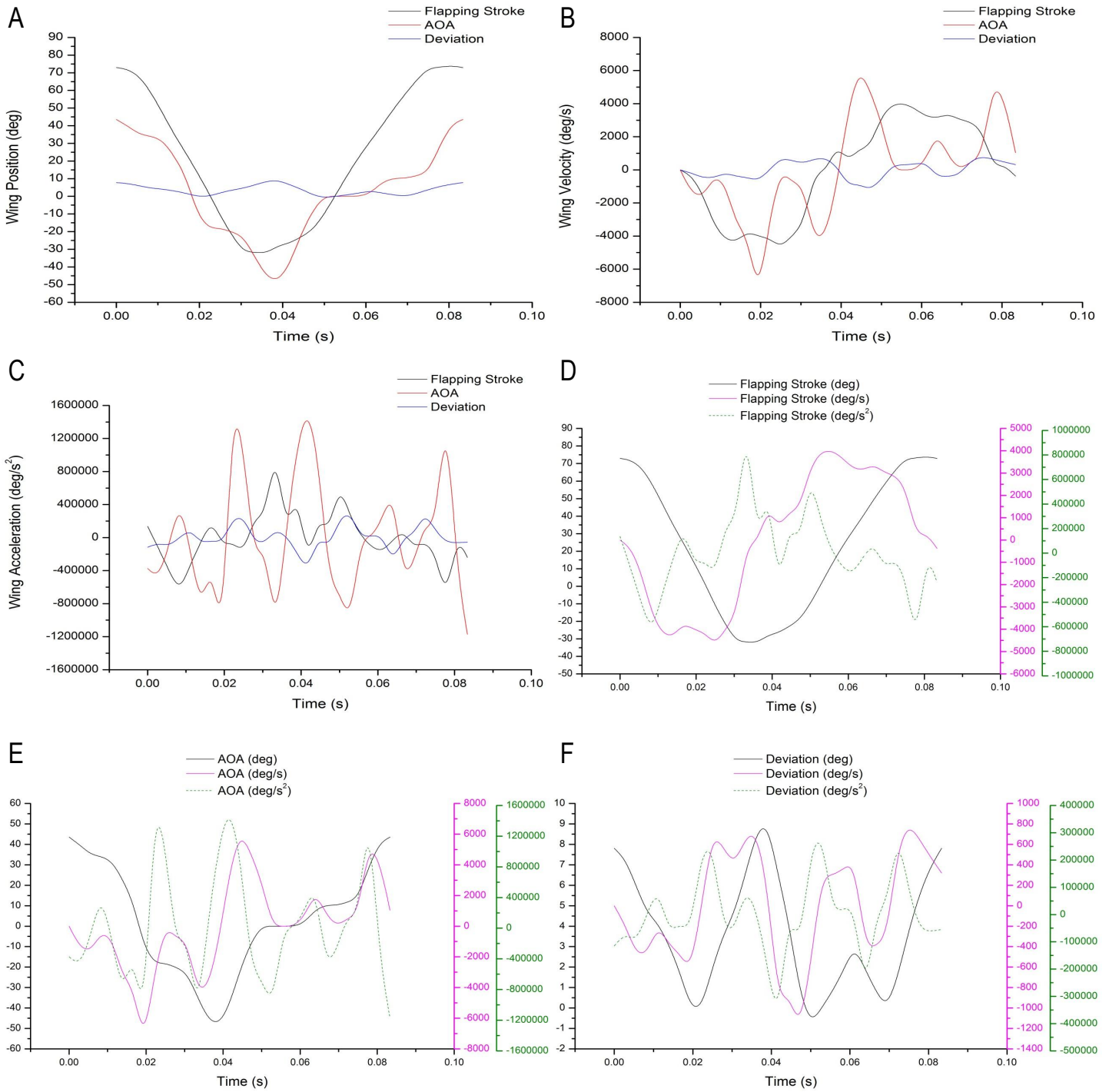


Figure 4.70: *Wing Kinematic Data for 26 mm Rigid Wings (WT1) 75 microns 2 mm exposed flexible area; A:Wing Position Plot; B:Wing Velocity Plot; C:Wing Acceleration Plot; D:Flapping Stroke Plot; E:Angle of Attack Plot; F:Deviation Plot*

Figure 4.68, presents the wing motion for a rigid wing flapping at 12 Hz with a mylar thickness of 75 microns and 2 mm exposed flexible area. This wing has more mass than the previous semi-rigid wing but other than that has the same wing area and aspect ratio. The white dots are tracked via software (can also be accomplished manually) and the kinematic data is output as aforementioned in this section. As previously seen the wing has its maximum positive AOA at the start downstroke position and maximum negative AOA at end downstroke, this relation is also seen in Figure 4.71, which has the same experimental parameters except that a 3 mm exposed flexible area is set for wing rotation. Also in both of these figures the mid-downstroke position has a negative AOA, this is due to the mass of the wing causing an advanced rotation earlier than previous wing motion results (Figure 4.66 ). The upstroke motion remains at a negative AOA for a brief period thereafter gradually rotating to 0 degrees AOA and continually rotates to a positive AOA towards the end of the upstroke motion.

From Figure 4.70, the flapping stroke angle seems to follow a cosine wave as expected, and as mentioned above the AOA is more or less zero for certain sections during the upstroke motion. The flapping stroke velocity moderately resembles a sine wave like trend (with numerous vacillations), with acceleration continually alternating in relation to velocity. The AOA velocity seems to continually fluctuate as would be expected from the various changes in wing AOA position throughout the cycle, and the acceleration resembles this behaviour as well. Figure 4.69 displays the images of wing deviation that produces angular movements of 9.5 degrees (max-min), which is significant considering the exposed flexible area for wing rotation is only 0.5 mm longer than test results reviewed in Figures 4.64 and 4.65. With the wing deviation continually changing and producing considerable distances from its original position (mainly in the positive directions as it rotates inwards when creating an AOA), the velocity and acceleration plots now show more of an erratic behaviour.

A similar outcome is also shown in Figure 4.72F, but the max-min deviation is much larger with a value of 23.5 degrees. This is a very large wing deviation from the original position and one that should be reduced if possible as very large deviations could produce some inaccuracies in AOA measurement (as the AOA is measured from a 2D image). This comparison test was carried out solely to demonstrate the effect a large pitching gap (exposed flexible area) would have and such large deviations would also cause damage to the mylar, deteriorating its condition faster as the wing is now swinging passively around 2 axes considerably and quite aggressively as well. The deviation of 9.5 degrees is very small compared to both the flapping

stroke and AOA amplitudes, thus we can view this as an acceptable deviation angle and as its a natural effect which is coupled with passive wing rotation there is nothing that can be done to prevent this motion, when such a pitching technique is exploited.

However, having said the above the AOA positioning of the wing seems more symmetrical for down and up strokes from the images in Figure 4.71 and observing the plots shown in Figure 4.72. The AOA resembles a cosine wave and this is reflected in a more organised velocity plot with a max to min of 150 degrees. Nonetheless, keep in mind that these wing AOA positions are not as accurate as has been seen in the previous images and plots due to such large deviations occurring in this test. The flapping stroke plots shown in Figures 4.70D and 4.72D, seem fairly similar but the 3 mm exposed flexible area tests produce a larger stroke amplitude of 132 degrees compared to 106 degrees for the 2 mm tests. The 3 mm test creates a larger stroke amplitude due to its larger exposed flexible area which is set for the purpose of wing rotation but in this enhances the stroke amplitude as well.

The images for front and side views were not recorded simultaneously as only 1 camera was available and a mirror configuration was setup at a later time. But this does not produce very sharp images as the larger image needs to be captured with the lens focusing on one location so the view which the lens does not have full focus on is slightly blurred. These tests were primarily done to capture and analyse wing motion, and due to the triggering method aforementioned the images can be matched using this as the start position is always the same, thus matching both sets of images is quite simple. This method cannot be used when recording force measurements as we need to ensure that the model or experimental rig should not be moved.

To summarise this section of wing motion analysis a direct comparison has been shown for all three angular motions and the tests considered in Figure 4.74 . The flapping stroke trend seems to be very similar for all the tests with small differences. The AOA plots seem to vary especially for the test which used a semi rigid wing with a 75 micron thickness mylar consisting of a 2 mm exposed flexible area. This trend produces much smaller AOA positions as discussed previously, and its actually quite similar to the rigid wing tests performed with 75 micron thickness mylar with 2 mm exposed flexible area for rotation. The AOA amplitudes for both SR 50 micron 1.5 mm exposed flexible area and rigid 75 micron 3 mm exposed flexible area are very similar, and the main difference in the curves is when the 1.5 mm exposed flexible area test experiences a reactional rotation during the start of the upstroke motion. The wing deviation plot shown seems to follow an obvious pattern and as the set distance for rotation increases, the deviation also increases producing large deviations

at the start and end of strokes. The 3 mm exposed flexible area test produces a fairly larger rotation at the end of downstroke motion as opposed to the start of downstroke.

A comparison of the wing deviation path has been shown for 2 mm and 3 mm exposed flexible area tests in Figure 4.74, which presents the deviation in different units to portray the horizontal displacement of the wing from its original position. The 3 mm exposed flexible area test clearly deviates much more than the 2 mm exposed flexible area test performing a skewed and irregular figure of '8' motion. Images have been shown in Figure 4.73 of the wing deviation tracked through a complete cycle, the white dot located at the edge of the wing tip is tracked and its path has been shown in green. The velocity plot is also shown in the adjacent diagram demonstrating the change in velocity where maximum velocity occurs in the mid region of the stroke (shown as orange) and minimum velocity occurs at the start or end of the stroke (shown as purple). In order to reduce wing deviation for factors stated above less than 3 mm exposed flexible areas were set to allow for passive wing rotation, small deviations would occur but this natural motion cannot be avoided when using a passive wing rotation, it can merely be reduced.

Although certain characteristics of the wing motion observed in the 0 degree body inclination experiments are rather expected seeing as natural forces would pull the angle of attack downwards (creating a negative AOA) before the end of downstroke motion and it is likely to remain in this downward state for a while. Thus, it should be borne in the mind that these experiments need to be carried out in order to understand what the actual effect is and what the outcome will be from such circumstances. A passive wing rotation flapping in this configuration at 0 degree body inclination, or any other body inclination angle is important to explore as FWMAV designers understand that the vehicle may be forced to change body inclination angle during flight. In some situations the FWMAV may need to change body inclination to fit through a small gap or continue flying through an area with confined space. Thus, dependent upon the geometry of the model it may be more suitable to alter body angle.

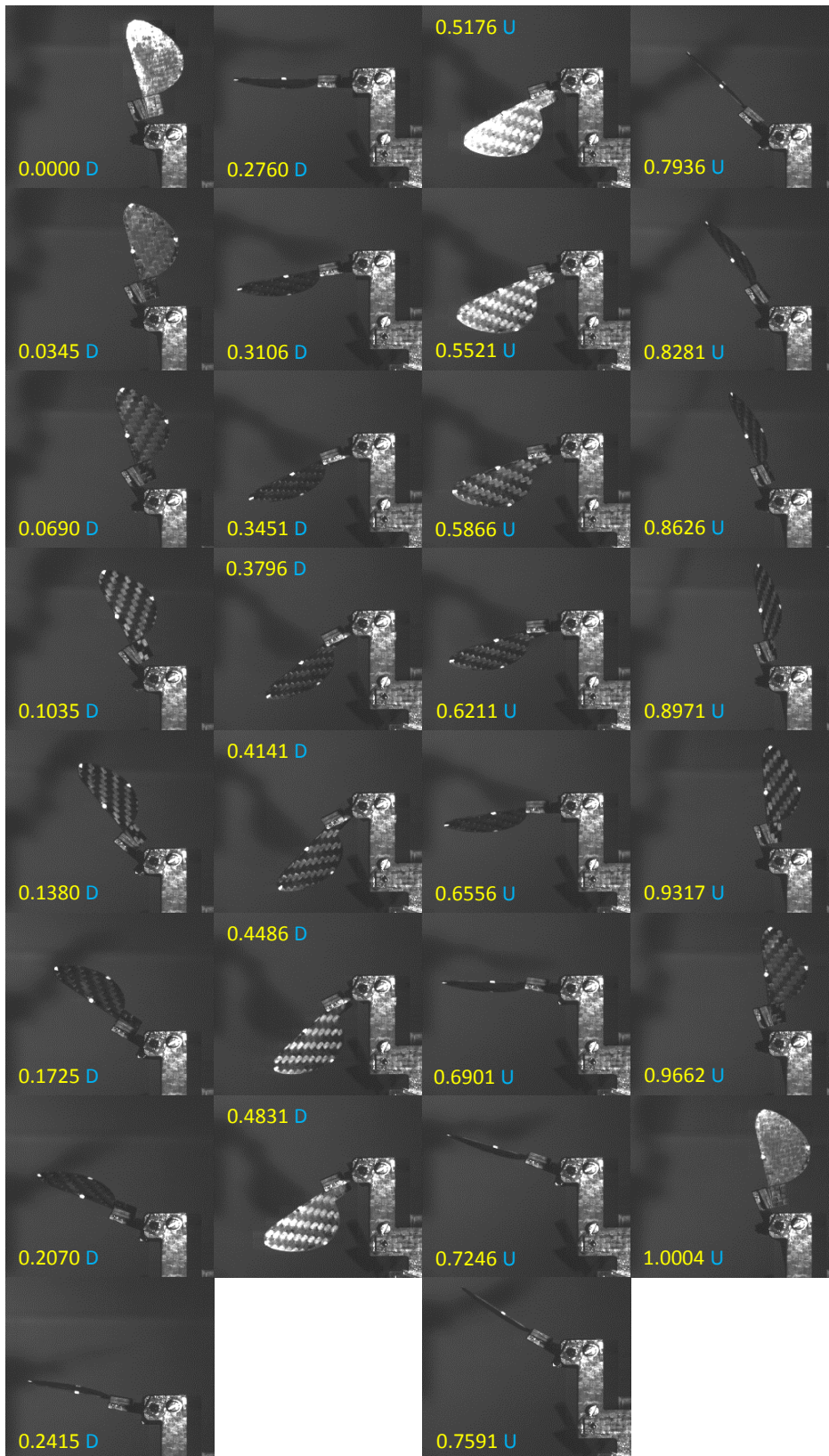


Figure 4.71: *Wing Motion for 26 mm Rigid Wings (WT1) 75 microns 3 mm exposed flexible area, Vertical Stroke Plane, D: Downstroke and U: Upstroke*

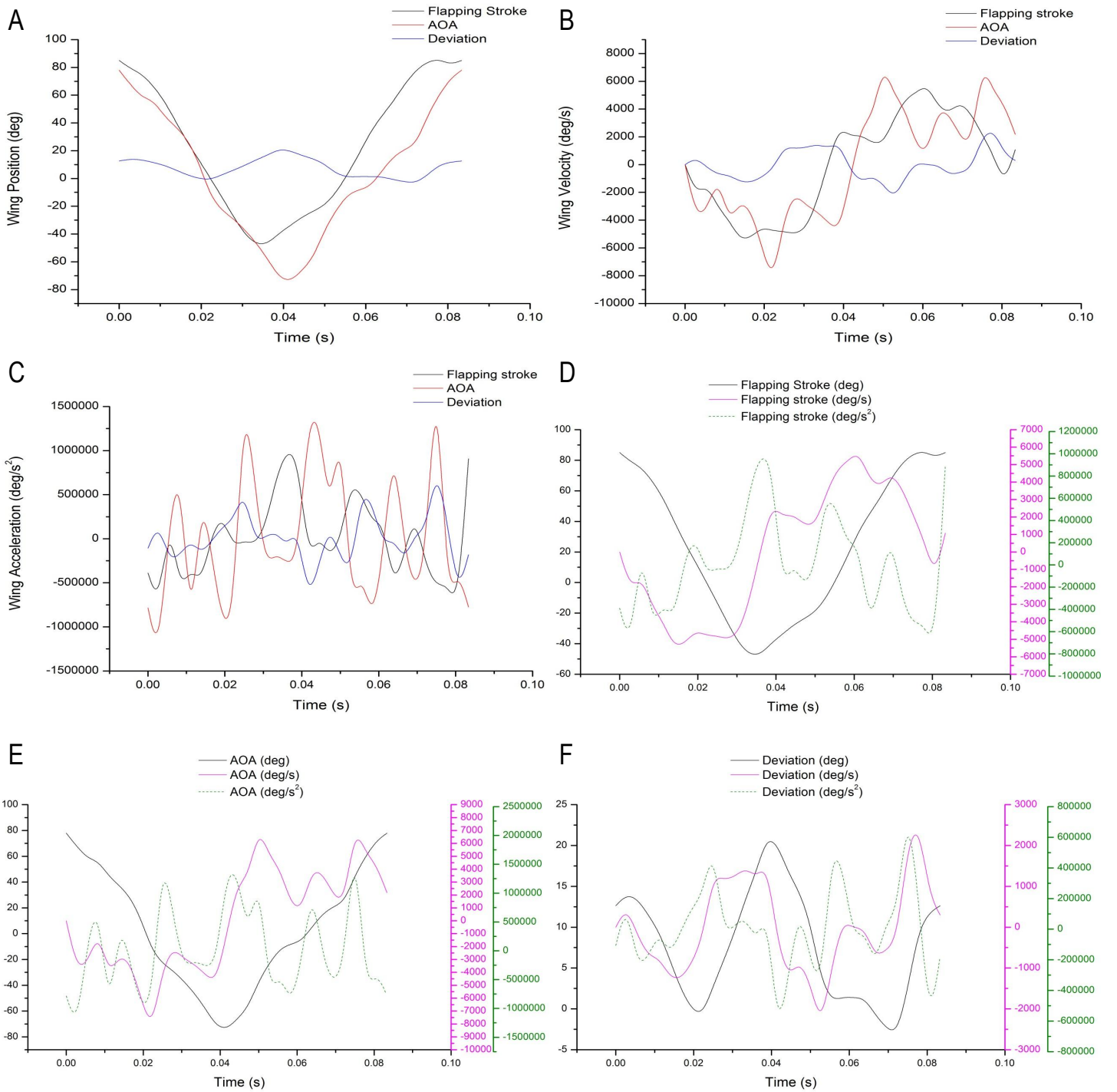


Figure 4.72: *Wing Kinematic Data for 26 mm Rigid Wings (WT1) 75 microns 3 mm exposed flexible area; A:Wing Position Plot; B:Wing Velocity Plot; C:Wing Acceleration Plot; D:Flapping Stroke Plot; E:Angle of Attack Plot; F:Deviation Plot*

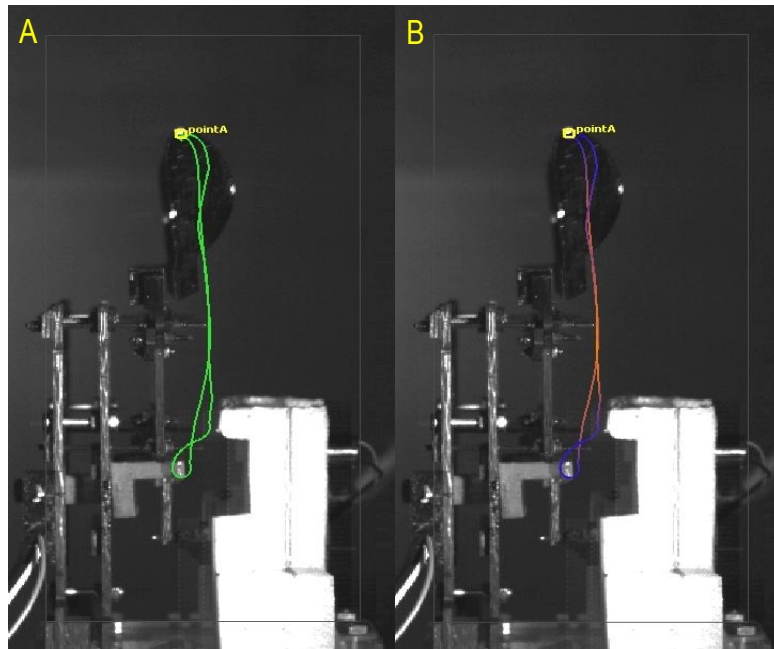


Figure 4.73: *Rigid Wing Deviation Trajectory 75mic 2 mm exposed flexible area; A:Deviation with Tracking Path; B:Deviation with Velocity Path*

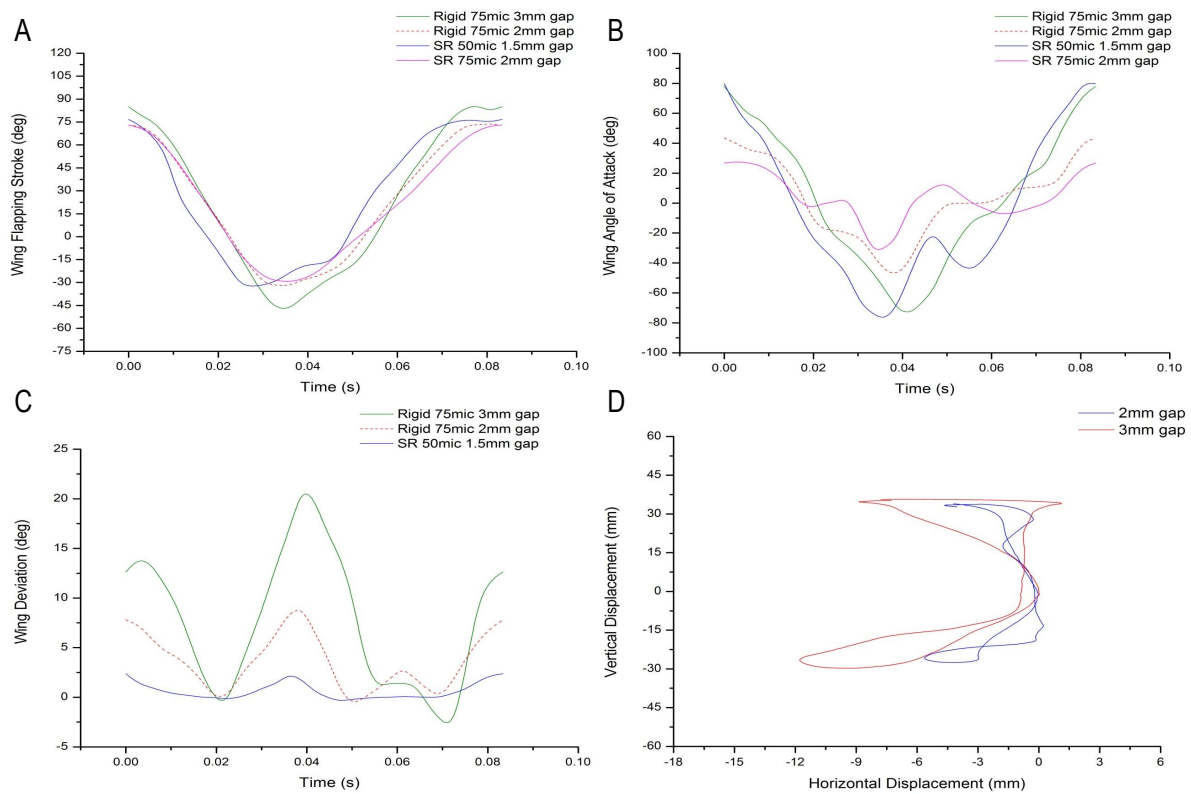


Figure 4.74: *Wing Movement Comparison for Various Mylar Thickness's and Lengths; A:Flapping Stroke Plot; B:Angle of Attack Plot; C:Deviation Plot; D:Deviation Motion Plot*

## Chapter 5

# Simulation Results

This fifth chapter expounds on the CFD investigations carried out for a single wing dynamically moving in a time dependent manner through an initial stationary fluid. Firstly a drosophila wing is modelled performing a hovering motion for which the results are compared to experimental and computational data from literature. Following this, a complete investigation is performed for a set of cases involving a rectangular wing travelling through the fluid in hovering mode where it flaps along the horizontal plane. And lastly, the 60 mm experimental wing (WT4) has been modelled performing a flapping only motion at 5 Hz, for which the experimental data from this thesis is compared to this simulation case.

Along with spatial discretisation, due to the nature of this analysis temporal discretisation is also a prerequisite in order carry out the transient simulations. In the current CFD study, the mesh density around the wing is clustered with a substantial amount of cells compared to the outer domain, to analyse and focus on the flow physics around the wing which is the area where rapid changes of the dependent variables would occur.

The Navier-Stokes equations which govern the flow of fluid are applied to the entire computational domain, where for example within this domain there could exist a body for which initial specifications are provided in the general form known as boundary conditions. The continuity and momentum equations which govern fluid flow are shown in Equations 5.1 and 5.2. For example, a spherical ball placed within the computational domain will cause the fluid to flow around it, as a boundary condition is put in place stating that fluid

cannot flow through this object, in addition to the application of the no-slip condition on the surface of the spherical ball. The determination of numerical solutions per cell are found by solving the set of equations per cell, where the solution is also influenced by its neighbouring cells (relating to the importance of a grid), thus the resultant of each cell will be dependent on its location within the computational domain. The flow is assumed to be incompressible in the entire numerical domain, which is sufficient as stated in (Anderson 1986), that flows with a Mach number of  $<0.3$  are treated as incompressible. For further information see (Ferziger & Peric 2002).

$$\frac{\partial \rho}{\partial t} + \nabla \bullet (\rho v) = 0 \quad (5.1)$$

$$\frac{\partial (\rho v)}{\partial t} + \nabla \bullet (\rho v v) = -\nabla p + \nabla \bullet (\bar{\tau}) \quad (5.2)$$

A commercial CFD software (Ansys Fluent) which utilises the finite volume discretisation methodology to solve the incompressible form (Equations 5.3 and 5.4) of the governing fluid dynamic equations was employed to investigate the fluid dynamics of flapping wings. Fluent consists of two numerical models of which the pressure based solver was utilised for these simulations.

$$\nabla v = 0 \quad (5.3)$$

$$\frac{\partial v}{\partial t} + \nabla \bullet (v v) = \nu \nabla^2 v - \nabla \frac{p}{\rho} \quad (5.4)$$

The governing equations are solved in a sequential fashion within the pressure based solver utilising a segregated algorithm such as Pressure-Implicit with Splitting of Operators (PISO). In order to obtain the solution at each time step, the equations are solved sequentially leading with the calculation of the velocity variables where the pressure is prescribed, thereafter the pressure correction is solved. Following this the velocity is corrected to ensure it is divergence free using the pressure correction from the previous step. This loop continues until convergence is achieved which will be followed by progression to the next time-step. Thus, with the application of this methodology the velocity and pressure progress separately, which results in cost-effectiveness for computational memory, but it is found to be more expensive in terms of

computational time to completion as convergence of the solution is slower because the equations are solved in a decoupled manner.

The PISO pressure velocity coupling scheme aids to improve efficiency over the Semi-Implicit Method for Pressure Linked Equations (SIMPLE) and Semi-Implicit Method for Pressure Linked Equations Consistent (SIMPLEC) schemes by applying joint neighbour and skewness corrections. The neighbour correction which is also known as the momentum correction shifts the repeated calculations that are required by the SIMPLE and SIMPLEC schemes to inside the pressure correction equation solution stage, which effectively decreases the number of iterations required to achieve convergence. The skewness correction is also applied in the SIMPLEC method, which overall aids to reduce convergence difficulties, effectively improving the amount of time required for convergence. Inaccuracies exist between the relation of pressure corrections in the adjacent cells and the mass flux at the cell face which is due to high cell skewness, thus in order to assist convergence once the pressure correction equation is solved the gradient of this is recalculated and utilised to update the mass flux corrections. Such a correction allows a solution to be found on highly skewed cells, which is vital for applications which exploit the moving grid technique. For further information see (Ansys Fluent Manual).

A grid sensitivity analysis has been performed within this study where mesh refinement is applied in the computational domains surrounding the wing. Thus, numerical solutions were obtained for a sequence of grids which became finer in order to determine a grid independent solution. Due to the dynamic mesh methodology adopted for this study, the grid sensitivity analysis was carried out on two different styles of grids where the domain surrounding the wing either acts in a dynamic fashion or remains stationary. Once the grid independent solution is obtained further simulations are performed on the most appropriate grid to obtain accurate numerical solutions with the least time required for completion.

The wing and grid movements were performed via the instructions of a UDF script which was read into Fluent during the simulation set-up stage. Due to the dynamics of the CFD simulations, the mesh will experience severe distortions which the solver will attempt to somewhat correct by the re-generation of cells through its dynamic meshing capabilities. Such a situation can be assisted by careful consideration of the time-step size and the total number of time-steps performed during the simulation, concurrently it is imperative to also keep in mind the expense of computational time and resources required. Adaptive time-stepping was also investigated in order to maintain mesh quality, improve the accuracy of the solution and reduce computational expenditure in terms of time, however such a technique was not employed unless

it was deemed necessary. For convergence and accuracy purposes the time step size and grid quality were paramount factors. The Courant number was found to be 0.8 for the dense grid. This was based on the wing tip velocity (determined by equation 5.50), average cell size within the inner domain where the cell sizes remain constant (unlike the outer domain which has a dynamic topology) and the time step size. The same was used for the rectangular wing as a very similar dense grid was utilised for the simulations. The convergence criterion for the simulations was set to  $1 \cdot 10^{-5}$  for every component such as mass and momentum. For each time step a fixed number of 100 iterations were set in order to reach the convergence criteria.

## 5.1 Wing Kinematics, Non-Dimensional Parameters & Further Aerodynamics

### 5.1.1 Wing Kinematics

The non-dimensionalised form of time (Equation 5.5) has been shown below, this definition is based on considering the real time and total periodic time. The flapping, angle of attack and deviation motions can be produced in a sinusoidal wave-formation by employing Equations 5.6 to 5.11. In more detail, the first two equations relate to wing flapping, thereafter the wing pitch equations are shown and lastly the final two equations are for wing deviation from the stroke plane. The flapping, pitching and deviation motions can be visually seen in Figure 2.5.

$$\tau = \frac{t}{T} \quad (5.5)$$

$$\phi = \Phi \cos(\omega t) \quad (5.6)$$

$$\dot{\phi} = -\Phi \omega \sin(\omega t) \quad (5.7)$$

$$\psi = \Psi \sin(\omega t) \quad (5.8)$$

$$\dot{\psi} = \Psi\omega\cos(\omega t) \quad (5.9)$$

$$\vartheta = \Theta\sin(\omega t) \quad (5.10)$$

$$\dot{\vartheta} = \Theta\omega\cos(\omega t) \quad (5.11)$$

The time dependent kinematic motion for both sets of simulations (drosophila wing and rectangular wing) was created by Equations 5.12 to 5.15. The flapping motion and its relative velocity was produced by Equations 5.12 and 5.14 respectively. And the pitching motion to set the angle of attack of the wings and its relative velocity was created by Equations 5.13 and 5.15 respectively, see (Berman et al. 2007) and (Liu et al. 2008) for further information. The wing stroke reversal duration is determined by  $\xi$  which can be set between 0 and 1, towards 0 the wave would produce a sinusoidal formation whereas towards 1 the wave formation will become much sharper representing a triangular wave form. Thus, the wing stroke reversal duration is much smaller at 1 opposed to the duration of stroke reversal at a value of 0. The angle of attack reversal duration is determined by  $\gamma$  which can be set from 0 to  $\infty$ , where at 0 the wave form becomes sinusoidal and towards  $\infty$  the wave represents a step function. Thus, as the value of  $\gamma$  moves away from 0, the wave form becomes sharper, with larger durations at a constant value, which in reference to AOA means that it will remain constant for longer durations. Figure 5.1, displays a plot where all four equations (5.12 to 5.15) are utilised for a frequency of 0.145 Hz.

$$\phi = \frac{\Phi}{\sin^{-1}\xi} (\sin^{-1}[\xi\cos\{\omega t\}]) \quad (5.12)$$

$$\psi = \frac{\Psi}{\tanh(\gamma)} (\tanh[\gamma\sin\{\omega t\}]) \quad (5.13)$$

$$\dot{\phi} = -\frac{2\pi f\xi\Phi\sin(2\pi ft)}{\left(\sin^{-1}(\xi) \left[\sqrt{1-\xi\cos\{2\pi ft\}}\right] \left[\sqrt{\xi\cos\{2\pi ft\}+1}\right]\right)} \quad (5.14)$$

$$\dot{\psi} = \frac{2\gamma f \Psi \pi \cos(2\pi ft) \left( \frac{1}{\cosh[\gamma \sin\{2\pi ft\}]} \right)^2}{\tanh(\gamma)} \quad (5.15)$$

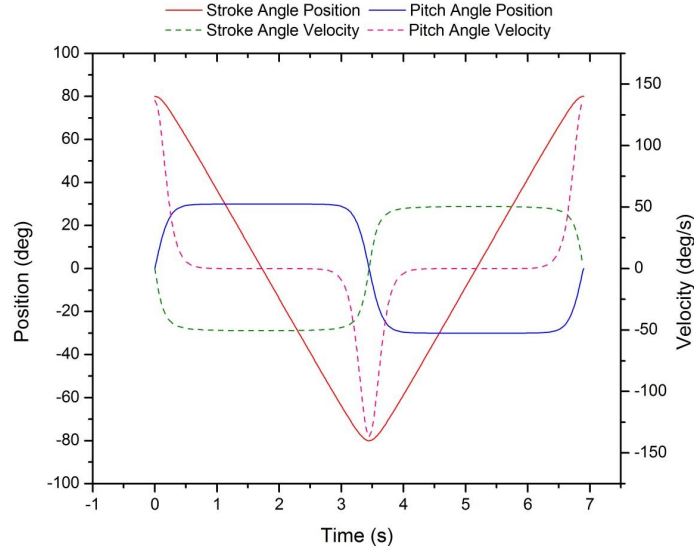


Figure 5.1: *Wing Kinematics for Instantaneous Position and Velocity*

The Fourier Equations 5.16 to 5.18, are usually chosen to model a very approximate wave formation of an actual insect, and the first order and second order derivatives will determine the velocity and acceleration respectively. These equations have been used in the past for modelling the kinematic motion of various insects, see (Liu 2009a) for further information.

$$\phi(t) = \sum_{n=1}^{n=m} [\phi_{an} \cos(2n\pi ft) + \phi_{bn} \sin(2n\pi ft)] \quad (5.16)$$

$$\psi(t) = \sum_{n=1}^{n=m} [\psi_{an} \cos(2n\pi ft) + \psi_{bn} \sin(2n\pi ft)] \quad (5.17)$$

$$\vartheta(t) = \sum_{n=1}^{n=m} [\vartheta_{an} \cos(2n\pi ft) + \vartheta_{bn} \sin(2n\pi ft)] \quad (5.18)$$

In order to improve accuracy the integer  $m$  should be increased.  $n$  is the range from 1 to  $m$ .

$\phi_{an}$ ,  $\phi_{bn}$ ,  $\psi_{an}$ ,  $\psi_{bn}$ ,  $\vartheta_{an}$ ,  $\vartheta_{bn}$  are the Fourier coefficients which can be measured from kinematic data for stroke angle, angle of attack and deviation angle respectively.

The body rotation matrix is shown in Equation 5.19, and the equations which fill this matrix are 5.20 to 5.28. The rotations incorporated into the matrix are roll, yaw and pitch about their respective axes. These can be visually seen in Figure 2.4. For further information see (Maeda et al. 2010), (Zuo et al. 2007) and (Jazar 2010).

$$body_{\varphi\sigma\varsigma} = \begin{bmatrix} a_{11} & a_{12} & a_{13} \\ a_{21} & a_{22} & a_{23} \\ a_{31} & a_{32} & a_{33} \end{bmatrix} \quad (5.19)$$

$$a_{11} = \cos\varsigma\cos\sigma \quad (5.20)$$

$$a_{12} = -\cos\varsigma\sin\sigma \quad (5.21)$$

$$a_{13} = \sin\varsigma \quad (5.22)$$

$$a_{21} = \sin\varphi\sin\varsigma\cos\sigma + \cos\varphi\sin\sigma \quad (5.23)$$

$$a_{22} = -\sin\varphi\sin\varsigma\sin\sigma + \cos\varphi\cos\sigma \quad (5.24)$$

$$a_{23} = -\sin\varphi\cos\varsigma \quad (5.25)$$

$$a_{31} = -\cos\varphi\sin\varsigma\cos\sigma + \sin\varphi\sin\sigma \quad (5.26)$$

$$a_{32} = \cos\varphi \sin\varsigma \sin\sigma + \sin\varphi \cos\sigma \quad (5.27)$$

$$a_{33} = \cos\varphi \cos\varsigma \quad (5.28)$$

The rotational matrix for a wing is shown in Equation 5.29, and the equations that fill this matrix are 5.30 to 5.38. This matrix operates on the wing base fixed coordinate system and creates the kinematic motions for flapping, pitching and deviation (shown in Figure 2.5). Different wave form kinematic equations are coupled with the equations stated above to create the wings motion.

$$wing_{\phi\psi\vartheta} = \begin{bmatrix} b_{11} & b_{12} & b_{13} \\ b_{21} & b_{22} & b_{23} \\ b_{31} & b_{32} & b_{33} \end{bmatrix} \quad (5.29)$$

$$b_{11} = \cos\vartheta \cos\psi \quad (5.30)$$

$$b_{12} = -\cos\vartheta \sin\psi \quad (5.31)$$

$$b_{13} = \sin\vartheta \quad (5.32)$$

$$b_{21} = \sin\phi \sin\vartheta \cos\psi + \cos\phi \sin\psi \quad (5.33)$$

$$b_{22} = -\sin\phi \sin\vartheta \sin\psi + \cos\phi \cos\psi \quad (5.34)$$

$$b_{23} = -\sin\phi \cos\vartheta \quad (5.35)$$

$$b_{31} = -\cos\phi\sin\vartheta\cos\psi + \sin\phi\sin\psi \quad (5.36)$$

$$b_{32} = \cos\phi\sin\vartheta\sin\psi + \sin\phi\cos\psi \quad (5.37)$$

$$b_{33} = \cos\phi\cos\vartheta \quad (5.38)$$

The product of both of the rotational matrices shown above is shown in Equation 5.39 and the respective equations 5.40 to 5.48 which fill this matrix. The body and wing can rotate about their respective coordinate frames simultaneously. Thus the body can perform rolling, yawing and pitching while the wing concurrently flaps, pitches to vary the AOA and deviates out of its stroke plane. The body and wing matrix is shown to merely present a coupled motion of different bodies within a single domain.

$$body \cdot wing_{\varphi\sigma\zeta, \phi\psi\vartheta} = \begin{bmatrix} c_{11} & c_{12} & c_{13} \\ c_{21} & c_{22} & c_{23} \\ c_{31} & c_{32} & c_{33} \end{bmatrix} \quad (5.39)$$

$$c_{11} = (\cos\zeta\cos\sigma)(\cos\vartheta\cos\psi) + (-\cos\zeta\sin\sigma)(\sin\phi\sin\vartheta\cos\psi + \cos\phi\sin\psi) + (\sin\zeta)(-\cos\phi\sin\vartheta\cos\psi + \sin\phi\sin\psi) \quad (5.40)$$

$$c_{12} = (\cos\zeta\cos\sigma)(-\cos\vartheta\sin\psi) + (-\cos\zeta\sin\sigma)(-\sin\phi\sin\vartheta\sin\psi + \cos\phi\cos\psi) + (\sin\zeta)(\cos\phi\sin\vartheta\sin\psi + \sin\phi\cos\psi) \quad (5.41)$$

$$c_{13} = (\cos\zeta\cos\sigma)(\sin\vartheta) + (-\cos\zeta\sin\sigma)(-\sin\phi\cos\vartheta) + (\sin\zeta)(\cos\phi\cos\vartheta) \quad (5.42)$$

$$\begin{aligned}
c_{21} = & (\sin\varphi\sin\zeta\cos\sigma + \cos\varphi\sin\sigma)(\cos\vartheta\cos\psi) + (-\sin\varphi\sin\zeta\sin\sigma + \cos\varphi\cos\sigma)(\sin\phi\sin\vartheta\cos\psi + \cos\phi\sin\psi) + \\
& (-\sin\varphi\cos\zeta)(-\cos\phi\sin\vartheta\cos\psi + \sin\phi\sin\psi)
\end{aligned} \tag{5.43}$$

$$\begin{aligned}
c_{22} = & (\sin\varphi\sin\zeta\cos\sigma + \cos\varphi\sin\sigma)(-\cos\vartheta\sin\psi) + (-\sin\varphi\sin\zeta\sin\sigma + \cos\varphi\cos\sigma)(-\sin\phi\sin\vartheta\sin\psi + \cos\phi\cos\psi) + \\
& (-\sin\varphi\cos\zeta)(\cos\phi\sin\vartheta\sin\psi + \sin\phi\cos\psi)
\end{aligned} \tag{5.44}$$

$$\begin{aligned}
c_{23} = & (\sin\varphi\sin\zeta\cos\sigma + \cos\varphi\sin\sigma)(\sin\vartheta) + (-\sin\varphi\sin\zeta\sin\sigma + \cos\varphi\cos\sigma)(-\sin\phi\cos\vartheta) + (-\sin\varphi\cos\zeta)(\cos\phi\cos\vartheta)
\end{aligned} \tag{5.45}$$

$$\begin{aligned}
c_{31} = & (-\cos\varphi\sin\zeta\cos\sigma + \sin\varphi\sin\sigma)(\cos\vartheta\cos\psi) + (\cos\varphi\sin\zeta\sin\sigma + \sin\varphi\cos\sigma)(\sin\phi\sin\vartheta\cos\psi + \cos\phi\sin\psi) + \\
& (\cos\varphi\cos\zeta)(-\cos\phi\sin\vartheta\cos\psi + \sin\phi\sin\psi)
\end{aligned} \tag{5.46}$$

$$\begin{aligned}
c_{32} = & (-\cos\varphi\sin\zeta\cos\sigma + \sin\varphi\sin\sigma)(-\cos\vartheta\sin\psi) + (\cos\varphi\sin\zeta\sin\sigma + \sin\varphi\cos\sigma)(-\sin\phi\sin\vartheta\sin\psi + \cos\phi\cos\psi) + \\
& (\cos\varphi\cos\zeta)(\cos\phi\sin\vartheta\sin\psi + \sin\phi\cos\psi)
\end{aligned} \tag{5.47}$$

$$\begin{aligned}
c_{33} = & (-\cos\varphi\sin\zeta\cos\sigma + \sin\varphi\sin\sigma)(\sin\vartheta) + (\cos\varphi\sin\zeta\sin\sigma + \sin\varphi\cos\sigma)(-\sin\phi\cos\vartheta) + (\cos\varphi\cos\zeta)(\cos\phi\cos\vartheta)
\end{aligned} \tag{5.48}$$

### 5.1.2 Non-Dimensional Parameters

**Reynolds Number:**

The Reynolds number for flapping flight is presented in two different forms due to the flight modes involved, which are forward flight and hovering flight. The traditional form of the Reynolds number equation applies for forward flight composed of a given reference length, reference velocity and the kinematic viscosity of the fluid shown in Equation 5.49. As the flapping wings generate forces such as lift and thrust required for insect flight, the appropriate reference length to consider is either the mean chord or the length of a single wing  $R$ . The freestream velocity is considered as the reference velocity for a forward flight scenario.

$$Re = \frac{U_{ref} L_{ref}}{\nu} \tag{5.49}$$

Under the hovering condition forwards velocity is non-existent, thus appropriate amendments are made to the existing equation as the reference velocity will now be considered as the wingtip velocity and the reference length is the span of a single wing, (Equation 5.50). The Reynolds number equation under the hovering condition is shown in Equation 5.51. For insect flight the general Reynolds number ranges from  $O(10^1)$  to  $O(10^4)$ , the aspect ratio and wing stroke amplitude do not have significant differences, on the contrary the flapping frequency increases as the insect size is reduced, thus the flapping frequency range is most certainly significant. A clear example of this is seen from a simple comparison of the flapping frequency of a hawk moth (*manduca sexta*) which beats its wings at 25 Hz, and a fruit fly (*drosophila melanogaster*) which beats its wings at 200 Hz (Shyy et al. 2013).

$$U_{ref} = 2\Phi f R = \omega R \tag{5.50}$$

$$Re_{hover} = \frac{\Phi f R^2}{\nu} \left( \frac{4}{AR} \right) \tag{5.51}$$

**Strouhal Number:**

The Strouhal number (Equation 5.52) is a dimensionless parameter known to characterise the vortex dynamics and shedding behaviour for unsteady fluid dynamics. This parameter is widely used when referring to the vortex shedding created by a cylindrical object producing the aerodynamic phenomena known as von

Karman vortex street where vortices are shed alternatively from either side of the bluff body creating a pattern downstream of the body. When an aerofoil is pitching and plunging in a fluid it can produce forward thrust for specific Strouhal numbers where the wake has a flow formation which is similar to a reverse von Karman vortex street as the direction of vorticity is reversed. In reference to flapping flight the Strouhal number (Equation 5.53) is a measure of propulsive efficiency, describing a ratio between the wing velocity and forwards velocity (Shyy et al. 2008) and (Shyy et al. 2013). For hovering wing motion, the Strouhal number has no actual meaning as the reference velocity is based on the flapping velocity. In most cases, for this flight condition the Strouhal number is twice the flapping frequency as vortex structures are shed per stroke either down or up.

$$St = \frac{fL_{ref}}{U_{ref}} \quad (5.52)$$

$$St = \frac{2fh_a}{U} \quad (5.53)$$

***Reduced Frequency:***

The reduced frequency refers to the ratio between the flapping velocity and forward velocity, which is composed of the flapping frequency, mean chord length and a reference velocity which relates to freestream velocity under the forward flight condition. Under the hovering condition the reference velocity can be defined as the wingtip velocity. The reduced frequency equation is shown in Equation 5.54. Furthermore, for a 2D hovering aerofoil the reduced frequency is shown in Equation 5.55 where the reference velocity is now defined as the maximum translational flapping velocity. With low speed forward flight the reduced frequency will be high, subsequently producing highly unsteady flow structures.

$$k = \frac{2\pi fL_{ref}}{2U_{ref}} = \frac{\pi}{\Phi AR} \quad (5.54)$$

$$k = \frac{2\pi fL_{ref}}{2U_{ref}} = \frac{\bar{c}}{2h_a} \quad (5.55)$$

***Advance Ratio:***

The advance ratio (Equation 5.56) is another dimensionless parameter which is relative to the forward

velocity and flapping velocity of an insect. The flapping velocity will vary along the span length of the wing, where it is minimum near the root section and maximum at the tip region. The advanced ratio is applicable for a forward flight condition and does not apply under hovering conditions as the forward velocity is non-existent. For example, consider a bumblebee which is in a hovering position, the stroke plane would be along the horizontal axis, where the down and up strokes are symmetrical, henceforth generating zero thrust and sufficient lift to support its body weight. Now when altering flight mode to forward flight, the bumblebee would tilt its body downwards towards the horizontal axis in order to reduce body drag, and as its flight speed increases the advanced ratio will follow this relation in accordance to Equation 5.56. As the body rotated, the stroke follows this action and reaches an angle approximately 40 degrees to the horizontal axis. Thus, for flight mode change a bumblebee tilts its stroke plane by approximately 40 degrees. In augmenting the advanced ratio, the force production per stroke is no longer the same as the downstroke demonstrates its supremacy in terms of force generation, where the downstroke path increases which results in higher velocities effectively producing larger forces. This dominance of downstroke is responsible for lift generation to support the insects weight along with some thrust force generation, the upstroke is quite different which is only suitable to produce thrust force (this flight mode alteration has been shown in Figure 2.3). The thrust force produced (approximately 10-20%) is actually quite small compared to the lift generated, which clearly states that the net aerodynamic force vector is tilted slightly forwards from the vertical axis. See (Ellington 1999) for further information.

$$J = \frac{U_{ref}}{2\Phi f R} = \frac{U_{ref}}{2\pi f h_a} = \frac{1}{\pi St} \quad (5.56)$$

### 5.1.3 Further CFD Review Related to Flapping Wings

A computational simulation study was carried out by Aono et al. (2007) to model the three dimensional near and far field fluid dynamics for a drosophila insect incorporating its realistic wing-body morphologies and wing kinematics. However, all the body volumes are assumed to be rigid, thus no wing or body deformations take place due to fluid interaction. Due to the dynamic wing motion, and complexities involved in flow dynamics the authors opted to use a multi-blocked overset grid methodology where three grids are utilised, two grids are used for wings and 1 for the entire domain which encloses the body and both grids around each wing. A similar grid methodology was chosen for the numerical simulations performed in this project as the

wing was enclosed by an inner virtual domain, and both of these volumes were enclosed by the much larger outer domain. As the body remains stationary throughout the simulation, only wing motions are carried out which utilise Equations 5.16 to 5.18.

Following end-upstroke, the early stages of pronation begins where the LEV and TV remained attached to the wing, but instabilities are evident, and shortly after the TV commences separation at approximately 70% wing span from the base as it pulls the LEV away from the surface of the wings. During the upstroke motion a doughnut shaped vortex ring existed (see Figure 5.2), which now detaches from the wings and moves into the wake. Understandably at such a low Reynolds number of approximately 134, the doughnut shaped vortex rings (one ring is formed per wing) have a strong full figured volumetric appearance which travels downwards into the insects wake formation. The authors mention at the latter stages of pronation a vortex forms on each wing as the insect rapidly rotates its wings in a similar fashion to the fling mechanism.

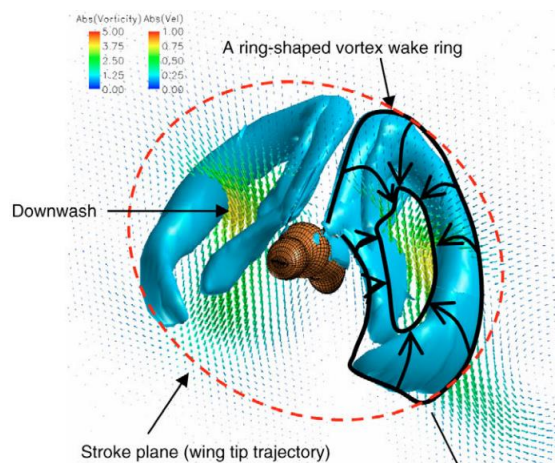


Figure 5.2: *Drosophila with Ring Shaped Vortex and Downwash*

Following pronation, downstroke commences where the wing continues to dynamically rotate increasing its AOA, and a trailing edge starting vortex is shed from both wings. From the shedding of the TEV (starting vortex), the bound vortex circulation is balanced and a downwards momentum is given to the air which is present in the region within the vortex ring, this downwards jet of fluid is termed the downwash. Analysing the downstroke motion further, its understood that a horseshoe shaped vortex is initially formed which wraps around the wing and is composed of the TEV which is connected to a TV and the LEV. Both LEV and TEV grow during the beginning of the downstroke and stretch along the wing span from base to tip, which have very weak axial flow velocity travelling through them. As aforementioned the TEV (starting

vortex) detaches from the wing surface but remains in the vicinity of the insect as it is connected to the TV, which encloses the doughnut shaped vortex ring on either side of the insect. An important feature to note is the intense downwash travelling through the hole of the doughnut shaped vortex ring which is acting throughout majority of the downstroke motion. The LEV remains attached to the wing surface for majority of the downstroke, and only starts to breakdown at the end of downstroke and start of supination where it detaches from the wing surface at approximately 70-80% from the wing base. Contemporaneously, the TV continues to grow and becomes unstable thereafter detaching from the wing surface. Thus, the vortices have now separated from the wings surface and the structure of the doughnut shaped vortex rings move downwards and form the far field wake beneath the insect. During the supination phase the authors mention that a stopping vortex forms around the leading edge due to the very slow translation motion of the wing. And during the second half of supination the wing begins to move through the wake formed from the prior stroke.

To complete the cycle as the wing starts to move through its upstroke phase travelling through the shed wake, a horseshoe vortex forms which is composed of the TEV, TV and LEV similar to the horseshoe shaped vortex formed during the early stage of downstroke. Following this, as featured during the downstroke motion, the trailing edge starting vortex will detach from the wings surface but remain in close proximity as it is connected to the TV, and shortly after a doughnut shaped vortex ring is formed which has more prominent structure than the vortex ring which was formed during the downstroke. As mentioned previously a strong downwards momentum jet of flow is present within the hole of both the vortex rings. During the stroke the LEV grows, with a tight and concentrated formation, which has its minimum diameter at the wing base location that gradually grows to an appearance of a tube-like structure along the wing span travelling towards the wing tip. Furthermore, this tube-like vortex structure looks and is very stable, and similar to the downstroke LEV, any axial flow velocity travelling through the vortex core seems to be very weak. A sufficient amount of spanwise axial flow velocity is actually observed behind the LEV and this increases towards the trailing edge. This stable LEV remains in this state for throughout the upstroke translation period, and both LEV and TV start to become unstable at the end of upstroke and start of pronation where the vortex ring structures are shed downwards into the wake and stopping vortices form at the leading edge of both wings. Finally the cycle is complete, the wing motion and vortex dynamics would start again and continue in this manner. Although downwards flow is present throughout a flapping cycle beneath the insect, only a limited region which is swept by the wings has the existence of a strong momentum jet, thus it is not beneath the insects

body but present beneath the area which the wings travels through.

A further simulation was performed for a hawk moth ( $Re = 6300$ ) to analyse the LEV properties for two different insects. As discussed in-depth in the literature review section of this thesis, distinct features exist between the LEV formations at these two Reynolds numbers. And from the CFD data provided here, it is evident that strong axial flow velocity exists at the LEV core for the hawk moth insect, and the LEV is more of a spiral structure that tends to stretch in a third dimension as it travels towards the wing tip. The hawk moth also has a sufficient spanwise flow present along majority of its chord when viewed at 60% from the wing base, this spanwise flow velocity is largest within the LEV core and reduces in velocity towards the trailing edge where it is still clearly evident. Such a structure is not present in the fruit fly LEV which has a more tube-like vortex that sticks to the leading edge surface of the wing, and is more stable with a less complicated composition. In direct relation to the LEV composition, the axial flow velocity within the LEV of the fruit fly is very weak, however the axial flow velocity behind the LEV is more pronounced which increases towards the trailing edge, where maximum spanwise velocity is present.

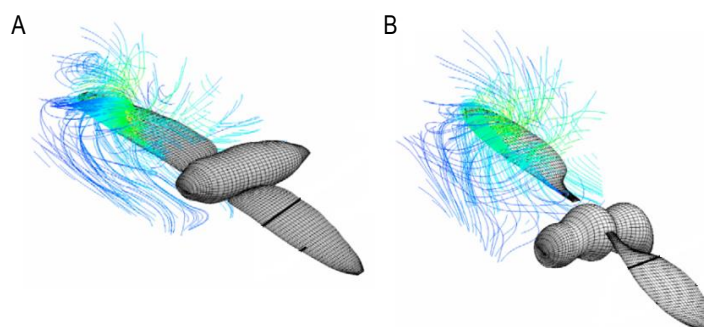


Figure 5.3: *Flow Field Around Insect Wings; A: Hawkmoth, B: Drosophila*

The force measurements had an average value of 2% greater than the fruit fly's weight, thus the simulated result shows that the insect can support its weight in hovering motion. The time history of lift force through a cycle shows a peak per stroke, which the authors state are most probably due to large negative pressure produced on the upper wing surface from the presence of the LEV and TV. Whereas the time history of the horizontal axis shows that drag force is produced during the downstroke, and thrust is produced during the upstroke which should cancel out one-another in order to perform precise hovering flight. As the wing kinematics are not symmetrical for each half stroke, a time history of identical vertical forces is not produced, likewise this applies for the horizontal forces as well. At the point where flapping wing velocity

and aerodynamic force produced both peak, is the position where maximum aerodynamic power is required, such a position existed at each mid-stroke.

Analysing the pressure gradient contours present on the wings of both of the insects, it was evidently shown that the pressure gradient along the span of a fruit fly is extremely weak when compared to that of a hawk moth, where a strong pressure gradient exists which is largest at the wing base to mid span at the leading edge and thereafter moves inwards towards the trailing edge. From the significant differences in comparison, the pressure gradient is seen to have a direct relation to the level of axial flow, and is the cause of the strong axial flow developed at the LEV core of the hawk moth wing, henceforth the pressure gradient directly assists LEV stability of the hawk moth. As the fruit fly wing has a small pressure gradient the axial flow velocity through the LEV core is very weak. The authors mention, that for flapping wing flight at the lower Reynolds number range of 100-250, the insect cannot generate a strong enough LEV which will create a steep pressure gradient at the core of the vortex, such a result is seen in the fruit fly wings which has an  $Re$  that lies in the range specified above. However, the structural tube-like formation of the vortex formed at the leading edge of the fruit fly wing is much more stable than the LEV generated by the hawk moth, which experiences vortex breakdown before the LEV of the fruit fly. In fact, the LEV of the fruit fly is seen to steadily grow and remain attached to the wing surface during both translation phases of down and up strokes, where detachment from the surface of the wing occurs at supination and pronation (wing rotational phases). As aforementioned a strong spanwise flow is found behind the LEV which progressively grew in strength towards the trailing edge (rearmost half) of the fruit fly wing, which the authors state may have been created by the centrifugal and Coriolis forces, as the pressure gradient on the fruit fly wing has clearly been seen to be far too weak to be the cause of the strong axial flow found behind the LEV along the rearmost half of the wing. As a general note, when the computed force results were analysed, they found that the hawk moth produced majority of the total lifting force (60-70%) during the downstroke motion (for this reason it is known as the power stroke) and the remaining during the upstroke. However, a contradictory result was found for the fruit fly where majority of the total lift force is produced during the upstroke (62%) and the remaining during the downstroke motion. Such a result gives an indication that forces generated for hovering flight tend to vary among insects and their dependency may be categorised by the size of the insect and its wing kinematics.

The fluid dynamic structures generated from the fruit fly wing motions did not show the production of the

root vortex, the likely cause of its absence is down to the presence of the insects body in the simulations. The doughnut shaped vortex ring pair which form during the insects wing motion as aforementioned has an intense downwash (jet stream of fluid) travelling through the holes, which break up into singular vortex rings at the rotational phases (supination and pronation) of the cyclic motion. Maximum lift forces are produced at mid-stroke, where the downwash seems to be very high as well. In accordance to the lift production data aforementioned for the fruit fly, the downwash during the upstroke is stronger than during the downstroke. In relation to the stronger downwash wake of the upstroke, the ring shaped vortex wake has a fuller structure during the upstroke than the down stroke. As the fruit fly has much less axial flow velocity through the core of its LEV in comparison to a hawk moth, it is reasonable to assume that the amount of vorticity fed into the tip vortex is likewise very small, and in contrast the amount of vorticity fed into the tip vortex by the wing motion of the hawk moth is very high as it has a much larger axial flow velocity travelling through the core its LEV. Thus, fundamentally the fruit fly LEV feeds less energy into its tip vortex, opposed to the amount of energy a hawk moths LEV feeds into its tip vortex. Finally, the authors found that the presence of the insects body during the simulations has very small effects on the vortex wake structure and the overall cycle averaged force measurements, thus they conclude that the body has negligible influence in the hovering aerodynamics. Nonetheless, this may not be the case during forward flight and manoeuvring as the body may have a significant role in these flight modes.

Ramamurti et al. (2002), carried out computational simulations on a large three dimensional drosophila wing undergoing a prescribed flapping wing motion. They employed a finite element incompressible in-house flow solver, which had the capability to re-mesh and eliminate distorted elements that were a result of the wing travelling through the domain. The movement of the rigid single wing will deform the cells which in turn alters the initial state of the volume grid. The wing is placed within a volume grid that has a symmetry plane in order to reduce the computational effort required and this domain consists of an unstructured tetrahedral mesh with 0.96 million cells. They simulated three different cases in which the wing rotational timing was altered to study the effect of advanced, symmetrical and delayed rotations on the instantaneous aerodynamic forces in comparison to the experimental data of Dickinson et al. (1999).

The fluid properties of the simulation are matched to the experimental by ensuring the Reynolds number is equivalent. Thus, in this case the viscosity of the oil, wing dimensions and flapping frequency were all chosen in relation to the Reynolds number of approximately 136. The exact wing kinematics as the experiment

were modelled into the simulation for the wing to dynamically perform, which applied to all three cases studied here. The wing travelled through a flapping stroke amplitude of 160 degrees, with an AOA of 40 degrees at both mid-strokes whilst rotating with a flapping frequency of 0.145 Hz. The advanced case has a wing rotation that precedes stroke reversal by 8%, the delayed case has a wing rotation which commences at 8% after stroke reversal, and the symmetric case where wing rotation occurs symmetrically in respect to stroke reversal. For comparison with the experimental results the drag force acting on the wing is found by Equation 5.57.

$$F_D = \sqrt{(F_x^2 + F_z^2)} \quad (5.57)$$

For the symmetrical wing rotation case, as the translation and wing rotation motions prescribed are symmetrical, the forces produced for both down and up strokes should likewise be symmetrical. The authors mention that due to mechanical play in the experimental rig, the output forces are not exactly symmetrical as expected. Such an outcome is actually expected because a perfect experiment is near impossible due to factors aforementioned in this thesis and the experimental procedure along with the defects stated by the authors, these have also been mentioned in the literature survey in this thesis for the experiment of Dickinson et al. (1999).

The lift and drag force data from the experiment of Dickinson et al. (1999) and Ramamurti et al. (2002) will be viewed in the following sub-section of this chapter. They find a peak in lift force at the onset of the downstroke motion which is attributed to the wing-wake interaction as the wing passes through the wake of the shed vorticity from the prior stroke, such an incident also occurs at the start of upstroke motion. For the symmetric case data comparison between the computed results and experimental data showed good agreement, but the initial peak at the start of each stroke was smaller than the experimental result. The drag data showed a really good comparison for both strokes. During mid-downstroke a LEV is seen attached to the wing from the formation of velocity vectors travelling around the leading edge of the wing. During the translation phases of both strokes the lift forces should be more or less constant as the translational acceleration is constant during this stage and the wing is held at a constant AOA, thus rotational acceleration is not varying. Due to the symmetrical nature of the wings motion a similar outcome of dynamic force measurements will be produced during the upstroke motion.

For the advanced case the wing rotates prior to stroke reversal, thus a peak in force is seen during the rotational phase, and as this rotational effect diminishes the lift forces drastically reduce. Thereafter, the

wing has a high angle of attack and moves through the wake of the previous stroke where a large pressure now exists on the lower surface of the wing which enhances the lift producing a peak in lift force. The peak lift force developed for the advance case from wake capture at the start of downstroke is approximately 0.48 N, which is much larger than the peak lift force of 0.28 N produced at the start of the symmetrical case.

In the delayed case, due to the absence of wing rotation before or during stroke reversal, no lift peak exists and the lift force generated is negative for the early stage of start downstroke due to the unfavourable orientation of the wing. This is followed by an increase in lift force from the combinational effect of the translational and rotational mechanisms. A brief plateau in lift force is experienced for a short period, due to the presence of the trailing edge vortex which is shed and lift forces start to increase as the wing continues with its downstroke motion. On the contrary, a very large peak exists for the drag force at the start of downstroke as the wing has an unfavourable negative AOA and it interacts with the wake from the previous stroke.

Analysing the velocity of the flow in the wake for all three cases presented that velocity was greatest for the advanced case, which was followed by the symmetrical case and finally found to be weakest in the delayed case. The average lift force generated is 0.318 N, 0.312 N, 0.206 N which refer to the symmetrical, advanced and delayed cases respectively (Ramamurti & Sandberg 2002). The average drag force generated is 0.375 N, 0.457 N, 0.457 N which refer to the symmetrical, advanced and delayed cases respectively (Ramamurti & Sandberg 2002). Finally, the average aerodynamic power required is 0.024 W, 0.039 W, 0.024 W which refer to the symmetrical, advanced and delayed cases respectively (Ramamurti & Sandberg 2002). The computational and experimental data seem to be in good agreement for all three cases, differences would exist between the two due to the complexities involved in the simulations and the highly unsteady fluid dynamics that exists in regards to the insect like wing motion. Furthermore, experimental data as aforementioned could have numerous uncertainties due to manufacturing tolerances, play in the mechanical devices among other parameters which are difficult to perfect during experimental work.

The unsteady vortex dynamics surrounding four different insect species which have significant differences in their flight parameters such as  $Re$ , wing-body morphologies and kinematics, body plane, stroke plane, AR and numerous others have been investigated by Liu et al. (2009). Numerical simulations were performed individually for all four insects and their respective body housed within a multi-blocked overset grid method which is based on a chimera grid scheme, their grid methodology has been elaborated upon in a previous

review in this section. The movement of the wings throughout the simulation would evidently distort the initial mesh, thus dynamic re-gridding was employed within the solver to generate mesh in necessary locations. Both body and wing volumes are modelled as rigid walls, thus neither experiences any deformation due to fluid loading. During all the simulations, the body is assumed to remain in the same position throughout, whilst the wing dynamically rotates about a wing base fixed coordinate system with rotations performed for stroke angle, AOA (feathering angle) and deviation angle. The authors mention that the wide range of Reynolds numbers related to insect flight is due to the significant differences in flapping frequency which tends to increase as the wing length decreases as the size of the insect reduces. Details for each of the insects studied have been provided in Table 5.1. The data provided shows a wide range in terms of wing length and flapping frequency which has been mentioned previously as contributions to the wide range of Re in consideration here.

| <b>Insect</b>    | <b>AR</b> | <b>f (Hz)</b> | <b>R (mm)</b> | <b><math>\Phi</math> (deg)</b> | <b>Re</b> | <b>k</b> |
|------------------|-----------|---------------|---------------|--------------------------------|-----------|----------|
| <i>Hawkmoth</i>  | 5.28      | 26.1          | 48.3          | 114.6                          | 6300      | 0.298    |
| <i>Honey Bee</i> | 8.12      | 229.8         | 9.7           | 90.5                           | 1123      | 0.244    |
| <i>Fruit Fly</i> | 6.13      | 218           | 2.39          | 139.8                          | 134       | 0.212    |
| <i>Thrips</i>    | 2.60      | 200           | 0.5           | 139.8                          | 12        | 0.249    |

Table 5.1: *Insect Data for Hovering Flight Mode (Liu et al. 2009)*

The authors have altered the thrips by simulating the insect with two wings opposed to four and any wing-wing interference effects have been neglected. In addition, the wings have been constructed as flat plate volumes to reduce further geometrical complexities of modelling a bristled wing. The kinematic wing motion of the thrips insect is based on the hovering fruit fly as the authors mention that wing and body kinematic data is not available at present for thrips insect. Validation for the hovering flight mode modelled was carried out by comparing the average lift force produced per cycle and the weight of the insect as it should be able to support itself during hovering mode, the results proved to show good comparison with negligible differences.

During the first half of the downstroke motion a horseshoe shaped vortex is formed around each of the hawkmoths wings which is composed of the LEV, TV and a TEV. During the downstroke motion the LEVs and TEVs present on both sides are seen to grow, and at the position of mid-downstroke both TEVs are shed from the wings surface. Upon shedding from the wings surface these two TEVs interact at the rear

of the insects body forming into a complex vortical structure. Shortly after mid-downstroke initial vortex breakdown is observed for the LEVs at approximately 70-80% wing span from the base. Vortex rings are formed during the downstroke around each wing which are composed of the LEV, TV and shed TEV (which is linked to the tip vortex).

Similar to the vortex ring mentioned in Aono et al. (2009), a strong downwards momentum jet exists in the hole of the vortex rings which is known as the downwash of fluid, however, dissimilar to the previous vortex ring dynamics, a vortex sheet exists inside of the vortex rings. Furthermore during the downstroke motion, behind each wing close to the wing tips a twisted vortical formation is present which is due to the interplay between the broken down LEV and the shed TV. During the upstroke motion the aforementioned vortical dynamics including downwash are replicated in the same order, but the presence of the downstroke wake has an influence as the upstroke vortex rings combine with the shed downstroke vortex rings, thus the upstroke vortex rings seem to deform and stretch whilst managing to maintain its ring-like structure.

Albeit, the wing geometries, kinematics, wing-body morphologies and  $Re$  are all fairly different between the hawk moth (whoms vortex dynamics have been described above) and the honey bee, but the near and far-field vortex dynamics formed from their respective wing motions have very similar characteristics. Similar to the hawk moth, horseshoe shaped vortices are present at early stroke which develop into vortex rings around each wing, and contributing to both the vortex structures are the LEV, TV and TEV. Furthermore, initial LEV breakdown is observed at 70-80% along the span from the base, which occurs after mid-downstroke. In the centre of these vortex rings exists the downwash of fluid which is an intense jet stream of fluid directed downwards. Noticeable differences exist in the size of areas covered by the streams of downwash produced by the hawk moth and the honey bee. The hawk moths downwash stream covers a very large area beneath the insects wings and a certain distance below the body section a connection of the two streams produced is observed. Such a connection does not exist in the downwash streams produced by the honey bee, and the area covered by the downwash is less where the area covered is directly beneath the wings, and lastly needless to mention both downwash streams have velocity vectors pointing downwards.

In comparison to the vortex structures formed from the wing motions of the hawk moth and honey bee, the horseshoe shaped vortices and vortex rings formed from the downstroke and upstroke phases by the fruit fly were found to be weaker but more stable. Thus, the LEV, TV and TEV generated by the fruit fly's wings were feeble but possessed more stability in comparison to the larger insects which had considerably

larger Reynolds numbers. The vortex rings have a smoother profile and no twisting of vortical structures is evident near the wing tip regions. Further to this, as the vortex rings are weaker, they deteriorate faster and hence expire quicker than the rings of the hawk moth and honey bee insects. The downwash wake regions are existent beneath the surface swept by the wings with a large gap present between both wake regions. In effect, the wake regions per wing are seen as separate columns and are much narrower when compared to the downwash wake regions produced by the hawk moth and honey bee insects. A region just below the body is occupied by fluid that is very close to zero speed which is known as a dead fluid zone.

The vortex dynamics for the thrips at such a low  $Re$  are fairly different to the three insects already discussed as the authors stated that the vortex structures suffer from much larger viscous forces, which results in very compact vortices formed at the edge of the wings that seem to remain close to the edges of the wings. The formation of both the horseshoe shaped vortices which develop in the stages of early down and up stroke motions are weak which gradually develop into vortex rings that are weak but stable. Furthermore, the LEVs are very stable throughout each stroke, and after shedding has taken place of the TEVs and TVs they still remain connected to the LEVs. The downwash wake formation for the thrips insect is considerably contrasting as column-like streams are not present beneath the wings, instead the downwash remains in the vicinity of the wings, showing a connection of the streams produced from each wing above the insects body and the velocity of the downwash wake maximises at both mid-strokes. Furthermore, the authors suggest that the existence of such a high viscosity due to the ultra low Reynolds number that thrips operate within may augment wing-wake, body-wake and wing-wing interference effects. Although, numerous simplifications and assumptions were employed when modelling the thrips insect, the fluid dynamics modelled here is a good approximation, more details have been shown below.

The vortex dynamics formed from flight at lower  $Re$  (fruit fly and thrips) in comparison to flight at higher  $Re$  (hawk moth and honeybee) clearly presents distinctions such as strength and stability of the vortical structures formed. As aforesaid the LEV is more stable but weaker in the lower  $Re$  cases, and this same result applies for the horseshoe shaped vortices and vortex rings formed. The vortex dynamics are stronger but more unstable at the higher range of  $Re$ , where the LEV has a more conical shape. Something interestingly noteworthy is that regardless of the wing geometry, kinematics and  $Re$  of the flow, a LEV is formed for all the insects in hovering flight mode which holds different characteristics but enhances the lifting forces for all these species. Further to this, the hawk moth and honey bee operate at considerably different Reynolds numbers,

have different stroke amplitudes and flapping frequencies but the vortex dynamics generated during wing motion such as the LEV and vortex rings are quite similar. Albeit, the stroke amplitude of the honeybee is shorter but its very high flapping frequency aids in generating sufficient lifting forces and producing a larger wing tip speed than the hawk moth. The fruit fly has a much smaller wing tip speed than the honey bee and hawk moth but has a LEV which is more stable than both of these insects. The pressure gradient paths along the wings of the hawk moth and honeybee were very similar but differed in terms of strength where the pressure gradient acting on the hawk moth wings was much larger. As aforementioned in a previous review, the pressure gradient acting on the fruit fly's wings is very small compared to the hawk moth. In general, the pressure gradient was greatest for the hawk moth and least for the fruit fly, giving some indication that the  $Re$  has an influence on the size and directional property of the pressure gradient produced along the wings during their respective motions. Furthermore, the  $Re$  or size of insect seems to have an influence on the downwash wake produced when hovering which is evident from the considerable differences in the wake formations, where the hawk moth downwash wake disc covers a much larger area than the fruit fly, whoms downwash wake stream is positioned only beneath the area swept by the wings. And the honeybee has a narrower downwash disc region than the hawk moth but larger than the fruit fly and notably no connection between the two downwash streams exists.

Analysing the force measurements, the authors state that the hawk moth produces two peaks per stroke (2 for downstroke, 2 for upstroke) whilst the lower  $Re$  insects such as the fruit fly and thrips produce a single peak per stroke. The honey bee data is an in between as the downstroke generates a single peak and the upstroke generates two peaks. And they go on to mention that the LEV is the source which is most likely to be responsible for most of the force generation, as a stable LEV is present throughout majority of the complete cycle for all of the insects. Furthermore, the stable vortex rings formed for each insect during each stroke may have some influence in force generation. A comparison of the mean force generated per stroke showed that the hawk moth produces majority of its lifting force during the downstroke, the honeybee generates approximately an equal sized lift force per stroke and the fruit fly generates majority of its lift force during the upstroke. The aforesaid provides some implication that force generation may be  $Re$  or size dependent where insects which fly in a higher  $Re$  range and are larger exploit their downstroke as the power stroke and insects which fly at the lower  $Re$  range and are smaller, do the opposite whereby they use the upstroke as their power stroke. As expected, the largest insect requires the most aerodynamic power and the smallest most lightweight insect required the least aerodynamic power to hover. This relation remains

consistent for all the insects considered where the hawk moth required the most aerodynamic power followed by the honeybee, fruit fly and finally the thrips insect.

The mean aerodynamic force produced for the thrips in the simulation is less than the weight of the insect, which raises concerns over the simplifications and computational method adopted to model the fluid dynamics of this insect. Simplifications such as using a membraned wing rather than a realistic bristled wing and modelling the kinematics of a fly rather than a real thrips. Also the fore and hind wing flap with a phase difference which may result in a cambered effect augmenting the aerodynamic performance this has been neglected in their simulation as the insect was modelled with only two wings. Furthermore, the body inclination and stroke plane angle would all have some effect on the flight forces generated which were not taken into consideration. Due to the number of differences the aerodynamic forces produced are not sufficient for the insect to hover, further information can be found in (Liu et al. 2009).

## 5.2 Cases Simulated

### 5.2.1 Drosophila

As an initial case, the methodology and boundary conditions employed within Fluent required validation for flapping wing simulations. Henceforth, the drosophila wing motion was modelled within Fluent and the results were compared to the experimental data of Dickinson et al. (1999) and the computational data of Ramamurti et al. (2002). The computational domain utilised for the simulations has been shown in Figures 5.4 and 5.5. The external domain commonly referred to as the outer domain includes the mesh in red and the inner domain is shown within this in a light blue shade. In the case where a SVID is utilised the domain is larger than the inner domain shown in the picture and covers the entire stroke angle region as it does not dynamically manoeuvre with the wing.

Further to this, a grid sensitivity study was carried out to achieve a grid independent solution, with the consideration of computational expenditure in terms of the time required for completion and moreover accuracy of the solution. For the grid sensitivity study, five different grids were examined which have been listed in Table 5.2 with their respective mesh densities. Slices have been presented in Figure C.7 to visualise the cells wrapped around the wing and the mesh on the wing surface has been shown in Figure

C.8. Furthermore, two dimensional slices which focus on the leading edge and present the cells in this region are shown in Figure C.9. The axis of wing rotation is also shown on the CAD image of the drosophila wing with a red line in the aforesaid figure.

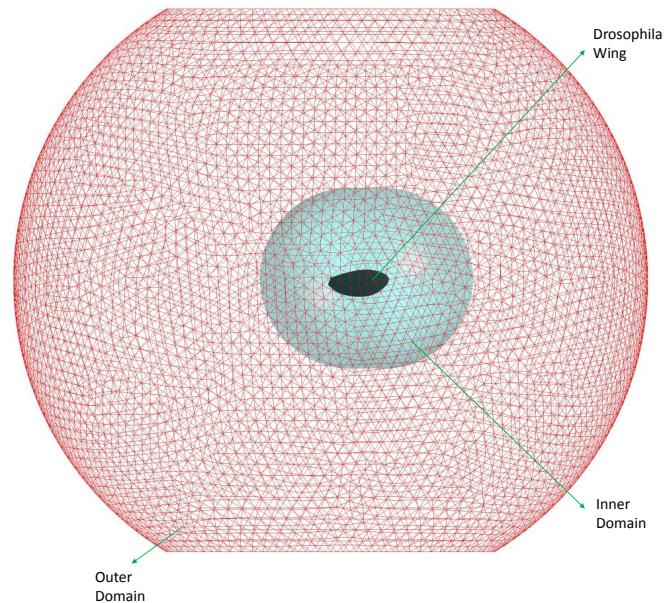


Figure 5.4: *Computational Domain with a Drosophila Wing*

A symmetrical plane is introduced to reduce the computational effort required for all the simulations presented in this chapter. As shown in Figures C.7 and C.8, an unstructured tetrahedral mesh was utilised for these computational simulations, this type of mesh was also employed for the remaining simulations presented in this chapter. The wing has a fixed wing-base coordinate system which it will rotate around which relates to the global world fixed coordinate system, and when a body is installed into the domain, it will too have a body fixed coordinate system which will relate to the global world fixed coordinate system. However, in such a case when a body is installed the wing based coordinate system will relate to the body coordinate system which will then relate to the global world fixed coordinate system.

In all the simulations considered in this thesis, the wing is assumed to be rigid and cannot deform. The initial state of the volume grid known as the outer domain will alter as a wing or any body dynamically moves through the tetrahedral 'net like' mesh structure, which will be re-meshed according to mesh quality, where poor cells can be eliminated and re-generated based upon the specified mesh criteria. As shown in Table

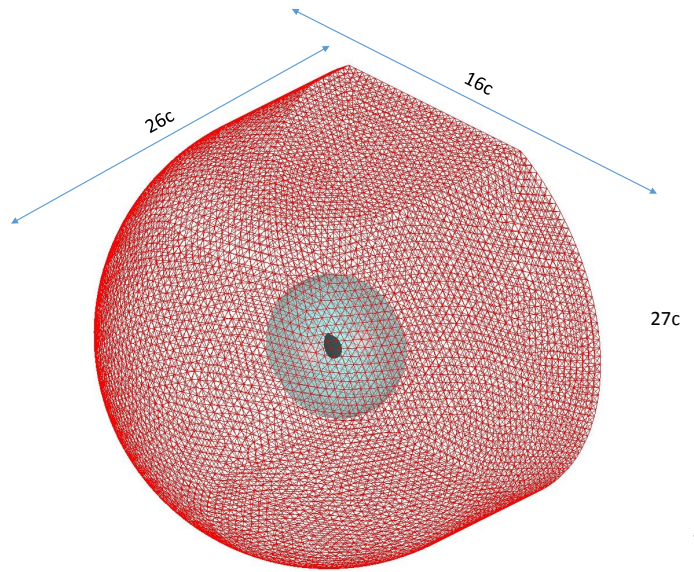


Figure 5.5: *Drosophila Wing Computational Domain with Dimensions*

5.2, two different categories of mesh have been developed, one which has a virtual inner domain (VID) that has the ability to follow the wings motion (known as a dynamic virtual inner domain DVID) and the other which is a VID that remains stationary allowing the wing to dynamically travel through its volumetric mesh. The former style would conserve a high quality mesh continuously around the wing as the VID would travel with the wing altering the mesh outside of this dynamic domain, thus the inner domain shell which encloses the wing and the outer domain would experience a change in state of its internal mesh as the VID moves through it. Employing this methodology would produce more accurate solutions due to the preservation of a high quality mesh continuously present around the wing, whilst reducing the computational cost in terms of time and reducing the computational resources required. The alternative method where the wing travels through a stationary virtual inner domain (SVID) could have lower quality cells wrapped around the wing or present in the near vicinity of the wing which would reduce the accuracy of the solution, whilst increasing both the computational time required and resources needed. Nevertheless, this method has to be utilised in certain situations, such as the presence of a stationary wall in the proximity of a dynamic wing as considered in the experimental investigations of this thesis.

The wing kinematics performed by the drosophila wing in this simulation has been shown in Figure 5.6A,

| <b>Grid Name</b>                                     | <b>Number of Cells</b> |
|--|------------------------|
| <i>Coarse with Dynamic Virtual Inner Domain</i>      | <i>0.425 Million</i>   |
| <i>Medium with Dynamic Virtual Inner Domain</i>      | <i>0.85 Million</i>    |
| <i>Dense with Dynamic Virtual Inner Domain</i>       | <i>1.7 Million</i>     |
| <i>Dense with Stationary Virtual Inner Domain</i>    | <i>1.7 Million</i>     |
| <i>Hyper Dense with Dynamic Virtual Inner Domain</i> | <i>3.4 Million</i>     |

Table 5.2: *Grid Density for Drosophila Wing*

although these are not the exact kinematics due to experimental tolerances and inaccuracies in the actual wing motion performed, the time dependent kinematics are accurate enough to model the wing motion. The lift force from the simulation can be found from the conventional Equation 5.58 and the formula to determine the drag force was mentioned earlier in this chapter. A graphical representation of the downstroke wing motion performed in the drosophila simulation has been shown in Figure 5.6B, to aid the reader in visualising the coupled motion of the wing as it rotates about a wing based coordinate system.

$$F_L = \frac{1}{2}\rho U_{ref}^2 SC_{FL} = qSC_{FL} \quad (5.58)$$

The aerodynamic data for lift and drag forces acquired from the grid sensitivity analysis has been displayed in Figure 5.6. The simulations were performed for three successive cycles and the data from the final cycle has been displayed, although very small differences existed between the second and third cycles. A general comparison of the lift curves, implies that the data for each grid produces similar results especially at the peak positions where the wing undergoes rotational effects and wing-wake interaction. Nonetheless, it can be clearly seen that the data during the translation phase of both strokes for the dense grid with a stationary VID and the remaining four grids has a clear distinction. Albeit, the grid consisting of a SVID has far more cells than the coarse and medium grids in the vicinity of the wing where measured data still presents perceptible discrepancies during the translation phase. The distinction found in the aerodynamic data relates directly to the quality of the cells in the vicinity of the wing and the ability of this grid to solve for the vortex lifting occurring at this stage of wing motion accurately.

Nevertheless, it should be kept borne in mind that certain techniques such as adaptive time-stepping and

mesh criteria can be applied to improve the accuracy of the solution when a stationary VID is chosen as the appropriate method for a simulation. Analysing the peak produced during the supination phase (Figure 5.6E) clearly presents that the dense DVID and hyper dense DVID grid produce very similar results which also applies for the medium grid as well. However, the dense grid with a SVID under predicts the size of the peak in comparison to the hyper dense grid and the coarse grid with a DVID over predicts the size of the lift force produced from the wings rotational effect. Finally, observing the drag plot shows that the data from all the grids match well, and the dense grid with a SVID only slightly over predicts the drag force produced at the start of each stroke.

At the commencement of each stroke lift enhancement occurs as the wing travels through its wake of shed vorticity from the previous stroke this in turn also produces a peak in drag force as seen from the data in Figure 5.6. The large peak occurs due to the orientation of the wing when it interacts with the shed vorticity. If the wing had a more favourable AOA the lift enhancement would be greater and the drag produced would be less, which is what occurred in the advanced wing rotation case mentioned in the publication of Dickinson et al. (1999) and Ramamurti et al. (2002). Furthermore, if the rate of rotation were altered this would also affect the peak lift force generated. If the rate of wing rotation increased, then lift enhancement would be achieved by a faster rate of rotation as well as developing a favourable AOA quicker in order to take more advantage of capturing the wake of the shed vorticity from the previous stroke.

To accurately model the experiment via numerical simulation, the fluid dynamic properties such as  $Re$  in this case would need to be the same. Thus, the geometrical properties of the wing such as span, chord and thickness should match the experimental wing features as close as possible. From an experimental point of view, when the wing was manufactured specific tolerances would have applied, thus an exact geometrical match is not possible between experimental and computational methods. However, in such an instance it is key to simply match with reasonable accuracy. Other factors such as surface roughness, edge finishings etc. would all have some form of effect on the near fluid dynamics of the wing, but as the effects are very small, they are deemed negligible, unless surface roughness on the surface of the wing is very high in which case this would need to be accounted for.

A comparison of the lift and drag forces produced from the present simulations have been compared to the experimental work of Dickinson et al. (1999) and the computational work of Ramamurti et al. (2002), the plots have been shown in Figure 5.7, it should be noted that the results presented are cyclic independent.

The simulation results of this project have good agreement with the experimental data, which applies moreso for the upstroke lift plots and especially the drag curve. The computational data of Ramamurti et al. (2002) have very good agreement with the simulated data of this project. At the start of each stroke where the wing has a coupled motion and interacts with its wake shed from the previous stroke, the lift force peak produced for the experimental data is larger than both the CFD results. Furthermore, symmetrical results are not produced for lift force data in both half strokes from the experimental data, especially during the translating phase where the wing is held at a constant AOA reducing the complications of a coupled motion. Such an asymmetry in the data may exist as the AOA for the downstroke differed to that held during the upstroke motion, the AOA held during the upstroke motion was more or less 40 degrees which matches that of the CFD data which is why the upstroke results have a better comparison for all three data sets. The kinematics modelled in the simulations of this project were symmetrical for both half strokes, hence the symmetrical nature of the lift and drag forces produced for each half stroke. The experimental and computational data for the drag curve relate very well, the only noticeable difference occurs for the peak produced during the rotation at the end of the stroke / start of supination or pronation and the very large negative drag force produced at the end of a stroke / start of the following stroke.

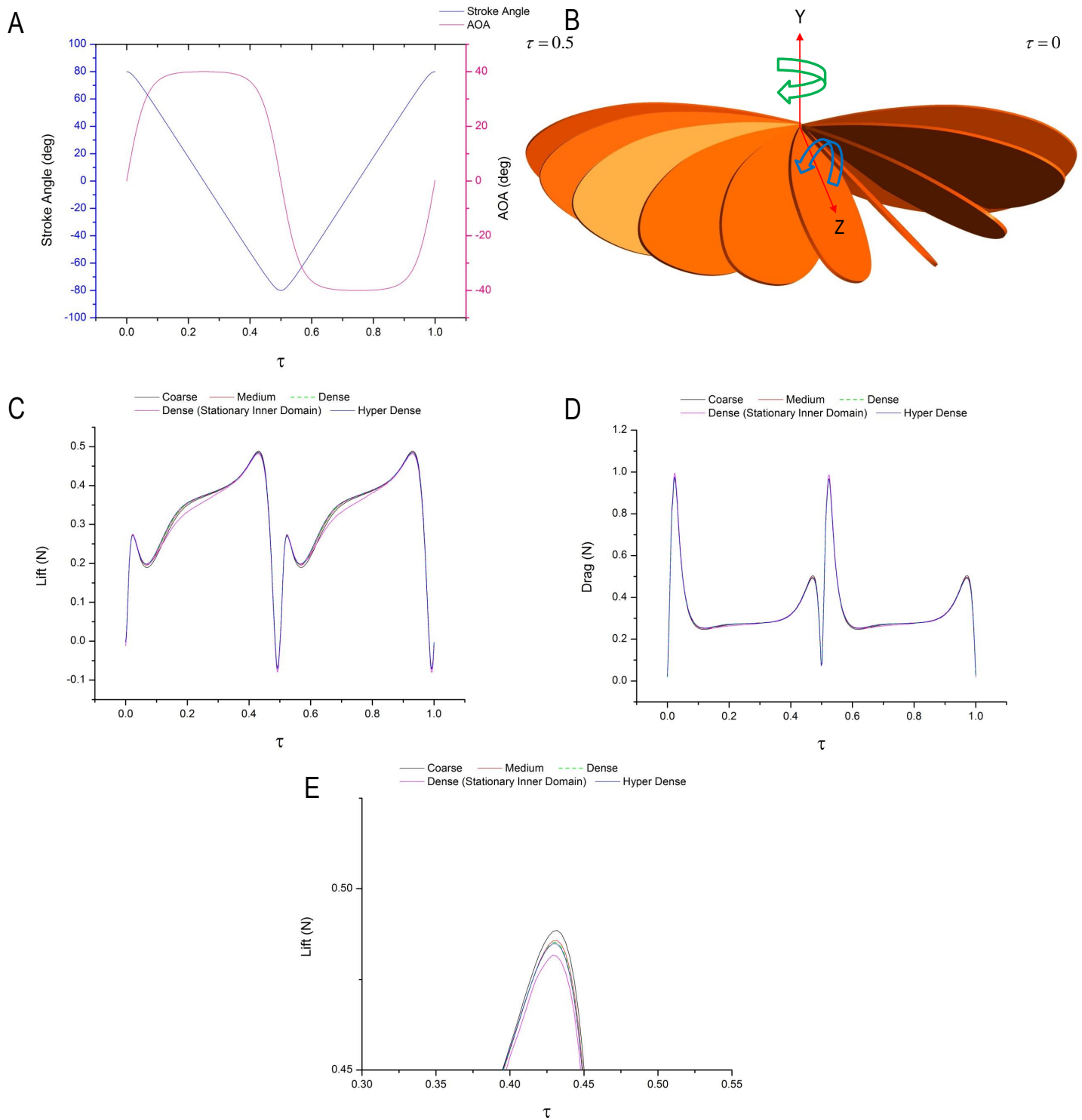


Figure 5.6: *Drosophila* Wing Kinematics and Measurement Comparison for Various Grid Densities; A: Wing Kinematics, B: Wing Motion (green arrow: flapping, blue arrow: pitching), C: Lift Force Comparison, D: Drag Force Comparison, E: Lift Force Comparison Close-Up

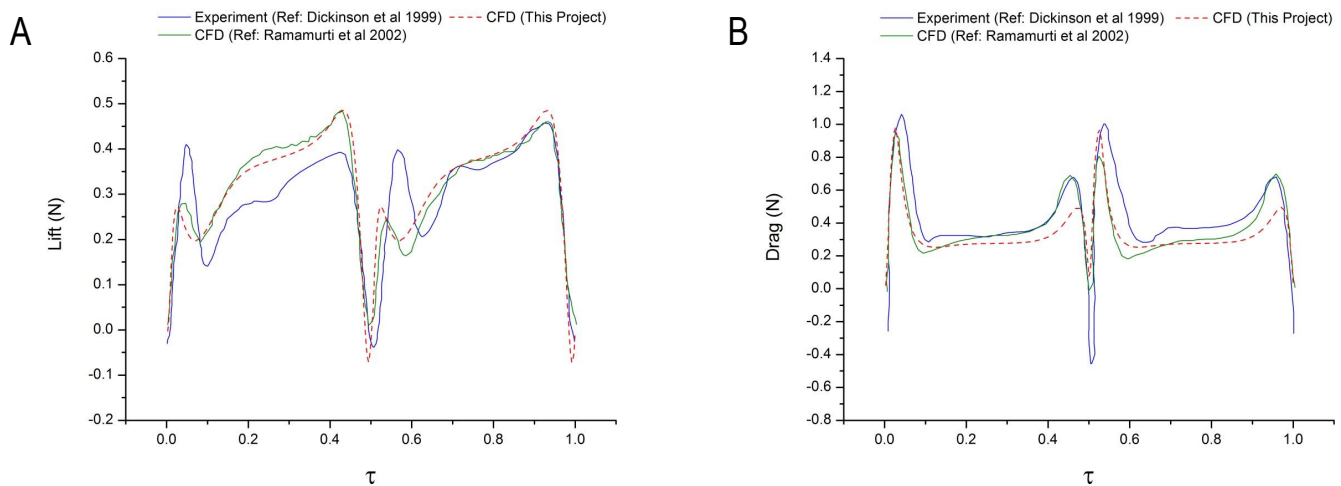


Figure 5.7: *Drosophila* Wing Measurement Comparison; A: Lift Force Comparison, B: Drag Force Comparison

In reality, attempting to match the experimental and computational results of such a complex nature is near impossible due to the number of uncertainties, inaccuracies and highly unsteady fluid dynamics involved. The differences between the experimental and computational results of this project could be due to a combination of the following: differences in the rate of wing rotation, differences in the axis of wing rotation, differences in the geometrical shape of the wing which would lead to distinctions in wing area and differences in time dependent AOA due to gear slippage and play in the experimental mechanism. Small differences also exist between the computational results from literature and those developed in this project as the wing kinematics differed, in addition the wing outer profiles have small differences which would have an effect on the fluid dynamics especially as the wing is dynamically rotated. The simulation results of Ramamurti et al. (2002) had similar kinematics to the experimental work as mentioned in literature.

Figure 5.8, illustrates flow visualisation images of the *drosophila* wing at mid-downstroke produced from the dense grid with a DVID. The flow movement shown by an inner vortex structure within the outer LEV travels from wing base to tip with a somewhat organised spiral formation travelling a curvilinear path, the outer vortex is shown with less instantaneous streamlines to clearly depict the tight tube-like structure of the inner vortex. At this very low Re of 136 the spanwise flow velocity travelling through the vortex structure is very weak (much smaller when compared to the velocity of the wing tip), this has been stated in various reviews of literature in this thesis. Albeit, the spanwise velocity may be weak, but this type of LEV is known to be more stable at low Re flows and alongside strength, vortex stability is a paramount factor in vortex lift enhancement phenomena. However, direct comparisons between the flow physics of this simulation and

a drosophila insect have considerable differences as the wing kinematics under hovering conditions are very different. The outer vortex structure attached to the leading edge has also been shown for clarity to help visualise its compressed and stable nature, which grows in diameter from the wing root towards the wing tip. The zoomed in view of the flow field describes the unsteady nature of the fluid which surrounds the wing with a complex formation. The self stabilising technique of the vortex and its importance have been highlighted earlier in this report.

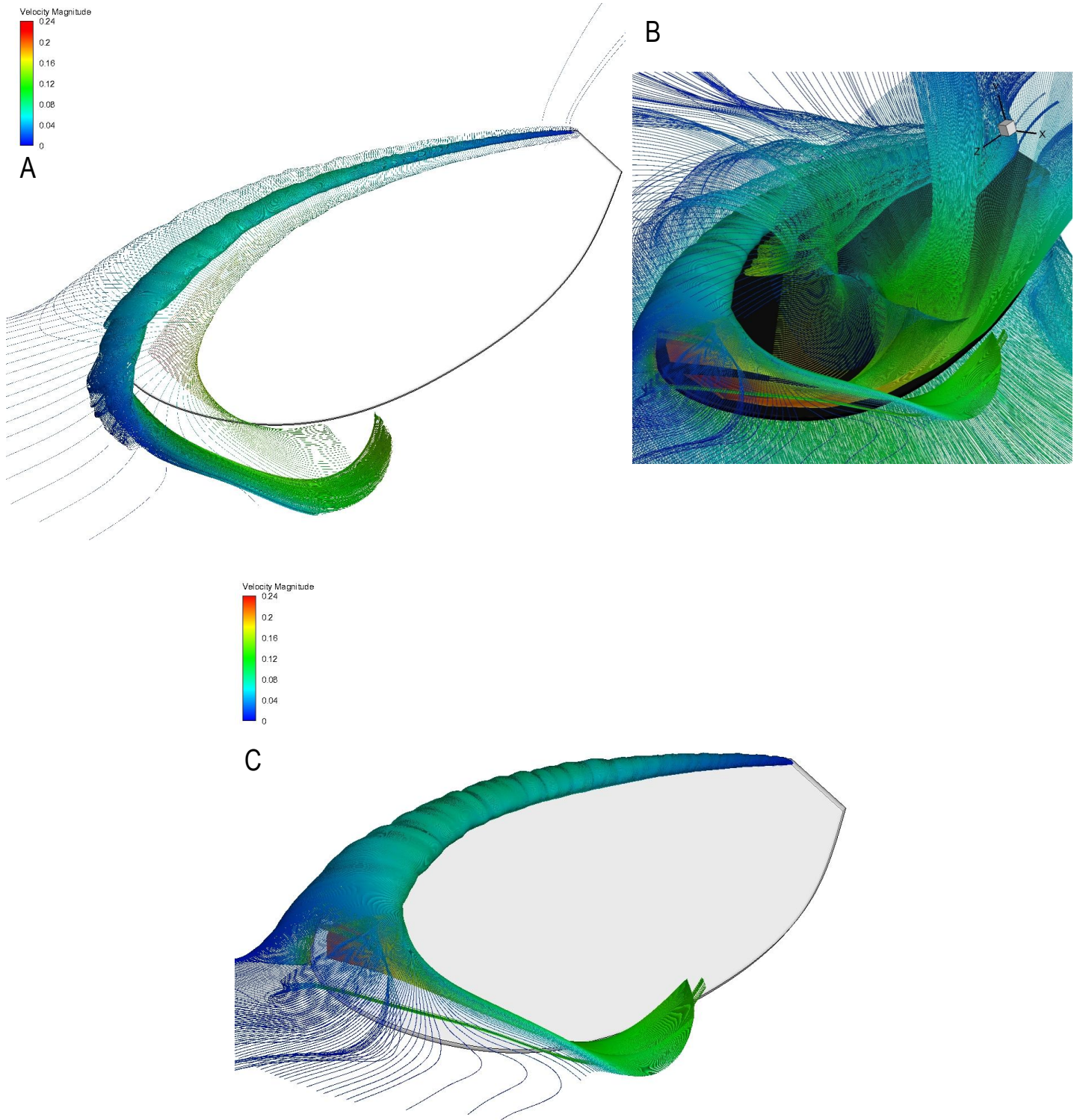


Figure 5.8: *Drosophila* Wing with Streamlines; A: Inner and Outer Vortex at  $\tau = 0.25$ , B: Flow Field Around Wing at  $\tau = 0.25$ , C: Full Outer Vortex Travelling from Root to Tip at  $\tau = 0.25$

### 5.2.2 Rectangular Wing

Simulations were conducted for a rectangular wing (refer to Table 5.3 for specifications) which underwent a flapping and rotating motion along the horizontal plane essentially producing a hovering motion. Twelve cases were compared in which the grid, type of wing, frequency, Reynolds number, flapping amplitude and pitching amplitude were all kept consistent. The wing rotation kinematics although modelled with the same equation for all cases, had alterations applied to some of its variables in order to control the duration of wing rotation. Along with variations in the rotational duration, the position of wing rotation was also varied at positions along the chord-wise axis from the leading edge to mid-chord. All the cases were simulated with a dense grid composed of 1.7M tetrahedral elements exploiting the DVID method. The force axis for the rectangular wing which also applies to the drosophila simulation has been shown in Figure 5.9. A slice of the two dimensional cells wrapped around the rectangular wing has been shown in Figure 5.11B, as expected the cells were heavily clustered around the wing to improve the accuracy of the solution. A grid sensitivity analysis has not been performed for the rectangular wing cases as major changes are not made from the original drosophila case previously presented. Taking this into consideration, the dense mesh has been chosen for these numerical simulations. All computational and experimental tests are performed under the condition of zero incoming flow.

The cases mentioned were investigated to determine the effects such alterations have on the aerodynamic forces, moments and power required as the wing moves through the fluid with a prescribed periodic motion. Due to the nature of the experiments performed in this project such control over the wing was impossible, thus computational explorations were carried out. The Reynolds number for these simulations is 155 which is slightly larger than the drosophila wing case. The kinematic motion executed by the wing was similar in comparison to the drosophila case which is shown in Figure 5.11A. The rotational position is an important factor for the obvious reason of its affect on the fluid dynamics and conjointly this parameter can actually be selected for a robotic FWMAV where the axial position of wing rotation can be set-up on the FWMAV during its design phase, however this cannot be amended during flight. Thus, such an analysis would aid in understanding and selecting the more auspicious rotational position. The maximum constant angle of attack for these cases is 30 degrees, which means at pronation and supination the wing will flip through an angle of 60 degrees during stroke reversal to position itself for the onset of the next stroke and the wing rotations for all the cases are performed in a symmetrical manner. Figure 5.12, displays the wings motion through a

single stroke and its respective rotational axes.

The twelve cases that have been investigated as part of this study have been listed in Table 5.4. Three rotational durations are analysed for the variable rotational positions along the chord-wise axis which is shown in Figure 5.11C, in which the mesh on the wing surface can also be seen. In more detail,  $\chi = D$  rotates about the span-wise axis at the leading edge of the wing,  $\chi = C$  rotates about the span-wise axis at 30% along chord from the leading edge,  $\chi = B$  rotates about the span-wise axis at 40% along the chord from the leading edge and finally  $\chi = A$  rotates about the span-wise axis at mid-chord position. The flow has been visualised around the wing for case 11, at early downstroke in Figure 5.11D, instantaneous streamlines were released at the leading, trailing and tip edges of the wing to view the vortical formations along these locations. The growth of the LEV and TEV have distinct similarities as both augment in diameter from the wing base to tip and both have a tight appearance with increasing flow velocity towards the tip. The TV has a much larger appearance opposed to the LEV and TEV vortices with a high velocity region on the inside of the TV above the wing tip, furthermore, a clear connection can be observed as the TV links all three vortical structures together. The axial rotations for the rectangular wing are the same as the drosophila wing as shown in Figure 5.6B. However, in the case of the rectangular wing the pitching motion occurs about 4 different positions along the chord rather than a single position.

The data in each of the plots is from the third flapping cycle as the data set produced for the second cycle had some differences when both were compared. On the other hand, when the data sets of the third and fourth cycles were compared very small differences existed, thus the solution was said to have converged with sufficient accuracy and overall the data of the third cycle will be used. Thus, simulating the fourth cycle for every case was said to be unnecessary, and in doing so would be inefficient due to the additional computational costs required for a considerable number of cases. The conventional equations for the horizontal and side forces have been shown below 5.59 and 5.60. Thereafter, the moment equation has been shown 5.61 which although is in reference to the x-axis, the formula is generic and can be applied to the remaining axes. The aerodynamic power required can be determined from Equation 5.62, which is calculated by both the flapping and wing pitching rotational moments and their respective time dependent wing positioning characteristics.

$$F_x = \frac{1}{2} \rho U_{ref}^2 S C_{Fx} \quad (5.59)$$

$$F_z = \frac{1}{2}\rho U_{ref}^2 SC_{Fz} \quad (5.60)$$

$$M_x = \frac{1}{2}\rho U_{ref}^2 SC_{Mx} L_{ref} \quad (5.61)$$

$$P_{req} = \left| My_{wing} \frac{\partial \phi}{\partial t} \right| + \left| Mz_{wing} \frac{\partial \psi}{\partial t} \right| \quad (5.62)$$

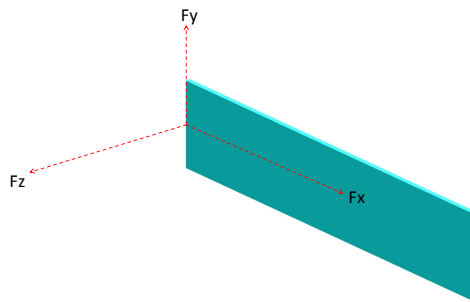


Figure 5.9: *Rectangular Wing with Force Axis, Flapping is About Fy & Pitching is About Fz (Moments Are Positive in The Anti-Clockwise Direction About Each Axes)*

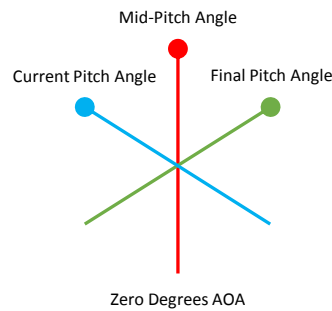


Figure 5.10: *Wing Pitching Schematic for Rotation Duration (Circle Represents Leading Edge)*

Figure 5.10, presents a simple schematic that describes the pitching motion of the wing during the rotational duration. The rotational duration is the time taken for the wing to reverse its pitch angle during supination or pronation. The diagram only describes the pitching motion, however, during this motion the wing also translates whilst rotating in pitch angle, which is detailed in Figure 5.11A.

| Parameter                      | Rectangular Wing |
|--------------------------------|------------------|
| <i>Wing Span (m)</i>           | 0.2612           |
| <i>Mean Chord (m)</i>          | 0.0852           |
| <i>Area (m<sup>2</sup>)</i>    | 0.0445           |
| <i>Aspect Ratio</i>            | 6.2              |
| <i>Flapping Frequency (Hz)</i> | 0.145            |
| <i>Thickness (m)</i>           | 0.0032           |

Table 5.3: *Rectangular Wing Specifications*

| Case Number | Case Title  |
|-------------|---|
| 1           | <i>Rotation Position : D, Rotation Duration : 3.3s for a Rectangular Wing</i> |
| 2           | <i>Rotation Position : D, Rotation Duration : 2.2s for a Rectangular Wing</i> |
| 3           | <i>Rotation Position : D, Rotation Duration : 1.1s for a Rectangular Wing</i> |
| 4           | <i>Rotation Position : C, Rotation Duration : 3.3s for a Rectangular Wing</i> |
| 5           | <i>Rotation Position : C, Rotation Duration : 2.2s for a Rectangular Wing</i> |
| 6           | <i>Rotation Position : C, Rotation Duration : 1.1s for a Rectangular Wing</i> |
| 7           | <i>Rotation Position : B, Rotation Duration : 3.3s for a Rectangular Wing</i> |
| 8           | <i>Rotation Position : B, Rotation Duration : 2.2s for a Rectangular Wing</i> |
| 9           | <i>Rotation Position : B, Rotation Duration : 1.1s for a Rectangular Wing</i> |
| 10          | <i>Rotation Position : A, Rotation Duration : 3.3s for a Rectangular Wing</i> |
| 11          | <i>Rotation Position : A, Rotation Duration : 2.2s for a Rectangular Wing</i> |
| 12          | <i>Rotation Position : A, Rotation Duration : 1.1s for a Rectangular Wing</i> |

Table 5.4: *Simulations Performed for a Rectangular Wing Moving in a Horizontal Plane*

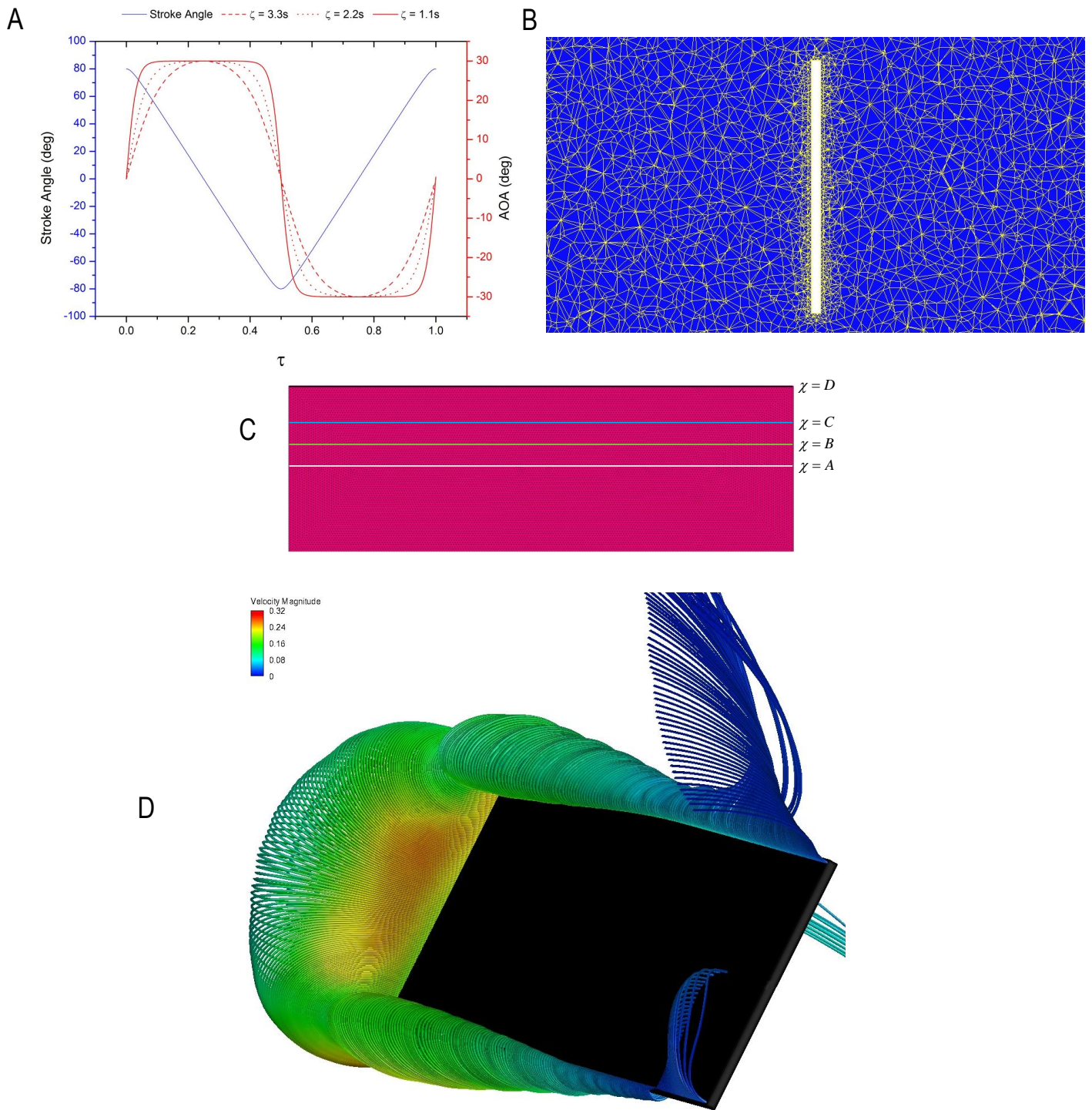


Figure 5.11: Kinematic and Flow Details for the Rectangular Wing; A: Kinematic Plot for Rectangular Wing Simulations, B: Cells Surrounding The Wing, C: Rotational Positions Investigated, D: Flow Around The Wing for case 11 at  $\tau = 0.045$ . Velocity Units: m/s

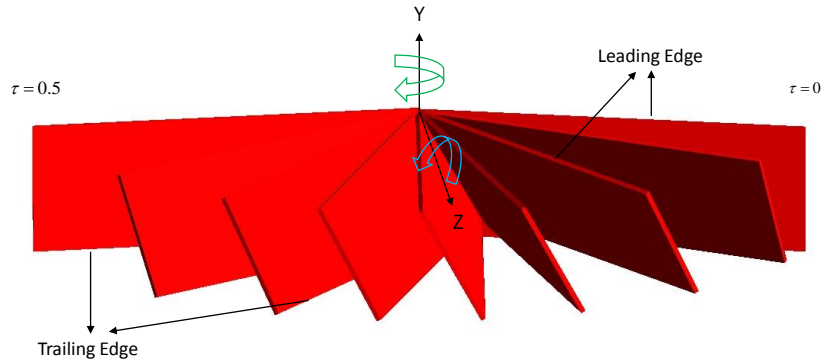


Figure 5.12: *Rectangular Wing Motion Through a Stroke (green arrow: flapping, blue arrow: pitching)*

A comparison of the lift forces generated by the wings (Figure 5.14A) whilst the wing rotates about the leading edge along the span-wise axis demonstrates that a rapid wing rotation during the supination and pronation phases has a significant beneficial impact to the lift force peaks produced. However, it must be kept in mind that along with a rapid wing pitch flip, the position of wing pitching is extremely vital. When  $\zeta = 1.1s$  a peak is produced as the wing rotates from 0 degrees to its maximum AOA of 30 degrees, thereafter the wing translates through its downstroke motion keeping a constant AOA and a near steady lift force is produced during this translation phase. Towards the end of the downstroke, the rotational phase termed supination commences where a peak is produced from the accelerative rotational effect of the wing, following this a second peak is produced as the wing continues to rotate and interacts with the shed vorticity from the previous stroke. This cyclic motion continues in the same manner during the upstroke as the prescribed kinematic motion is symmetrical.

As the rotational duration increases to  $\zeta = 2.2s$  the size of the peaks produced at the end and start of the strokes heavily reduce, albeit, their presence is still notable opposed to the lift data produced when the rotational duration increases further to  $\zeta = 3.3s$ . In the latter, the wing has a constant AOA for a very short period, thus for majority of the cycle the wing has a dynamic AOA altering very slowly when compared to the previously mentioned two rotational durations. At the end of the downstroke as supination commences a peak is produced for  $\zeta = 2.2s$  and as the vortices are shed from the wing they move into the wake which the wing captures at the onset of the next stroke where a peak force is produced. For  $\zeta = 3.3s$ , at the onset of the following stroke a small peak is produced as the wing continues to rotate and captures the vorticity present in the wake from the prior stroke, but this peak is much smaller compared to when  $\zeta = 2.2s$  and

$\zeta = 1.1s$ . The average lift force produced per cycle has been shown for all three rotational durations in Figure 5.14B, where it is clearly seen that the largest lifting force is generated when  $\zeta = 1.1s$  and the lift force declines as the rotational duration increases.

Figures 5.14 C and D, present lift force data for  $\chi = C$  whilst comparing all three rotational durations. For  $\zeta = 1.1s$  a peak is produced at the start of every stroke where the wing is performing a rotational motion whilst capturing the shed vorticity from the previous stroke (see Figure 5.13). And interestingly as the rotational axis has moved downwards along the wing chord from the leading edge, no peak force is produced towards the end of the stroke when supination and pronation commences. Similarly at the start of a stroke a peak is produced when  $\zeta = 2.2s$  and a very small peak as seen in the previous plot is present when  $\zeta = 3.3s$ , the wake capture of the vorticity shed in the previous stroke is a paramount enhancement feature which contributes to the overall lift force produced per cycle. During the translation phase of both strokes when  $\zeta = 2.2s$  an almost steady lift force is generated as the AOA is held constant and the LEV is stabilised enhancing the lift force. The bar plot of the average lift generated displays that as  $\zeta$  is increased the mean lift force produced per cycle declines, thus a near continual wing rotation throughout each stroke at a slow velocity is not beneficial for generating lift.

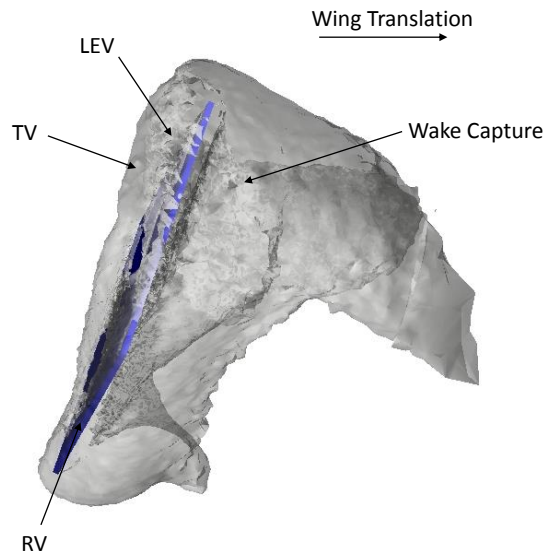


Figure 5.13: *Flow Around The Rectangular Wing with Rotation Position D and Duration of 1.1s, Early Downstroke*

As the wing approaches the end of the translation phase it has a fixed AOA of 30 degrees, which will dynamically alter as the supination or pronation phases begin. At the onset of a rotational phase as the wing rotates about the leading edge a large favourable pressure acts on the under surface of the wing, as the wing forces its way through the fluid present in the vicinity of its lower surface. As a result an upward lifting force is generated which is greater for shorter rotational durations as the velocity of the wing flicking effect is larger which has a direct relation to the force generated. If the rotational axis is moved downwards along the wing chord as has been analysed in this study, this favourable pressure which acts on the wings under surface is reduced as the area of the lower surface forcing its way through the fluid is reduced, and in addition the upper surface which is moving in the opposite direction is also forcing its way through the fluid present in its near vicinity which produces a force in the opposing direction. In effect, the positive lift force produced is heavily reduced due to the reduction in area of the lower surface interacting with the fluid (which has a positive vertical force vector) and the upper surface which interacts with the fluid whilst rotating generates a force vector in the downwards direction. Overall, in the cases presented in this study it would be more beneficial to have the wing rotational axis located along the leading edge to generate a sufficient peak force at the end of a stroke or at least near to the leading edge to take advantage of this force enhancement mechanism.

Figures 5.14 E and F, displays a comparison of the data for all three rotational durations for the axis of wing rotation located at  $\chi = B$ . At the start of both strokes a peak is produced similar to the previous plots which is an enhancement of lift production as the wing captures the shed wake whilst rotating to reach a fixed AOA. Almost steady lift force is produced for a sufficient amount of time when  $\zeta = 1.1s$  and  $\zeta = 2.2s$  during the translation phase, whilst a small inclination is found in lift force during this phase for  $\zeta = 3.3s$  as the wing continues to rotate at a slow rate. Similar to the previous average cyclic lift force produced, as  $\zeta$  increases the amount of lift force generated seems to decrease. Such an outcome exists as a much smaller peak or even a plateau in lift force is produced at the onset of both strokes and continuous rotation at a slow rate generates a lower lift force throughout the cycle when compared to the plots of  $\zeta = 2.2s$  and  $\zeta = 1.1s$ .

The lift force data of the final rotational axis along the span located at mid-chord has been shown in Figures 5.15 A and B. A lift enhancement is noticed at the onset of each stroke as the shed vorticity from the prior stroke is captured whilst the wing rotates to approach its fixed AOA. For the simulation when  $\zeta = 3.3s$  a plateau is noticed instead of a small peak which means that as the rotational axis moves downwards from

the leading edge lift force generation at the onset of a stroke is affected, this will be further revealed in the following plots regarding lift force production. When  $\zeta = 2.2s$  and  $\zeta = 1.1s$  the lift force produced during the translation phase is almost steady unlike when  $\zeta = 3.3s$  where a small inclination is shown due to the continuous wing rotation. The overall average lift produced throughout the cycle is largest when  $\zeta = 1.1s$  and smallest when  $\zeta = 3.3s$ , thus the trend aforementioned for the previous plots still applies for this mid-chord rotational axis as well.

A comparison of the time history of lift generation per cycle with a consistent rotational duration and variable rotational axial locations have been shown in Figures 5.15 C and D. A similar trend existent between the individual curve lines is evident where some difference exists during the wings rotation towards the end of each stroke especially when the pitching axis is located along the leading edge of the wing. As aforementioned, as the pitching axis is moved downwards along the chord (where the leading edge is seen to be the top and mid-chord denoted as bottom) the lift force peak towards the end of the stroke reduces until effectively no peak actually exists during this phase. As expected the time history of the lift force data for each stroke is equivalent as the prescribed wing kinematics are symmetrical for each stroke, this applies to all the lift force plots displayed in this section. The average lift force comparison per periodic motion demonstrates that the largest lift force is generated when the wing pitching position is located along the leading edge of the wing. This reduces as the pitching position moves further down the wing in the chord-wise direction where the smallest lift force is produced when the wings rotation acts about the spanwise axis at its mid-chord.

Figures 5.15 E and F, display lift force data when  $\zeta = 2.2s$ , for a variety of wing pitching locations. Clear distinctions are present at the stroke reversal stages. At the start of each stroke a peak exists which is similar when  $\chi = A, B$  and  $C$ , but fairly different when  $\chi = D$  where the force generated is much larger as the wake capture mechanism has a much stronger effect. As the peak declines, the pitching about the mid-chord (when  $\chi = A$ ) has the greatest dip in force production as the wing continues to rotate and translate. During the translation phase where the wing has a fixed AOA, a very consistent lift force is produced which lasts longer when  $\chi = C$ . Towards the end of the stroke the wing begins to pitch as it approaches stroke reversal, a large lifting peak is generated when the pitching occurs about the leading edge spanwise axis. Peaks are not clearly evident for the remaining pitching locations and the size of the forces tend to reduce as the pitching position moves downwards from the leading edge. The pressure acting on the surface of the wing is much more favourable as the wing moves back towards an AOA of zero degrees when  $\chi = D$  as opposed

to the pressure acting on the lower and upper surfaces of the wing when  $\chi = A$ . As the favourable pressure is reduced heavily due to mid rotation this has a direct effect on the lift force produced in the upwards direction. The average cycle data explains a similar result to the previous average plot where the largest lift force is produced when  $\chi = D$  and is lowest when  $\chi = A$ . Furthermore, this same result is seen in Figure 5.15F where the average cyclic lift force generated decreases as the wings pitching axis moves downwards along the chord from the leading edge to the mid-chord.

Time history lift force data when  $\zeta = 1.1s$  for all four rotational positions has been shown in Figure 5.16A. Large peaks are observed during the rotational phases when the wing rotates about the leading edge spanwise axis. For the remaining three wing pitch positions, peaks are not observed during the first half of supination. During the translation phase when the wing is held at a fixed AOA, an almost steady lift force is generated for  $\chi = A, B, \text{ and } C$ , such a result does not exist when  $\chi = D$  where the force is seen to gradually decline until the start of supination or pronation.

For the sake of a clear comparison, the lift force data for both of the extreme wing pitch positions have been shown in Figures 5.16C and D. Lift generation between these two rotational locations has a large variance, which is evidently reflected in the averaged lift cyclic data, where the lift force produced when wing pitching occurs at the leading edge is larger for all rotational durations opposed to when wing pitching takes place at mid-chord. A three dimensional surface plot (Figure 5.16E) has been presented to compile the average lift force data on a single plot as both the rotational position and durations are altered. The colour bar provides an indication of the lift force to aid in understanding the size of lift forces generated. Clearly when the wing pitch position is at the leading edge and  $\zeta = 1.1s$  the largest average lift force is produced per cycle, and when the wing pitch position is located at mid-chord with  $\zeta = 3.3s$  the smallest lift force is produced. However, interestingly when the wing rotation is at  $\chi = A$  and  $\zeta = 1.1s$  a larger average lift force is generated opposed to when  $\chi = D$  and  $\zeta = 3.3s$ , thus the rotational duration has a significant effect on the average lift force data produced during a cyclic motion.

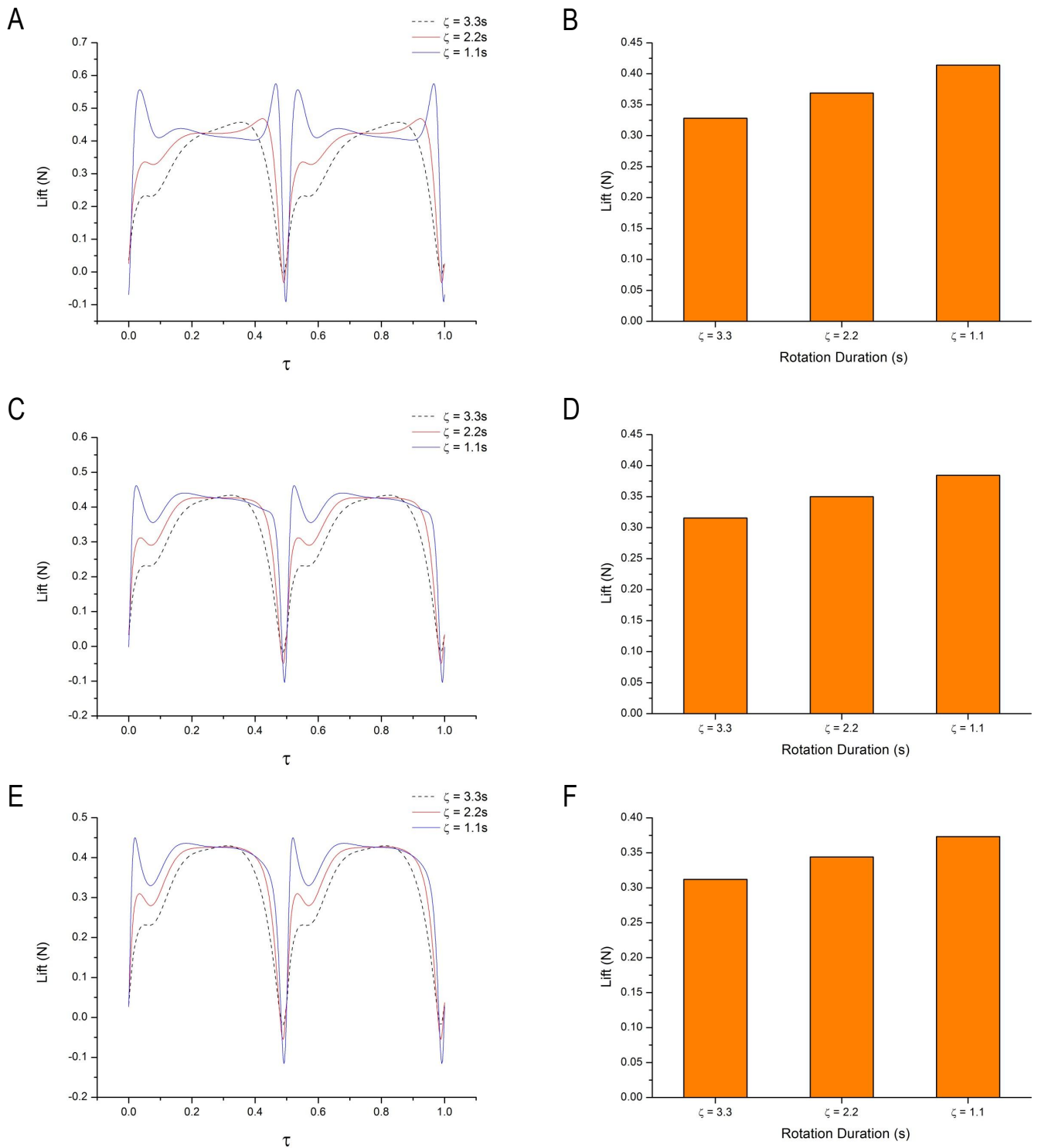


Figure 5.14: *Lift Force Comparison; A: Rotation Position D, B: Rotation Position D (average), C: Rotation Position C, D: Rotation Position C (average), E: Rotation Position B, F: Rotation Position B (average)*

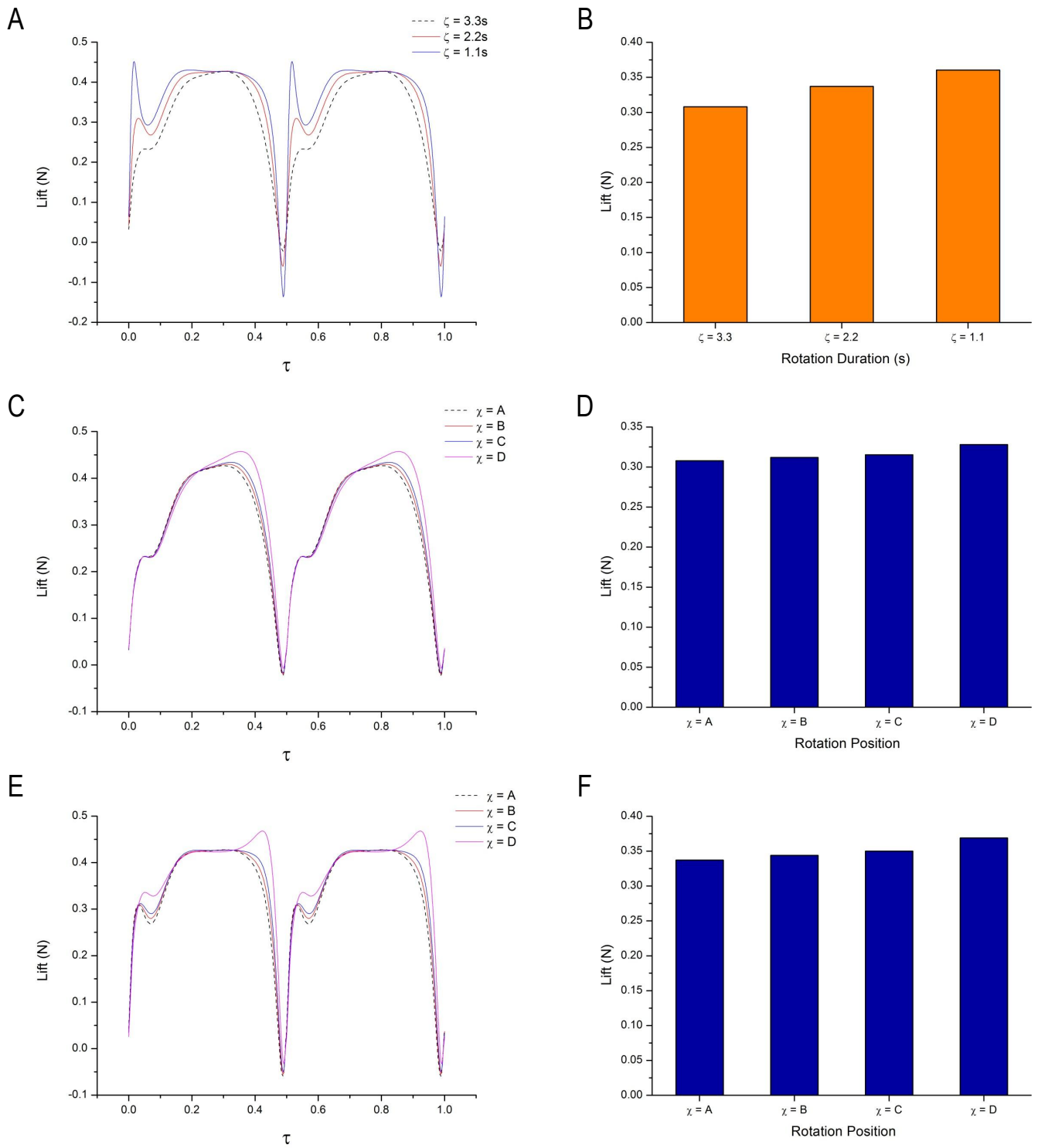


Figure 5.15: Lift Force Comparison; A: Rotation Position A, B: Rotation Position A (average), C: Rotation Duration 3.3s, D: Rotation Duration 3.3s (average), E: Rotation Duration 2.2s, F: Rotation Duration 2.2s (average)

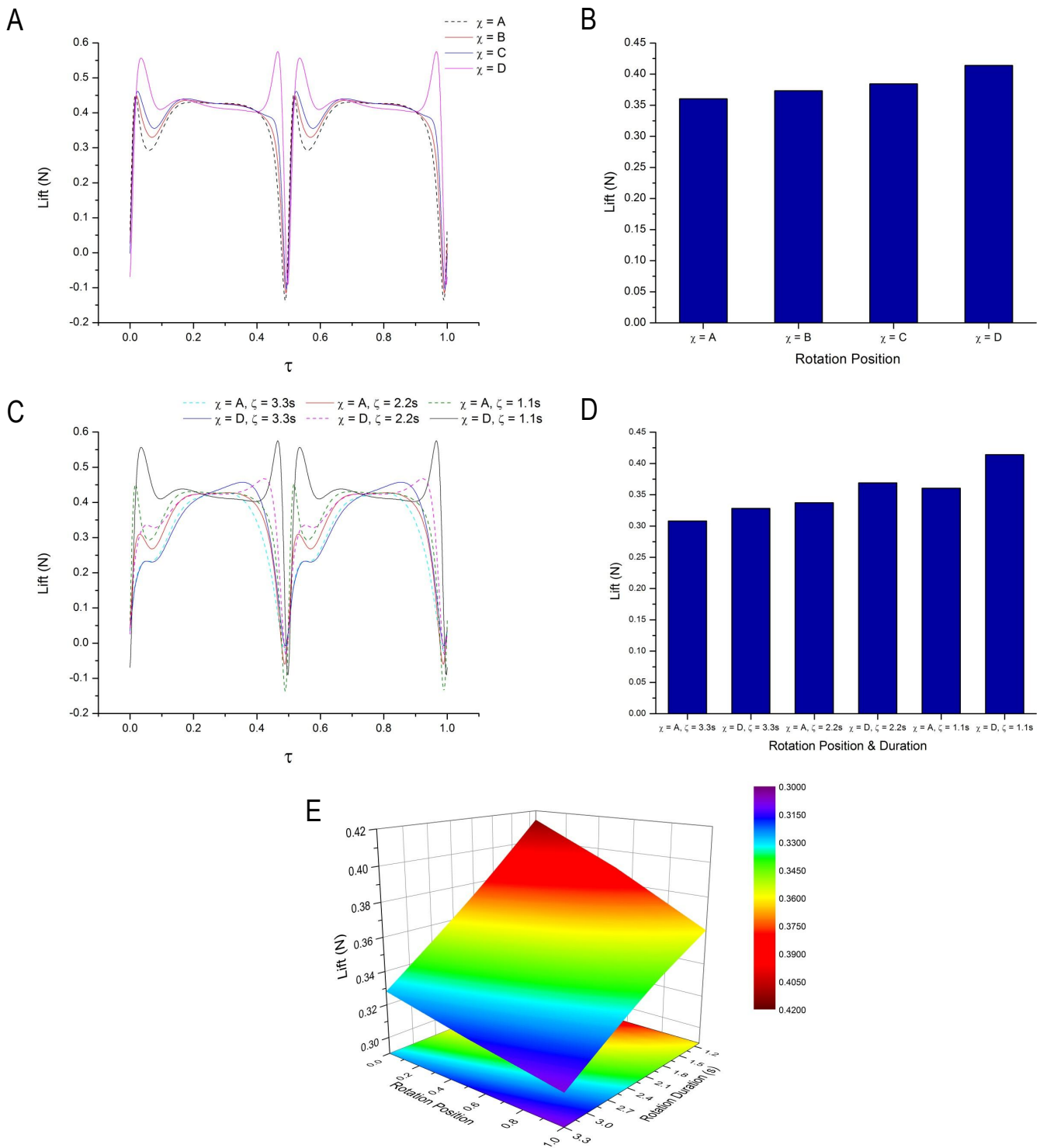


Figure 5.16: *Lift Force Comparison; A: Rotation Duration 1.1s, B: Rotation Duration 1.1s (average), C: Leading Edge Mid-Chord Positions, D: Leading Edge Mid-Chord Positions (average), E: Average Lift For All Cases (Legend Represents Lift Force)*

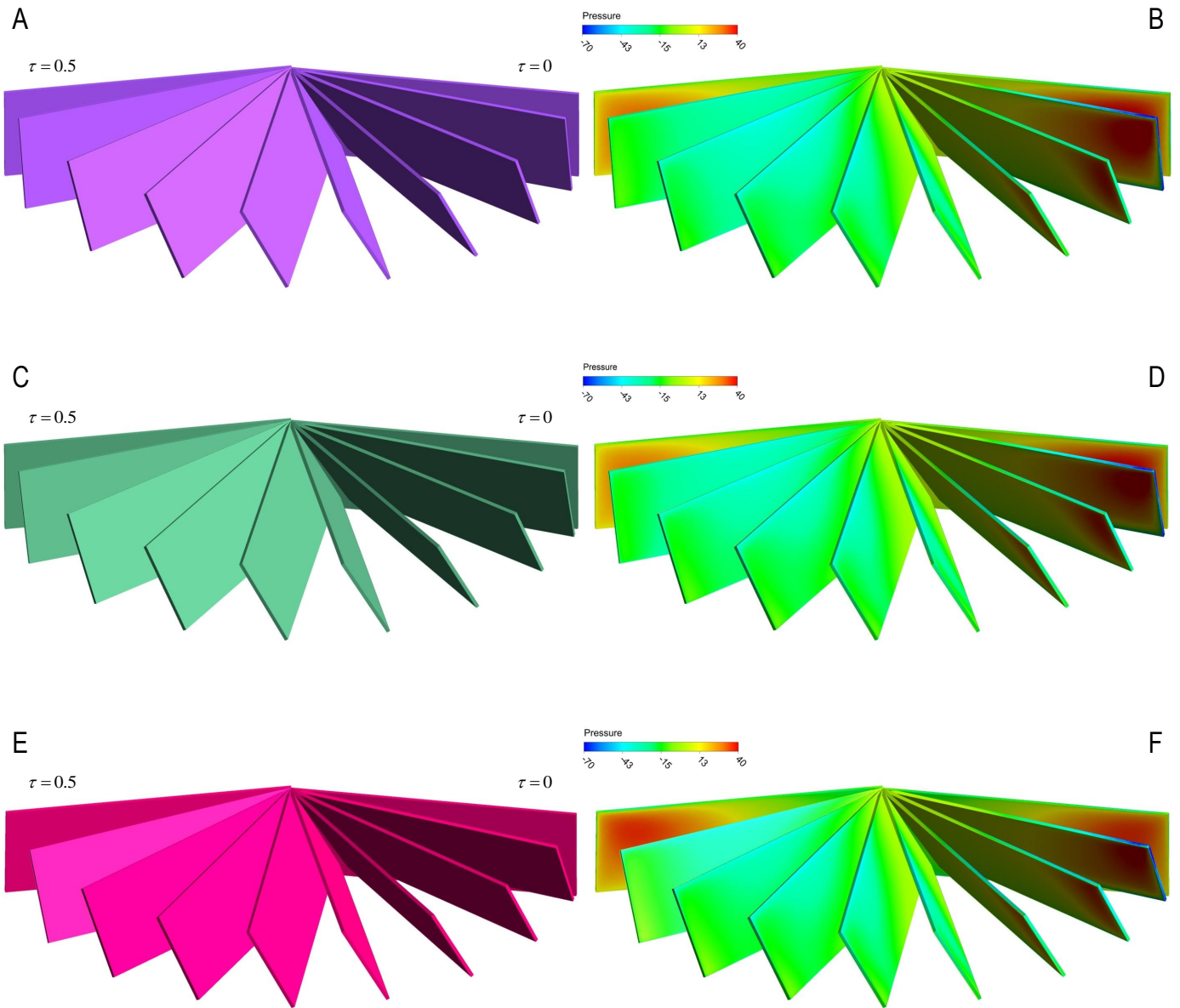


Figure 5.17: *Rectangular Wing Motion for Cases 1-3; A: Case 1, B: Case 1 with Pressure on Wing Surfaces, C: Case 2, D: Case 2 with Pressure on Wing Surfaces, E: Case 3, F: Case 3 with Pressure on Wing Surfaces*

The three different rates of rotation for a specific location of pitching have been shown in Figure 5.17, which are accompanied with colour pressure mappings on the wings surface during the downstroke motion of the third cycle. The pressure acting on the frontal wing surface near the tip region is larger for  $\zeta = 1.1s$  and that decreases as the rate of rotation decreases. Further to this, the lower pressure region shown on the back surface of the wing in the images is where the vortex is heavily present, this is more dominant as the rate of rotation increases.

Figures 5.18A and B, illustrate horizontal force data for all the  $\zeta$  rates when the wing is pitching at the leading edge, where a negative value denotes a thrust force. All three curves follow a general trend where no significant outlier exists. The key distinctions are present during the rotational phases of each stroke where small peaks are produced, more-so during the start of a stroke. The largest peak is produced at approximately mid-stroke when the wing has reached maximum velocity and its stroke position is almost perpendicular to the measuring axis (it would be exactly perpendicular if the AOA was 0 degrees), this is shown for both strokes which is in agreement with the prescribed symmetric kinematics. When  $\zeta = 1.1s$  the wing holds an AOA of 30 degrees for much longer which will have a reduced form drag compared to a case where  $\zeta$  has lower AOAs for longer durations or slow continual changes in AOA which occurs when  $\zeta = 3.3s$ . If the AOA were zero degrees or very close to this during the translation phase the drag generated during the downstroke would be greater, when  $\zeta = 3.3s$  the wing has a small AOA slowly changing for considerable durations during a stroke, thus it has a larger form drag acting on it. For  $\zeta = 3.3s$  a peak is not produced towards the end of a stroke as the wing continues to rotate slowly rather than rapidly rotating which is what occurs when  $\zeta = 1.1s$ . The net horizontal force produced for all the cases analysed would be 0 N as the forces generated for both down and upstrokes would cancel one-another. The average horizontal force in plot 5.18B has been determined by averaging the time history of the forces for a single stroke (either the downstroke or positive values of the upstroke). The greatest horizontal force is generated for the slowest rate of rotation which is when  $\zeta = 3.3s$  as the wing has a larger form drag acting on it for both strokes, opposed to the two remaining rotation rates which are faster. As the rotation rate increases the total horizontal force produced decreases, where it is smallest when  $\zeta = 1.1s$ .

As the wing pitch position moves chord-wise downwards to  $\chi = C$ , the peaks during the onset of a stroke become more prominent where the greatest peak is generated by the case which has the slowest rate of rotation  $\zeta = 3.3s$  (see Figure 5.18C). The wing translates at the same rate in all the cases with increasing

velocity and a large acceleration, which means that if the AOA is small than a larger form drag will be generated in the horizontal direction which is what occurs for  $\zeta = 3.3s$  and as the rate of rotation increases the size of the peak reduces. The horizontal forces reach a maximum and minimum at mid-stroke for both down and upstrokes respectively. At this location the wing has an approximate AOA of 30 degrees for all three  $\zeta$ 's and the translation properties are the same, thus the force generated should be very similar. Furthermore, as the location of rotation moved downwards along the chord from the leading edge, the differences in slope for all three  $\zeta$ 's have reduced opposed to that seen in Figure 5.18A. The total horizontal force generated has the same relation as mentioned previously where the force produced increases as the rate of rotation decreases which is shown in Figure 5.18D.

Figures 5.18E and F, display the horizontal force data as the rotational axis moves further down from the leading edge to  $\chi = B$ . As seen previously peaks are produced during the onset of each stroke which is greatest when  $\zeta = 3.3s$  and smallest when  $\zeta = 1.1s$  as the faster rotation rate experiences much smaller form drag in the horizontal direction. Again maximum and minimum horizontal forces are generated at mid-strokes for which the reasons have been previously mentioned and noticeably the distinctions between the curves have reduced as the wing approaches the end of the stroke. Likewise, the greatest total horizontal force is produced for the slowest rate of pitching whereas the smallest force has been generated when the wing carries out the fastest pitching motion. This relationship is observed again when the wing pitches about its spanwise axis located at mid-chord (Figure 5.19A and B).

The final rotational position is at mid-chord (Figure 5.19A) for which similar to the previous plots a peak is produced at the onset of a stroke that is found to be greatest for the slowest rotational duration and lowest for the fastest wing rotation. Towards the end of the stroke the trend found earlier continues where the difference between the curves has reduced even further. As expected from the previous data analysed the maximum and minimum horizontal force generated occurs at mid-stroke for both strokes, and the curves follow one-another very well apart from the clear distinctions at the commencement of each stroke.

Figures 5.19C and D, consists of horizontal force data for which the wing rotation duration is kept constant at  $\zeta = 3.3s$  to compare the effect of all the locations of wing rotation. All four curves follow one-another well, where the only clear distinction exists towards the end of the stroke during the rotational phase where a rotation about the leading edge spanwise axis has a greater horizontal force production. And a small difference exists at the onset of each stroke as less drag force is generated in the positive horizontal direction

when the wing rotates about the leading edge. Thus an overall reduced peak is formed for the force acting in the horizontal direction. However, the total horizontal force cyclic data shows that the greatest horizontal force is generated when the wing pitches about the leading edge, and this reduces very slowly as the pitching axis moves further down along the chord with very small differences present in the total horizontal force generated when  $\chi = A, B$  and  $C$ .

As the rotational duration decreases the distinctions of horizontal force data for wing pitch occurring about the leading edge are more evident during the rotational phases (see Figure 5.19E). This becomes even more prominent as the rotational duration decreases further to  $\zeta = 1.1s$ , where clear peaks are produced towards the end of each stroke, which has been shown in Figure 5.20A. Both of these plots have maximum and minimum horizontal force values at approximately mid-stroke when the wing has a near to perpendicular alignment with the horizontal (which aids in maximising the force produced in the perpendicular direction) when the AOA held by the wing is neglected. As the rotational axis moves further downwards from the leading edge the total horizontal force produced decreases as well, where the maximum force is generated when wing pitching occurs about the leading edge, this description describes the data found for both plots in Figures 5.19F and 5.20B.

A comparison of the horizontal force data for rotations about both the leading edge and mid-chord are shown in Figures 5.20C and D, where the horizontal force generated when rotation occurs about the leading edge is larger for all individual rotational durations, when compared to the force produced when pitching occurs about the mid-chord spanwise axis. All six curves have also been presented to show the clear contrast which exists between the time history of the horizontal force data. A complete comparison of the average horizontal force produced whilst the rotational duration and position are varied has been shown in Figure 5.20E. The colour bar to the right of the surface plot describes the size of the horizontal forces, for a simpler understanding. The horizontal force is clearly seen to be at a maximum when the wing pitching occurs about the leading edge with the slowest rate of rotation. The minimum horizontal force is produced when the wing has the fastest rate of rotation which is when  $\zeta = 1.1s$  and the wing pitches about the mid-chord spanwise axis. Thus, both extremes occur at opposite ends of rotational location and duration. The average horizontal force declines as the rotational position moves chordwise downwards and as the rotational duration decreases.

A sequence of pressure contours whilst the wing is travelling through a downstroke motion has been illustrated

in Figure 5.21, which describes the flow dynamics in the proximity of the wing when rotated about its spanwise leading edge axis at a rate of  $\zeta = 2.2s$ . The low pressure region located on the upper surface of the leading edge has a clear growth when comparing images A and B, which is expected as the wing is travelling in its translation phase holding a fixed AOA with a stable three dimensional vortex attached to the leading edge. This low pressure region on the upper surface (negative pressure region) of the wing continues to grow through the sequence of images as the wing translates through the downstroke with a fixed AOA which starts to dynamically alter as it approaches the end of this downstroke motion. As the wing rotates towards a zero degree AOA which will denote the end of the downstroke motion, the low pressure region on the upper surface of the wing has a significant growth, as does the LEV present at the leading edge which also begins to stretch. Further to this, a vortex begins to form at the trailing edge as the wings rotation promotes large flow separations at the bottom of the wing where the complete connection is formed above the wings surface for the low pressure region enclosing the LEV and newly formed TEV. The area of positive pressure acting on the lower surface of the wing seems to widen between images A and B, and continues in this fashion whilst becoming weaker as the wing starts to decelerate its flapping motion which is clear by the lighter shade of red shown in image E. As the wings rotational velocity augments the pressure acting on the lower surface follows this behaviour whilst moving further downwards from the leading edge and maximising towards the trailing edge region.

For the same non-dimensional timings velocity vector plots have been presented in Figure 5.22 which describes the velocity and directional movement of the fluid in the proximity of the wings. As the sequence of images progress from A to E, there is a clear development of diametral size of the LEV as it stretches out during the rotational phase. Also the velocity acting on the upper rearward surface increases during the translation phase and continues in this fashion when performing a coupled motion of flapping and pitching. Effectively as the translational velocity of the wing decreases and the rotational velocity increases an enlarged region of high velocity is present for majority of the distance along the chord which is evident in image F, this relates directly to the large region of low pressure present near the wings upper surface as shown in Figure 5.21F. As the wing commences rotation the vortex attached to the leading edge starts to stretch which is linked to its growth in diameter. During the translation phase when the wing is held at a prescribed fixed AOA the LEV is more compact and has a tighter structure relating to it being more stable which is paramount when attempting to maximise the vortex lifting effect.

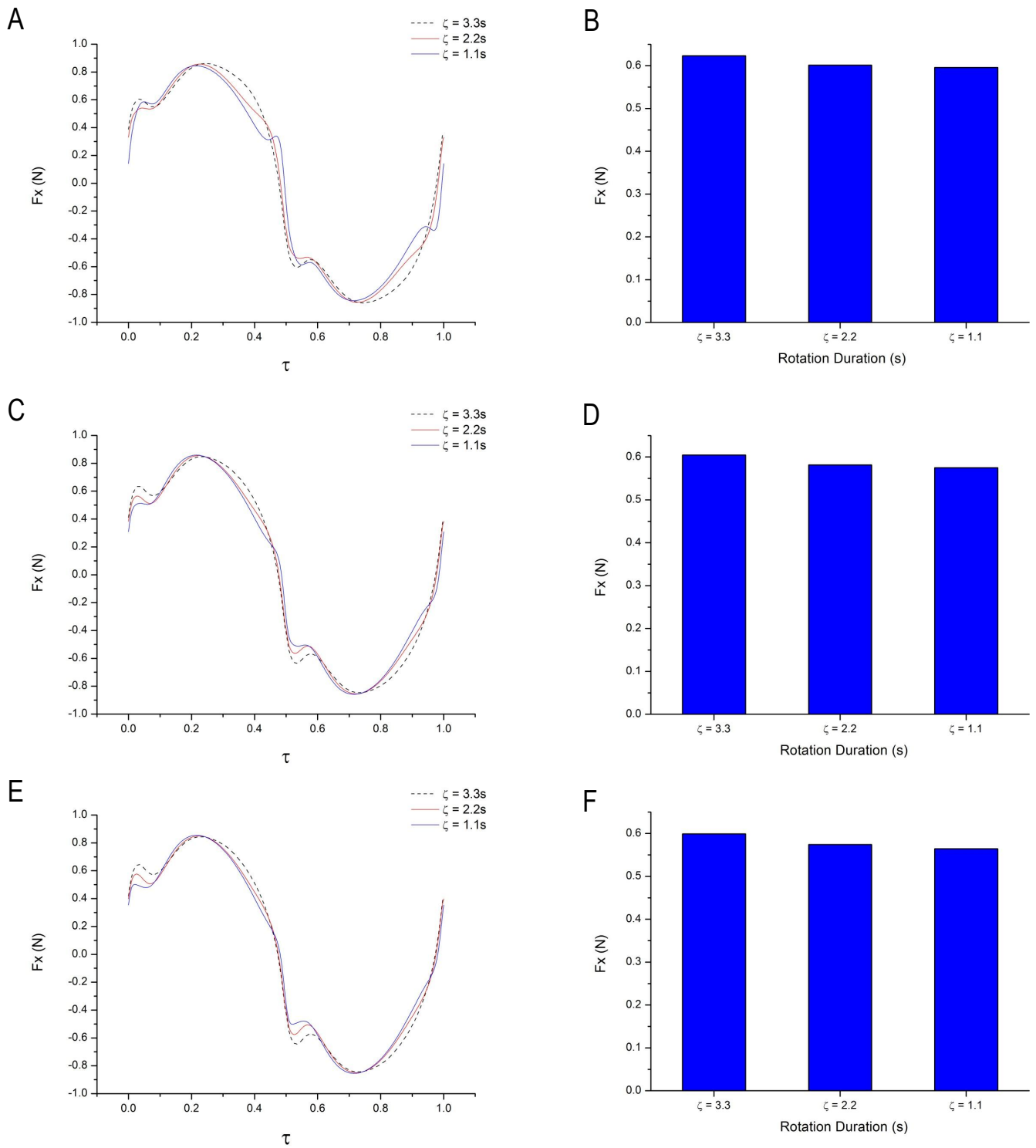


Figure 5.18: *Horizontal Force Comparison; A: Rotation Position D, B: Rotation Position D (average), C: Rotation Position C, D: Rotation Position C (average), E: Rotation Position B, F: Rotation Position B (average)*

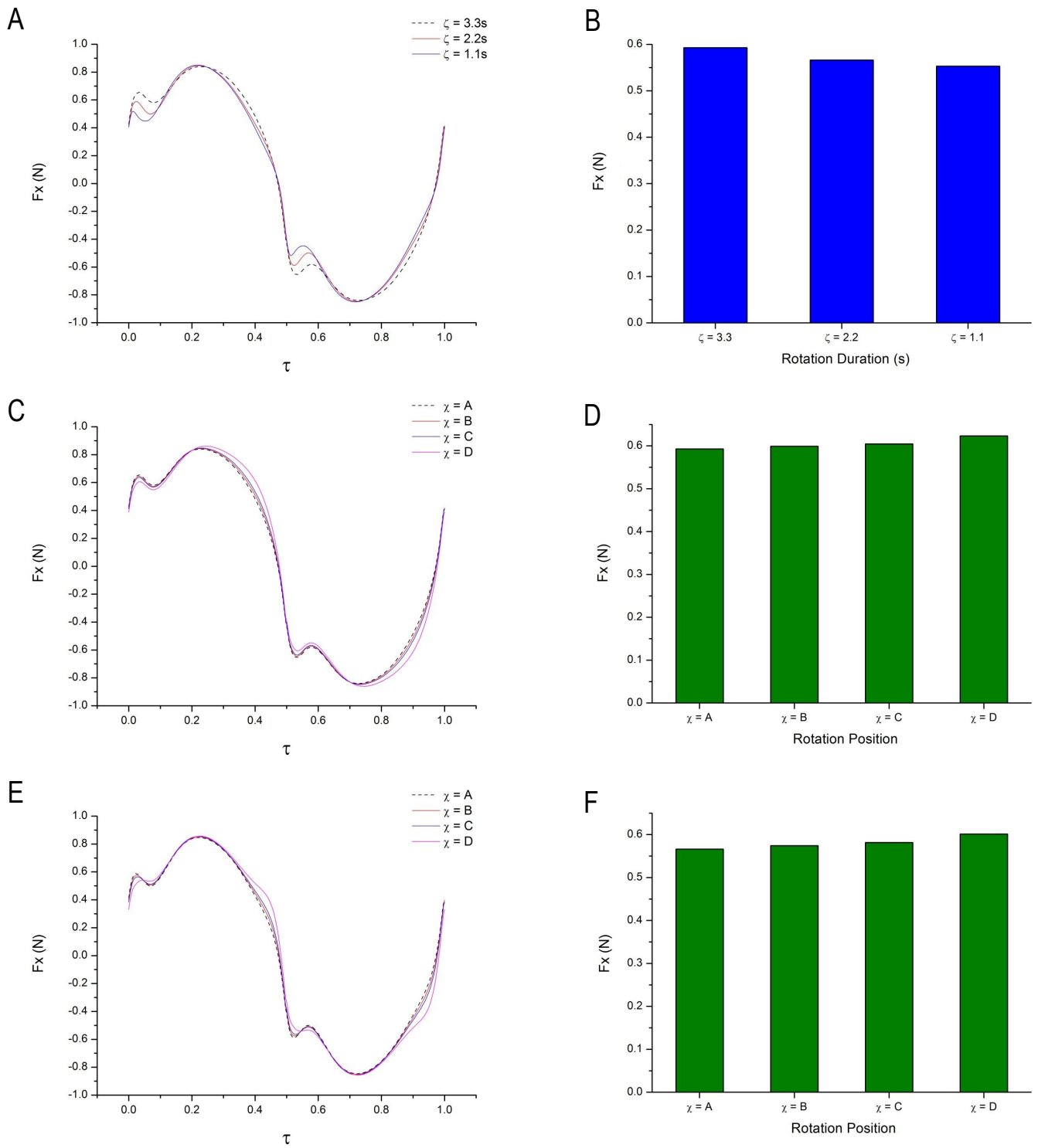


Figure 5.19: *Horizontal Force Comparison; A: Rotation Position A, B: Rotation Position A (average), C: Rotation Duration 3.3s, D: Rotation Duration 3.3s (average), E: Rotation Duration 2.2s, F: Rotation Duration 2.2s (average)*

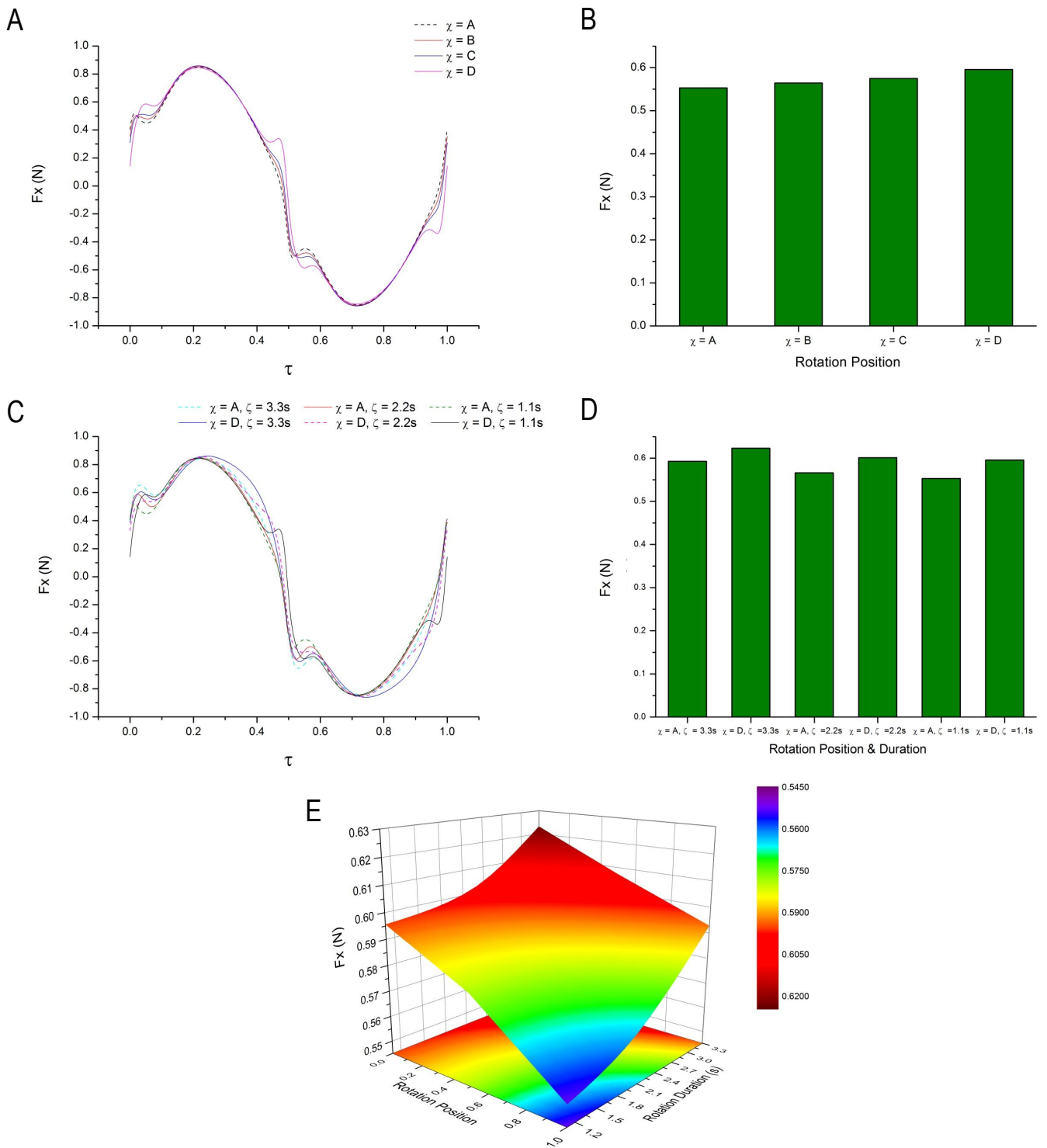


Figure 5.20: Horizontal Force Comparison; A: Rotation Duration 1.1s, B: Rotation Duration 1.1s (average), C: Leading Edge Mid-Chord Positions, D: Leading Edge Mid-Chord Positions (average), E: Average Thrust For All Cases (Legend Represents Thrust Force)

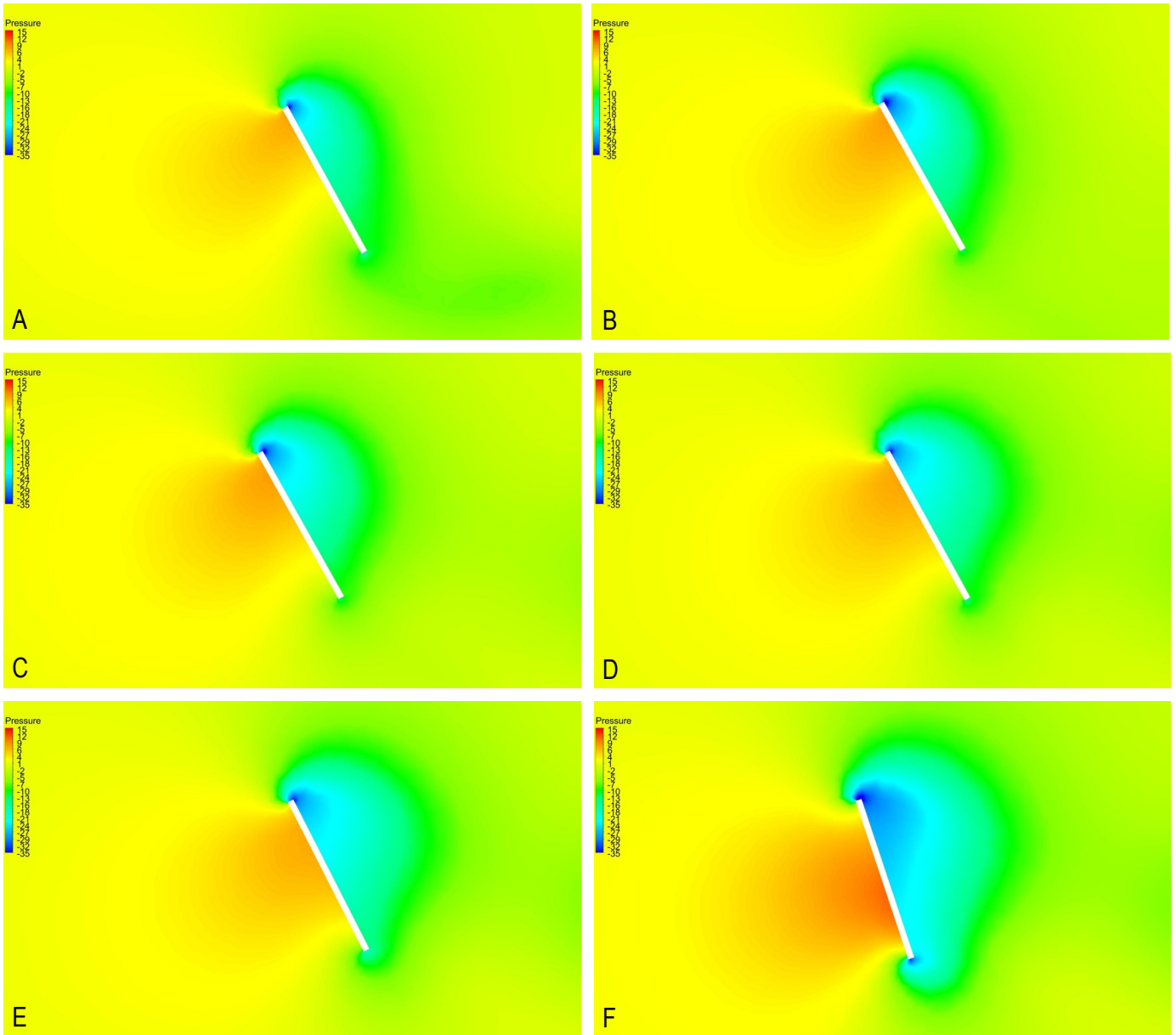


Figure 5.21: *Pressure Contours of Flow Around Rectangular Wing at Mid-Span (Case 2); A: During Downstroke  $\tau = 0.161$ , B: During Downstroke  $\tau = 0.219$ , C: During Downstroke  $\tau = 0.277$ , D: During Downstroke  $\tau = 0.335$ , E: During Downstroke  $\tau = 0.393$ , F: During Downstroke  $\tau = 0.451$ . Pressure Units: Pa*

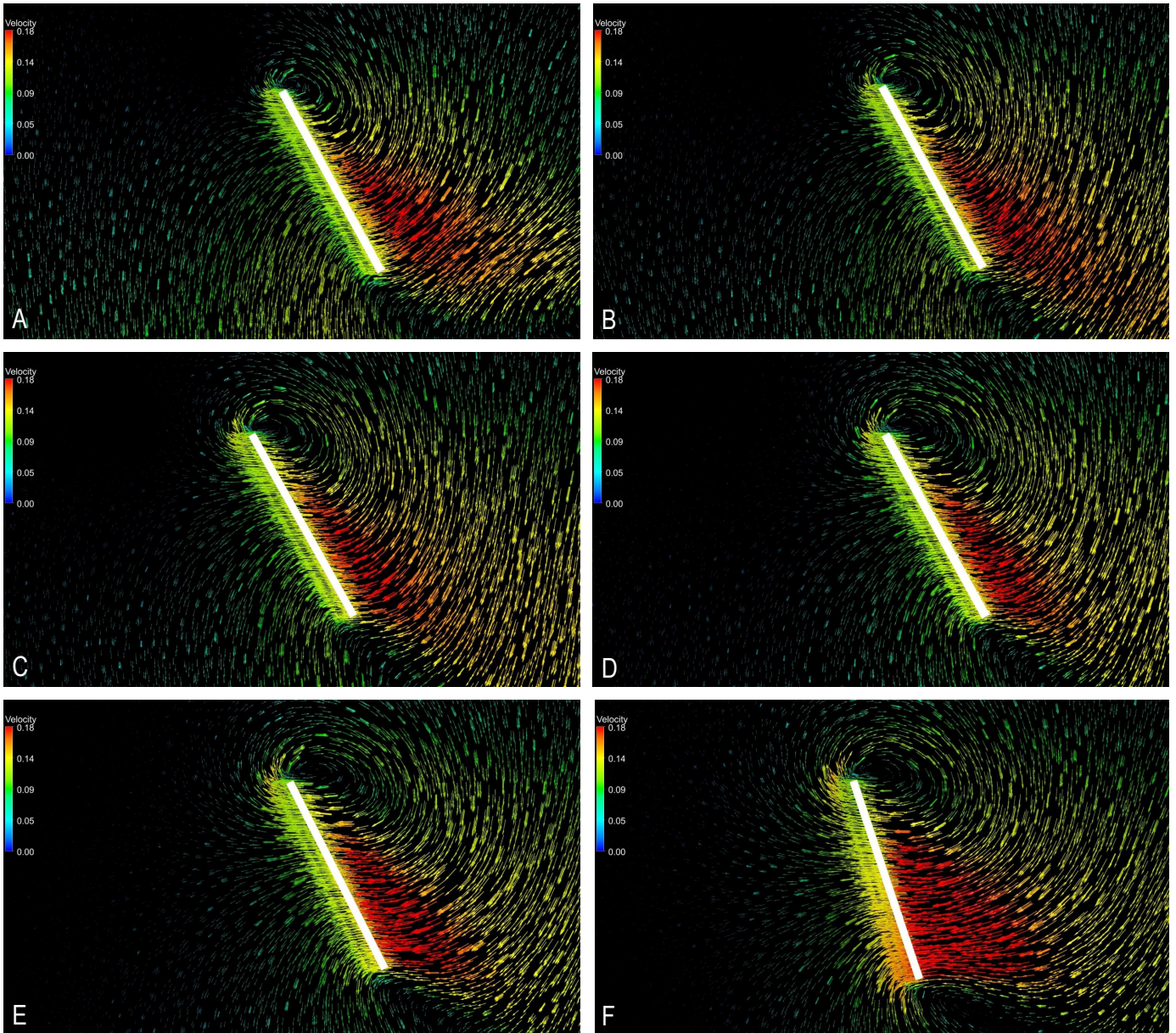


Figure 5.22: *Velocity Vectors of Flow Around Rectangular Wing at Mid-Span (Case 2); A: During Downstroke  $\tau = 0.161$ , B: During Downstroke  $\tau = 0.219$ , C: During Downstroke  $\tau = 0.277$ , D: During Downstroke  $\tau = 0.335$ , E: During Downstroke  $\tau = 0.393$ , F: During Downstroke  $\tau = 0.451$ . Velocity Units: m/s*

As the flapping motion is symmetrical when modelling whilst exploiting a symmetrical plane the rolling and yawing moment at instantaneous times throughout the cyclic time history will cancel out, whereby the average rolling and yawing moment generated will be 0 Nm at all times during a flapping cycle. Such an outcome does not apply for the pitching moment as the wings are both pitching around the axis in the same direction rather than in opposite directions which occurs for both rolling and yawing moments. As pitching occurs about the same axis, the moments generated by both wings are summed together for each stroke, where a cancelling effect applies when considering the entire cycle rather than instantaneous times throughout the flapping cycle. Thus, to simplify, a moment about the pitching axis will exist for the downstroke, which will be balanced out and cancelled once the upstroke has completed its motion, thus the counteraction occurs in the following stroke.

Pitching moment data plots have been shown in Figure 5.23 which contains data for three rotational durations and their respective average data which is determined by the average moment generated for a single stroke which in this case was the downstroke. The total moment generated throughout the cycle will be equal to 0 Nm due to the aforementioned balancing effect. A further time history plot is found in Figure 5.24A which consists of data when the wing pitches about the mid-chord. For all time history plots the pitching moment peaks during the start of each stroke with opposite signs for all three rates of rotation with the greatest moment generated when  $\zeta = 1.1s$  and lowest being when  $\zeta = 3.3s$ . As the rotational axis on the wing moves further downwards along the chord, the peak created during the start of each stroke becomes sharper but reduces in size in terms of the value of pitching moment. Furthermore, when the wing rotates about the leading edge the rapid rotation of  $\zeta = 1.1s$  creates a peak as the wing approaches end downstroke and end upstroke. Such a result does not occur as the wing rotational location moves further back towards the mid-chord as the pressure now acts on the upper and lower surfaces of the wing, which prevents a large imbalance of pressure acting considerably on one side of the wing opposed to the other. In general, for all three rotation locations ( $\chi = B, C$  and  $D$ ) the pitching moment is maximum for the fastest rate of rotation and lowest for the slowest rate of rotation (see Figure 5.23B, D and F). This relation is not found at the mid-chord as the longest rotational duration now produces the largest moment in the opposite direction, the average size of the pitching moment generated during the downstroke is much smaller as the wing pitches about its mid chord axis opposed to pitching about the leading edge. In addition, the pitching moment produced is negative when  $\zeta = 3.3s$  and  $2.2s$ , thus the wing is rotating on average in the clockwise direction opposed to anti-clockwise which is found when  $\zeta = 1.1s$ .

The rotational duration has been kept constant in order to compare the four rotational positions along the chordwise axis ranging from the leading edge to mid-chord in Figures 5.24 and 5.25. When  $\zeta = 3.3s$  the greatest pitching moment is generated when the leading edge is chosen as the rotational axis which augments in size as the rotational duration decreases. Overall, all four curves in each of the plots (Figures 5.24C, E and Figure 5.25A) all show very similar trends where this curved path is replicated during the upstroke with the difference being an opposing sign. Analysing the average moment data from the downstroke motion it is evident that the moment generated decreases as the rotational location moves chordwise downwards and as previously mentioned when  $\zeta = 3.3s$  and  $2.2s$  the wing pitches with a clockwise rotation which is opposite to all the other pitching moments recorded for the 12 cases. The pitching moment data for each singular case can be seen in Figures C.3 and C.4 which also includes the summation of the two in a time history format.

A comparison of the pitching moment generated during a cycle when wing rotation occurs about both extreme locations has been shown in Figures 5.25C and 5.25D, the plots include the time history and an average of the moment data found during the downstroke motion. Due to the uneven pressure acting on the surface of the wing during its motion when it is rotated about the leading edge, the size of the pitching moment generated is much greater opposed to the pressure acting on the wings surface when rotation acts along the mid-chord spanwise axis. Thus, during the hovering motion an insect would experience a pitching moment acting in the anti-clockwise direction unless it is counteracted upon by the insects body as it has control of each segmental part. However, if the body does not take part in providing stabilisation and cancelling the momentary pitching moment developed during the downstroke, the following upstroke motion will counteract the prior pitching moment formed to restore equilibrium.

Overall, the moment generated when the wing rotates about the mid-chord spanwise axis is substantially smaller when compared to the moment values shown for a rotation located at the leading edge. The surface plot compiles a comparison between both variables which are the location of rotation and its duration and presents the moment generated during the downstroke motion as average data. The greatest pitching moment is present when the wing rotates about the leading edge and the rate of rotation is fastest, this decreases as the rate of rotation decreases due to the differences in pressure acting on the wings surface, which has significant peaks during the rotational phases of a single stroke when  $\zeta = 1.1s$ . As the location of wing rotation declines along the chord-wise direction towards the mid-chord, the moment generated decreases almost linearly with

a precipitous nature with a rotational duration of  $\zeta = 1.1s$ , thereafter the moment further decreases in size becoming negative as the rotational duration increases towards  $\zeta = 3.3s$ . Similar to the previous surface plots described in this section the colour bar represents the size of the measured parameter, which in this evaluation is the pitching moment that is positive when rotating in the counter-clockwise direction and negative when rotating in the clockwise direction.

Images have been illustrated in Figure 5.26 with the wing performing a downstroke motion at both extreme rotation locations with a rotational duration of 2.2s. A sweeping motion of the wing swinging through its downstroke whilst pitching at its mid-chord about the spanwise axis has been shown in Figure 5.26C with a solid colour to solely represent its motion. A comparison has been shown in the remaining images which are A, B, D and E (A and E display pressure visualisations on the lower surface of the wing, whilst B and D display pressure visualisations on the upper surface of the wing). Observing the initial few pressure contour images shown in images A and E, it becomes clear that the pressure acting on the wing when  $\chi = D$  lasts for a longer duration as the third wing in both images have a clear distinction with a stronger presence when  $\chi = D$ .

Pressure contours of the flow field surrounding the wing tip at quarter downstroke have been shown in Figures 5.27A, B and C, which correspond to the three different rotational durations as the wing pitches about its spanwise leading edge axis. A large pressure region exists on the lower surface of the wing, whilst a low pressure region acts on the upper surface of the wing which seems to grow as the rotational duration decreases. Furthermore, a much lower pressure is present near the leading edge in image C for the fastest rotational duration opposed to the remaining two images. Lastly, the image in 5.27D, illustrates the velocity field present at the mid-span via a contour flooded slice and three dimensional vectors depicting the direction of the flow in this slice. A very low pressure area exists at the centre of the vortex depicted by the single coloured vectors. The velocity acting on the upper surface is greatest on the rearward half of the wing towards the trailing edge.

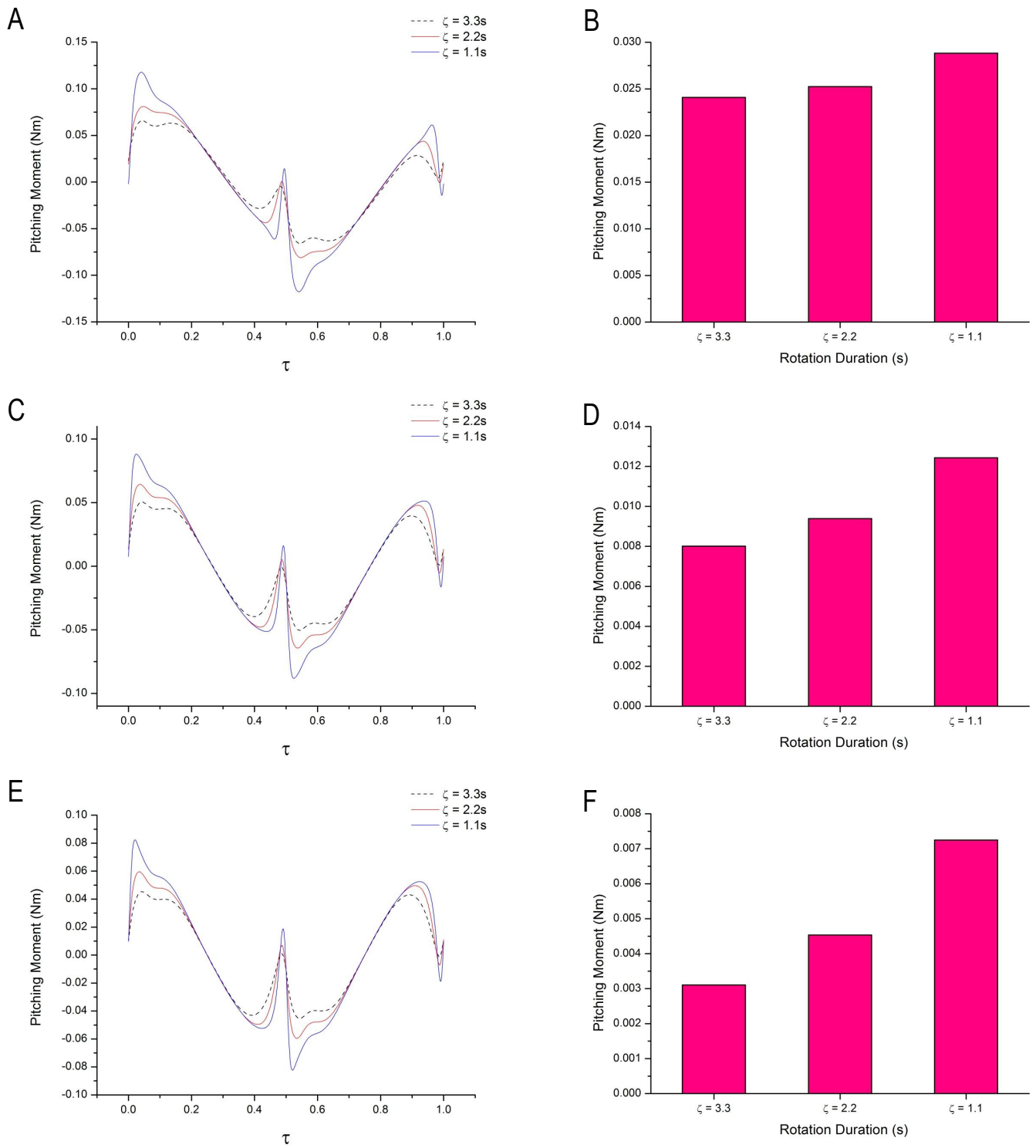


Figure 5.23: *Pitching Moment Comparison; A: Rotation Position D, B: Rotation Position D (average), C: Rotation Position C, D: Rotation Position C (average), E: Rotation Position B, F: Rotation Position B (average)*

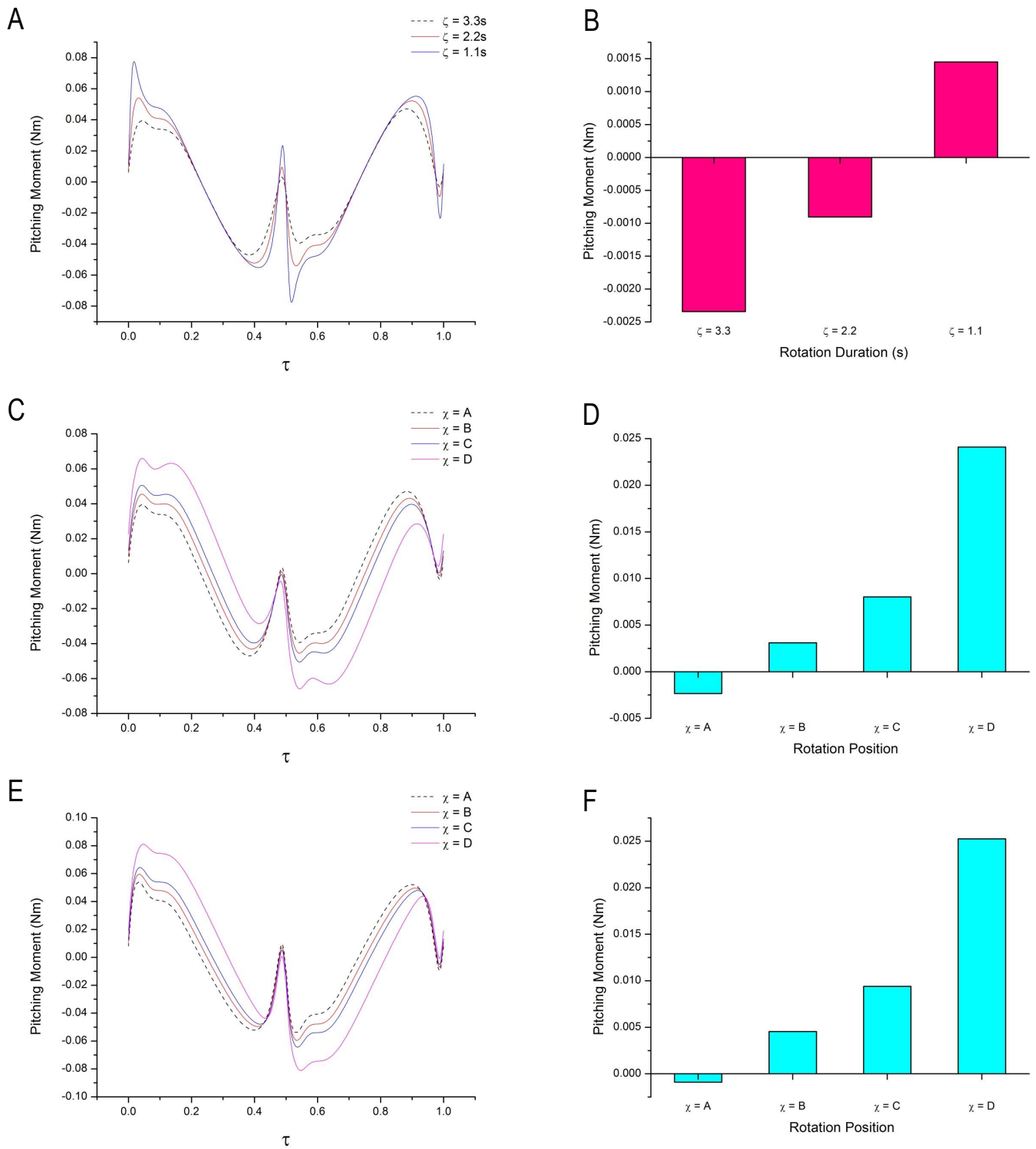


Figure 5.24: *Pitching Moment Comparison; A: Rotation Position A, B: Rotation Position A (average), C: Rotation Duration 3.3s, D: Rotation Duration 3.3s (average), E: Rotation Duration 2.2s, F: Rotation Duration 2.2s (average)*

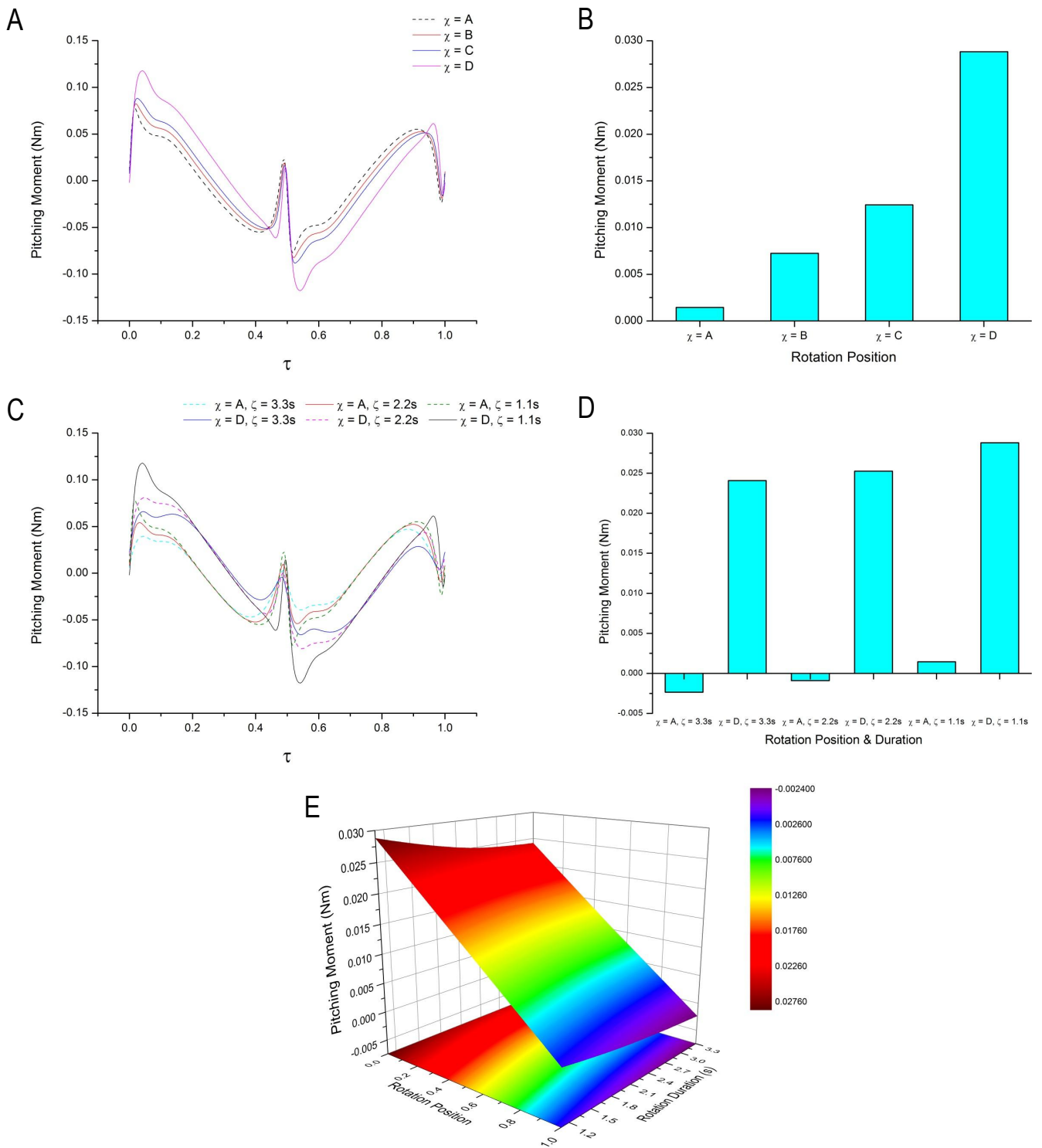


Figure 5.25: *Pitching Moment Comparison; A: Rotation Duration 1.1s, B: Rotation Duration 1.1s (average), C: Leading Edge Mid-Chord Positions, D: Leading Edge Mid-Chord Positions (average), E: Average Pitching Moment For All Cases (Legend Represents Pitching Moment)*

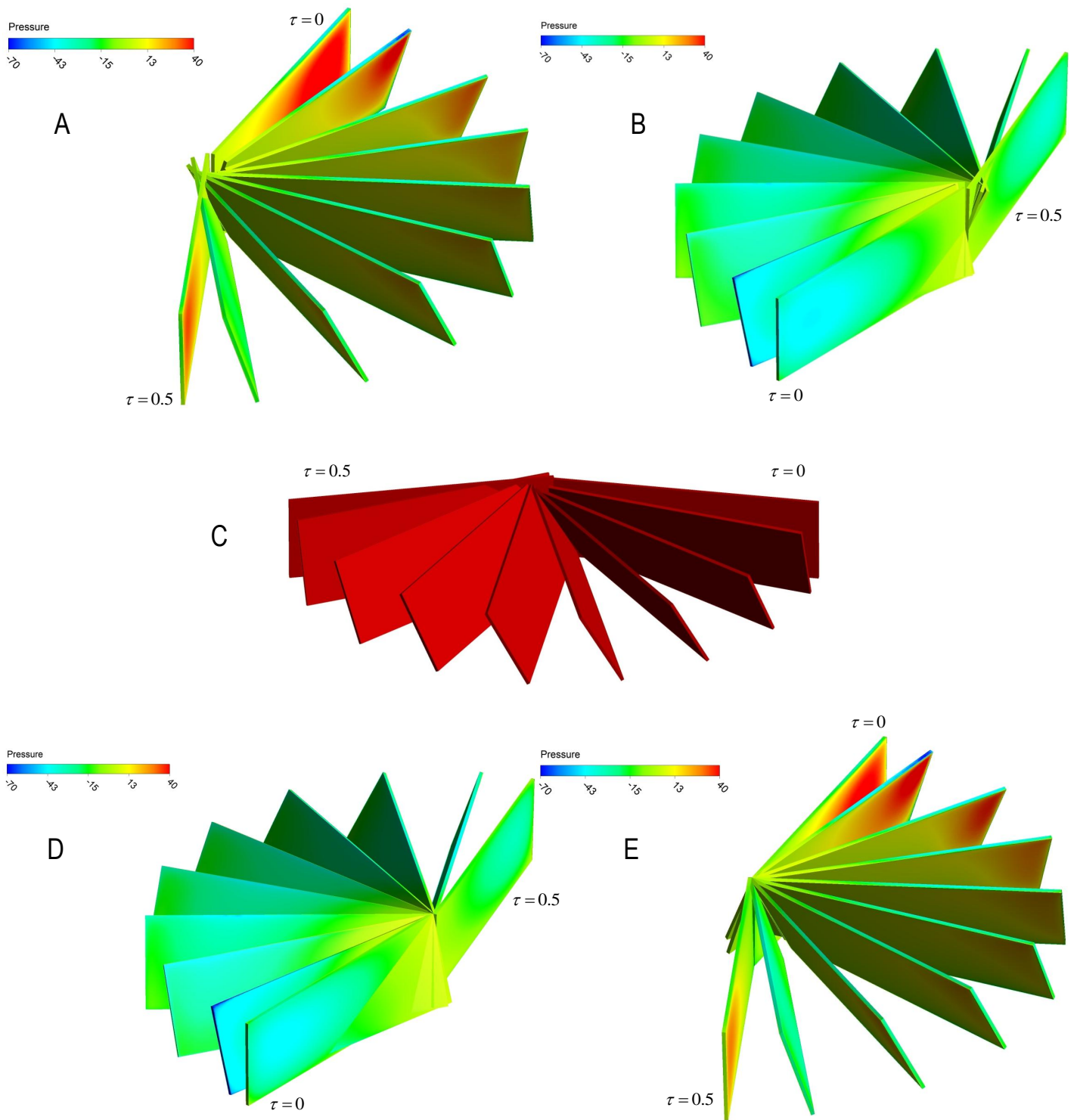


Figure 5.26: *Rectangular Wing in Downstroke Motion with Rotation about Mid-Chord and Leading Edge for  $\chi = 2.2s$ ; A: Pressure on Wing with Mid-Chord Rotation View 1, B: Pressure on Wing with Mid-Chord Rotation View 2, C: Wing Motion with Mid-Chord Rotation, D: Pressure on Wing with Leading Edge Rotation View 1, E: Pressure on Wing with Leading Edge Rotation View 2. Pressure Units: Pa*

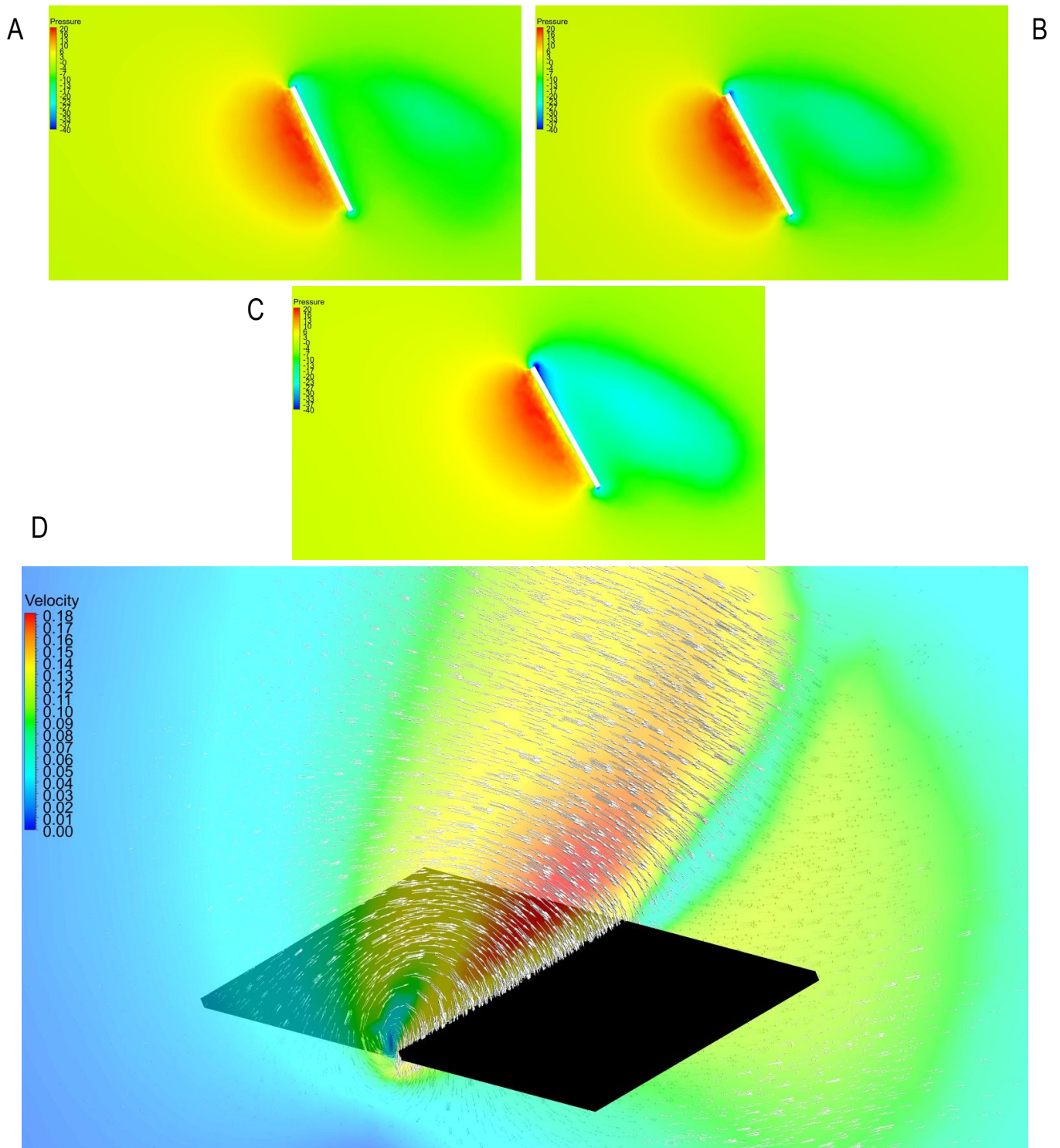


Figure 5.27: *Rectangular Wing in Downstroke Motion with Rotation about the Leading Edge; A: Pressure Contour of Flow Around Wing Tip with Rotation Duration as  $\zeta = 3.3s$  at  $\tau = 0.125$ , B: Pressure Contour of Flow Around Wing Tip with Rotation Duration as  $\zeta = 2.2s$  at  $\tau = 0.125$ , C: Pressure Contour of Flow Around Wing Tip with Rotation Duration as  $\zeta = 1.1s$  at  $\tau = 0.125$ , D: Velocity Magnitude Contour and Vectors through the Mid-Span at  $\tau = 0.219$ . Pressure Units: Pa, Velocity Units: m/s*

Clear distinctions exist in the power plots shown in Figures 5.28 and 5.29 which refer to the aerodynamic power required to perform wing motions at three different pitching durations and four different rotational locations. The aerodynamic power is calculated using Equation 5.62 for all the cases. Large peaks are produced during wing rotations for all rotational durations which are clearly more pronounced when  $\zeta = 1.1s$  at the start of each stroke where the wing also makes its way through the shed vorticity present in the wake from the previous stroke. During the translation phase the aerodynamic power required when  $\zeta = 1.1s$  seems to decline steadily which occurs for all four rotational positions for which the plots have been shown in the Figures stated above. Towards the end of downstroke a peak is produced for all three  $\zeta$  timings which is greatest when the wing pitches about the spanwise leading edge axis for  $\zeta = 2.2s$  and  $1.1s$  and reduces in size as the rotational location moves chordwise downwards where a peak is actually non-existent when  $\chi = A$  for  $\zeta = 1.1s$ .

Further to this, a small peak exists just before the end of each stroke which grows as the rotational location moves chordwise downwards. Thus a sudden requirement of aerodynamic power is present at this time which is most probably due to the wing heavily slowing down, but also continually travelling through its prescribed motion whilst the shed flow is creating a resistive effect. Although the size of the peak towards end downstroke for  $\zeta = 3.3s$  decreases in size as the rotational location moves chordwise downwards, its reduction in size is much less than the remaining two  $\zeta$  timings.

Due to the slow pitching motion of the wing when  $\zeta = 3.3s$  the aerodynamic power required does not reach a steady state as the wing motion through each stroke seems to be in almost continual motion. As  $\chi$  moves downwards from the leading edge towards mid-chord, the peak aerodynamic power generated at the start of each stroke seems to decrease in size. This relation applies to all three  $\zeta$  timings but is more prominent when  $\zeta = 1.1s$  due to such a rapid pitching motion. The general trend of the average aerodynamic power required per cycle demonstrates that the greatest power is needed when  $\zeta = 3.3s$ , this is shown for all the rotational locations investigated except for when  $\chi = D$ . When  $\chi = D$  the aerodynamic power required for  $\zeta = 1.1s$  is slightly greater than when  $\zeta = 3.3s$  and the lowest power is needed when  $\zeta = 2.2s$ . Thus, the large peaks of aerodynamic power generated for  $\zeta = 1.1s$  during the rotational stages of the cycle contribute significantly towards the overall average power needed. In addition the average power required seems to reduce for all rotational durations as the location of wing pitching moves chordwise downwards from the leading edge to the mid-chord.

Figures 5.29C and D, display plots for which the rotational duration is kept consistent at 3.3s whilst the rotational location along the chord is varied. As mentioned previously peaks are produced during the stages of wing pitching for all the rotational locations and the power generated in between the peaks is greatest for  $\chi = D$  and least for  $\chi = A$ . The average data shows that the largest aerodynamic power is needed when  $\chi = D$  which declines as the rotational location moves chordwise downwards from the leading edge towards mid-chord which requires the smallest average aerodynamic power throughout a cycle. This same trend is seen for the following plots when  $\zeta = 2.2s$  and  $1.1s$  are held constant and the rotational locations are varied. As the rotational duration decreased to  $\zeta = 2.2s$ , the peaks during the rotational stages became sharper and larger with a more steady aerodynamic power during the translation phase as the AOA is held constant at 30 degrees. Both peaks are greater when  $\chi = D$  which declines as the rotational position moves downwards from the leading edge towards the mid-chord, the distinction is more prominent for the peak generated towards the end of the downstroke motion.

Lastly, in Figure 5.30A  $\zeta$  is held at 1.1s whilst  $\chi$  varies for which considerable peaks are generated at all the rotational stages except when  $\chi = A$  towards the end of a stroke, where no peak is existent apart from the very small peak produced just before the end of a stroke as aforementioned. The greatest peaks are generated when  $\chi = D$ , which decline as the rotational location moves chordwise downwards from the leading edge, which is the same trend that was found in the previous plots discussed for the remaining two rotational durations. During the translation phase all the curves seem to have a region of steady decline for the aerodynamic power required as the plots collapse on top of one-another until the rotational phase near the end of a stroke commences.

Both extreme rotational locations have been compared in time history format and via average bar plots for the aerodynamic power required in a complete cycle (see Figure 5.30C and D). A clear variance is evident amongst the plots depicted in the time history plot with the largest peaks generated at the start of each stroke for  $\chi = A$  and  $\chi = D$  where  $\zeta = 1.1s$  for both curves. Additionally for all  $\zeta$  timings, the average aerodynamic power required when the spanwise pitching occurs about the leading edge is greater than that found when pitching occurs about the mid-chord. The final surface plot shown in Figure 5.30E, compiles the rotational location, duration and the aerodynamic power required due to both of these variables in a single averaged plot where the colour bar presents the power required values. The greatest average aerodynamic power is required when the wing rotates about the leading edge with the fastest rotational duration. A steep,

almost linear decline is found for the aerodynamic power required as the rotational position moves chordwise downwards, where the smallest aerodynamic power is recorded with pitching occurring at the mid-chord about the spanwise axis when  $\zeta = 1.1s$ . This gradually augments as the rotational duration increases whilst maintaining the rotational position of mid-chord. Overall, this states that the greatest aerodynamic power is generally required when the wing pitches about the spanwise axis at the leading edge of the wing, and a much smaller aerodynamic power is required when the wing pitches about the mid-chord, regardless of the  $\zeta$  timing which applies to both statements.

Figure 5.31, consists of flow visualisations of the LEV attached to the wing for all three rotational durations at quarter downstroke with wing pitching occurring about the spanwise axis of the leading edge. Instantaneous streamlines were released at the leading edge to visualise the inner and outer vortices for which a reduced number of streamlines were set to view the outer vortex. The pressure contour has been shown for the upper surface of the wing where a negative pressure region exists in the vicinity of the vortex, the lower surface of the wing will have a much higher positive pressure acting on it especially near the tip section.

The vortices shown in the individual images seem to show a more compressed appearance as the rotational duration decreases from 3.3s to 1.1s. Furthermore, as the vortex travels from root to tip it grows in diameter for each image which for a certain period seems to have a fairly consistent diameter near to the mid-span of the wing. The vortex has a much larger rate of growth and larger diameter as the rotational duration increases from 1.1s to 3.3s. Figures 5.32A, C and D show the same set of streamline flow visualisation images. In this set of images the streamlines have been colour mapped by velocity which becomes larger towards the wing tip. As expected the velocity at the root is much lower than that found at the tip and it has a gradual growth from the root to tip. Moreover, the growth of the vortex is clearly much larger for  $\zeta = 3.3s$  when compared to  $\zeta = 1.1s$ , which leads directly to instabilities opposed to the very compressed appearance of the LEV when  $\zeta = 1.1s$ , which has a very tight formation along the span of the wing and a much smaller rate of growth. At the tip section of the wing, the vortices break apart and move away from the wings surface. Overall, at this low Reynolds number each rotational duration does create a tube-like structured LEV which is evidently more prominent when  $\zeta = 1.1s$ .

The highly unsteady three dimensional vortical flow field is shown in Figure 5.32B, which clearly illustrates how unsteady the flow is in the proximity of the wing with large flow velocities present above the tip section of the wing. The LEV feeds vorticity into the tip vortex and breaks apart when travelling through the enlarged TV. Note a fuller, more enlarged LEV is shown in the flow field image as much more instantaneous streamlines were released from a position set back from the leading edge.

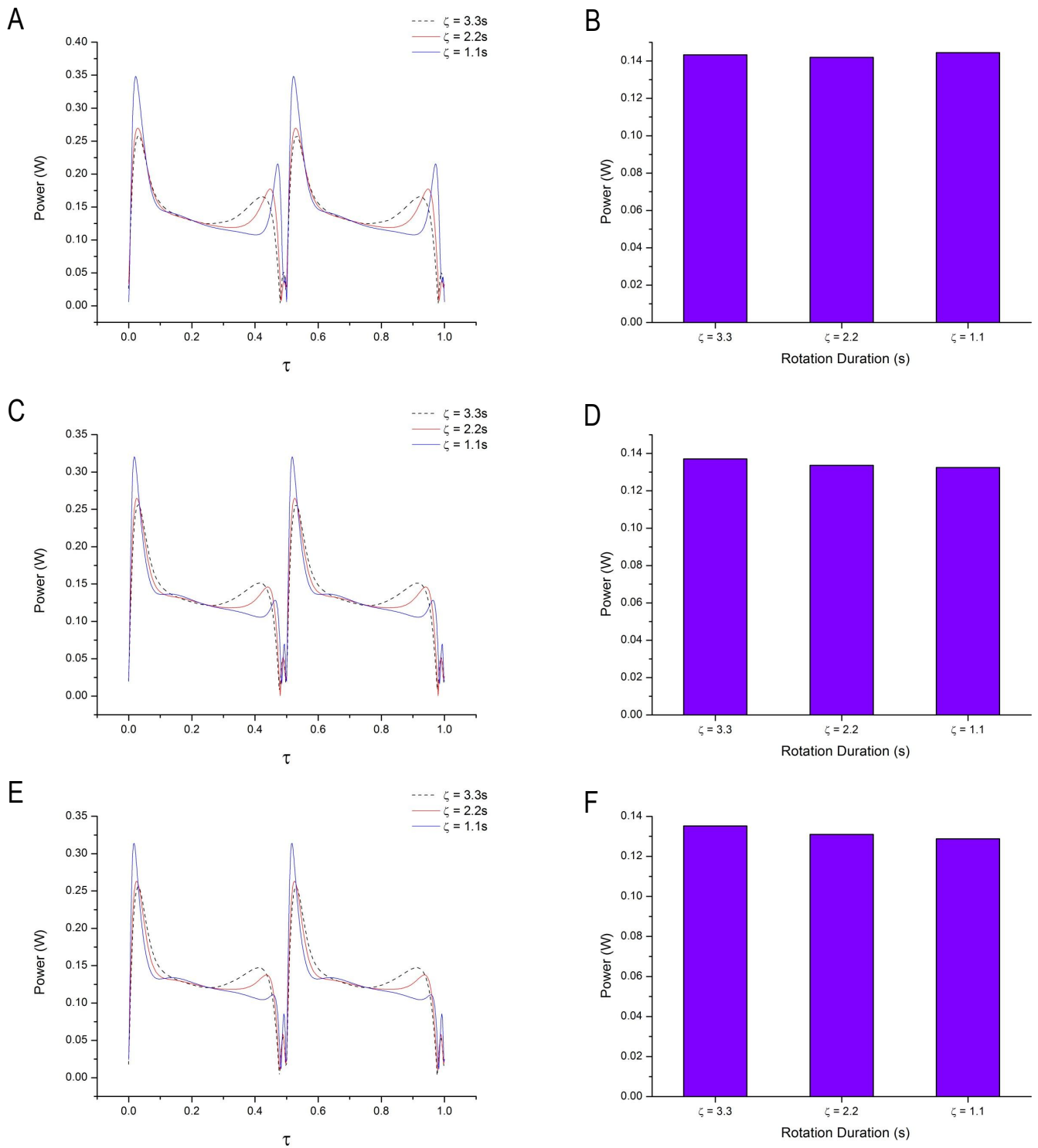


Figure 5.28: Aerodynamic Power Comparison; A: Rotation Position D, B: Rotation Position D (average), C: Rotation Position C, D: Rotation Position C (average), E: Rotation Position B, F: Rotation position B (average)

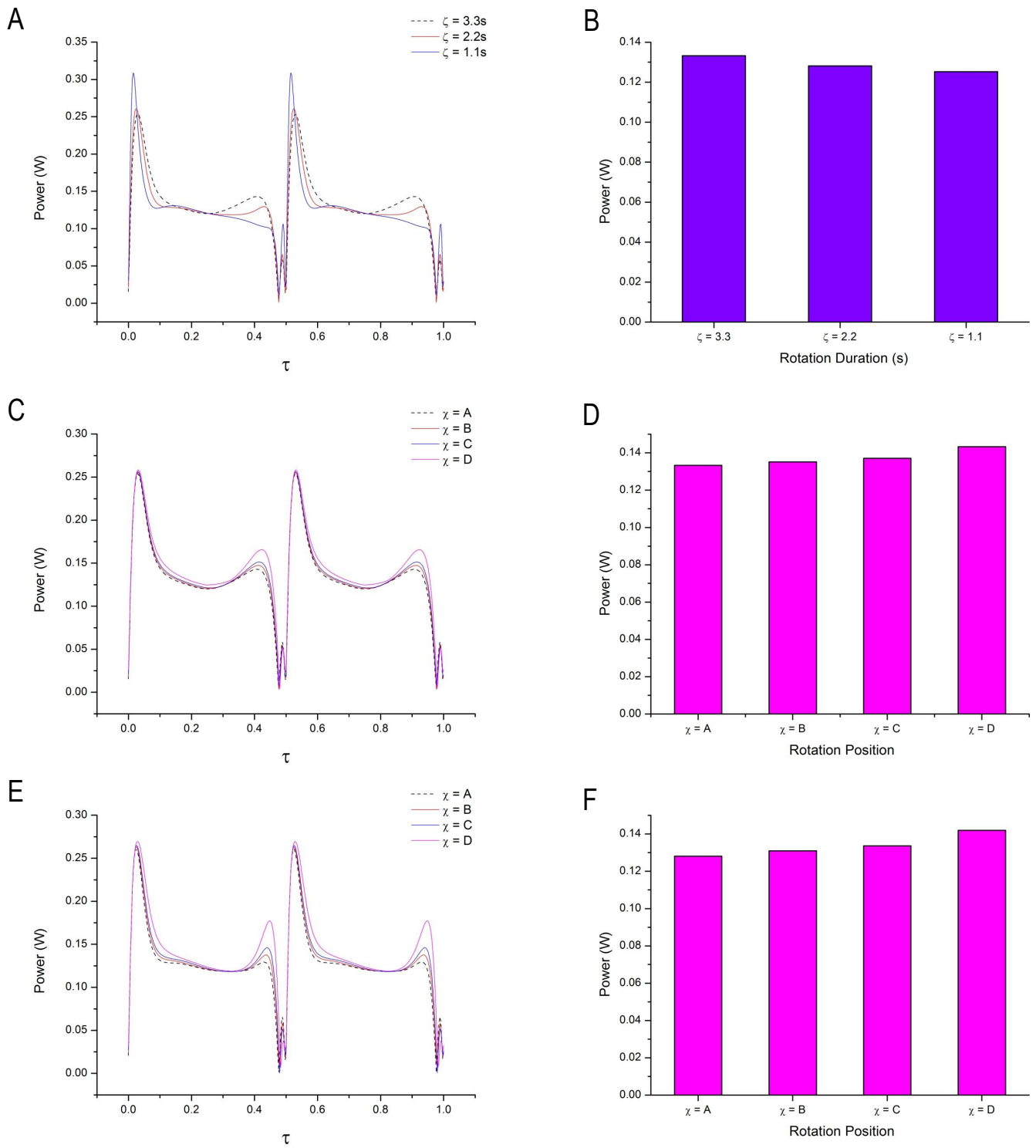


Figure 5.29: Aerodynamic Power Comparison; A: Rotation Position A, B: Rotation Position A (average), C: Rotation Duration 3.3s, D: Rotation Duration 3.3s (average), E: Rotation Duration 2.2s, F: Rotation Duration 2.2s (average)

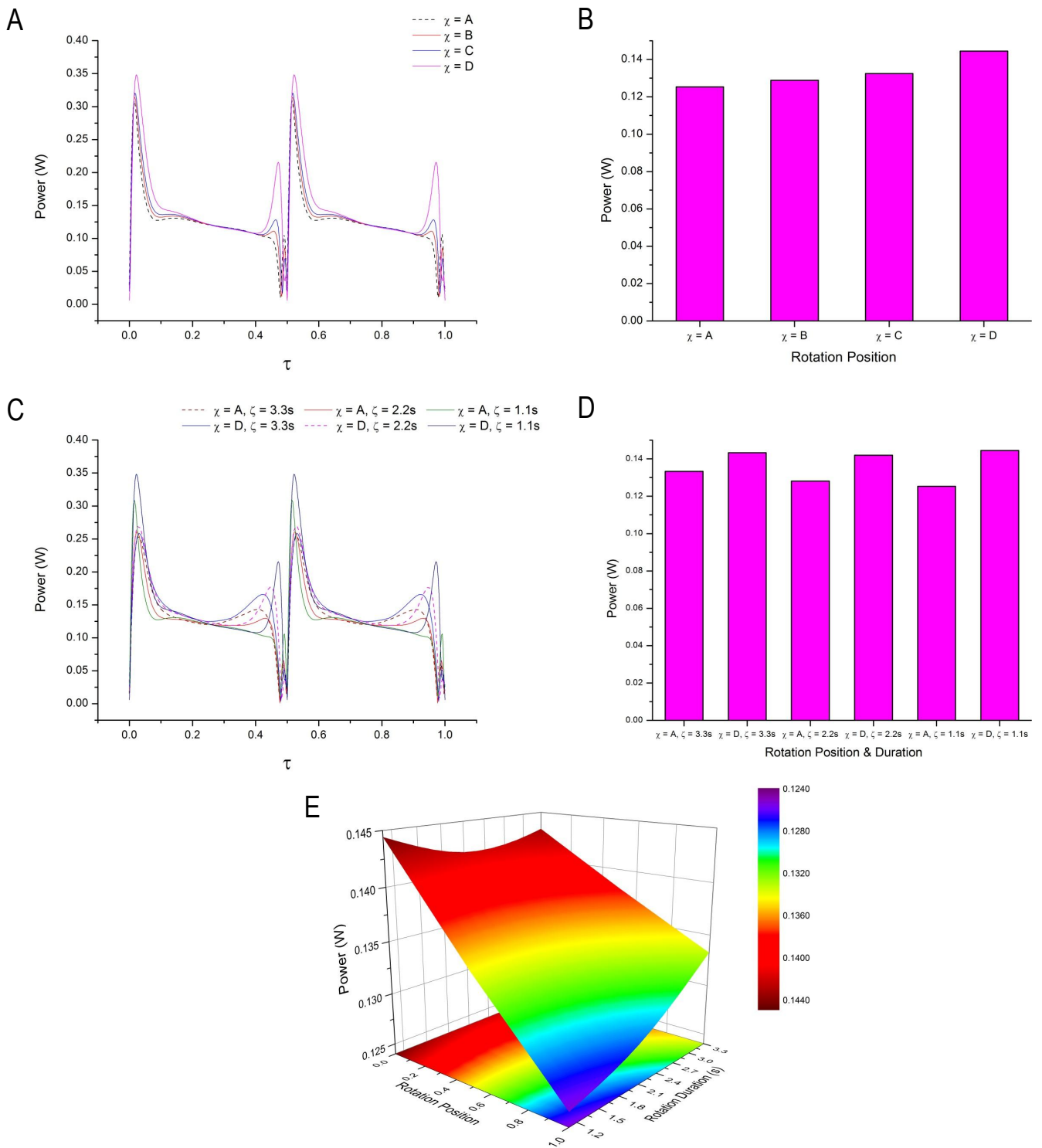


Figure 5.30: Aerodynamic Power Comparison; A: Rotation Duration 1.1s, B: Rotation Duration 1.1s (average), C: Leading Edge Mid-Chord Positions, D: Leading Edge Mid-Chord Positions (average), E: Average Aerodynamic Power For All Cases (Legend Represents Aerodynamic Power)

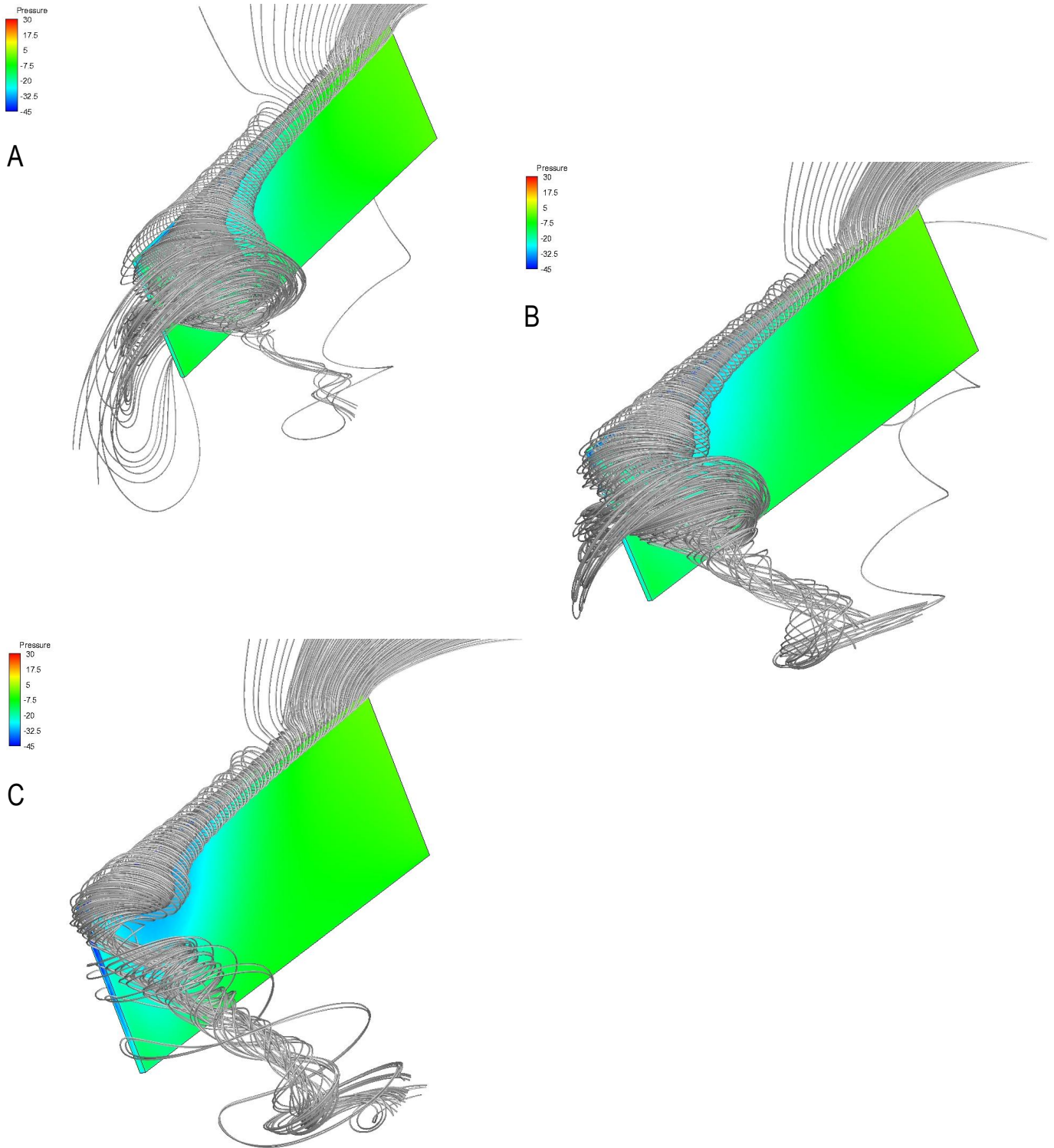


Figure 5.31: *Rectangular Wing with Rotation About the Leading Edge Cases 1-3 at  $\tau = 0.125$ ; A: Streamlines & Pressure Contour on Wing Surface for  $\zeta = 3.3s$ , B: Streamlines & Pressure Contour on Wing Surface for  $\zeta = 2.2s$ , C: Streamlines & Pressure Contour on Wing Surface for  $\zeta = 1.1s$ . Pressure Units: Pa*

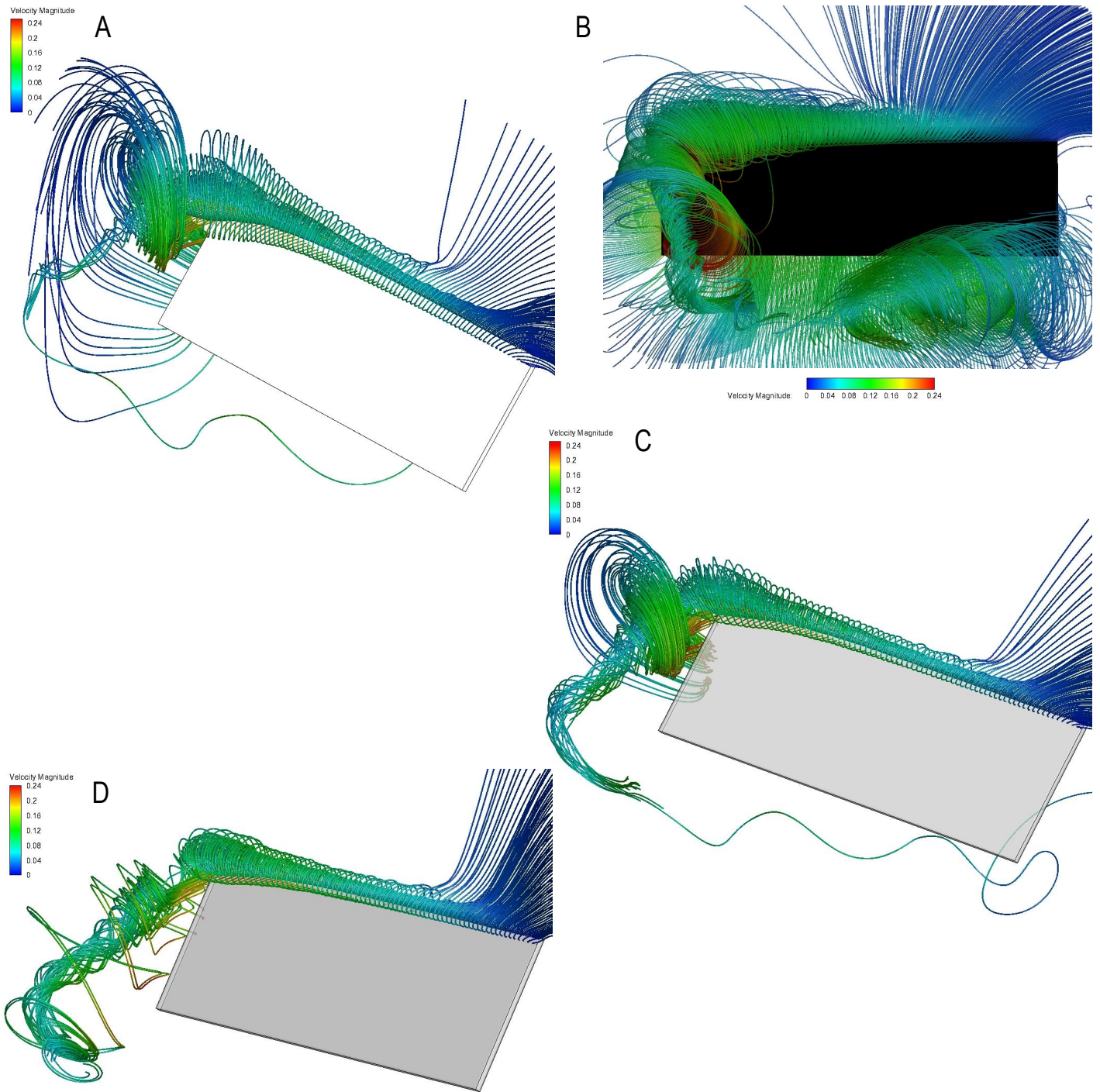


Figure 5.32: *Rectangular Wing with Rotation About the Leading Edge Cases 1-3 at  $\tau = 0.125$ ; A: Streamlines with Velocity Magnitude for  $\zeta = 3.3s$ , B: Flow Field Around the Wing for  $\zeta = 1.1s$ , C: Streamlines with Velocity Magnitude for  $\zeta = 2.2s$ , D: Streamlines with Velocity Magnitude for  $\zeta = 1.1s$ . Velocity Units: m/s*

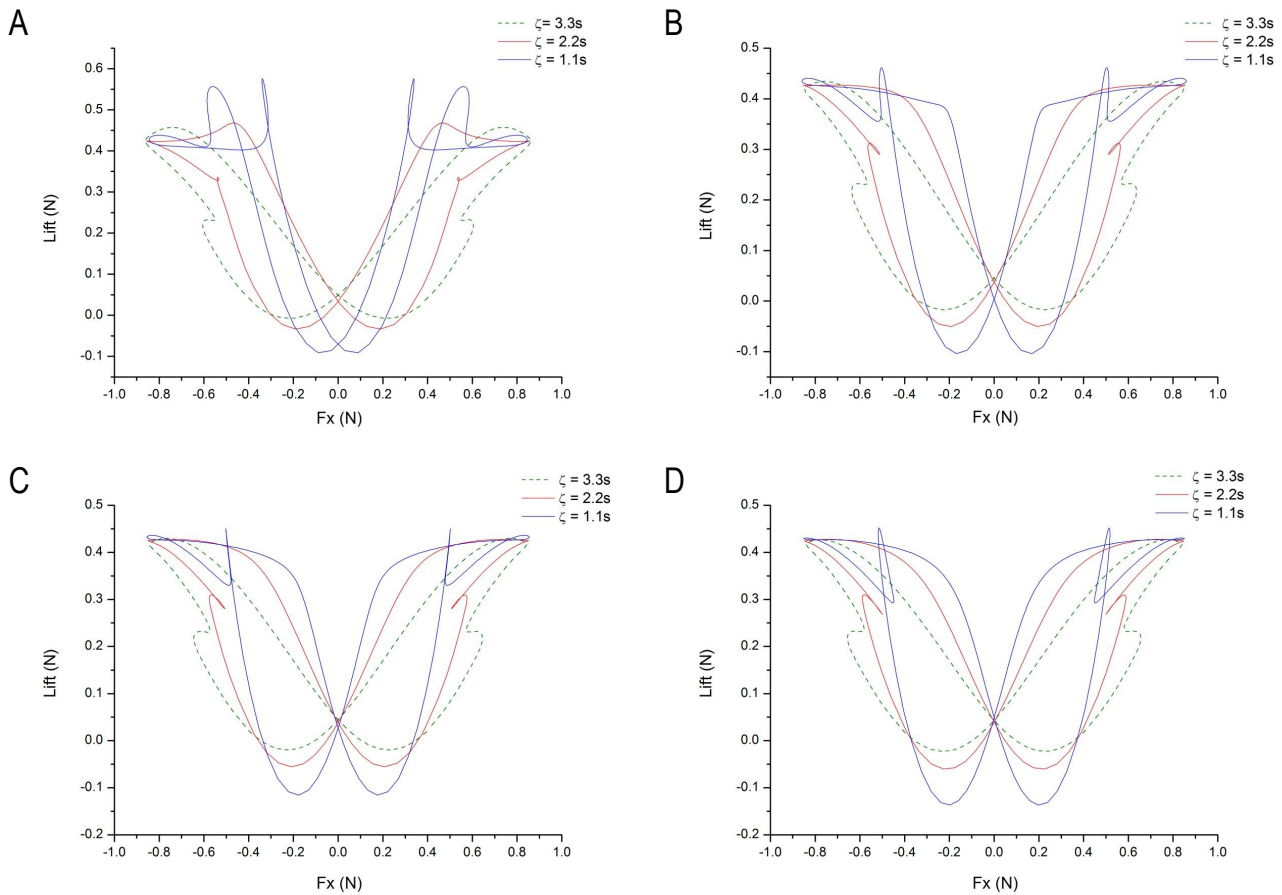


Figure 5.33:  $F_x$  Vs Lift Limit Cycle Comparison; A: Rotation Position D, B: Rotation Position C, C: Rotation Position B, D: Rotation Position A

Limit cycles have been shown in Figure 5.33 for all four rotational locations along the chord of the wing. A symmetrical mirror line in the vertical direction exists at point  $F_x = 0$  for all the plots as the lift and  $F_x$  data is equivalent for both strokes as the prescribed wing kinematics are symmetrical. The shapes of the curves have clear distinctions for the three rotational durations as some of the curves intersect themselves on numerous occasions whilst others have no intersections whatsoever. When  $\zeta = 1.1s$  the curve for all the rotational positions seems to have numerous intersections for which a considerable number of loops are present, especially when the wing pitches about the leading edge which is primarily due to the sharp peaks produced for lift force. As the rotational location moves chordwise downwards when  $\zeta = 1.1s$  the large loop in the limit cycle plot becomes wider, which can be clearly seen by comparing plot A and D, where the large loop is considerably thin when the wing pitches about the leading edge. The aforementioned trend applies to the remaining two rotational durations as well.

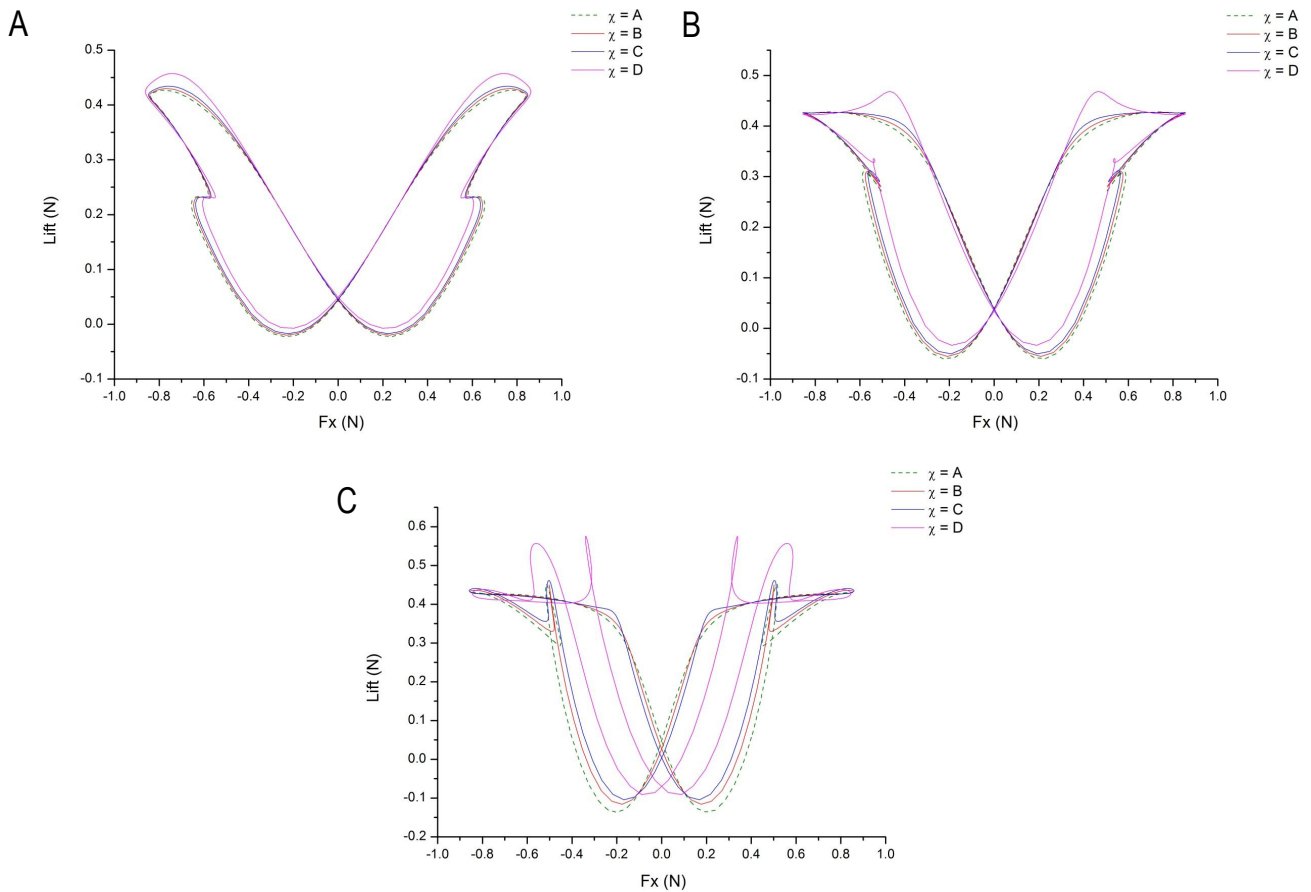


Figure 5.34: *Fx Vs Lift Limit Cycle Comparison; A: Rotation Duration 3.3s, B: Rotation Duration 2.2s, C: Rotation Duration 1.1s*

Figure 5.34, consists of limit cycle plots where the rotational duration is kept consistent and the position of rotation along the chord is varied from the leading edge to mid-chord. For the largest rotational duration the limit cycle has two cusps and all the curves follow one-another very well with some distinction present when the wing pitches about the leading edge. As the rotational duration becomes faster the curves start to intersect themselves and the distinction between the wing pitching about the leading edge and the remaining three locations augments, this trend continues as the rotational duration reaches its smallest value of 1.1s. When the wing pitches about the leading edge spanwise axis, the distinctions between this curve and the remaining three become more prominent as the rotational duration becomes smaller. Essentially, as the rotational duration increases the shape of the limit cycle plot becomes less complex where no loops are present, thus the curve consists of no self intersection regions. Individual plots of the limit cycles can be found in the appendix section of this report.

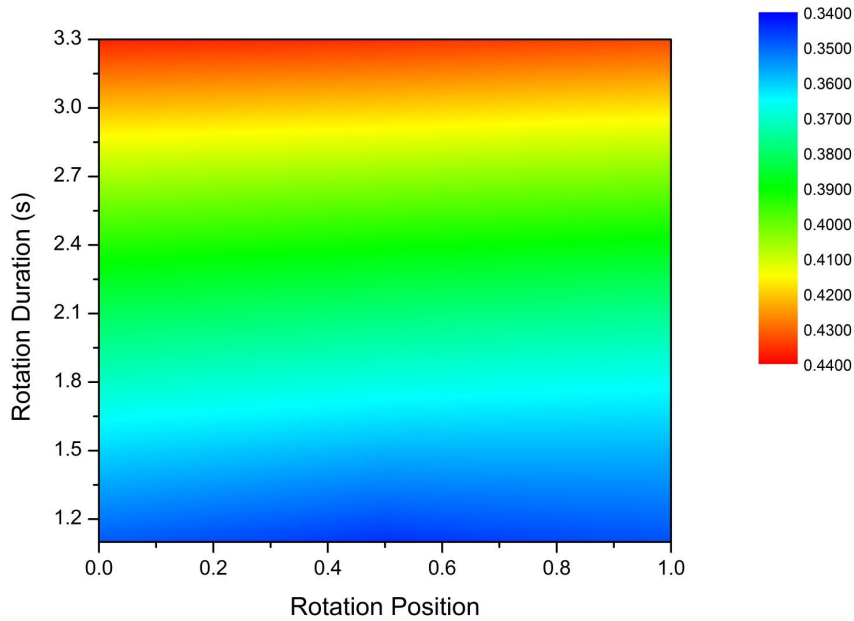


Figure 5.35: *Contour Plot for Average Aerodynamic Power / Average Lift Force For All Cases (Legend Represents Average Power, W / Average Lift, N)*

Figure 5.35, illustrates a contour plot which compares the average aerodynamic power required to lift force generated for both of the variable parameters which are the rotational location and duration. Evidently the greatest ratio of power to lift occurs for the slowest rotational duration which is 3.3s and declines as the duration decreases towards 1.1s, this applies for all rotational positions. As seen previously, the most aerodynamic power is required when  $\zeta = 3.3s$  (for most of the rotational locations), which declines as the rotational duration decreases. Fundamentally, more aerodynamic power is required per lift force generated when the wing rotates slowly and almost continually throughout the periodic motion for most of the rotational positions. On the contrary, the longest rotational duration seems to produce the lowest average lift force for all the rotational locations examined. Furthermore, it is encouraging to note that the ratio of aerodynamic power required per lift force generated for the shortest rotational duration forms a reasonable relationship, as excessive power is not required for such large lift force generations. As seen from the previous plots of the individual measurement parameters, the largest average lift force produced per cycle occurs when  $\zeta = 1.1s$  whilst the least average power required also occurs when  $\zeta = 1.1s$  with the exception of pitching about the leading edge for reasons aforementioned during the power data discussion.

Flow visualisations have been presented in Figure 5.36 of the TV formed at quarter downstroke for all three different rotational durations. The streamlines for both the LEV and TV were created by releasing instantaneous streamlines very close to both edges. The streamlines are colour mapped for the velocity magnitude, where maximum velocity seems to be present near the upper wing surface. As the rotational duration decreases the vortices at the tip seem to converge into a somewhat conical structure opposed to the more cylindrical shape formed when  $\zeta = 3.3s$ . The grey streamlines represent the LEV which feeds vorticity into the TV, the images clearly depict the connection between both of these vortices. The break-up of the LEV and its distancing from the surface of the wing tip was mentioned earlier which can be seen clearly as the LEV connects with the TV and breaks apart whilst travelling through the much larger TV, this flow movement is visualised in all three images. The conical-like formation of the TV in image C has a very similar diameter to the LEV which is clearly illustrated at the point where they connect.

Figure 5.37, displays the frontal view of the LEV and TV structures formed at quarter downstroke which were described above. The detachment of the LEV from the leading edge can be seen clearly for all three rotational durations which occurs at approximately three quarter wing span from the root. More specifically, the detachment of the LEV when  $\zeta = 3.3s$  occurs earlier than when  $\zeta = 1.1s$ . In general, the LEV detaches earlier for the slowest rotational duration and at a later position along the wing span from the root as the rotational duration decreases. Furthermore, the connection between the two types of vortices formed for each wing motion is clearly visualised as the LEV moves into the TV. The position of the TV seems to be further away from the wings tip surface with greater stretching when  $\zeta = 3.3s$  as the wing rotates very slowly. The growth in diameter of the LEV from the root to tip is clearly shown as the vortex travels along the leading edge of the wing in the spanwise direction towards the tip, eventually detaching from the wings surface and moving into the TV, which is much larger in diameter and unstable opposed to the compressed tube-like LEV. The TV also has a more intense appearance for the smallest rotational duration when compared to that of the largest rotational duration which is more unstable as well.

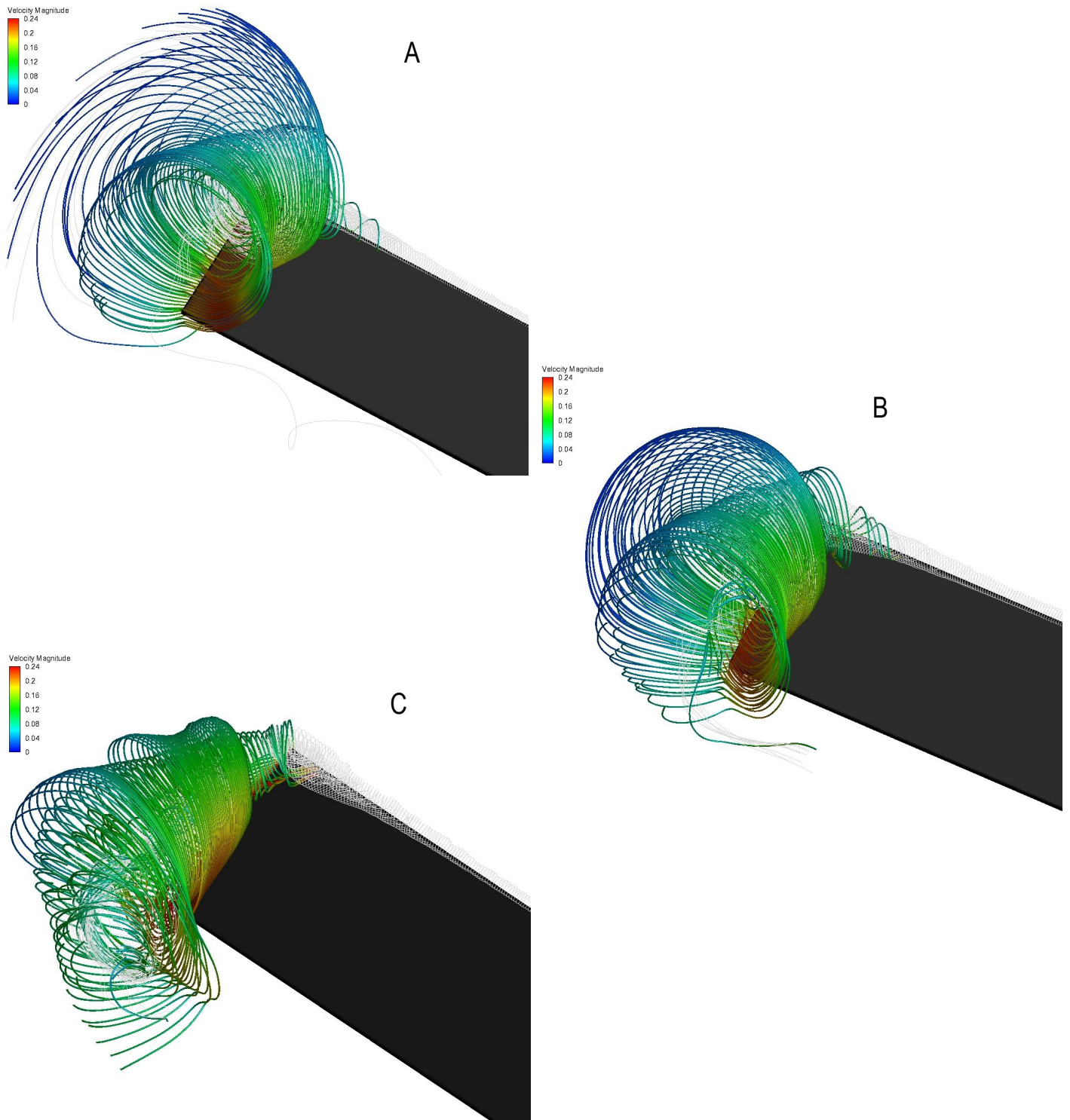


Figure 5.36: *Rectangular Wing with Rotation About the Leading Edge Cases 1-3 at  $\tau = 0.125$ ; A: Streamlines with Velocity Magnitude at Wing Tip for  $\zeta = 3.3s$ , B: Streamlines with Velocity Magnitude at Wing Tip for  $\zeta = 2.2s$ , C: Streamlines with Velocity Magnitude at Wing Tip for  $\zeta = 1.1s$ . Velocity Units: m/s*

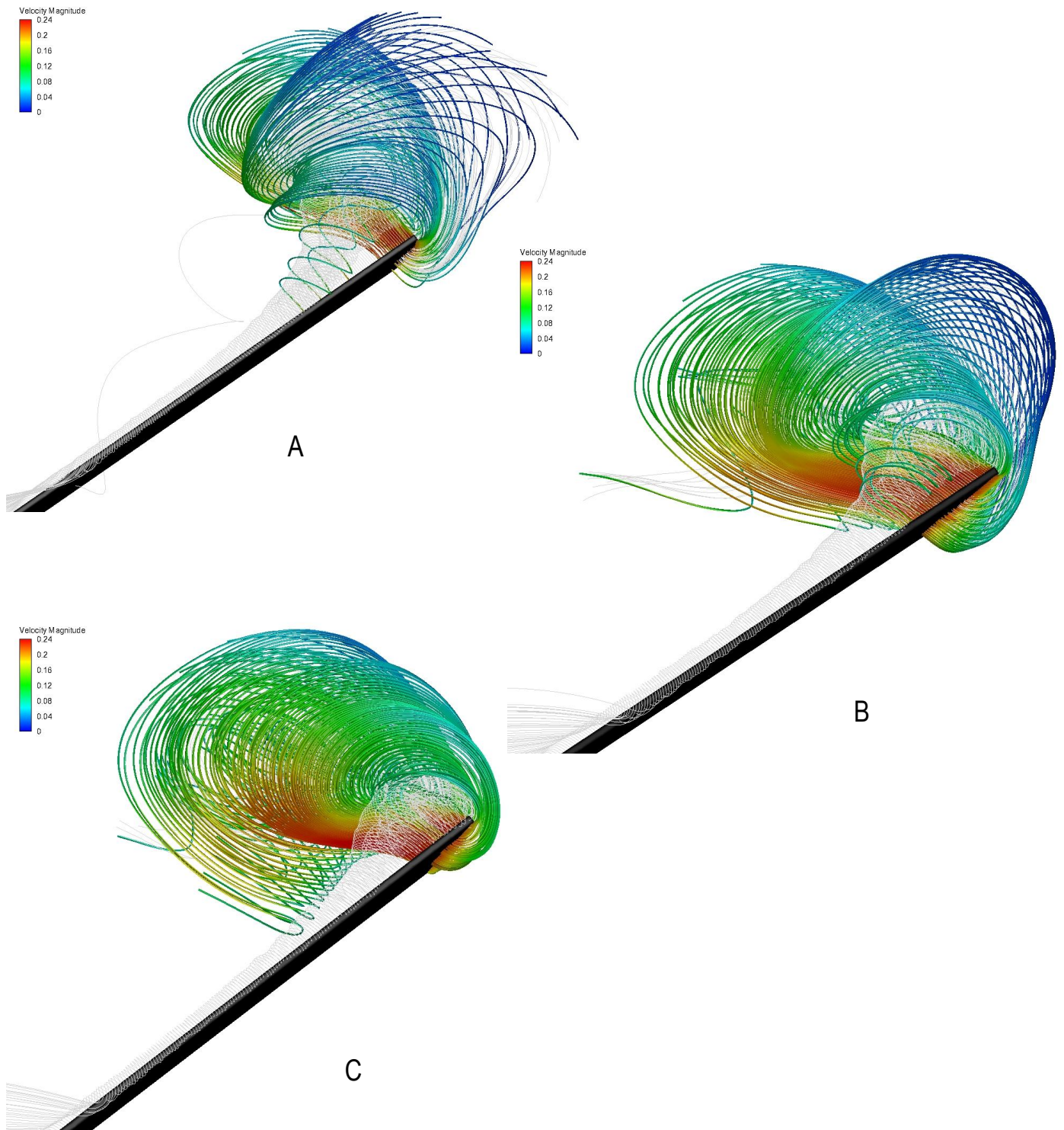


Figure 5.37: *Rectangular Wing with Rotation About the Leading Edge Cases 1-3 at  $\tau = 0.125$ ; A: Frontal View of Streamlines with Velocity Magnitude at Wing Tip for  $\zeta = 3.3s$ , B: Frontal View of Streamlines with Velocity Magnitude at Wing Tip for  $\zeta = 2.2s$ , C: Frontal View of Streamlines with Velocity Magnitude at Wing Tip for  $\zeta = 1.1s$ . Velocity Units: m/s*

### 5.2.3 Flapping Experimental Wing

A simulation was performed for the 60 mm wing (WT4) travelling through a flapping motion only to form a comparison with the experimental data which is presented in the following chapter. Large flow separation would occur in such a case as the wing is essentially a flat plate moving through an initial static region of air with a AOA of zero degrees, thus flow would effectively separate at every edge. Furthermore, as expected a wing performing a periodic flapping only motion with an AOA of zero degrees would produce an equal sized lifting force per half stroke but with an opposing sign, thus generating a net lift force of zero. The kinematic motion of this flapping wing is shown in Figure 6.11, which is located in the next chapter. The computational domain for the experimental wing with descriptions and dimensions is shown in Figures 5.38 and 5.39 respectively.

| Grid  | Number of Cells |
|---|-----------------|
| <i>Coarse with Stationary Virtual Inner Domain</i>      | 0.2 Million     |
| <i>Medium with Stationary Virtual Inner Domain</i>      | 0.4 Million     |
| <i>Dense with Stationary Virtual Inner Domain</i>       | 0.8 Million     |
| <i>Hyper Dense with Stationary Virtual Inner Domain</i> | 1.6 Million     |

Table 5.5: *Grid Density for 60 mm Experimental Wing (WT4)*

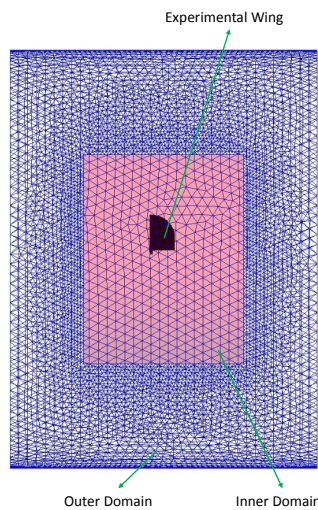


Figure 5.38: *Computational Domain with The Experimental Wing*

A grid sensitivity study was performed for the simulation involving the 60 mm wing (WT4), the results have been shown in Figure 5.40 and the mesh sizes have been provided in Table 5.5. The overall comparison for data produced from each grid seems to be in good agreement as the plots lay on top of one-another and in general the data is very similar to the hyper dense grid which has a much smaller resolution in the key regions surrounding the wing. Distinctions exist at the peak of both mid-strokes, where the coarse grid produces over predicted lift force data compared to the hyper dense case and fluctuations are present which affect the expected smooth curvature of the peaks. The final set of data presented will belong to the dense grid as a grid independent solution was achieved and its data has the best comparison to the hyper dense grid data and it is computationally less expensive than the hyper dense grid. All the grids consisted of a SVID housing a wing, and both of these volumes were enclosed by an outer domain. A DVID was not employed in this simulation as an SVID would be more suitable in future simulations when a stationary wall is present in the proximity of the dynamic flapping wing.

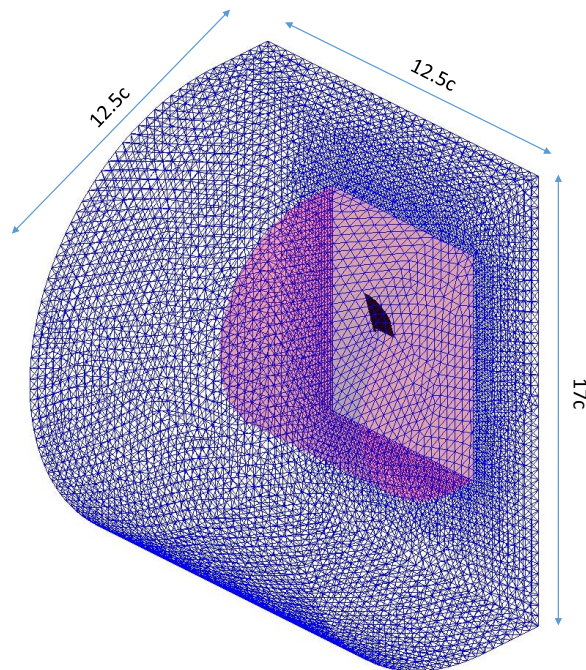


Figure 5.39: *Experimental Wing in The Computational Domain with Dimensions*

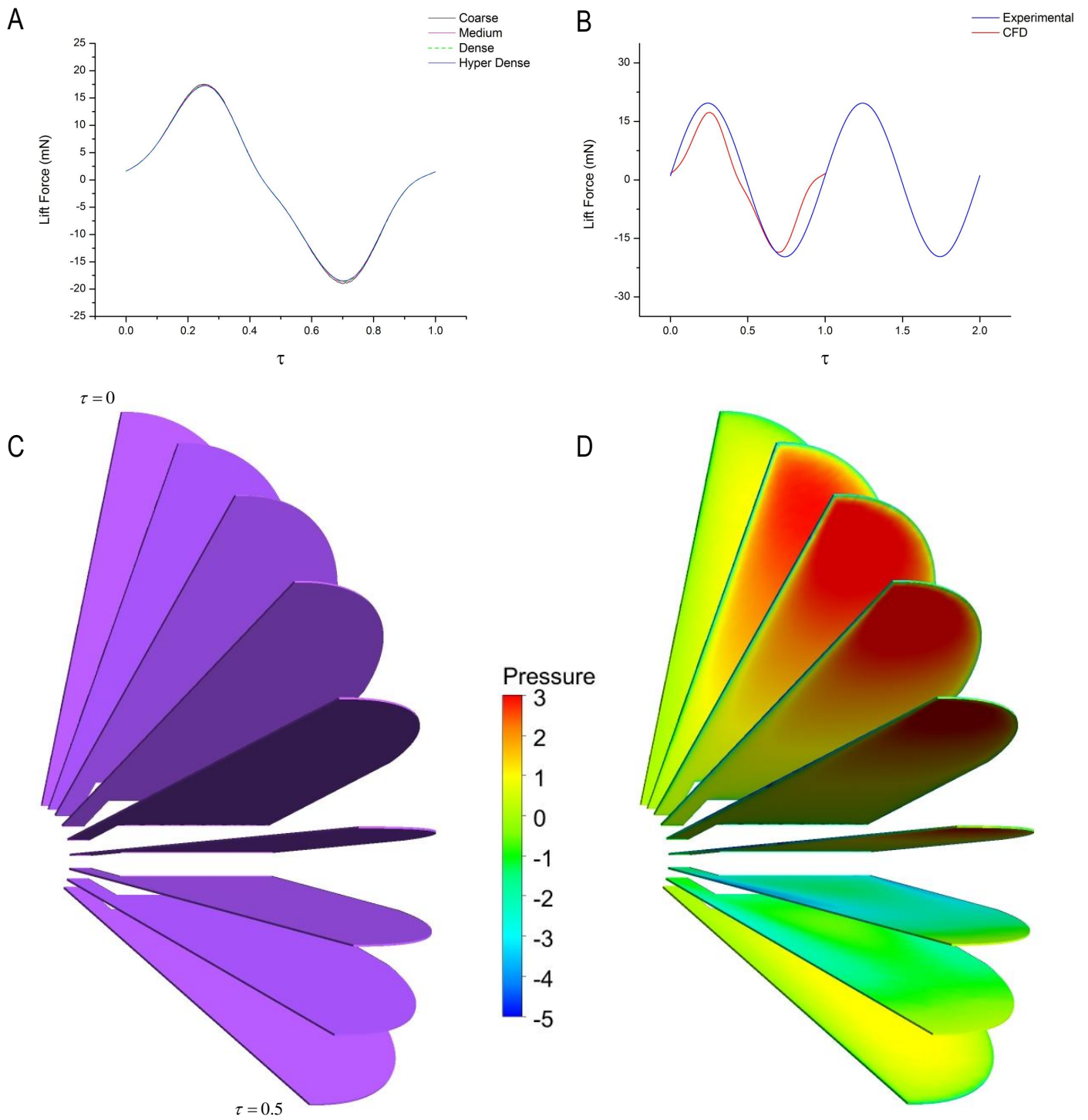


Figure 5.40: 60 mm Wing (WT4) Data with Motion and Pressure Visualisation; A: Grid Sensitivity Comparison for Lift Force Data, B: Experimental and CFD Lift Force Comparison, C: Flapping Wing Motion of Downstroke, D: Flapping Wing Motion of Downstroke with Pressure Contours on Wing Surfaces. Pressure Units: Pa

A comparison between the experimental and computational data has been shown in Figure 5.40, in which it can be seen that the two data sets follow a very similar trend. However, differences exist between the two curves as the computational curve does not produce a near perfect sine wave as expected, and on the other hand the experimental data does demonstrate a near perfect sine wave. The change of sign for lift force occurs earlier for the CFD result in comparison to the experimental, this could be due to difficulties in solving the amount of separated flow within the proximity of the wing. A comparison between this form of experiment where the sensor measures the force generated by the entire model at such a small scale becomes far more complicated opposed to when the sensor is located on the wing arm where direct measurements are acquired. The measurement uncertainty is very small for this range of force measurement and has been reported in chapter 4. In this method more uncertainties are introduced, one of which is the level of vibrations present when acquiring measurements from an entire dynamic system. Nonetheless, with the aforementioned in mind the data comparison between the experimental and computational results align well, with the computational method experiencing clear difficulties in convergence of the solution during the simulation due to the sheer volume of separated flow creating a highly unsteady fluid behaviour in the region of the wing. An attempt to address this difficulty was carried out by reducing the size of the time step, thus the wing travels a smaller angle having less distortional effects on the surrounding mesh. The simulations were performed for three successive flapping cycles, and the data shown in the comparison is from the third cycle. Furthermore, any distinctions between the second and third lift force data cycles were minute, so in future the second cycle can be used as a final set which would be more beneficial in terms of computational time.

An image of the wing travelling through a downstroke motion has been presented in Figure 5.40, and the corresponding pressure acting on the wings surface from fluid interaction is accompanied. The greatest pressure acts towards the tip of the wing where velocity is larger, and this would reach a maximum at mid-stroke position which is reflected directly by the peaks produced on the force plots. During most of the downstroke motion the upper surface of the wing has very low pressure acting on it which can also be negative on regions of the wing, however, at extreme positions such as start downstroke / end downstroke a much greater pressure will be acting on the upper surface (as seen in the image).

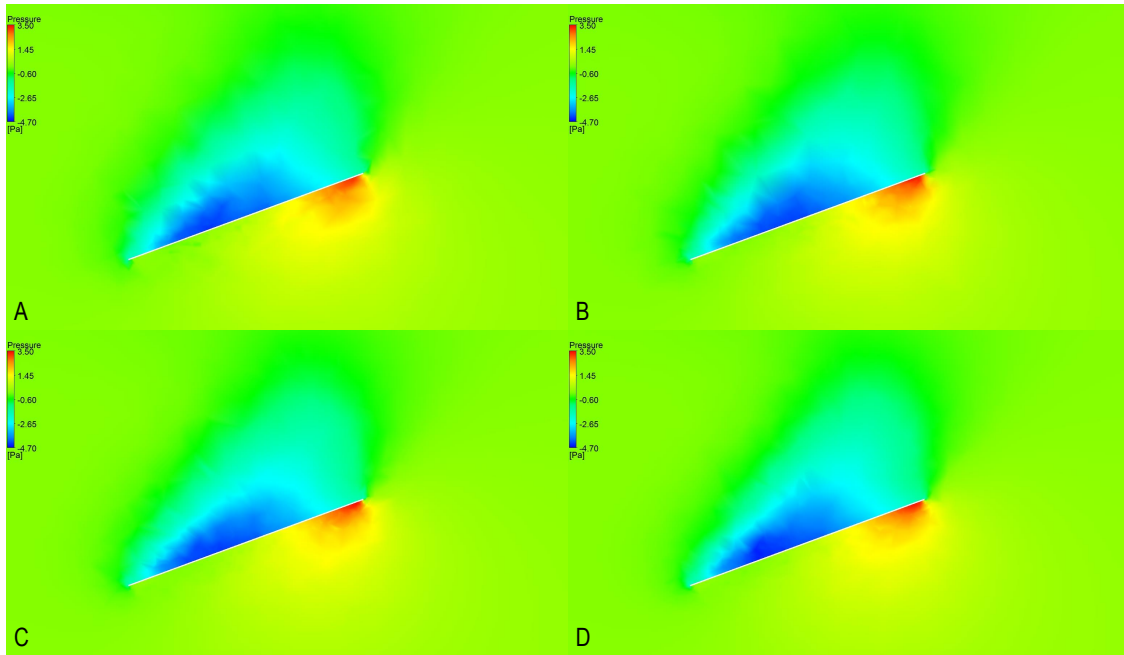


Figure 5.41: *60 mm Experimental Wing (WT4) with Pressure Distribution; A: Coarse Mesh, B: Medium Mesh, C: Dense Mesh, D: Hyper Dense Mesh. Pressure Units: Pa*

A comparison of the pressure distribution at mid-stroke along the span of the wing for all four grid densities considered is shown in Figure 5.41. The slices display the wing travelling through its downstroke motion with maximum positive pressure occurring on the under surface at the tip of the wing, at which point the wing has maximum velocity. The negative pressure region on the upper surface of the wing becomes more concentrated as the grid density increases, this can be clearly seen when comparing image A and D. Furthermore, the region covered by the darker blue shade (lowest pressure region) becomes smaller and more concise as the grid density increases. A very similar result is seen for the red positive pressure region, where the area covered is smaller and intensity of the red shade becomes more evident at the tip under surface of the wing as the grid density increases.

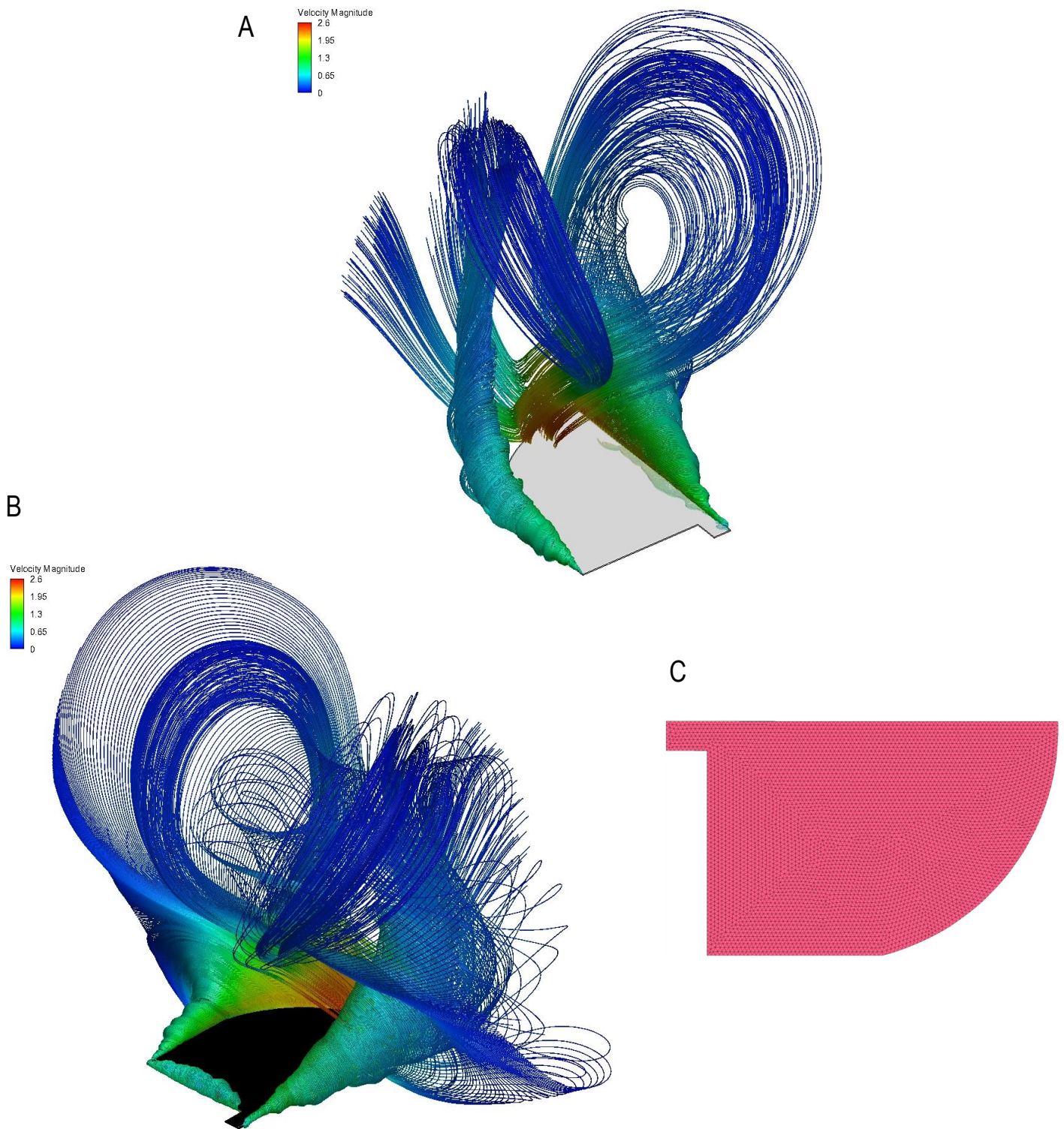


Figure 5.42: 60 mm Experimental Wing (WT4) with Streamlines and Mesh; A: Flow Characteristics During Downstroke at  $\tau = 0.25$ , B: Flow Field Around Wing at  $\tau = 0.25$ , C: Mesh on Wing Surface, Velocity Units:  $m/s$

Figure 5.42, consists of flow visualisations relating to this flapping wing and an image of the triangular mesh on the surface of the wing. The mesh on the surface of this wing belongs to the dense grid which consisted of 800,000 elements within the computational domain. The flow visualisations have been composed when the wing (set to flap at 5 Hz) was positioned at mid-downstroke, therefore peak force production. Figure 5.42A, illustrates the vortex dynamics in the form of streamlines which were instantaneously released at the leading edge to view the flow behaviour at this specific position. The vortical structure of the flow present at the leading edge is substantially different when compared to the structure of the vortex when the wing adopts a sufficiently large AOA as seen from previous flow visualisations shown in this chapter.

The Reynolds number of the flow in these simulations and experiments was 2716. The flow dynamics at the trailing edge is also visualised as instantaneous streamlines are released very close to this edge, which has a much shorter geometrical length than the leading edge, and a curved profile linking the leading and trailing edges. As the wing travels downwards with a profile of a flat plate held at zero degrees AOA, the fluid separates at every edge and tends to roll-up in the form of a vortex which is highly unstable, with an extremely large growth in diameter along the span of the leading and trailing edges. The vortex along the span of the leading edge experiences significant stretching as it grows from wing base to tip, and its instability is clearly evident, this also applies to the flow formation at the trailing edge. Both flow topologies seem as though they are being pulled off the edge of the wing and a zero degree AOA effects the operation of any vortex self-stabilising mechanism as presented in literature where the wings have a considerable sized AOA.

The complex unsteady flow field present around this flapping wing has been shown in a more organised manner where streamlines have been released around the edges only rather than the entire wing, this has been shown in Figure 5.42C. The development of a much smaller and compact vortex has been shown along the length located at the base of the wing. The wing velocity along this wing base length is much smaller when compared to the tip, and for this reason the velocity of the fluid is also much smaller. This aids in forming a more stabilised vortical structure which does not experience the form of stretching that acts at the leading and trailing edges of this wing. Flow separation is clearly present at the curved edge of the wing which has a higher velocity of flow opposed to the wing base vortical structure as presented by the colours on the streamlines representing velocity magnitude.

## Chapter 6

# Experimental Results

This chapter presents the experimental results produced from the tests mentioned in the experimental arrangements chapter. The first section considers the force and moment measurements for model 1 in various arrangements as well as fluid-wall interactions due to the effect of rigid boundaries. This will be followed by an evaluation and comparison of the results produced by model 2 in both of its configurations in order to scrutinise the effect of configuration change on aerodynamic forces and related power requirement. Sub-sections within this chapter will review the wing motion kinematics for the tests conducted and depict images of wing rotation with a passive rotational mechanism. An 'open-air' experimental rig and 'vacuum chamber' experimental rig were utilised for these experiments. Two models were designed in this thesis, both are based on the same mechanical actuation concept. However, the only difference is that model 1 performs symmetrical flapping only and model 2 performs both symmetrical and asymmetrical flapping motions. The experimental results reported have been produced from the tests listed in Table 6.1.

| Model | Flapping Style & Wing  | Flapping Configuration | Stroke Plane      | Unique Identifier                           |
|-------|--|------------------------|-------------------|---|
| 1     | <i>Flapping Only with Wing Type 3 (47 mm)</i>                  | <i>Symmetrical</i>     | <i>Vertical</i>   | <i>M1 – F – WT3 – S – V</i>                 |
| 1     | <i>Flapping Only with Wing Type 4 (60 mm)</i>                  | <i>Symmetrical</i>     | <i>Vertical</i>   | <i>M1 – F – WT4 – S – V</i>                 |
| 1     | <i>Flapping Only with Wing Type 4 (60 mm) &amp; Boundaries</i> | <i>Symmetrical</i>     | <i>Vertical</i>   | <i>M1 – F<sub>wB</sub> – WT4 – S – V</i>    |
| 1     | <i>FR with Wing Type 4 (60 mm)</i>                             | <i>Symmetrical</i>     | <i>Vertical</i>   | <i>M1 – FR – WT4 – S – V</i>                |
| 1     | <i>FR with Wing Type 4 (60 mm) &amp; Boundaries</i>            | <i>Symmetrical</i>     | <i>Vertical</i>   | <i>M1 – FR<sub>wB</sub> – WT4 – S – V</i>   |
| 1     | <i>FR with Wing Type 4 (60 mm)</i>                             | <i>Symmetrical</i>     | <i>Horizontal</i> | <i>M1 – FR – WT4 – S – H</i>                |
| 1     | <i>FR with Wing Type 4 (60 mm) &amp; Boundaries</i>            | <i>Symmetrical</i>     | <i>Horizontal</i> | <i>M1 – FR<sub>wB</sub> – WT4 – S – H</i>   |
| 1     | <i>FRAP with Wing Type 4 (60 mm)</i>                           | <i>Symmetrical</i>     | <i>Vertical</i>   | <i>M1 – FRAP – WT4 – S – V</i>              |
| 1     | <i>FRAP with Wing Type 4 (60 mm) &amp; Boundaries</i>          | <i>Symmetrical</i>     | <i>Vertical</i>   | <i>M1 – FRAP<sub>wB</sub> – WT4 – S – V</i> |
| 2     | <i>Flapping Only with Wing Type 4 (60 mm)</i>                  | <i>Symmetrical</i>     | <i>Vertical</i>   | <i>M2 – F – WT4 – S – V</i>                 |
| 2     | <i>Flapping Only with Wing Type 4 (60 mm)</i>                  | <i>Asymmetrical</i>    | <i>Vertical</i>   | <i>M2 – F – WT4 – A – V</i>                 |
| 2     | <i>FR with Wing Type 4 (60 mm)</i>                             | <i>Symmetrical</i>     | <i>Vertical</i>   | <i>M2 – FR – WT4 – S – V</i>                |
| 2     | <i>FR with Wing Type 4 (60 mm)</i>                             | <i>Asymmetrical</i>    | <i>Vertical</i>   | <i>M2 – FR – WT4 – A – V</i>                |
| 2     | <i>FR with Wing Type 4 (60 mm)</i>                             | <i>Asymmetrical</i>    | <i>Horizontal</i> | <i>M2 – FR – WT4 – A – H</i>                |

Table 6.1: Experiments Performed with Both Models

## 6.1 Force & Moment Measurements for Model 1 (Sym Only)

Force and moment measurements related to model 1 will be shown in this section for various cases. Fundamental experiments were carried out in the form of flapping only which led to developments in the form of passive wing rotation via elastic bending, which was then followed by the boundary experimentations where a rigid boundary is located in the near vicinity of the dynamic wing motion. Boundary tests were initially carried out for flapping only as a base evaluation, thereafter the additional coupled motion of the wing was introduced, via mechanical motion and elastic dynamics. In aerodynamic terms the vertical force will be denoted as lift force and the horizontal force will be denoted as thrust force, both can be seen as flight force vectors.

### 6.1.1 Flapping Only for 47 mm Wings (WT3)

Flapping only tests at various frequencies ranging from 3-10 Hz in increments of 1 Hz for wings with a semi span of 47 mm were conducted. The frequency was altered by setting the appropriate voltage on the power supply in accordance to the desired frequency and the current was drawn by the motor as required, an ESC was not required as a brushed DC coreless motor was used for both FW models. Each of the tests were performed in air and under vacuum conditions. Thereafter the aerodynamic force was determined through the subtraction of total force (found during tests in air) and inertial force (found during tests in the vacuum chamber). Before the subtraction stage, the raw data requires filtering due to the contributions of the structural vibrations from the experimental rig and electrical noise present in the experimental instrumentation, namely the F/T sensor components. The data also consists of structural vibrational modes from the excitation of the FW model. These structural vibrational modes would appear at regular intervals which are multiples of the flapping frequency. Thus, low-pass filtering is performed for each dataset to acquire the force/moment produced at each flapping frequency for both the total force and vacuum chamber data. The average aerodynamic power was determined through the subtraction of the average power input for total force and vacuum chamber tests.

Figures 6.1 to 6.3 display the data acquired from the flapping tests. Spectral analysis has been presented in the form of spectrograms for each case where the dominant frequency namely the flapping frequency is presented as the darkest red line. For example plot A in Figure 6.1 clearly represents a flapping frequency

of 3 Hz where the darkest shade occurs. The modes of vibration of the flapping frequency are shown in the spectrogram plots which are a noticeably lighter shade than the actual flapping frequency. A peak is produced in the form of a harmonic series in relation to the flapping frequency, for example, when the flapping frequency is 9 Hz a peak is produced at 18 Hz, 27 Hz, 36 Hz and 45 Hz. It is worth noting that beyond the actual flapping frequency the amplitude of the peak considerably reduces in size, thus as the harmonic frequency increases its effect on the measured data reduces. These harmonic peaks are a structural response from the experimental rig and vehicle itself. This form of structural modes are expected when performing experiments on a dynamic system. For lucidity a spectrogram plot has been shown for each different frequency. The plots along the right-side of the above mentioned figures show the vertical forces and aerodynamic power required by the wings when moving through air. Time has been shown along the horizontal axis as non-dimensional time for two cycles, which is normalised by the instantaneous time and the period of oscillation.

The aerodynamic plots clearly show a sinusoidal behaviour and its respective inertial plot relates well to the behaviour of a cosine curve. As the frequency increases the peaks of the aerodynamic curves also increase as expected and this relation is also shown in the aerodynamic power plots. Naturally this observation is clearly shown in the inertial data as well, as the flapping velocity of the wing increases, with an increase in frequency. At the start of downstroke, the inertial force is at its maximum positive value and at the end of this stroke the inertial force reaches its maximum negative value, and at these respective positions the aerodynamic force produced is more or less zero, as the wing velocity is zero. The wing tip will experience maximum wing velocity at mid-downstroke and mid-upstroke positions. These are the locations where pressure will peak on the surface of the wing in accordance to the respective stroke direction. This peak in pressure acting on the wing surface particularly near the wing tip which experiences the largest velocity is directly related to the peaks shown in the aerodynamic plots. The maximum positive aerodynamic force peak is experienced during the mid-downstroke position, and the maximum negative peak aerodynamic force is experienced during the mid-upstroke position. Whilst the wing approaches maximum velocity at both mid-down and upstrokes the aerodynamic peaks will directly relate to this. During a flapping cycle the wing-root will undergo the smallest velocity, whereas the wing-tip will undergo the largest velocity. Maximum pressure will occur at the location on the wing which experiences maximum flapping velocity.

To provide a complete view, during linear translation of a wing, each chord-wise section of the wing moves at

the same velocity through a fluid, thus the velocity at the base and tip of the wing are identical as the wing travels through a straight path. In such a scenario the pressure encountered at the wing tip and base should also be identical. A flapping wing actually performs a circular motion about a pivot point in mechanical terms, thus in this case each chord-wise section will not be rotated at the same velocity, instead the wing tip will move at a faster velocity than the wing root. In essence, the velocity along the wing chord-wise sections increases linearly from root to tip, thus there will be a substantial difference between the pressure encountered due to the fluid at the wing tip and root regions.

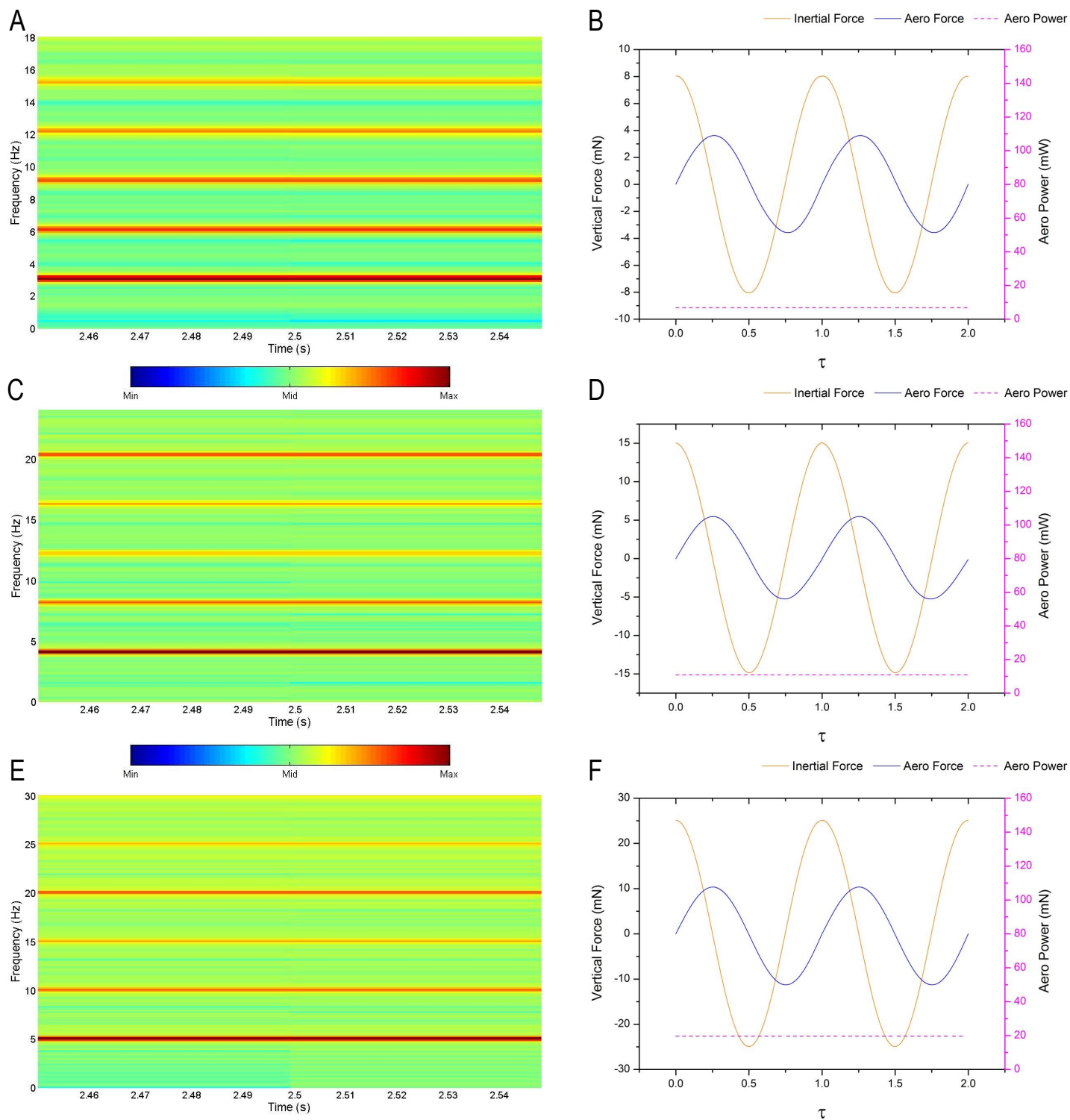


Figure 6.1: *Flapping Wing Measurements for 47 mm Wings (WT3); A: 3 Hz Spectrogram, B: 3 Hz Force & Power Data, C: 4 Hz Spectrogram, D: 4 Hz Force & Power Data E: 5 Hz Spectrogram, F: 5 Hz Force & Power Data. Colour Bar Represents Size of Amplitude. UI: M1-F-WT3-S-V*

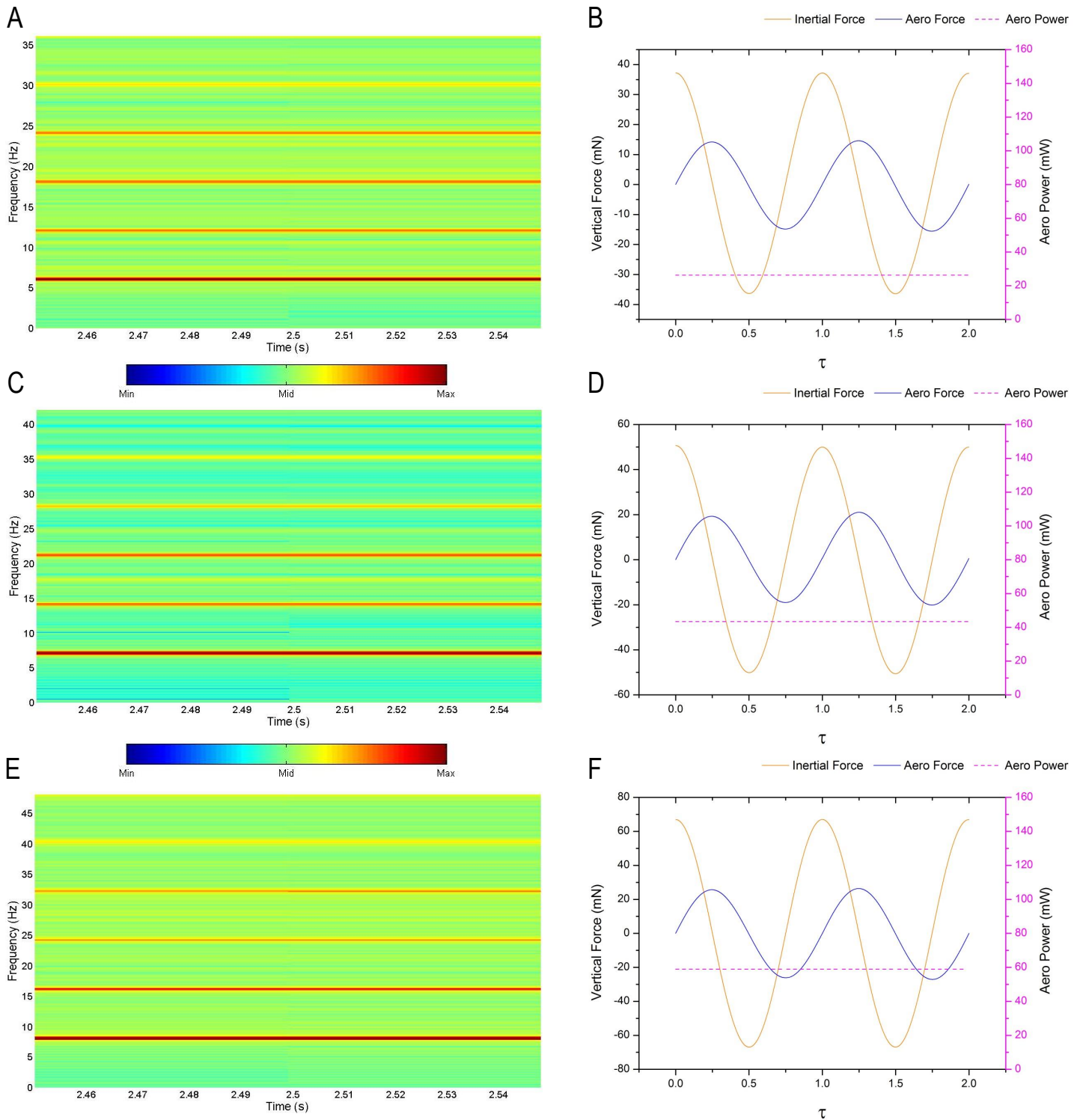


Figure 6.2: *Flapping Wing Measurements for 47 mm Wings (WT3); A: 6 Hz Spectrogram, B: 6 Hz Force & Power Data, C: 7 Hz Spectrogram, D: 7 Hz Force & Power Data E: 8 Hz Spectrogram, F: 8 Hz Force & Power Data. Colour Bar Represents Size of Amplitude. UI: M1-F-WT3-S-V*

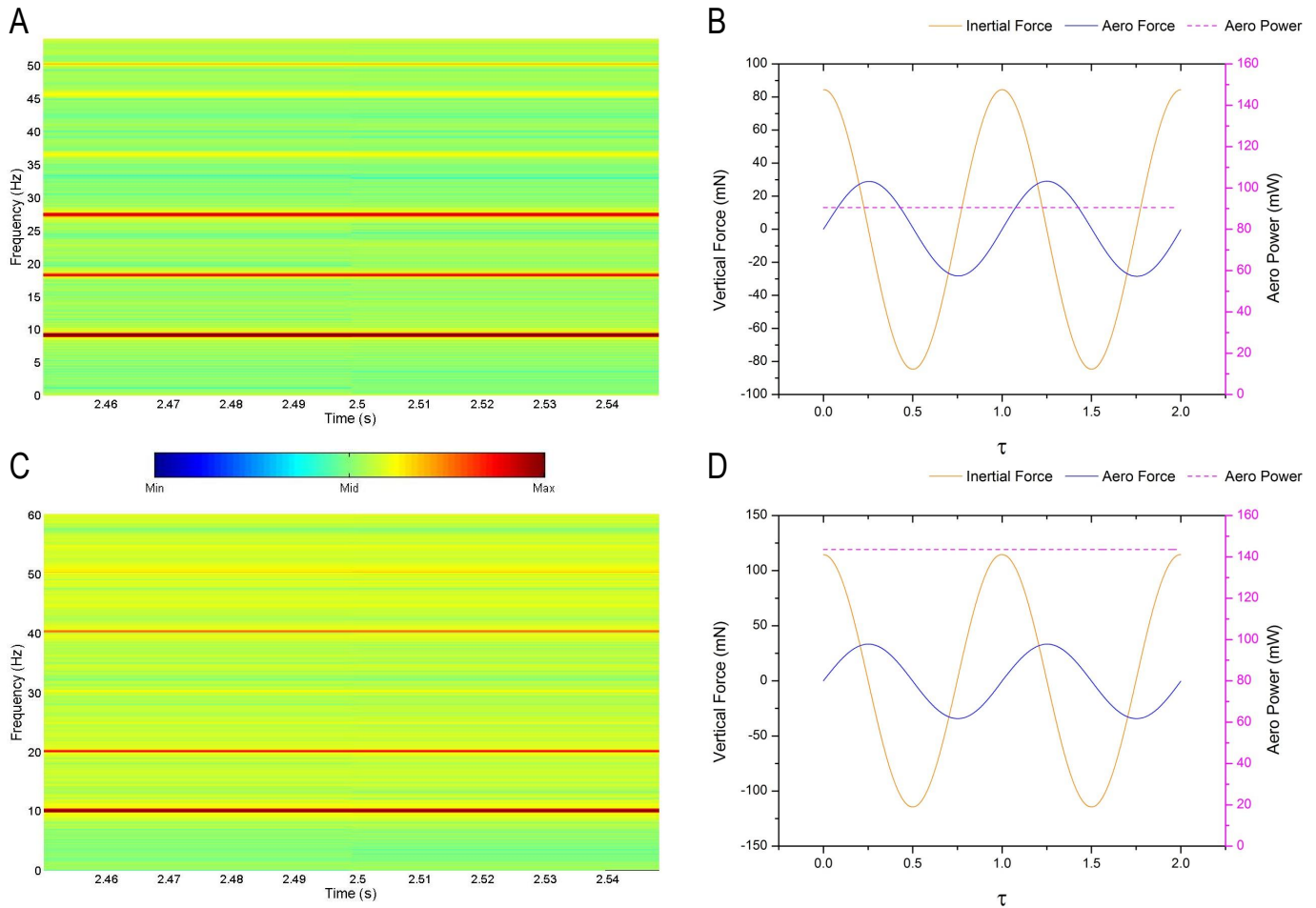


Figure 6.3: *Flapping Wing Measurements for 47 mm Wings (WT3); A: 9 Hz Spectrogram, B: 9 Hz Force & Power Data, C: 10 Hz Spectrogram, D: 10 Hz Force & Power Data. Colour Bar Represents Size of Amplitude. UI: M1-F-WT3-S-V*

Figure 6.4, displays various data plots all related to the flapping wing tests for the 47 mm wings (WT3). A comparison of the peak aerodynamic forces produced in all the cases has been shown in plot A. The relation between the aerodynamic forces and flapping frequency displays that as the frequency increases the aerodynamic forces also increase. There is a significant increase in aero force measured between flapping frequency at 3 Hz and 10 Hz as expected due to the large differences in pressure which would exist on the surface of the wing. The tests were performed at a range of Reynolds numbers under hovering conditions (Equation 5.51) which increased as the flapping frequency increased. Scrutinising the comparison of aerodynamic plots, an appreciable higher increase is observed between 4 and 5 Hz compared to between 3 and 4 Hz. This may be directly related to the mechanism as the mechanical motion of the system must have improved considerably when set to 5 Hz as opposed to the two lower frequencies as the lag created by the mechanical gear system had reduced.

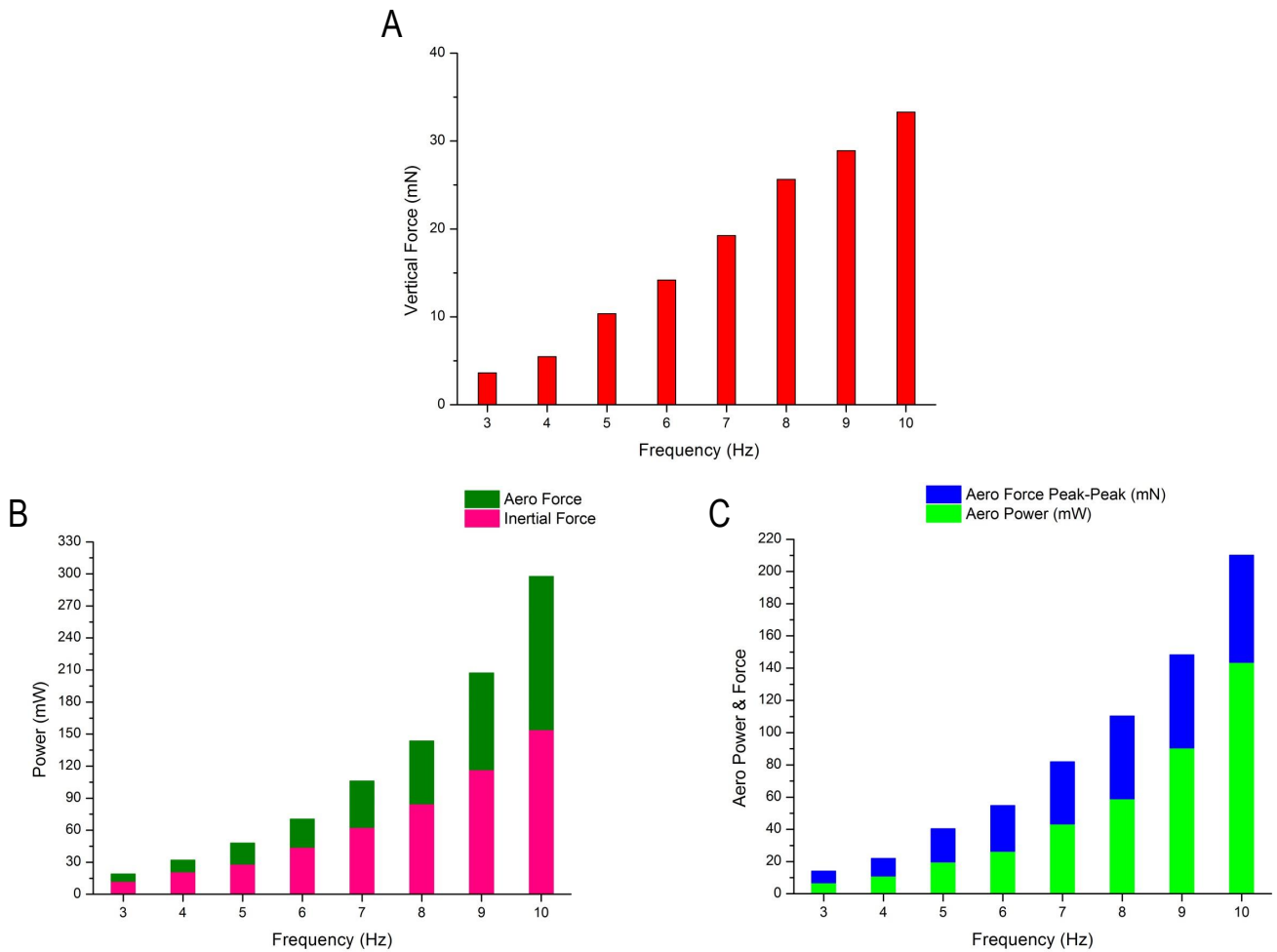


Figure 6.4: *Flapping Wing Measurements for 47 mm Wings (WT3)*; A: *Aerodynamic Force Comparison*, B: *Power Data for Inertia and Aerodynamic Forces*, C: *Aerodynamic Power & Force Relation*. UI: M1-F-WT3-S-V

Figure 6.4B and C compare the power required by the system and its relation to the peak aerodynamic force. It should be noted that the power required for the inertial forces includes the power needed to overcome the frictional forces within the system. As the frequency increases the power required by the model in vacuum conditions increases exponentially, this also applies for the power needed to produce the aerodynamic forces achieved. A noticeable jump in aerodynamic power required exists between 8-9 Hz and 9-10 Hz, which is due to the system needing a much larger voltage to obtain these flapping frequencies. The relation between the aero power required per force production for all frequencies presents a consistent behaviour as the power needed increases, the output peak-peak aerodynamic force also increases. For majority of the frequencies tested it can be seen that substantial power has not been drawn, except for 9 Hz and especially 10 Hz where the aerodynamic power required is considerably large in comparison to the peak-peak aero force produced.

### 6.1.2 Wing Motion Analysis for Model 1

This section will provide some kinematic images and data plots of the wing motion created through a complete stroke cycle. As aforementioned images were taken via the HS camera and relevant kinematic data was extracted from the images to understand the wings motion when free to rotate under the influence of aerodynamic loading.

A sequence of images have been shown in Figure 6.5 for the flapping only motion produced by the 60 mm wings (WT4) flapping at 5 Hz which meant the duration of a complete cycle lasts 0.2 seconds. The sequence commences from the downstroke position, and ends at the end upstroke position as shown in the images. Needless to mention stroke reversal occurs at the end of the downstroke and start of the upstroke motion. Subsequently a sequence of kinematic images for the flapping with wing rotation motion and flapping with AP wing rotation have been illustrated in Figures 6.6 and 6.7 respectively. The sets of images displayed were captured during the tests when the model was flapping along the vertical stroke plane. Henceforth, another sequence of images have been shown where the model has now been mounted at 90 degrees (Figure 6.8) to the vertical axis, thus the flapping stroke plane is now along the horizontal axis. The wing performs a flapping wing with rotation motion, where the wings trailing edge and the top of the optics table had a substantial distance between them to ensure the measurements are acquired accurately. The wings start from a start downstroke position and ends with an end-upstroke position. Due to the mirror set-up for this particular style of experiments the motions seems to be moving in the opposite direction in comparison to the previous sets of images.

Figures 6.9 and 6.10, all present a sequence relating to the motion of the wing during a boundary test acting as a ground platform. For the vertical flapping only test, the wing travels towards the rigid ground effect base and comes to rest at its maximum downstroke position where its tip is approximately 1 mm away from the surface of the ground effect base. When the model is rotated about a 90 degree angle, its stroke plane now occurs through the horizontal plane, thus when the boundary is located below the model it is now adjacent to the wings trailing edge. In this fashion the boundary has a role as a wall placed directly behind the trailing edge of the wings when flapping through a horizontal stroke plane. Referring to Figure 6.9, the wing sweeps through the fluid, and commences to rotate prior to the start upstroke position through a combination of effects, some of which are due to inertia, fluid loading and the deformational properties of the polyester exploited. Thus a slightly thinner polyester at the wing base would have altered the time

dependent AOA, likewise altering the exposed area which promoted wing rotation would lead to a difference in the AOA per time during the cycle. Thereafter, the wing approaches the boundary where the distance between the wings trailing edges and the upper surface of the boundary is approximately 1.2-1.4 mm apart, shortly after the wing will reverse in stroke and travel in the opposite direction. Unlike the ground effect base acting during a vertical stroke plane arrangement the wall is now in the proximity of the wing for longer durations. Lastly, under the actions of passive rotation when the model is flapping through the vertical stroke plane the curved portion of the wing neighbouring the trailing edge approaches the ground effect base towards end downstroke in the FRAP motion shown in Figure 6.10. As seen previously, prior to stroke reversal under a free-to-rotate condition the wing opens up as it nears the ground effect base where the distance between the two is approximately 1-1.5 mm. However, in contrast to the flapping only motion the tip does not reach the wall to create such a small distance between the two bodies. Henceforth, as shown in the sequence the wing continues to open up, augmenting its AOA whilst it commences the upstroke phase of the cyclic motion.

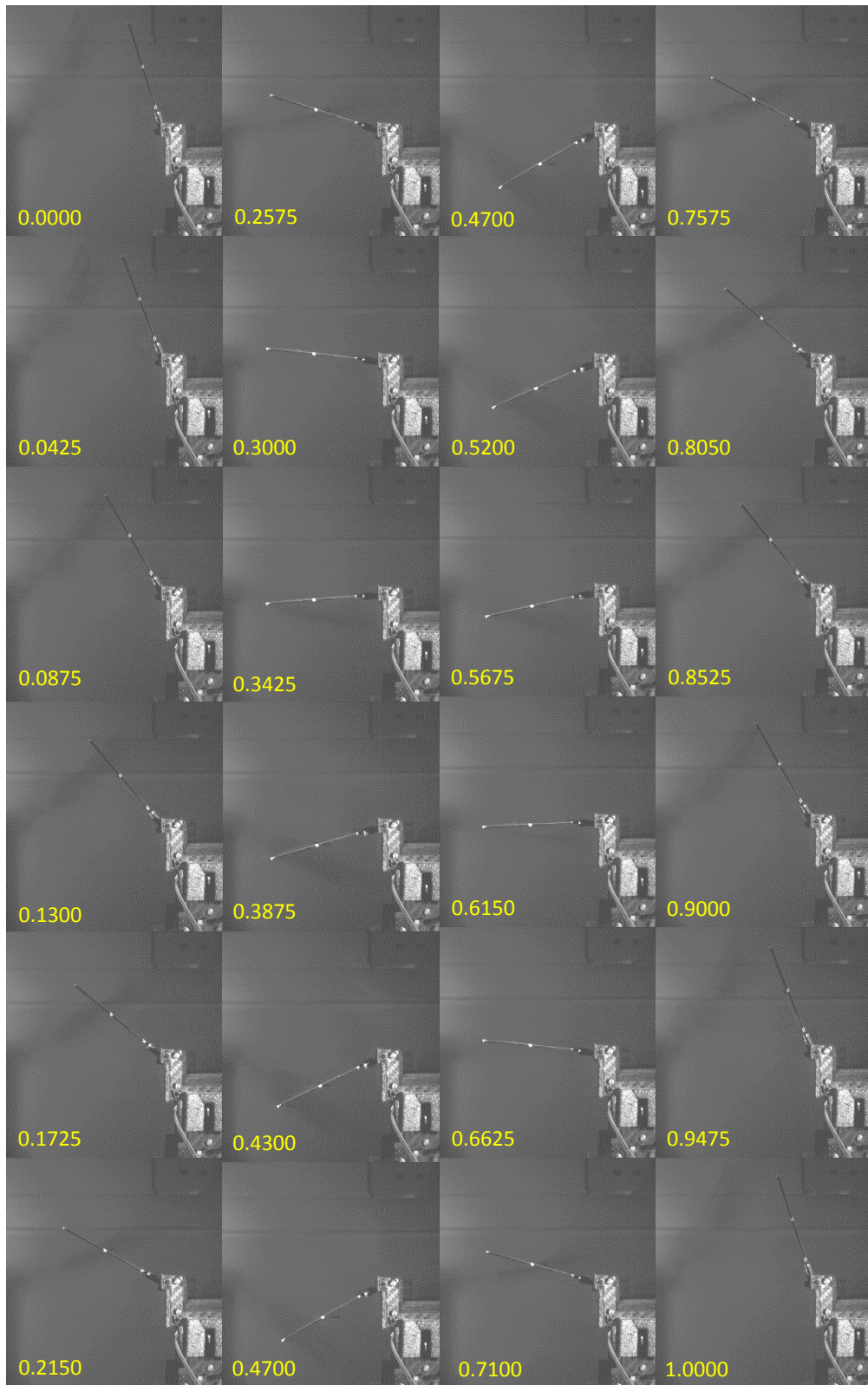


Figure 6.5: *Wing Position for Flapping Motion Sequence with Non-Dimensional Time. UI: M1-F-WT4-S-V*

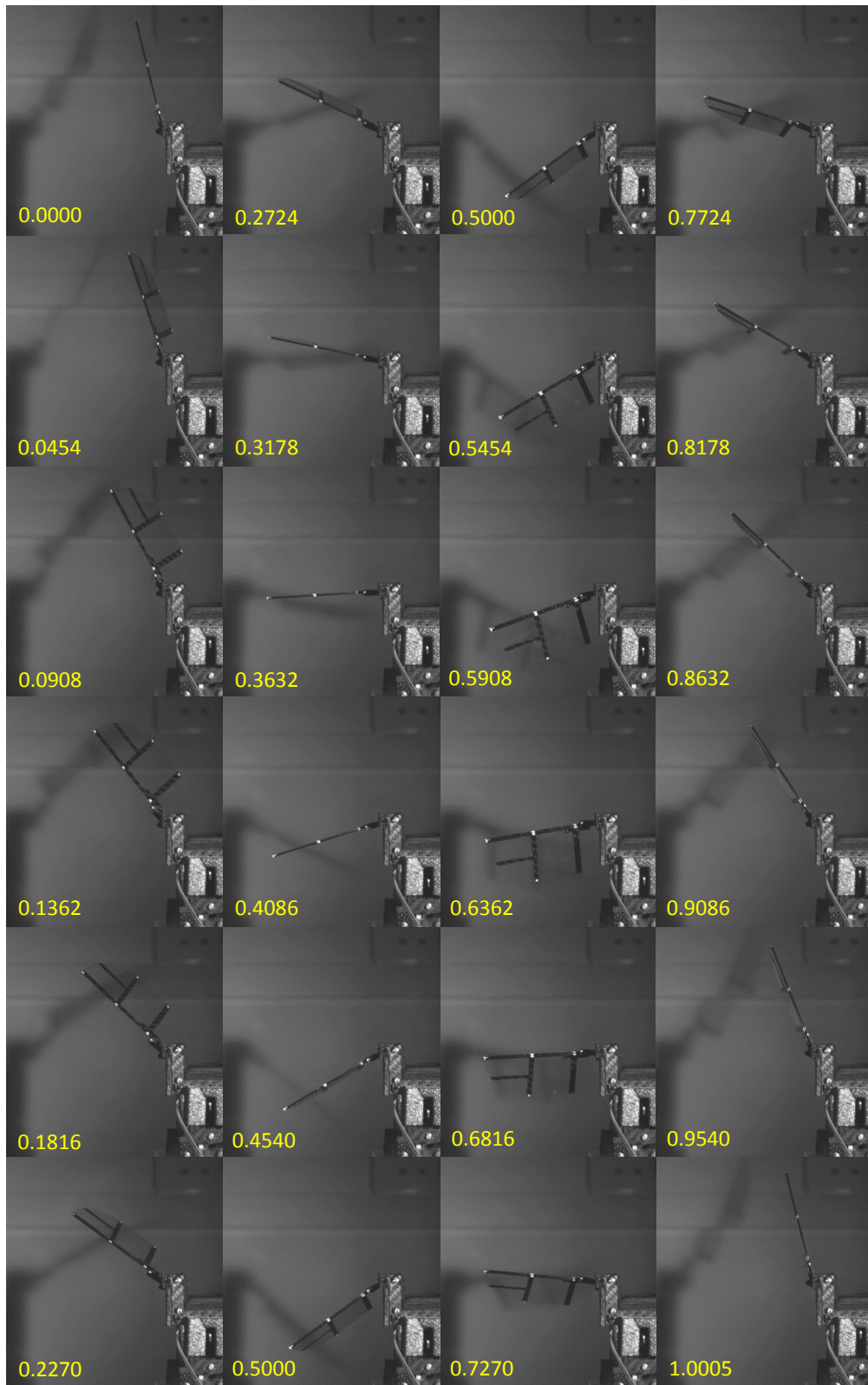


Figure 6.6: *Wing Position for FR Motion Sequence with Non-Dimensional Time. UI: M1-FR-WT4-S-V*

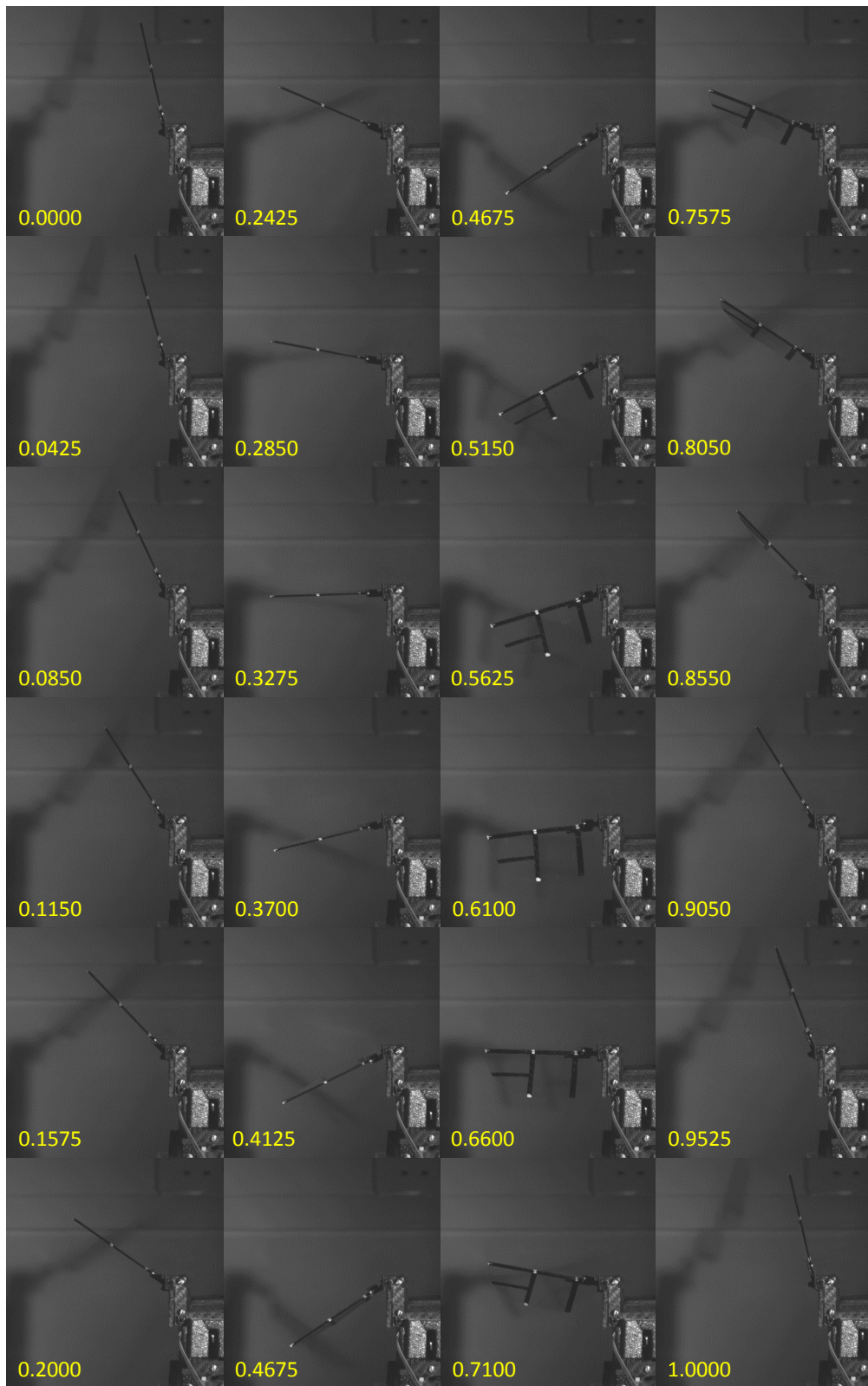


Figure 6.7: *Wing Position for FR with AP Motion Sequence with Non-Dimensional Time. UI: M1-FRAP-WT<sub>4</sub>-S-V*

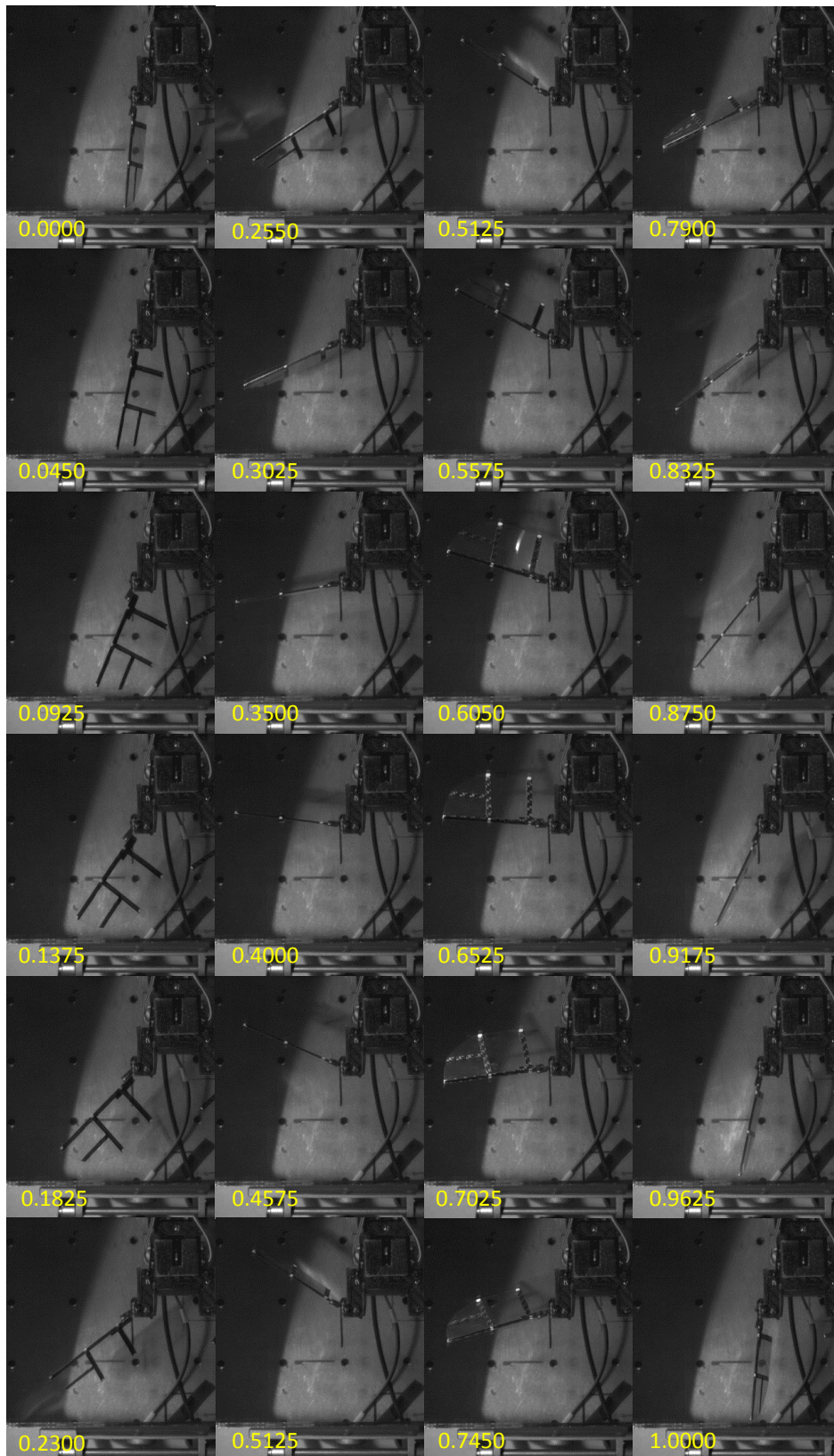


Figure 6.8: *Wing Position for FR Motion in Hovering Mode Sequence with Non-Dimensional Time. UI: M1-FR-WT4-S-H*

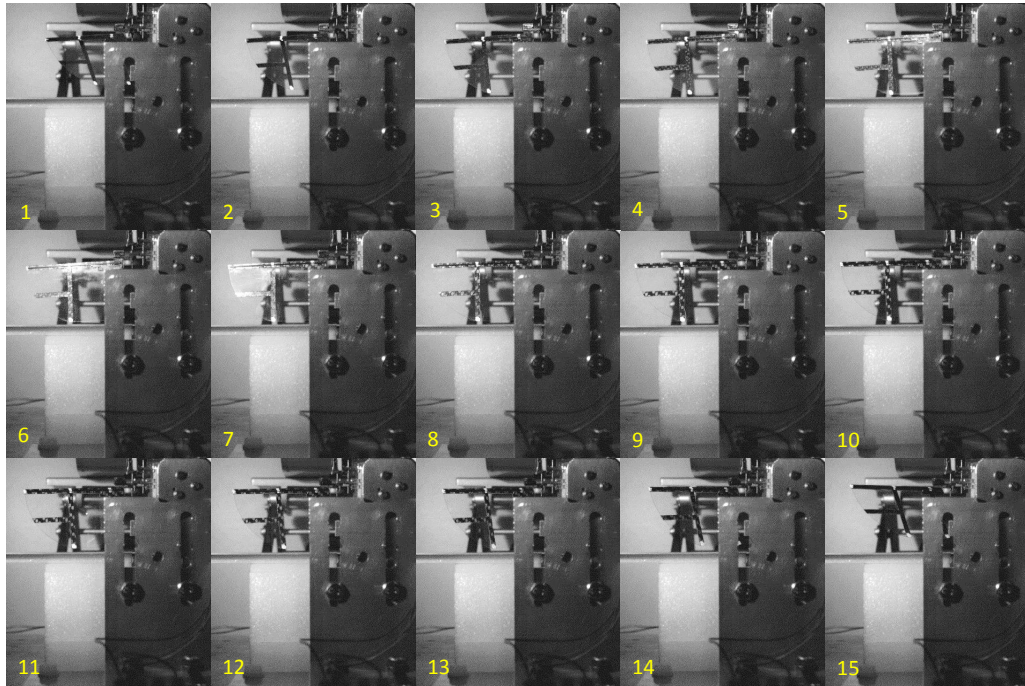


Figure 6.9: *Wing Position from Ground Effect Base for FR Motion in Hovering Mode, 1-8 Downstroke, 9-15 Upstroke. UI: M1-FRwB-WT4-S-H*

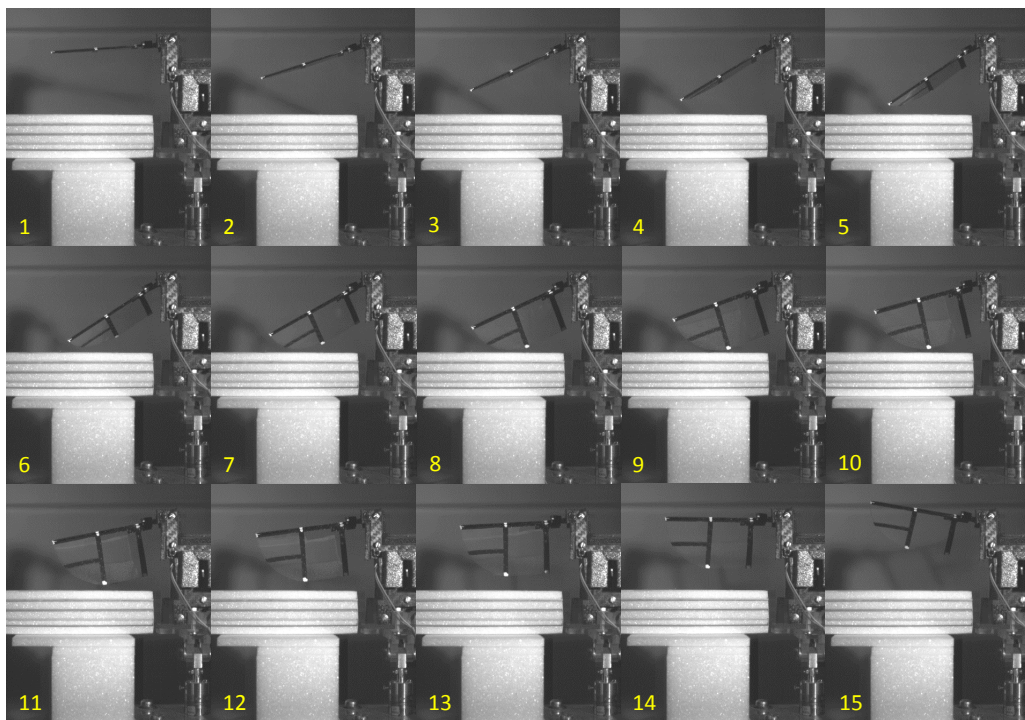


Figure 6.10: *Wing Position from Ground Effect Base for FR with AP Motion, 1-8 Downstroke, 9-15 Upstroke. UI: M1-FRAPwB-WT4-S-V*

Unlike the kinematic plot for a singular flapping motion which had a close correspondence to a traditional cosine wave, the flapping stroke curve for the coupled motion (refer to Figure 6.11B) is slightly distorted which is caused by the passively rotating wing. Under such a condition where the wing is passively rotating, this rotational effect will always have an influence on the flapping stroke kinematics. The AOA curve has a somewhat relation to a sinusoidal curve which also consists of some distortions as expected from a free-to-rotate wing under the influence of aerodynamic loading and ones which have quite a large mass compared to its size. Under future flight conditions the wings mass would need to decrease substantially which will naturally adopt some form of flexibility as a thinner and lighter sheet will be utilised for its membrane surface. A similar flapping stroke was created when the model was rotated 90 degrees to flap through a horizontal stroke plane (refer to Figure 6.11D), both of these plots seem to have a very close resemblance. Albeit, the AOA curves for both stroke planes showed some correlation such as a peak produced per half stroke. However, due to the nature of passive rotation the size of the peaks produced, exact timings and start/end positions were all different.

The flapping stroke plot for the FRAP arrangement (see Figure 6.11C) seems to show a similar correspondence to the flapping only kinematic curve for majority of the downstroke phase, and once the AOA starts to vary the flapping stroke plot starts to show a resemblance to the flapping with wing rotation arrangement. The duration where the AOA is constantly zero produces a smoother plot. As aforementioned and in concurrence with the images seen, the AOA does not remain at zero degrees for the entire duration of the downstroke motion, it actually starts to rotate in advance of the upstroke motion. A comparison of the passive AOA rotational kinematic curves has been shown in Figure 6.11E. As aforementioned, although the shapes of the curves for the AOA motion for both vertical and horizontal flapping stroke planes have a correspondence to one-another, numerous distinctions exist which is expounded upon in this chapter. The largest peak AOA was produced for the FRAP arrangement which was in the region of -54.8 degrees. The other two datasets were not far off reaching angles of -53.6 degrees and -50.7 degrees for flapping with wing rotation in the vertical and horizontal planes respectively.

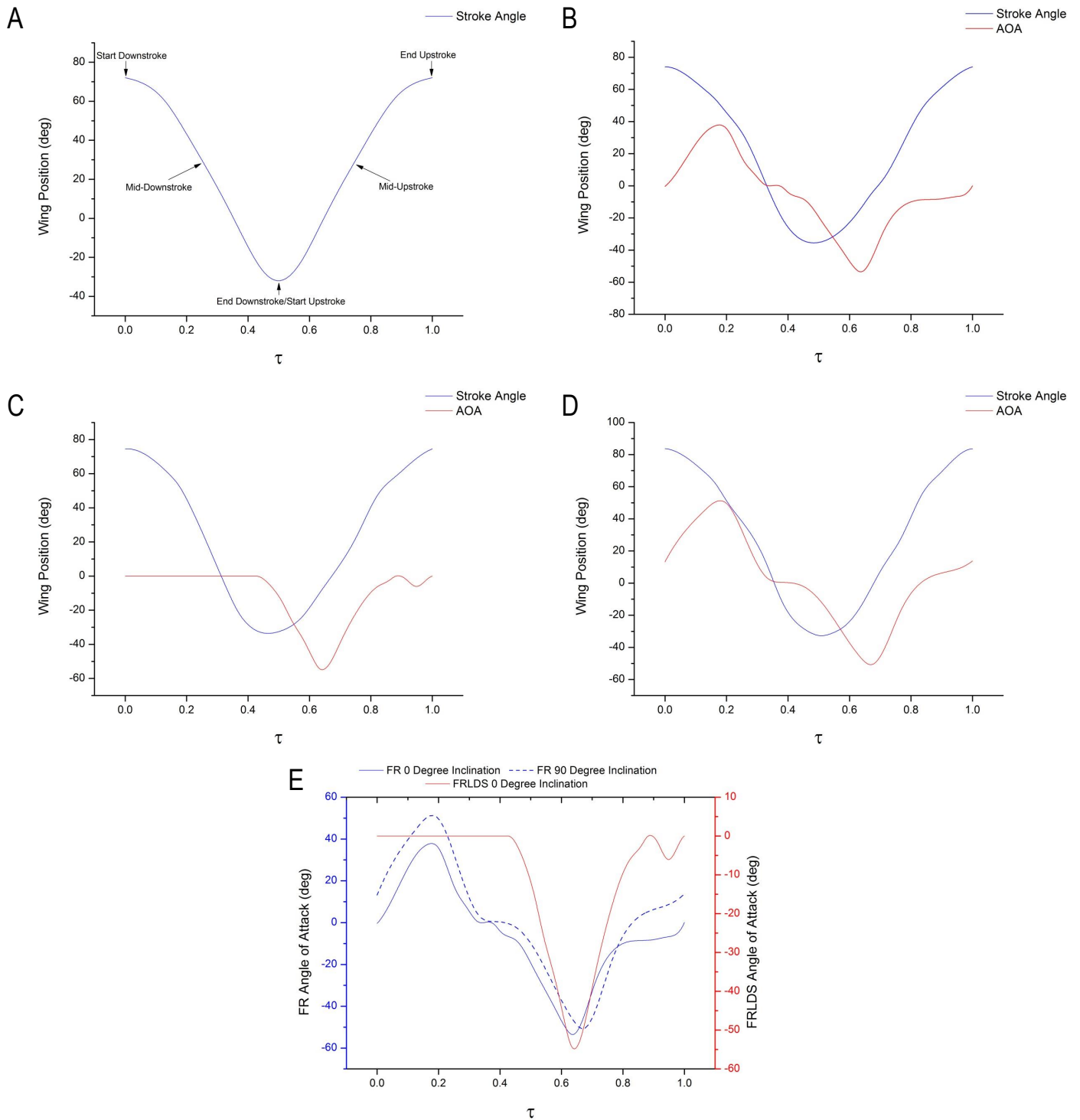


Figure 6.11: *Wing Kinematics for a Compilation of Arrangements Tested with Model 1; A: Flapping, B: FR with 0 Degree Inclination, C: FRAP with 0 Degree Inclination, D: FR with 90 Degree Inclination, E: AOA Comparison for FR and FRAP Configurations*

### 6.1.3 Flapping Only for 60 mm Wings (WT4)

During everyday flight an insect would normally fly near to some form of boundary that interacts with the flow field generated by the dynamic movement of its wings. The amount of effect this boundary has on the flow field and flight forces/moments is dependent on parameters such as the distance of the boundary from its wings, type of boundary and surface of the boundary. Similar to an insect a FWMAV would also encounter such situations, especially when reconnoitring in compact spaces for military missions, travelling through the remains of a collapsed building etc. Such situations have been explained previously in this thesis where the vast number of roles which are suitable for FWMAVs, were explained in detail. Whilst flying in the proximity of boundaries it is important to understand the affect this will have on the vehicles flight forces and even the energy consumed during such experiences as these situations must be accounted for when designing these robotic devices. For example, if more energy is consumed by the device then this will need to be accounted for when planning specific missions. It may not be suitable to simply add a much larger power supply as this will increase the weight of the entire vehicle where carrying excess energy now becomes unnecessary additional payload, thus estimating the approximate addition of energy consumption would aid in the addition for a more appropriate sized power supply.

To begin a complete analysis one needs to commence an investigation with a simpler case such as a wing performing a flapping motion only, thereafter further complexities can be introduced by altering variables and forming comparisons to the base case. A wing with a span of 60 mm (shown in chapter 3) was flapped at 5 Hz through a stroke amplitude of 104 degrees per stroke this would be used as the base case. The 60 mm wings (WT4) were chosen for this part of the study because of its partly straight trailing edge profile for boundary tests and its significantly larger wing area. Reducing the flapping frequency meant that the model would produce less vibrations, thus the data will have much less contributions from the harmonic structural modes of the vehicle and experimental rig. Furthermore, considering the amount of tests planned, reducing the frequency meant that repairs to the model could be prevented or at least reduced, in addition, reducing the number of repairs increases the chances of upholding consistent frictional forces between tests. Following the base case, rigid boundaries were introduced in the near vicinity of the flapping wings to create an enforced fluid-boundary interaction. Fluid-wall interaction occurs in this experiment when the rigid wing is flapping through a fluid. The dynamic motion of a flapping wing causes an alteration to the previous state of the stationary fluid which is present in the territory of the wing, by forcing it to move dependent on the

specific wing motion, which shortly after adopts a cyclic time dependent formation due to the continuous periodic wing motion. Thus, the installation of a boundary in the near region of the active wing would force the fluid to adopt a different formation when compressed within a narrow gap between two walls, where one is moving and the other is stationary. The consistency found in the cyclic force/moment measurements meant that flow formation is periodically consistent. Thus, as long the wing performs a consistent motion and the conditions between itself and the boundary are unaltered per cycle, the fluid behaviour will again adopt a cyclic time dependent formation.

Flapping wing investigations were conducted where a wall is placed near its trailing edge, on the ground and in combination of both. The 60 mm wing (WT4) incorporates a trailing edge which is straight for up to 50% of its span which meant that a sufficient section of the wing was in the near region of the wall located at the trailing edge. The boundary tests reported in this section have been shown as separate cases in Table 6.2. The experimental arrangements have been shown in Figures 6.12 and 6.13 to alleviate the reader from constantly turning back to chapter 4 to visualise the experimental layouts whilst viewing the results.

| <b>Case</b>    | <b>Case Description</b>                 | <b>Figure</b> |
|----------------|---|---------------|
| <i>Case F1</i> | <i>Flapping Only</i>                    | 6.12A         |
| <i>Case F2</i> | <i>Flapping with Foam Table</i>         | 6.13A         |
| <i>Case F3</i> | <i>Flapping with TE Boundary</i>        | 6.13B         |
| <i>Case F4</i> | <i>Flapping with TE + GE Boundaries</i> | 6.13C         |
| <i>Case F5</i> | <i>Flapping with GE Boundary</i>        | 6.12B         |

Table 6.2: *Flapping Cases for 60 mm Wings (WT4)*

Force and power measurements have been presented for the 60 mm wing (WT4) flapping alone and in the near vicinity of boundaries in Figure 6.14. The graphs display the aerodynamic forces for all the cases investigated along with the aerodynamic power required to produce the respective aerodynamic forces. The aerodynamic forces take up a sinusoidal wave-form directly related to the wing motion and velocity of this flapping wing which as mentioned previously peak at the mid-stroke positions. The inertial curve relates well to a cosine curve, where maximum and minimum peak occurs at the start and end of a stroke cycle respectively. The aerodynamic force is more or less zero when the inertial force approaches maximum/minimum, as seen in Figure 6.14A. Understandably, the same inertial force dataset was used to determine the aerodynamic forces

for all the tests shown in this Figure, as the vacuum chamber data should be the same. The vacuum chamber and total force measurements showed very good periodic consistency, and to enhance accuracy they were both cyclically averaged. This involved averaging a group of five cycles from each total force measurement and vacuum chamber dataset, which were then subtracted to determine the aerodynamic measurements. The sole purpose of averaging was to augment accuracy by attempting to account for any minute random variations present in periodic cycles. Evidently the boundaries do have some affect on the aerodynamic force and power drawn by the system, both of these will be further analysed in the following paragraphs. The spectrogram clearly presents the dominant frequency as the flapping frequency at 5 Hz, thereafter shades of red occur at regular multiples of the flapping frequency as a harmonic series.

The aerodynamic and inertial forces are shown with the wing kinematics in Figure 6.14A, where it is clearly presented that the aerodynamic force peaks at both mid-stroke positions where the wing experiences maximum pressure acting on its surface. It is worth noting that the measurements are taken after approximately 5 cycles, when the flow field has had sufficient time to initialise and the fluid formation in the region of the wing path has approached a time independent periodic formation (although flow visualisation was not performed the flow behaviour must be consistent as the forces measured have cyclic consistency).

From the five cases investigated all the boundary tests have produced a larger aerodynamic force for both down and upstrokes (shown in Figure 6.14B). Case F2 is not counted as a boundary case, it was merely conducted to ensure the table has negligible effect on the aerodynamic forces as it is a significant distance from the wing, even when the wing is in extreme downstroke position. The data shown in the comparison plot for all tests clearly shows that the table has negligible effect on the aerodynamic forces. The smallest inflation occurred for case F5 as this GE boundary does not continuously act on the flow dynamics as it is placed at the end downstroke position. The ground effect will have a very small contribution as the wing is still a fair distance away from it at mid-downstroke position, however as the wing is moving downwards it does push the fluid beneath the wings surface downwards where it is interfered by the rigid boundary below.

The other two cases which had walls located very close to the trailing edge of the wing had a much more noticeable effect on the downstroke peak force. As the TE wall in case F3 is positioned closer to the trailing edge of the wing at approximately 1 mm compared to 1.7 mm for case F4 (combined boundary case), the case F3 test would have the largest effect on the peak aerodynamic force for both the downstroke and upstroke. Considering the wing area and flapping frequency, the aerodynamic forces produced would not be

substantially large, with this in mind the walls were placed as close as possible to the trailing edge without touching the wing to enhance the boundary effect. Due to a symmetrical motion and unaltered conditions the downstroke motion of the wing with the TE wall will be considered for the following analysis. When the wing actively moves downwards, part of the fluid under the wings surface will be pushed downwards and some of it will travel/leak around the wing separating from the surface. As fluid travels around the trailing edge attempting to move to the upper surface of lower pressure, this fluid motion is obstructed by the wall as it is so close to the TE of the wing. Thus, the fluid will apply a pressure on the surface of the wall as it travels through its stroke whilst an additional pressure will also be applied to the lower surface of the wing in the trailing edge region, simultaneously some of the fluid may leak through the narrow gap but actual occurrences can only be examined in thorough detail by the utilisation of flow visualisation. As the fluid is somewhat compressed between the lower surface trailing edge and the wall, an overall additional pressure would be applied to the lower surface of the wall continuously which will peak as the wing velocity peaks at the mid-stroke position. The same theory would apply during the upstroke phase as well. As the boundary moves further away from the wing trailing edge the additional pressure applied due to the forced compression of fluid will reduce which can be seen from the downstroke phase between case F3 and case F4.

The upstroke aerodynamic peak force is larger than that produced on the downstroke due to effect of the 'GE' wall. When the wing approaches end downstroke the wing tip is approximately 1 mm away from the 'GE' wall surface, this boundary also causes an effect in case F4 as the aerodynamic peak force for this case is also larger for the upstroke compared to the downstroke peak. As the wing approaches the GE wall at the end of its downstroke, its velocity is approaching zero where it eventually comes to rest and thenceforth commences to move in the opposite direction through its upstroke motion. As both walls meet the fluid is again under compression where it leaks around the wings edges and is now present above the surface of the wing, thus as the wing moves through its upstroke motion an additional pressure will be applied to the upper surface of the wing. It can be said that the GE boundary blocks the movement of fluid further downwards, which means some of the fluid may travel around the edges of the wing, thus additional fluid exists above the wings surface during the upstroke motion, relating to the augmentation of aerodynamic force during the upstroke motion. The peak again occurs when the wing reaches maximum velocity in its stroke cycle, but by this point sufficient differences exist between case F1, case F5 and case F4. Differences actually start to become evident from the start upstroke position which can be seen from the plot in Figure 6.14B.

The enhancements in aerodynamic force can be evidently seen in the aerodynamic power data shown in Figure 6.14C, where all the boundary tests require more power than the base 'flapping only' case. The power consumed for case F2 is basically the same as case F1 which was expected as there was no noticeable difference in force production. Case F4 requires the most aerodynamic power but generates less peak-peak aerodynamic force when compared to case F3. Due to the additional pressure acting on the surface of the wing for case F5 when travelling through the upstroke motion, more power is drawn by the mechanical system. The aerodynamic power required for all cases when assessed with the peak-peak force generation seems to agree well for all the cases, as no excess power was drawn by the mechanism in any of the cases investigated.

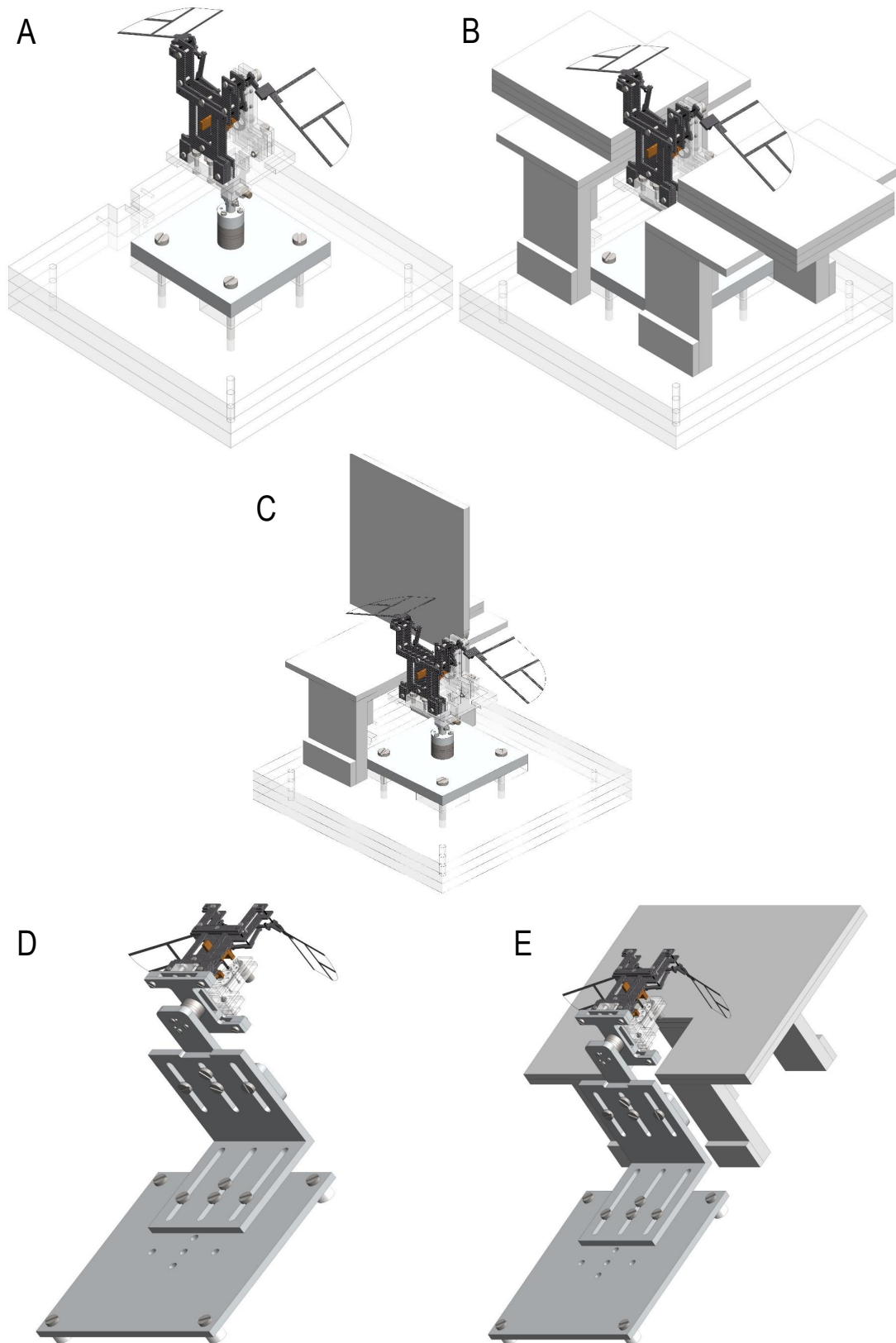


Figure 6.12: *Various Experimental Layouts; A: Cases F1, FR1 & FRAP1, B: Cases F5 & FRAP2, C: Case FR3, D: Model at 90degrees, E: Model at 90 degrees w/GE*

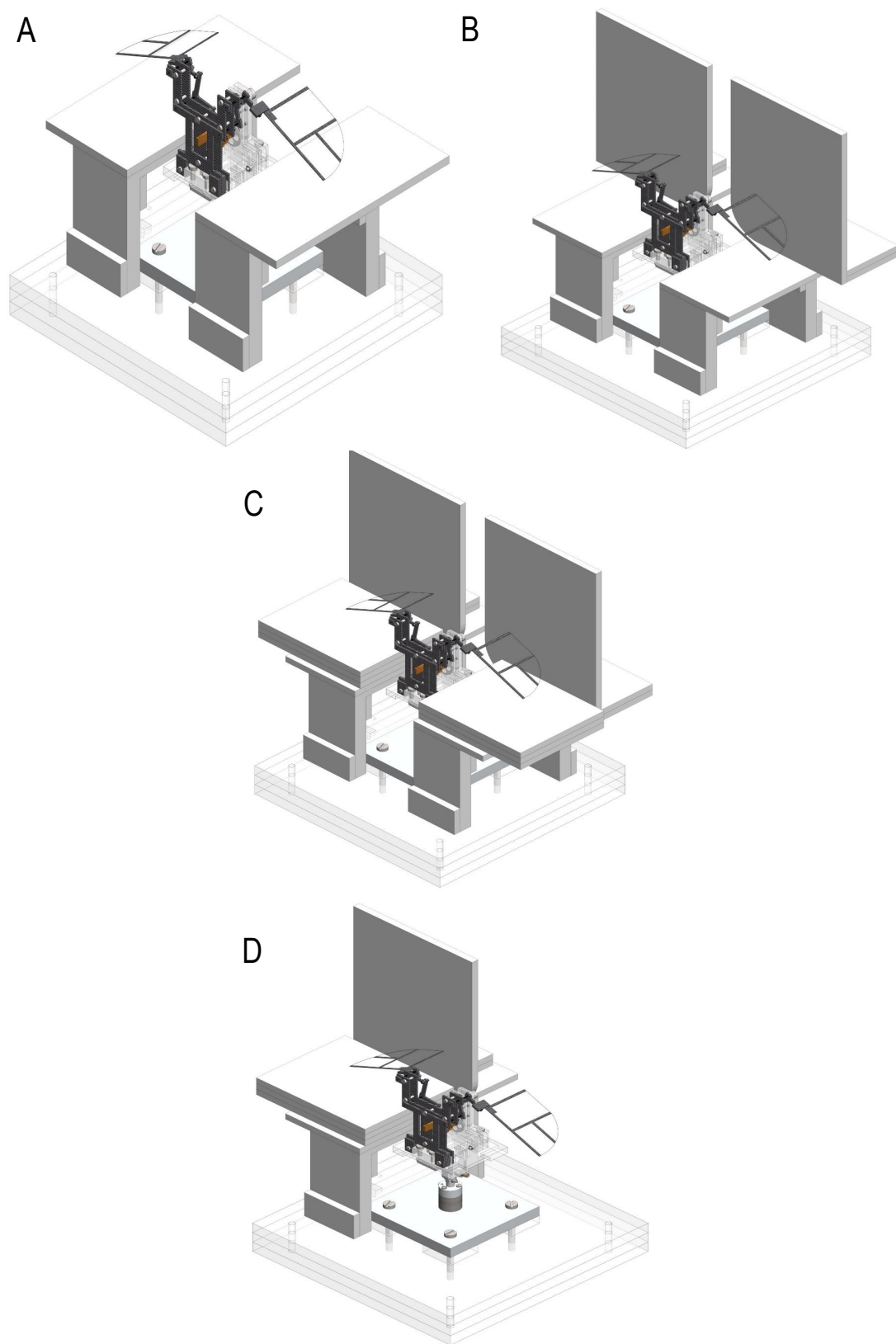


Figure 6.13: *Various Experimental Layouts; A: Case F2, B: Cases F3, FR2 & FRAP4, C: Cases F4, FR4 & FRAP3, D: Case FR5*

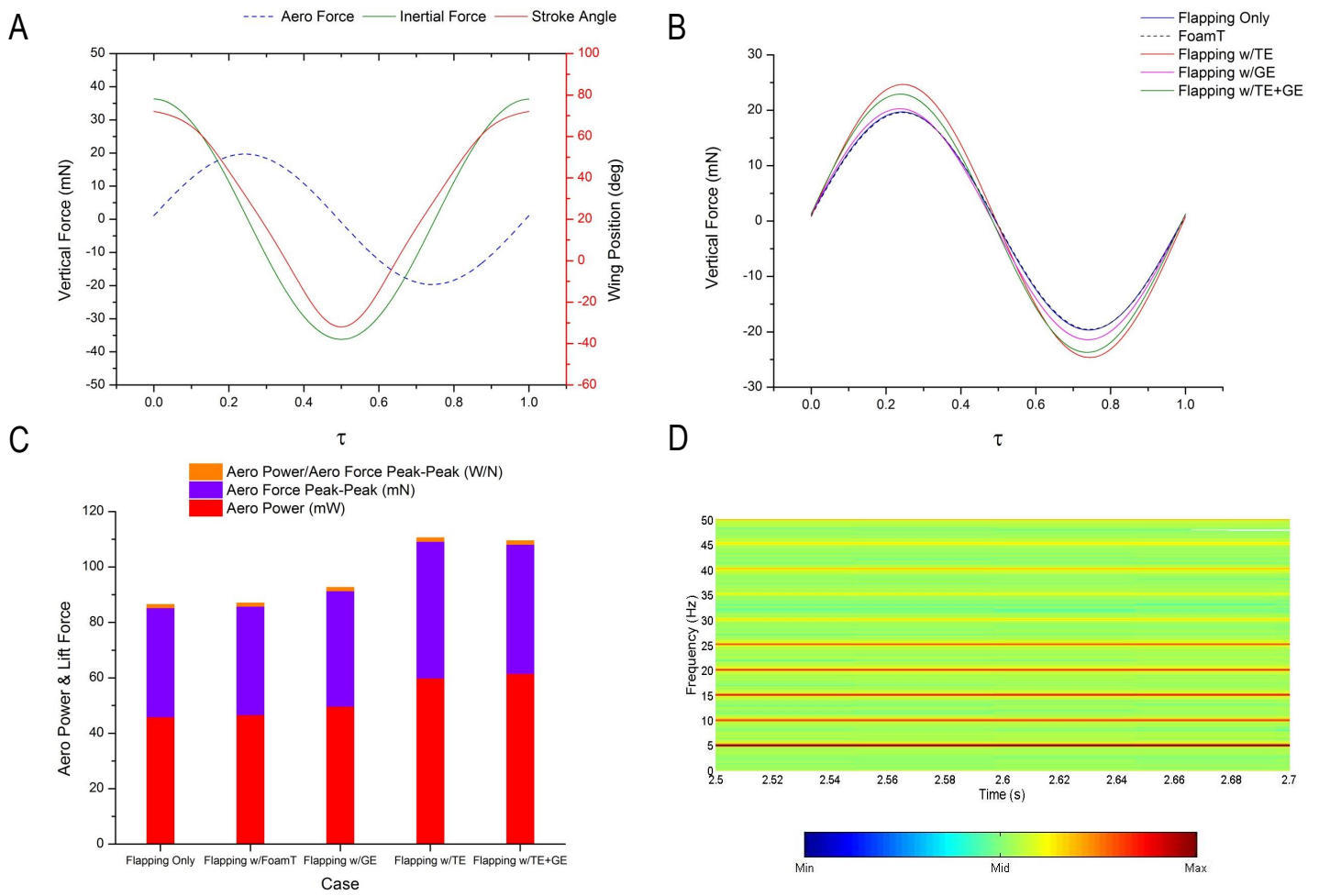


Figure 6.14: *Flapping Wing Measurements for 60 mm Wings (WT<sub>4</sub>); A: Flapping Only Aero and Inertial Forces with Stroke Angle, B: Comparison of Flapping Aero Forces, C: Aerodynamic Power & Force Relation, D: Spectrogram for Vertical Axis in Air. Colour Bar Represents Size of Amplitude. UI: M1-F-WT<sub>4</sub>-S-V & M1-FwB-WT<sub>4</sub>-S-V*

### 6.1.4 Flapping & Rotation for 60 mm Wings (WT4)

Progressing with the addition of wing rotation indicated that the model can now perform a coupled wing motion from a single actuator by adopting a passive wing rotation methodology as discussed in chapters 3 and 4. Similar to the flapping only experiments the 60 mm wings (WT4) were utilised for these experiments and the vehicle was provided the required voltage to perform at a flapping frequency of 5 Hz. Both F/T and power measurements were recorded for air and vacuum condition tests, which would adequately provide the aerodynamic forces and moments produced by the wings motion. Proceeding on from the base test of flapping and passively rotating wings, rigid smooth surfaced boundaries were introduced to provide interference to the original flow field generated from the periodic motion of the wings. Analogous to the flapping wing tests previously discussed, the boundaries were positioned in the near vicinity of the wings forcing a flow-boundary interaction, whereby the development of the flow formation has been given sufficient time until the flow possesses periodic consistency as the conditions during a test have reached a steady state. Each boundary test consists of a somewhat dynamic wall (known as the wing) as well as a stationary wall which now has a varying distance from the edge of the wing due to the additional rotational motion of the wing.

| Case            | Case Description   | Figure |
|-----------------|--|--------|
| <i>Case FR1</i> | <i>Flapping &amp; Rotation Only</i>                                | 6.12A  |
| <i>Case FR2</i> | <i>Flapping &amp; Rotation with TE Boundary</i>                    | 6.13B  |
| <i>Case FR3</i> | <i>Flapping &amp; Rotation with TE Boundary 1 Side Only</i>        | 6.12C  |
| <i>Case FR4</i> | <i>Flapping &amp; Rotation with TE + GE Boundaries</i>             | 6.13C  |
| <i>Case FR5</i> | <i>Flapping &amp; Rotation with TE + GE Boundaries 1 Side Only</i> | 6.13D  |

Table 6.3: *Flapping and Rotation Cases at 0 Degree Inclination for 60 mm Wings (WT4)*

Due to the nature of the experimental work and complexities involved measurement uncertainty will always exist. There are various uncertainties, some of which are measurement errors in the transducer, measurement errors from camera images, wing rotation in air and vacuum chamber tests, impossibility of creating a perfectly equal stroke angle and AOA on both sides for the flapping model and the vacuum condition was just below 100%. The very small uncertainties of the transducer were mentioned in Chapter 4 of this report and the original data for the flapping and rotation case was analysed to determine the effect of the uncertainty percentages. The data has been manipulated to consider the effect of the uncertainty percentage for both

total and inertial forces, thereafter new instantaneous aerodynamic forces are found (shown in Figure 6.15). The plot clearly demonstrates that extremely small differences are produced for each component analysed. Thus, the uncertainties of the transducer can be seen as near negligible due to the minute differences found. On another aspect one must keep in mind that as the wing rotation is created by a passive rotation via an elastic material, there will be differences present in the wing rotation produced in air and in a vacuum chamber. Inertial effects will also become stronger as there is no fluid in the chamber to resist the wings motion, thus identical wing motions in the two different tests are impossible in such experiments. For the type of vehicle developed in this project it must be understood that small asymmetries may exist between the wing motions of both sides, due to manufacturing errors, errors when assembling the model, differences in linkage stiffness on both sides, differences in rotational gap (gap of exposed polyester to promote wing rotation) and differences in the quality of the carbon pins used to connect the parts of the vehicle. Such differences will always exist in these forms of mechanical devices, where the designer/assembler should attempt to minimise the effects caused as much as possible.

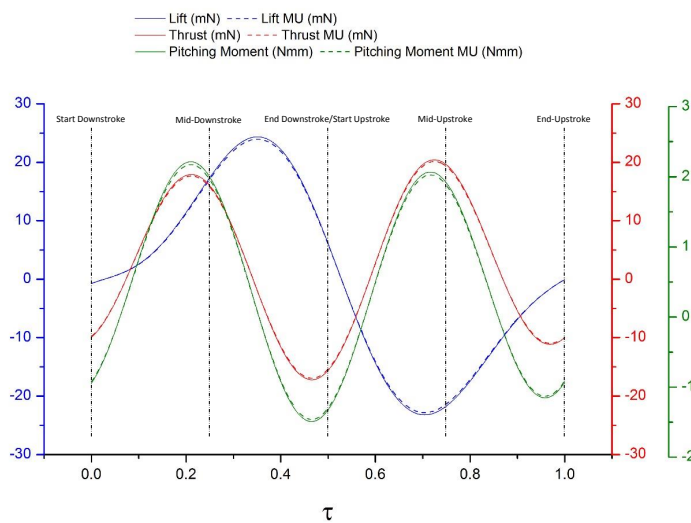


Figure 6.15: *Flapping and Rotation Measurements with Uncertainty Applied*

The boundary tests investigated in this section have been shown in Table 6.3. The placement of boundaries solely on one side of the model was carried out to investigate the effect on flight aerodynamics and power requirements when a single boundary applies an obstruction as such scenarios can intermittently occur in everyday flight. Such an event would encourage an asymmetrical flow field formation that would prove to produce interesting flow visualisations to directly compare flow compositions from both sides per time

step throughout a complete cycle. Experimentally visualising the flow as the wing approaches and departs from the boundary region would aid in understanding the structure of the flow field and the extent of the obstruction caused by the boundary. Furthermore, analysing the pattern of the flow field with and without a boundary would provide interesting results. Future investigations focusing on a boundary in the near vicinity of the leading edge of a dynamic wing, would likewise produce compelling results to study the forced breakdown/obstruction of the LEV which is known to provide a substantial enhancement to flapping wing flight aerodynamics based on techniques exploited by insects. Flow visualisation alongside F/T measurements would assist in understanding the affect of encouraging the breakdown/obstruction of the LEV, in auxiliary to establishing the changes in power requirement to maintain flight, and even maintain the vehicles current altitude.

The force and moment measurements alongside their power requirements for all the tests involving the flapping and rotation arrangement for model 1 are shown in Figure 6.16. The lift curve resembles a sinusoidal wave, but has a slanted appearance due to the coupled motion which likewise affects the lift force generation as this proceeds at a slower rate in the beginning stages of the downstroke motion as the wing flicks in the opposite direction. The lift curve peaks twice per cycle approximately at the mid locations of both strokes, thus a similar behaviour to flapping only is observed. During this time the thrust force completes two cycles where it moves at almost twice the rate of the lift curve, this is related to the rotational effects of the wings.

Unlike the case of flapping only, the FR case benefits from two motions which combined provide larger positive and negative lift peaks. The combination of the wing attacking the air through its rotational motion whilst performing its controlled flapping stroke results in the peak forces produced which surpass that found for the flapping only case. Significant portions of the thrust curves lie on the positive half of the relative force axis, thus the average thrust force throughout the cycle will be a positive value, the size of each varies per individual case which will be expanded upon in the latter part of this sub-section. Supplementary to this, positive thrust peaks are produced approximately near to the mid-stroke positions of the both half strokes and negative peaks are developed towards the end of the stroke.

The data plots shown in Figure 6.16, displays that the first lift peak does not align well with the positive thrust peak when compared to the alignment of the lift and thrust force peaks in the second half stroke. The distinction between the two peaks in the first half stroke is directly related to the expeditious dynamic

changes of the AOA for both wings. A general comparison of aerodynamic power required for the flapping only case and FR only case epitomises the clear distinction that an additional motion requires substantially more power. However when considering this augmentation in power, the ancillary force produced, namely thrust force should also be taken into account.

The pitching moment for all cases moves almost identically with the pattern of the thrust force curve as the peaks of both curves align well to one-another, differing moderately in amplitude as the moment accounts for the distance between the location where the force acts on the wings and the central axis of the transducer. In order to maintain consistency all the moment measurements for these experiments have been reported for the model as measured from the transducers tool plate position (see Figure 4.34). The aero power required per case varies as boundaries are introduced which prove to be more power demanding when compared to case FR1. Although the wing motion is now composed of an additional rotation, the foam table was still found to have negligible effect on the aerodynamic forces and power required.

In order to maintain consistency and accuracy the same set of inertial data was used to determine the aerodynamic forces and moments from the individual total force datasets. The distances of the boundaries from the wings are as follows, for the case with the 'TEwall' on both sides the wall was approximately 1 mm behind the trailing edge of the wings, this boundary position was held for the test involving a 'TEwall' on one side only. Cases which had a dual boundary in the form of a wall placed at the trailing edge and a ground effect base, had the wall positioned slightly further which was approximately 1.7 mm from the trailing edge of the wings this was primarily due to alignment issues when fixating two boundaries to the foam table whilst attempting to ensure both are flush against one-another to avoid the existence of a gap, likewise a dual boundary was placed on one side only as well maintaining the same distances aforementioned. In all the cases which involved the ground effect base, this was positioned to be a distance of approximately 1-1.5 mm from the wing edge which was setup with the assistance of the HS camera. The wing edge approaches its minimum position at the end of its downstroke motion which is repetitive for every cycle.

Figure 6.16B, illustrates the spectrogram for the 'FR' motion of the wings in air, this plot has been shown as the wings now perform a coupled motion. The deepest shade of red signifies the dominant frequency for each dataset which evidently shows the dominance of the flapping frequency of the vehicle. Vibrational modes are signified by the shades of red/yellow seen at regular multiples of the flapping frequency. Note the time shown in the spectrogram plots have no particular significance to the force and moment measurements, a random

clip of data was selected for the spectrogram plots. As the wing now produces a coupled motion where the wing rotational frequency is twice as large as the flapping frequency, that data cannot be simply filtered to include the flapping frequency only, instead it must be filtered with the consideration of the combination of motions, thus a low pass filter is applied above x2 of the flapping frequency (more specifically the filter was applied at x2.5 of the flapping frequency).

A comparison for the lift force curves for all 'FR' tests has been shown in Figure 6.17A. The lift force curves for all the tests follow the same trend which is originally set by the base case (case FR1). The maximum amplitude is found to occur for case FR2 for both half strokes as this boundary is positioned closest to the wing and has the most effect when the trailing edge of the wings are in the proximity of this wall. As the wing abruptly rotates whilst performing a flapping stroke, the flow is somewhat compressed when in the near region of the wall, this compression occurs as the wings sweeps across a stationary wall with a mere gap of 1 mm, thus an additional pressure would act on the wings surface near the trailing edge portion as the flow cannot easily pass through such a gap. Since the wing is away from the wall for certain periods during a complete cycle, a time dependent vortex will develop at the trailing edge which may remain attached to this surface or breakdown. When in the proximity of the wall this vortex will be forced to diminish due to the reduction in space, thus the vortex may in some way peel off the trailing edge of the dynamic wing by the stationary wall. An accurate detailed analysis of the time dependent composition of the flow around the wings in the vicinity of the trailing edge wall or any boundary can only be carried out by flow visualisation.

The lift force peaks for both half strokes seem to line up fairly well for all the tests performed. The peak for the second half stroke occurs approximately at the expected timing where the flapping stroke approaches maximum velocity. Upon close examination of the amplitude of the peak force, it is clear that the peak force produced during the downstroke motion is larger than that produced during the upstroke motion. This difference is largely due to the varying AOA, which consistently applies throughout all the tests performed in this arrangement as shown in this comparison plot. Distinctions amongst the results will become more evident at the peak positions where the velocity of the flapping stroke is near maximum and the AOA will have a contribution as well. A single wall placed solely on one side creates a smaller difference in lift force production for both half strokes as expected because the boundary effect has now been reduced when compared to a pair of walls placed at the trailing edge of the wings.

The plots shown for the tests where the boundary is positioned on one side only (case FR3 and case FR5)

seem to produce similar peak amplitudes which slightly differ for the second half stroke peak, nevertheless they seem to produce similar results. The case with dual boundaries located on both sides of the model, namely case FR4 produces peak amplitudes below that found for case FR2 as the walls near the trailing edge are now slightly further as aforementioned, thus the effect of the boundary will be accordingly reduced. It should be noted that although the vertical force has been labelled as the lifting force, the model was not expected to create a substantial amount of lift force or for that matter more specifically the model was ideally expected to create an averaged lift force of zero per cycle, which would mean that the wing kinematics are identical for both half strokes. Although this is not exactly the case, the average lift force produced per cycle is basically negligible.

Figures 6.17B and 6.17C, illustrate the thrust force and pitching moment plots respectively. During the start of the downstroke motion the thrust plots all differ from the FR only plot due to the presence of the wall which causes the wing to possess a small angle of attack, whereby it was experiencing an advanced rotation flicking to the opposite side during the final phase of the upstroke motion. The near wing effect of the flow has a direct consequence on the initial thrust values during the start of a stroke, as the values at the start of the cycle are well below the FR only case. At every peak position of both cycles created for the thrust force of a single flapping cycle, the boundaries exhibit larger thrust forces, and similar behaviour has been reproduced in the pitching moment measurements.

Apart from case FR3, the other three involving boundaries produce very similar peak amplitudes for the first half stroke which applies for both thrust forces and pitching moments. Analysing the images it was found that the tests which had wall boundaries acting behind the trailing edge of the wing had a slightly larger angle of attack, which directly represents the contribution the wall has on the auxiliary thrust forces produced. Due to the flexible nature of the wings rotation via an elastic material the boundaries can cause changes in the AOA. Furthermore, if a thinner mylar was used and the wing trailing edge was highly deformable compared to the rather rigid nature of the current wings the trailing edge would most probably have experienced significant deformation when in the proximity of the boundary. Further research could be performed focusing on the flexibility effects at the trailing edge of the wings due to the presence of a boundary, and how such a scenario effects the aerodynamic characteristics of a FWMAV.

For the second half stroke the cases involving dual boundaries produce the largest peaks for both thrust force and pitching moment as the ground base evidently has some form of effect here, where maximal effect is

produced for the case which has dual boundaries acting on both sides. The peak thrust force for the second half stroke for the cases which incorporated a ground effect base had a slightly larger AOA compared with the cases which had the wall placed near the trailing edge only, which is shown by the supplementary peak thrust force created during the upstroke motion. As the wing approaches the ground base, flow would leak and travel around the edge which is in the proximity of the boundary where it will now be present on the opposite surface (the leading surface during the upstroke motion) as it is additionally bound by the wall in this dual boundary configuration. If the dynamic flow present in this region has a considerable amount of velocity, when the wing moves through its upstroke motion the flow would apply an additional pressure on the wings surface which would essentially reduce the rate of change in AOA. Thus at the position of maximum velocity for the flapping stroke during the upstroke motion the AOA is effectively larger in the dual boundary cases opposed to its single boundary counterpart cases. The boundary effect of a single wall placed on one side will be lesser when compared to a case with walls placed on both sides, in turn the peak thrust force produced will consequently be smaller.

The kinematic time history of wing displacement has been plotted with the lift and thrust force measurements for case FR1 in Figure 6.18A. The peak of the lift curve on the first half stroke is a clear amalgamation of the flapping and wing rotation motions, where the peak is delayed beyond mid-stroke but augmented from a large contribution of the wing energetically moving through the air, whose actions consist of various variables. Some of these are the elastic behaviour of the mylar, inertial domination as the wing rotates it does not hold its angle attack through the downstroke and instead flicks in the opposite direction. It should be noted that the AOA is measured relative to the horizontal axis. When the wing is positioned along the horizontal the AOA is equal to 0 degrees, an angle above this axis is referred to as a positive angle and therefore below this axis is referred to as a negative angle. Considering the wing is essentially a flat plate with a coupled motion which has numerous parameters producing its movement including the controlled flapping stroke by the mechanical system, would effectively create a larger peak than that produced by a singular flapping motion. Following the change in direction of the wing AOA, the thrust force starts reducing, reaching a minimum peak position at the end of the downstroke motion. As the wing starts to travel through the upstroke motion the AOA alters favourably and the thrust force begins to grow positively. The second lift force peak produced during the upstroke motion is evidently produced from the combined motion but in this case the AOA rotational motion does not have such a large contribution as it is part way through its rotation. The second positive thrust peak is slightly larger than the first positive thrust

peak as the flapping stroke is near mid-stroke thus it has maximal velocity which contributes significantly in the thrust production as the wing has a sufficient AOA at this point as well. Henceforth, the thrust force starts reducing as the flapping stroke velocity will decrease as it approaches a rest position at end-upstroke, and the AOA tends to move towards much smaller angles eventually approaching zero degrees. In terms of angle of attack and pressure acting on the surface of the wing, this can be analysed by considering a single directional stroke and assuming various wing rotation angles.

Average thrust force and pitching moment data has been displayed in Figures 6.18B and 6.18C. The largest average thrust force was produced when the dual boundary was installed on both sides of the model, this was followed by the case which had two walls placed closer to the trailing edge on both sides. Although the peak of the dual boundary applied to one side was larger on the upstroke motion than the 'FR w/TE' case, the negative peaks of this single dual boundary were quite large as well, thus this reduced the average value. The pitching moments as expected have a direct relationship with the thrust force as they are partially formed by the thrust force. The tests involving the single boundaries showed similar thrust force production where the larger of the two was created by the dual boundary case, this same relation was observed for the pitching moment as well. All the boundary tests had larger average thrust force and pitching moment values than the base 'FR Only' case. Furthermore, all the tests produced an average positive thrust force signifying the importance of wing rotation.

The aerodynamic power required to create the aerodynamic forces and moments associated with this FW-MAV is shown in Figure 6.18D, where the aero power and thrust relation for all tests performed in this arrangement are compared. The most power demanding case is FR2 which demands a considerable amount of more power when compared to the base case. The least power demanding boundary case is for the dual boundary positioned solely on one side of the model followed by the case which has a single wall placed on one side of the model, as this wall is closer to the trailing edge it will cause more resistance as the wing sweeps across it during its cyclic motion. Interestingly so, when comparing the aerodynamic power required per thrust force produced, the base case produces the largest ratio, which in effect means it requires more power to output an average thrust force of 2.46mN. The combined boundary case applied to both sides (case FR4) seems to have the smallest ratio followed by case FR5. Overall, propitious results are seen in terms of aerodynamic power requirement per thrust force production when a dual boundary arrangement is in the presence of such a wing motion.

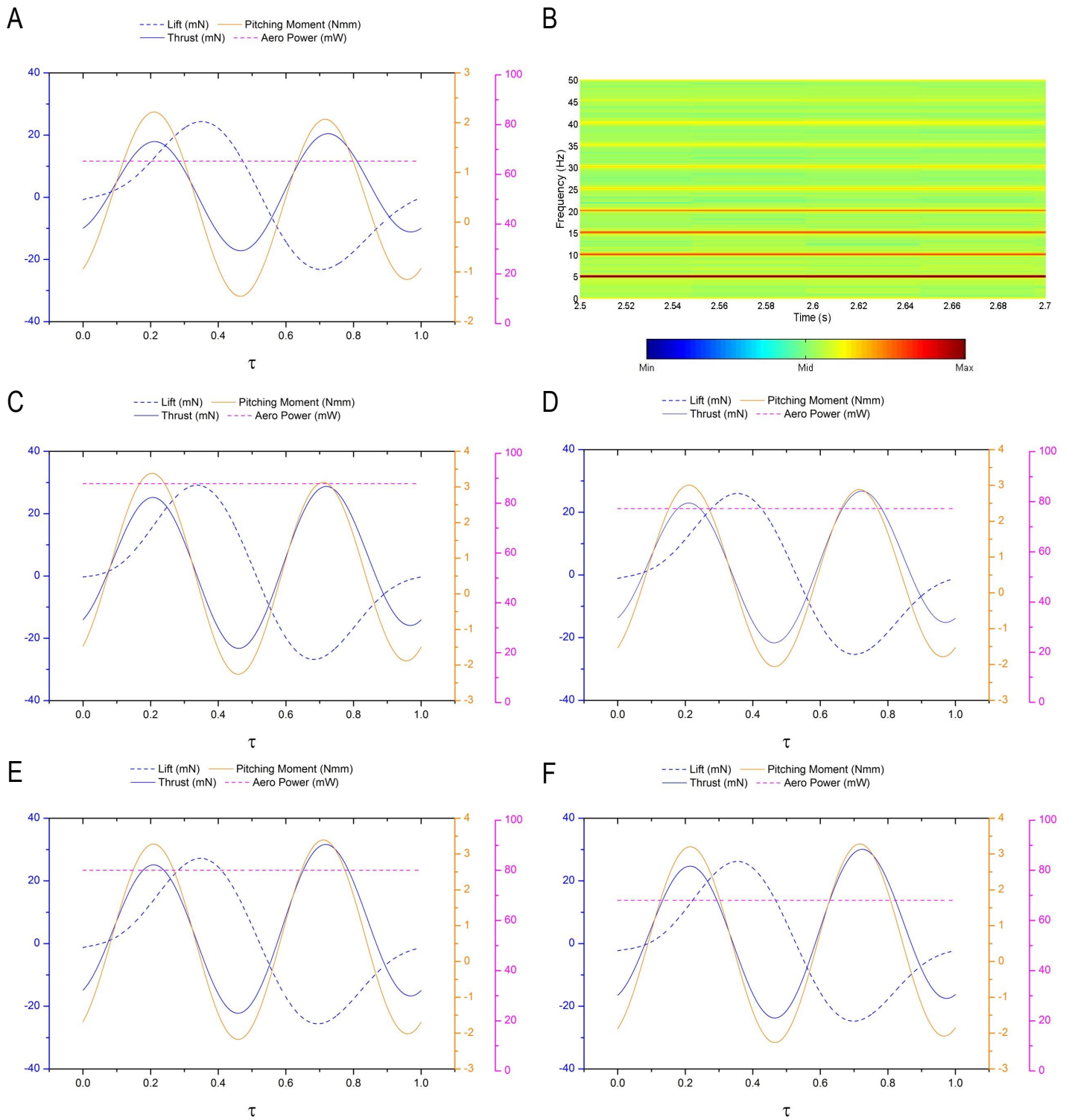


Figure 6.16: *Flapping & Rotation Wing Measurements for 60 mm Wings (WT4); A: Case FR1, B: Spectrogram for Vertical Axis in Air, C: Case FR2, D: Case FR3, E: Case FR4, F: Case FR5. Colour Bar Represents Size of Amplitude. UI: M1-FR-WT4-S-V & M1-FRwB-WT4-S-V*

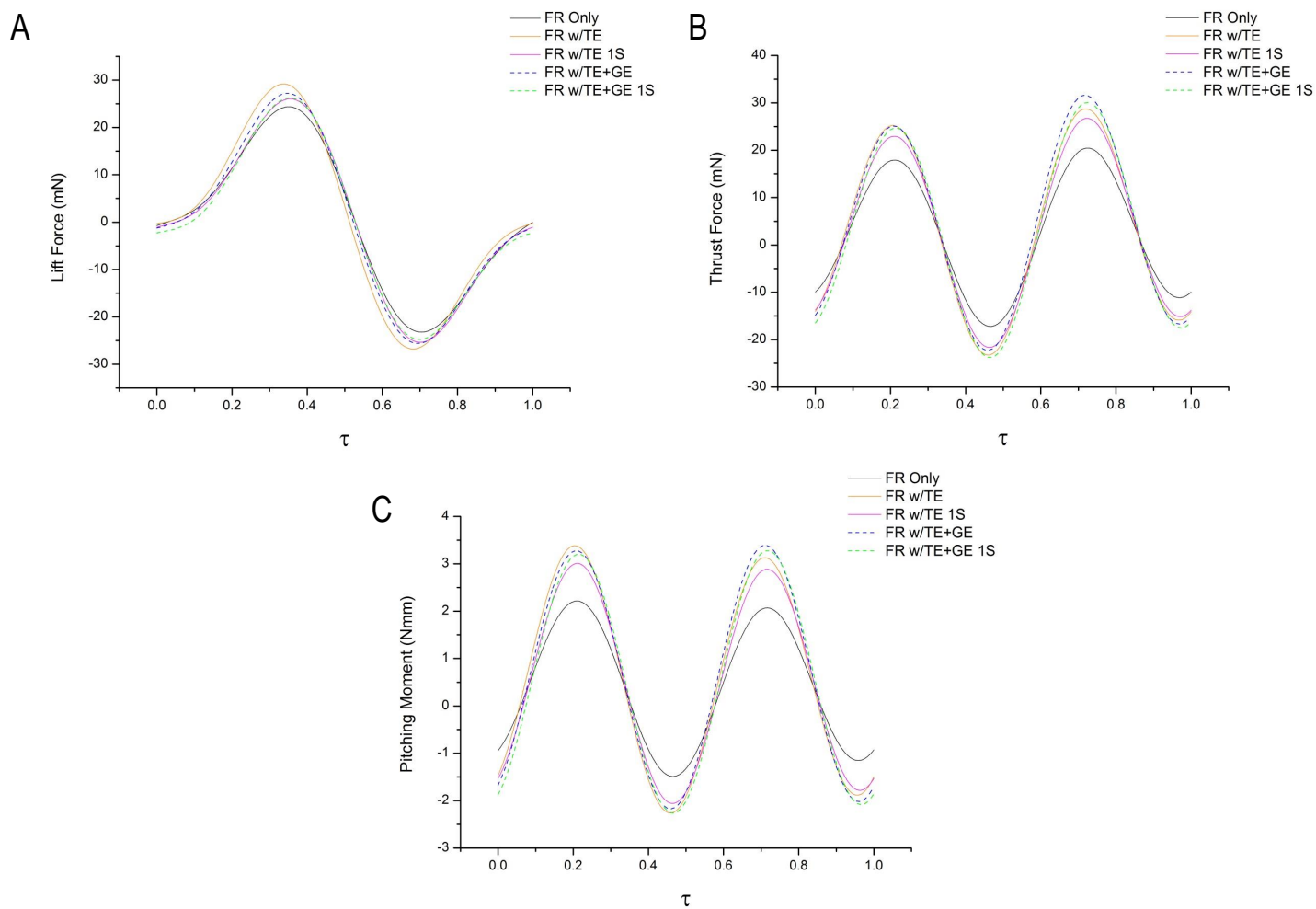


Figure 6.17: *Flapping & Rotation Wing Measurements for 60 mm Wings (WT<sub>4</sub>); A: Comparison of Lift Force, B: Comparison of Thrust Force, C: Comparison of Pitching Moment. UI: M1-FR-WT<sub>4</sub>-S-V & M1-FRwB-WT<sub>4</sub>-S-V*

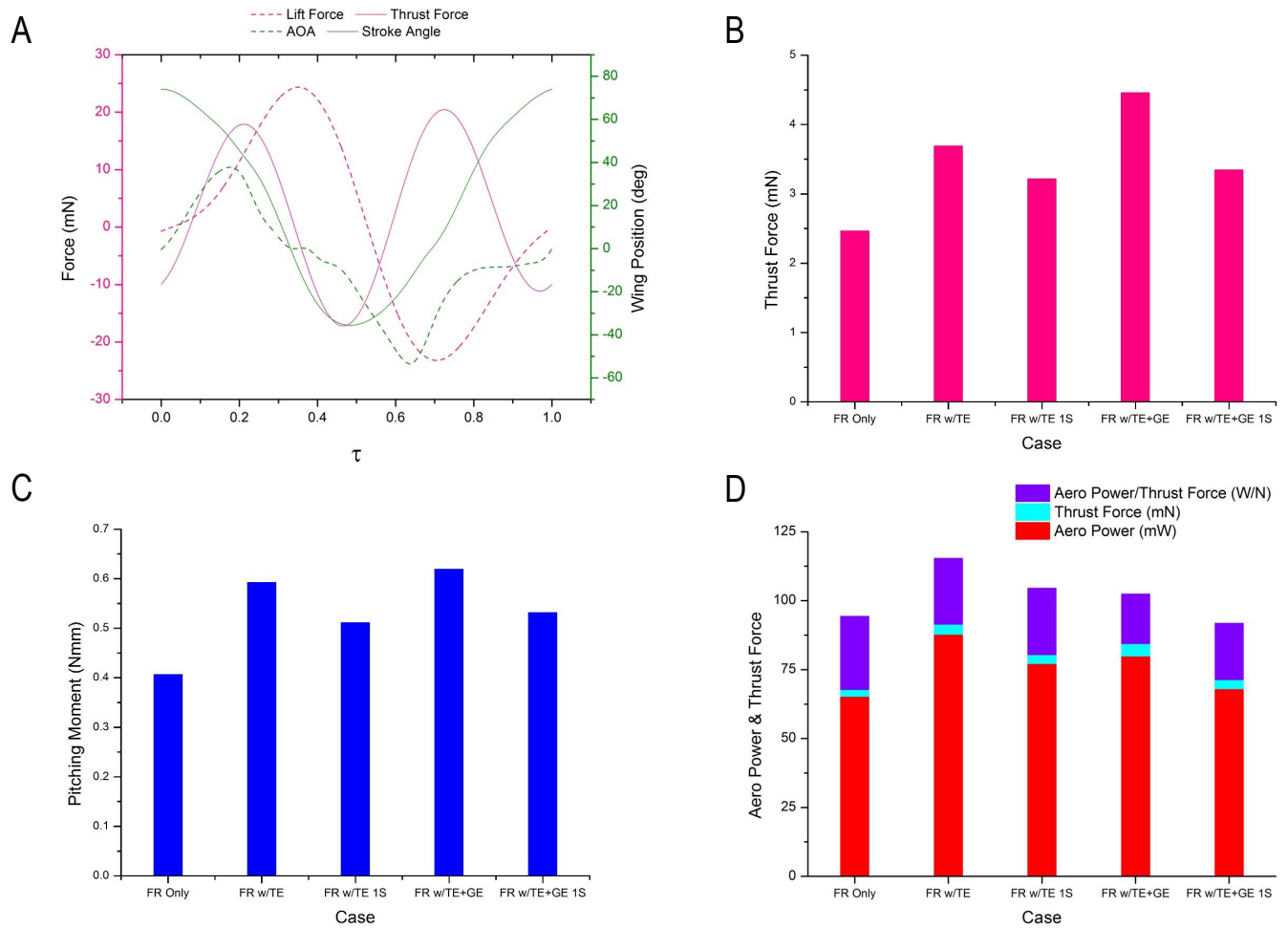


Figure 6.18: *Flapping & Rotation Wing Measurements for 60 mm Wings (WT<sub>4</sub>); A: FR Only Data with Wing Displacement Kinematics, B: Average Thrust Force for All Cases, C: Average Pitching Moment for All Cases, D: Average Aerodynamic Power & Force Relation. UI:M1-FR-WT<sub>4</sub>-S-V & M1-FRwB-WT<sub>4</sub>-S-V*

The model was rotated 90 degrees which meant that its flapping stroke is now in the horizontal plane, commonly known as the hovering position where ideally a positive lifting force is generated to sustain the vehicles altitude, whilst it remains in the current location through a net thrust force of zero. The model was flapped at the same frequency of 5 Hz with the 60 mm wings (WT4) attached to its flapping arms as it produced a coupled flapping and rotating wing motion. In the previous position (mounted to flap in the vertical plane) it can be said that the gravitational force would have an additional effect during the downstroke especially on the wing rotation due to its passive nature, and a more restrictive force would be applied during the upstroke as the wing is travelling in the opposite direction.

The labels applied to each axis as shown in chapter 3 remain consistent, thus shapes of the curve will now differ compared to the data previously analysed as flapping direction has now switched. Thus, when flapped along a horizontal stroke plane the effect of gravity should be equivalent on both half strokes. Aerodynamic readings were obtained for a base case 'FR Only (90 Deg)' and a boundary case where a ground effect is created in the proximity of the trailing edge of the wings similar to the TE wall tests.

As seen previously the thrust curve resembles a somewhat skewed sinusoidal wave which again has a delay in producing a peak force at the mid-downstroke position, and in fact the peak produced during the upstroke occurs moderately earlier than expected (see Figure 6.11 for positions during a cycle). Similar to the previous set of results, the rotational motion of the wing has a direct effect on the time that the peak thrust force will occur. The peaks for both thrust and lift force during the downstroke motion do not align which is the opposite result of what occurs during the upstroke motion where the peaks occur at a fairly similar time, this observation applies to both cases where the data plots have been shown in Figures 6.19A and 6.19B. The ground effect boundary case requires significant amounts of more power compared to the base case, this will be expanded upon in the latter part of the sub-section. The lift force peaks line up well with the peaks of the pitching moment curve which as mentioned previously, a relationship should exist amongst these two measurement axes as the pitching moment is partially composed of the lift force data.

Individual plots for comparison of the thrust, lift and pitching moment data produced from both cases have been shown in Figures 6.19C, D and E. Both curves line up well in all the plots where the peaks for both sets of data occur in the same time history, thus the boundary does not cause significant phase differences. Both peaks on each half stroke for the thrust data are larger when the ground effect boundary is used. The thrust peak produced for the 'FR w/GE' case during the downstroke is larger than that produced on the

upstroke as the flapping velocity will be larger at the time of the peak for the first half stroke and the AOA is smaller, thus this combined effect along with the presence of the wall provides the augmented peak. As the wing approaches the wall the same theory expounded upon in the previous section regarding the flapping and rotating wing in the near vicinity of a boundary located at the trailing edge will apply here as the wall is likewise located at the trailing edge of the wing, however the wall was a slightly larger distance away of approximately 1.2-1.4 mm. Similarly the ground effect wall creates larger lift force peaks opposed to the no boundary case, as the wall effects the AOA of the wing as the flow induces a larger peak AOA which overall produces larger lifting forces. Furthermore, the lift peaks for both cases present that the same size of peak is produced per individual case for each half stroke, such a result was not observed when the model was flapping along the vertical plane. The pitching moment data clearly shows larger peaks for the boundary case as expected from the data presented in the lift force comparison plot, and the time history of the peaks aligns well with the peaks found for the lift force plot.

A time history plot of generated forces and kinematic wing displacement is presented in Figure 6.20A, which clearly shows that when the AOA peaks on both half strokes, the lift force peaks occur at the same time, thus full advantage is taken of the wing AOA position and its vigorous rotational characteristic. Furthermore, as the peak amplitudes of the AOA are very similar on both half strokes, the lift force also produces very similar positive peak values for each half stroke. As the wing rotation reduces from its peak position in the first half stroke, the lift force plot follows this behaviour, which is an expected result as lifting force will decline as the AOA decreases. As the AOA curve has a somewhat resemblance to a sinusoidal wave, the lift force curve will behave in a similar fashion, as lift force generation in this arrangement is dependent upon the wing possessing an angle of attack. The AOA motion also has a contribution from the sinusoidal motion of the flapping mechanism which creates the flapping stroke.

The thrust force peak in the first half stroke occurs when the surface of the wing is progressively striking the fluid and advancing through the wings rotational motion towards a zero AOA, henceforth becoming negative. During this motion the wing also possesses a flapping stroke velocity, and the combination of this produces the peak in thrust force (the larger proportion of the combined effect will be from the wing rotational characteristic as the peak is delayed well beyond the maximum flapping stroke velocity). The peak thrust force in the second half stroke is smaller than that produced in the previous half stroke, as it occurs when the wing has a large AOA and quite early during the upwards flapping stroke, thus the velocity

is fairly below its maximal value. As the AOA does not remain constant at its peak value, the lift force curve reacts in the same fashion, thus larger peaks are required to produce a more sizeable lift force that would make such a vehicle airborne.

The average lift force generated for the boundary case is seemingly larger when compared to the base case, as shown in Figure 6.20B. Correspondingly, the pitching moment for the ground effect boundary follows this trend producing a larger average moment compared to the base case in this horizontal flapping plane. As determined earlier from Figure 6.19 the boundary case requires a consequential amount of more power than the base case, clearly stating that a larger resistance was formed when the wing was dynamically active in the presence of a wall. Analysing the aerodynamic power requirement opposed to the lift force generated in both cases, it was found that the base case produced a larger ratio opposed to its counterpart ground effect boundary case.

Albeit, the boundary case does require more power but it also generates a significant lifting force. Furthermore, its performance in terms of power required and lift produced is better than the base case, thus an FWMAV with a ground effect boundary present in the close proximity of the trailing edge should enhance the vehicles lift force capabilities. Bear in mind, that the distance between the boundary and trailing edge of the wing, condition of the surface and the area of the ground surface (as in some situations the rigid surface behind the wing may not cover its entire stroke amplitude range, or may not exist in certain locations of its flapping stroke arc) are all influential factors in the level of lift force enhancement. It should also be kept in mind that more power would be required in such boundary cases, thus the vehicle should be equipped with an energy source of sufficient capacity.

A comparison of the results acquired when the model was positioned vertically and horizontally are shown in Figures 6.20C and D. The axis labels were swapped over when the flapping stroke plane was changed, thus the data has been compared as vertical and horizontal forces to avoid confusion. Both curves evidently have the same trend of slope and their peak amplitudes are also very similar, however a specific distinction such as the phase difference is quite noticeable especially in the latter part of the upstroke motion (Figure 6.20C). Such distinctions are expected as the time history of the AOA between both datasets differ (the differences become increasingly noticeable during the tests performed in the vacuum chamber). The peak amplitudes for the horizontal and vertical forces in Figure 6.20D are very similar except for the negative peaks produced at stroke reversal. Such a difference may exist due to the direction of flapping as gravity

has a different effect on the up and down strokes when flapping in a vertical plane as opposed to flapping along a horizontal plane. These comparisons were performed merely to present that due to a passive wing rotation some disparities in force measurements would tend to exist.

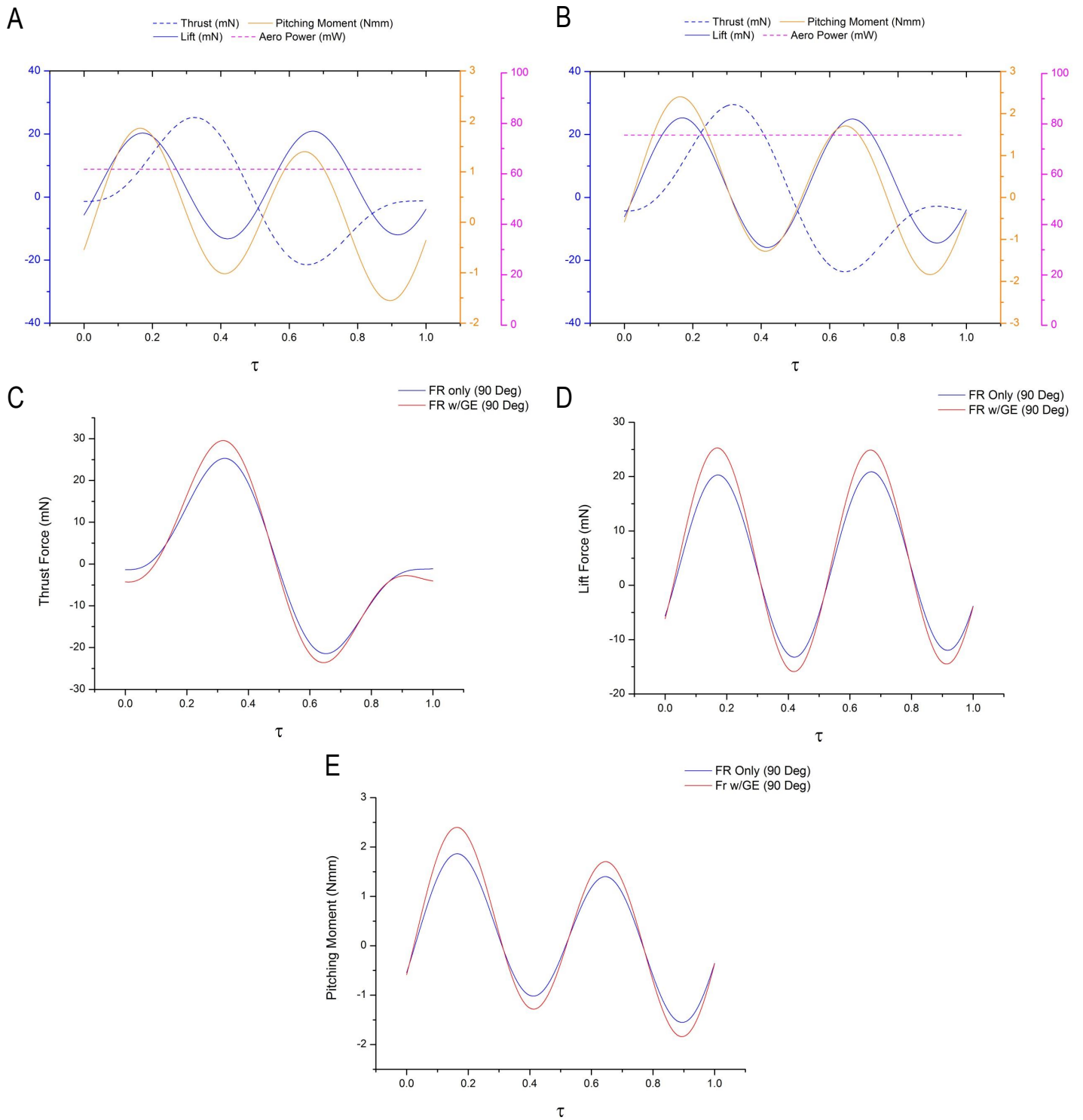


Figure 6.19: *Flapping & Rotation Wing Measurements for 60 mm Wings (WT<sub>4</sub>) with Model in Hovering Position; A: FR Only (90 Deg), B: FR w/GE Boundary (90 Deg), C: Comparison of Thrust Force, D: Comparison of Lift Force, E: Comparison of Pitching Moment. UI: M1-FR-WT<sub>4</sub>-S-H & M1-FRwB-WT<sub>4</sub>-S-H*

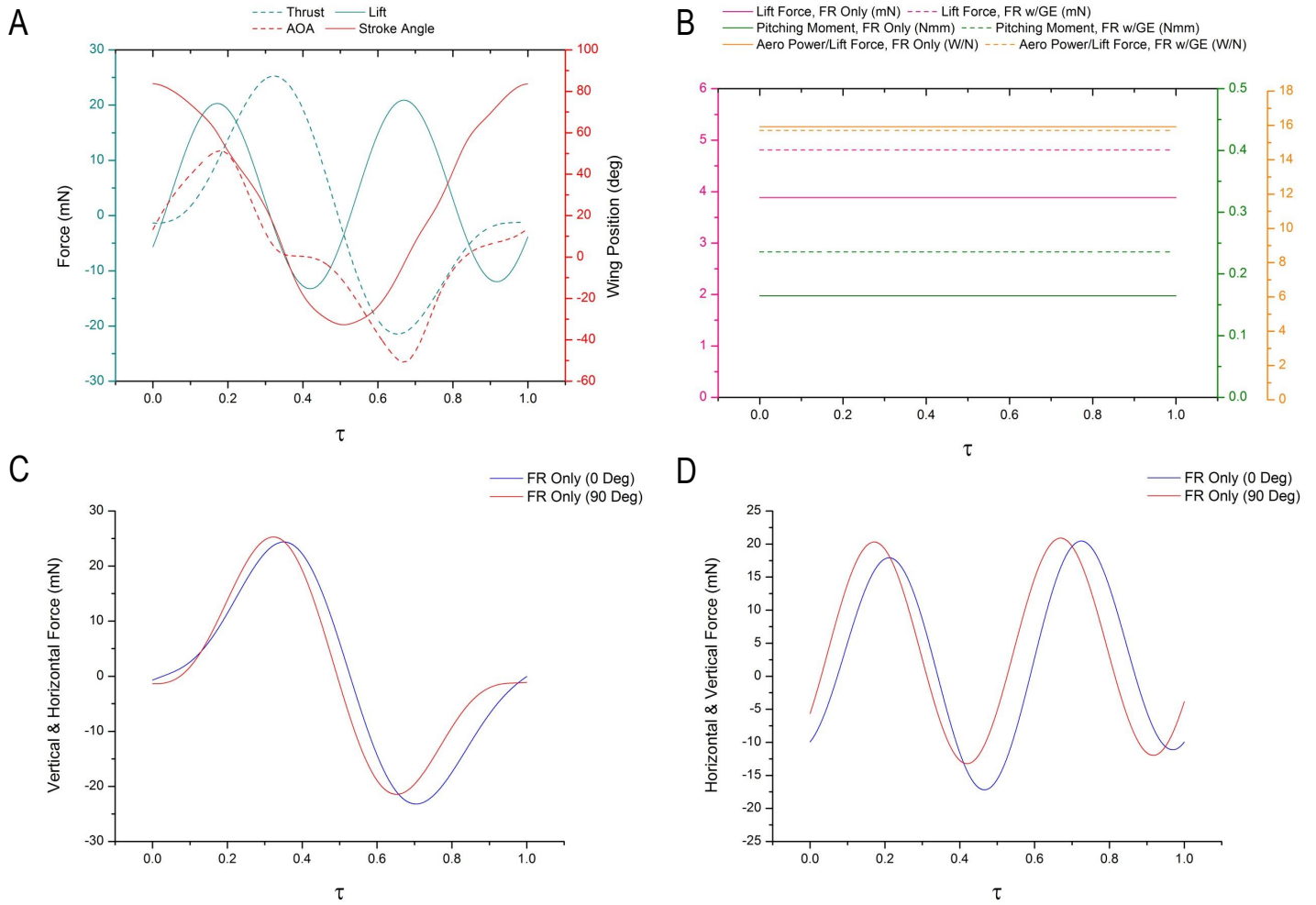


Figure 6.20: *Flapping & Rotation Wing Measurements for 60 mm Wings (WT<sub>4</sub>); A: FR Only (90 Deg) with Wing Displacement Kinematics, B: Average Pitching Moment, Average Lift & Average Power (90 Deg Data), C: Comparison of Vertical & Horizontal Forces at Different Inclinations, D: Comparison of Horizontal & Vertical Forces at Different Inclinations. UI: M1-FR-WT<sub>4</sub>-S-V, M1-FR-WT<sub>4</sub>-S-H & M1-FRwB-WT<sub>4</sub>-S-H*

### 6.1.5 Flapping & Rotation with Asymmetric Pitching for 60 mm Wings (WT4)

Altering the wing fixture configuration to create a combination of the two previous configurations which are, flapping only and flapping with wing rotation, gave rise to a novel form of wing motion denoted as flapping and wing rotation with a limitation applied during one half-stroke, namely the downstroke in the present study (FRAP). In this form of wing motion, the downstroke will have negligible wing rotation in comparison to the upstroke as the AOA produced during this particular half stroke will be zero degrees. The dataset tested here, has a limitation applied during the downstroke and the wing is free to rotate passively during the upstroke motion. The ideal effect is to exploit the downstroke as the dominant lift generating stroke (power stroke) and utilise the upstroke as the thrust generating stroke generated from the wings rotation. In addition dependent on the wings rotational motion the upstroke may produce a reduced amount of negative lift force, which should give a net lift force in the upwards direction. Consequently, this amalgamated approach of wing motion should lead to the reduction of aerodynamic power required by the FWMAV when producing this wing motion. With the application of passive wing rotation the AOA for the FWMAV cannot be controlled, thus user specified actions cannot be carried out. Figure 6.21, displays a simple schematic of the wings motion during both down and upstrokes as well as the kinematic displacement curve of the wings motion during a complete cycle under passive pitching during the upstroke motion only. The schematic presents an idealistic situation where the AOA during the downstroke holds at zero degrees and passive wing rotation activates during the upstroke only where a negative AOA is produced via passive effects, the dashed red line merely represents the neutral position of the wing.

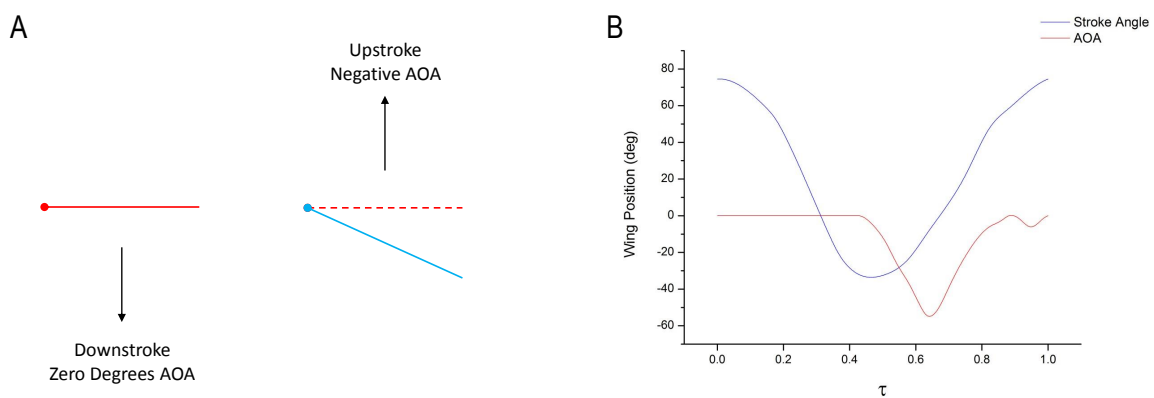


Figure 6.21: *Flapping with Restricted Wing Pitching; A: Schematic of Wing Pitching Motion, B: Wing Kinematic Motion for Complete Cycle; Circle Represents Leading Edge*

When this type of FWMAV is airborne whether it be autonomous or user controlled, applying alterations to the vehicles wing AOA is not optional as the wing rotation is not performed by a programmed wave, instead a passive application is exploited. Therefore, somewhat controlling the AOA by limitations provides a feasible option which can be actioned during flight by using a mechanism such as an electromagnetic hinge which can be constructed to be very light weight and operate on the flapping arms of the vehicle. The hinge could act in a fashion where it flicks a rigid lightweight component above or below the elastic material which produces the wing rotation, this would effectively block the deformation of the elastic material creating a zero or limited AOA. In this manner, the AOA will have some form of control and principally the vehicle can still adopt the passive mechanism to create its dynamic AOA motion. Thus, torque control can be produced by asymmetric flapping strokes which is analysed in the kinematic data and wing motion can be partially controlled by AOA limitation as aforementioned. Further research on the FWMAV could be to examine the flight aerodynamics when both of these techniques are applied simultaneously.

Experimentations were performed using the FRAP wing motion with the same wings and flapping frequency as the previous three datasets. The flapping stroke was along the vertical axis where the wing was restricted to produce an AOA on the downstroke by a small carbon piece attached to the flapping arm placed a distance above the elastic polyester material, and free to rotate passively during the upstroke phase. A base case was initially evaluated, followed by various boundary tests to study the effect the boundary has on the aerodynamic characteristics. The results for lift force, thrust force, pitching moment and aerodynamic power required to sweep the wings through the air with its unconventional motion have been illustrated in Figure 6.22. The experiments performed in this section have been listed in Table 6.4. As aforementioned the aerodynamic power presented is an average value throughout a cycle.

| <b>Case</b>       | <b>Case Description</b>                                   | <b>Figure</b> |
|-------------------|---|---------------|
| <i>Case FRAP1</i> | <i>Flapping &amp; Rotation AP Only</i>                    | 6.12A         |
| <i>Case FRAP2</i> | <i>Flapping &amp; Rotation AP with GE Boundary</i>        | 6.12B         |
| <i>Case FRAP3</i> | <i>Flapping &amp; Rotation AP with TE + GE Boundaries</i> | 6.13C         |
| <i>Case FRAP4</i> | <i>Flapping &amp; Rotation AP with TE Boundary</i>        | 6.13B         |

Table 6.4: *Flapping and Rotation with AP Cases for 60 mm Wings (WT4)*

The lift force curve has a resemblance to a typical sinusoidal wave, particularly for the downstroke phase

where a negligible AOA is produced. Distinctly, the downstroke generates a larger lift force peak compared to that produced during the upstroke, thus the term 'power stroke' and ideology aforementioned relating to the lift force production on both half strokes justly applies. Neither of the lift force peaks align well with the thrust force peaks, which is dissimilar to data presented previously in case FR1. This is most probably due to the type of rotation produced and enforcing no rotation on the downstroke, in addition to actual thrust force being produced on the upstroke in comparison to the downstroke. Furthermore, the pathway to the lift force peak in the first half-stroke is now much steeper in comparison to case FR1 as a flapping motion is produced rather than a coupled motion.

Nevertheless, small wing deflections do exist during this downstroke motion which is partially the reason why a thrust force peak is produced during the first half stroke. Although the first half-stroke is a flapping only motion, the complete cyclic stroke is a coupled motion, thus the same filtering method stated for the flapping and rotation tests was applied. When a filter is applied to a very small frequency range, very small disturbances are included from the model and measuring system. When this filtering range is increased the level of disturbances from the experimental rig and measuring system will likewise increase. Henceforth, applying a filtering technique which accounts for the forces and moments produced by the combined motion would as expected consist of some small contributions from the experimental rig and measuring system. This will be expanded upon later in this section, but for now it must be understood that the thrust peaks during the downstroke are a combinational effect from the wing deflection and contributions from both the experimental rig and filtering process. If the forces were measured directly from the wing rather than a complete model, the contributions aforementioned would be vastly smaller. Furthermore, the amplitude of the thrust force peak during the first half stroke is much smaller than that produced during the second half stroke, this is principally due to the second half stroke actually producing sufficient wing rotations. Although these contributions exist in the FR tests as well, as the wing produces a sufficiently large AOA on both half-strokes, thrust forces are generated as expected. To reduce unwanted contributions vacuum chamber data was subtracted from total force data, but some contributions still exist for this type of dynamic experiment.

As expected the pitching moment peaks line up well with the peaks of the thrust force curve, where the pitching moment peak generated on the first half stroke is considerably smaller than that produced on the second half stroke. A small wing deflection must have existed during the downstroke motion as a small exposed flexible area existed between the carbon piece attached at the wing root and carbon piece attached

to the flapping arms to restrict wing rotation. However, although the angle consistently held its position it was quite small and could not accurately be measured from the images, thus it has been presented as zero degrees in the kinematic data plots. All the boundary tests required more aerodynamic power than the base case, which corresponds well with the previous experimental datasets, which also presented that when dynamic wing and stationary boundary are juxtapositional more aerodynamic power is drawn by the system.

The dominant frequency for both tests is shown to be the flapping frequency at 5 Hz (refer to Figure 6.22E and Figure 6.23B). Significant vibrational modes exist in the vacuum chamber tests clearly shown by the shades of red at regular multiples of the flapping frequency. Both spectrogram plots have noticeable differences as the vibrational modes present in the air spectrogram plot also exist at regular multiples of the flapping frequency but majority of these are shown in a yellow shade presenting a lower amplitude. The core reason behind such disturbances produced during the vacuum chamber tests is due to the wing root colliding with the carbon piece placed on the flapping arm to restrict the wing rotation, as the wing approaches the end of its upstroke motion and starts its downstroke motion, it collides aggressively with this carbon piece. In comparison, tests performed in air would create a resistive force acting in the opposite direction to which the wing is travelling and reduce its velocity, thus the size of impact is much less.

Due to the collision between the wing and the carbon restriction part, the aerodynamic force composed of the subtraction between total force and inertial force would be affected which is clearly present at the early stage of downstroke where the lift force curve is somewhat skewed and experiences a delay in generating positive lift. The lift force peak produced in the downstroke phase is clearly larger than that produced during the upstroke phase (Figure 6.23A), where the wing has a large AOA which will affect the lift force produced. As the wing had just reversed direction in terms of wing pitch angle its effect on the fluid is rather weak, thus its contribution to the force acting in the vertical direction is not sufficiently strong in order to produce a significant effect. During the second half stroke the wing rotational motion aids in producing a large thrusting peak force, which occurs when the flapping velocity is near to maximum and the wing is positioned at a sufficient AOA. The combined motion of the wing dynamically rotating as it is forced to move through the upstroke allows it to generate such a sizeable peak thrust force.

An averaged comparison of lift force produced through the complete cycle has been presented in Figure 6.23C, where a large lifting force is produced for the case where the wall boundary is placed very close to the

wings trailing edge. Evidently the wing will take advantage of the downstroke phase as the wall continually applies an additional pressure on the leading surface (bottom face) of the wing around the trailing edge region. The ground effect case produces a slightly negative lift force, keep in mind that the wing is flapping through a vertical plane thus the ground effect does not act on the trailing edge of the wing as it did in the previous data set where the model was rotated to flap along the horizontal axis. The case with a combined boundary also produces an averaged lift force less than the base case most probably due to the existence of the ground boundary. A further imperative result to note here, is the positive average lift force produced for the base case.

All the cases produce an average positive thrust force for the complete cycle (Figure 6.23D), where the largest thrust is produced by the combined boundary case (case FRAP3), followed by case FRAP4 which is composed of a single wall on either side placed approximately 1 mm away from the wing trailing edge. The thrust generated by the base case was larger than that found for the one with the installation of the ground effect boundary in the vicinity of the wings. Likewise, the pitching moment data was also positive for the averaged data of a complete cycle with the same order as the thrust force data except that in this case the ground effect seemed to generate a larger moment than the base case (refer to Figure 6.23E). Considering solely the base case (case FRAP1), it has shown to produce a positive average lifting force and a positive average thrust force, which clearly presents the advantage of controlling the AOA using the foregoing technique.

The average thrust force produced based on the wings AOA has been illustrated in Figure 6.23F, where the thrust force has been averaged according to the duration the AOA was at zero degrees (basically negligible) and when the AOA was variable. First and foremost, the clear result shown for all the cases states that when the wing has a variable AOA, a massive thrust force is produced when compared to the duration when the wing possesses a zero degree AOA. Secondly, as mentioned previously during the downstroke phase a small AOA was produced which was regarded as negligible and contributions from the entire system exist due to the filtering method applied, all the aforementioned are regarded as the reason why a small averaged thrust force exists during the limited rotation phase. During the variable AOA duration the largest average thrust was produced by the combined boundary case, and the remaining cases seemed to produce similar average thrust data. The average thrust force generated in the duration when the AOA is regarded as zero degrees demonstrated to produce similar results for all the cases, where the largest results were produced for the

cases which consisted of walls behind the trailing edge and the minimal result of -0.0215 mN was generated for the ground effect case.

A comparison of the lift force through the time history of a complete cycle has been shown in Figure 6.24A. Case FRAP4 produced the largest lift force during the downstroke phase, when the wing is very close to the wall, and the fluid would find it difficult to pass through such a gap. Thus an intense build up of fluid is continuously present on the lower surface of the wing around the trailing edge region (as less separation occurs due to the presence of the wall) which would provide an additional pressure to this under surface effectively augmenting lift force production and reducing flow separation at the trailing edge. However, this benefit comes at the expense of power required as the wing is experiencing a larger resistive force acting against its motion. As case FRAP4 has a smaller gap of approximately 1 mm between the wall and the trailing edge of the wings compared to case FRAP3 where the gap is larger of approximately 1.7 mm, a smaller lift force peak is produced during the downstroke motion. It is worth noting that the lift force curves produced by all the cases follow the same trend and the peaks also occur in the same positions. Small differences existed in the AOA curve for the boundary cases which consisted of a wall placed adjacent to the wings trailing edge and base case, which included a slightly earlier commencement of the variable AOA phase and a slightly larger peak amplitude for the AOA motion. The very small difference which exists between the timings of when the peak forces are produced during the upstroke phase for each case could be due to small differences that exist in the AOA.

The largest negative peaks for the lift force are produced by both cases which consist of walls located behind the trailing edge of the wings. Both cases seem to produce the same size of peak, where the ground boundary augments the negative vertical force produced which is why the peak of the dual boundary is now equal to the peak of case 'FRAP w/TE'. This is substantiated by the case which only has a ground effect boundary acting, where the negative peak is noticeably larger than the base case with no boundary. As the wing approaches the ground effect wall, fluid will travel around the edges of the wing which is sweeping forwards towards the ground effect boundary. This fluid will gather above the wings surface and apply an additional resistive force to the wings motion, effectively causing more power to be drawn by the mechanical system (shown in Figures 6.22 and 6.24D) to move beyond this region and carry out its upstroke motion.

Due to the different rotational start times, and the difference in amplitude for AOA the wings in the trailing edge wall boundary case had more time to generate a sufficient rotational velocity and smaller AOA in order

to produce larger peaks. This effect along with the ground effect assisted the dual boundary in creating a larger negative lift force peak compared to the base case. Although the differences commence early during the upstroke phase, due to the formation and properties of a sinusoidal motion the differences become more evident at the peak positions of sinusoidal waves, thus significant differences are found at the peaks of the curves. Furthermore, the AOA motion during its dynamic phase (where its free to rotate) produces one half of a somewhat sinusoidal wave as it gradually moves away from the zero position, peaks at a maximum, thereafter moves back towards a zero position.

Figures 6.24B and C, display plots of the thrust force and pitching moment measurements obtained from all the cases flapping with an FRAP arrangement. Both plots show the same trend where the first peak is much smaller than the second for the reason which has been aforementioned. All the cases show the same trends for thrust force and pitching moment plots where all the peaks occur at the same time. The largest positive thrust peak produced during the second half stroke where the AOA is now free to rotate passively under the influence of aerodynamic loading is produced by case FRAP3 followed by case FRAP4. A similar result was seen in the dataset where the wing was performing a flapping and rotation motion. This positive thrust peak occurs where the wing possesses a sufficient AOA and the wing is approximately at mid-upstroke where the flapping stroke velocity peaks. As the difference in AOA between the base case and boundary cases is small, the boundary has a reduced effect, thus substantial differences do not exist between the positive thrust peaks in this second half stroke. The positive thrust peak produced for the ground effect boundary is very similar to the base case result as the boundary has not created a significant effect on the wing pitch angle. As the angle of attack in all cases starts and ends at an angle which is more or less zero degrees the start thrust data all starts and ends very near to one another with minute distinctions, this is clearly illustrated in the pitching moment data as well. A comparison of the aerodynamic power required for each case clarified that for all boundary cases the mechanical system drew more power, as the wings travelled through regions which formed larger resistances to its cyclic motion. The most power demanding case of all, was where the walls were placed closest near the trailing edge region, namely case FRAP4, this was followed by case FRAP3. The case which had the walls placed closest to the trailing edge of the wings produced the largest ratio of aerodynamic power required per thrust force generated, which simply presents that its efficiency in producing thrust is lower than all the other cases. In this situation the most efficient result was produced by the base case where no boundary existed in the near vicinity of the wings.

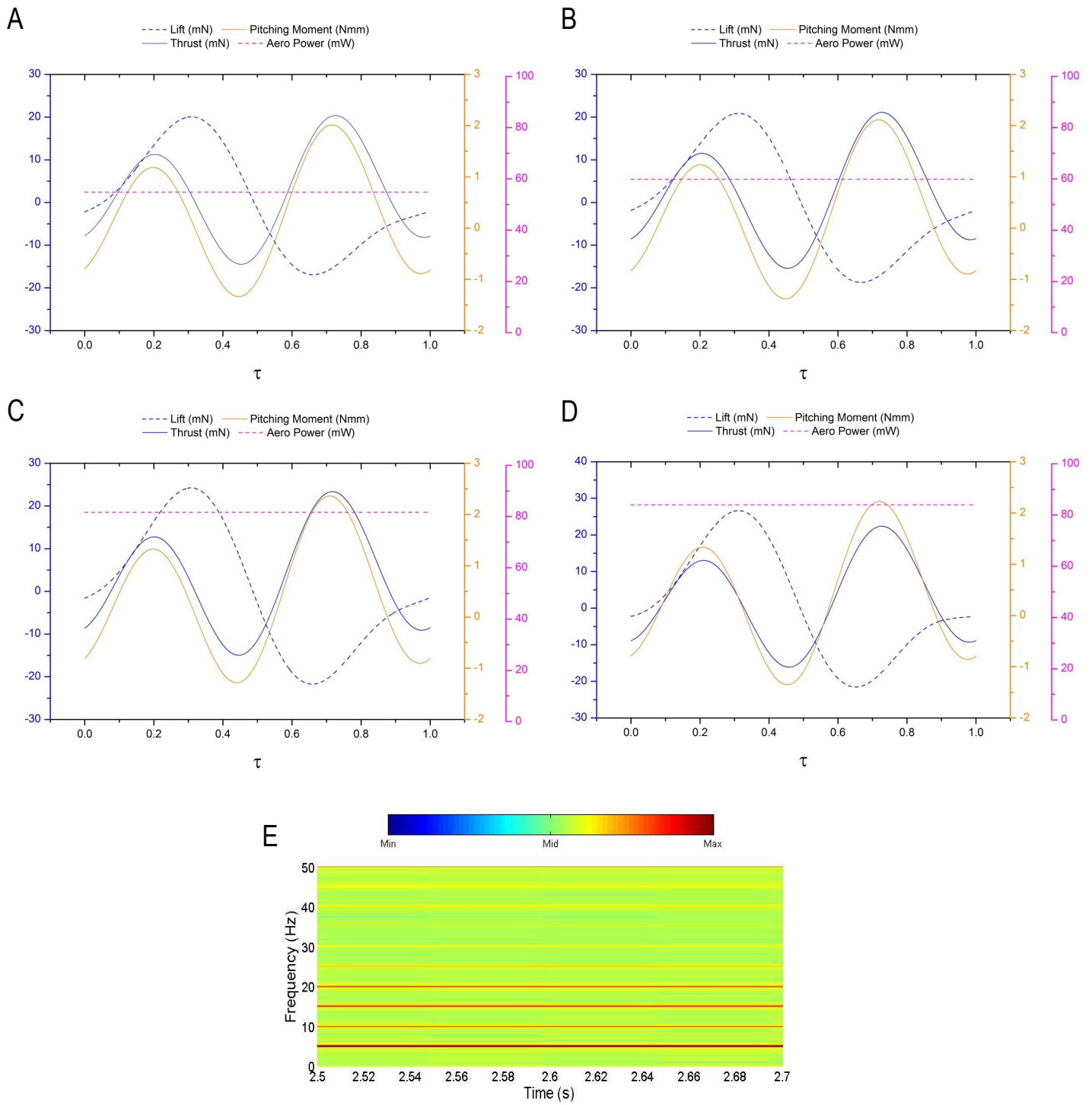


Figure 6.22: Flapping and Rotation with Asymmetric Pitching Measurements for 60 mm Wings (WT4); A: Case FRAP1, B: Case FRAP2, C: Case FRAP3, D: Case FRAP4, E: Spectrogram for Vertical Axis in Air. Colour Bar Represents Size of Amplitude. UI: M1-FRAP-WT4-S-V & M1-FRAPwB-WT4-S-V

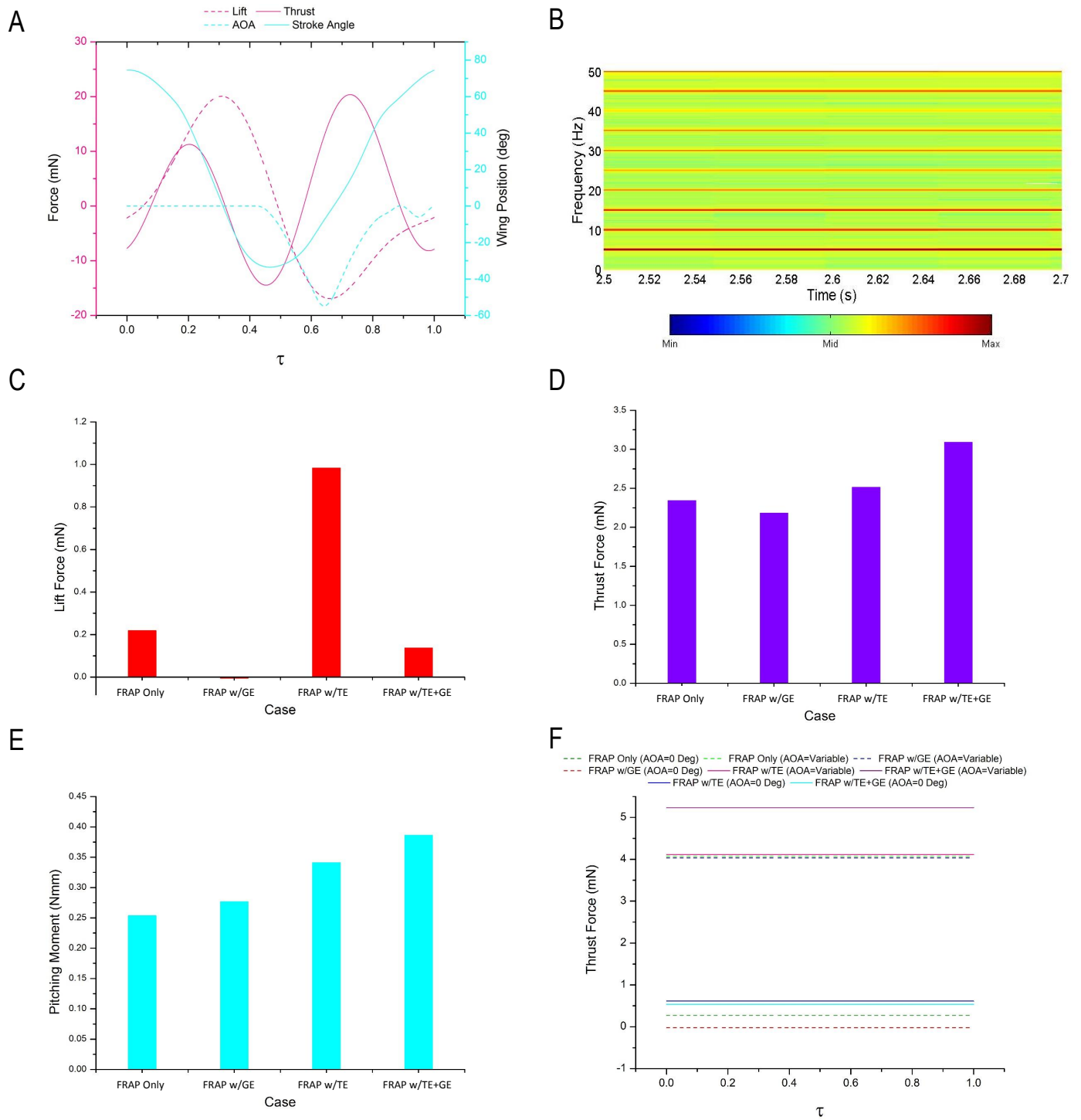


Figure 6.23: *Flapping and Rotation with Asymmetric Pitching Measurements for 60 mm Wings (WT<sub>4</sub>); A: FRAP Only with Wing Displacement Kinematics, B: Spectrogram for Vertical Axis in Vacuum Chamber, C: Average Lift Force, D: Average Thrust Force, E: Average Pitching Force, F: Average Thrust Force Based Upon AOA Duration. Colour Bar Represents Size of Amplitude. UI: M1-FRAP-WT<sub>4</sub>-S-V & M1-FRAPwB-WT<sub>4</sub>-S-V*

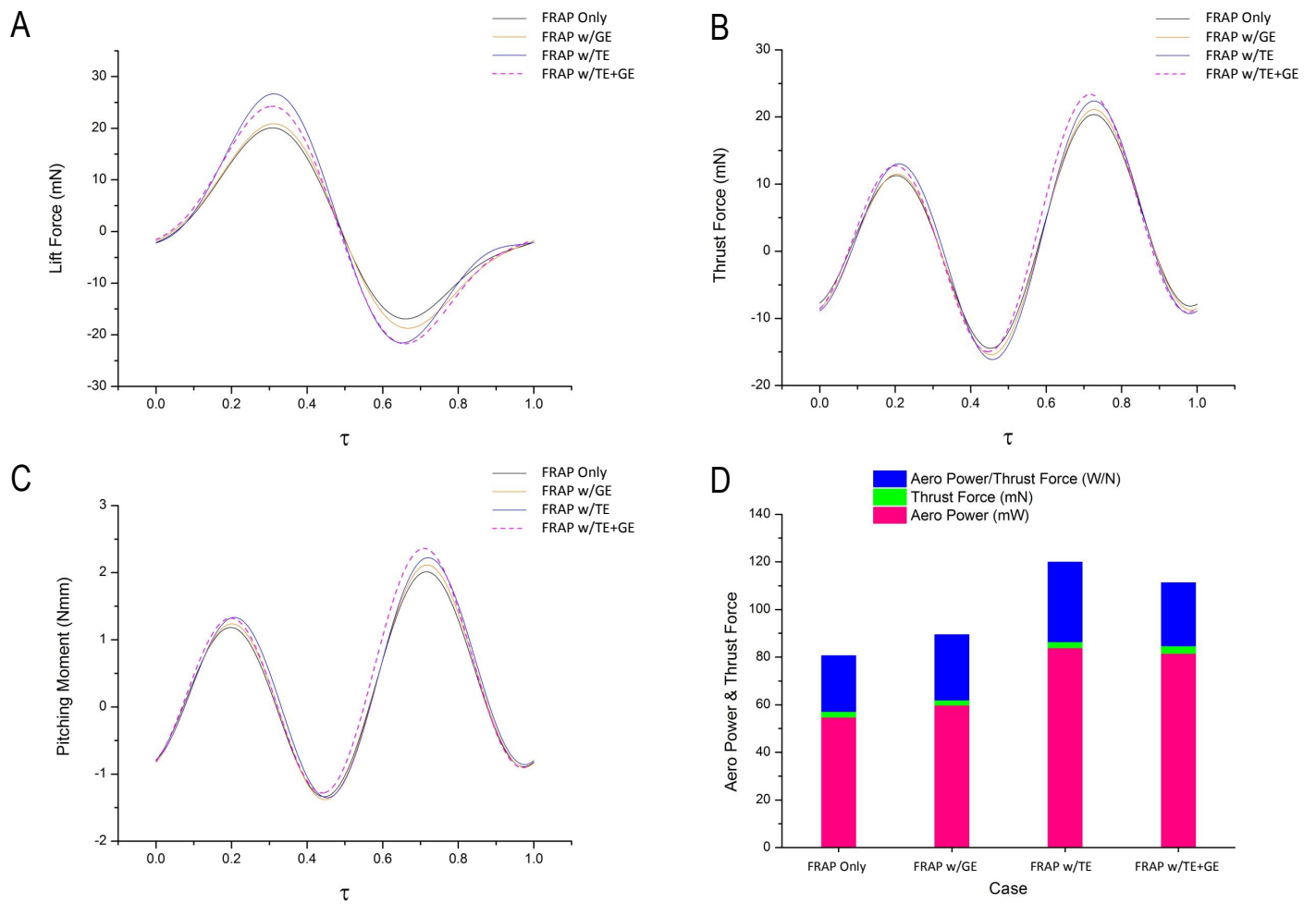


Figure 6.24: *Flapping and Rotation with Asymmetric Pitching Measurements for 60 mm Wings (WT4); A: Comparison of Lift Force, B: Comparison of Thrust Force, C: Comparison of Pitching Moment, D: Aero Power & Thrust Force Relation. UI: M1-FRAP-WT4-S-V & M1-FRAPwB-WT4-S-V*

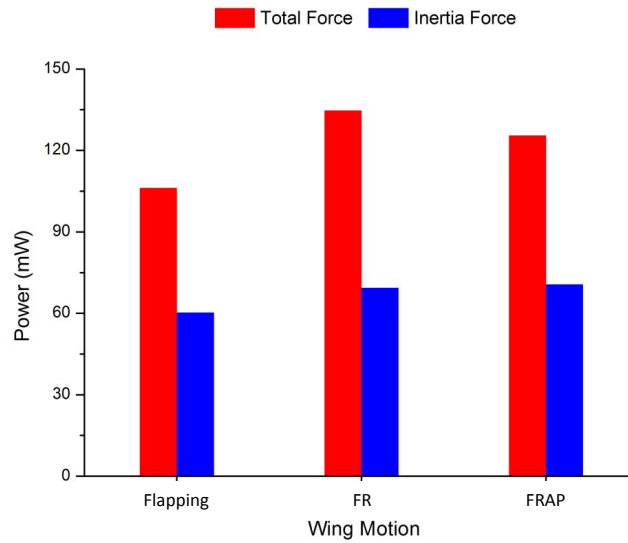


Figure 6.25: *Power Input for Various Wing Motions with Model 1 Inclined at 0 Degrees*

Figure 6.25 displays a power comparison for the power required during total and inertia force measurements. As expected the total force would require more power as air resistance is present during these experiments in comparison to inertia force measurements. For a clear breakdown the power required during total force is composed of aerodynamic, inertia and frictional forces within the complete system. The power drawn during the inertia tests is composed of the aforementioned forces except aerodynamic. The power drawn during the inertia tests are quite similar for all the wing motions assessed, especially for FR and FRAP. However, the total power required is greater for FR than FRAP which clearly states that the power drawn for aerodynamic force is greater due to the coupled wing motion produced for a complete cycle. Using a lighter wing and reducing the frictional forces within the system would lead to a decrease in the total power required. The least power drawn is for flapping experiments where the wing performs a singular motion which clearly requires less power during the inertial tests as the wing accelerates about one axis.

## 6.2 Force & Moment Measurements for Model 2 (Sym & Asym)

Similar tests were conducted on model 2 (ref. section 3.3) in both of its configurations to perform symmetric and asymmetric flapping motions. For this model the stroke amplitude for the second half of the stroke was deliberately reduced to avoid linkage locking (see Figure 6.26 where the minimum angle is -16 degrees in comparison to model 1 where the minimum angle is -32 degrees). This was done because the asymmetric configuration would produce a larger stroke amplitude on one side, thus to avoid any locking effect the linkage mechanism was raised (hence the larger height of Model 2), fundamentally this was a method of precaution to avoid unnecessary repairs. Core tests were carried out in both configurations to merely assess the affect if any, that a change of configuration would introduce, in addition to investigating the aerodynamic characteristics such as F/T measurements. Consequently boundary effects were not studied for model 2 as these investigations had been pursued using model 1, future research along these lines could revolve around near wing boundaries for asymmetric flapping motions to understand the effect of rigid boundary-fluid interaction and its outcome on aerodynamic torques acting on an FWMAV.

### 6.2.1 Wing Motion Analysis for Model 2 (Sym & Asym)

This section will provide some kinematic images and data plots for model 2 under both of its configurations, which are symmetrical and asymmetrical flapping. Both types of flapping styles will be presented such as flapping and flapping with wing rotation. Finally, comparisons are presented for the wing motion of this model under operation and the behaviour of its passive pitching motion.

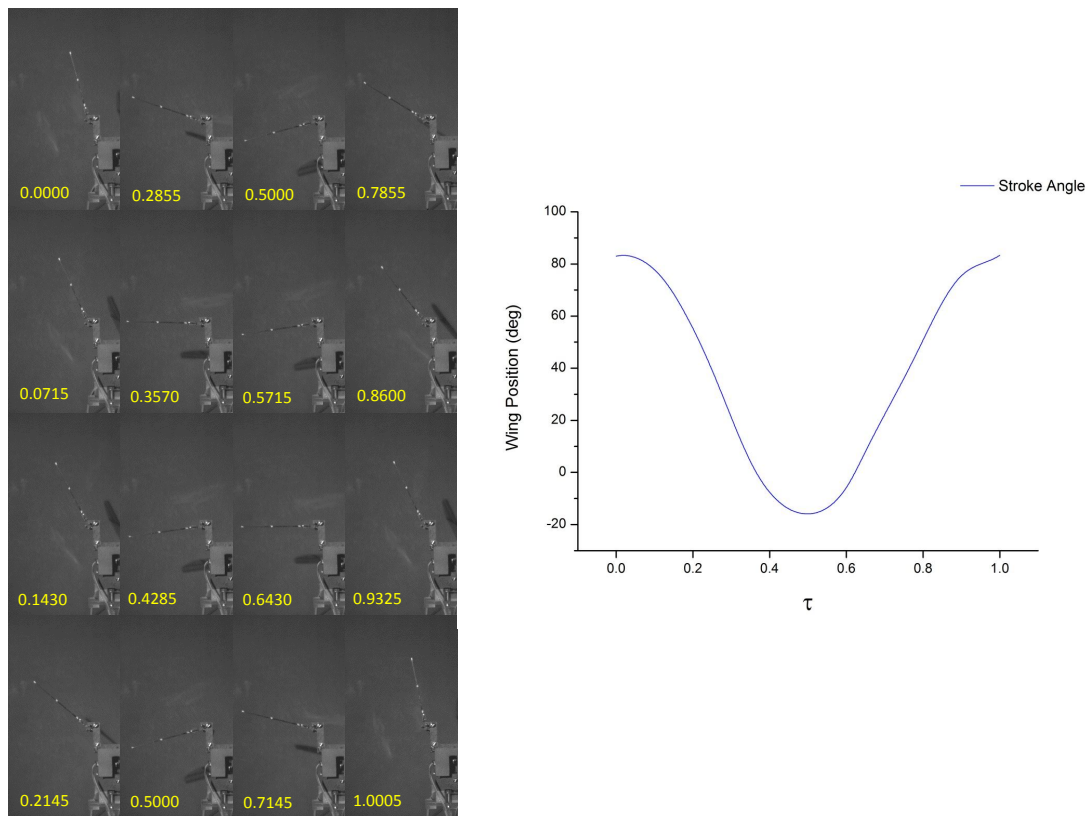


Figure 6.26: *Wing Position for Model 2 in Sym Configuration Undergoing Flapping Motion Sequence with Non-Dimensional Time. UI: M2-F-WT4-S-V*

Figure 6.26, illustrates a sequence of images for the flapping motion of model 2 in its symmetric configuration along with the kinematic data plot elaborating upon the wings position during a complete stroke cycle. The plot has a clear resemblance to a typical cosine curve, where the first and final peaks relate to the start downstroke and end upstroke positions respectively. The wing position was determined by the use of the white dots marked on the leading edge of the wing. As aforementioned in order to avoid unnecessary damage to the models mechanism, the size of the negative angle created at end-downstroke was reduced as it was established during the design phase that the asymmetrical configuration will produce a significant sized stroke amplitude on one side.

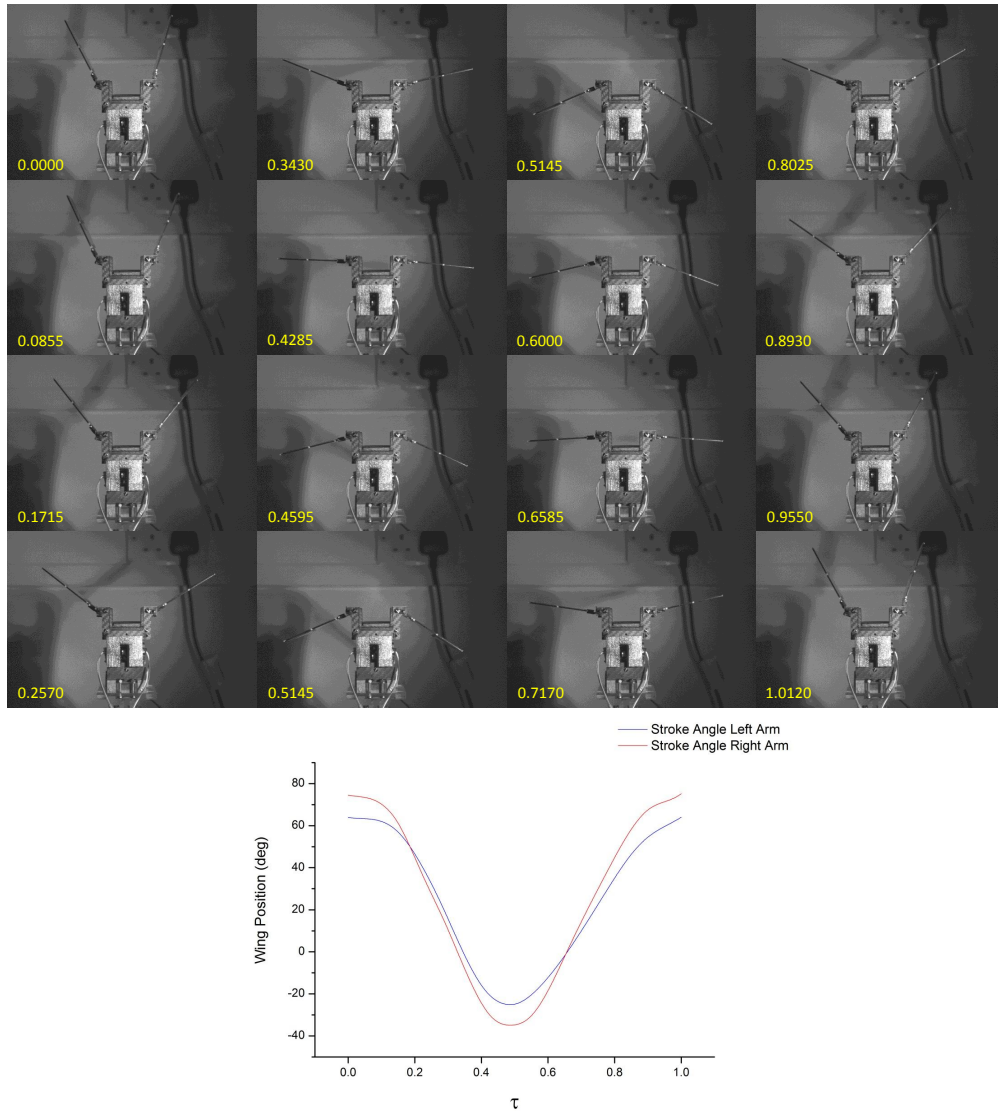


Figure 6.27: *Wing Position for Model 2 in Asym Configuration Undergoing Flapping Motion Sequence with Non-Dimensional Time. UI: M2-F-WT4-A-V*

Figure 6.27, consists of a sequence of images and a kinematic plot relating to model 2 performing a flapping motion in its asymmetric configuration. Separate plots have been shown for both flapping arms as they travel through different stroke amplitudes, where the right arm seems to travel through a larger stroke amplitude which is accomplished within the same time duration as the left arm moving through a smaller stroke amplitude. The images along with the plot clearly show the differences which commence at the initial downstroke position, thus as aforementioned in the data analysis section a moment will be produced during the downstroke phase, which will balance out during the upstroke phase.

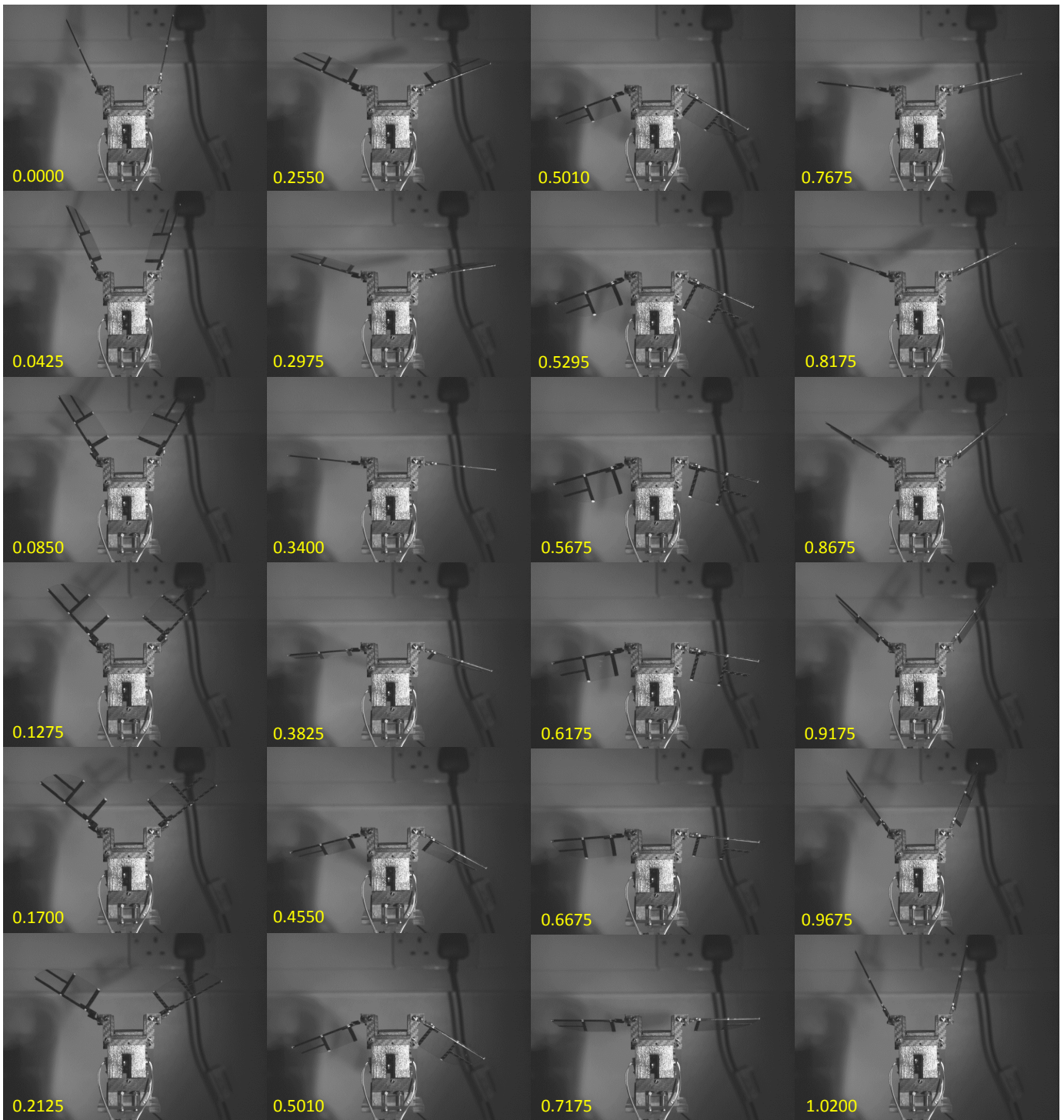


Figure 6.28: *Wing Position for Model 2 in Asym Configuration Undergoing FR Motion Sequence with Non-Dimensional Time. UI: M2-FR-WT4-A-V*

Figure 6.28, presents a sequence of images for model 2 in its asymmetric configuration performing a flapping with wing rotation motion. The right side of the model has a larger flapping stroke amplitude and correspondingly has larger AOA peaks for both half strokes. In compliance with the singular asymmetric flapping only motion, the right side travels a larger stroke amplitude in the same time duration that it takes the left wing to travel a smaller amplitude, which clearly signifies that the right side travels faster. The result in terms of aerodynamic characteristics of such kinematics is presented in this chapter and the wing position plots for the coupled motion of model 2 in both of its optional configurations have been illustrated in Figure 6.29.

Model 2 in a symmetric configuration produces a distorted flapping stroke in comparison to the curve produced when the model was performing a singular flapping motion (see Figure 6.26, as before this is due to the addition of the rotational feature). The AOA curve has a similar shape to the passive wing rotation created by model 1 when operating under this free-to-rotate condition, two peaks are produced in total (one for each half stroke). The kinematic plot relating to the sequence shown in Figure 6.28, is illustrated in Figure 6.29B, where both sets of flapping and wing rotational wing positions have been plotted separately. Similar to all the plots related to the coupled wing motion, the flapping stroke curves for the asymmetric configuration are also distorted, this was an expected result as it has been observed in previous datasets. The AOA peak amplitude for the right wing is considerably larger than its neighbouring left wing, where large distinctions are formed near to the peak AOA locations. The right arm also remains at the end-downstroke/start-upstroke position for a shorter duration in comparison to the left arm. Whilst in the asymmetric configuration, the model was rotated 90 degrees to flap along the horizontal plane, the kinematic data has been presented in Figure 6.29C. The flapping stroke amplitude and AOA peaks for the right arm were larger than its neighbouring left arm, and the shapes for the flapping stroke amplitude and AOA for both datasets did show some similarities. The AOA seems to remain near to a zero degree wing pitch position when progressing to the latter stage of the downstroke motion, before turning negative near to the start upstroke stage.

A comparison of the AOA for both configurations whilst flapping through a vertical stroke plane has been shown in Figure 6.29D, evidently the symmetric configuration produces the largest peaks for both half strokes. The curve also shows a smoother trend signifying a more gentle progression when travelling through this continuous dynamic motion. When in the asymmetric configuration the linkages of the mechanical system

would not move as smoothly as they do when in the symmetric configuration as the links are slightly slanted when the plunger is displaced horizontally. In turn, this will have an effect on the flapping arms which will subsequently affect the smoothness of the passive rotational motion. Furthermore when progressing passively the AOA differs on both sides which would reduce the chances of such a gentle dynamic motion. Lastly, the AOA kinematics have been compared for the model in its asymmetric configuration when flapping through two different stroke planes which are perpendicular to one-another. The AOA seemed to linger in the region of zero degrees for a short duration (notably for the right arm) when placed in the hovering mode, such an event did not occur when flapping in the vertical plane where the AOA simply progressed from positive to negative angles. A similar result where the AOA lingers near to zero degrees AOA when flapping through the horizontal stroke plane is observed for model 1 as well, thus the wing is rotating back from the peak position far too quickly. Significantly reducing the wings mass or altering the specifications related to the polyester adopted for wing rotation would aid in improving the motion of the wings AOA, as inertial effects are affecting the wings rotational characteristics. Overall, future alterations would need to improve the rotational motions of the AOA, as it should ideally be held at a desired AOA for a large duration of each half stroke thereafter producing a rapid rotation prior to or at stroke reversal.

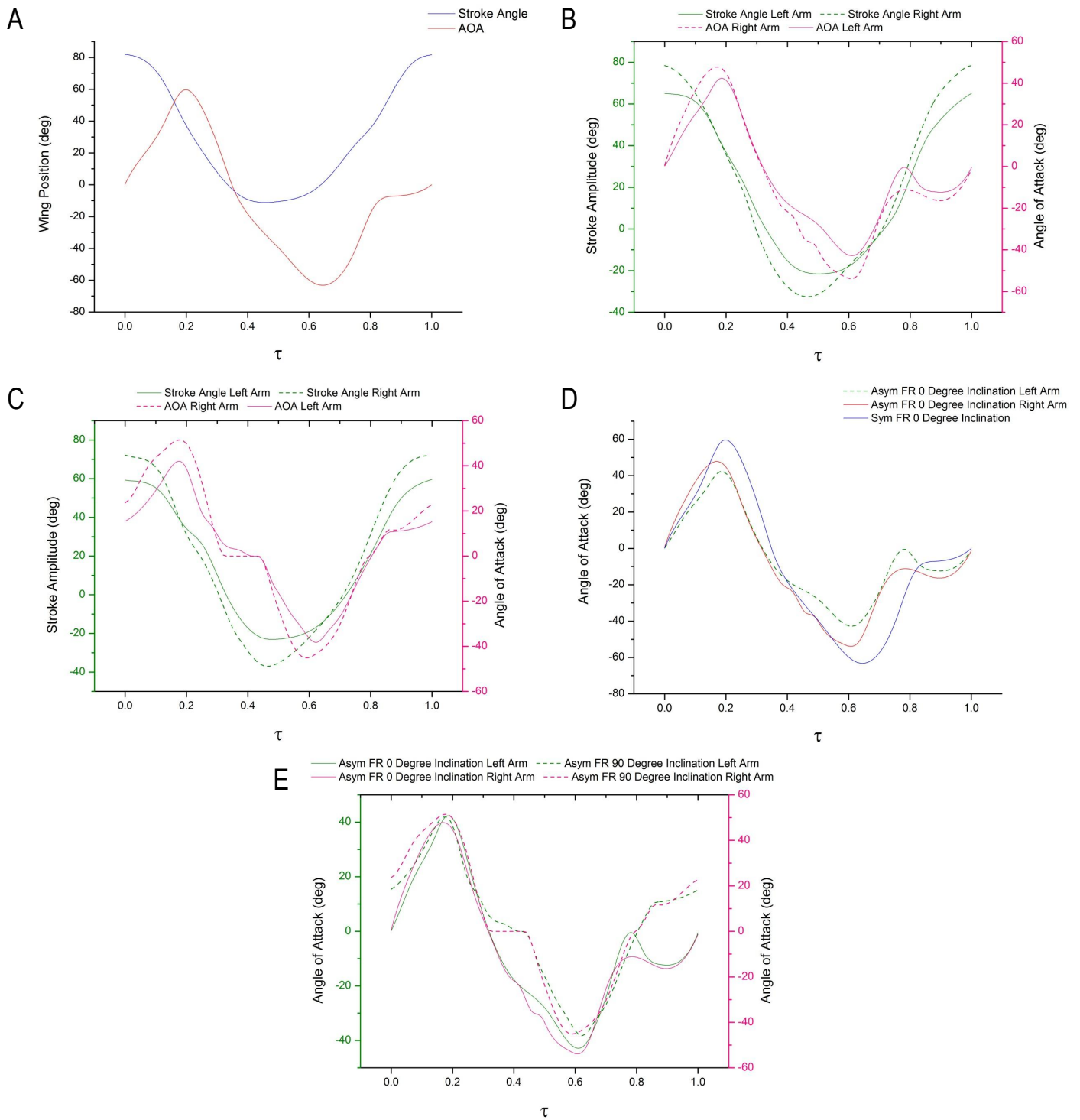


Figure 6.29: *Wing Kinematics for a Compilation of Arrangements Tested with Model 2; A: Sym Configuration with FR Motion, B: Asym Configuration with FR Motion, C: Asym Configuration with FR Motion with 90 Degree Inclination, D: AOA Comparison for Sym & Asym Configurations, E: AOA Comparison for Asym Configuration in 0 Degree & 90 Degree Inclinations*

## 6.2.2 Flapping Only for 60 mm Wings (WT4)

For these tests a comparison was made between both configurations to determine any gain or loss in aerodynamic forces and power required for flapping wings with a singular span of 60 mm at 5 Hz. The wing displacements have been shown in Figures 6.26 and 6.27, for both symmetric and asymmetric flapping respectively. Both configurations were tested with the same method in air and individual inertia experiments were conducted due to the differences which exist in stroke amplitude and additional/reductions in mechanical friction as a result of switching the backing plate.

Figures 6.30A and B, illustrate individual plots for the inertial and aerodynamic forces as well as the average aerodynamic power required to move the wings through the air. The same trend is observed for both sets of force plots where the inertial force peaks at the start and end of a stroke whilst closely resembling a cosine curve that also defines the flapping motion. The relationship between inertial and aerodynamic forces clearly shows that when inertia reaches maximum/minimum values the aerodynamic forces are more or less zero as the wing approaches a rest condition. As the aerodynamic forces peak, the inertial plots move towards a zero value as the acceleration of the wing approaches zero. The sinusoidal motion of the wings is well represented by the time dependent inertia forces. The aero power required for both configurations is found to be very similar, which is satisfactory as the aero forces produce similar values.

Spectrograms for the asymmetric configuration have been shown in Figure 6.30, both illustrate that the dominant frequency occurs at the flapping frequency. The spectrogram plot for both air and vacuum tests seems to have a fair amount of 'yellow' especially for the latter which is a resultant of larger vibrations. Unlike the tests in air no aerodynamic damping is experienced when in vacuum condition. Although the model produces larger vibrations under a vacuum condition, the inertial measurements are not affected at the frequencies at which the data is analysed primarily due to the low pass filtering method as a cut-off procedure is executed. This model in general already seemed to produce larger vibrations due to it experiencing larger frictional forces which was discussed in chapter 3 of this thesis.

Both aerodynamic force cycles compare well to one-another where the asymmetric curve seems to have a larger downstroke peak, but a reduced upstroke peak. This is clearly shown by the line plots shown in Figure 6.30, where the peaks between both configurations show noticeable distinctions. The difference between both upstroke peaks is larger than the difference between both downstroke peaks which is directly related to the

wing kinematics. When comparing each case individually it seems clear that the down and up stroke peaks for the symmetrical configuration do not have large discrepancies, especially in comparison to the distinctions found for the down and up stroke peaks of the asymmetric curves. The considerable discrepancy found for the peaks of the asymmetric case relates to the wing motion as the left side of the wing during the upstroke is moving at a slower rate, shown in the wing displacement plot where a larger duration is required for a change in wing displacement. Such differences in addition to a slightly swifter downstroke compared to the upstroke phase will result in a larger aero peak force during the downstroke stage and a smaller peak force during the upstroke phase.

Overall, no significant reduction in aerodynamic force was found between both configurations which proves to be a satisfactory result, where changes in flapping mode will not result in large differences of peak-peak force production. Although an FWMAV cannot lift itself when performing a single flapping motion as the net aero force will be close to zero, it is vital to perform such investigations as base experimentations. The aerodynamic power required for peak-peak force output is displayed in Figure 6.30D, where it is shown that the asymmetric configuration requires slightly more power than the symmetric configuration even though it generates a smaller peak-peak aero force. As a whole, the difference in peak-peak force generated and power required does not have substantial differences, which is why the aero power required per force output data is very similar. This can be viewed as a positive result as power requirements and force generation between both configurations do not have considerable discrepancies, however for even larger asymmetries considerable differences in both power required and force produced may occur.

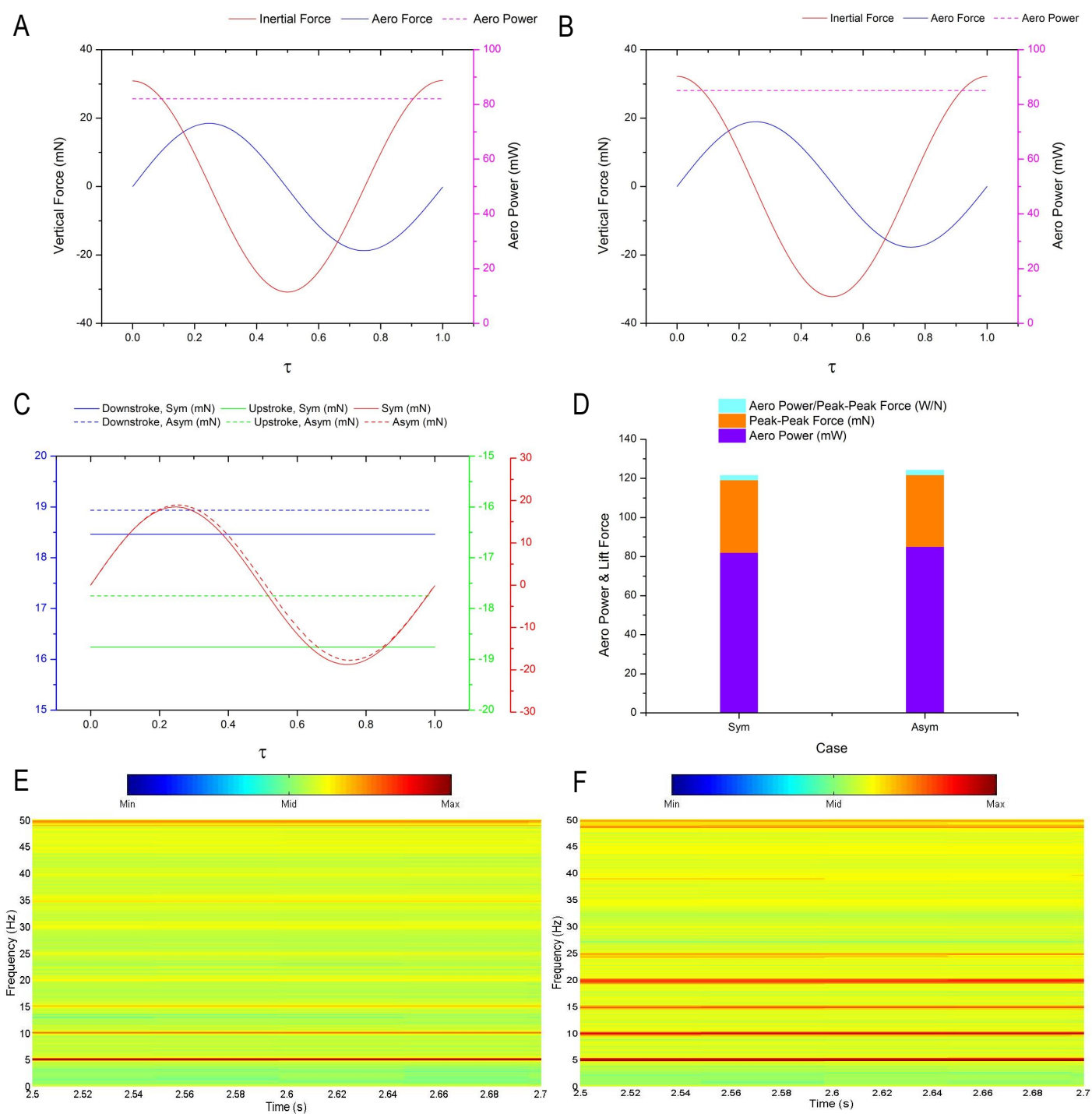


Figure 6.30: *Flapping Wing Measurements of 60 mm Wings (WT<sub>4</sub>) for Model 2; A: Symmetric Configuration, B: Asymmetric Configuration, C: Comparison of Lift Force and Peak Data, D: Aero Power & Lift Force Relation, E: Spectrogram for Vertical Axis in Air for Asymmetric Configuration, F: Spectrogram for Vertical Axis in Vacuum Chamber for Asymmetric Configuration. Colour Bar Represents Size of Amplitude. UI: M2-F-WT<sub>4</sub>-S-V & M2-F-WT<sub>4</sub>-A-V*

### 6.2.3 Flapping and Rotation for 60 mm Wings (WT4)

With the introduction of an additional degree-of-freedom, the coupled wing motion is expected to promote supplementary asymmetries when the model is in the asymmetric flapping configuration. In turn, this may have consequences on the aerodynamic forces and power required to generate these forces which will be reported in this section. To uphold consistency with the flapping only experiments, these tests were performed on the same wings and flapped at the same frequency. Due to the passive nature of wing rotation utilised on this FWMAV, difficulties arise when estimating the AOA of a wing especially when the stroke amplitudes can be different for either side of the vehicle. Nonetheless, from a general point of view, a larger wing rotation (AOA) should be created for a wing which travels a larger stroke amplitude.

The aerodynamic force generated and power required in the symmetric configuration for a pair of wings in a flapping and rotating motion has been shown in Figure 6.31A. Similar to the data presented for model 1, whilst the lift curve shows two peak locations and completing a single cycle, the thrust curve peaks four times completing two cycles all within the same duration. When compared to the flapping only case for the symmetric configuration (Figure 6.30), it can be clearly seen that the aerodynamic power required to move the wings with a coupled motion through the air requires considerable amounts of more power, but in the coupled motion case two forms of aerodynamic forces are now generated acting in perpendicular axes to one-another.

The vertical aero force peaks are now slightly skewed due to the lag applied from the additional motion and the flow dynamics involved in generating the aerodynamic forces is much more complicated. Positive thrust peaks are produced in both half strokes, and the larger of the two occurs during the first half stroke as the wing rapidly flicks in the opposite direction of the flapping motion due to aerodynamic loading, effectively producing a positive AOA. Whilst combined with the velocity of the flapping stroke (which for a flapping cycle will peak at mid-stroke, gradually increasing from rest and maximising at each mid-stroke) produces the larger positive peak. Due to the additional friction felt by wing actuating components of this model, a slightly larger exposed flexible area was intentionally adopted in these tests to promote sufficient wing rotation.

Also partly due to the method of rotation and inertial effects the wing has already assumed a negative angle of attack before the start of upstroke, thus the thrust force does not fully take advantage of this flicking effect

in the positive thrust direction. Negative thrust forces are produced as the wing AOA changes direction and becomes negative during its present flapping stroke direction which is too early for such a change in AOA. Ideally the wing should maintain a fixed AOA of 45 degrees through majority of each half stroke maximising the generation of thrust force and rapidly rotating at the end of each stroke taking advantage of rotational accelerations. The collective size of the positive thrust peaks are clearly larger than the negative thrust peaks, where the majority of the thrust curve lies on the positive half of the force axis. The lift force peaks although out of phase from the positive thrust peaks, align better with the positive thrust peaks than the negative thrust peaks, part of the reason for the small negative thrust peak is also due to the flapping stroke velocity which tends towards zero at the end of each stroke. In terms of time history, if the wings are slightly off in terms of flapping angle or wing rotation small asymmetries may be created which will effectively become negligible as the amplitudes of each motion are equal. Thus, as long as the overall flapping amplitude and rotational amplitudes on both sides are very similar the net asymmetry will result towards zero deeming it negligible. The aforementioned would not apply for a FWMAV which has been prescribed an asymmetric motion as amplitudes per side would not balance one-another which will effectively create some form of average body torque.

Before analysing the moments for the asymmetric configuration, the moment data for the symmetric configuration will be analysed first. Thus, due to the additional frictional forces encountered in model 2, augmented torques may be present in the time history data. Moment results have been shown in Figure 6.31B, where the time history of both rolling and yawing clearly shows some discrepancies between both sides which is more prominent for the rolling moment as the values produced are larger. Both of these moments when averaged throughout the cyclic data tend towards a zero value which means that no overall moment will be created about both of these axes. Note the vehicle may produce a moment on the first half stroke, but this will be countered on the second half stroke, to effectively balance out. The pitching moment data lies dominantly in the positive half of the moment axis following the behaviour of the thrust curve, which produces an overall positive pitching moment as shown in the plot when the data is averaged over the entire cycle. The spectrogram plot for the asymmetric configuration has been shown in Figure 6.31 C, where it can be clearly seen that in addition to the harmonic series of structural modes, additional vibrations were present within the system that have been shown by the shades of yellow.

Lift and thrust force measurements along with aerodynamic power for the asymmetric configuration have

been displayed in Figure 6.32A. The asymmetric configuration has shown to require more power, which is due to the additional stroke angle travelled by the wings. The power required for total force which consists of contributions from the system and flow dynamics, is larger for the asymmetric model, which in this case is as mentioned due to stroke angle travelled but moreover created by the friction forces acting on the slider when moving along its vertical guide slot. The thrust peak of the upstroke motion is larger than the peak of the downstroke motion, this result seems to display the opposite result of what was seen for the symmetric configuration thrust data. Similar to the symmetric configuration the lift curve resembles a skewed sinusoidal wave due to the coupled wing motion, where the start downstroke for both demonstrates a lagging effect in lift force generation from the reduced gradient opposed to the gradient seen in Figure 6.30 for a flapping only motion during start downstroke.

All three moments were analysed for the asymmetric configuration for a complete stroke cycle and the averages are all presented in Figure 6.32B. As expected differences evidently exist on both sides as this was prescribed on the model before the test, and such a design was created to promote overall averaged differences. The rolling moment for such a configuration may not necessarily have a large distinction due to the asymmetries of flapping stroke and AOA on both sides. The rolling moment curves for the vertical and horizontal (see Figure 6.33) flapping planes have differences in the size of amplitude and slope peaks during the stroke reversal phase. When the model was flapping in the horizontal plane it experienced much more friction and the wing rotation also had some differences (see Figure 6.29) this directly affects the rolling moment. The linkages became tighter as the vertical slider was offset from the line of symmetry and inertial forces were applied to the wing arms, this became apparent when the asymmetrical configuration required more power. Furthermore the tightness in linkages would also have some effect on the AOA when the model is tested by vacuum conditions. The amalgamation of these differences are the reasons for the differences found, in addition to the additional vibrations this model produces in the horizontal position. Further during the total force tests the asymmetrical configuration was found to draw much more power when flapping along the horizontal plane in comparison to the vertical plane. Aside from this the curves do start and end travelling in the same directions and have similar values at these positions. Moreover, the most important result is the cyclic average which for both tests is near to zero. Before analysing a complex coupled motion, consider a singular flapping motion of both sides where the right side has a larger stroke amplitude than the left side. Now during the first half of the stroke, as one side has a larger flapping amplitude than the other, a moment should be produced, where the model rotates in the anti-clockwise direction (model

would rotate downwards on the left side and upwards on the right side). However, as the second half of the stroke completes, the imbalance generated from the first half stroke will now become neutralised as the model rotates back to its equilibrium position. The general moment in such a scenario is created from the distinction in force production of both sides. Thus, it can be said that throughout a complete stroke cycle the resultant averaged moment will be zero. With the introduction of an AOA for both sides would alter the situation, but if the AOA is controlled and exactly symmetric for both up and down strokes, then the overall averaged rolling moment for the cycle should result in zero as the difference in lift produced in the downstroke is counter balanced with the difference in lift produced during the upstroke motion. For a passive AOA, the dynamics becomes more complicated as difficulties arise in producing such symmetrical wing rotations especially in a time dependent manner. Nonetheless, so long as the AOA amplitude during the downstroke is similar to the AOA during the upstroke, the average rolling moment generated should be small. Although time dependent asymmetries exist as expected for this asymmetric configuration as shown in the data plot, the overall averaged rolling moment for the complete cycle is slightly below zero, which proves to be a sufficient result when exploiting passive wing rotation. The pitching moment generated lies prominently on the positive half of the moment axis, producing a net averaged positive pitching moment, which consists of a contribution created by the distance from the central axis of the sensor to the position of thrust force production.

Finally, the yawing moment unsurprisingly has time dependent asymmetries where the curve lies more prominently on the negative half of the moment axis which results in an overall negative yawing moment. The moments about the axes on the sensor are positive when acting in the anti-clockwise direction, thus if a negative yawing moment is created this means that the moment about the  $T_z$  axis was acting in the clockwise direction, overall resulting in the right wing moving forwards per cycle according to the measurements. Correctly so, as the right side had a larger stroke amplitude and AOA opposed to the left side, a negative (clockwise acting) yawing moment was created producing a successful result for this configuration as its asymmetrical motion results in an imbalance around the yawing axis. This effectively demonstrates that when the model utilises its asymmetric capability, a directional turn with the leading edge moving forwards on one side will be executed. Further tests can be performed by producing a symmetric stroke amplitude for both sides and creating a larger wing rotation for one side (by increasing the gap of exposed polyester) to determine the effect of the moment created by the difference in AOA only. However, such a test may only be worthy if differences in AOA can be created during flight like using the FRAP method. If changes

cannot be implemented to the vehicle during flight then such functionalities may not be suitable features for this type of vehicle. As the type of flapping configuration can be actioned during flight from symmetric to asymmetric as explained previously in this report, such a function is suitable as well as the FRAP method which can be executed during flight with the addition of a very lightweight hinge like feature placed near the flapping arm.

Both configurations showed very similar trends and peak amplitudes in the lift force direction, where noticeable distinctions are seen at the start and end of the cycle due to differences in the AOA from both sets of data (shown in Figure 6.32C). The thrust peaks as mentioned previously show largest peaks on opposite strokes for both configurations as the symmetrical configuration has a larger AOA, this largely developed a greater thrust peak due to large wing rotational accelerations. On the upstroke both the lift peak and thrust peak for the asymmetric configuration line up well, thus the large pressure acting on the wings upper surface as it moves through this upstroke creating a peak in negative lift contributes to the peak in thrust force where the wings on both sides have large enough AOAs to generate such a peak thrust force. Compared to the lift force curves, the thrust curves seem fairly out of phase from one another, where the time history data for the thrust force of the symmetric configuration is lagging behind. When closely examined this was due to the tests in the vacuum chamber where the inertial curve for this test lagged behind the asymmetric inertial data. The peak wing rotational angles for both configurations also presented a slight phase shift, which is primarily due to the rate of wing rotation.

The aerodynamic power required to sweep the wings through the air differed for both models as shown in Figure 6.32, where the asymmetric configuration was more power demanding than its counterpart configuration, which consequently affected the ratio of aero power required to average thrust force output. In general, for a very similar thrust force output the asymmetric configuration required more power, which has been elaborated upon previously in this section. From the comparison of moment data, it can be seen that both configurations produce positive pitching moments which is moderately larger for the asymmetrical configuration. The symmetric configuration encounters zero yawing moment and near zero rolling moment, which overall states that when the model is in this configuration the only turning effect which it will experience will be due to the pitching moment. As for when the model is in the asymmetric configuration, a small rolling moment and large yawing moment will be experienced, creating a turning effect with the leading edge moving forwards, accompanied by a pitching moment.

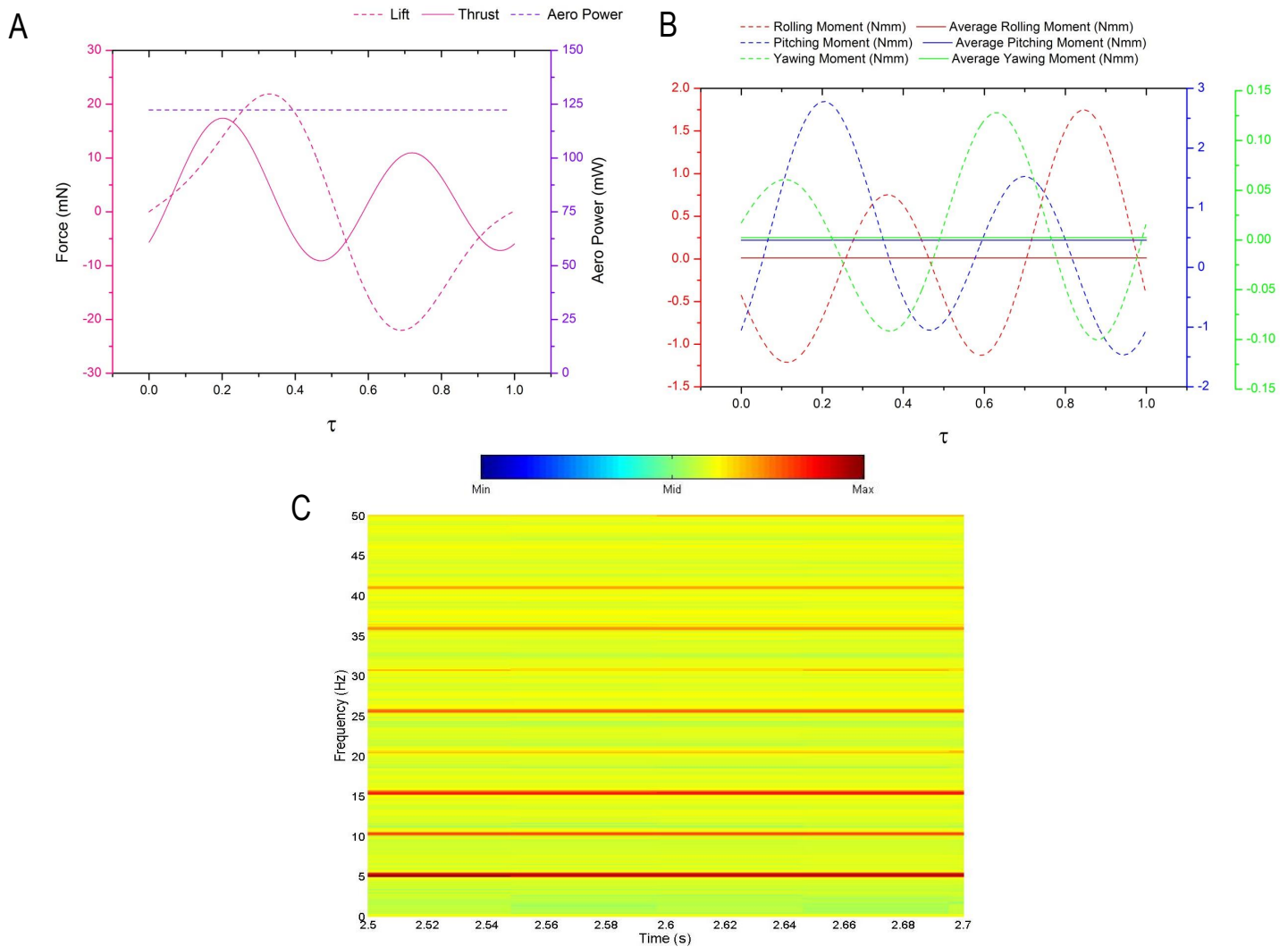


Figure 6.31: *Flapping & Rotating Wing Measurements of 60 mm Wings (WT<sub>4</sub>) for Model 2; A: Symmetric Configuration Force & Power Data, B: Symmetric Configuration Moment Data, C: Spectrogram for Vertical Axis in Air for Asymmetric Configuration. Colour Bar Represents Size of Amplitude. UI: M2-FR-WT<sub>4</sub>-S-V & M2-FR-WT<sub>4</sub>-A-V*

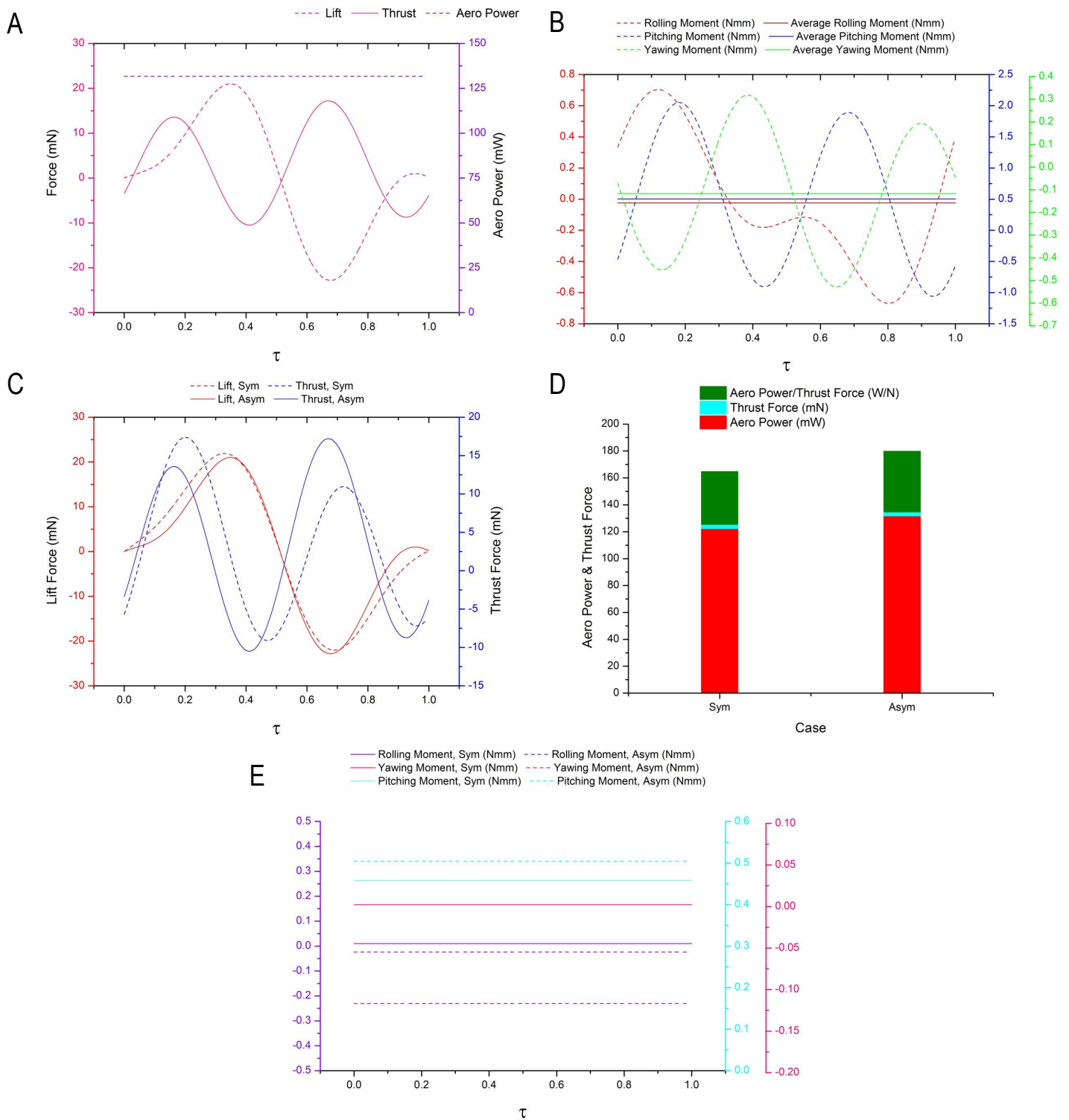


Figure 6.32: Flapping & Rotating Wing Measurements of 60 mm Wings (WT4) for Model 2; A: Asymmetric Configuration Force & Power Data, B: Asymmetric Configuration Moment Data, C: Comparison of Lift & Thrust, D: Aero Power & Thrust Force Relation, E: Comparison of Moments. UI: M2-FR-WT4-S-V & M2-FR-WT4-A-V

Model 2 in its asymmetric configuration was tested when placed in a horizontal hovering mode flapping its wings at 5 Hz, where the lift and thrust axis are acting in the vertical and horizontal directions respectively. Lift, thrust and aero power measurements are shown in Figure 6.33A, where the lift force seems to produce fair sized peaks for both down and up strokes, which lies prominently in the positive half of the force axis, demonstrating an average lifting force in the upwards direction. The thrusting force more or less lies near to zero, producing near to equivalent peaks of opposite signs on both half strokes. The aerodynamic power required is much less in this case compared to when the model was positioned with a flapping stroke plane in the vertical direction, this may have been due to the differences in AOA and larger stroke amplitude travelled when positioned at 0 degrees inclination.

Moment data (Figure 6.33B) in this stroke plane presented the same behaviour as was seen for a vertical stroke plane, where the pitching moment lies more on the positive side, resulting in a stroke averaged positive pitching moment. The rolling moment data averages near to zero lying on the negative side of the axis similar to the previous result. If the rolling moment data was exactly zero, then asymmetries between the down and upstrokes would be seen to have become negligible. Nonetheless, as the rolling moment data found in the tests for both flapping planes are close to zero when compared to the pitching and yawing moments, they can be seen as negligible. As the right side of the model continues to travel with the larger stroke amplitude as prescribed, the yawing moment as expected shows time dependent asymmetries which average out on the negative half of the moment axis generating a similar sized yawing moment when compared to flapping in a vertical plane. The overall negative yawing moment demonstrates that rotation around the yawing axis is in the clockwise direction, stating the side with the larger amplitude as before will have a leading edge moving forwards effect. The small difference in the size of yawing moment generated for the two different stroke planes is due to the differences in peak AOA, and also to generate a force pointing ahead of the leading edge would require the wing to have an AOA. When the wing is flapping in the horizontal plane for a brief period the AOA is zero, which would affect the overall force created in the direction ahead of the leading edge of the wing. When flapping in the vertical direction with a passive wing rotation under a gravitational effect, the AOA of the wings decreases rapidly moving to a negative AOA, this dropping effect meant that the wings would continue to have an AOA throughout its motion aiding in the generation of yawing moment.

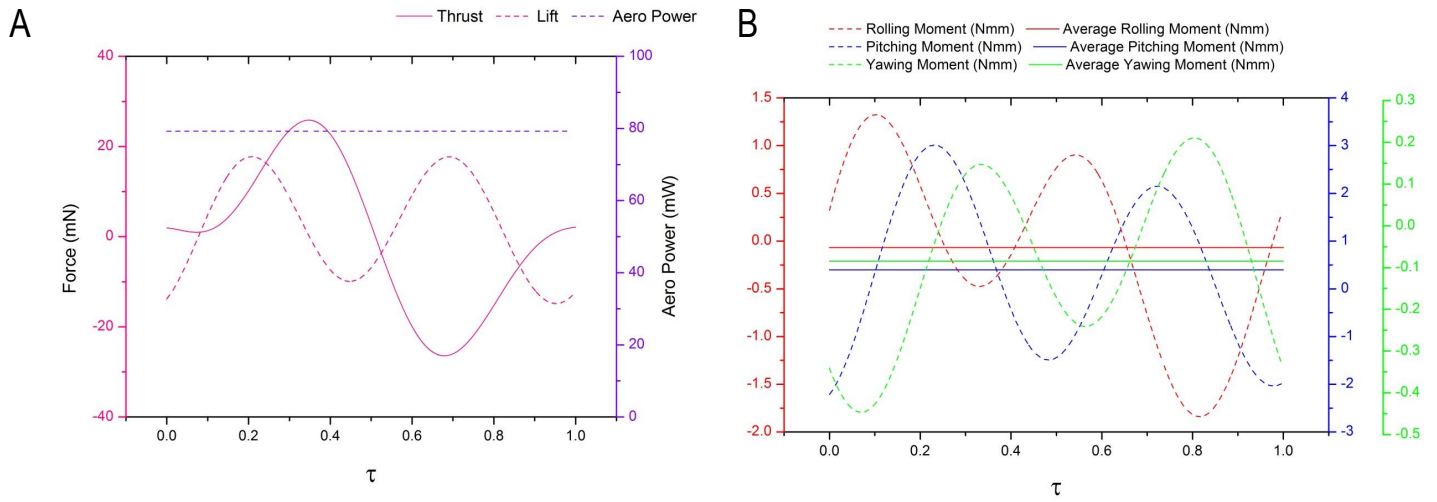


Figure 6.33: *Flapping & Rotating Wing Measurements of 60 mm Wings (WT<sub>4</sub>) for Model 2 in Hovering Position; A: Asymmetric Configuration Force & Power Data, B: Asymmetric Configuration Moment Data.*  
 UI: M2-FR-WT<sub>4</sub>-A-H

## Chapter 7

# Conclusion and Recommendations

The final chapter draws a close to the work conducted in this research programme whilst summarising and concluding on the results obtained from the various investigations performed. Experimental and computational methods were exploited to analyse the aerodynamics of flapping wing motion with a dynamically passive AOA wing motion via an elastic material which is currently in operation for various other FWMAVs. The fundamental aspect of performing such studies was to understand, further investigate and critically analyse the effects certain wing motions have on the force and moment generations per cyclic motion as well as the power required to perform such kinematic motions. Aside from this, the design of an FWMAV was also thoroughly scrutinised to develop a model which can be exploited for experimental purposes, with the capability of being downsized significantly for future flight applications in addition to being cost effective in terms of materials and time required to construct such models. Following the conclusion of the tests conducted and results obtained, recommendations will be provided for future research related to this field of engineering some of which have been discussed in detail throughout this thesis.

### 7.1 Conclusion

In the present study, various disciplines and methods were exploited to investigate the aerodynamics of insect inspired flapping wing flight. It is paramount to note that various extensive research studies had

to be conducted prior to the design of the FWMAV and the experimental rig. In furtherance, the entire experimental laboratory had to be assembled which meant that a substantial amount of equipment as well as the assembly of all the components was needed to provide an operable experimental FWMAV rig. The initial design of the FWMAV led to the creation of a second model which has the ability to successfully perform asymmetrical flapping for which various types of experimental measurements were taken.

Experimental studies were conducted to analyse the different types of wing motion such as flapping only, flapping with wing rotation and flapping with AP wing rotation as a dynamic AOA was prevented during the downstroke motion. In furtherance to the aforementioned both models were investigated upon to determine the effects of asymmetrical wing motion on lift force production in comparison to symmetrical wing motion. Experimental data was captured via force & moment measurements, power readings and images of the wing kinematics.

Computational explorations were conducted for hovering flight mode in a three dimensional numerical domain with the capability to simulate a moving boundary. A validation study was commenced initially to determine the accuracy of the computational solver before performing numerous further cases which compare the rotational duration and location along the chord of the wing. A simulation was also conducted for the 60 mm wing (WT4) performing a flapping motion in a stationary fluid condition which can be directly compared to a flapping wing experiment in this thesis.

This thesis has various novel contributions such as the design, development and analysis of two micro air vehicles, where the secondary model has the ability to perform two types of flapping modes namely symmetrical and asymmetrical motions. Experimental comparisons of force, moment and power measurements for symmetrical and asymmetrical motions were examined. Experimental measurements for boundary effects present in the near vicinity of the wings for various types of wing motions were investigated. A different type of wing motion labelled as Flapping and Rotation with Asymmetric Pitching (FRAP) was introduced and experimentally tested for use in future flight worthy vehicles. Also it can be said that passive wing pitching produced insufficient lifting forces in comparison to the weight of the test models, especially when significant inertial forces are continuously present. Lastly, a complete set of simulations were performed to compare force, moment and power measurements for various axial locations of wing rotation and the rates of rotation.

Flapping only experiments were conducted using model 1 and the 47 mm span wings (WT3). The maximum and minimum aerodynamic forces are produced at mid-down and upstrokes for which a sinusoidal curve is formed per cycle. The peak aerodynamic force generated per stroke grows, which in effect means that the peak-peak force enlarges as the flapping frequency increases. As expected the difference in aerodynamic force generated when flapping at 3 Hz and 10 Hz is considerable and this relation continues for the power required measurements as well. More specifically, the power required per frequency of measurement increases almost parabolically for tests in both air and vacuum conditions. Furthermore, the power demanded by the mechanical system per force output for each set of flapping frequency seems to be reasonable as no single frequency set demands extreme amounts of power when compared to its force output.

Further flapping only experiments with 60 mm span wings (WT4) attached to the model which had a constant chord-wise length for a significant span length were exploited in near wing, stationary boundary experiments. In such tests, the wings would continue to move dynamically as prescribed by its motor mechanism whilst a stationary wall is present in the wings proximity, acting as a ground effect when horizontal or trailing edge wall effect when positioned vertically. In the latter scenario, the flow around the wing is continually influenced by the stationary wall throughout the wings periodic motion, thus in such a situation the flow dynamics are more affected as opposed to when the boundary is utilised in a ground effect configuration. It was found that all the boundary tests produced a larger aerodynamic force when compared to the flapping test with no boundary present, and the boundary which created the smallest effect in aerodynamic force generation was for the ground effect case. The greatest aerodynamic peak forces were generated when a TE wall was present behind both wings, as in such a case the boundary was placed very close to the wings trailing edge, having the greatest effect on the near wing fluid dynamics which will effectively alter the aerodynamic force measurements. Furthermore, the aerodynamic power required per test in reference to the force output generated seems reasonable for all the tests with no outliers existent. Thus, if more power is demanded for specific tests such as when a TE boundary is present or when TE+GE boundaries are present, the output aerodynamic force generated for these tests is relatively larger as well, thus the overall aerodynamic power required in comparison to the aerodynamic force output has a consistent relation.

The addition of an elastic material located near the root of both wings allowed the wings to pitch passively under the effect of aero and inertial loadings whilst the mechanism was dynamically actuated by a single motor. Boundaries were positioned in the proximity of the wings when dynamically travelling through the

enforced arc-like motion with a passive AOA free to rotate in the positive and negative directions. The greatest lift force peaks were reported when stationary walls were placed behind the trailing edge of both wings. The lift force peaks generated for both strokes were greater when stationary boundaries were present in the proximity of the wings motion as opposed to when no boundaries were utilised. The greatest thrust force was generated for the combined boundary effect, which was found to be significantly larger than the base case. Moreover, all the cases which had a boundary present as the wings performed their coupled motion generated more thrust than the base case, and as a direct result the pitching moments for the boundary cases were also greater than the base case. Interestingly, an overall positive thrust force is generated as a consequence of the wing pitching motion that produces two large peaks for all cases during a complete cycle. The aerodynamic power required for all the boundary tests was found to be larger than that required for the base case. More specifically, the largest aerodynamic power drawn was when walls were placed very close to the trailing edge of both wings. Interestingly, the smallest ratio of aerodynamic power required to thrust force generation was obtained when a dual boundary arrangement was placed in the proximity of both wings, as the thrust generated in this test was found to be the largest of all the cases investigated. The body of the FWMAV was rotated about 90 degrees to position the model in its hovering mode where the wings travel through a horizontal stroke plane performing the aforementioned coupled wing motion. The overall lift force generated for the base case and ground effect boundary case were positive with large peaks present in the positive half of the lift axis. The ground effect base enhanced lift force production significantly, and as a result the pitching moment generated for this boundary case was also larger than the base case. The enhanced lift production for the boundary case was derived at the expense of consuming more power during the wings motion, but the ratio of aero power to lift force generated was lower for the boundary case.

An optimised form of wing motion amalgamating the aforementioned flapping only and flapping with wing rotation was developed and tested to investigate the resultant forces and moments generated per periodic wing motion. As the wing pitches through the upstroke only the thrust force may be affected as a sufficient sized AOA is required to generate enough thrust force per cycle. Analysing the cyclic data for lift force it was found that the downstroke generated a greater aerodynamic peak force than the upstroke. As the downstroke produced a greater lifting force a successful result was acquired and this proved that the amalgamated design is performing its primary role appropriately where the downstroke can be exploited as the power stroke. This form of stroke is required in many forms of flight which would appreciably assist vertical force generation, in addition to prolonging the quality of the elastic material exploited for wing pitching. The greatest

aerodynamic lift force generated during the downstroke was found when a rigid stationary boundary was positioned very close to the trailing edge of the wings and furthermore, this boundary effect provided the largest average lift force produced for the wings cyclic motion. This average lift was approximately four times greater than that found for the base case where no boundary existed in the wings proximity at all stages of the wings motion. When analysing the average thrust force produced per cycle it was found that the combined boundary of the trailing edge wall and ground effect base generated the greatest horizontal force, which consequently lead to the largest production of average pitching moment per cycle as well. All the boundaries required more aerodynamic power than the base case, the greatest being when walls were located very close to the TE of both wings. Consequently, the greatest ratio of aerodynamic power required per thrust force output was found for the aforementioned boundary effect as well.

Model 2 was tested in both of its configurations to determine whether the asymmetric motion has any reduction in lift force generation opposed to its symmetric configuration. Overall the model had very similar lift force curves throughout a single cycle, but when in the asymmetric configuration slightly more power was consumed as the wings travel through a larger stroke amplitude. As similar lift force curves were found in the comparison, it can be concluded that the asymmetric configuration with a flapping only motion does not cause any considerable losses in lift force production.

Following the simplified flapping only tests, model 2 was set-up to perform a flapping with wing rotation motion in both of its configurations. Similar to the previous analysis, it was imperative to analyse whether any lift force reduction is caused by the asymmetric configuration. Comparisons were made by evaluating the F/T measurements and aerodynamic power required by both the configurations to generate the respective aerodynamic forces recorded. The thrust force generated by the asymmetrical configuration is greater than that produced when in a symmetrical configuration whilst both curves create larger peaks on opposite strokes due to the differences in wing motion. The cyclic lift force produced similar peaks for both strokes as both curves followed one another well, which is a satisfactory result as no significant lift is lost when the configuration is altered. However, the asymmetric configuration did seem to draw more aerodynamic power as the wings travelled through a larger overall stroke amplitude. Furthermore, the power consumed when analysing total force was also greater for the asymmetric configuration which is partly due to the larger overall stroke amplitude but predominantly due to the greater frictional forces experienced by the vertical slider when translating along the vertical guide slot. This is an aspect which requires further work and was discussed

in this thesis. As a result of the larger consumption of power for the asymmetric configuration, the ratio of aerodynamic power to thrust force generated was greater than that found for the symmetric configuration. Pitching moments were generated when the model was in both configurations which was found to be larger for asymmetric wing motion, and more importantly a yawing moment was generated when the model was actuated in its asymmetric configuration. This successful result meant that the model can manoeuvre or even regain stability when its orientation is affected for example by gust winds. Subsequently the body was rotated through 90 degrees to position the model in hovering mode where the wings stroke plane is now along the horizontal plane. The lift force curve is made up of four peaks and the average force generated is positive, thus when the model is in hovering mode and in a asymmetric configuration an overall vertical force is obtained. Furthermore, similar to the vertical stroke plane moment generation, both pitching and yawing moments are generated when cyclically averaged.

Simulations with a drosophila wing were conducted under a hovering condition where the wings swept along the horizontal plane with a coupled motion which was modelled into the solver. The results showed good agreement to experimental and computational data obtained by other researchers working in this field, this comparison also validated the computational methodology. A comparison of the different types of grids studied namely DVID and SVID demonstrated that both produced similar results, but the former method would provide more accuracy due to its consistent grid quality in the proximity of the wing.

Following the validation of the simulation method, a rectangular wing was placed within the numerical domain to perform a similar motion to the drosophila wing with changes applied to the rate of rotation and the location of wing rotation. A total of 12 cases were compared in terms of lift force, horizontal force, moments, aerodynamic power required and limit cycles. Symmetrical wing kinematics were prescribed for all the cases, which lead to identical time history data for both half strokes. The vortex dynamics were compared for all three rotational durations, for which it was found that the when the wing rotated at a faster rate the vortex structure was tighter and its diametral growth towards the wing tip was less, when compared to the growth for the slowest rotational duration. Furthermore, the tip vortex when  $\zeta = 1.1s$  illustrated a more conical formation opposed to that visualised when  $\zeta = 3.3s$ , in addition for the faster rotational duration the vortex seemed to be closer to the wings surface.

For all the rotational positions it was found that the lift force was greatest when  $\zeta = 1.1s$  which declined as the rotational duration increased to  $\zeta = 3.3s$ . As the rotational location was varied, it was found that

for all the rotational durations the greatest cyclic lift force was found when the wing pitched about the leading edge spanwise axis which declined as the rotational location moved chord-wise downwards towards the mid-chord. The maximum average lift force per cycle was generated when the wing pitched about the leading edge axis with the fastest rotational duration ( $\zeta = 1.1s$ ). Subsequently, at this rotational duration of  $\zeta = 1.1s$  the average cyclic lift force declined almost linearly as the rotational location moved further down the chord from the leading edge towards mid-chord. Furthermore, as the rotational location is held constant, the average lift force declines linearly as the rotational duration increases from  $\zeta = 1.1s$  to  $\zeta = 3.3s$ . The minimum average periodic lift force produced occurs when the wing pitches about its spanwise axis located at mid-chord with the slowest rotational duration.

Although the net horizontal force throughout a cycle is equal to zero, an average of a single stroke was calculated to analyse which motion generates the greatest horizontal force per stroke. The greatest average horizontal force is produced for the slowest rotational duration which applies for all the rotational locations explored along the chord, this declines as the rotational duration decreases towards  $\zeta = 1.1s$ . In the instance when the rotational duration is held constant, the greatest horizontal force is generated when the wing is pitched about the leading edge spanwise axis. The force decreases as the rotational location moves chord-wise downwards towards the mid-chord which produces the lowest average horizontal force for all rotational durations. The maximum average horizontal force was generated when the wing rotated about the leading edge with the slowest rate of rotational duration, this force then declined linearly as the rotational duration was held constant and the rotational location moved towards the mid-chord from the leading edge. As the rotational location was now held constant a gradual decline in the average horizontal force produced was found as the rotational duration decreased towards  $\zeta = 1.1s$  from  $\zeta = 3.3s$ . The minimum average horizontal force produced for the downstroke motion was obtained when the wing pitched about the mid-chord spanwise axis with a rotational duration of  $1.1s$ .

Similar to the horizontal force the pitching moment was averaged for a single stroke as the net moment generated throughout a cycle is zero. During the downstroke, a moment will be generated which will balance out at the end of the upstroke and equilibrium will be regained. More precisely, the moment generated is actually momentary lasting a specific amount of time dependent on the flapping frequency. The largest positive pitching moment was generated when the wing travelled through its fastest rotational duration of  $\zeta = 1.1s$  which applies for all the rotational locations previously mentioned, and as the rotational duration

increases the size of the pitching moment decreases. When the wing rotates about the mid-chord spanwise axis, the pitching moment generated is much smaller and even becomes negative where rotation is acting in the opposite direction. Whilst the rotational duration is held constant and the location of wing pitching is altered, it was found that the greatest pitching moment is produced when the wing pitches about its spanwise axis at the leading edge, and as the pitching location moves towards the mid-chord from the leading edge the size of the moment decreases, where it even becomes negative. The maximum pitching moment is obtained when the wing pitches about the leading edge with a rotational duration of 1.1s, the pitching moment then declines with a steep linear attitude as the rotational duration is held constant and the rotational location is moved chordwise downwards from the leading edge towards the mid-chord. A small gradual decline in pitching moment is also noticed when the rotational duration increases from 1.1s to 3.3s whilst the wing pitching position is held constant about the leading edge. Lastly, the minimum pitching moment which rotates in the opposite direction is generated when the wing pitches about the mid-chord whilst its rotational duration is the slowest tested value of  $\zeta = 3.3s$ .

Lastly, the aerodynamic power required for the wings to sweep through their prescribed kinematic motion was calculated, where it was found that when  $\chi = A, B$  &  $C$  the greatest average aerodynamic power required occurred at  $\zeta = 3.3s$  which declined as the rotational duration decreased. However, when the wing is pitched about the leading edge the greatest average aerodynamic power required is when  $\zeta = 1.1s$  followed by  $\zeta = 3.3s$ . For each rotational duration the greatest average aerodynamic power required was found when the wing pitched about the leading edge and this declined as the pitching location moved chordwise downwards from the leading edge towards the mid-chord. The greatest aerodynamic power is drawn when the wing pitches about the leading edge whilst pitching at the fastest rotational duration, this gradually declines as the pitching location is held constant and the rotational duration is increased towards 3.3s. As the rotational location moves chordwise downwards from the leading edge and the wing rotational duration is held constant as 1.1s, the average aerodynamic power required declines precipitously with a linear path. Lastly, the smallest aerodynamic power is required when the wing rotates about the spanwise axis located at the mid-chord with the smallest rotational duration of 1.1s.

A simulation was also performed for the 60 mm wing (WT4) performing a flapping motion at 5 Hz to compare the vertical force measurement in a time dependent manner to the experimental data. The data curves for the experimental and computational results follow the same trend, with some distinctions. It is also worth

noting that a comparison in this manner is quite complex as the sensor exploited to acquire measurements of the experimental model is located a distance underneath the model, thus considerable vibrations are read by the sensor which contaminate the measurements acquired and although filtering is carried out, not all the vibrations can be filtered.

The FWMAVs designed and thoroughly tested in this research programme have demonstrated their applicability as part of an experimental rig which can be considerably downsized for future flight applications. The linkage mechanism was evaluated experimentally and computationally whilst examining the small input deflection and the large output angular motion. The results presented a very good relation between the two which meant that the linkage mechanism design operated well physically and the manufacturing along with assembly of the pieces was conducted accurately. Furthermore, a highly admirable characteristic is the small linear deflection applied to the vertical plunger in order to alter the type of flapping from symmetrical to asymmetrical which expands the forms of flight this FWMAV is capable of performing.

Overall, to produce a FWMAV which can fly autonomously would require a lot more research which would initially begin by downsizing and reducing the weight of model 2 presented in this thesis, and performing additional experiments with the incorporation of the second actuator for user controlled flight mode change. As previously mentioned, a more efficient and powerful motor would be needed, in addition to a Li-Po battery which the model would carry on-board. The wings would need to become lighter in which case they would become more flexible and a thinner mylar piece can be used for passive wing rotation. Further research in terms of stability, control, fluid dynamics analysis and assisted flight tests would need to take place to optimise the model in the hope to achieve autonomous flight.

## 7.2 Recommendations

The following are some recommendations for future research in this field of engineering which can be carried out experimentally and/or computationally to evaluate the aerodynamics of insect inspired flapping wings.

- Further experimentations should be performed exploiting the FR and FRAP methods to obtain greater pitching angles whilst attempting to have a somewhat large constant AOA for a considerable duration to augment lift forces when positioned in the horizontal mode. Such implementations would augment the thrust

force generation when the wings are flapping through a vertical plane.

- Flow visualisation studies should be conducted on the passively rotating flapping wings to understand the vortex dynamics whilst measuring the time dependent forces and moments.
- Downsizing the FWMAVs reported in this thesis would move them a step closer to being flight worthy FWMAVs in terms of size and mass which are two key characteristics. Although further experimental tests will need to be conducted, the FWMAVs can be tested along a vertical and horizontal guide to evaluate its lift and thrust force generation.
- Further experiments can be performed using the asymmetrical method of the FWMAV design to investigate the effects on torque generation when rigid stationary boundaries are introduced in the proximity of the wings.
- Improve the mechanical mechanism of model 2 namely the vertical slider (plunger) as large frictional forces are present as determined from the experimental results.
- Add lightweight hinges to the wing arms to alter the type of wing motion during flight and determine the effect this has on the F/T measurements during the transition phase of wing motion. Furthermore, add a lightweight linkage mechanism including an actuator to dynamically alter the type of flapping motion from symmetric to asymmetric and determine the effect this has on flight F/T measurements.
- Simulations can be performed for some of the base experiments detailed in this thesis to understand the time dependent vortex dynamics throughout a cyclic period. Furthermore, boundaries can be positioned in the near vicinity of the dynamic wings to obstruct the flow dynamics surrounding the wings. Lastly, asymmetric wing motion simulations as performed in the experiments can be simulated to understand the vortex dynamics of the highly unsteady flow as well as analyse the moments generated from the wing motion kinematics.
- Conduct further experiments where a combination of FR and FRAP motions are incorporated onto the experimental rig at the same time for each side of the model to determine the moment generated from this asymmetrical motion. The active hinge can make this a realistic option of wing motion, thus experimentations should be performed to determine the effect of this dual motion.
- A stationary boundary can be placed at the leading edge of the wings when dynamically moving to determine the effect this has on the forces produced and the vortex dynamics via flow visualisation as the

LEV provides significant lift force enhancements which are imperative to insect flight.

- Coupled simulation in the form of FSI to determine the effect of the stationary boundary on the very flexible membrane of the wings, which would evidently deflect in a different manner if boundaries are present in their proximity.
- Further simulations can be performed on the rectangular wings to determine the effect of a stationary boundary when the wings are travelling with the variable parameters studied in this thesis. Furthermore, larger AOA's more specifically 40-50 degrees can be studied to determine the differences found in the forces, moments and power evaluated in this research.
- Experimental three dimensional flow visualisation can be utilised to study the vortex dynamics when a stationary boundary is in the proximity of the wings and compare the differences when a boundary is not present, or when the boundary has a rough surface. Furthermore, various shapes of boundaries and surface textures can be placed in the proximity of the active wings to analyse the F/T measurements and flow dynamics.
- Experimental studies can be conducted in the wind tunnel when the model performs FR, FRAP and asymmetric wing motions. In addition, a ground effect boundary can be introduced to model an FWMAV in forward flight with a ground effect acting in the proximity of the wings. Lastly, flow visualisation can be carried out to study the vortex dynamics in such cases.

# Bibliography

- [AeroVironment BBC] [www.bbc.co.uk/news/world-us-canada-12513315](http://www.bbc.co.uk/news/world-us-canada-12513315)
- [AeroVironment Inc A] [www.avinc.com/uas/adc/pointer](http://www.avinc.com/uas/adc/pointer)
- [AeroVironment Inc B] [www.avinc.com/uas/adc/blackwidow](http://www.avinc.com/uas/adc/blackwidow)
- [AeroVironment Inc C] [www.avinc.com/uas/](http://www.avinc.com/uas/)
- [AeroVironment Inc D] [www.avinc.com/downloads/Wasp III.pdf](http://www.avinc.com/downloads/Wasp%20III.pdf)
- [AeroVironment Inc E] [www.avinc.com/downloads/WaspAE.pdf](http://www.avinc.com/downloads/WaspAE.pdf)
- [AeroVironment Inc F] [www.avinc.com/resources/press release/aerovironment develops worlds first fully operational life size hummingbird](http://www.avinc.com/resources/press%20release/aerovironment%20develops%20worlds%20first%20fully%20operational%20life%20size%20hummingbird)
- [AeroVironment Inc G] [www.avinc.com/media gallery/](http://www.avinc.com/media%20gallery/)
- [Alexander 2002] Alexander, D., 2002. Natures flyer's. Johns Hopkin's University Press
- [Anderson 1986] Anderson, J.D., 1986. Fundamentals of Aerodynamics. McGraw Hill International Editions
- [Anderson et al. 2011] Anderson, M.L., Sladek, N.J., Cobb, R.G., 2011. Design, Fabrication, and Testing of an Insect-Sized MAV Wing Flapping Mechanism. 49th AIAA Aerospace Science Meeting, AIAA 2011-549
- [Anderson 2011a] Anderson, M.L., 2011. Design and Control of Flapping Wing Micro Air Vehicles. PhD Thesis
- [Ansys Fluent Manual] Ansys Fluent. Fluent Manual and User Guide

- [Aono et al. 2007] Aono, H., Liang, F., Liu, H., 2007. Near and Far Field Aerodynamics in Insect Hovering Flight: An Integrated computational Study. *The Journal of Experimental Biology* 211, 239-257
- [AV media gallery] [www.avinc.com/media gallery/](http://www.avinc.com/media_gallery/)
- [Avadhanula et al 2003] Avadhanula, S., Wood, R., Steltz, E., Yan, J., Fearing, R., 2003. Lift Force Improvements for the Micromechanical Flying Insect. IEEE, International Conference on Intelligent Robots and Systems
- [ATI] [www.ati-ia.com/Library/documents/ATI FT Catalog.pdf](http://www.ati-ia.com/Library/documents/ATI_FT_Catalog.pdf)
- [ATI-Staff] Personal Discussion
- [Azuma 2006] Azuma, A., 2006. *The Biokinetics of Flying and Swimming*. Second Edition. AIAA
- [Berman et al. 2007] Berman, G. J., Wang, J. Z., 2007. Energy minimizing kinematics in hovering insect flight. *Journal of fluid mechanics*, Vol. 582, pp. 153-168
- [Beta CAE] Beta CAE  $\mu$ ETA Post Processor User Guide
- [Birch et al. 2001] Birch, J. M., Dickinson, M. H., 2001. Spanwise Flow and The Attachment of The Leading Edge Vortex on Insect Wings. *Nature*, Vol. 412
- [Birch et al. 2003] Birch, J.M., Dickinson, M.H., 2003. The Influence of Wing-Wake Interactions on the Production of Aerodynamic Forces in Flapping Flight. *The Journal of Experimental Biology*, 206, 2257-2272
- [Birch et al. 2003] Birch, J. M., Dickson, W. B., Dickinson, M. H., 2003. Force Production and Flow Structure of The Leading Edge Vortex on Flapping Wings at High and Low Reynolds Numbers. *The Journal of Experimental Biology* 207, 1063-1072
- [Bolsman et al. 2008] Bolsman, C.T, Goosen, J.F.L, Van Keulen, F., 2008. Insect-Inspired Wing Actuation Structures Based on Ring-Type Resonators. *Active and Passive Smart Structures and Integrated Systems*. Proceedings of SPIE Vol. 6928
- [Bolsman et al. 2009] Bolsman, C.T., Goosen, H.F.L., Van Keulen, F., 2009. Design and Realization of Resonant Mechanisms for Wing Actuation in Flapping Wing Micro Air Vehicles. 3rd International Conference on Integrity, Reliability and Failure

- [Bolsman et al. 2009] Bolsman, C.T., Goosen, J.F.L., Van Keulen, F., 2010. Design Overview of a Resonant Wing Actuation Mechanism for Application in Flapping Wing MAVs. *International Journal of Micro Air Vehicles*. Vol. 1, Number 4, pp 263-272
- [Croon et al. 2009] Croon, G., Clercq, K., Ruijsink, R., Remes, B., Wagter, C., 2009. Design, Aerodynamics, and Vision Based Control of the Delfly. *International Journal of Micro Air Vehicles*
- [Delfly Website A] [www.delfly.nl/](http://www.delfly.nl/)
- [Delfly Website B] [www.delfly.nl/?site=DIImenu=medialang=en](http://www.delfly.nl/?site=DIImenu=medialang=en)
- [Delfly Website C] [www.delfly.nl/?site=DIImenu=lang=en](http://www.delfly.nl/?site=DIImenu=lang=en)
- [Designation Systems] [www.designation-systems.net/dusrm/app4/wasp.html](http://www.designation-systems.net/dusrm/app4/wasp.html)
- [Dickinson et al. 1995] Dickinson, M., Lighton, J., 1995. Muscle Efficiency and Elastic Storage in the Flight Motor of *Drosophila*. *Science*, ProQuest Engineering Collection
- [Dickinson et al. 1999] Dickinson, M.H., Lehmann, F.O., Sane, S.P., 1999. Wing Rotation and the Aerodynamic Basis of Insect Flight. *Science*. Vol. 284, no. 5422, pp. 5422-1960
- [Dudley 2002] Dudley, R., 2002. *The Biomechanics of Insect Flight (Form, Function and Evolution)* Princeton University Press
- [Ebrahimi et al. 2012] Ebrahimi, A., Mazaheri, K., 2012. Aerodynamic Performance of the Flapping Wing. *Applied Aerodynamics*, Dr. Jorge Colman Lerner (Ed.). InTech
- [Ellington 1984] Ellington, C., 1984. The Aerodynamics of Hovering Insect Flight I-VI, *Philosophical Transactions of The Royal Society of Biological Sciences*
- [Ellington et al. 1996] Ellington, C. P., Van Den Berg, C., Willmott, A. P., Thomas, A. L. R., 1996. Leading Edge Vortices in Insect Flight. *Nature*, Vol. 384
- [Ellington 1999] Ellington, C.P., 1999. The Novel Aerodynamics of Insect Flight: Applications To Micro Air Vehicles. *The Journal of Experimental Biology* 202, 3439-3448
- [Femto-Tools] [www.femtotools.com/index.php?id=applications-lift-fly](http://www.femtotools.com/index.php?id=applications-lift-fly)

- [Ferziger & Peric 2002] Ferziger, J., H., Peric, M., 2002. Computational Methods for Fluid Dynamics. 3rd Edition. Springer
- [Finio et al. 2009] Finio, B.M., Shang, J.K., Wood, R.J., 2009. Body Torque Modulation for a Microrobotic Fly. IEEE International Conference on Robotics and Automation, pp 3449-3456
- [Finio et al. 2009a] Finio, B.M., Eum, B., Oland, C., Wood, R.J., 2009. Asymmetric Flapping For a Robotic Fly Using a Hybrid Power Control Actuator. IEEE, International Conference on Intelligent Robots and Systems, pp 2755-2762
- [Finio et al. 2010] Finio, B.M., Whitney, J.P., Wood, R.J., 2010. Stroke Plane Deviation for a Microrobotic Fly. IEEE International Conference on Intelligent Robots and Systems, pp 3378-3385
- [Galinski et al. 2010] Galinski, C., Mieloszyk, J., Piechna, J., 2010. Progress in the Gust Resistant MAV Programme. ICAS
- [Go Radio Controlled] [www.goradiocontrolled.com/acatalog/interactive-toy-concepts-ify-vamp.html](http://www.goradiocontrolled.com/acatalog/interactive-toy-concepts-ify-vamp.html)
- [Goodman 2003] Goodman, L., 2003. Form and Function in the Honey Bee. International Bee Research Association (IBRA)
- [Grasmeyer & Keennon 2001] Grasmeyer, J., Keennon, M., 2001. Development of the Black Widow Micro Aerial Vehicle. AIAA
- [Grodnitsky 1999] Grodnitsky, D.L., 1999. Form and Function of Insect Wings, The John Hopkins University Press, Baltimore and London
- [Hall et al. 2012] Hall, A., Riddick, J., 2012. Micro-Electro Mechanical Flapping Wing Technology for Micro Aerial Vehicles. Bioinspiration, Biomimetics and Bioreplication. Proceedings of SPIE, Vol. 8339, Article ID 83390L, pp 9
- [Hu et al. 2010] Hu, H., Kumar, A.G., Abate, G., Albertani, R., 2010. An Experimental Investigation on the Aerodynamic Performances of Flexible Membrane Wings in Flapping Flight. Aerospace Science and Technology, pp 575-586
- [Jazar 2010] Jazar, R.N., 2010. Theory of applied robotics: Kinematics, dynamics and control, 2nd Edition. Springer

- [Josephson et al. 2000] Josephson, R., Malamud, J., Stokes, D., 2000. Asynchronous Muscle: A Primer. *Journal of Experimental Biology*
- [Kawamura et al. 2008] Kawamura, Y., Souda, S., Nishimoto, S., Ellington, C.P., 2008. Clapping Wing Micro Air Vehicle of Insect Size. *Bio-Mechanisms of Swimming and Flying*, pp 319-330. Springer
- [Kim et al. 2003] Kim, S.W., Jang, L.H., Kim, M.H., Kim, J.S., 2003. Power-Driven Ornithopter piloted by remote controller. Patent No: US 6550716B1
- [Kramer 1932] Kramer, M., 1932. Die Zunahme des Maximalauftriebes von Tragflügeln bei plotzlicher Anstellwinkelvergrosserung (Boeneffekt). *Z. Flugtech. Motorluftschiff*. Vol. 23
- [Lehmann 2004] Lehmann, F.O., 2004. *The Mechanisms of Lift Enhancement in Insect Flight*. Springer-Verlag 2004
- [Lehmann et al. 2005] Lehmann, F.O., Sane, S.P., Dickinson, M., 2005. The Aerodynamic Effects of Wing-Wing Interaction in Flapping Insect Wings. *The Journal of Experimental Biology* 208, pp. 3075-3092
- [Lentink et al. 2009] Lentink, D., Jongerius, S.R., Bradshaw, N.L., 2009. *The Scalable Design of Flapping Micro-Air Vehicles Inspired by Insect Flight*. *Flying Insects and Robots*. Springer
- [Lentink et al. 2010] Lentink, D., Jongerius, S., Bradshaw, N., 2010. *The Scalable Design of Flapping Micro-Air Vehicles Inspired by Insect Flight*. *Flying Insects and Robots*, 2010, pp 185-205, Springer Berlin Heidelberg
- [Liu et al. 2009] Liu, H., Aono, H., 2009. *Size Effects on Insect Hovering Aerodynamics: An Integrated Computational Study*. *Bioinspiration and Biomimetics*. IOP Science
- [Liu 2009a] Liu, H., 2009. Integrated modeling of insect flight: From morphology, kinematics to aerodynamics. *Journal of computational physics*, 228, pp. 439-459
- [Liu et al. 2008] Liu, Y., Sun, M., 2008. *Wing kinematics measurement and aerodynamics of hovering drone-flies*. *The Company of Biologists*
- [Maeda et al. 2010] Maeda, M., Gao, N., Nishihashi, N., Liu, H., 2010. A free flight simulation of insect flapping flight. *Journal of Aero Aqua Bio-mechanisms*, Vol. 1, No. 1

- [Mazaheri et al. 2011] Mazaheri, K., Ebrahimi, A., 2011. Experimental Investigation on Aerodynamic Performance of a Flapping Wing Vehicle in Forward Flight. *Journal of Fluids and Structures*
- [Miller et al. 2004] Miller, L. A., Peskin, C. S., 2004. A Computational Fluid Dynamics of Clap And Fling in The Smallest Insects. *The Journal of Experimental Biology* 208, 195-212
- [Muren 2008] Muren, P., 2008. Passively stable rotor system for indoor hovering UAS. *Royal Aeronautical Society*
- [Nagai et al. 2008] Nagai, H., Isogai, K., Hayase, T., 2008. Measurement of Unsteady Aerodynamic Forces of 2D Flapping Wing in Hovering to Forward Flight. *International Congress of the Aeronautical Sciences 2008*
- [Nakata et al. 2011] Nakata, T., Liu, H., Tanaka, Y., Nishihashi, N., Wang, X., Sato, A., 2011. Aerodynamics of a Bio-Inspired Flexible Flapping Wing Micro Air Vehicle. *Bioinspiration Biomimetics*. IOP Science
- [Nguyen et al. 2007] Nguyen, Q.V., Park, H.C., Goo, N.S., Byun, D., 2007. A Flying Insect Like Flapper Actuated by a Compressed LIPCA. *International Conference of Robotics and Biomimetics*. IEEE
- [Nguyen et al. 2008] Nguyen, V.Q., Syaifuddin, M., Park, H.C., Byun, D.Y., Goo, N.S., Yoon, K.J., 2008. Characteristics of an Insect Mimicking Flapping System Actuated by a Unimorph Piezoceramic Actuator. *Journal of Intelligent Material Systems and Structures*. Vol. 19
- [Nguyen et al. 2009] Nguyen, Q., Truong, Q., Park, H., Goo, N., Byun, D., 2009. A Motor Driven Flapping Wing System Mimicking Beetle Flight. *International Conference on Robotics and Biomimetics IEEE*
- [Nguyen et al. 2009a] Nguyen, Q.V., Park, H.C., Goo, N.S., Byun, D., 2009. An Insect Like Flapping Wing Device Actuated by a Compressed Unimorph Piezoelectric Composite Actuator. *Intelligent Unmanned Systems: Theory and Applications*. Vol. 192, pp 101-117. Springer
- [Nguyen et al. 2009b] Nguyen, Q.V., Park, H.C., Goo, N.S., Dyun, D., 2009. Aerodynamic Force Generation of an Insect Inspired Flapper Actuated by a Compressed Unimorph Actuator. *Chinese Science Bulletin*. Vol. 54, Issue 16, pp 2871-2879. Springer
- [Nguyen et al. 2010a] Nguyen, Q., Park, H., Goo, N., Byun, D., 2010. Characteristics of a Beetles Free Flight and a Flapping-Wing System that Mimics Beetle Flight. *Journal of Bionic Engineering*

- [Nguyen et al. 2010b] Nguyen, Q., Truong, Q., Park, H., Goo, N., Byun, D., 2010. Measurement of Force Produced by an Insect-Mimicking Flapping-Wing System. *Journal of Bionic Engineering*
- [PAR-Group] [www.par-group.co.uk/engineering-plastics/lexan-polycarbonate-sheet.aspx](http://www.par-group.co.uk/engineering-plastics/lexan-polycarbonate-sheet.aspx)
- [Park et al. 2008] Park, J., Yoon, K., 2008. Designing a Biomimetic Ornithopter Capable of Sustained and Controlled Flight. *Journal of Bionic Engineering*
- [Percin et al. 2011] Percin, M., Hu, Y., Van Oudheusden, B.W., Remes, B., Scarano, F., 2011. Wing Flexibility Effects in Clap-and-Fling. *Proceedings of the International Micro Air Vehicles Conference*
- [Plantraco A] [www.microflight.com/Online-Catalog/Ready-to-Fly-Airplanes/Carbon-Butterfly-Livingroom-Flyer](http://www.microflight.com/Online-Catalog/Ready-to-Fly-Airplanes/Carbon-Butterfly-Livingroom-Flyer)
- [Plantraco B] [www.microflight.com/Online-Catalog/Ready-to-Fly-Airplanes/MicroMAV-chevron](http://www.microflight.com/Online-Catalog/Ready-to-Fly-Airplanes/MicroMAV-chevron)
- [Pornsirak et al. 2001] Pornsin-Sirirak, T., Tai, Y., Ho, C., Keennon, M., 2001. Microbat: A Palm-Sized Electrically Powered Ornithopter
- [Prox Dynamics A] [www.proxdynamics.com/r d/micro-helicopters-and-ornithopters/](http://www.proxdynamics.com/r d/micro-helicopters-and-ornithopters/)
- [Prox Dynamics B] [www.proxdynamics.com/r d/micro-helicopters-and-ornithopters/](http://www.proxdynamics.com/r d/micro-helicopters-and-ornithopters/)
- [QTRCO] [www.qtrco.com/wp-content/uploads/2012/07/DCN00190-SYWhtPaper042511.pdf](http://www.qtrco.com/wp-content/uploads/2012/07/DCN00190-SYWhtPaper042511.pdf)
- [Remote Controlled Toys] [www.remotecontrolledtoys.co.uk/rc-toys/ifly-vamp-bat](http://www.remotecontrolledtoys.co.uk/rc-toys/ifly-vamp-bat)
- [Ramamurti & Sandberg 2002] Ramamurti, R., Sandberg, W. C., 2002. A Three Dimensional Computational Study of The Aerodynamic Mechanisms of Insect Flight. *The Journal of Experimental Biology* 205, 1507-1518
- [Richter & Lipson 2011] Richter, C., Lipson, H., 2011. Untethered Hovering Flapping Flight of a 3D-Printed Mechanical Insect. *Artificial Life*, Spring 2011 Volume 17, Number 2, pp 73-86
- [Sane & Dickinson 2002] Sane, S.P., Dickinson, M.H., 2002. The Aerodynamic Effects of Wing Rotation and a Revised Quasi-Steady Model of Flapping Flight. *The Journal of Experimental Biology* 205, 1087-1096

- [Sane 2003] Sane, S.P., 2003. The Aerodynamics of Insect Flight. *The Journal of Experimental Biology* 206, 4191-4208
- [Shang et al. 2009] Shang, J.K., Combes, S.A., Finio, B.M., Wood, R.J., 2009. Artificial Insect Wings of Diverse Morphology for Flapping Wing Micro Air Vehicles. *Bioinspiration and Biomimetics*. IOP-Science
- [Shyy et al. 2007] Shyy, W., Liu, H., 2007. Flapping Wings and Aerodynamic Lift: The Role of Leading Edge Vortices. *AIAA Journal*, Vol. 45, No. 12, Aerospace Letters
- [Shyy et al. 2008] Shyy, W., Lian, Y., Tang, J., Viery, D., Liu, H., 2008. Aerodynamics of Low Reynolds Number Flyers. *Cambridge Aerospace Series*
- [Shyy et al. 2009] Shyy, W., Trizila, P., Kang, C-K., Aono, H., 2009. Can Tip Vortices Enhance Lift of a Flapping Wing. *AIAA Journal*, Vol. 47, No. 2, Aerospace Letters
- [Shyy et al. 2013] Shyy, W., Aono, H., Kang, C.K., Liu, H., 2013. An Introduction to Flapping Wing Aerodynamics. *Cambridge Aerospace Series*
- [Skybotix Helicopter Robot Shop A] [www.robotshop.com/media/files/pdf/coax-datasheet-coax-pack.pdf](http://www.robotshop.com/media/files/pdf/coax-datasheet-coax-pack.pdf)
- [Skybotix Helicopter Robot Shop B] [www.robotshop.com/en/skybotix-coax-autonomous-uav-micro-helicopter-drone.html](http://www.robotshop.com/en/skybotix-coax-autonomous-uav-micro-helicopter-drone.html)
- [Sladek et al. 2011] Sladek, N.J., Anderson, M.L., Cobb, R.G., 2011. Aero and Structural-Dynamic Repeatability of a Novel MAV Wing Manufacturing Process. *AIAA Atmospheric Flight Mechanics Conference*, AIAA 2011-6393
- [Srygley et al. 2002] Srygley, R.B., Thomas, A.L.R., 2002. Unconventional Lift Generating Mechanisms in Free Flying Butterflies. *Nature*, Vol. 420
- [Steltz et al. 2007] Steltz, E., Avadhanula, S., Fearing, R., 2007. High Lift Force with 275 Hz Wing Beat in MFI. *IEEE, International Conference on Intelligent Robots and Systems*.
- [Sun et al. 2002] Sun, M., Tang, J., 2002. Unsteady Aerodynamic Force Generation by a Model Fruit Fly Wing in Flapping Motion. *The Journal of Experimental Biology* 205, 55-70

- [Syaifuddin et al. 2006] Syaifuddin, M., Park H.C., Goo N.S., 2006. Design and Evaluation of a LIPCA Actuated Flapping Device. Smart Materials and Structures. IOP Science
- [Tanaka & Wood 2010] Tanaka, H., Wood, R.J., 2010. Fabrication of Corrugated Artificial Insect Wings Using Laser Micromachined Molds. Journal of Micromechanics and Microengineering. IOP Science
- [Teoh et al. 2012] Teoh, Z.E., Fuller, S.B., Chirarattananon, P., Prez-Arancibia, J.D., Greenberg, J.D., Wood, R.J., 2012. A Hovering Flapping-Wing Microrobot with Altitude Control and Passive Upright Stability. IEEE International Conference on Intelligent Robots and Systems, pp 3209-3216
- [Truong et al. 2011] Truong, Q.T., Nguyen, Q.V., Park, H.C, Byun, D., Goo, N.S., 2011. Modification of a Four-Bar Linkage System for a Higher Optimal Flapping Frequency. Journal of Intelligent Material Systems and Structures
- [University of California Berkeley] [www.berkeley.edu/news/media/releases/99legacy/robotfly3.jpg](http://www.berkeley.edu/news/media/releases/99legacy/robotfly3.jpg)
- [Van Den Berg et al. 1997] Van Den Berg, C., Ellington, C.P., 1997. The Vortex Wake of A Hovering Model Hawkmoth. Philosophical Transactions of The Royal Society of Biological Sciences, Vol. 352, no. 1351, pp. 317-328
- [Wagner 1925] Wagner, H., 1925. ber die Entstehung des dynamischen uftriebes von Tragflgen. Z. Angew. Math. Mech. 5, 17-35
- [Weis-Fogh 1973] Weis-Fogh, T., 1973. Quick Estimates of Flight Fitness in Hovering Animals, Including Novel Mechanisms For Lift Production. Journal of Experimental Biology, 59, 169-230
- [Whitney et al. 2011] Whitney, J.P., Sreetharan, P.S., Ma, K.Y., Wood, R.J., 2011. Pop-Up Book MEMS. Journal of Micromechanics and Microengineering. IOPScience
- [Wolfram Scotch] [www.demonstrations.wolfram.com/ComparingSimpleCrankSliderAndScotchYokeMechanisms/](http://www.demonstrations.wolfram.com/ComparingSimpleCrankSliderAndScotchYokeMechanisms/)
- [Wood 2007] Wood, R., 2007. Liftoff of a 60 mg Flapping Wing MAV. IEEE, International Conference on Intelligent Robots and Systems
- [Wood 2007a] [micro.seas.harvard.edu/papers/IROS07/Wood.mpg](http://micro.seas.harvard.edu/papers/IROS07/Wood.mpg)
- [Wood 2007b] Wood, R., 2007. Design, Fabrication and Analysis of a 3DOF, 3 cm Flapping Wing MAV. IEEE, International Conference on Intelligent Robots and Systems

- [Wood 2008a] Wood, R., 2008. The First Take-off of a Biologically Inspired At Scale Robotic Insect. IEEE, Transaction on Robotics
- [Xtreme Quadcopter Robot Shop] [www.robotshop.com/en/xtreme-20-gen-ii-quadcopter.html](http://www.robotshop.com/en/xtreme-20-gen-ii-quadcopter.html)
- [Yoon et al. 2002] Yoon, K.J., Shin, S., Park, H.C., Goo, N.S., 2002. Design and Manufacture of a Lightweight Piezo-Composite Curved Actuator. Smart Materials and Structures, Vol. 11, Number 1. IOP Science
- [Zuo et al. 2007] Zuo, D., Peng, S., Chen, W., Zhang, W., 2007. Numerical simulation of flapping wing insect hovering flight at unsteady flow. International Journal of Numerical Methods in Fluids, Vol. 53, pp. 1801-1817

## Appendix A

# Experimental Images and Arrangements

The boundaries used for experimental work were constructed of Depron foam which can be purchased in many sizes and thickness ready to cut as needed. A sharp blade such as an X-Acto knife is ideal to cut this foam into the desired shapes and can be done precisely. Depron foam is extremely lightweight and rigid, subsequently it is commonly used for RC model aircrafts and even boats due to its moisture resistant properties. By virtue of the rigidity of Depron foam, it can be easily machined or sanded down to create curvatures which is highly beneficial when crafting models. The walls were designed to explore the effect it has on force measurements due to wall-fluid interaction in a domain consisting of a continuously moving wing. Some of the boundaries used in the experiments have been illustrated in this section via CAD diagrams and photographs. The main dimensions have been shown in the CAD diagrams in order to give the reader an insight of the approximate sizes of the boundaries. All the dimensions shown in the diagrams are in mm.

Figures A.1 to A.4 show pictures of some of the boundaries used in these experiments.

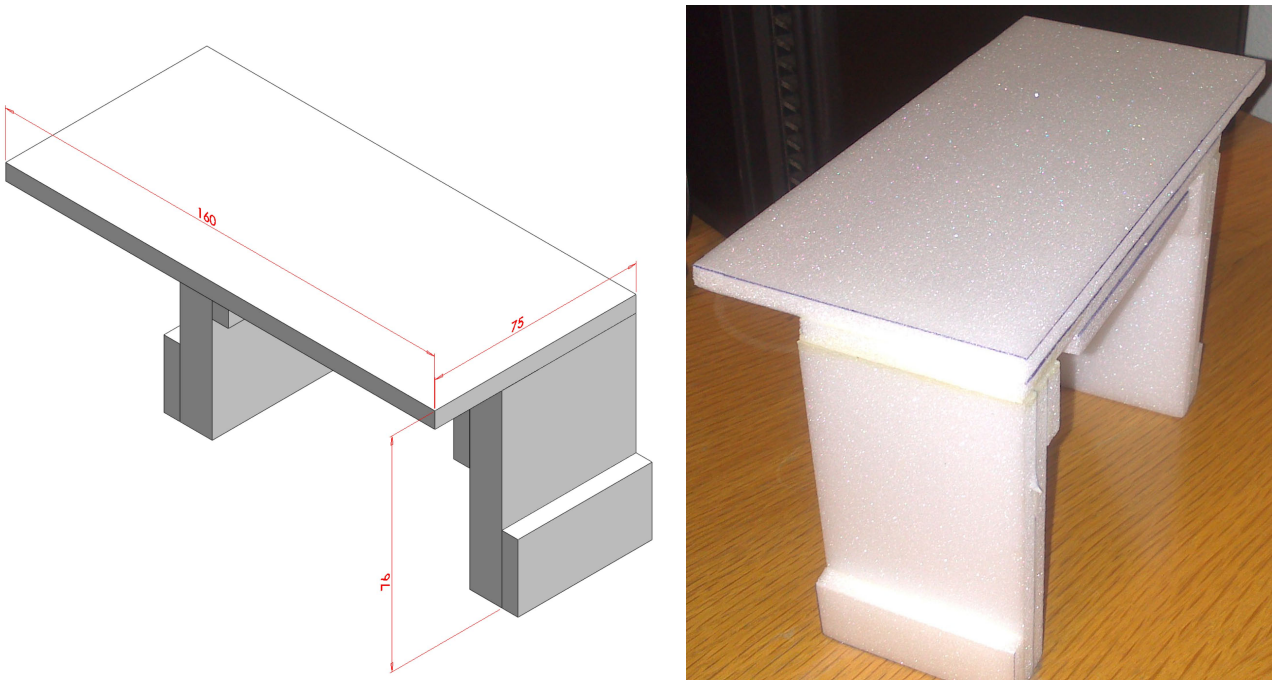


Figure A.1: *Table for Experiments*

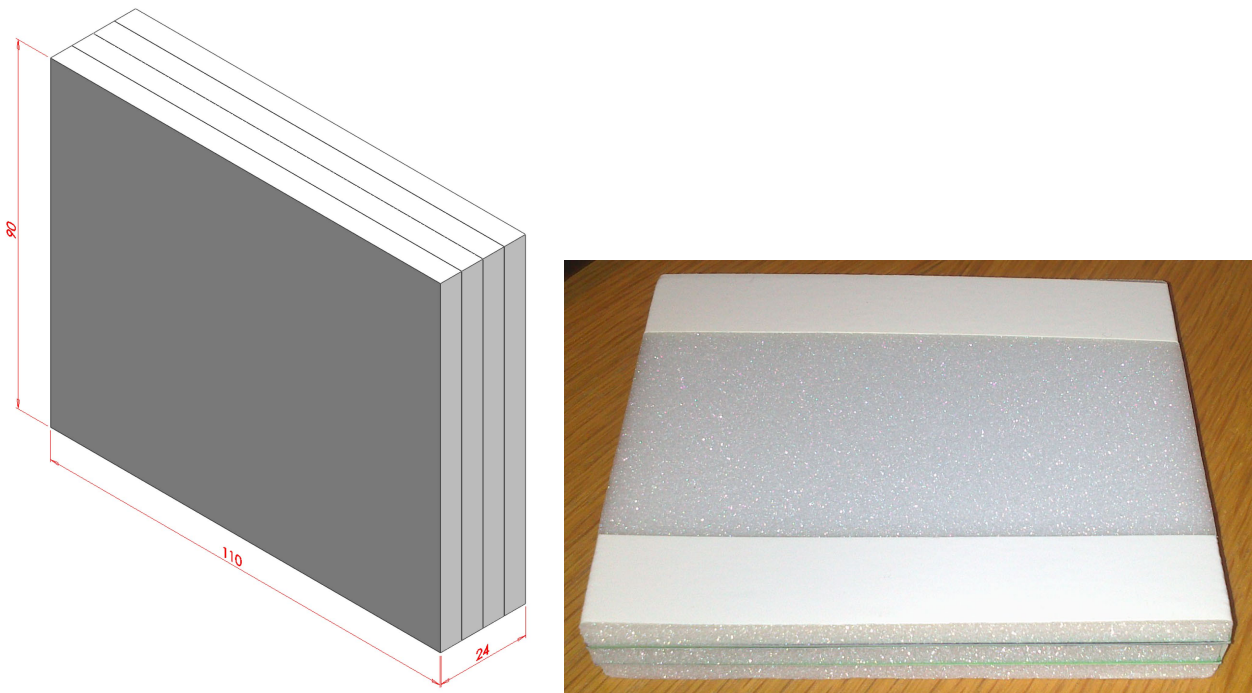


Figure A.2: *Ground Effect Boundary for Experiments*

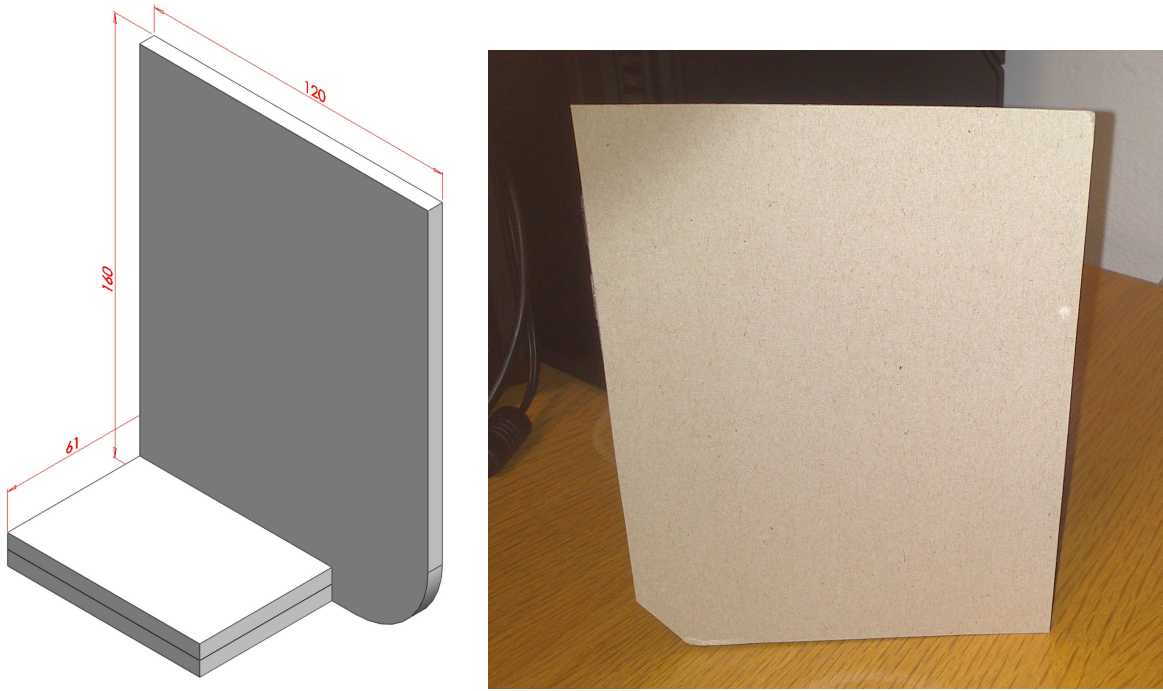


Figure A.3: *Trailing Edge Wall Boundary for Experiments*

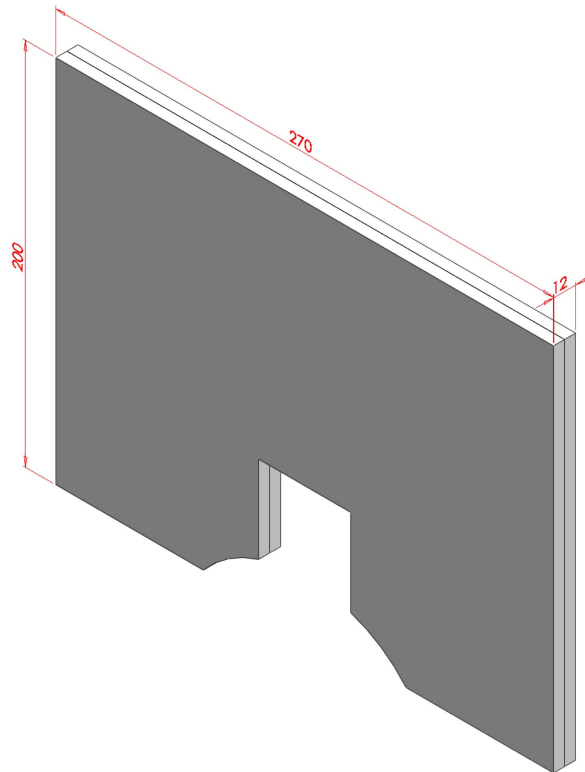


Figure A.4: *CAD of Ground Effect Boundary for 90Deg Body Inclination Experiment*

## Appendix B

# Further Experimental Results

Spectrogram plots which represent the frequency-time data for some additional axes that were exploited to determine thrust force, lift force and pitching moment have been shown as examples in Figures B.1 and B.2. The former illustrates data analysed from air tests and the latter are plots for the data analysed from vacuum chamber tests.

The plots in Figure B.1, represent various types of experiments such as FR, FRAP and FR in hovering mode. In all these tests as aforesaid in the main part of this thesis, the flapping frequency was set to 5 Hz. The green shade aligns well at 5 Hz and 10 Hz, stating that these were the dominant frequencies, which agree with the flapping frequency selected in the apparatus setup. Although the flapping frequency was set at 5 Hz, the main axis which is known as the Fz axis (lift force direction in all the 0 degree inclination tests) would normally show a dominance at 5 Hz as the wings are flapping in this plane directly and large forces are applied along this direction. However, the more dominant frequency can be 10 Hz opposed to 5 Hz for the Fx and Ty axes as wing rotation has a strong effect and overall large contributions to their respective values produced during wing motion. Green shades are thereafter seen at regular intervals, which are actually multiples of the flapping frequency demonstrating the vibrational modes of the rig. Evidently, additional vibrations were present in the moment axis as seen from the plots in Figures B.1B, B.1D and B.1F, especially when compared to their counterpart thrust / lift force axis.

The vacuum chamber plots in Figure B.2, present the data from the same tests described above which are

FR, FRAP and FR in hovering mode. The vacuum chamber data seems to have more vibrational effects present and as expected shades of green are present along frequencies which are multiples of the flapping frequency. Some plots such as B.2A, B.2B and B.2D seem to show more influence of the vibrational effects from the greater regions of green shade present as the frequency values along the y-axis increase.

Figure B.3, displays numerous images of the wing motion captured during the various experiments performed. Some of the images contain the boundaries that were exploited in the experiments that had a rigid stationary surface in the form of a trailing edge wall or ground effect base. A dual boundary configuration has been shown in images B.3B and B.3D where the trailing edge wall and ground effect surface are both present. Hovering mode images have been shown in B.3E and B.3F, the former has no boundary and the latter has a ground effect boundary which is continuously present during the wings motion. The final two images were captured when the wing was in the vacuum chamber, as it can be seen, the images are more difficult to analyse due to the the guard placed above the glass bell jar for safety reasons. Lexan was utilised to create a window within the cylindrical guard in order for the HS camera to capture the wings motion.

Figure B.4, illustrates an image to the left which shows the path of the wing via the green lines and the locations of the white dots with their labels according to their respective positions. The data output for each according to their two-dimensional positions and frame number has been shown to the right of the Figure. Evidently the root point has travelled the smallest trajectory which is shown by the declivity of the curve through the downstroke (first half of the curve) and the tip point travels the largest trajectory as its downstroke has the largest declivity of the three curves.

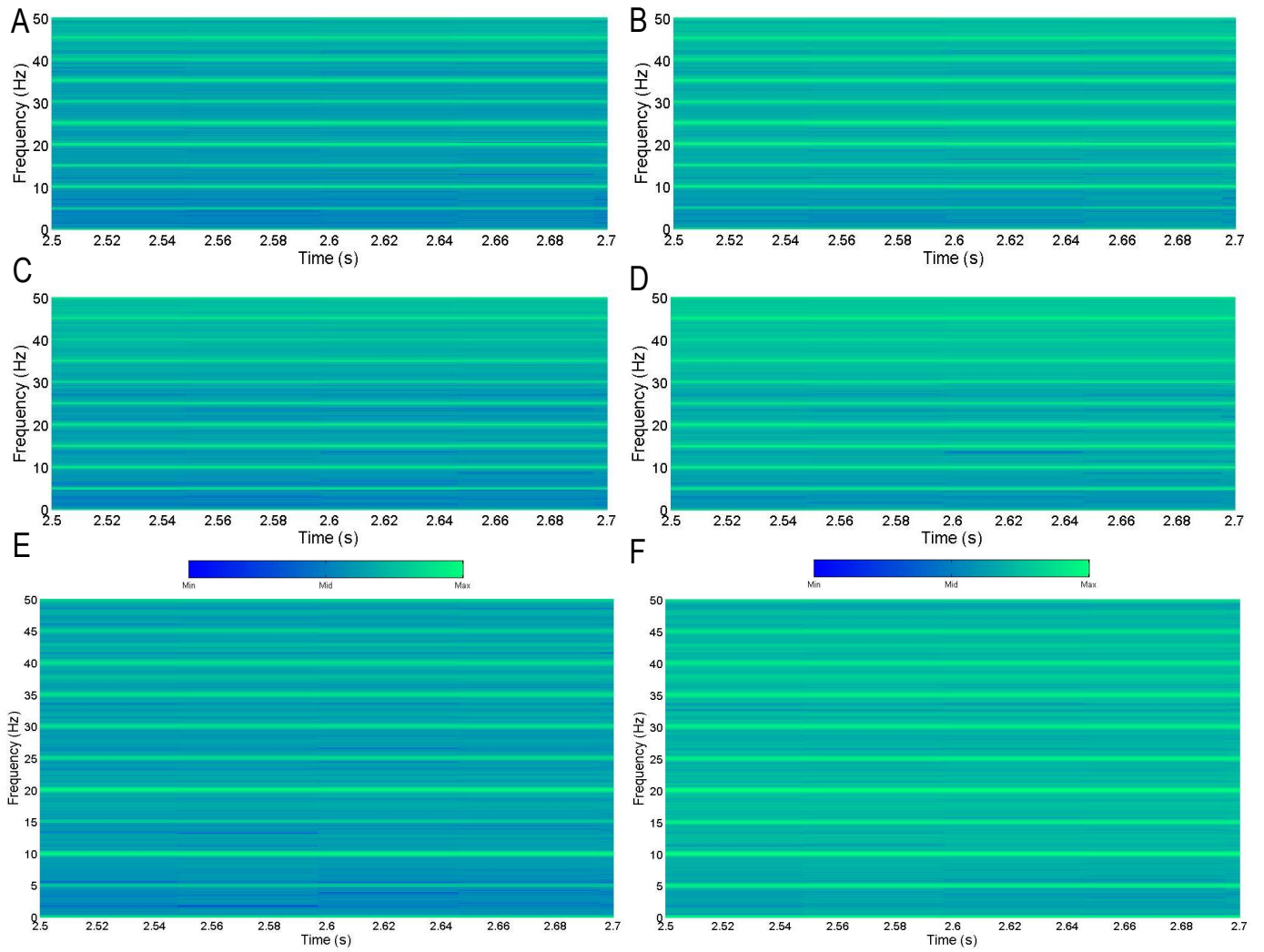


Figure B.1: Spectrogram Plots for 60 mm Wings ( $WT_4$ ) in FR & FRAP Configurations; A: FR for Fx Axis, B: FR for Ty Axis, C: FRAP for Fx Axis, D: FRAP for Ty Axis, E: FR in Hovering Mode for Fx Axis, F: FR in Hovering Mode for Ty Axis. Colour Bar Represents Size of Amplitude. UI: M1-FR- $WT_4$ -S-V, M1-FR- $WT_4$ -S-H & M1-FRAP- $WT_4$ -S-V

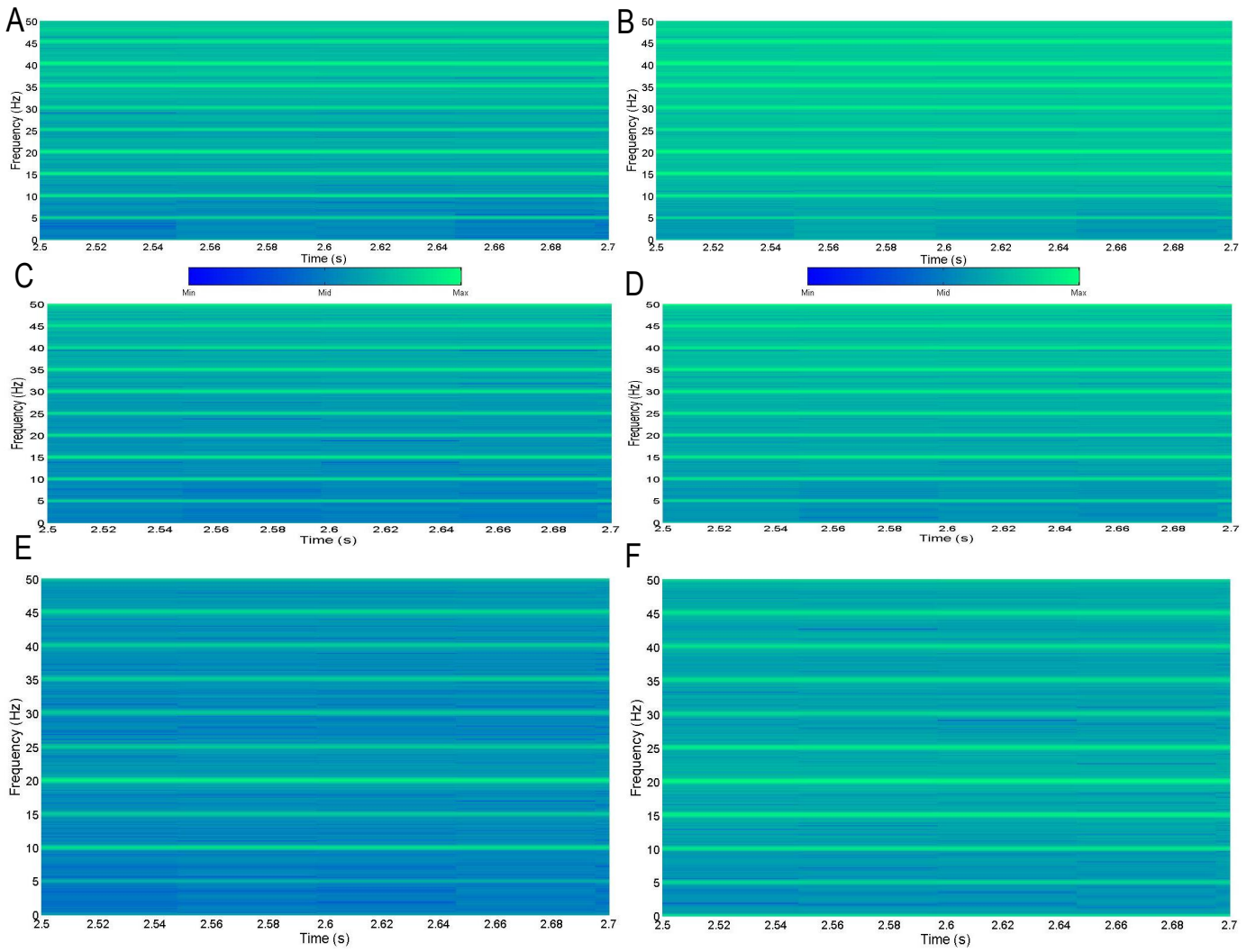


Figure B.2: Spectrogram Plots for 60 mm Wings ( $WT_4$ ) in FR & FRAP Configurations During Vacuum Chamber Tests; A: FR for  $F_x$  Axis, B: FR for  $T_y$  Axis, C: FRAP for  $F_x$  Axis, D: FRAP for  $T_y$  Axis, E: FR in Hovering Mode for  $F_x$  Axis, F: FR in Hovering Mode for  $T_y$  Axis. Colour Bar Represents Size of Amplitude. UI: M1-FR-WT<sub>4</sub>-S-V, M1-FR-WT<sub>4</sub>-S-H & M1-FRAP-WT<sub>4</sub>-S-V

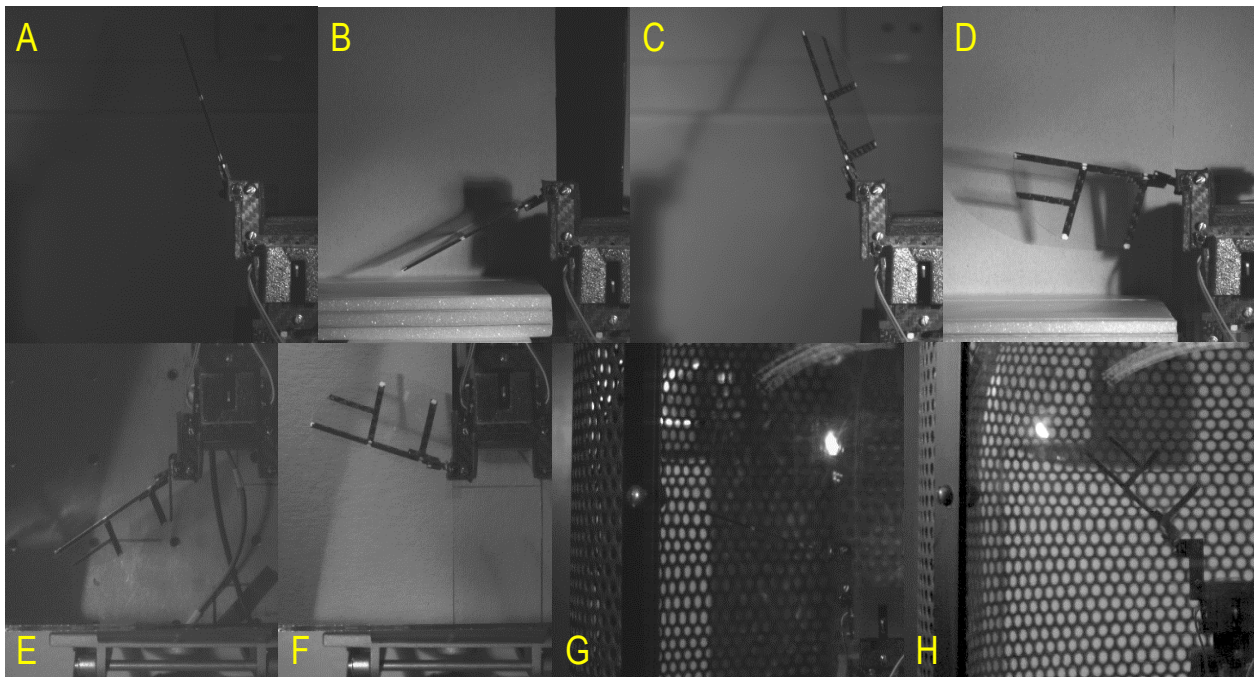


Figure B.3: *Example of Experimental Images to Capture Wing Motion with Various Arrangements; A: Flapping Only, B: Flapping with TEWall and GE Boundaries, C: FR Only, D: FR with TEWall and GE Boundaries, E: FR Only in Hovering Mode, F: FR in Hovering Mode with GE Boundary, G: Flapping Only in Vacuum Chamber, H: FR Only in Vacuum Chamber*

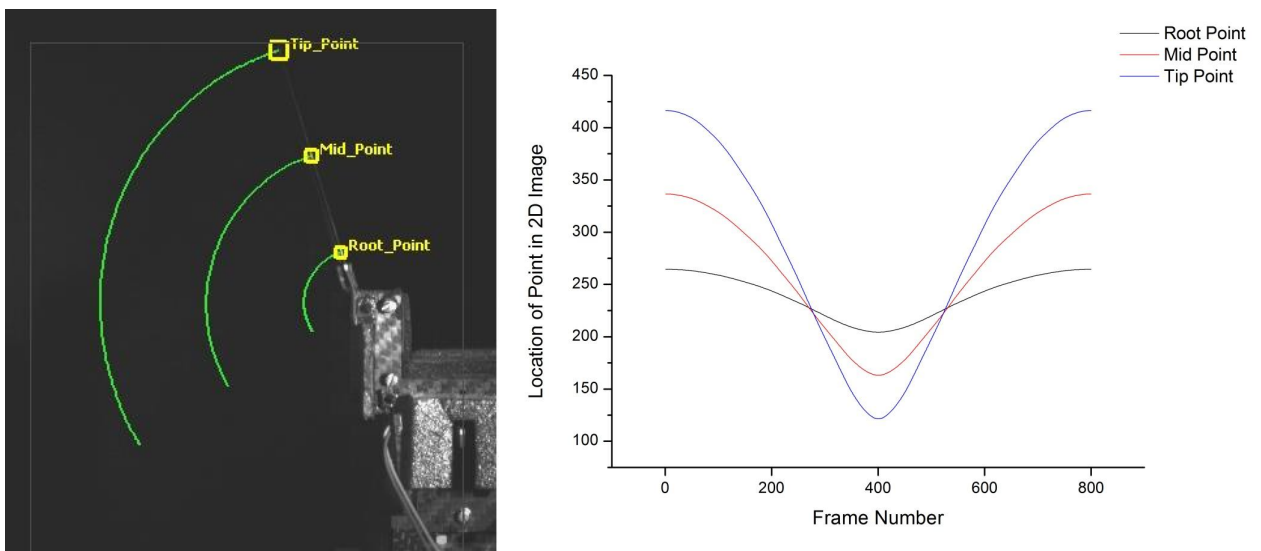


Figure B.4: *Point Tracking for Flapping Wing and Location Data Output*

## Appendix C

# Further CFD Results and Grids etc.

Limit cycle plots are presented in Figures C.1 to C.2, in an individual style to present the curve more clearly without superimposing another curve for comparison sake. The plots are the complete set of results for all 12 cases simulated. They have been discussed in comparison form previously in the main content of this thesis. Aerodynamic moments have been plotted in Figures C.3 and C.4, which have clear differences dependent on the wings rotational timings and position along the chord-wise direction. When wing rotation occurs along position D, an additional peak is created at the end of each stroke when the supination / pronation stage occurs. And the size of the peak is dependent on the wings rotational timing. The overall moment produced about the rolling axis would continually balance out resulting in zero rolling moment throughout the entire time history of a cycle due to two wings travelling the exact same motion on both sides, and the same would apply for the yawing moment. In contrast, the pitching moment would be balanced out when the entire cycle is complete and not throughout the instantaneous time history as the wings are rotating in the same direction which would effectively result in a summation of the two per stroke. This summation per stroke is balanced out in the following stroke as the summation generated in the following stroke is of opposite sign, hence the equilibrium is reached. The pitching moment produces a large peak at the start of a stroke when the wings rotation duration is 1.1s, and the size of the peak decreases as the wing rotation duration increases.

Aerodynamic power plots have been shown in Figures C.5 and C.6 for all the cases compared with the

rectangular wing. The plots merely present a simpler format of the power contributions from the wings motion to the total aerodynamic power required per cycle. When considering wing rotation along position D, large peaks are produced for the smallest wing rotation duration (1.1s) at the start of a stroke, more precisely during the supination or pronation stage as the wings rotate very rapidly with large accelerations. Thereafter, a steady zero power is required for wing rotation as the wings hold a steady AOA during the translation phase, thus no power is needed to perform wing rotation. For the case where wing rotation has the longest duration such as 3.3s ( C.5A), aerodynamic power for wing rotation is required throughout most of the cycle as the wings rotation is very slow and a steady AOA is held for a short duration during the translation phase per stroke. A similar outcome is seen in plots C.5D to C.5F, where the rotation position has moved along the chord and now occurs at position C. In general when a rapid wing rotation takes place with the shortest rotational duration large peaks in power occur as seen in Figures C.6C and C.6F. For these cases the AOA is held constant for the longest durations as wing rotation completes in the shortest duration, thus rotational power is zero during the long wing translation phases, and peaks are produced during supination and pronation. Further to this, all the plots in both of these Figures show large total aerodynamic peaks at the onset of a stroke, which are clearly larger for the cases that undergo wing rotation in a duration of 1.1s. In general, the power peak produced due to flapping is largest for the cases which have the longest wing rotation duration as the wing endures large form drag during these cases, due to the slow dynamic rate of AOA change.

For Figures C.7 and C.8, the former displays the various grids employed during the grid sensitivity study and the latter presents the two dimensional mesh on the surface of the drosophila wings for the grid sensitivity study, along with an image of the wing depicting the wing rotational position (red line) employed for the drosophila simulations. As evidently seen, the cell size reduces considerably as the mesh becomes denser from a coarse mesh to a hyper dense mesh. This is seen for both sets of grid images which are, the outer elements surrounding the wing and the two dimensional cells on the wings surface. Additional slices which focus on the mesh situated at the leading edge of the wing are displayed in Figure C.9.

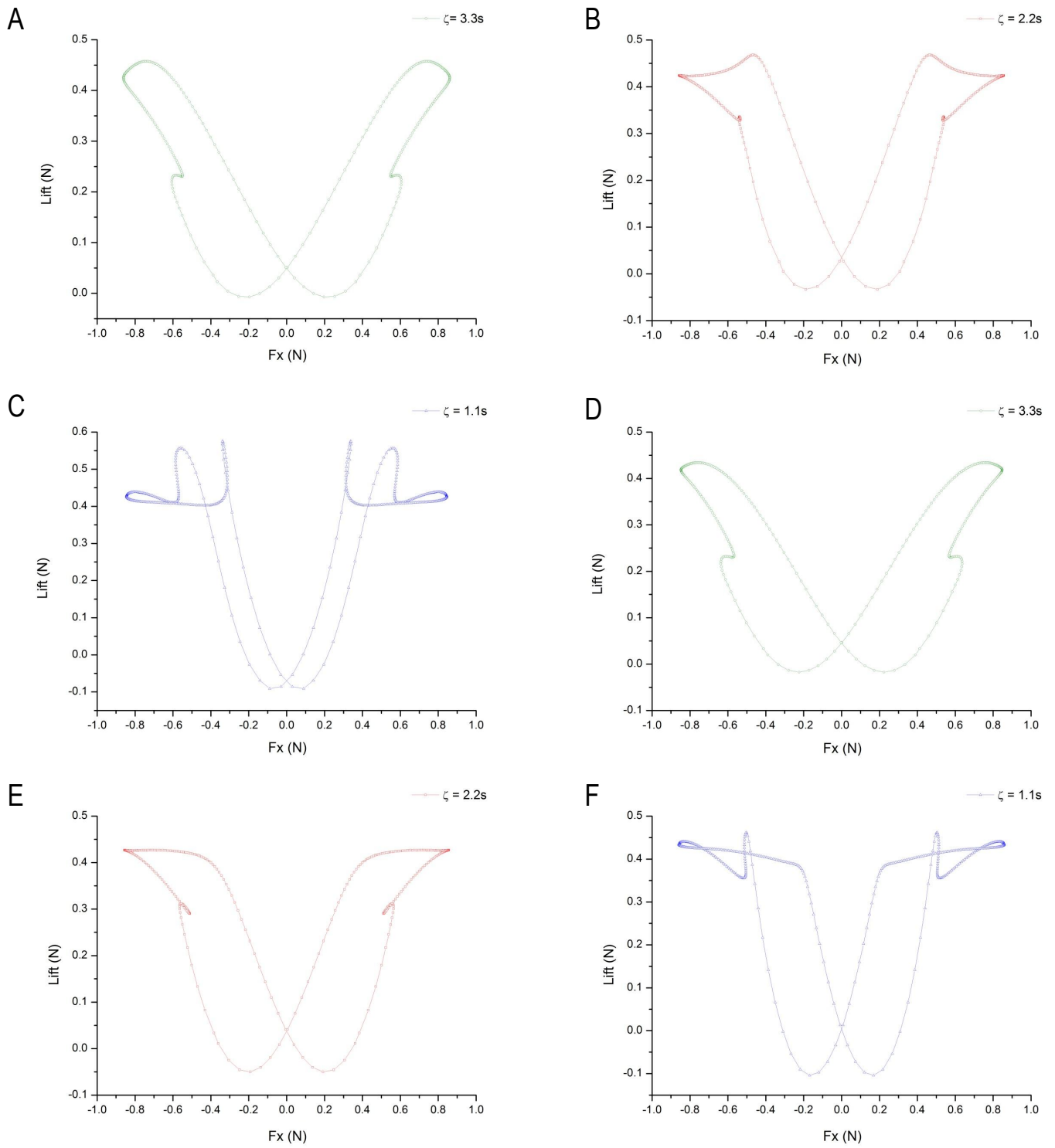


Figure C.1: *Fx Vs Lift Limit Cycles; A: Rotation Position D, B: Rotation Position D, C: Rotation Position D, D: Rotation Position C, E: Rotation Position C, F: Rotation Position C*

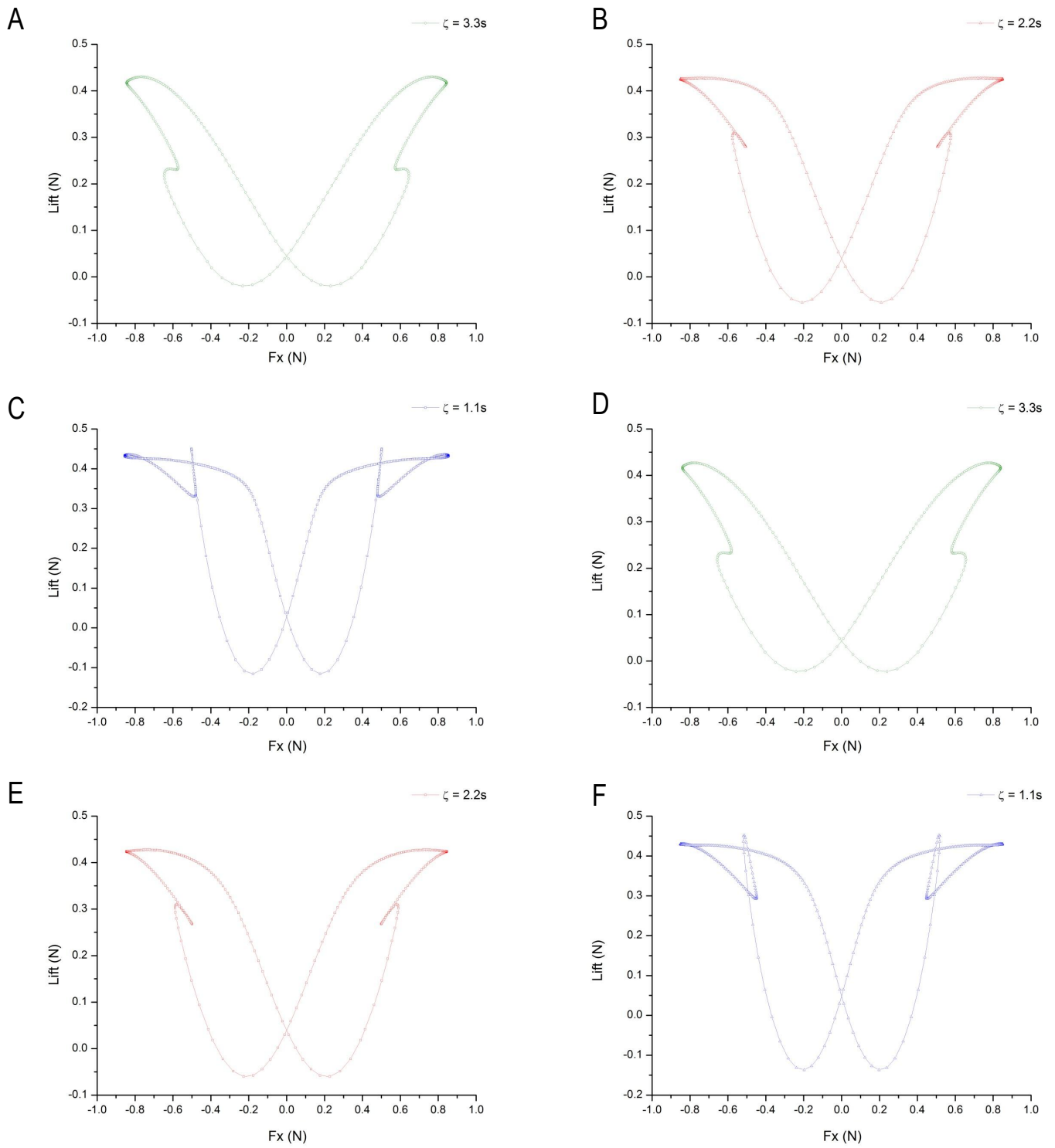


Figure C.2: *Fx Vs Lift Limit Cycles*; A: *Rotation Position B*, B: *Rotation Position B*, C: *Rotation Position B*, D: *Rotation Position A*, E: *Rotation Position A*, F: *Rotation Position A*

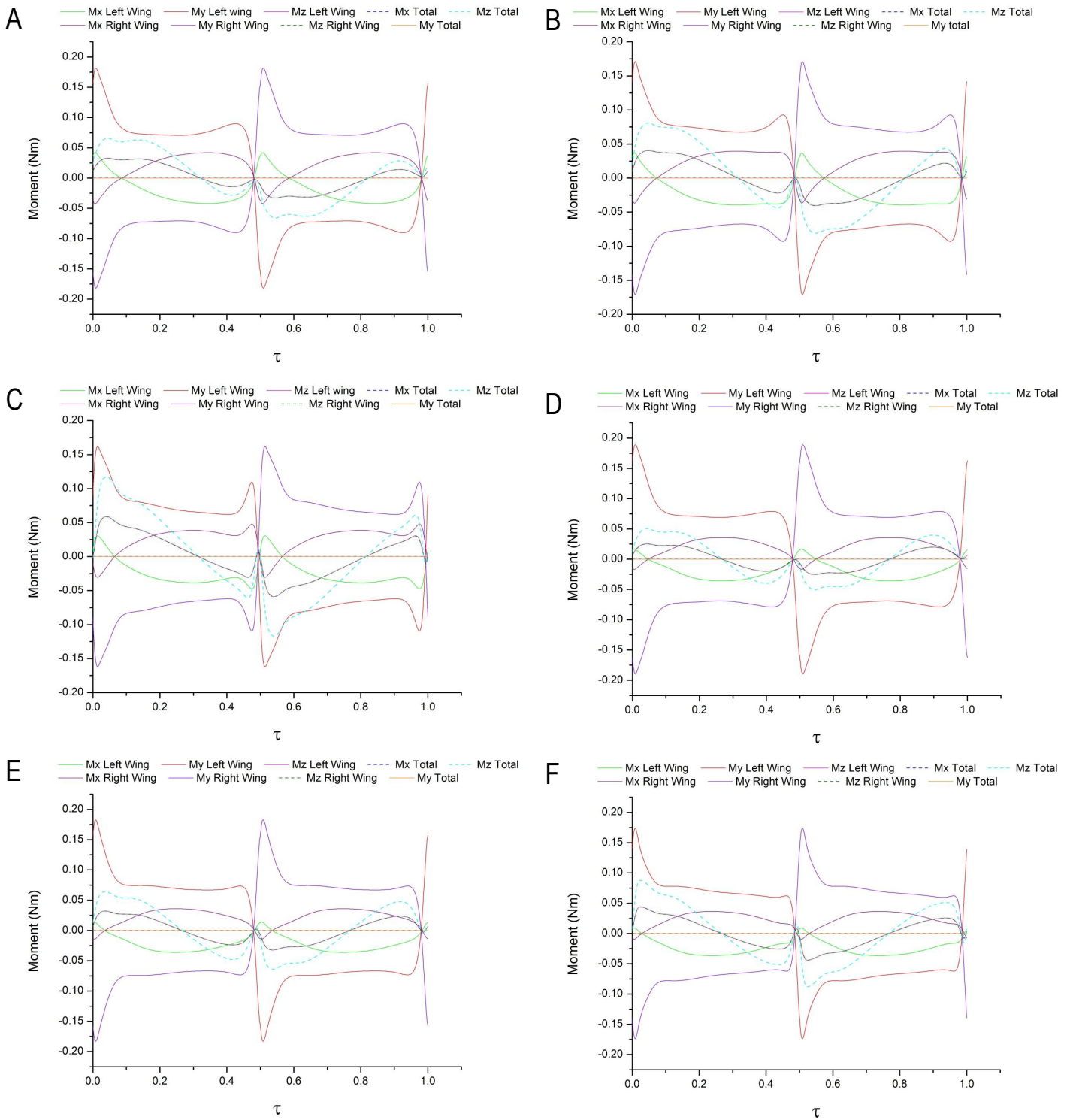


Figure C.3: Moments for Rotation Position D and Rotation Position C ; A: Rotation Position D and Duration 3.3s, B: Rotation Position D and Duration 2.2s, C: Rotation Position D and Duration 1.1s, D: Rotation Position C and Duration 3.3s, E: Rotation Position C and Duration 2.2s, F: Rotation Position C and Duration 1.1s

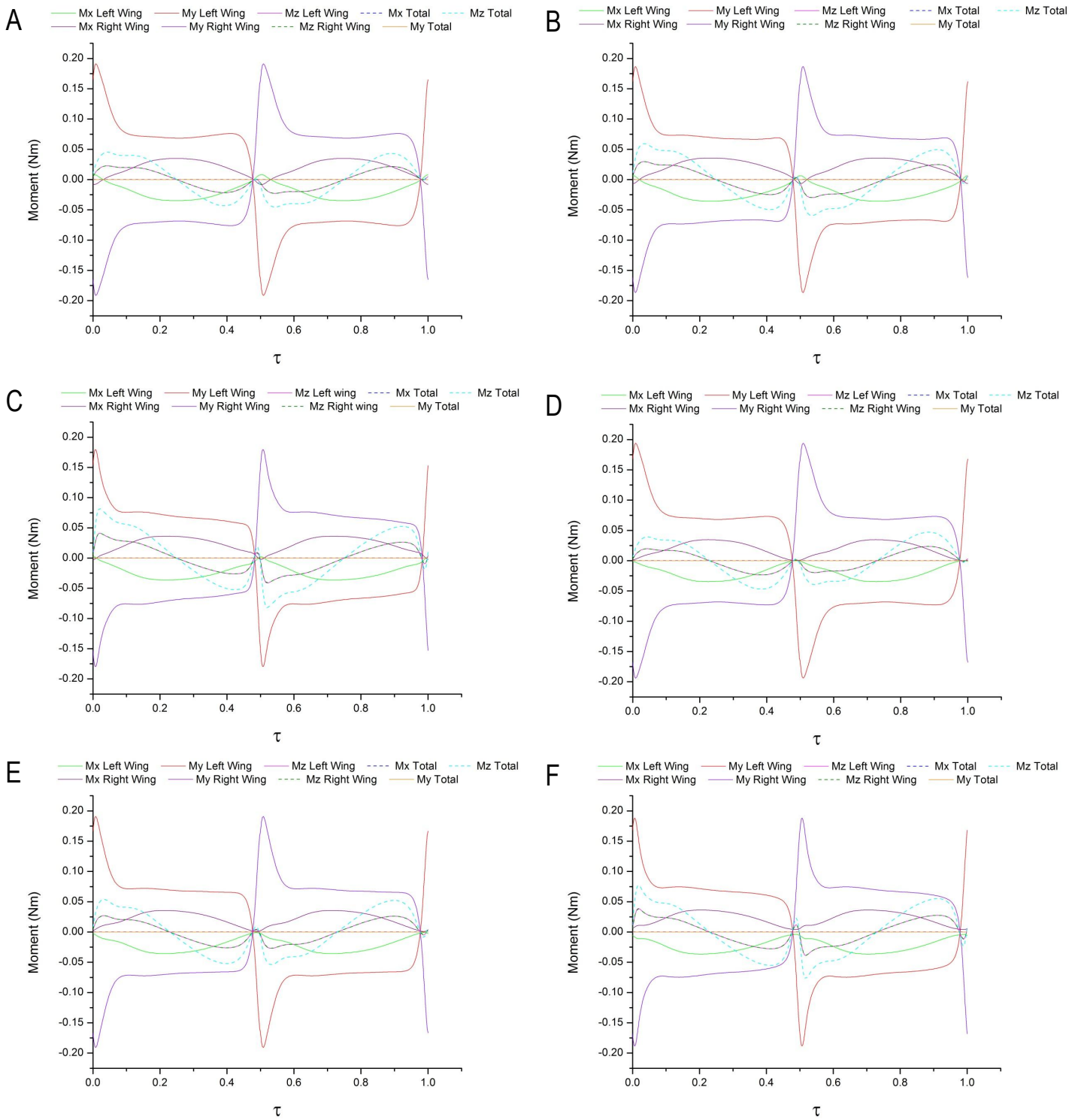


Figure C.4: Moments for Rotation Position B and Rotation Position A ; A: Rotation Position B and Duration 3.3s, B: Rotation Position B and Duration 2.2s, C: Rotation Position B and Duration 1.1s, D: Rotation Position A and Duration 3.3s, E: Rotation Position A and Duration 2.2s, F: Rotation Position A and Duration 1.1s

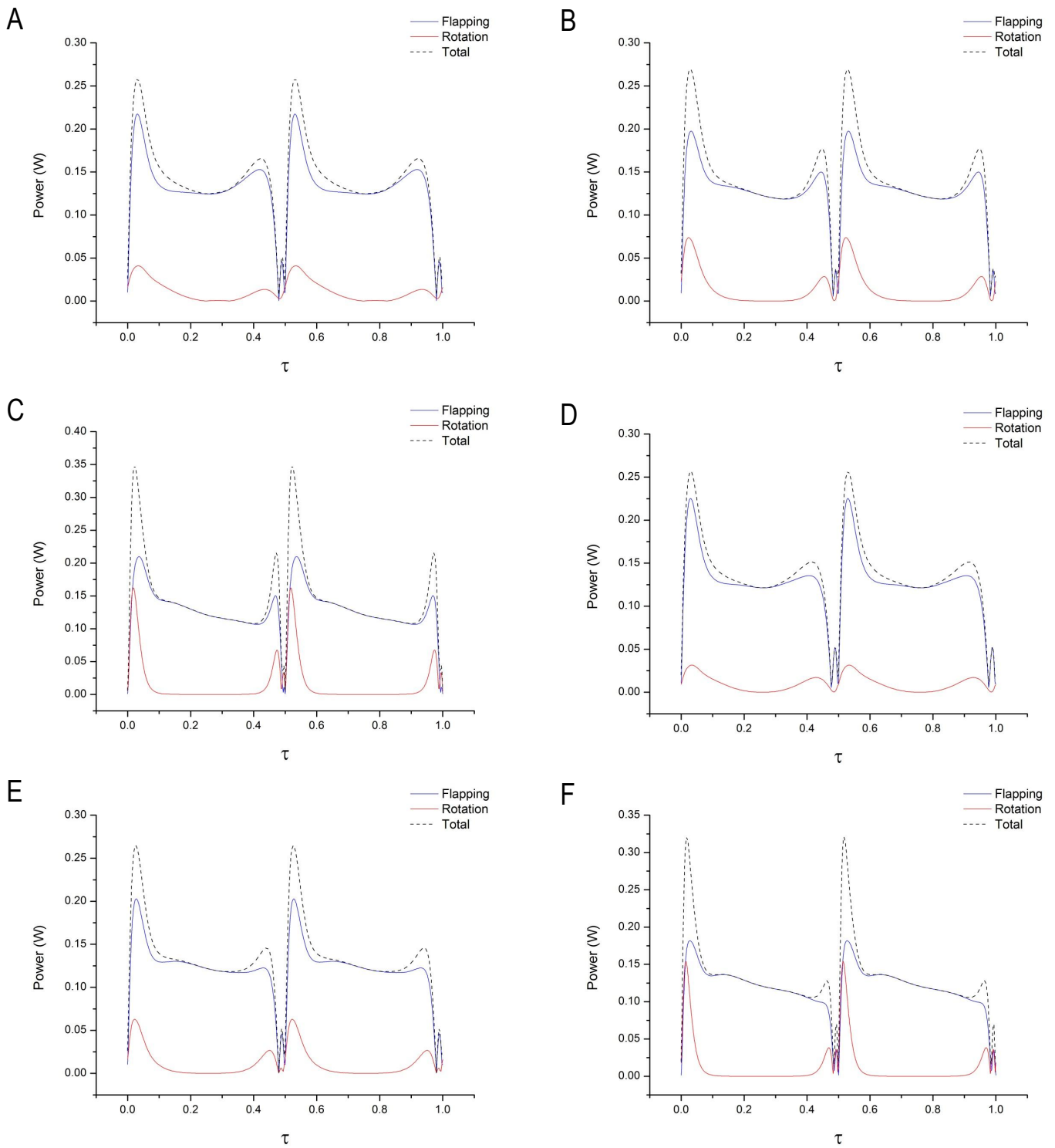


Figure C.5: Aerodynamic Power for Rotation Position D and Rotation Position C ; A: Rotation Position D and Duration 3.3s, B: Rotation Position D and Duration 2.2s, C: Rotation Position D and Duration 1.1s, D: Rotation Position C and Duration 3.3s, E: Rotation Position C and Duration 2.2s, F: Rotation Position C and Duration 1.1s

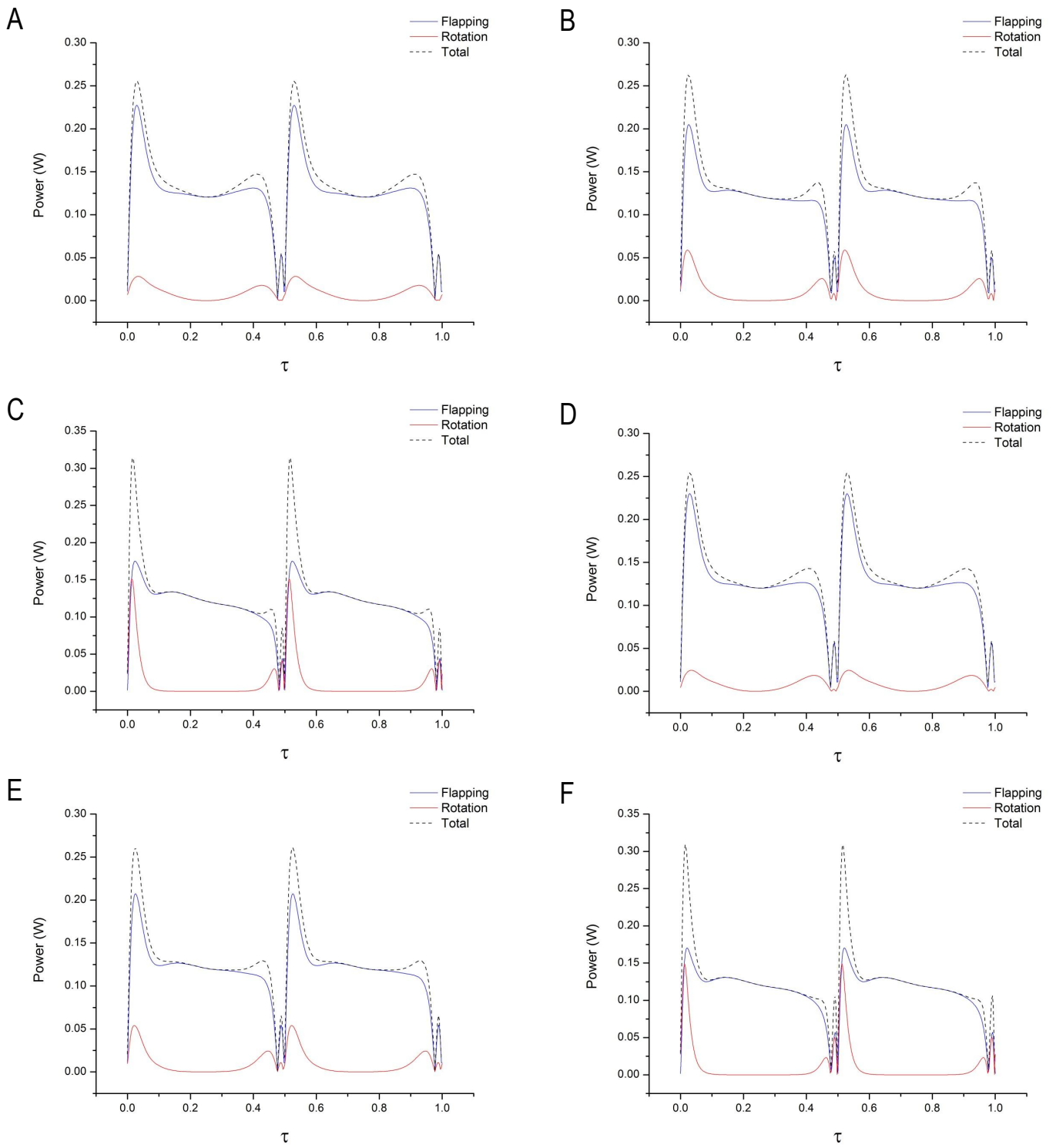


Figure C.6: Aerodynamic Power for Rotation Position B and Rotation Position A ; A: Rotation Position B and Duration 3.3s, B: Rotation Position B and Duration 2.2s, C: Rotation Position B and Duration 1.1s, D: Rotation Position A and Duration 3.3s, E: Rotation Position A and Duration 2.2s, F: Rotation Position A and Duration 1.1s

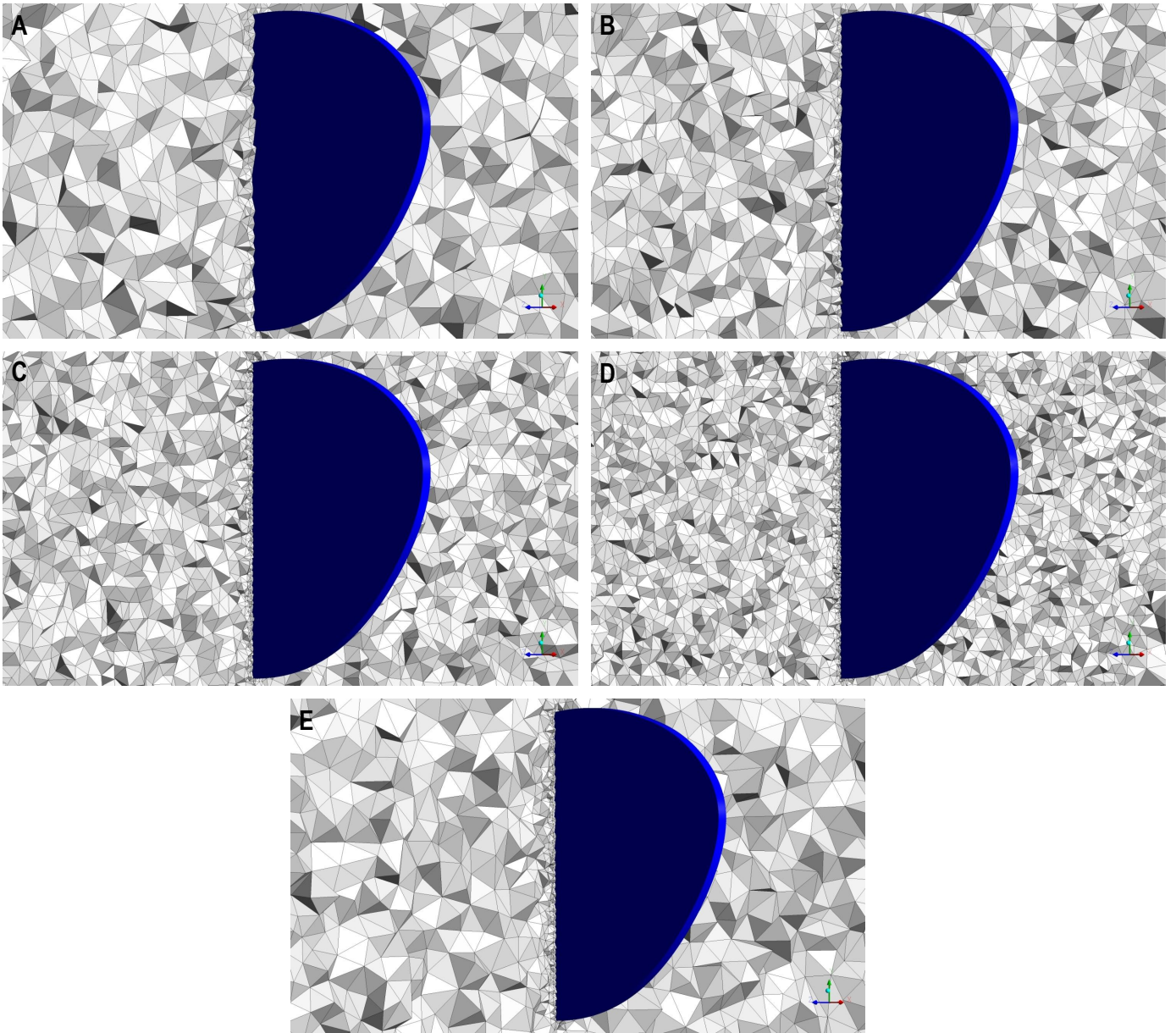


Figure C.7: *Mesh Around Drosophila Wing for Grid Independence Study; A: Coarse Mesh, B: Medium Mesh, C: Dense Mesh, D: Hyper Dense Mesh, E: Dense Mesh with Stationary Inner Domain*

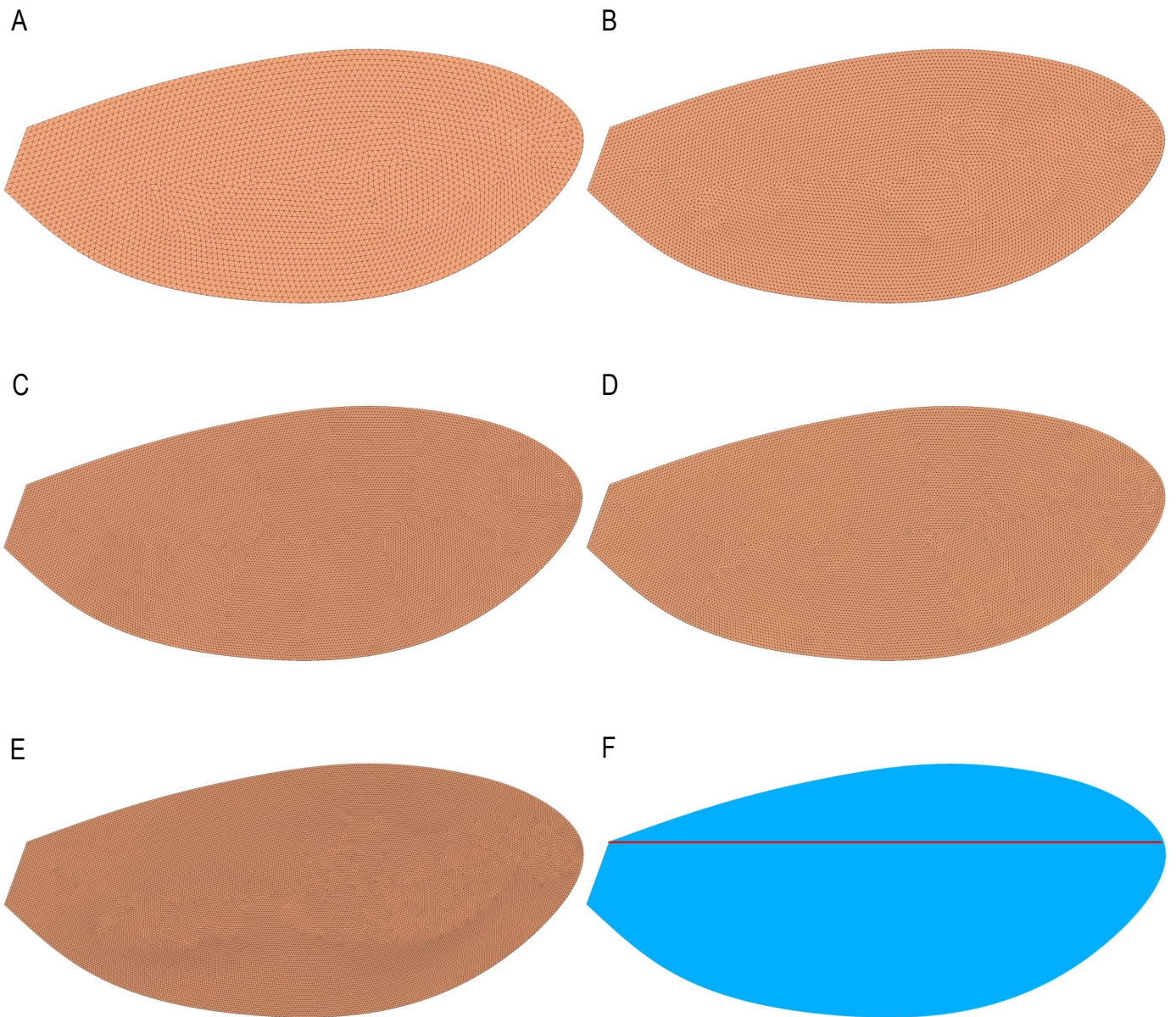


Figure C.8: *Mesh on Drosophila Wing for Grid Independence Study; A: Coarse Mesh, B: Medium Mesh, C: Dense Mesh, D: Dense Mesh with Stationary Inner Domain, E: Hyper Dense Mesh, F: Wing Rotation Location*

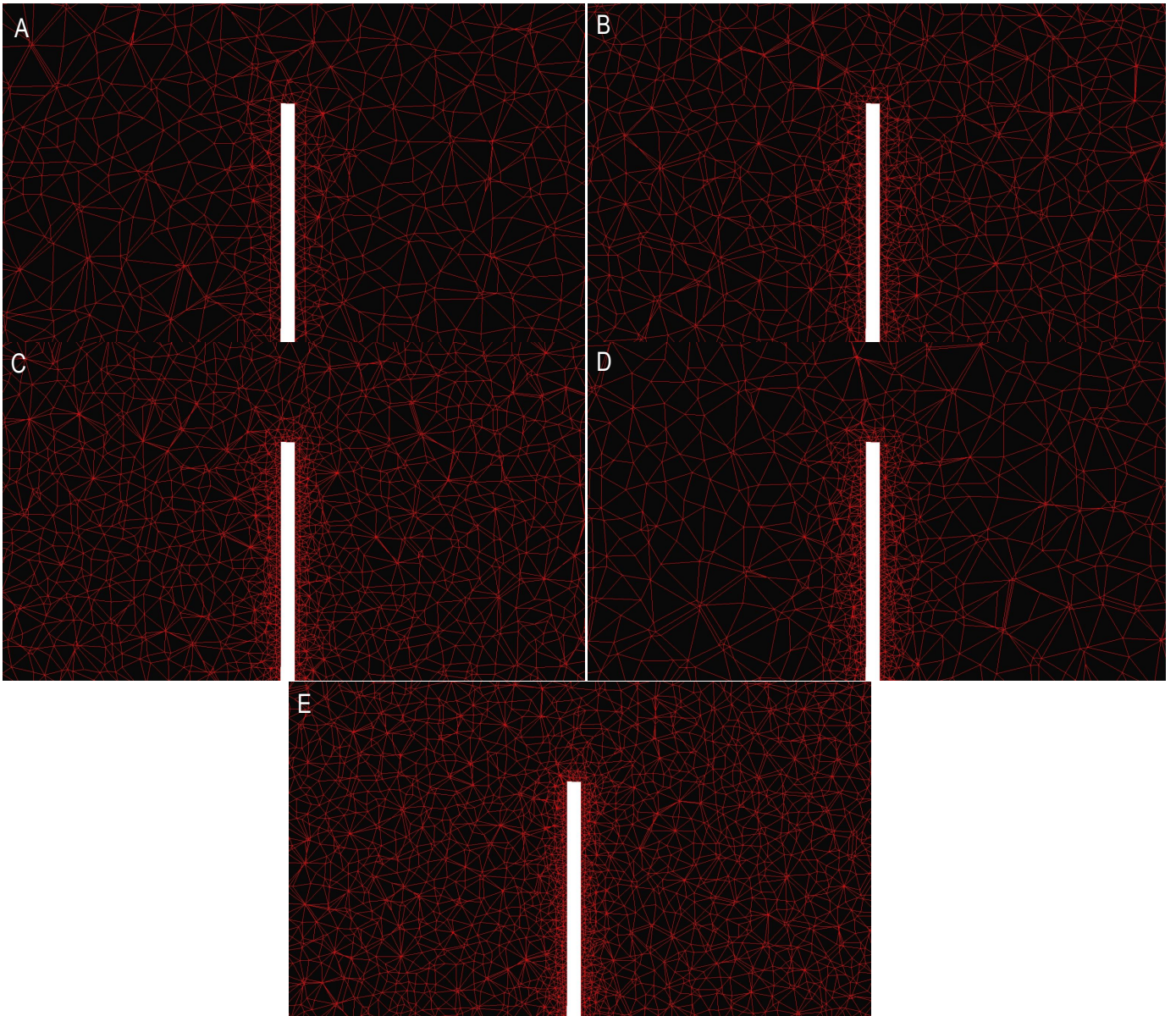


Figure C.9: *Two Dimensional Slices of the Grid and Drosophila Wing at the Leading Edge; A: Coarse Mesh, B: Medium Mesh, C: Dense Mesh, D: Dense Mesh with Stationary Inner Domain, E: Hyper Dense Mesh*

## Appendix D

### FWMAV Models I and II extras

Figure D.1, consists of numerous CAD images of the FWMAV model designed in this project with the body attached in various views. The body was constructed using 3 mm and 6 mm Depron foam. The black colour was applied as the original white colour of the foam was reflecting a bright white shade in the images which would make it difficult to view the dots on the wing. The body was securely taped to model, and this was checked before every test as any change such as a body part peeling off the model may affect the results. Furthermore, the body entraps the fluid motion formed by the circular rotating gearbox which could also affect the fluid dynamics of the FWMAV and overall the force / moment measurements, as a strong circular fluid motion is created by the rapid spinning of the gears and connected components. The wings did not touch the body when in motion for any of the tests, and during vacuum chamber tests the body was taken off as Depron foam may expand in the chamber.

Figure D.2, presents exploded CAD images of both backboards, linkage mechanism, linear slider and various other pieces for the assembly of model 1. A set of different views are provided to aid the reader to understand the connections required to connect the linkage system to the support frame of the model. M2 screws and nuts were used to maintain a consistent spacing between both of the frame boards. This method of assembly assists in keeping the pins straight and is employed as a prevention technique to ensure extra stress is not applied on the pins from any mis-alignments. The FWMAV models were designed and constructed within the duration of this project for the primary purpose of experimental research where downsizing and weight

reduction were the key characteristics in mind for future advancements.

Figure D.3, displays various exploded views of the linkage mechanism. These images focus solely on the connections required to assemble the linkage mechanism, where the components are connected via pins and pin ends. The linkage mechanism is connected to the linear slider which then connects to the crank arm which essentially pushes and pulls the linear slider. The method and accuracy of the connections for all the components assembled within the linkage mechanism is crucial for the mechanical flapping mechanism as the core movement is produced from this mechanical construction. However, it should be noted that the method and accuracy of connecting the remaining components is also important, but additional precision is required for the connection of the linkage mechanism and gearbox system.

Figure D.4, delineates the connections of the remaining components. Images D.4A to D.4C, depict various views of the connections of the model to its base and the fixations needed to secure them together. And images D.4D to D.4F, shows various views of the connections for the gearbox support board and the rotary actuation components installed in this mechanical device. As seen from the images the motor is slotted into the top holes of both support boards whilst the gears and pins are secured to the support boards via pin ends. The alignment of the teeth for the three gears exploited has been shown in the main contents of this thesis. These connection diagrams disclose how the gearbox is assembled and all the parts required except for a power source as the mains power was utilised in these experiments. Thus, Figures D.2 to D.4 present the complete assembly of the FWMAV model utilised in the experimental work of this project. As explained previously, the model is composed of various materials and components which all have specific roles to perform in order for the mechanical model to operate successfully. In future, specific components can be downsized in order to develop a much smaller and lighter FWMAV and test its flight ability under tethered conditions with a string or supported via a vertical guide stand.

Figures D.5 to D.10, consist of photographs of the actual model without the gearbox system to solely view the backboard and mechanical linkage system in various views. The linkages were painted with white strips in order to track its movement accurately when comparing the physical mechanical system and the CAD assembly model. Additional images also present the base of the model and the aluminium component acting as an adaptor to connect the model to the sensor. From the image taken above the model, the layout of the backboards, linkage mechanism and pins can be seen clearly, along with the screws and nuts exploited to maintain consistent spacings.

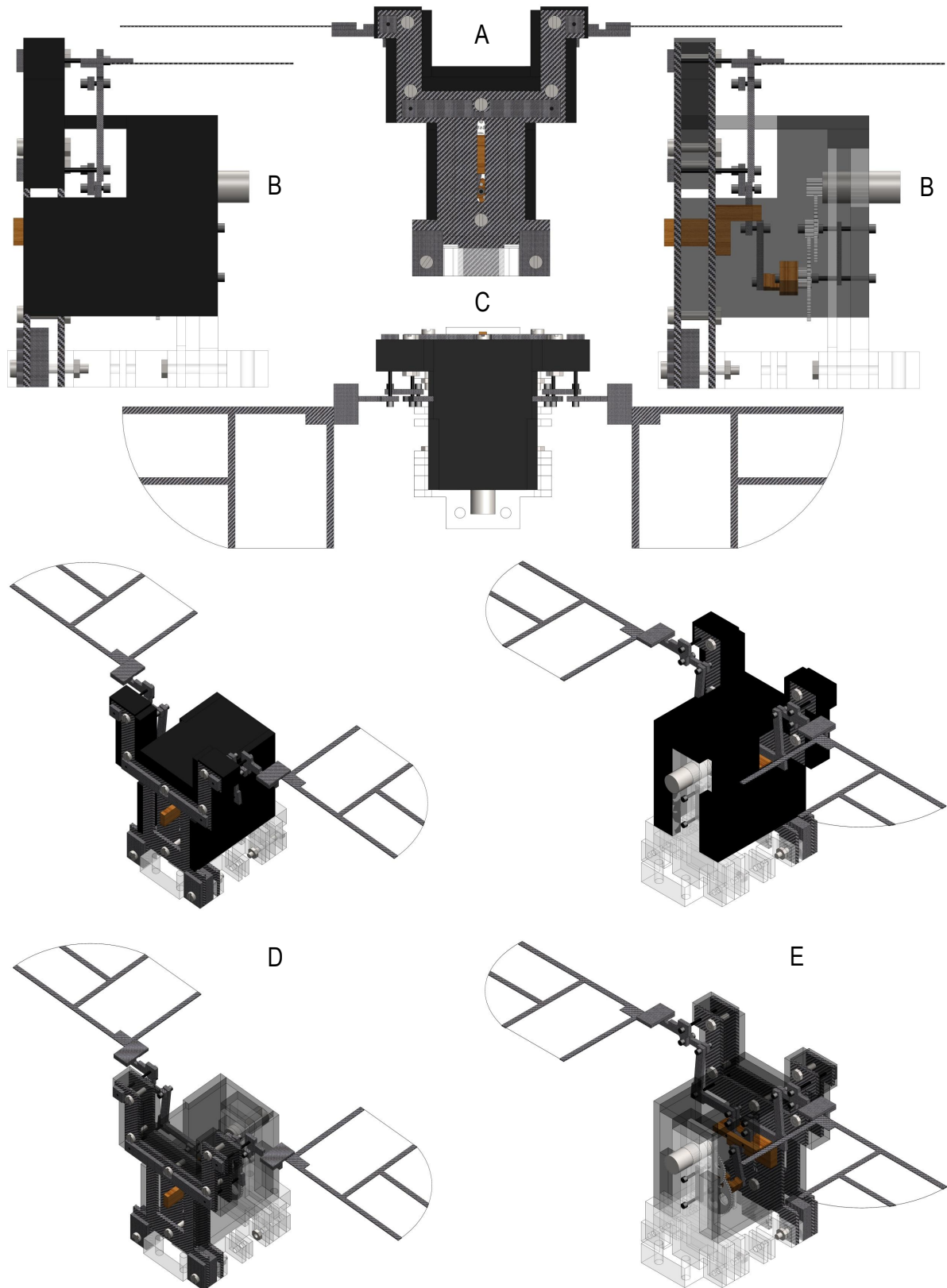


Figure D.1: *Model 1 with Body and 60 mm Wings (WT4) in Flapping Arrangement; A: Front View, B: Side View (Opaque and Transparent), C: Top View, D: Front Isometric View (Opaque and Transparent), E: Back Isometric View (Opaque and Transparent)*

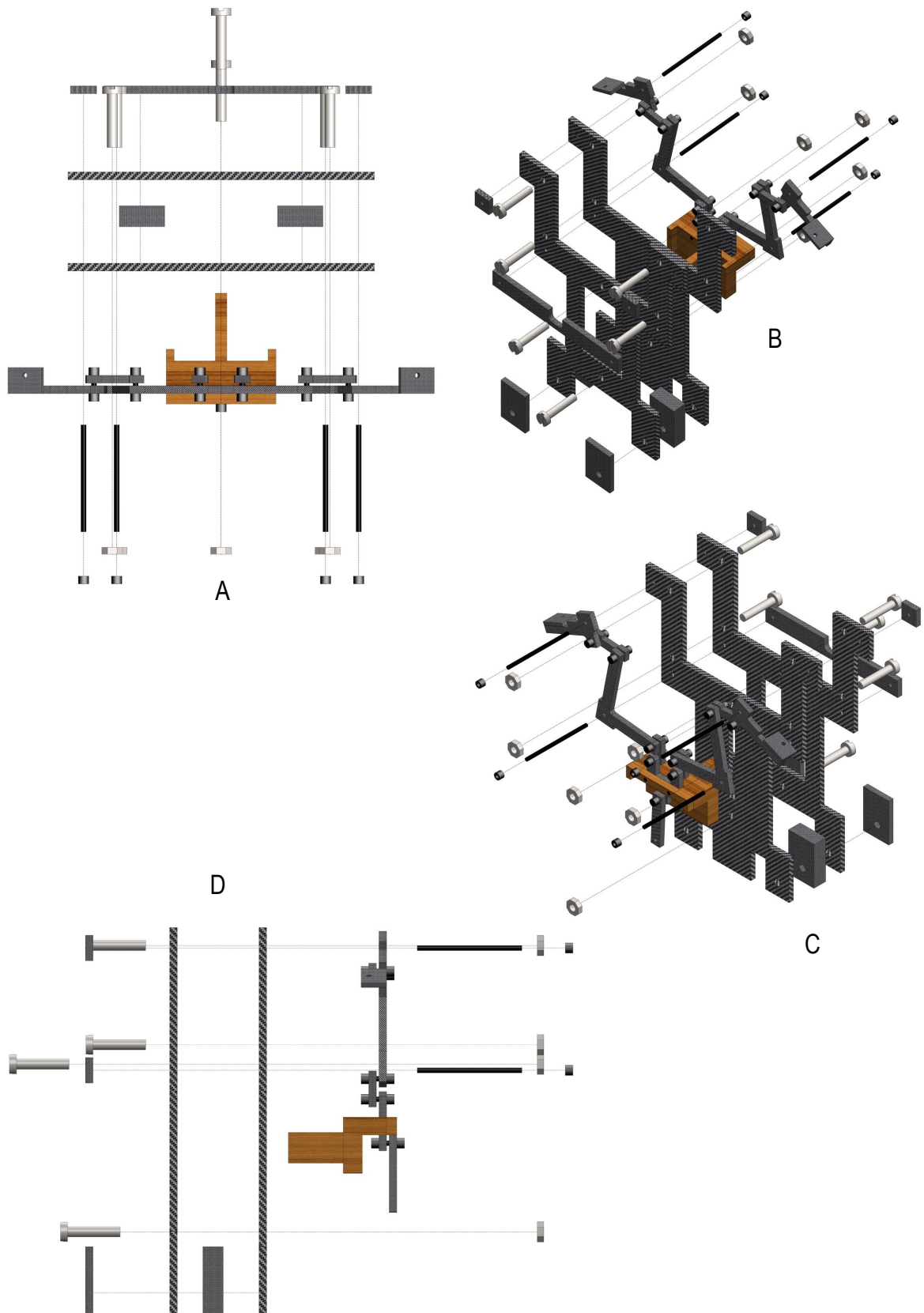


Figure D.2: *Model 1 Support Board and Linkage Mechanism with Connection Lines; A: Top View, B: Front Isometric View, C: Back Isometric View, D: Side View*

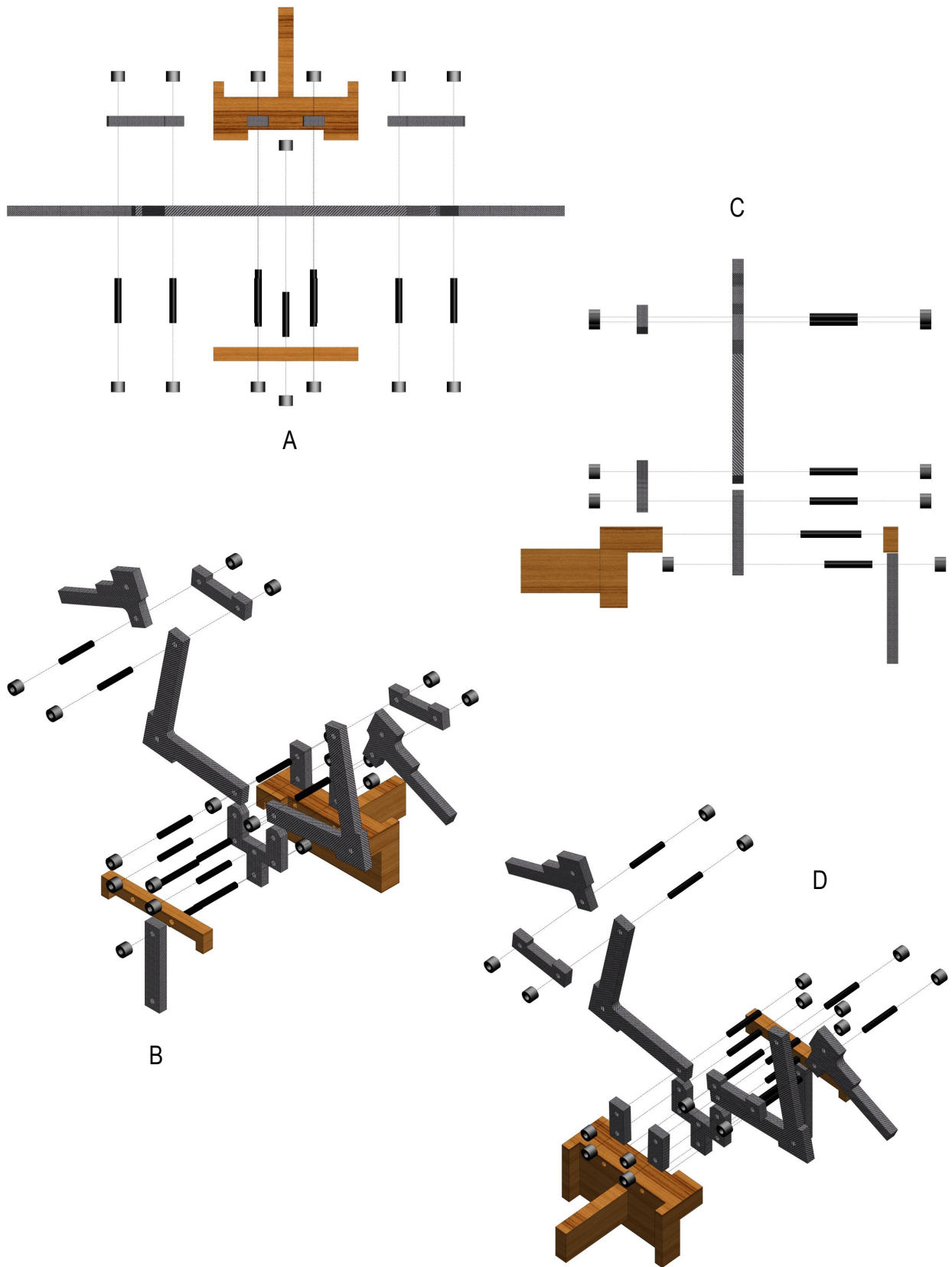


Figure D.3: *Model 1 Complete Linkage Mechanism with Connection Lines; A: Top View, B: Back Isometric View, C: Side View, D: Front Isometric View*

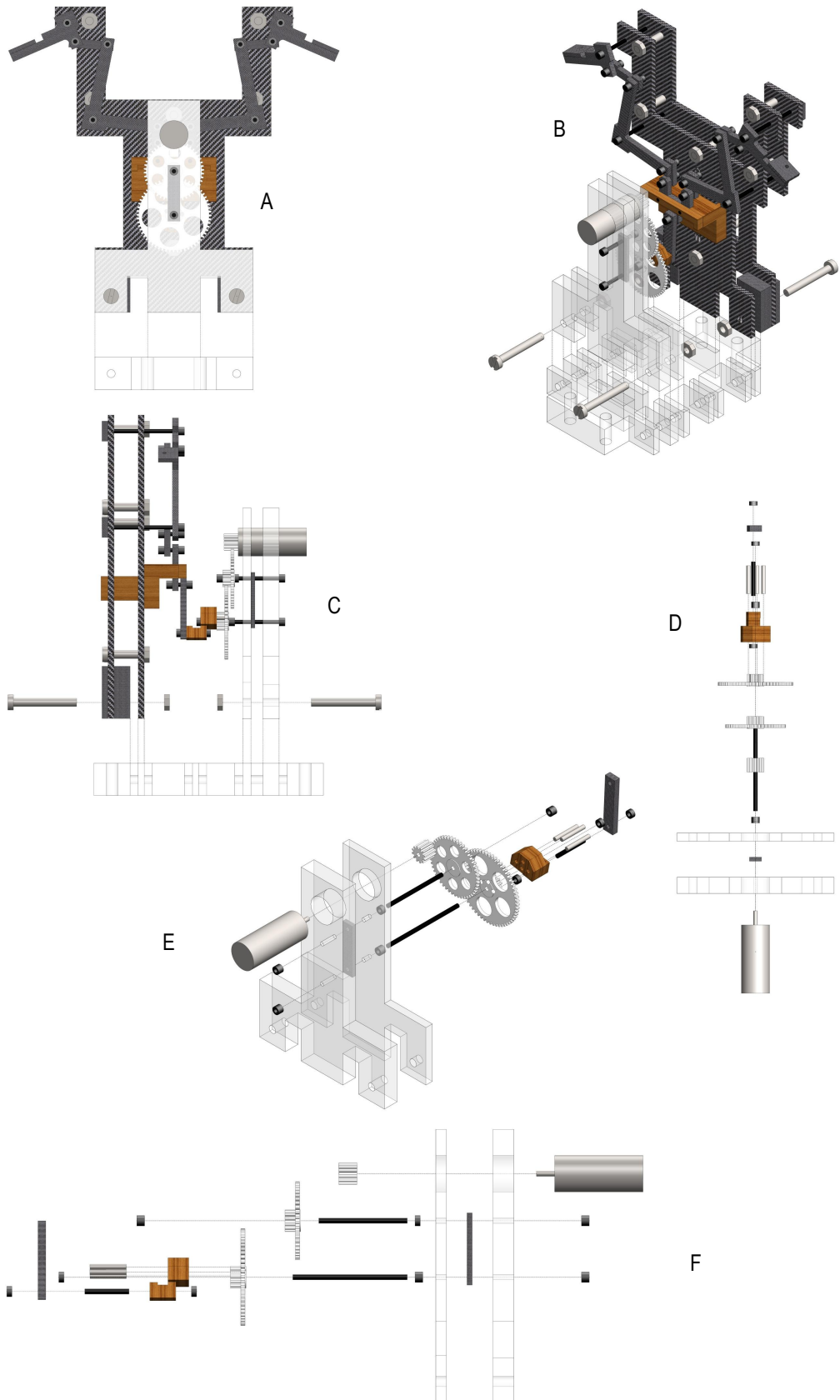


Figure D.4: Model 1 Base and Gearbox with Connection Lines; A: Back View, B: Back Isometric View, C: Side View, D: Top View, E: Back Isometric View, F: Side View

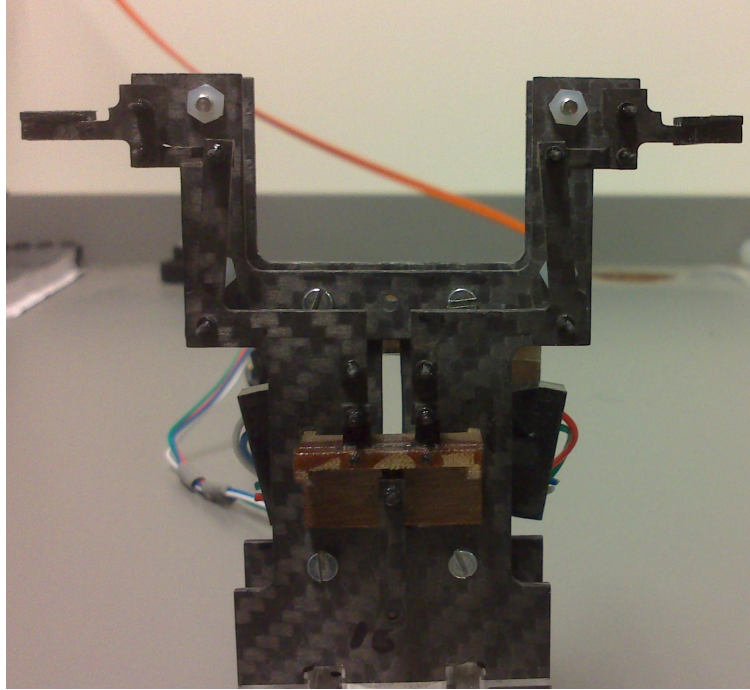


Figure D.5: *Photograph of Model 2 Backboard and Linkage Mechanism*

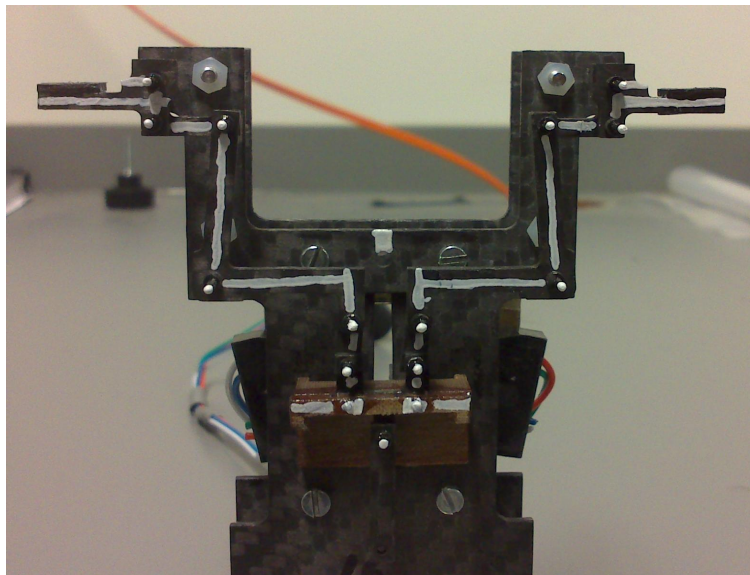


Figure D.6: *Photograph of Model 2 Linkage Mechanism with White Lines for Measurements*

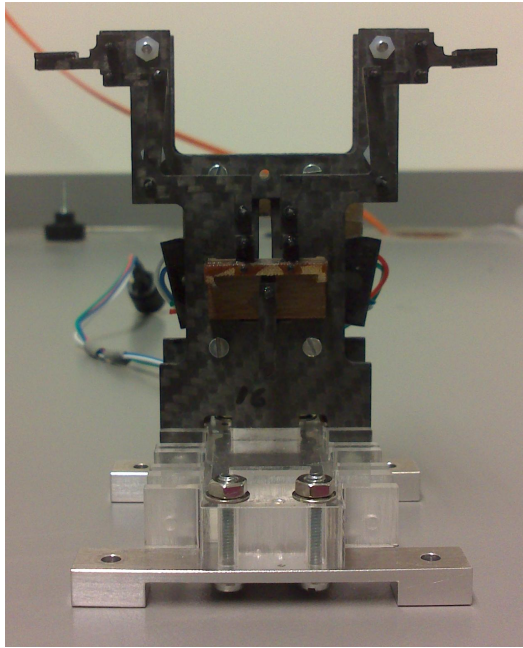


Figure D.7: *Photograph of Model 2 Linkage Mechanism and Base*

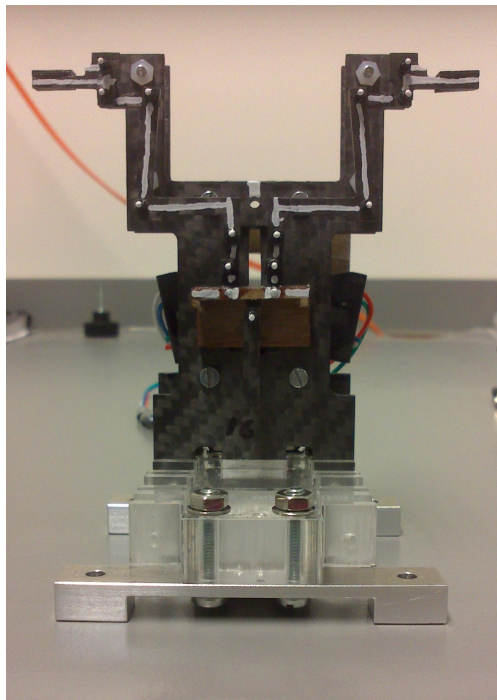


Figure D.8: *Photograph of Model 2 Linkage Mechanism Marked and Base*

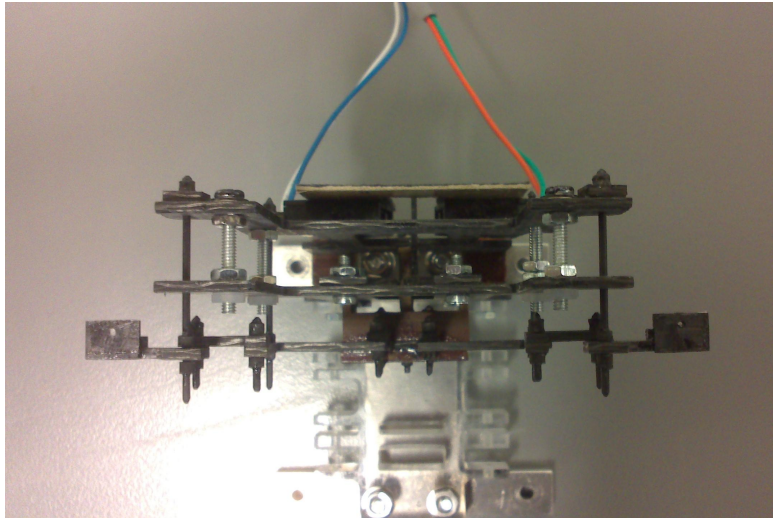


Figure D.9: *Photograph of Model 2 Top View*

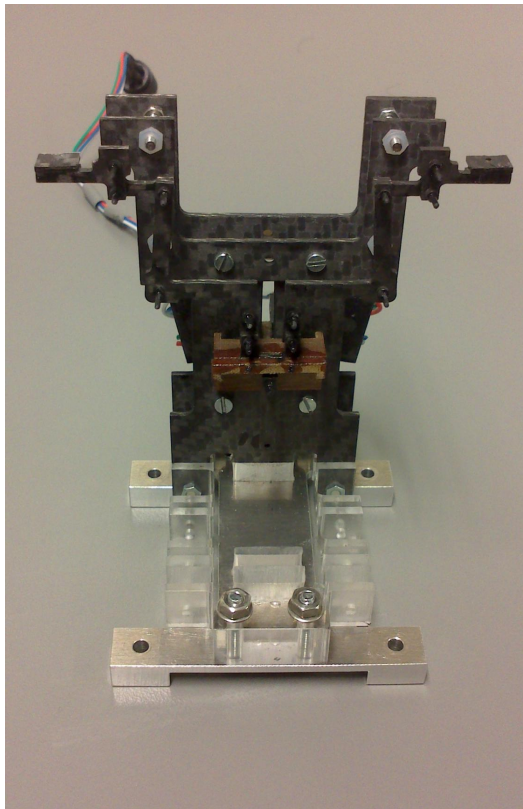


Figure D.10: *Photograph of Model 2 Linkage Mechanism and Base*